Geochemical investigation of the fluid records and recycling of a Palaeoarchean silicified seafloor in the Barberton granitoid-greenstone terrain (3.5-3.2 Ga, South Africa)

Lungele Steve Kitoga

To cite this version:

Lungele Steve Kitoga. Geochemical investigation of the fluid records and recycling of a Palaeoarchean silicified seafloor in the Barberton granitoid-greenstone terrain (3.5-3.2 Ga, South Africa). Geochemistry. Université Clermont Auvergne; Universiteit Stellenbosch (Afrique du Sud), 2024. English. NNT : 2024UCFA0069 . tel-05430793

HAL Id: tel-05430793
https://theses.hal.science/tel-05430793v1

Submitted on 24 Dec 2025

UNIVERSITE CLERMONT AUVERGNE
Collège des Ecoles Doctorales
Ecole Doctorale des Sciences Fondamentales

STELLENBOSCH UNIVERSITY
Faculty of Sciences
Department of Earth Sciences

DOCTORAL THESIS

Field: Structure and Evolution of the Earth and of other Planets.

Presented and defended publicly on 24 September 2024 by
Lungele Steve KITOGA

Geochemical investigation of the fluid records and recycling of a Palaeoarchean silicified seafloor in the Barberton granitoid-greenstone terrain (3.5-3.2 Ga, South Africa).

Directors: Professors Jean-Francois Moyen, Gary Stevens and Johanna Marin-Carbonne

Jury members:

Marc Chaussidon, DR CNRS	IPGP, Paris Cité University	President
Luc André, Professor	Royal Museum of Central Africa	Reporter
Axel Hofmann, Professor	University of Johannesbug	Reporter
Marion Garcon, CR CNRS	Clermont Auvergne University	Examiner
Nadja Drabon, Assistant Professor	Harvard University	Examiner
Maud Boyet, DR CNRS	Clermont Auvergne University	Invited
Jean-Francois Moyen, Professor	Université Jean Monnet Clermont Auvergne University	Director
Gary Stevens, Professor	Stellenbosch University	Director
Johanna Marin-Carbonne, As. Professor	University of Lausanne	Director

A tous ceux qui m'ont prêté un peu de leur temps pour poursuivre ce rêve

A mon père *Laurent Lungele*

A ma mère *Jeanne Ilunga*

A ma moitié *Francine Rhulole*

A tous les miens.

CONTENT OF THE THESIS

THESIS ABSTRACT

Silica-rich rocks generated on the palaeoarchean seafloor could preserve crucial information about the composition and temperature of the hydrothermal fluids and seawater that existed on the early Earth. Furthermore, isotopic studies have identified the recycling of these rocks into the source zone of tonalite-trondhjemite-granodiorites (TTG) constituting the core of early continents. Conducted in the Barberton granitoid-greenstone terrain (3.5–3.1 Ga, South Africa), this study focuses on silica-rich rocks to constrain palaeoarchean fluid compositions and recycling processes.

Firstly, petrographic, geochemical and thermometric data allow discussing the elemental composition and temperature of the paleoarchean hydrothermal fluids that generated the silicified lavas and cherts occurring in the Onverwacht Group. The acquired data allow distinguishing petrographic and geochemical effects of regional metamorphism and meteoric fluid circulations from those of the silicifying hydrothermal fluids. Collectively, the studied rocks are found to have undergone regional metamorphism that re-equilibrated their mineralogical assemblages without affecting significantly their bulk-rock elemental composition. Late-stage circulations of oxidised weathering fluids testified by Ce anomalies modified also the composition of a few samples. Based on compositional features that were not considerably modified by late-stage processes, the silicifying hydrothermal fluids are argued to have been free of positive Eu anomaly unlike most high-temperature hydrothermal fluids, and to have featured a relatively low temperature (>150 °C).

Secondly, the O and Si isotope compositions of the silicifying hydrothermal fluids and palaoeoarchean seawater are discussed using the isotopic composition of pervasively silicified lavas and sediments. Similarity of δ^{30}Si values in silicified lavas and sediments and in seawater-precipitated cherts is interpreted to show that the palaeoarchean hydrothermal fluids and seawater might have been undistinguishable in terms of Si isotope composition. Besides, the O isotope composition of silicified clastic sediments and lavas is different from that of seawater-precipitated cherts, reflecting lower δ^{18}O values for the silicifying hydrothermal fluids compared to modern analogues. While the O isotope composition of hydrothermal fluids points to a low-δ^{18}O palaeoarchean seawater, post-depositional modification of seawater-precipitated cherts due to interaction with hydrothermal fluids near the seafloor is shown to preclude a straightforward determination of seawater properties by studying these cherts.

Thirdly, the O and Si isotopic compositions of silicified lavas and cherts from the Onverwacht Group are used to improve our understanding of geodynamic processes that recycled similar rocks towards the source zone of TTGs. A correlation between the variations of δ^{18}O values over time in TTGs and in the silica-rich rocks demonstrates that a younger seafloor was progressively added to the TTG source zones in the Barberton. The variation of δ^{18}O values in the silica-rich rocks is considered as an effect of lithospheric cooling. A mass balance calculation constrains the possible O and Si isotope composition of the reworked silica-rich rocks, and stratigraphic units matching the calculated isotopic values are identified in the Onverwacht Group. Our calculation suggests that seafloor-derived silica-rich rocks represented 5–12 vol.% of the TTG source zones. The possible burial depth estimated for these silicified lavas fits best with their recycling due to sporadic subduction events that operated already before 3.45 Ga ago.

Overall, this thesis supports that seawater-crust interactions influenced the generation of the earliest felsic continents.

Keywords: Hydrothermal fluids, seafloor, seawater, silicification, Recycling, TTG magma

RESUME DE LA THESE

Titre : « Étude géochimique des enregistrements de fluides et du recyclage du plancher océanique silicifié dans les roches paléoarchéennes de la région de Barberton (3.5-3.2 Ga, Afrique du Sud). »

Les roches riches en silice formées sur le plancher océanique paléoarchéen conservent des informations cruciales sur la composition et la température des fluides hydrothermaux et des océans sur la Terre primitive. En outre, des études géochimiques ont mis évidence le recyclage de ces roches vers la zone source des tonalite-trondhjemite-granodiorite (TTG) constituant le noyau des premiers continents. Focalisée sur la ceinture de Barberton (3,5−3,1 Ga, Afrique du Sud), cette étude porte sur la composition des roches riches en silice afin de contraindre les compositions des fluides et les processus géodynamiques Paléoarchéens.

Premièrement, des données pétrographiques, géochimiques et thermométriques permettent de d'étudier la composition élémentaire et la température des fluides hydrothermaux génératrices des laves silicifiés et cherts du groupe d'Onverwacht. Grace à ces données, des témoins du métamorphisme régional et des circulations de fluides météoritiques sont différenciés de ceux des fluides hydrothermaux. Toutes les roches étudiées ont subi un métamorphisme régional qui a rééquilibré leurs assemblages minéralogiques sans affecter significativement la composition élémentaire des roches totales. Des circulations tardives de fluides météoritiques oxydés, attestées par des anomalies en Ce, ont également modifié la composition de certains échantillons. Toutefois, des critères compositionnels indifférentes des processus tardifs permettent de montrer que les fluides hydrothermaux du fond marin ne présentaient pas d'anomalie positive en Eu et avaient une température relativement basse (<150 °C).

Deuxièmement, les compositions isotopiques en O et Si des fluides hydrothermaux et de l'eau de mer Paléo-archéens sont discutées grâce aux compositions des laves et sédiments silicifiés. La similitude des valeurs de δ^{30}Si des laves et sédiments silicifiés avec celles des cherts précipités de l'eau de mer suggère que les fluides hydrothermaux et l'eau de mer paléoarchéens auraient eu des valeurs de δ^{30}Si similaires. En outre, la composition isotopique des sédiments clastiques et des laves silicifiés est différente de celle des cherts précipités de l'eau de mer et reflète des valeurs de δ^{18}O des fluides hydrothermaux paléoarcheennes plus faibles que celles des fluides modernes. Alors que le δ^{18}O des fluides hydrothermaux indique une eau de mer paléoarchéenne à δ^{18}O négatif, l'interaction des cherts avec ces fluides hydrothermaux sur le fond marin aurait considérablement modifié leur composition isotopique de l'O, ce qui questionne les reconstructions d'eau de mer qui en ont découlé.

Troisièmement, les compositions isotopiques en O et Si des laves silicifiées et des cherts du groupe d'Onverwacht sont utilisées pour améliorer notre compréhension des processus géodynamiques qui ont recyclé des roches similaires vers la zone source des TTGs de Barberton. La corrélation entre les variations des valeurs de $\delta^{18}O$ dans les TTG et dans les roches riches en silice au fil du temps montre qu'un plancher océanique de plus en plus jeune qui a passé moins de 200 Ma au fond de l'océan a été recyclé dans la zone sources des TTGs. L'évolution temporelle du $\delta^{18}O$ des roches riches en silice est considérée comme un effet d'un refroidissement lithosphérique progressif. Un calcul de bilan de masse contraint la composition isotopique possible de l'O et du Si des roches riches recyclées, repérant des unités stratigraphiques qui ont les valeurs isotopiques calculées dans le groupe d'Onverwacht. Ce calcul suggère que les roches riches en silice du plancher océanique représentaient 5−12 vol.% des zones sources du TTG. La profondeur d'enfouissement estimée pour ces roches du plancher océanique suggère que leur recyclage serait dû à des événements de subduction sporadiques.

Globalement, cette thèse soutient que les interactions entre l'eau de mer et la croute ont influencé la formation des premiers continents.

Mots-clés : Fluides hydrothermaux, plancher océanique, eau de mer, silicification, recyclage, magma TTG

ACKNOWLEDGMENTS

Firstly, Professors *Jean-Francois Moyen*, *Gary Stevens*, *Johanna Marin-Carbonne* and *Maud Boyet* are gratefully thanked for having accepted me as a candidate for this study. Their patience, support and pedagogy while transmitting to me the art of conducting geochemical research over the last three years is sincerely acknowledged. I was impressed by your speed to proofread my drafts which positively influenced the completion of this work almost within the agreed three years. I also thank you for the freedom you granted me to explore new directions in this project. Our relationship was complex, and I am certain that you have strongly influenced my growth as a human and a scientist. I must also thank *Jeff* and *Myriam* for having introduced me to the Eglise Protestante Unie de Clermont-Ferrand that has positively influenced our stay.

Secondly, I sincerely thank Professors *Marc Chaussidon*, *Axel Hofmann*, *Luc André*, *Nadja Drabon* and Dr. *Marion Garcon* who accepted to evaluate this work despite their numerous occupations.

Prof. *Erwan Thébault*, Prof. *Regis Doucelance* and Prof. *Vincent Bussigny* provided insightful remarks on this study during the follow up meeting a year ago. Dr. *David Zakharov* provided exciting collaboration on part of the research featured in this thesis. Prof. *Nicolas Olivier* provided continued support from the remote interview for the doctoral contract to in-person discussions on sedimentary samples. Dr. *Martin Guitreau* was always available for insightful discussions on the isotopic composition of the Barberton TTGs. Prof. *Andreas Pack* and Dr. *Thomasso Di Rocco* assisted with triple oxygen isotope analyses at the University of Gottingen in Germany. *George Olivier*, *Mareli Grobbelaar* and *Madeleine Frazenburg* provided technical assistance at Stellenbosch University. *Clara Gorce*, *Krzysztof Suchorski*, *Mathis Neimard*, *Mouhcine Gannoun*, *Delphine Auclair*, *Chantal Bosq* and *Federica Schiavi* provided technical assistance during the analytical work at Laboratoire Magmas et Volcans. *Anne-Sophie Bouvier* and *Thomas Bovay* helped with SIMS analyses at the University of Lausanne. I also thank *Audrey Chaza*l, *Angélique Chanut*, *Elia Sharmazanova* and *Emilie Habouzit* from Clermont Auvergne University as well as *Gillian Strydom* and *Dorothy Stevens* from Stellenbosch University who helped a lot with the administrative paperwork. Moreover, our field campaign in the Barberton terrain was facilitated by permission from SAPPI to access the land and the hospitality of Mountain View Estate. I must also thank Ms. *Maud Adam* from Campus France Bukavu who helped through the visa process.

I am really grateful towards my colleagues with whom I spent memorable times over the last years around a drink, dinner or simply in the office we shared in Stellenbosch or in Clermont-Ferrand. Particularly, *Marcel Vinicius* from Stellenbosch University, who shared my first steps into this journey, is thanked for having helped with driving in the Barberton Mountains, and *Tristan Engels* and *Syro Lacerda* from LMV (representative sample of all other colleagues) are thanked for their help when I needed assistance.

I also thank my previous Professors *Jacques Batumike, Charles Nzolang* and *Sebastian Tappe* who passionately told me about geochemistry during Bachelor and Master studies.

In addition, I sincerely thank my family and friends for all the support and for never complaining about my absence from home over the years. I really thank my brothers and sisters for the encouragement to pursue this journey, and I hope this achievement will be a source of motivation for *Henock* who is also willing to embrace a scientific journey and discover how life can be different abroad. I am particularly grateful for the regular and always mindful calls of our parents that made my wife and myself occasionally feel like we were still at home. Our friends from Clermont-Ferrand are also thanked for their support because life in Clermont would have been (negatively) different without their presence; sincere thanks to *Constantine* and *Samuel Bonnefoy* who helped welcoming Francine in Clermont.

Finally, my most emotional and devoted gratitude to my soulmate *Francine* who kept our oath valid even in the darkest moments of the last three years. Thank you for having stood by me when I somehow isolated from anything else: you are probably the reason why I succeeded to keep my mind out. I am convinced now that “For the best and the worst” has always been more than a simple slogan, and I will spend a lifetime respecting this principle of our engagement.

The Centre National de la Recherche Scientifique (CNRS) awarded the funding for my doctoral contract to my PhD supervisors and I am grateful for that. Further funding resulted from the BUCOMO project awarded to Jean-Francois Moyen and Gary Stevens by the CNRS in France and the National Research Foundation in South Africa, the STROMATA and ISOREE grants awarded by the European Research Council respectively to Johanna Marin-Carbonne and Maud Boyet. An additional AAP 20-25 grant received from the Collège des Ecoles Doctorales of Université Clermont Auvergne covered part of my different trips to Lausanne for analyses. I will be grateful forever to the BEBUC scholarship system that funded my bachelor and master studies, therefore importantly setting the stage for a successful doctoral journey.

REMERCIEMENT

Tout d'abord, les Professeurs *Jean-François Moyen*, *Gary Stevens*, *Johanna Marin-Carbonne* et *Maud Boyet* sont remerciés pour m'avoir pris pour ce projet de thèse. Leur patience, leur soutien et leur pédagogie lors de la transmission de l'art de la recherche géochimique au cours des trois dernières années sont sincèrement remerciés. J'ai été impressionné par la rapidité avec laquelle vous avez relu mes manuscripts, ce qui a influencé positivement l'achèvement de ce travail presque dans les trois ans convenus. Je vous remercie également pour la liberté que vous m'avez accordée d'explorer de nouvelles directions dans le cadre de ce projet. Notre relation a vraiment été complexe durant ces trois années, et vous aurez été incontournables dans la forge de ma personnalité d’humain et de chercheur.

Deuxièmement, je remercie sincèrement les Professeurs *Marc Chaussidon*, *Axel Hofmann*, *Luc André*, *Nadja Drabon* et Dr. *Marion Garcon* qui ont accepté d'évaluer ce travail malgré leurs nombreuses occupations.

Dr. *Erwan Thébault*, Prof. *Regis Doucelance* et Prof. *Vincent Bussigny* ont fait des remarques très constructives sur cette étude lors du comité de suivi de thèse de 2023. Dr. *David Zakharov* a collaboré avec beaucoup d’intérêt sur une partie de la recherche présentée dans cette thèse. Dr. *Nicolas Olivier* a apporté un soutien continu depuis l'entretien à distance pour le contrat doctoral jusqu'aux discussions en personne sur les échantillons sédimentaires. Dr. *Martin*

Guitreau a toujours été disponible pour répondre à mes questions sur la composition isotopique des TTG de Barberton. Prof. *Andreas Pack* et Dr. *Thomasso Di Rocco* ont aidé avec les analyses isotopiques triples de l’oxygène à l'université de Gottingen. *George Olivier*, *Marelli Grobbelaar* et *Madeleine Franzenburg* ont fourni une assistance technique à l'université de Stellenbosch. *Clara Gorce*, *Krzysztof Suchorski*, *Mathis Neimard*, *Mouhcine Gannoun*, *Delphine Auclair*, *Chantal Bosq* et *Federica Schiavi* ont fourni une assistance technique lors des travaux d'analyse au Laboratoire Magmas et Volcans. *Anne-Sophie Bouvier* et *Thomas Bovay* ont participé aux analyses SIMS à l'Université de Lausanne. Je remercie également *Audrey Chazal*, *Angélique Chanut*, *Elia Sharmazanova* et *Emilie Habouzit, Etienne Traverner* de l'Université Clermont Auvergne ainsi que *Gillian Strydom* et *Dorothy Stevens* de l'Université de Stellenbosch qui ont beaucoup aidé avec les procédures administratives et logistiques. De plus, notre campagne de terrain dans la région de Barberton a été facilitée par l'autorisation d’accéder aux zones forestières de la SAPPI et par l'hospitalité de Mountain View Estate. Je remercie également Mme *Maud Adam* de Campus France Bukavu qui m'a beaucoup aidé durant la procédure de demande de visa.

Je suis aussi reconnaissant envers mes collègues avec qui nous avons passé des moments mémorables autour d'un dîner ou dans le bureau partagé à Stellenbosch ou à Clermont-Ferrand. Je remercie tout particulièrement *Marcel Vinicius* de l'université de Stellenbosch, qui a partagé mes premiers pas dans ce voyage, pour m'avoir aidé à conduire dans les montagnes de Barberton. Je remercie également *Tristan Engels* et *Syro Lacerda* (pour représenter tous les autres) du LMV pour leur disponibilité à chaque fois que j'ai eu besoin d'aide.

Je remercie aussi mes anciens Professeurs Jacques Batumike, Charles Nzolang et *Sebastian Tappe* qui m'ont passionnément parlé de géochimie au niveau de la licence et du master.

Je ne peux oublier de remercier ma famille biologique et mes amis pour leur soutien et pour ne s’être jamais plaints de mon absence au fil des ans. Je remercie vraiment mes frères et sœurs de m'avoir encouragé à poursuivre cette aventure, et j'espère que cette fin sera une source de motivation pour *Henock*, qui souhaite lui aussi se lancer dans le domaine scientifique et découvrir à quel point la vie peut être différente à l’étranger. Je suis particulièrement reconnaissant à nos parents pour leurs appels réguliers qui nous ont permis, à ma femme et moi-même, de sentir comme si nous étions encore à la maison. Nos amis de Clermont-Ferrand sont également remerciés pour leur soutien, car la vie à Clermont aurait été (négativement) différente sans leur présence ; sincères remerciement *Constantine* et *Samuel Bonnefoy* qui m’ont aidé à accueillir Francine à Clermont.

Enfin, ma gratitude la plus émue et dévouée revient à mon âme sœur *Francine* qui a maintenu notre serment valide même dans les moments les plus sombres de ces trois dernières années. Merci de m'avoir soutenu même lorsque j'avais l'impression de m'isoler de tout : c'est probablement grâce à toi que j'ai réussi à garder mes esprits. Je suis maintenant convaincu que "Pour le meilleur, et pour le pire" c’est bien plus qu'un simple slogan, et je passerai une vie (ou plus) à respecter cet engagement.

Le Centre National de la Recherche Scientifique (CNRS) a accordé le financement du contrat doctoral à mes directeurs de thèse. D'autres financements proviennent du projet BUCOMO attribué à Jean-François Moyen et Gary Stevens par le CNRS en France et la National

Research Foundation en Afrique du Sud, des bourses STROMATA et ISOREE accordées par le conseil européen de la recherche respectivement à Johanna Marin-Carbonne et Maud Boyet. Une bourse supplémentaire AAP 20-25 reçue du Collège des Ecoles Doctorales de l'Université Clermont Auvergne a couvert une partie de mes différents voyages à Lausanne pour les analyses. Enfin, je serai à jamais reconnaissante au système de bourses BEBUC qui a financé mes études de licence et de master, préparant ainsi le terrain pour mes études de doctorat.

LIST OF FIGURES

LIST OF TABLES

Part I.

General Introduction

1.1. Motivation and objectives

Earth is, so far, the only planet of the solar system that is inhabited by complex living species including humans. The origin of life represents an existential question that is still not answered despite its profound implications on the adaptability of the living to natural and anthropogenic changes in Earth's environment. The precise environment in which the primitive living cells evolved remains mostly unconstrained, justifying continued investigation of archean (4.0 – 2.5 Ga) geological terrains that are still accessible at the surface of the Earth. The primitive environment on Earth (see artist's impression in **Figure 1-1**) must have been tightly correlated with the evolution of surface temperature (Lowe and Byerly, 2020), the chemical composition of oceans (Kasting et al., 2006; Jaffrés et al., 2007; Albarede et al., 2020), the constitution of the atmosphere (Catling and Zahnle, 2020), the proportion of continental surface (Kamber, 2010; Bindeman et al., 2018) and the onset of plate tectonics (Cawood et al., 2018; Windley et al., 2021), which could collectively govern the emergence of life on Earth.

Figure 1-1. Artist's impression of the archean environment with volcanic eruptions, minor emergent terrains, a toxic atmosphere, seawater and a faint sun light (artist: Andrey Atuchin, https://theconversation.com).

Seawater must have particularly influenced the development of life because putative marine microfossils have been observed in archean marine sediments (Westall et al., 2001; Javaux and Marshall, 2005; Alleon and Summons, 2019). This importantly motivates the search for understanding the composition and the temperature of the archean seawater. Archean seawater was anoxic and therefore featured some unique compositional properties such as a higher amount of dissolved iron compared to modern oceans. In addition, seawater has always reacted with the underlying crust to generate hydrothermal fluids that could have created favourable conditions for the proliferation of living cells on the archean seafloor (Furnes et al., 2004; Hofmann and Harris, 2008). Together with the input of continental erosion, the discharge of hydrothermal fluids represents an important supplier of major and trace element contents to the seawater reservoir. Therefore, different contributions of hydrothermal fluids and continental erosion in the past could generate compositional differences between archean and modern oceans (Kamber, 2010; Bindeman et al., 2018; Albarede et al., 2020), although the precise composition of the archean seawater and hydrothermal fluids is still to be determined.

Silica-rich rocks (cherts and related rocks) that are common in archean geological terrains could reveal the properties of contemporaneous hydrothermal fluids and seawater (Sugitani et al., 1996; Robert and Chaussidon, 2006; Hofmann and Wilson, 2007; Brengman and Fedo, 2018; Byerly et al., 2019; André et al., 2022). These rocks formed on the archean seafloor and are quite complex petrologically. They include pure chemical precipitates derived from seawater on one side, and lavas and sediments that were intensely silicified by interacting with hydrothermal fluids on the other side (**Figure 1-2**) (Paris et al., 1985; André et al., 2022). Seawater-precipitated cherts could allow constraining the composition and the temperature of the archean seawater (Clayton et al., 1972; Robert and Chaussidon 2006; Sharp et al., 2016), whereas silicified clastic sediments (or secondary cherts) and lavas could disclose the geochemical composition and temperature of archean hydrothermal fluids (Hofmann and Harris, 2008; Abraham et al., 2011). However, these different silica-rich rock types can be difficult to distinguish petrographically because seawater-precipitated cherts are commonly associated with hydrothermally silicified fine-grained clastic sediments. This could complicate the reconstruction of archean seawater composition and temperature in two different ways. Firstly, samples considered as seawater proxies might not really represent pure seawater precipitates and this can lead to erroneous interpretations (Lowe et al., 2020). Secondly, pure seawater-precipitated cherts could have undergone post-depositional interactions with the silicifying hydrothermal fluids that could considerably modify their original composition (Zakharov et al., 2021). Several studies were aimed to reconstruct the temperature of archean oceans using the composition of cherts and, based on different assumptions on seawater composition, different temperatures (from ~0 to ~90 °C) have been proposed for archean oceans (Knauth and Lowe, 1978; Kasting et al., 2006; Jaffrés et al., 2007; Robert and Chaussidon 2006; Lowe and Byerly, 2020). In most cases, the assumptions on seawater composition are not verified, resulting in vigorous debates about the actual temperature of archean oceans.

Additionally, only a few studies were interested in the geochemistry of silicified lavas and clastic sediments (Hofmann and Harris, 2008; Abraham et al., 2011; Brengman et al., 2016; Brengman and Fedo, 2018) such that the temperature of hydrothermal fluids and its potential effect on the composition of seawater-precipitated cherts still requires in-depth investigation. In a well-preserved geological context, a study of seawater-precipitated cherts and hydrothermally silicified lavas and sediments collectively could allow evaluating the possible records of the archean seawater and hydrothermal fluid properties.

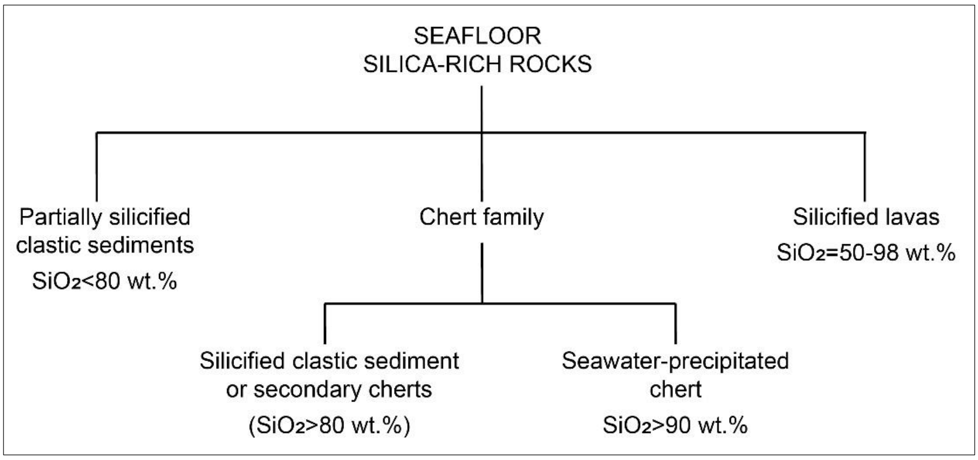

Figure 1-2. Classification of studied silica-rich rocks derived from the palaeoarchean seafloor of interest for this study

Geochemical signatures of silica-rich rocks derived from the archean seafloor were recently identified in tonalite-trondjhemite-granodiorite (TTG) bodies, the dominant constituents of continents on the early Earth (Trail et al., 2018; André et al., 2019; Deng et al., 2019). This evidence of seafloor recycling into the source zone of archean granitoids (TTGs) has provided a unique opportunity to investigate the geodynamic context in which the earliest continents were generated on Earth. Understanding the origin of the earliest continents is important for our continued study of primitive life because continental erosion supplied nutrients that favoured the proliferation of life in submerged continental platforms (Flament et al., 2008; Fralick and Riding, 2015). However, since more than five decades, the geodynamic mechanisms through which TTG melts were generated on the early Earth have been debated between models suggesting reworking in a subduction-like context (Martin, 1993; Sotiriou et al., 2023) and models proposing melting in intra- or infra-crustal setting far from subduction zones (Johnson et al., 2017; Bédard, 2018). Despite the recent geochemical evidence that seafloor-derived rocks were recycled towards TTG source zones, this geodynamic debate is still ongoing. In fact, explanations for the evidenced recycling have not yet succeeded to discriminate geodynamic transportation such as subduction (Deng et al., 2019; Roman and

Arndt, 2020) from what is named passive burial in this thesis (Hernández-Uribe, 2024). Therefore, the difficulty to distinguish recycling by transportation from recycling by burial is the next challenge that is still hindering the use TTG compositions for understanding the geodynamic setting in which specific TTG magmas were generated. We hypothesise here that analysing different TTG generations together with seafloor-derived rocks of known burial depth in a well characterised geological terrain could reveal the burial depth (or crustal position due to accumulation of younger lavas on the seafloor) of the seafloor-derived rocks that were reworked in the source zone of specific TTG melts. We will attempt using this new hypothesis to discriminate burial from transportation in a proposed model of seafloor recycling.

The fact that archean seafloor-derived rocks interacted with other fluids (e.g. metamorphic and weathering fluids) after their residence on the seafloor complicates the use of these rocks to constrain the composition of the archean seawater and hydrothermal fluids and to understand archean recycling processes (Weis and Wasserburg, 1987a; Lowe and Byerly, 2007b). Metamorphic and weathering fluids can substantially modify the mineralogical and geochemical composition of seafloor-derived rocks, precluding our ability to capture a clear signature related to the archean seawater or hydrothermal fluids (Knauth and Lowe, 2003; Lowe and Byerly, 2007b; Bonnand et al., 2020). Therefore, reconstructing the influence of late-stage metamorphic and weathering fluids on the composition of archean seafloor-derived rocks is necessary for using these rocks to constrain the properties of archean hydrothermal fluids and seawater, or to study archean recycling processes.

The present thesis investigates the fluid record and recycling processes of silicified lavas and cherts in the Barberton granitoid-greenstone terrain (South Africa) formed between 3.55 and 3.1 Ga ago. It firstly investigates the mineralogical and geochemical composition of the silicified lavas and cherts to characterise the properties of the palaeoarchean seawater and hydrothermal fluids after evaluating potential effects of metamorphic transformation and weathering. Then, considering the composition of silicified lavas and cherts, it reappraises the signature of seafloor recycling previously identified in the Barberton TTGs in order to determine the geological processes that were responsible for the recycling of seafloor-derived rocks toward the source zone of TTGs. The following four specific objectives are pursued in the thesis:

- Disentangling mineralogical and geochemical transformations acquired near the palaeoarchean seafloor from the effects of subsequent processes including regional metamorphism and weathering,

- Determining the geochemical properties (e.g. REE anomalies, O isotope composition, Si isotope composition and temperature) of the silicifying hydrothermal fluids,
- Evaluating the potential of cherts from the Barberton terrain to reconstruct the composition and temperature of the palaeoarchean seawater,
- Constraining the geological processes that transported seafloor-derived rocks towards the source zone of the Barberton TTGs.

1.2. Subdivision of the thesis

In addition to the present introductory part, the rest of the thesis is subdivided in five parts. **Part II** presents the relevant background information, including theoretical considerations and descriptions of the geochemical tools used in the thesis (e.g. elemental anomalies, stable O and Si isotopes and radiogenic Sm-Nd and La-Ce isotopes). It also provides a review on archean cratonic terrains and their geodynamic significance, and a review on archean silica-rich rocks and their record of ancient fluid properties. **Part III** corresponds to a paper that was under review at *Geochimica et Cosmochimica Acta* when this thesis was evaluated. It presents new petrographic and geochemical data for different sections of silicified lavas and cherts cropping out in the Barberton terrain. This part aims to disentangle the effects of hydrothermal silicification near the palaeoarchean (3.6 – 3.2 Ga) seafloor from those of subsequent metamorphic and weathering processes. It provides also some clues on the properties (e.g. temperature and chemical composition) of silicifying hydrothermal fluids. Subsequently, **Part IV** corresponds to a paper that was under revision upon submission of the thesis and now published in *Chemical Geology*. It uses O and Si isotopic compositions in silicified lavas and cherts (including silicified clastic sediments and seawater-precipitated cherts, **Figure 1-2**) to constrain the isotopic composition of hydrothermal fluids. This part discussed also the post-depositional modification of O isotope compositions in seawater-precipitated cherts and the potential causes for the evolution of O isotope composition over time in both the silica-rich rocks and the TTGs of the Barberton terrain. Then, **Part V** attempts to quantify the proportions and compositions of silica-rich rocks reworked in the source zone of the Barberton TTGs, to propose the potential crustal position of reworked rocks and discuss possible geodynamic implications. This part of the thesis is based on thermodynamic modelling and on a reappraisal of O and Si isotopic compositions in the Barberton TTGs. Finally, **Part VI** summarises the major results and perspectives arising from the entire work.

1.3. Brief description of the doctoral program

The thesis was realised in a “co-tutelle” program between Clermont Auvergne University in France and Stellenbosch University in South Africa where I spent respectively two years (July 2022 – October 2024) and one year (October 2021 – July 2022). In addition, several trips to Lausanne were made for analytical purpose and discussion with Prof. Johanna Marin-Carbonne.

Part II.

State of the Art

Part II. State of the Art

This part of the thesis presents background information on (1) theoretical and geochemical principles, (2) archean cratonic terrains and dynamics with an emphasis on the geology of the Barberton granitoid-greenstone terrain investigated in this work, and (3) archean seafloor-derived silica-rich rocks, their types, origin, fluid records and paleo-environmental significance.

2.1. Theoretical and geochemical principles

The present section starts with basic principles to facilitate the understanding of results and discussions embodied in the rest of the thesis. In a first place, principles of fluid-rock interactions that allow using the composition of altered rocks to reconstruct the properties (e.g. composition, temperature and redox state) of ancient fluids are introduced. Then, the properties of geochemical tools that have been used in this thesis, such as elemental anomalies and isotopic compositions, are described.

2.1.1. Fluid-rock interaction and fluid types

Crustal rocks coexist with varying amounts of aqueous fluids in different geological contexts (**Figure 2-1**). By interacting with these fluids, the rocks undergo mineralogical and geochemical transformation in pursuit of thermodynamic equilibrium, which generally remains out of reach in such open systems (Nabelek, 1987; Steefel et al., 2009). The three main types of fluids that commonly circulate in the crust are hydrothermal, metamorphic and meteoric fluids.

Hydrothermal fluids are restricted in this thesis to aqueous fluids that percolate from the seafloor to inner parts of the oceanic crust, where they interact with crustal rocks before ascending back to the seafloor. These fluids generally react with the crust all along the descending and ascending path (**Figure 2-1a**) (Elderfield et al., 1999; Zakharov et al., 2021). The circulation of hydrothermal fluids results from temperature gradients existing between the cold ocean and the hot inner parts of the oceanic crust. Due to thermal gradient, hydrothermal fluids interact with the submarine crust at varying depths and temperatures (Alt and Bach, 2006; Alt et al., 2010). Consequently, the altered oceanic crust contains low-temperature secondary minerals (e.g. clay) at shallow depth, and high-temperature phases (e.g. amphibole and epidote) at greater depth (> 800 m below seafloor) (Gillis and Robinson, 1990; Alt et al., 2010).

Metamorphic fluids (**Figure 2-1b**) are aqueous fluids interacting with crustal rocks during regional or contact metamorphic events (Crawford and Hollister, 1986; Newton, 1989). These fluids generally originate from dehydration reactions due to the mineralogical transformation of the rocks at higher pressure or temperatures. Such dehydration reactions are common during the metamorphic evolution of fluid-rich crustal rocks and are particularly ubiquitous in subduction zones due to the progressive transformation of altered lavas into amphibolites or eclogites. Although some studies consider transformations resulting from hydrothermal circulation of seawater-derived fluids in the crust as a form of metamorphism (e.g., Cloete, 1991; Shibuya et al., 2007), the choice to distinguish hydrothermal and metamorphic fluids in this study is justified because these distinct fluids operate in different types of geological contexts and at different times. In some cases, fossil hydrothermal pipes can clearly document the circulation of hydrothermal fluids in an ancient submarine crust, distinguishing them from a potential circulation of metamorphic fluids (de Wit and Furnes, 2016).

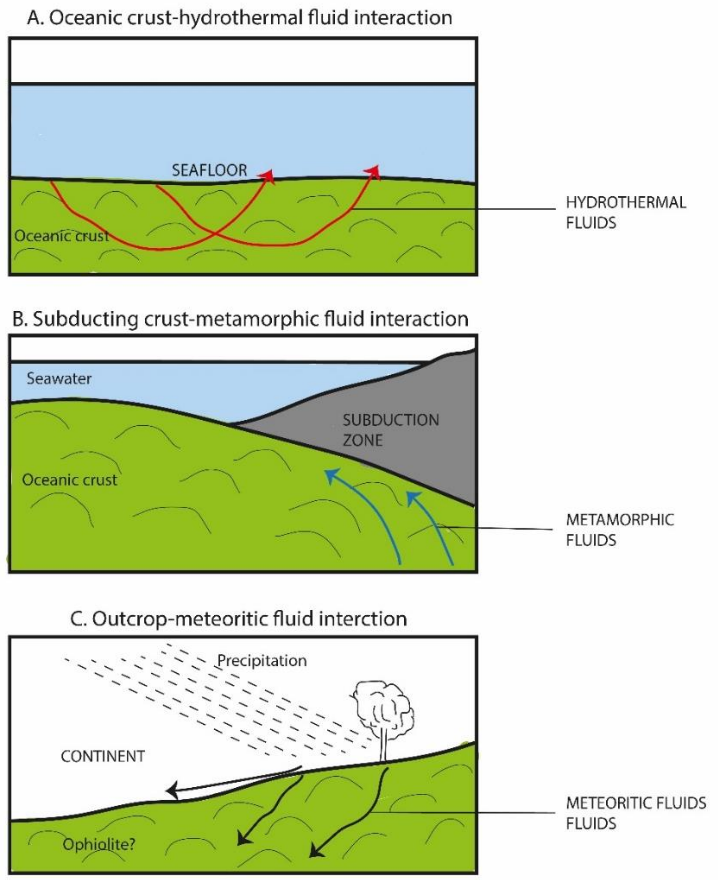

Figure 2-1. Cartoons illustrating the circulation of A) hydrothermal fluids, B) metamorphic fluids and C) meteoric fluids in crustal rocks. Cartoon A illustrates how hydrothermal fluids circulate from seawater into the crust and discharged back on the seafloor. Cartoon B shows metamorphic fluids originating from the deep crust where metamorphic transformation of hydrous minerals liberates aqueous fluids. Finally, cartoon C shows how meteoric fluids originating from precipitations in a continent interact with the rocks exposed near the surface.

Meteoric fluids (e.g. **Figure 2-1c**) are aqueous fluids associated with the hydrologic system of continents. Meteoric fluids are considered to include precipitation, runoff and continental aquifer water and are generally responsible for the alteration of exhumed continental rocks.

In addition to these three major types of fluids that alter the composition of crustal rocks, sedimentary rocks interact also with diagenetic fluids (Kolodny and Epstein, 1976; Yanchilina et al., 2020). These are pore fluids captured from the seawater column that evolve compositionally by dissolving chemical elements from the hosting sediments. Unlike the three major fluid types that can alter any crustal rock, diagenetic fluids are only restricted to interaction with sedimentary rocks and occurs shortly (i.e. up to a few tens of Ma) after their deposition.

Archean rocks commonly record multiple stages of fluid-rock interaction, with each stage involving a specific type of fluid. This constitutes a significant challenge for the investigation of individual fluid-related events (e.g. hydrothermal alteration) based on the mineralogy and geochemistry of ancient rocks (Weis and Wasserburg, 1987; Toulkeridis et al., 1998; Marty et al., 2018; Reimann et al., 2021; Zakharov et al., 2021). For example, in the theoretical case illustrated in **Figure 2-1**, mineralogical and geochemical transformations due to the late-stage metamorphic and weathering processes (i.e. **Figure 2-1B and C**) would obscure geochemical signatures inherited from hydrothermal fluids. This would complicate the use of outcropping rocks to reconstruct the properties (e.g., composition, temperature, redox state) of the hydrothermal fluids (**Figure 2-1A**).

2.1.2. Elemental anomalies and their use to determine fluid properties

During fluid-rock interactions, preferential mobilisation (i.e. addition or removal) of an element and dilution/enrichment of other elements due to such mobilisation constitute the two main processes that modify the concentration of an element in the rock and the fluid. These modifications generate abnormal elemental concentrations (anomalies) that can be identified by comparing the composition of altered rocks with that of fresh (or least-altered) rocks. Due to fluid-rock interactions, an element becomes anomalous in the altered rock if it is sequestrated from or released into the rock more efficiently than other elements. The concentration of an anomalous element in an altered rock therefore differs from its initial concentration in the fresh rock. A positive anomaly of an element in a rock or a fluid means that the considered rock or fluid gained more or lost less of this element than of other elements, and the opposite applies to define a negative anomaly. High field strength elements (HFSE) such as Zr and some heavy rare earth elements (HREE) are reputed to be relatively immobile during fluid-rock interactions, and therefore allow tracking the effect of dilution to identify truly mobilised elements.

To quantify elemental anomalies observed in altered rocks, we normalise the concentration of the considered element in the altered rocks to fresh rock concentration using the following simple **Equation 2-1** (e.g. Zhang and Smith-Duque, 2014):

$$X_N = \frac{X_{AR}}{X_{FR}} \quad \textbf{(Equation 2-1)}$$

where X_N is the fresh-rock normalised value for element X, X_{AR} is the concentration of X in the altered rock and X_{FR} is the concentration of X in the fresh rock. Theoretically, in absence of dilution, immobile elements should display a X_N of ~1 in altered rocks as their concentration remains constant, enriched elements should have a X_N that is higher than 1, and an X_N lower than 1 should occurs in depleted elements. In practice, however, dilution or concentration of some element due to the addition or removal of other elements can generate X_N values that are different from 1 even for elements that were not mobilised by fluid-rock interaction (Grant, 1986; Grant, 2005). Therefore, instead of a X_N ratio of 1, the actual X_N ratio of immobile elements can be used as a reference to identify elements gained or lost by altered rock. For REEs, instead of normalising their concentration to fresh rock composition, it is traditionally normalised to a reference reservoir such as the chondrite uniform reservoir (CHUR) (e.g. Anders and Grevesse, 1989). This facilitates the comparison of REE compositions in different terrestrial reservoirs.

Anomalous concentrations of elements in altered rocks can be associated with the properties of altering fluids. Three cases of such anomalies, namely alkali anomalies, Eu anomaly and Ce anomaly, are relevant here.

2.1.2.1. Positive alkali anomalies related to low-temperature (<150 °C) hydrothermal fluids

The alkali content (K, Rb and Cs) generally increases in rocks that interact with low-temperature hydrothermal fluids (<150 °C), but these elements are more easily scavenged from rocks that react with high-temperature hydrothermal fluids (Hart and Staudigel, 1982; Rouchon and Orberger, 2008). For instance, **Figure 2-2** show a pattern of fresh-rock normalised elements in altered lavas derived from the top 120 m of the modern oceanic crust (Zhang and Smith-Duque, 2014). In this figure, the positive anomalies in K, Rb, Cs and Ba are due to clay formation, replacing magmatic phases at temperature below 150°C.

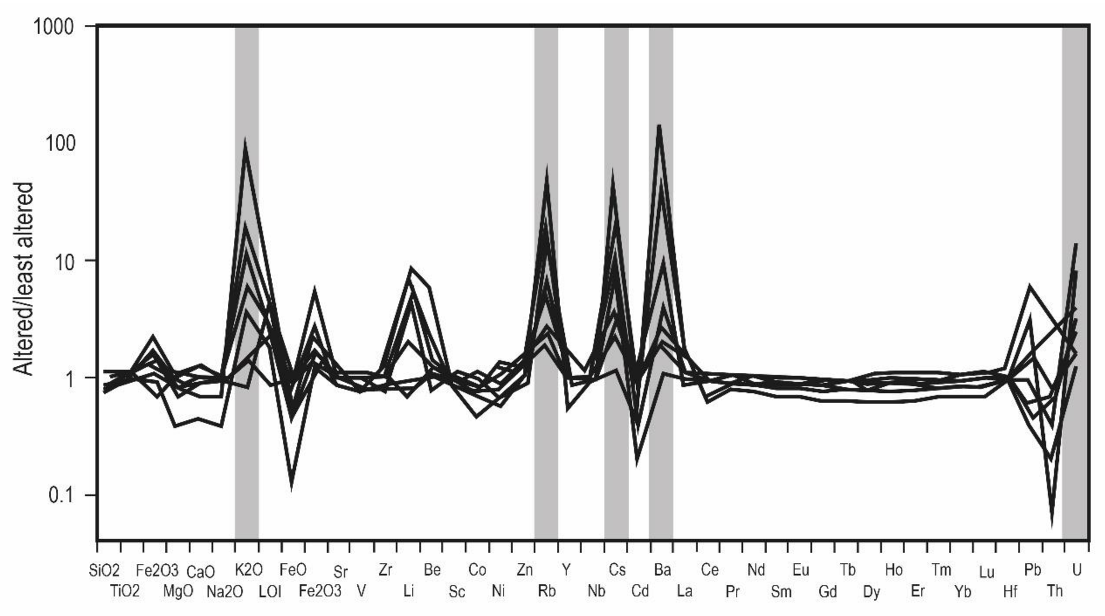

Figure 2-2. Fresh-rock normalised pattern of major and trace element concentrations in hydrothermally altered lavas derived from the top 120 m of the modern oceanic crust (modified after Zhang and Smith-Duque, 2014). The positive anomalies in K, Rb, Cs, Ba and U shown with grey fields are due to sequestration of alkali elements from low-temperature (<150 °C) hydrothermal fluids.

2.1.2.2. Eu anomaly reflecting high-temperature (>250 °C) hydrothermal fluids

Europium is systematically leached out of rocks that interact with hydrothermal fluids above 250 °C, but remains immobile when fluid-rock interaction operates at lower temperature (Gillis and Robinson, 1990; Bau, 1991; Mills and Elderfield, 1995). In fact, at temperature exceeding 250 °C, Eu shifts its valence from III+ to II+ in aqueous systems and becomes more soluble than other REEs. Therefore, hydrothermal fluids discharged at the modern seafloor as smokers feature positive Eu anomalies in chondrite-normalised REE pattern (**Figure 2-3**), indicating that these fluids result from interaction between seawater and the basaltic crust at temperature above 250 °C. **Equation 2-2** allows quantifying Eu anomaly (Lawrence et al., 2006):

$$\frac{\mathrm{Eu}}{\mathrm{Eu}^*} = \frac{\mathrm{Eu_{CN}}}{(\mathrm{Sm_{CN}})^{2/3} \times (\mathrm{Tb_{CN}})^{1/3}} \quad \textbf{(Equation 2-2)}$$

where Eu* is the theoretical abundance extrapolated from neighbouring REE concentrations (Sm and Gd) in chondrite-normalised REE patterns, and $\mathrm{Eu_{CN}}$, $\mathrm{Sm_{CN}}$, $\mathrm{Gd_{CN}}$ are measured concentrations of the respective elements normalised to the chondrite.

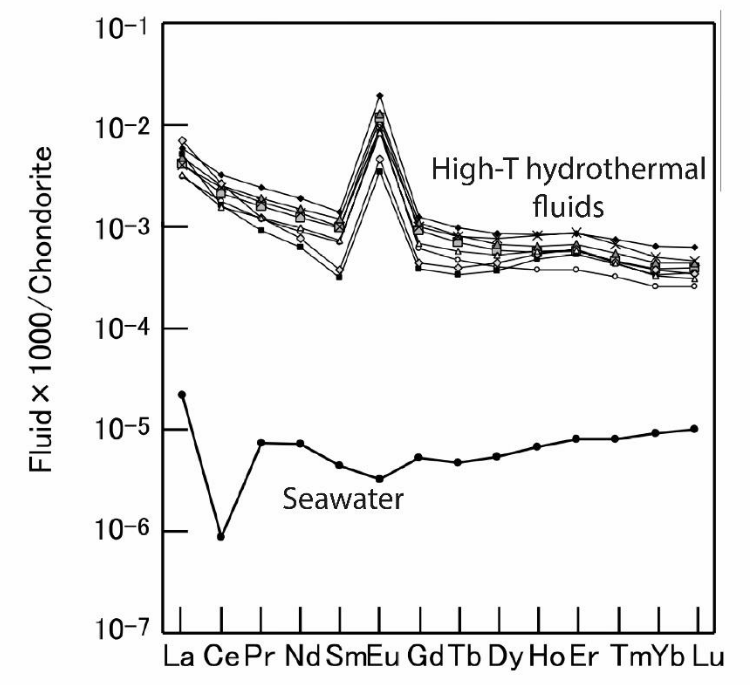

Figure 2-3. Rare earth patterns of modern high-temperature hydrothermal fluids and seawater (modified after Hongo et al., 2007). The positive Eu anomaly of hydrothermal fluids is ascribed to interaction with the basaltic crust at high-temperature (>250 °C). The negative Ce anomaly in modern seawater is due to the presence of Ce^{4+} under oxidized conditions. Under this IV+ valence, Ce is highly insoluble and therefore removed from seawater.

2.1.2.3. Ce anomaly as a characteristic of oxidised fluids

Cerium changes its valence from III+ to IV+ in oxidised environments and becomes less soluble than other REE. Therefore, Ce becomes less mobile than other light rare earth element (LREE). This change in the valence of cerium explains the negative Ce anomaly of modern oxidised oceans as Ce is preferentially retained in continents during their erosion and preferentially scavenged from oceans by the first chemical sediments precipitated (**Figure 2-3**) (Tanaka et al., 1990; Shimizu et al., 1991). When oxidised fluids interact with crustal rocks, cerium behaves differently from other REE and this process can produce Ce anomaly in altered rocks (Shimizu et al., 1991; Cotten et al., 1995; Bonnand et al., 2020). In fact, the oxidised fluids could add to the rocks or remove from them all the other REE except Ce. Therefore, Ce anomalies allows to track the contribution of oxidised fluids to altered rocks (Cotten et al., 1995). We use the **Equation 2-3** to quantify Ce anomaly:

$$\frac{Ce}{Ce^*} = \frac{Ce_{CN} \times Nd_{CN}}{(Pr_{CN})^2} \quad \textbf{(Equation 2-3)}$$

where Ce* is the theoretical values considering a perfect alignment of Ce with Pr and Nd.

2.1.3. Stable isotope geochemistry

2.1.3.1. Principles

Isotopes are different atoms displaying the same number of protons and electrons but different numbers of neutrons. Stable isotopes that do not decay into any other isotope (see reviews by Hoefs, 2009; Sharp, 2017) are differentiated from radioactive isotopes. The latter are unstable and decay spontaneously into less unstable isotopes called radiogenic, that can be themselves stable or radioactive. For light stable isotope systems, we generally use a delta (δ) notation (**Equation 2-4**) to quantify the isotopic abundance of a given substance:

$$\delta_{\mathrm{Sample}} = 1000 * \frac{\mathrm{R_{Sample}}}{\mathrm{R_{Standard}}} - 1000 \quad (\textbf{Equation 2-4})$$

In this equation, δ is expressed in permil (‰), R_{Sample} represents ratios of heavy over light isotopes in the analysed material and $R_{Standard}$ is the same ratio in a conventional international standard. A δ value above or below 0‰ means that the analysed material has a higher or lower proportion of heavy isotopes than the standard.

Because isotopes of the same element feature by definition different atomic masses, they exhibit slightly different thermodynamic properties, leading to isotopic fractionation between distinct substances (Hoefs, 2009; Sharp, 2017). Isotopic fractionation is the process through which distinct isotopic abundances appear between different substances. We distinguish two different types of stable isotope fractionation in nature: equilibrium and kinetic fractionations. Kinetic fractionations result from irreversible and unquantifiable reactions (e.g. metabolic reactions), while equilibrium fractionation is by definition due to reversible reactions that can be quantified or predicted. The extent of equilibrium fractionation is higher for light elements such as H, O and C because they have relatively high differences of mass. Equilibrium fractionation is negligible for heavy elements (e.g. REEs) because the relative difference of mass between different isotopes of these elements is not significant enough to generate notable isotopic fractionations. In equilibrium fractionation scenarios, heavier isotopes generally show a preference for substances where the considered element is linked to atoms with the strongest bounding energy (Sharp, 2017). Thus, for example, heavier isotopes would become more concentrated in solids than in aqueous fluids when these two different substances co-exist in an equilibrated system. In a specific system involving different substances, isotopic fractionation between these substances is generally higher at low temperature because an excess of free energy at high temperature minimises the effect of atomic mass on isotopic fractionation.

The fractionation of stable isotopes between two substances is most commonly expressed by the cap-delta (Δ) that generally depends on the temperature of equilibrium (Hoefs, 2009; Sharp, 2017). However, the Δ notation can also be used to express a deviation from natural correlation curve between two isotopic ratios of the same element (e.g. $\delta^{18}O$ vs. $\delta^{17}O$, see **sub-section 2.1.3.2.**). An effort will therefore be made to clearly distinguish these two different parameter despite the similar notation. The following formula (**Equation 2-5**) allows calculating Δ as an isotopic fractionation between two different substances:

$$\Delta = \delta_{\text{Substance A}} - \delta_{\text{Substance B}} \quad \textbf{(Equation 2-5)}$$

Oxygen and silicon isotopes are the main stable isotopes investigated in this thesis and are therefore described below with their respective applications.

2.1.3.2. Oxygen isotope geochemistry

Oxygen comprises three different isotopes with variable natural abundances: ^{16}O (99.8%), ^{17}O (0.038%) and ^{18}O (0.205%). We conventionally use an average seawater standard (Vienna Standard of Mean Ocean Water, VSMOW) to quantify the $\delta^{18}O$ and $\delta^{17}O$ values of natural material using **Equation 2-4** (Perry, 1967; Knauth and Lowe, 1978). Thus, modern seawater typically has a $\delta^{18}O$ and $\delta^{17}O$ of ~0 ‰ because it is equivalence in O isotope composition to the standard (Muehlenbachs, 1998; Luz and Barkan, 2010). Traditionally, only the $\delta^{18}O$ values of terrestrial substances (e.g. rocks and fluids) were analysed (e.g. Perry, 1967; Knauth and Lowe, 1978; Muehlenbachs, 1998). But, due to its limitation in solving some geological problems, coeval measurements of $\delta^{18}O$ and $\delta^{17}O$ were introduced as the “triple O” isotope tool (e.g. Luz and Barkan, 2010; Bao et al., 2016; Bindeman, 2021; Zakharov et al., 2021). The triple O isotope technique relies on the quantification of the $\Delta'^{17}O$ parameter that represents a deviation of samples from the alignment of terrestrial samples in the $\delta'^{18}O$ – $\delta'^{17}O$ space (**Figure 2-4**). The $\Delta'^{17}O$ and $\delta'^{18(17)}O$ parameters are given by **Equations 2-6** and **2-7**:

$$\Delta'^{17}O = \delta'^{18}O - 0.528 \times \delta'^{17}O \quad \textbf{(Equation 2-6)}$$

and

$$\delta'^{18(17)}O = 1000 \times \ln\left(\frac{\delta^{18(17)}O}{1000} + 1\right) \quad \textbf{(Equation 2-7)}$$

In this thesis, two major applications of O isotope compositions are relevant, namely the use of O isotope composition in cherts as a paleo-thermometer, and the use of O isotope fractionation in felsic magmas in the study of their source zone composition.

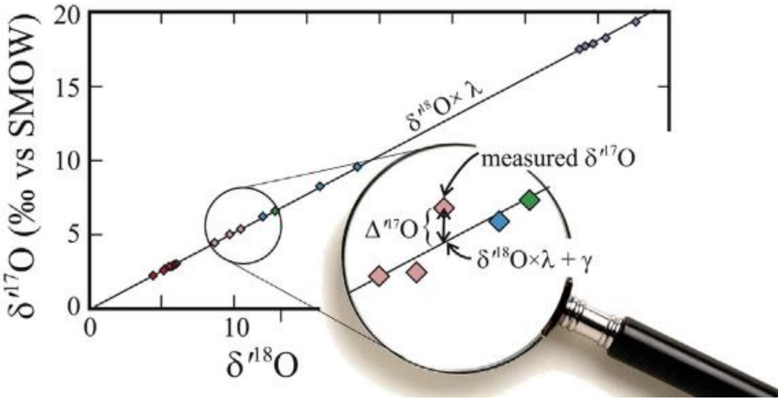

Figure 2-4. Graphical illustration of the Δ'^{17}O parameter (Sharp et al., 2016).

A. Oxygen isotope compositions of chert as a fluid paleo-thermometer

Three main thermometers of low-temperature fluid-related processes that operated near the past seafloor rely on the fractionation of oxygen isotopes between minerals and fluids. Firstly, the temperature of ancient seawater could be determined based on the δ^{18}O of cherts, using the following formula (**Equation 2-8**) obtained from modern cherts (Clayton et al., 1972; Knauth and Lowe, 1978):

$$\Delta^{18}O_{(qz-wt)} = \frac{3.09\times10^{6}}{T^{2}} - 3.29 \quad \textbf{(Equation 2-8)}$$

with T in Kelvin. The main issue with the application of this formula is that it involves the δ^{18}O of ancient seawater which is generally unknown and not necessarily equivalent to the modern one (Jaffrés et al., 2007; Bindeman, 2021). In addition, this application considers that cherts precipitated directly from seawater although their O isotope composition has been shown to evolve at diagenetic stage (Kolodny and Epstein, 1976; Yanchilina et al., 2020; Ibarra et al., 2022).

Secondly, the temperature of fluids could be determined from O isotope fractionation between quartz and carbonate (**Figure 2-5a**) that co-precipitated at equilibrium from the same fluids (**Equation 2-9**) (Sharp and Kirschner, 1994; Marin-Carbonne et al., 2011; Galili et al., 2019):

$$\Delta^{18}O_{(qz-cal)} = \frac{0.87(\pm0.06)\times10^{6}}{T^{2}} \quad \textbf{(Equation 2-9)}$$

Thirdly, the temperature of fluids can be reconstructed using the triple O isotope composition of precipitated silica. The determination of δ^{18}O and Δ'^{17}O could allow determining both the temperature and the δ^{18}O value of fluids, as illustrated in **Figure 2-5b**

(Sharp et al., 2016). These two different parameters can be theoretically obtained by solving the following system of equations (**Equations 2-10** to **2-12**):

$$\Delta^{18}O_{(qz-wt)} = \frac{4.28 \times 10^{6}}{T^{2}} - \frac{3.5}{T} \qquad \textbf{(Equation 2-10)}$$

$$\Delta'^{17}O_{(qz-wt)} = \left(\frac{4.28 \times 10^{6}}{T^{2}} - \frac{3.5}{T}\right) \times \left(0.5305 - \frac{1.85}{T} - 0.528\right) \qquad \textbf{(Equation 2-11)}$$

$$\Delta^{18}O_{(qz-wt)} = \Phi \times \Delta^{17}O_{(qz-wt)} \qquad \textbf{(Equation 2-12)}$$

In these equations, T is expressed in kelvin and Φ (see **Equation 2-12**) is comprised between 0.524 and 0.531 (Sharp et al., 2016). Note that the Δ symbol relates to isotopic fractionation between quartz and water in **Equations 2-8** to **2-12**, but to deviation from the curve defined by natural rocks in **Equation 2-6** and **Figure 2-4**, and this difference should be kept in mind.

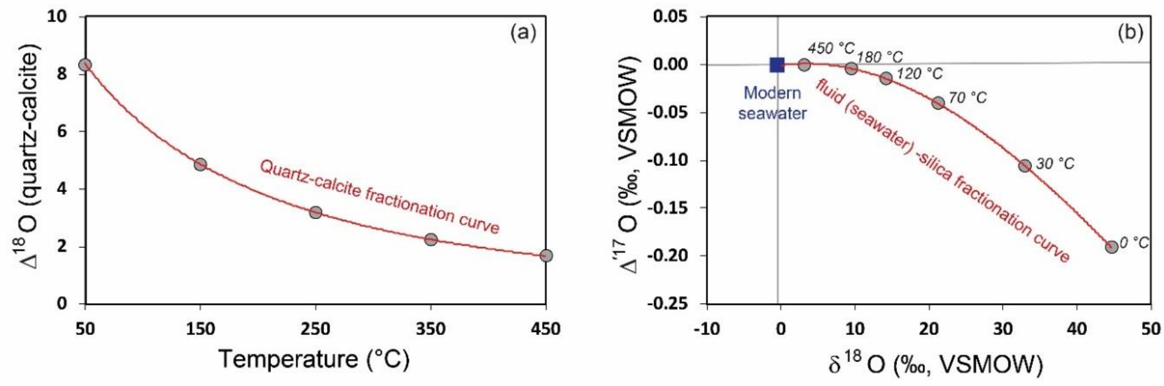

Figure 2-5. Temperature control on the fractionation of O isotopes in the quartz-water system. Plate (a) illustrates the relationship between $\Delta^{18}O_{qz\text{-}cal}$ and the temperature (Knauth and Lowe, 1978). Plate (b) shows the evolution of $\delta^{18}O$ and $\Delta'^{17}O$ in silica (or chert) precipitating from the modern seawater at different temperatures (Sharp et al., 2016).

The two thermometers respectively based on quartz-carbonate O isotope fractionation and triple O isotope measurement in quartz that are illustrated in **Figure 2-5** have the advantage of not requiring to know the O isotope composition of the fluids for which we need to determine the temperature. However, their application requires that analysed quartz and carbonates formed in equilibrium with the fluids and remained preserved from subsequent processes like metamorphism and weathering. A temperature of 70-150 °C has been obtained from the triple O isotope composition of archean cherts and was contrastingly interpreted to represent (1) the circulation of post-depositional fluids (e.g. hydrothermal or diagenetic fluids) (e.g. Sengupta et al., 2020; Zakharov et al., 2021) or (2) a hot archean seawater (Lowe et al., 2020). These two different interpretations are legitimate as, on one side, seawater-precipitated cherts capture the temperature and triple O isotope composition of the modern seawater (Sharp et al., 2016), and on the other side, the O isotope composition of modern cherts is known to evolve during their diagenetic maturation (Yanchilina et al., 2020; Ibarra et al., 2022). Concerning the quartz-carbonate thermometer (**Figure 2-5b**), it was only applied by one study in the Barberton greenstone belt, which obtained relatively high temperatures (> 200 °C) representing the circulation of metamorphic fluids (Marin-Carbonne et al., 2011). It is therefore important to understand the different stages of fluid-rock interaction undergone by a chert in order to determine fluid temperatures from its O isotope composition (Lowe et al., 2020).

B. Oxygen isotope fractionation in felsic magmatic systems

The measurement of oxygen isotope ratios in felsic rocks and their minerals (e.g. zircon) is useful for determining the $\delta^{18}O$ value of felsic magmas, which depends on the lithology of their source region. Two important advances in this field are noteworthy as they have improved our capacity to constrain the O isotope composition of rocks that constituted source zones of felsic magmas. Firstly, an important constrain on the fractionation of O isotopes between a mafic crust and felsic magmas that it generates by melting was provided by numerical calculations of Bindeman et al. (2005). These authors showed that felsic magmas are 0.5 to 1 ‰ higher in $\delta^{18}O$ than a mafic crust from which they originate because residual minerals after melting have a preference for lighter O isotopes (**Figure 2-6a**). This information is important for reconstructing the average O isotope composition of the source zone using the composition of a magma.

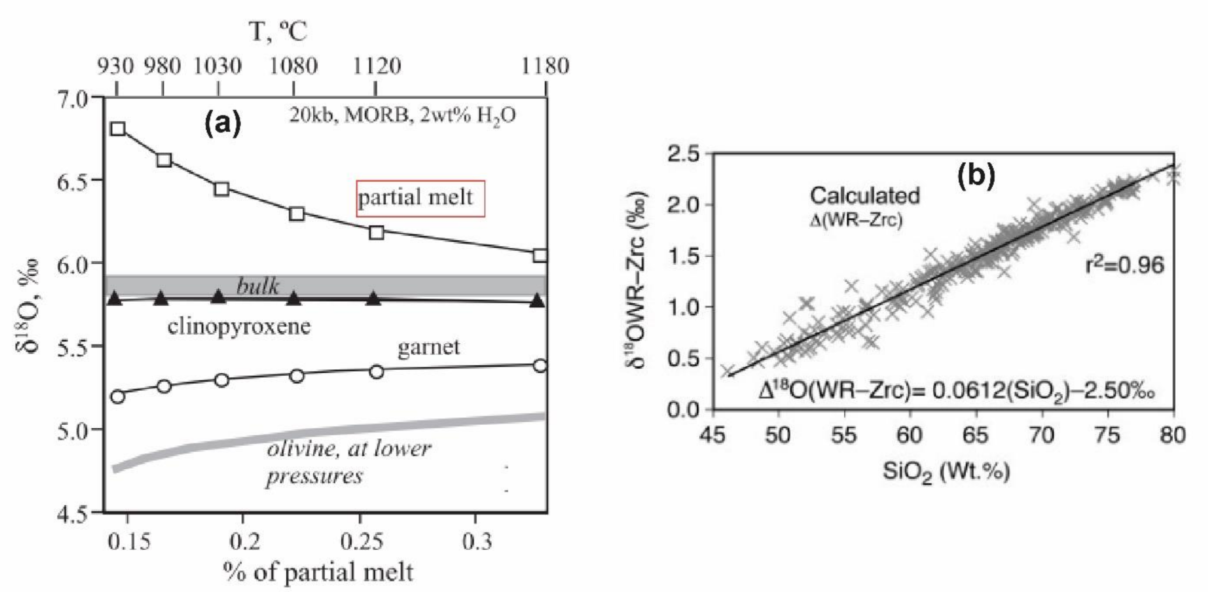

Figure 2-6. Illustration of O isotope fractionation in magmatic systems. (a) shows how the $\delta^{18}O$ value of the melt and of residual phases evolves with the degree of batch melting (Bindeman et al., 2005). (b) shows that the fractionation of $\delta^{18}O$ between felsic melts and zircon depends on the SiO_2 content of the melt (Lackey et al., 2008).

Secondly, as zircon is generally considered as a proxy for O isotope composition in felsic melts, Lackey et al. (2008) calibrated an empirical equation that can be used to determine the fractionation of O isotopes between zircon and a melt:

$$\Delta^{18}O_{(WR-zircon)} = 0.0612 \times SiO_2 - 2.5 \quad (\textbf{Equation 2-13})$$

In this equation, $\Delta^{18}O_{WR\text{-zircon}}$ is expressed in ‰ and SiO_2 is in wt.%. This calibration shows that the SiO_2 content of a magma is correlated with the fractionation of O isotopes between this magma and its zircons. Fractionation is more important in felsic rocks (SiO_2 = 65-75 wt.%, $\Delta^{18}O_{WR\text{-zircon}}$ = ~1.5‰) than in ultramafic rocks derived from the mantle (SiO_2 ~30-40 wt.% $\Delta^{18}O_{WR\text{-zircon}}$ = ~0.3‰) (Faure and Harris, 1991; Valley et al., 1994). Unlike previously proposed, similar $\delta^{18}O$ values in zircons from felsic rocks and those from mantle-derived ultramafic rocks may not necessarily mean a mantle-like $\delta^{18}O$ (~5.3±0.3‰) in the source zone of felsic magmas. Therefore, previous assumptions that TTG melts originated from melting of fresh mantle-derived mafic magmas based on the O isotope composition of their zircons (Wang et al., 2022; Lei et al., 2023) need to be revisited.

2.1.3.3. Silicon isotope geochemistry

Silicon has three different stable isotopes: ^{28}Si (92.23%), ^{29}Si (4.67%) and ^{30}Si (3.1%) (Poitrasson, 2017). The $\delta^{30}Si$ and $\delta^{29}Si$ are respectively calculated based on $^{30}Si/^{28}Si$ and $^{29}Si/^{28}Si$ ratios, using NBS-28 as the conventional standard for normalising Si isotopes (**Equation 2-4**). In this study, we focus on the conventionally studied $\delta^{30}Si$ (Ding et al., 2005; Abraham et al., 2008).

A. Silicon isotope composition of cherts as a tracer of fluid?

Archean cherts display a large range of $\delta^{30}Si$ values (from less than -2 to more than +2‰) (**Figure 2-7a**) that could be explained in three different ways. Firstly, this isotopic range could reflect coexistence of silica from different sources, including seawater, hydrothermal fluids and continental erosion into cherts (van den Boorn et al., 2007, 2010; Geilert et al., 2014; Sun et al., 2023; Trower and Fischer, 2019a). In this perspective, cherts with negative $\delta^{30}Si$ values were considered to have an important hydrothermal contribution, whereas cherts with a positive $\delta^{30}Si$ values were considered to represent seawater precipitates (**Figure 2-7a**). This suggests a tight correlation between the isotopic variation of Si in cherts and the cycle of Si on the Precambrian Earth (**Figure 2-7b**) (Siever, 1992; van den Boorn et al., 2010; André et al., 2006, 2022), where different sources of Si could infer different isotopic compositions. Secondly, the large range of

δ^{30}Si in cherts could be explained by a Rayleigh fractionation in the residual fluids during continuous precipitation of silica (Abraham et al., 2011; Marin-Carbonne et al., 2011; André et al., 2022). Thirdly, this large range of δ^{30}Si could also be explained by kinetic isotopic fractionation of Si isotopes (e.g. Stefurak et al., 2015; Kleine et al., 2018).

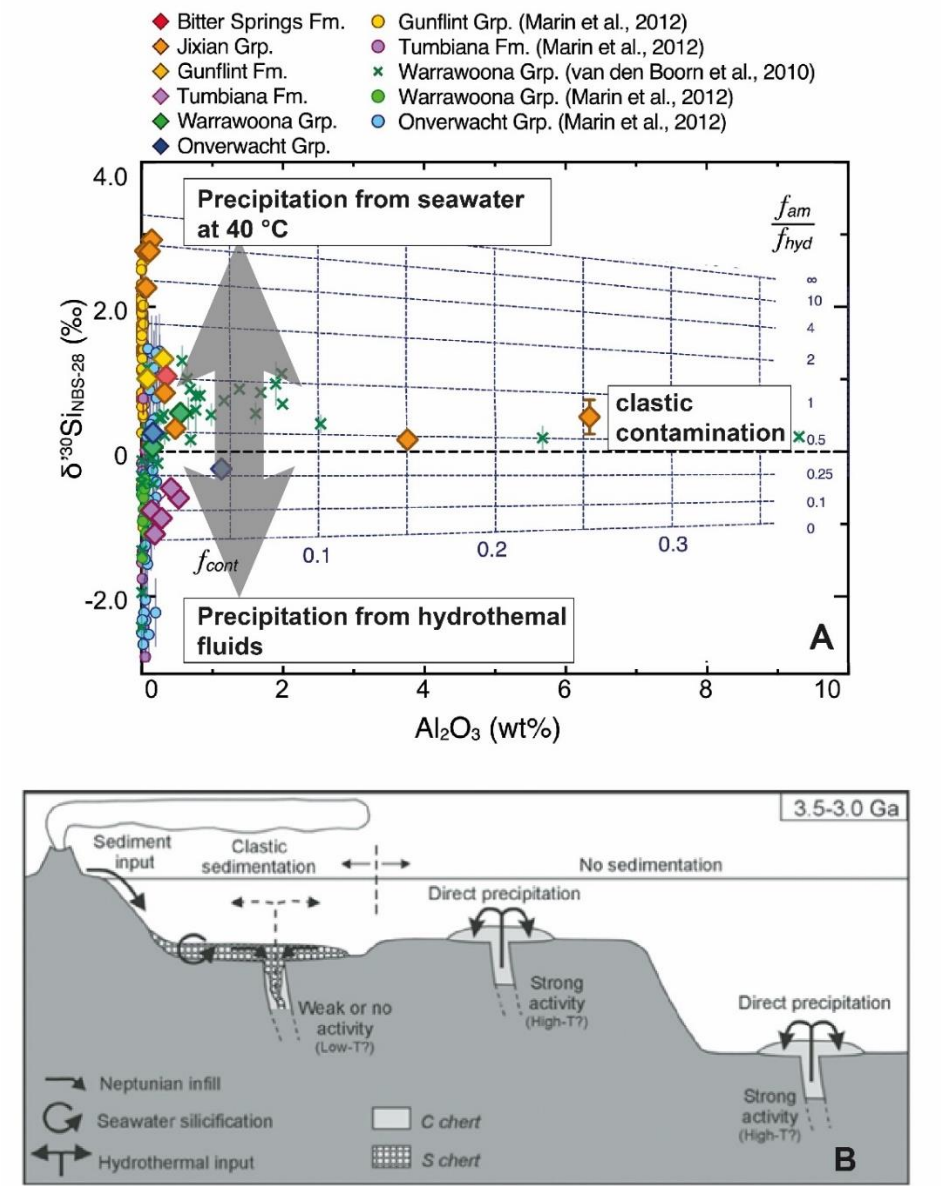

Figure 2-7. (a) Range of Si isotope composition in Precambrian cherts from various fields with possible endmember contributions of seawater-precipitation, precipitation from hydrothermal input and clastic contamination (modified after Sun et al., 2023). (b) Possible Si isotope cycle in the archean ocean-crust system (van den Boorn et al., 2010). The C and S type cherts shown in the figure respectively represent seawater-precipitated cherts and pervasively silicified clastic sediments.

The different interpretations proposed to explain the variation of Si isotope composition in archean cherts demonstrate that the origin of Si isotope compositions measured in archean cherts is not well understood. Yet, it is also important to note that Si isotope compositions of cherts were considered as a possible thermometer for archean fluids, considering a known isotopic composition for the fluids (Robert and Chaussidon, 2006; Tatzel et al., 2024), providing valuable insights into the temperature of ancient oceans or diagenetic fluids. While the average δ^{30}Si value of Archean cherts is generally positive, negative δ^{30}Si values generally occur in archean shales and BIFs and were suggested to show that BIFs and shales could represent the sink of isotopically lighter silica complementing cherts (André et al., 2006; Stefurak et al., 2015; Trower and Fischer, 2019).

B. Silicon isotopes applied to the study of magmatic systems

Two important contributions facilitate the use of Si isotopes in the study of magmatic systems. The first is the observation an igneous array based on the relationship between bulk-rock δ^{30}Si value and SiO_2 concentration of most igneous magmas of Phanerozoic age by André et al. (2019) (**Figure 2-8a**) as expressed by the following equation:

$$\delta^{30}\mathrm{Si} = 0.0056\ \times \mathrm{SiO_2}\ (\mathrm{wt.\%}) - 0.567 \quad (\textbf{Equation 2-14})$$

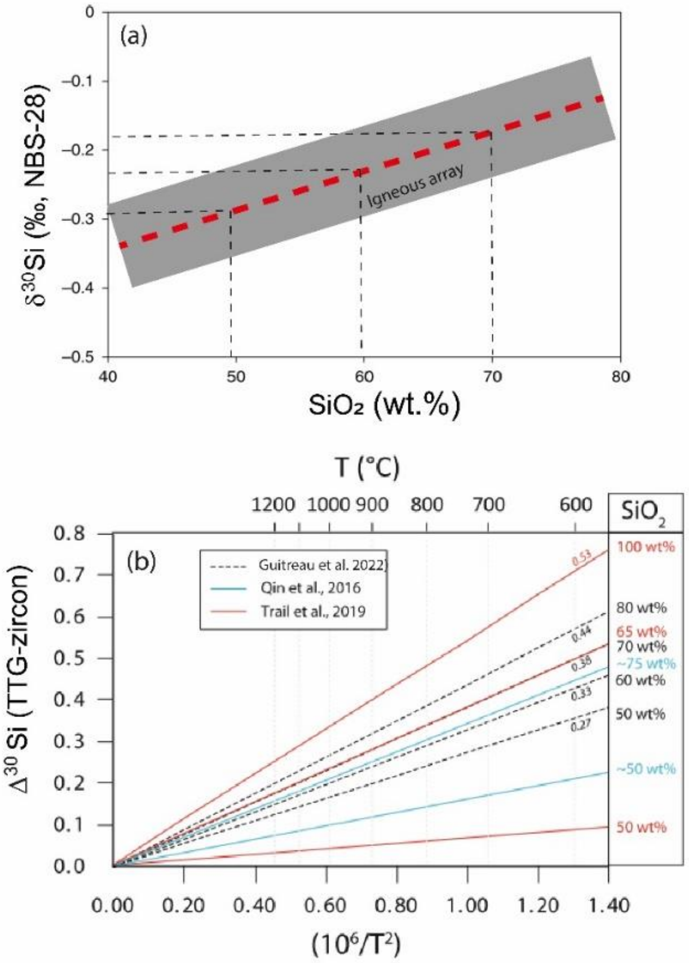

Figure 2-8. Illustration of Si isotope fractionation in magmatic systems. (a) igneous array representing the δ^{30}Si value of melts as a function of their SiO_2 content (André et al., 2019). (b) fractionation of δ^{30}Si between zircon and melt as a function of SiO_2 concentration and temperature of the system (Qin et al., 2016; Guitreau et al., 2022).

The deviation of archean TTGs from this array to slightly higher δ^{30}Si values (from -0.1 to +0.1‰) was importantly proposed to trace the recycling of silicified lavas or cherts from the seafloor towards the source zone of TTG bodies (André et al., 2019; Deng et al., 2019). Secondly, the fractionation of Si isotopes between zircons and TTG magmas was calibrated and allows to use the isotopic composition of zircon to reconstruct the Si isotope composition of the magma from which it crystallised (Qin et al., 2016; Guitreau et al., 2022). We consider in this thesis the empirical fractionation proposed by Guitreau et al. (2022) as adapted to natural systems (**Figure 2-8a**):

$$\Delta^{30}\mathrm{Si}_{(\mathrm{melt-zircon})} = 0.0054 \times \frac{10^6}{\mathrm{T}^2} \times \mathrm{SiO}_2 \quad \textbf{(Equation 2-15)}$$

Based on this fractionation, recent analyses of Si isotope compositions of magmatic zircons (Trail et al., 2018; Guitreau et al., 2022; Lei et al., 2023) confirmed the recycling of seafloor-derived silica-rich rocks towards the source zone of archean TTGs that was initially proposed based on bulk-rock measurements.

2.1.4. Radiogenic isotope geochemistry

2.1.4.1. Principle

Radioactive isotopes are unstable atoms that release radiations by decaying into more stable atoms named radiogenic. The decay of a radioactive isotope into a radiogenic isotope occurs at a constant rate that is specific to each radioactive-radiogenic isotope system (Peter and Shields, 1997). Over time, the relative amount of radiogenic isotope increases while the amount of radioactive isotopes decreases in the system. The quantity of radiogenic isotopes produced in a sample over time depends on the initial amount of radioactive isotopes present when the system was closed, the parent/daughter ratio, and the elapsed amount of time. A half-life time is defined as the time required for half of the radioactive isotopes to decay into radiogenic isotopes, and each isotopic system having a specific half-life time. Additionally, an isochron is a line followed by samples of the same age and same starting relative abundance of radiogenic isotopes, in parent (x-axis) *versus* daughter isotope (y-axis) diagram (e.g. **Figure 2-9**). The slope of isochrons is controlled by the radioactive decay constant and the time elapsed since closure of the system; while the position of each sample depends on its initial parent/daughter ratio.

Conventionally, radiogenic isotopes are normalised to chondritic uniform reservoir (CHUR), which theoretically represents the isotopic composition of the bulk Earth. This allows defining the epsilon (ε) parameter:

$$\varepsilon_{\mathrm{Sample,T0}} = \left(\frac{\mathrm{R}_{\mathrm{Sample,\ T0}}}{\mathrm{R}_{\mathrm{CHUR,\ T0}}} - 1\right) * 10000 \qquad \textbf{(Equation 2-16)}$$

with R_{sample} and R_{CHUR} representing the ratio between a radiogenic and a stable isotope at a certain time (T0), respectively in the sample and in CHUR. Among the radioactive systems, we were particularly interested in the ^{147}Sm-^{143}Nd and ^{138}La-^{138}Ce systems described below.

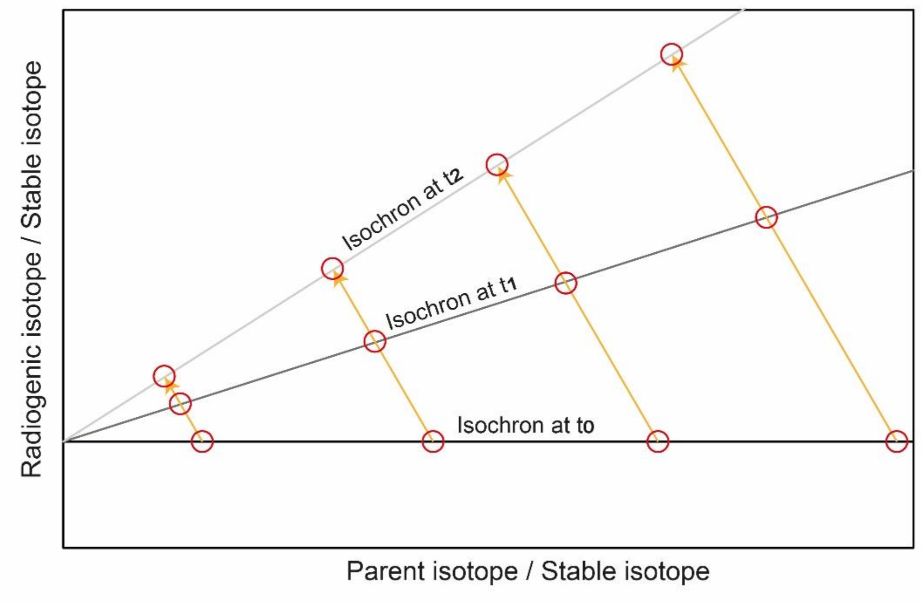

Figure 2-9. Illustration of an isochron diagram. At t_0, cogenetic materials with different parent /daughter ratios share the same initial ratio for radiogenic isotopes. At t_1 and t_2, the different rocks/minerals are aligned along lines called isochrons due to the decay of radioactive isotopes: the longer the elapsed time, the steeper the isochrons.

2.1.4.2. The Sm-Nd and La-Ce isotope systems

Samarium, neodymium, lanthanum and cerium are all LREE with more than two different natural isotopes. Cerium comprises three stable isotopes (^{136}Ce – 0.185 wt.%, ^{140}Ce – 88.450 wt.% and ^{142}Ce – 11.114 wt.%), and one radiogenic isotope (^{138}Ce – 0.251 wt.%) (Rosman and Taylor, 1998; Meija et al., 2016). Samarium displays six stable isotopes (^{144}Sm – 3.08 wt.%, ^{148}Sm – 11.3 wt.%, ^{149}Sm – 13.8 wt.%, ^{150}Sm – 7.37 wt.%, ^{152}Sm – 26.7 wt.% and ^{154}Sm – 22.7 wt.%) and one radioactive isotopes (^{147}Sm – 15 wt.% and) (O'Nions, 1979). Neodymium has seven stable or nearly stable isotopes (^{142}Nd – 27.2 wt.%, ^{144}Nd-23.8 wt.%, ^{145}Nd – 8.3 wt.%, ^{146}Nd – 17.2 wt.%, ^{144}Nd – 23.8 wt.%, ^{148}Nd – 5.7 wt.% and ^{150}Nd – 5.6 wt.%) and one radiogenic isotope (^{143}Nd – 12.2 wt.%).

^{138}La decays into ^{138}Ce with a half-life time of ~292.4 billion years. Similarly, ^{147}Sm decays into ^{143}Nd with a half-life time of ~106 billion years (**Table 2-1**). These two different systems have been combined to study the differentiation and evolution of terrestrial reservoirs including the different endmembers of the mantle and the composition of the oceanic and continental crusts (e.g. Willbold and Stracke, 2010; Tappe et al., 2014; Israel et al., 2020). Here, we consider a different application of these isotopic systems consisting of the determination of the timing of LREE perturbation due to fluid-rock interactions (e.g. Weis and Wasserburg, 1987; Toulkeridis et al., 1998; Hayashi et al., 2004; Bonnand et al., 2020).

Table 2-1. Decay rate and half-life time values for ^{137}Sm-^{143}Nd and ^{138}La-^{138}Ce isotopic systems

Reference	**System**	λ (year^{-1})	$T_{1/2}$ (year)
(Lugmair and Marti, 1978)	^{137}Sm-^{143}Nd	6.54×10^{-12}	1.05986E+11
(Israel et al., 2020)	^{138}La-^{138}Ce	2.37×10^{-12}	2.92467E+11

Constraining interactions with oxidised fluids using La-Ce and Sm-Nd isotopes

Lighter LREEs are relatively more mobile and soluble in fluid than HREE , such that the portion of LREE sequestrated by rocks from fluids during fluid-rock interactions generally works to decrease the ^{147}Sm/^{144}Nd and increase the ^{138}La/^{142}Ce ratios (Bonnand et al., 2020). In addition, as already, mentioned, oxidised fluids are characterised by a negative Ce anomaly because they cannot dissolve Ce as efficiently as other LREE (Shimizu et al., 1994; Cotten et al., 1995). Thus, the sequestration of LREE from oxidised altering fluids drastically increases the ^{138}La/^{142}Ce of altered rocks. **Figure 2-10** illustrates an example of La-Ce and Sm-Nd isotopic resetting in 3.2 Ga old sediments from the Moodies Group (Barberton terrain, South Africa) due to their interaction with Cenozoic oxidised fluids (Bonnand et al., 2020). In this case study, the intensive sequestration of LREE from an oxidised fluid with a considerably high ^{138}La/^{142}Ce due to negative Ce anomaly allowed dating the weathering event to less than 100 Ma. Thus, LREE isotopes can be used to identify and estimate the age of late fluid circulations in ancient rocks.

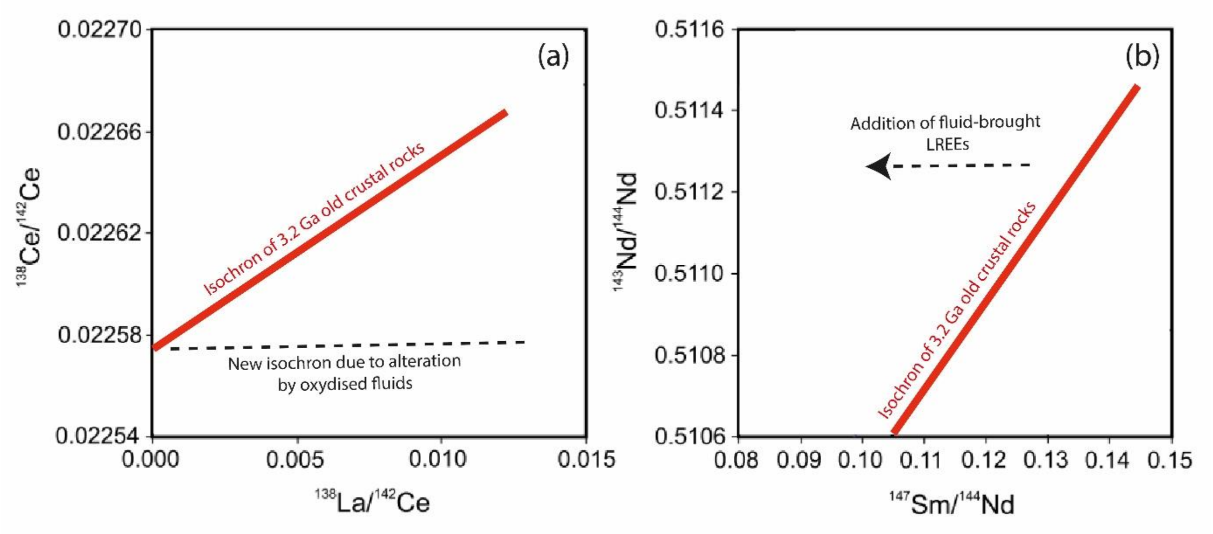

Figure 2-10. Illustration of the effect of oxidised fluid circulations on La-Ce and Sm-Nd isotope systematics (modified after Bonnand et al., 2019). By decreasing Sm/Nd ratios and increasing La/Ce ratios, oxidised fluids remove samples from their isochrons.

2.2. Archean cratonic terrains and Early Earth dynamics

Following the description of geochemical tools in the previous section, presented here is a geological background on archean cratonic terrains (with a focus on the geology of the studied Barberton granitoid-greenstone terrain) and archean geodynamics. The Archean Eon (4.0 – 2.5 Ga) is the second Eon of Earth's history during which the oldest crustal rocks still accessible at outcrops formed. It was preceded by the Hadean Eon that started with the formation of the Earth ~4.6 Ga ago. The Archean Eon is subdivided in four main Eras (**Figure 2-11**), namely the Eoarchean (4.0 – 3.6 Ga), the Palaeoarchean (3.6 – 3.2 Ga), the Meso-Archean (3.2 – 2.8 Ga) and the Neoarchean (2.8 – 2.5 Ga). Below, I present (1) an overview of archean cratonic terrains and rocks, (2) the geology of the studied Barberton granitoid-greenstone terrain, and (3) different geodynamic models previously proposed for the early crust with an emphasis on geochemical constrains.

2.2.1. An overview of archean cratonic terrains and rocks

Cratonic terrains of archean age (4.0 – 3.6 Ga) occur on every continent of the globe and constitute the best record of the crust that existed on the early Earth (**Figure 2-12**). Surviving vestiges of the preceding Hadean Eon are scarce. These include a small piece of mafic crust of debated age preserved in northern Quebec (Nuvvuagittuq greenstone belt, Canada, O'Neil et al., 2008) and Hadean zircons occurring in several cratons, of which detrital zircons from Jack Hills in Australia (Yilgarn craton) are the most studied (Compston and Pidgeon, 1986; Byerly et al., 2018). Thus, most of the rock record from the Hadean Eon is no longer accessible for geological investigation due to crustal recycling into the mantle, reworking and erosion. Contrastingly, Archean terrains are still accessible at the surface of the Earth. Their studies are crucial for understanding the geodynamic processes that were operating during the Early history of the Earth (e.g. Martin, 1993; Bickle et al., 1994). Because only small fragments of the archean crust are scattered in modern continents (**Figure 2-12**), they might not represent the full array of archean geological settings. Therefore, preservation biases could complicate comparisons between the archean and the modern Earth (Brown et al., 2020). While these preservation issues preclude the acquisition of a global picture on the archean Earth, accessible archean terrains remain precious as they can reveal processes and conditions that existed at least in certain parts of the early Earth.

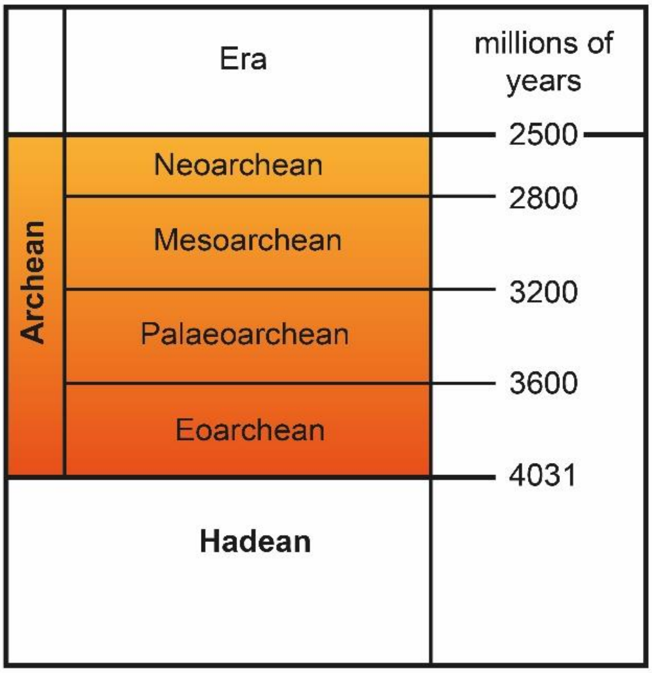

Figure 2-11. Chronological subdivision of the Archean eon

Archean cratons generally comprise supracrustal rocks (lavas and sediments) assembled in greenstone belts, and intrusive rocks occurring as granitoids (commonly with a gneissic aspect) (Anhaeusser, 2014). These two different types of rocks (i.e. supracrustal and intrusive) are generally incorporated in geological assemblages called granitoid-greenstone terrains. From the archean sedimentary records and the geochemistry of granitoids and gneisses, we know that a hadean (4.6 – 4.0 Ga) crust existed on Earth up to 360 Ma before the onset of the Archean Eon (e.g. Wilde et al., 2001).

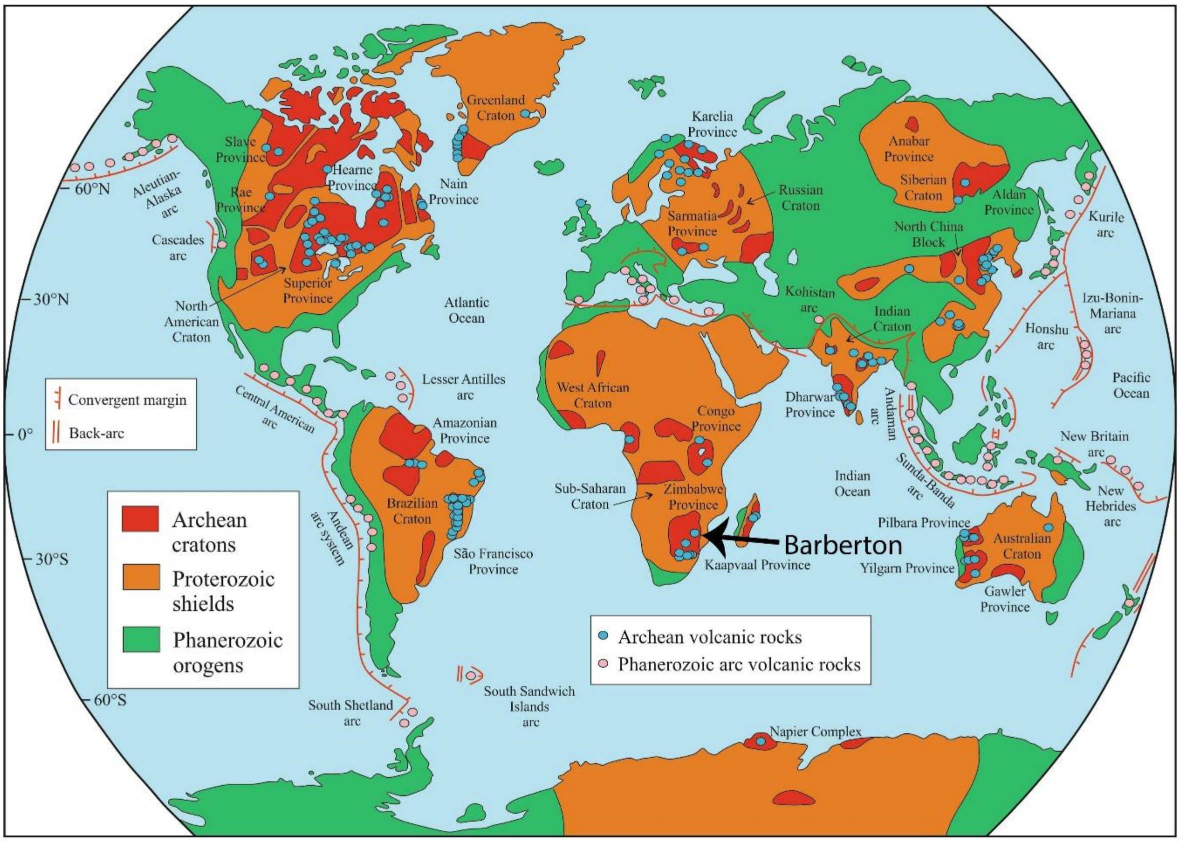

Figure 2-12. Global distribution of archean cratons (in red) (taken from (Sotiriou et al., 2022). The black arrow shows the location of the Barberton granitoid-greenstone terrain investigated in this study.

A nearly exhaustive list of archean cratonic terrains was recently inventoried by Condie (2019). Although it is impossible to enumerate all these terrains here, some of them feature considerably old ages (>3.6 Ga) making them emblematic in the study of the geology of the early Earth. These are the 4.03-3.6 Ga Acasta complex in the Slave craton, ~3.8 Ga (highly discussed age: up to > 4.15 Ga; O'Neil et al., 2012) Nuvvuagittuq greenstone belt in the Superior craton, 3.8 – 3.7 Ga Issua greenstone belt and 3.9 – 3.7 Ga Itsaq Gneiss complex in SW Greenland. Unfortunately, these oldest cratonic terrains on Earth generally feature high degrees of deformation and high-grade metamorphism that can hinder their characterisation. Preservation from high-grade metamorphism or from intense deformation have motivated geological studies of slightly younger terrains, including the Pilbara craton (3.5 – 3.2 Ga) (e.g. Nakamura and Kato, 2004; Smithies et al., 2009; Johnson and Wing, 2020), the Singhbum craton (3.5 – 3.1 Ga) (e.g. Hofmann et al., 2022), the Abitibi greenstone belt (2.7 Ga) (e.g. Brengman and Fedo, 2018), and the Barberton granitoid-greenstone terrain (3.5 – 3.1 Ga) (e.g. de Wit, 1982; McLennan et al., 1983) in the search of unambiguous features preserved from the early crust. Amongst those, the Pilbara and Barberton granitoid-greenstone terrains are two well-studied examples as they are (i) reasonably accessible, (ii) sufficiently large to display a variety of rocks and structures and (iii) the oldest featuring such aspects. The geology of the Barberton granitoid-greenstone terrain studied in this thesis will be detailed in **Sub-section 2.2.2.** but we firstly introduce the principal supracrustal and granitic rocks occurring in most archean terrains.

2.2.1.1. Supracrustal rocks and their geological significance

Archean supracrustal rocks comprise volcanic and sedimentary sequences that emplaced in a submarine setting (**Figure 2-13**).

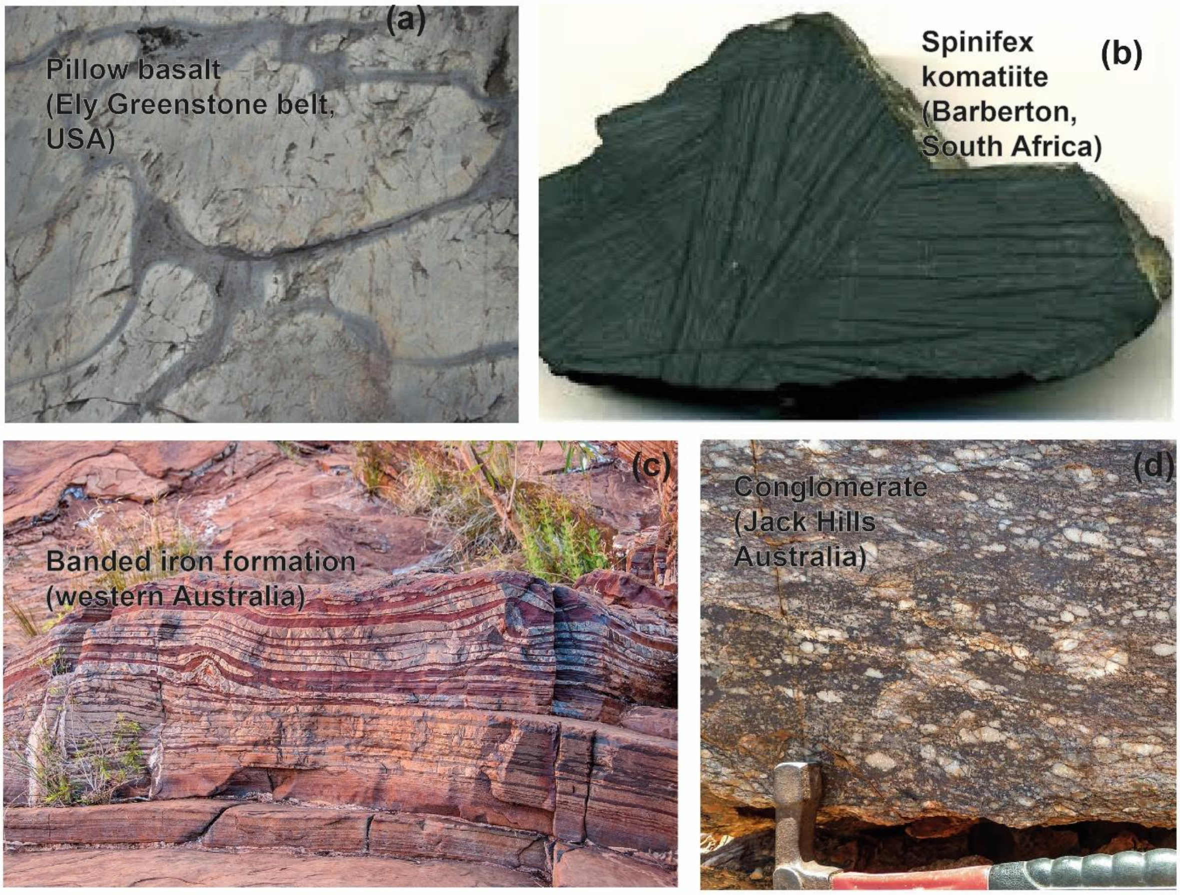

Figure 2-13. Photographs of some supracrustal rocks occurring in archean greenstone belts. (a) Pillowed basalt (https://www.angelfire.com/), (b) komatiite with the characteristic spinifex texture, (c) banded iron formation (BIF) (https://en.wikipedia.org/), (d) conglomerate (https://iugs-geoheritage.org/).

Volcanic rocks include ultramafic to mafic lavas, represented by komatiites, basaltic komatiites and basalts (**Figure 2-13a-b**) (Arndt, 1998; Sotiriou et al., 2022). Some greenstone belts contain also felsic lavas that are generally linked to an episode of granitic magmatism (Agangi et al., 2018; Laurent et al., 2020). In the field, ultramafic to mafic lavas occur as pillows or massive lava flows. These archean lavas are richer in incompatible elements compared to modern Mid-Ocean Ridge Basalts (MORB) and could have originated from a more fertile mantle source than that of modern MORBs (e.g. Moyen and Laurent, 2018). In addition, archean lavas were hotter than modern analogues, as suggested by their relatively high MgO content. This was interpreted to show that their mantle source could be up to 200 °C hotter than its modern equivalent due to the cooling of the Earth (Herzberg et al., 2010; Brown et al., 2020).

Archean sedimentary rocks comprise chemical sediments precipitated directly from seawater and lithic sediments representing submarine volcaniclastic materials or continental-eroded clasts. Among these sediments, banded iron formations and cherts are the main chemical sediments of archean age in most cratons (e.g. **Figure 2-13c**). The composition of these sediments can reveal the properties (e.g. composition, temperature, redox state and pH) of archean seawater (Dauphas et al., 2004; Maliva et al., 2005; Ackerman et al., 2023). On the other side, conglomerates, sandstones and shales are major clastic sediments (e.g. **Figure 2-13d**). These rocks are useful for studying the constitution of archean continents that are not accessible anymore, and testify of the presence of emerged continents with both felsic and mafic compositions (e.g. Garçon et al., 2017; Garçon, 2021).

The emplacement of archean lavas and sediments deposited in submarine settings fuelled a vigorous debate whether greenstone belts are equivalent to the modern oceanic crust (Bickle et al., 1994; Grosch and Slama, 2017). This debate is important because the consideration of greenstone belts as analogous to the modern oceanic crust has been deemed to imply their generation at mid-ocean ridges, which would suggest that modern-style plate tectonics was already operational during the Archean Eon (de Wit, 1982; Sotiriou et al., 2022). Several studies considered some greenstone belts as equivalent to the oceanic crust preserved in Phanerozoic ophiolitic complexes (Kusky and Polat, 1999; Dilek and Furnes, 2014; Condie and Stern, 2023). However, the vertical accumulation of mafic lavas that is common in archean greenstone belts, is incompatible with progressive production of magmas in an extensive regime such as at mid-ocean ridge (Puchtel et al., 1998). In addition, greenstone belts are generally free of sheeted dyke complexes and sheared ultramafics that are major constituents of the modern oceanic crust. The formation of greenstone belts is rather ascribed to high-degree melting as the one resulting in the large igneous provinces resembling to modern oceanic plateaus (Abbott, 1996). Whatever the geodynamic setting in which they were produced, greenstone belts were initially formed in a submarine environment and represent our best archive of a mafic crust that interacted with seawater-derived hydrothermal fluids during the Archean Eon.

2.2.1.2. Felsic intrusive rocks: Tonalite-Trondhjemite-Granodiorite bodies and other granitoids

Granitoids or their deformed analogues (orthogneisses) are present in every archean cratonic terrain. In most cratons, they include early generations of tonalite-trondjhemite-granodiorites (TTGs) (i.e. granitic bodies constituted by these different rock types) that generally predate the formation of more potassic granitoids (**Figure 2-14**) (Martin et al., 2005; Laurent et al., 2014). The mechanisms of TTG formation could be crucial for the stabilisation and preservation of archean cratons as these granitoids generally represent their oldest preserved components. TTGs rocks are generally part of plutons or smaller dykes and comprise quartz, sodic plagioclase, biotite and accessory minerals, including zircon, apatite, allanite/epidote, Fe-Ti oxides and monazite (Condie, 2014; Laurent et al., 2024). Geochemically, TTGs are sodic (K/Na ratio <0.6) and characterised by highly fractionated REE patterns (La/Yb > 15) as well as elevated Sr/Y ratio (>15) (Moyen, 2009).

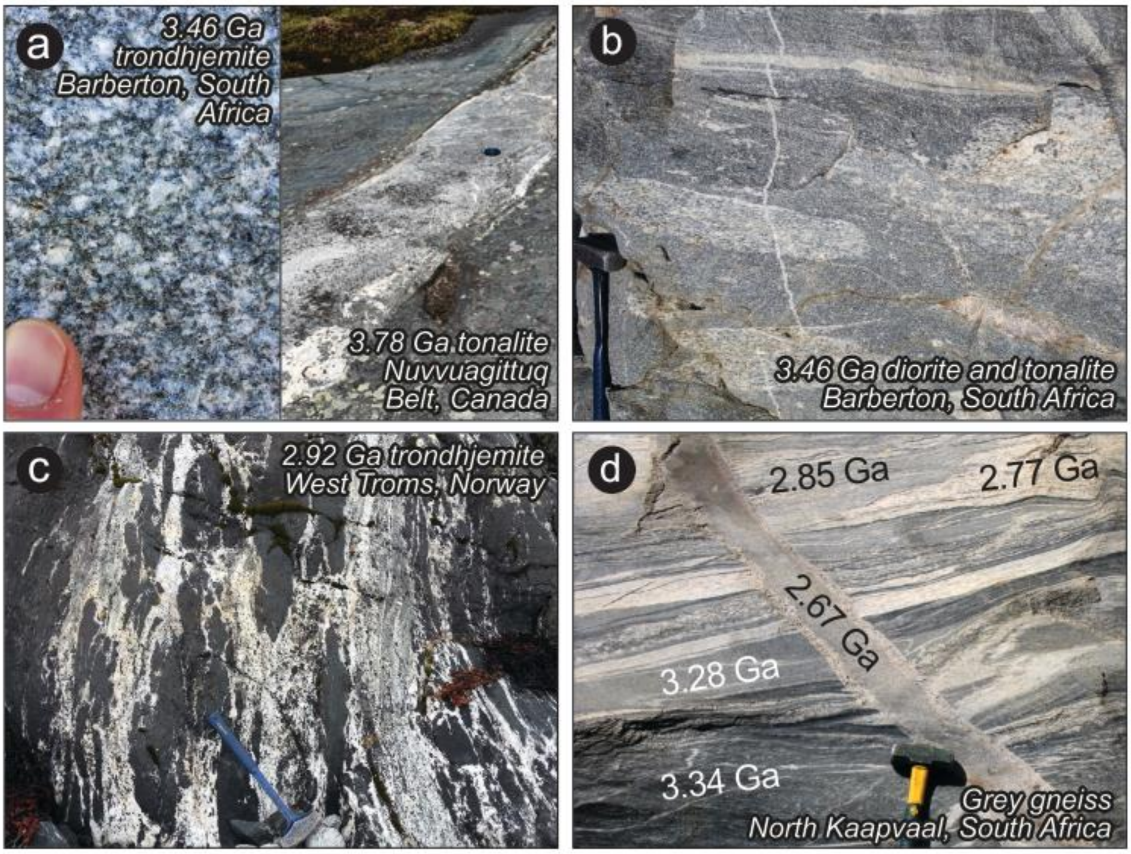

Figure 2-14. Different outcrops aspects of archean TTGs (taken from Laurent et al., 2024). Note the different rock types belonging to the large group of TTGs. In (d) it is shown that TTGs can also consist of composite complexes including meta-TTGs, amphibolites, leucosomes and even dykes.

Different petrological models were previously proposed to explain the formation of archean TTGs. Firstly, these sodic granitoids were considered as primitive undifferentiated liquids. In this case, their formation was explained either by fluid-absent (Martin, 1987) or fluid-present melting of a modern-like mid-ocean ridge basalt (Laurie and Stevens, 2012), or of a more enriched basaltic source (Smithies et al., 2009; Martin et al., 2014; Moyen and Laurent, 2018). Secondly, TTGs were proposed to result from differentiation of a primary arc magma due to fractional crystallisation (Jagoutz et al., 2013). Thirdly, TTGs could also represent cumulates resulting from a primitive tonalitic liquid, for which complementary melts were systematically erupted on the seafloor (Laurent et al., 2020). A conventional interpretation is that TTGs are chilled, primary or near primary melts. Under this hypothesis, their major and trace elements composition can be interpreted as reliable barometers. This was assumed in studies that considered La/Yb and Sr/Y ratios in bulk TTGs as reliable barometers due to their dependence on the proportion of residual garnet or plagioclase, which in turn depends on melting depth for specific source compositions (e.g. Rapp et al., 1991; Moyen and Stevens, 2006). However, since recent studies have proposed that fractional crystallisation and mineral accumulation processes could considerably change the bulk-rock composition of original TTG melts (Laurent et al., 2020; Rollinson, 2021), the inferences on the pressure of TTG melting based on trace element compositions should be regarded cautiously.

In addition to TTGs, archean terrains contain also different other types of more potassic granitoids reflecting different petrological origins. For further details on these granitoids and their geodynamic significance, the reader is referred to the papers of Laurent et al. (2014) as they are out of the scope of this study.

2.2.2. The Barberton granitoid-greenstone terrain

After the general presentation of palaeoarchean rocks, this section focuses on the geology of the investigated Barberton granitoid-greenstone terrain (**Figure 2-15**). The age of rocks cropping out in the Barberton granitoid-greenstone terrain extends between the palaeoarchean and mesoarchean Eras (3.55-3.1 Ga) (Byerly et al., 2019). The Barberton terrain is located in the Kaapvaal Craton and crops out in the Republic of South Africa and in the Kingdom of eSwatini. The Barberton terrain has been instrumental for understanding the environments and processes that characterised the early Earth because of its particular preservation from high-grade metamorphism and its constitution by different crustal rock types (i.e. ultramafic-to-mafic lavas, sedimentary rocks and granitoids) (Lowe and Byerly, 2007a; Stevens and Moyen, 2007; Puchtel et al., 2013; Moyen et al., 2019). The Barberton granitoid-greenstone terrain comprises a succession of volcano-sedimentary formations representing the Barberton greenstone belt and several sets of granitic bodies illustrated in **Figure 2-15**.

2.2.2.1. Supracrustal formations of the Barberton greenstone belt

The supracrustal rocks cropping out in the Barberton greenstone belt (**Figure 2-15**) incorporate volcanic materials erupted and sedimentary layers deposited in a sub-aquatic environment between 3550 and ca. 3200 Ma ago (Heubeck and Lowe, 1994; de Wit et al., 2011; Furnes et al., 2012; Hofmann et al., 2013; Byerly et al., 2019; Heubeck, 2019). On the geological map and stratigraphic chart of South Africa, the Barberton greenstone belt is identified as the "Swaziland Supergroup" and represents the "Swazian" period, but this terminology is generally not used in the recent scientific literature. The earliest group of lithologies occurring in the Barberton greenstone belt as the 3.5-3.3 Ga old Onverwacht Group dominated by volcanic rocks (**Figure 2-15**). This group is stratigraphically overlain by the 3.3-3.2 Ga old Fig Tree and Moodies Groups that are made of siliciclastic sediments, orthochemical BIF, felsic lavas and terrigenous sediments (Heubeck, 2019; Drabon and Lowe, 2021).

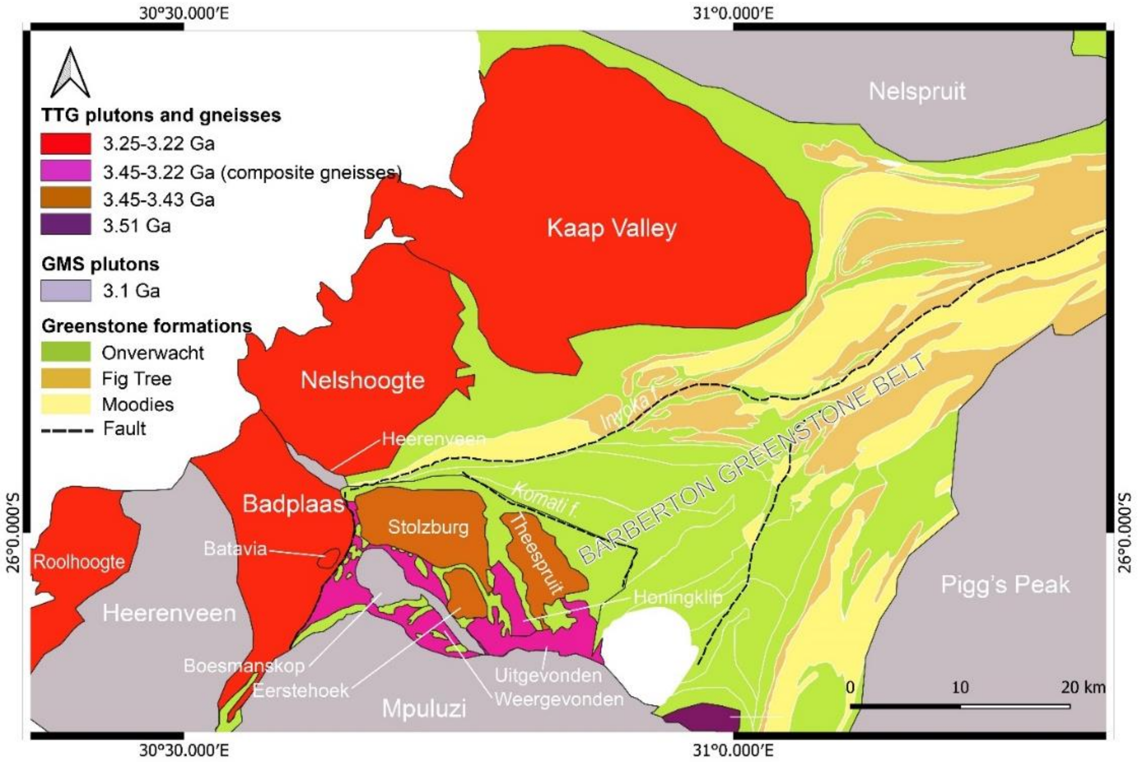

Figure 2-15. Simplified geological map of the Barberton granitoid-greenstone terrain showing Greenstone formations and surrounding granitic bodies.

A. The Onverwacht Group: a record of submarine palaeoarchean crust

Dominant lava flows of the Onverwacht Group intercalate with minor sedimentary layers that deposited on the seafloor during periods of volcanic quiescence (**Figure 2-16**) (de Wit et al., 2011; Byerly et al., 2019). In the anticline situated in the east of Inyoka fault (the Onverwacht anticline), the Onverwacht Group exhibits a continuous stratigraphic succession reaching ~10 km of thickness. The nature of volcanic rocks erupted in the Onverwacht Group is quite variable. They are dominated by ultramafic to mafic lavas but comprise also felsic lavas at some stratigraphic levels (Furnes et al., 2013; Agangi et al., 2018). The ultramafic to mafic lavas (i.e. komatiites, komatiitic basalts and basalts) are interpreted as owed to melting of a mantle plume at variable temperatures and depths (Robin-Popieul et al., 2012). The felsic lavas cropping out in the Onverwacht Group are due to the same felsic magmatism that generated the granitic bodies surrounding the Barberton greenstone belt (Agangi et al., 2018; Laurent et al., 2020). Sedimentary rocks occurring in the Onverwacht Group include clastic components comprising air-fall volcaniclasic materials and possible products of continental erosion. Generally, the clastic sediments and underlying lava tops are variably silicified due to interactions with seawater-derived fluids (Paris et al., 1985; Lowe and Byerly, 1986; Hofmann and Harris, 2008;); the nature of these silicified rocks and their link to silicifying fluids are dedicatedly discussed in **Section 2.3.**

The Onverwacht Group is subdivided in five formations, each of which comprises one or several volcanic and sedimentary units. At least four of these formations, namely the Komati, Hooggenoeg, Kromberg and Mendon formations, represent a continuous stratigraphic succession (**Figure 2-16**). On the other side of the Inyoka fault, the Weltevreden Formation emplaced coevally with the Mendon Formation (Lowe and Byerly, 1999; Kareem and Byerly, 2003) but in a different crustal block (**Figure 2-15**). In addition to these classical formations of the Onverwacht Group, de Wit et al. (2011) proposed to rename the uppermost part of the Hooggenoeg Formation as the “Noisy complex”, although this name is not unanimously adopted. Each Formation of the Onverwacht Group is subdivided in one or several members and each member comprises both sediments and lavas (Byerly et al., 2019). The stratigraphic members of the Onverwacht units are conventionally named by a ‘code’ including the first letter of the formation to which they belong followed by their stratigraphic order of occurrence. For example, H3 is the stratigraphic member of the Hooggenoeg formation made of its third sedimentary layer together with underlying lava (Lowe and Byerly, 2007a; Byerly et al., 2019).

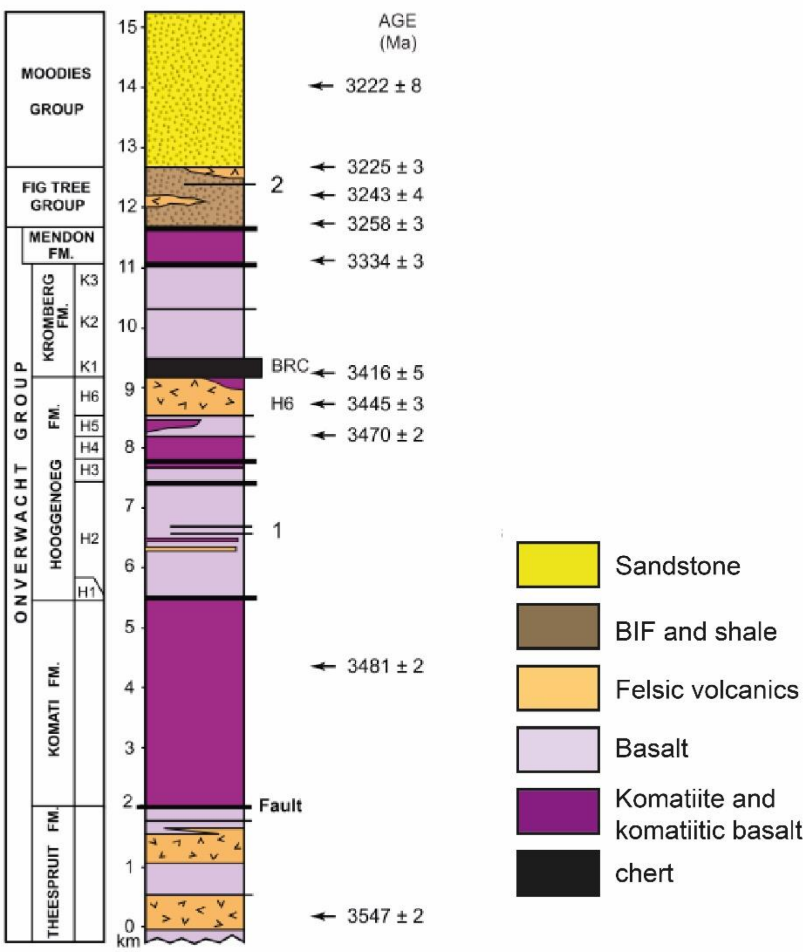

Figure 2-16. Simplified stratigraphic succession of the Barberton greenstone belt (modified after Lowe et al., 2020).

B. The Fig Tree and Moodies Groups

The Fig Tree and Moodies groups, stratigraphically above the Onverwacht Group are dominated by sedimentary rocks although they also contain subordinate amounts of lava flows (**Figure 2-16**) (Lowe and Byerly, 2007a). Lithologically, the Fig Tree and the Moodies Groups are notably different. Finely grained clastics and chemical sediments (i.e. shales and banded iron formations) dominate the Fig Tree Group (Drabon et al., 2019; Drabon and Lowe, 2021; Stoll et al., 2021) whereas coarse-grained and mature clastic sediments (i.e. sandstones) dominate the Moodies Group (Heubeck and Lowe, 1994; Heubeck, 2019). The striking abundance of sedimentary deposition in these two groups over a restricted timeframe shows that their deposition was linked to an important uplift event that facilitated erosion of emerged terrains between 3.3 and 3.2 Ga ago (Lowe and Byerly, 2007a).

2.2.2.2. The Barberton granitoids: Four different generations of felsic magmas

Four different generations of granitic bodies crop out in the Barberton area during the Palaeoarchea and Mesoarchean Eras (**Figure 2-15**) (Anhaeusser and Robb, 1980; Anhaeusser, 1981; Robb et al., 1986; Clemens et al., 2010; Moyen et al., 2019; Moyen et al., 2021). The first generation consists of Tonalite-Trondjhemite-Granodiorites (TTG) constituting the 3.5 Ga-old Steynsdorp gneisses in tectonic contact with the south-western extremity of belt (Kisters and Anhaeusser, 1995). These gneisses are equivalent to the large gneissic complex called Ancient Gneissic Complex cropping out to the east of the Barberton granitoid-greenstone terrain in Swaziland (Kröner et al., 2016). The second consists of the 3.45 Ga-old Theespruit, Stolzburg and Eerstehoek TTG plutons intruding the southern part of the belt. The third comprises the 3.3-3.2 Ga TTG plutons including the Kaap-Valley, Nelshooghte and Badplaas bodies intruding the western part of the belt, and some composite gneisses like the Honingklip, Uitgevongeden and Wergenvonden composite gneisses between the ca. 3.45 Ga plutons. Finally, the fourth generation of granitoids is represented by the ~3.1 Ga-old granodiorite-monzonzogranite-syenogranites (GMS) surrounding the older Barberton Greensotne Belt and TTG bodies. These include the Nelspuit body in the north, the Pigg's Peak batholith in the east, the Boesmanskop and Mpuluzi plutons in the south, as well as the Heerenveen pluton in the west of the belt. The three different generations of TTG magmatic episodes followed by an episode of GMS magmatism were proposed to document a progressive stabilisation of an early granitoid-greenstone crust into a cratonic domain (Moyen et al., 2021).

2.2.2.3. Metamorphism and late-stage episode of fluid circulation

An earlier metamorphic event could have occurred around 3.45 Ga ago in the belt but this event remains poorly constrained (Kisters and Anhaeusser, 1995; Knauth and Lowe, 2003). The most important metamorphic event is dated around ~3.2 Ga using metamorphic phases (e.g. garnet and titanite), coevally with the major episode of deformation that faulted and folded the Barberton greenstone belt (Stevens and Moyen, 2007; Cutts et al., 2014). This episode generated different degrees of metamorphism on both sides of the Komati fault: high-grade amphibolite-facies metamorphism to the south and greenschist facies low-grade metamorphism to the north. In addition, bulk-rock radiogenic isotope studies suggested that other metamorphic events might have affected the Barberton granitoid-greenstone terrain between 2.7 and 2.2 Ga ago (Toulkeridis et al., 1998; Weis and Wasserburg, 1987; Mühlberg et al., 2021), although these apparent isochron ages could have also resulted from other open system processes such as mobilisation of trace elements by fluids. In addition, an intense circulation of fluids in the Barberton greenstone terrain generated localised gold mineralisation between 3.1 and 3.0 Ga ago (Agangi et al., 2019). Post-archean fluid circulations in continental setting have also been evidenced in the Barberton greenstone belt. Firstly, ironstone bodies occurring in the belt were demonstrated to document quaternary fluid circulation in continental setting based on a detailed field observations in the field by Lowe and Byerly (2007b). These authors considered relationship of the ironstone bodies with recent landslides to demonstrate that the circulations of meteoric fluids at the origin of these ironstone bodies was of quaternary age. The study of Bonnand et al. (2019) demonstrated also that recent (i.e. Cenozoic) weathering fluids could have modified the composition of the Barberton rocks in continental setting, as supported also by Reimann et al., (2021) and Saitoh et al. (2021). Thus, although the Barberton granitoid-greenstone terrain is certainly one of the best-preserved geological assemblages of its age, the composition of its rocks must have been modified to some extent by metamorphic and weathering processes.

2.2.2.4. Deformation of the Barberton granitoid-greenstone terrain

Several episodes of deformation affected the Barberton granitoid-greenstone terrain before its stabilisation, but most outcrops accessible to the north of Komati fault do not register penetrative deformation (Kisters and Anhaeusser, 1995; Kisters et al., 2010; Schmitz and Heubeck, 2021). The earliest episode of deformation in the south of the belt were estimated around 3.45 Ga ago (Kisters and Anhaeusser, 1995; Kisters et al., 2003) but the extent of this deformation is unclear. As already mentioned, the main episode of deformation that generated the main faults and folds observed in the entire belt occurred around ~3.2 Ga ago. The 3.2 Ga episode of deformation was also associated with the amalgamation of at least two different geological assemblages, including the two crustal portions assembled through the NE-SW-trending Inyoka fault (**Figure 2-15**) (Lowe and Byerly, 2007a; Anhaeusser, 2019).

2.2.3. Archean crustal dynamics and the role of stable isotope compositions in TTGS

Geodynamic processes that operated on the early Earth must have influenced the formation and the stabilisation of archean cratonic terrains. The archean geodynamic system was probably different from modern plate tectonics because the mantle was likely 100-200 °C hotter than it is today (Herzberg and Ohtani, 1988; Herzberg et al., 2010). Modern plate tectonics is defined by a global network of convergent (subduction zone) and divergent (mid-ocean ridge and rift zone) boundaries between distinct lithospheric plates (Cawood et al., 2018). Today, subduction is the main process that recycles materials derived from the oceanic crust back to the mantle, but during the Archean Eon, other processes like burial by accumulation of younger mafic rocks on the seafloor could also lead to the recycling of crustal materials. The onset of plate tectonics with long-lived subductions and the nature of geodynamic processes that preceded plate tectonics represent topical questions in Earth sciences that have been investigated using different approaches (e.g. Moyen and van Hunen, 2012; Van Hunen and Moyen, 2012; Nebel et al., 2018; Cawood et al., 2018; Windley et al., 2021).

2.2.3.1. Approaches commonly used to study archean geodynamic processes

Structural analyses in the field constitute the first approach that was used to understand archean geodynamic processes. Observations of shear zones, folds and dome-and-keel structures played a major role in the definition of different geodynamic models (see **sub-section 2.2.3.2.**) that were controversially debated in the literature (e.g. Windley et al., 2021). Particularly, different geodynamic interpretations resulted from structural studies in the Barberton granitoid-greenstone terrain alone. Some researchers proposed the operation of modern-style plate tectonics during the Archean Eon based on the presence of shear zones that they interpreted to generate stratigraphic repetition in a setting resembling modern subduction zones (de Wit, 1982; Grosch and Slama, 2017; Grosch et al., 2020). Contrastingly, other researchers interpreted the different structures observed in the belt to rather imply a geodynamic setting where horizontal movements were insignificant, and that was rather dominated by vertical sagging or drip (Van Kranendonk, 2011; Van Kranendonk et al., 2014; Schmitz and Heubeck, 2021). The main challenge in using structural data to investigate archean geodynamic settings resides in the fact that only small portions of the archean crust were preserved and these portions may be insufficient for the acquisition of a unified picture of crustal dynamics on the early Earth.

The second approach consists of petrological and geochemical studies of TTGs based on their major and trace element compositions that allow determining the pressure at which TTG melts were generated, as already presented in **sub-section 2.2.12**. The use of the geochemical approaches has been challenged by the fact that these data may not represent primary liquids (Manning et al., 2006; Doucet et al., 2020). In fact, the elemental composition of TTGs may have been considerably modified by petrological processes including fractional crystallisation and accumulation of the solid phases.

The third classically used approach consists of numerical modelling simulating the deformation of an archean crust, with the consideration that both the crust and the mantle were hotter than modern analogues (van Hunen and van den Berg, 2008; Sizova et al., 2015; Van Hunen and Moyen, 2012). A pitfall in this approach is that the physical properties (e.g. viscosity and temperature) of the crust and the mantle considered in the models are subject to uncertainties, which could lead to important biases in the models. Overall, both structural analyses, TTG petrology and numerical modelling do not provide unambiguous evidence on the nature of archean geodynamic processes. This justifies the fact that the different geodynamic models described below were proposed for the early Earth.

2.2.3.2. Geodynamic models previously proposed for the early Earth

Multiple geodynamic models have attempted to explain the major geological features observed in archean cratons, together with the reworking of mafic rocks to produce TTG magmas (Brown et al., 2020; Cawood et al., 2018; Nebel et al., 2018). The large spectrum of proposed geodynamic models can be subdivided into three major groups (**Figure 2-17**): (1) models supporting the operation of modern-style plate tectonics, (2) models supporting an immobile mafic crust, and (3) hybrid models combining the first two.

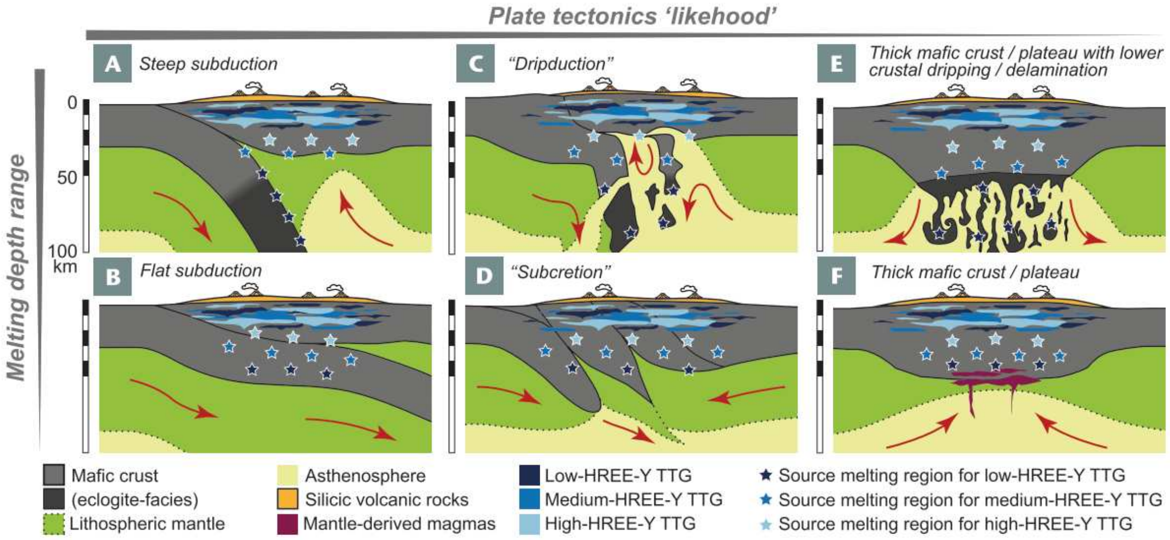

Figure 2-17. Different models of crustal geodynamic proposed for the Early earth with possible sites of TTG melting shown by stars (taken from Laurent et al., 2024). Panels A and B illustrate modern-like subductions where slab melting is possible, while panels E and F illustrate a different geodynamic setting where TTG melting occurs due to delamination processes, in intra- to infra-crustal settings. Panels C and D show intermediate scenario where incipient subductions are interrupted but allow the recycling of seafloor-derived rocks towards the deep Earth.

A. Models supporting modern-style plate tectonics

Geodynamic models supporting the operation of plate tectonics during the Archean Eon were based on structures (e.g. shear zones) and metamorphic conditions supporting the existence of horizontal movements in the archean crust (De Wit et al., 1992; Kusky and Polat, 1999; Moyen et al., 2006; Windley et al., 2021). These models were also supported by petrological arguments proposing the melting of subducted slabs to explain the generation of TTG magmas mainly because the source of TTG magmas must have contained water (Martin, 1993; Clemens et al., 2006; Laurie and Stevens, 2012; Martin et al., 2014). The lack of mantle contamination in most TTGs is not compatible with percolation of these melt from a steeply-subducted slab through the mantle wedge, such that shallow subductions were suggested to be more adapted to explain the origin of TTGs (e.g., Foley et al., 2003; Martin & Moyen, 2002). In addition, to reconcile the pate tectonic model with the higher thermal gradient of the archean Earth, lithospheric plates were proposed to have been smaller than modern plates, allowing high thermal fluxes at plate boundaries (Martin et al., 2006).

Models supporting modern-style plate tectonics with a global network of convergent and divergent plate boundaries were highly criticized for several reasons. Firstly, numerical modelling studies, considering that the Earth was hotter during the Archean Eon than it is today, showed that sustained slab pulls were not possible because the crust was not yet rigid enough (van Hunen and van den Berg, 2008; Moyen and van Hunen, 2012; Sizova et al., 2015). Secondly, structural studies interpreted the shearing structures associated with convergence as rather related to vertical sinking from the bottom of the ultramafic-to-mafic crust. Such sinking events are due to gradients of density between the crust and the hot (and therefore light) mantle (e.g. Van Kranendonk et al., 2009). Thirdly, modern-style plate tectonics is incompatible with the vertical accumulation of archean lavas into continuous successions (sometimes reaching 10 km in thickness), because motions of the juvenile crust would result into a thin oceanic crust similar to the modern one (< 7km thick, except in oceanic plateaux).

B. Models supporting a horizontally immobile crust

In opposition to models that proposed the operation of modern-like plate tectonics during the Archean Eon, alternative models suggested a horizontally immobile archean crust called a stagnant lid (Bédard, 2024). These models are generally compatible with the accumulation of mafic magmas observed in most greenstone belts, and most of them interpret structural features observed in archean granitoid-greenstone terrains (e.g. dome-and-keel, folds and shear zones) as related to density-driven sinking of portions of the mafic crust into the hot archean mantle (Kisters et al., 2010; Van Kranendonk et al., 2009, 2014). Such vertical recycling from the base of the crust were called “delamination”, “dripping” or “sagduction” in the literature, and suggested that TTGs formed due to melting in intra-crustal to infra-crustal settings.

The models proposing a horizontally immobile crust were also highly criticised on a few points including their incapacity to explain water-fluxed melting of mafic lavas at the source of TTG magmatism. But in response, it was argued that the quantity of water required in the source of archean TTGs could have been deeply buried together with seafloor-derived rocks due to accumulation of juvenile lavas and sediments (Nebel et al., 2018; Hartnady et al., 2022). While completely immobile greenstone belts may not explain the generation of high-pressure TTG magmas at depths exceeding 50 km, vertical movements associated with delamination/dripping/sagduction processes were proposed as an alternative to subduction on the early Earth (Sizova et al., 2015; Bédard, 2018).

C. Hybrid models

Alleviating most drawbacks of the two previous types of models, hybrid models are considered as models supporting the possibility that intermittent subduction-like processes could be occasionally due to mantle upwelling in an archean lithosphere where delamination/dripping/sagduction process were also operational (Moyen et al., 2019; Laurent et al., 2024) (**Figure 2-18**). The hybrid models are based on numerical thermodynamic models (Moyen and van Hunen, 2012; Sizova et al., 2015) and explain most available geological features, including the different aspects of archean TTG composition. According to these models, slight horizontal movements in the lithosphere due to entrainment by convection of the underlying asthenosphere (Nebel et al., 2018), could generate plate boundaries and subduction-like processes that were rapidly terminated by detachment of the generally hot and relatively flexible slabs (Nebel et al., 2018; Chelle-Michou et al., 2022). In addition, an interplay between convections in the asthenosphere and density gradient through the lithospheric occasioned delamination from the bottom of mafic crusts as observed in numerical models (Sizova et al., 2015).

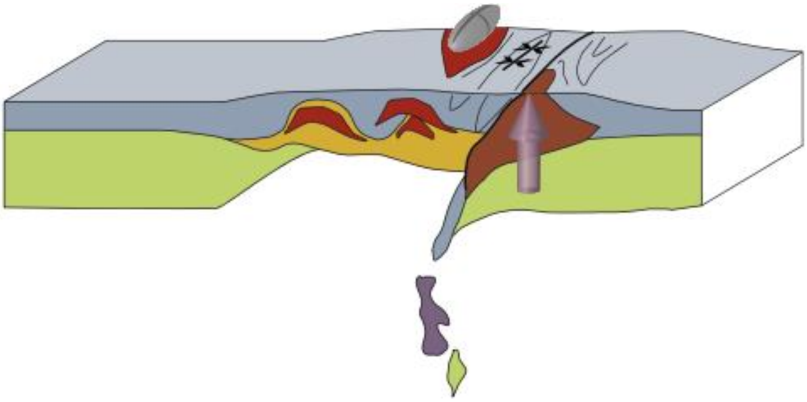

Figure 2-18. An example of a hybrid geodynamic model featuring both a subduction-like movement and a delamination (taken from Moyen et al., 2019).

2.2.3.3. Geodynamic debates and the contribution of stable isotope analyses

It remains challenging to discriminate TTGs that formed in subduction zones – even sporadic archean ones – from TTGs generated in infra-crustal to intra-crustal settings or those due to delamination processes (Vézinet et al., 2018; Hartnady et al., 2022; Tamblyn et al., 2023). Yet, discriminating TTGs formed in these different contexts remains important for understanding how the Earth evolved from a potentially different geodynamic regime to the modern plate tectonics (Nebel et al., 2018; Moreira et al., 2020; Bédard, 2024). Petrologically, these different geodynamic contexts would produce similar signatures in the elemental composition of produced TTGs melts, challenging the use of major or trace element compositions to determine the geodynamic setting in which TTG magmas formed. Therefore, as an alternative, stable isotopes have been growingly investigated to study archean geodynamic processes that led to the generation of TTG magmas (Cavosie et al., 2005; André et al., 2019; Deng et al., 2019; Smit et al., 2019).

When fractionated by hydrosphere-crust interactions at relatively low temperature, stable isotopes offer an opportunity to trace the recycling of the uppermost crustal rocks into the isotopically distinct mantle reservoir. Wilde et al. (2001) was among the first to evidence the recycling of seafloor-derived materials into the TTG source zone based on O isotope analyses in archean zircons. In addition, Si isotope analyses in bulk-rock samples or in separated zircons have shown that silicified lavas or cherts could represent the reworked seafloor-derived material (**Figure 2-19**) (Trail et al., 2018; André et al., 2019; Deng et al., 2019; Lei et al., 2023). While the isotopic signature of recycling processes is generally interpreted as subduction-related, isotopic data do not provide enough information to distinguish subduction from delamination-like processes (Vezinet et al., 2018; Hartnady et al., 2022). An important step in using isotopic data to understand archean geodynamic processes is the determination of the crustal position (shallow versus deep) of supracrustal rocks prior to their reworking into TTG source zone: the reworking of shallow rocks (<10 km deep) can only be explained by a movement resembling to subduction, whereas deep rocks (>20 km, Laurent et al., 2024) could be reworked in an immobile crust or due to delamination-like processes. Determining the crustal depth of reworked seafloor-derived rocks is complicated because the reworked mafic crust is not accessible anymore for stratigraphic characterisation. Considering that currently accessible greenstone belts are equivalent to the source of archean TTGs (Smithies et al., 2009; Moyen et al., 2019) is the only way of circumventing this issue. In this perspective, potential isotopic variations in the archean silica-rich rocks still accessible today would reveal the burial depth of the silicified archean seafloor that was reworked in TTG source zones.

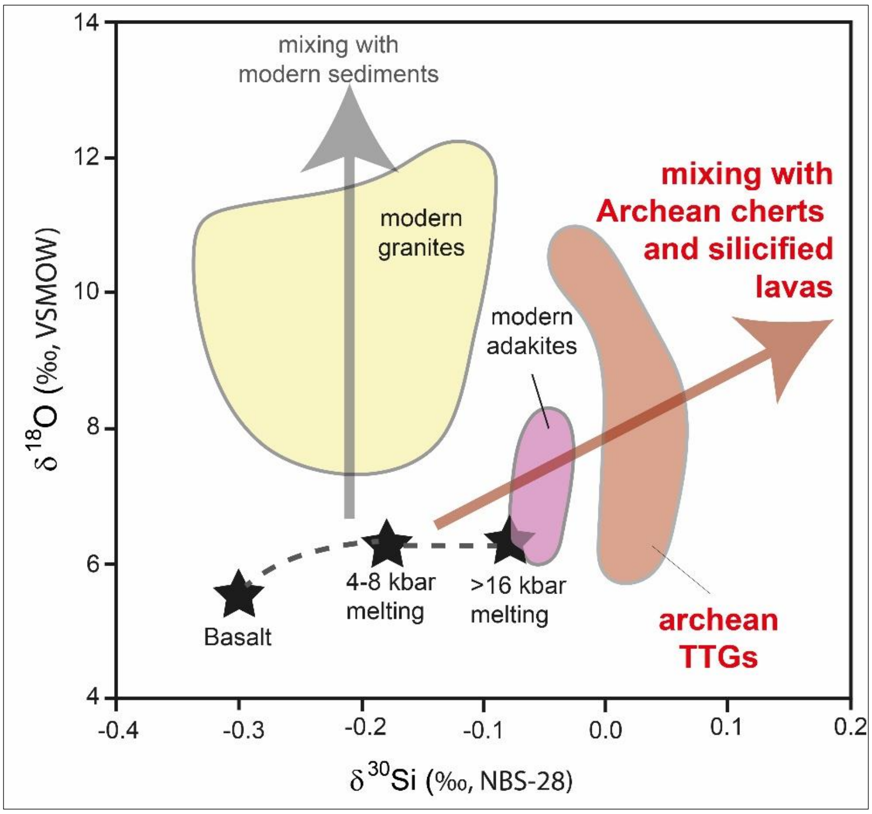

Figure 2-19. Binary plot of δ^{18}O and δ^{30}Si values in different granitoids, including modern TTGs (modified after Deng et al., 2019). The most important information shown on this figure is that the high δ^{30}Si and δ^{18}O of archean TTGs can only be explained by the mixing between silicified lavas or cherts derived from the seafloor and fresh mantle-derived basalts in the TTG source zone. The isotopic composition of modern adakites can be explained by melting of a basalt at pressures exceeding 16 kbar. The composition of other modern granites can be explained by sources containing both basalts and modern sediments with high δ^{18}O but mantle-like δ^{30}Si.

2.3. Archean seafloor-derived silica-rich rocks: types, origin, fluid records and environmental significance

This section presents the different types of silica-rich rocks occurring in archean cratonic terrains, the distinct geological processes explaining their formation, and their paleo-environmental significance with a focus on O isotope composition.

2.3.1. Classification and geochemistry of the seafloor-derived silica-rich rocks

Three different types of silica-rich rocks are present in Palaeoarchean terrains, namely silicified lavas, silicified clastic sediments and seawater-precipitated cherts. It is noteworthy that banded iron formations (BIF) (Aquila, 2024) could also be part of the Archean seafloor silica-rich rocks, but these rocks are not considered in this thesis as they are mostly absent or minor in the studied Onverwacht Group.

2.3.1.1. Seawater-precipitated cherts

Seawater-precipitated or sensu-stricto cherts are generally translucent and free of clastic features that would represent detrital relicts (Perry, 1967; Perry and Tan, 1972; Knauth and Lowe, 1978; Lowe et al., 2020) (**Figure 2-20**). The translucent cherts were called massive white cherts by Ledevin et al. (2019), who recognised also some massive detritus-free black cherts that they interpreted as chemical precipitates. The black cherts inherit their colour from oxides, sulphides and blackish carbonaceous materials that they contain and that could represent the earliest forms of life on Earth (Tice and Lowe, 2006; van Zuilen et al., 2007). Geochemically, seawater-precipitated cherts generally occur as pure silica, and their Al_2O_3 content was previously considered to constrain the contribution of detrital impurities (van den Boorn et al., 2010; Geilert et al., 2014). Seawater-precipitated cherts are commonly characterised by a high Y/Ho ratio (> 30) resulting in positive Y anomaly in REE+Y patterns that reminisce the REE composition of the modern seawater (Sugahara et al., 2010).

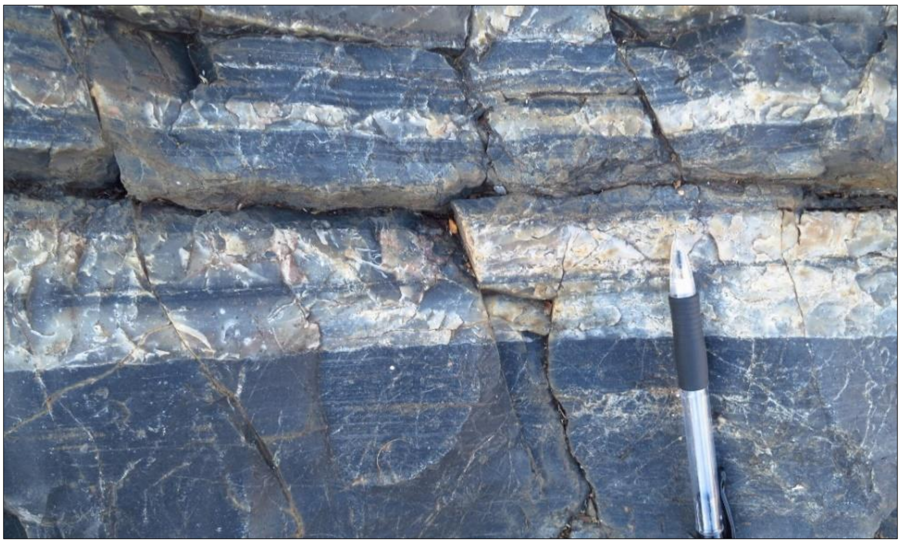

Figure 2-20. Black and white layers of seawater-precipitated cherts from the Barberton greenstone belt.

2.3.1.2. Silicified clastic sediments (or secondary cherts)

Silicified clastic sediments commonly preserve sedimentary features (e.g. cross-bedding and grading) that reveal their clastic nature (**Figure 2-21**). In the literature, these silicified sediments are called S-type cherts (or secondary cherts) and comprise silicified pyroclastites associated with submarine volcanism and clastic sediments derived from emerged terrains (Stanistreet et al., 1981; Lanier and Lowe, 1982; Hofmann et al., 2013). The mineralogy of these rocks is dominated by micro-quartz that is accompanied with muscovite, chlorite, oxides, carbonates and sulphides. Sometimes, coarse detrital phases such as quartz, feldspar and chromite can be distinguished from quartz-rich zones with discrete boundaries or recrystallised rims (e.g. Ledevin et al., 2014). Resistant accessory minerals like zircon and chromite are commonly preserved in the silicified sediments. These silicified sediments can carry also carbonaceous materials considered by some authors to represent fossilised microorganisms (Westall et al., 2001; Tice and Lowe, 2006; Hickman-lewis et al., 2018; Alleon and Summons, 2019). Geochemically, silicified clastic sediments display large variations in major element compositions due to differences in their degree of silicification. HFSE (e.g. Ti, Zr, Hf, Nb and Ta) were proposed to have remained almost immobile in the silicified sediments and have been used to study the nature and the provenance of the archean detrital sediments (Rouchon and Orberger, 2008; Rouchon et al., 2009).

Figure 2-21. Example of silicified clastic sediments (sandstones) from the Barberton greenstone belt, Kromberg Formation (taken from Ledevin et al., 2014).

2.3.1.3. Silicified lavas

Below cherts, whatever their type (seawater precipitated and silicified clastic sediments), the topmost part of submarine archean lavas (mafic or felsic) is generally silicified (Paris et al., 1985; Lowe and Byerly, 1986). Silicified lavas can extend up to several hundreds of meters below these chert layers and they can preserve their magmatic structure such as pillow morphologies (**Figure 2-22**), even if their mineralogy is replaced by secondary quartz-dominated assemblages. Quartz, muscovite, chlorite, carbonate, oxides and sulphides are common minerals observed in these rocks. It is noteworthy that the proportion of silica in the silicified lavas increases towards their contact with chert layers, with SiO_2 concentration ranging from near-magmatic compositions up to more than 95 wt.% SiO_2 (Hofmann and Harris, 2008; Abraham et al., 2011). Silicification is generally associated with an uptake of alkalies (K_2O, Rb, Cs, Ba) and other elements like U and Pb, whereas MgO, FeO and CaO are generally depleted in the silicified lavas due to the break-down of magmatic phases (Hanor and Duschac, 1990; Hofmann and Harris, 2008). In addition, silicification was proposed to increase slightly the LREE content of the lavas (Hofmann and Harris, 2008), although the REE and HFSE ratios are generally considered to have remained unchanged during silicification.

Figure 2-22. Silicified pillowed lavas from the Barberton greenstone belt, (taken from Furnes et al., 2004).

2.3.2. Formation of the archean silica-rich rocks

To explain the formation of the different types of silica-rich rocks described above, models involving precipitation of pure silica from seawater, diagenetic silicification, and hydrothermal silicification of pre-existing material (lavas and sediments) were proposed. These models are not exclusive and could have operated coevally.

2.3.2.1. Precipitation of silica from the archean seawater

Pure cherts could precipitate directly from the archean seawater (Siever, 1992; André et al., 2022) (**Figure 2-23**). Mechanisms that triggered the precipitation of silica are not well constrained, but the abundance of cherts in archean terrains has been interpreted to show that silica was close to saturation in the archean seawater (Siever, 1992; Ackerman et al., 2023). The dissolved silica that was precipitated could have originated from hydrothermal discharges (Paris et al., 1985; Sugitani, 1992), but a contribution of continentally eroded silica cannot be completely excluded (Trower and Fischer, 2019). After deposition of silica at the seafloor probably as amorphous silica or gel, cherts evolved to their microquartz-dominated texture at diagenetic stage (Kolodny and Epstein, 1976).

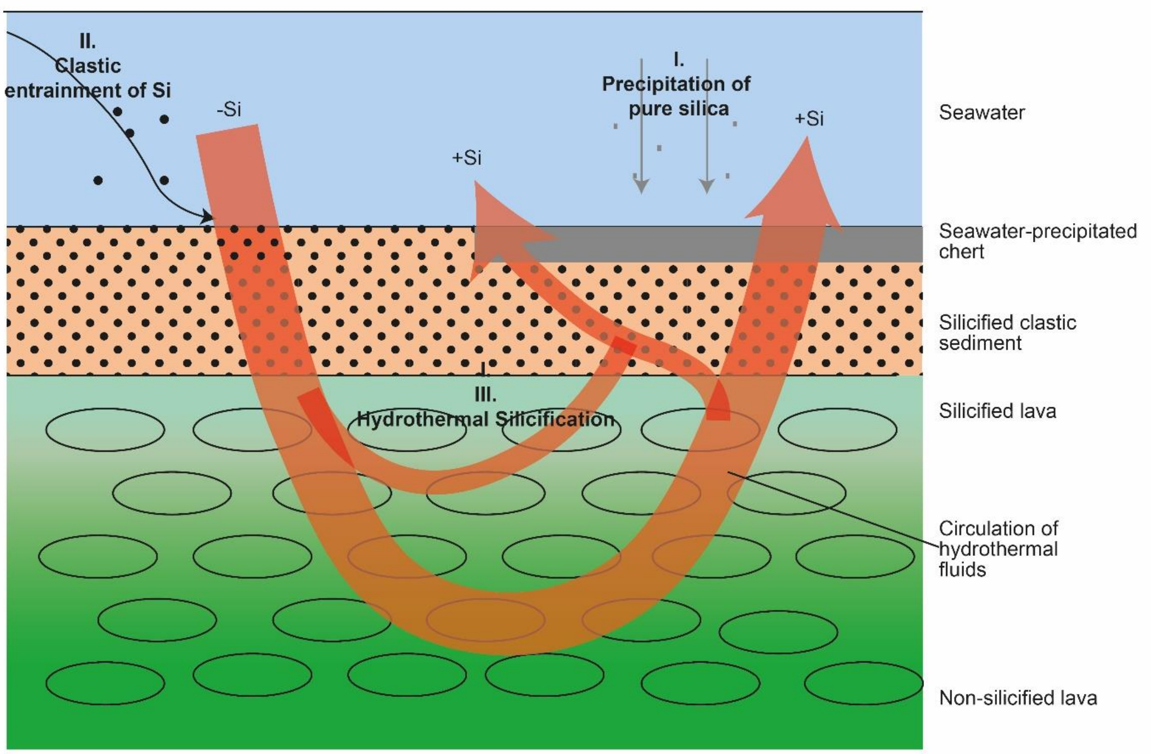

Figure 2-23. Formation of silica-rich rocks near the archean seafloor. The processes include (I) precipitation of pure silica, (II) silica entrainment by clastic precipitation and (III) deposition of silica from hydrothermal fluids. This cartoon was drawn based on the models of Paris et al. (1985) and André et al. (2022).

To explain the formation of silicified clastic sediments, Ledevin et al. (2014) suggested that these sediments could have scavenged Si from seawater. In this model, silica was proposed to have accumulated at the interface of suspended phyllosilicates. Subsequently, interaction between the precipitated silica and lithic phases at diagenetic stage could generate silicified clastic sediments (Rouchon and Orberger, 2008; Rouchon et al., 2009). In addition, Stefurak et al. (2014) proposed also that archean cherts could form as an accumulation of primary, sub-millimetric silica granules deposited on the seafloor. Consequently, cherts as we know them today represent a complex family of different rock types (i.e. silicified clastic sediments and seawater-precipitated silica) and this complexity must be considered in the use of their composition to reconstruct the properties of archean oceans (Lowe et al., 2020).

2.3.2.2. Hydrothermal silicification

Hydrothermalism (**Figure 2-23**) was proposed to explain the silicification of lavas and clastic sediments near the archean seafloor based on observations of hydrothermal breccia (**Figure 2-24**) and veins in these silicified rocks.

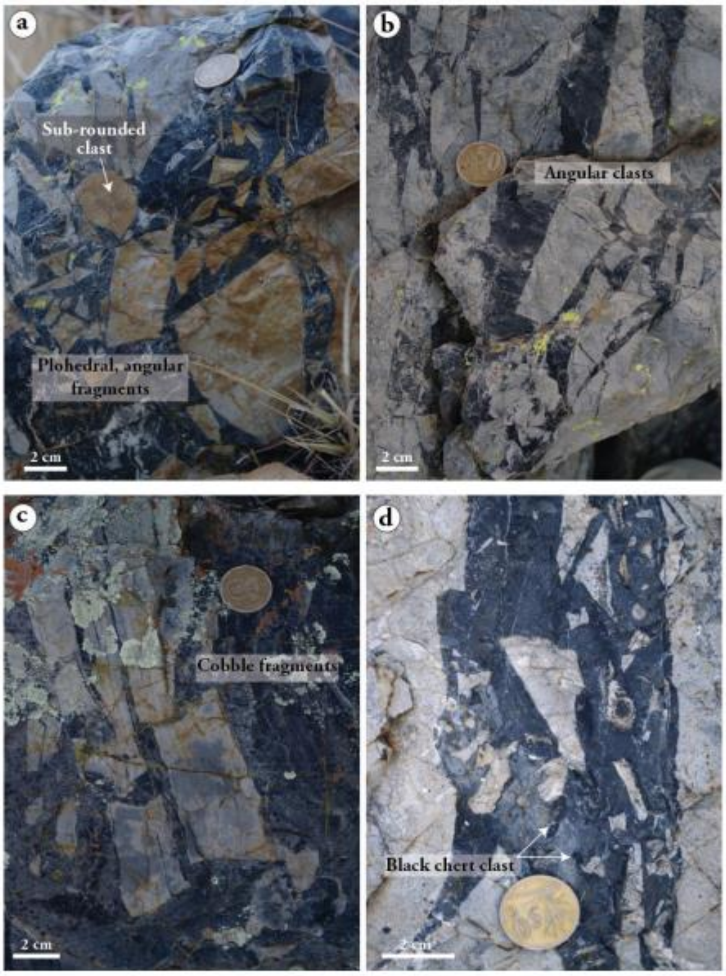

Figure 2-24. Brecciated cherts supporting the circulation of silica-rich hydrothermal fluids in the Barberton greenstone belt (Ledevin et al., 2015).

Hydrothermally silicified rocks are important for reconstructing the composition and the temperature of palaeoarchean hydrothermal fluids, which could reveal geochemical exchanges that operated between the palaeoarchean hydrosphere and the submarine lithosphere (Albarede et al., 2020). A low temperature (<150 °C) was constrained for the silicifying hydrothermal fluids based on O isotope analyses in these rocks and on their sequestration of elements like alkalis, Pb, Th and U, and on fluid inclusion studies (De Ronde et al., 1997; Hofmann and Harris, 2008). However, in some cases, other thermometric techniques such as chlorite chemistry or Raman spectroscopy of carbonaceous materials were used to suggest that hydrothermal silicification could have also operated at temperatures as high as 300 °C (Cloete, 1991; Johnson and Wing, 2020; Zakharov et al., 2021). Abraham et al. (2011) analysed Si and O isotope compositions of silicified lavas and proposed that silicification could be explained by deposition of silica from a descending flux of warming seawater-derived fluids, and an ascending flux of cooling hydrothermal fluids derived from the deeper within the crust. These authors suggested also that the dissolved silica could originate from interactions between hydrothermal fluids and deep crustal rocks at a temperature that exceeded 150 °C. Importantly, Brengman and Fedo (2018) proposed that hydrothermal silicification could communicate a signature reminiscing mixing between seawater and hydrothermal fluids in the REE pattern of silicified lavas and clastic sediments characterised by a positive Eu anomaly.

2.3.3. Environmental significance of chert composition

2.3.3.1. Silica-rich rocks as proxies for Early Earth environment

Silica-rich rocks are among the best proxies for the composition and temperature of the archean seawater and hydrothermal fluids (Perry and Lefticariu, 2007). Although the archean seawater must have been instrumental for the development of earliest forms of life on Earth, its temperature remains highly debated. Constraining unambiguously the temperature of the archean seawater is important for our investigation of the archean atmosphere because the temperature of seawater is an important parameter for numerical estimations of the concentration of greenhouse gases (e.g. CO_2 and CH_4) in early Earth's atmosphere (Catling and Zahnle, 2020; Charnay et al., 2020; Kasting et al., 2006). The geochemical composition of the archean seawater remains also poorly constrained, although we know that the an anoxic archean atmosphere must have co-existed with a reduced seawater (Herwartz et al., 2021). Due to their potential record of seawater composition and temperature, archean silica-rich rocks represent an important asset for understanding the environment that prevailed on the early Earth. A continued investigation of chert composition can therefore improve the knowledge of the way the initially reduced atmosphere progressively became oxidised on the early Earth.

2.3.3.2. Secular evolution of O isotopes and its different interpretations

The global compilation of O isotope composition in cherts displays a secular evolution from low $\delta^{18}O$ values of 15–23‰ in palaeoarchean cherts to 30–40‰ in modern cherts (**Figure 2-25**). This evolution has been interpreted in three different ways.

Firstly, this evolution was proposed to reflect the evolution of seawater composition from a low $\delta^{18}O$ (-10 to -5‰) during the Palaeoarchean Era to the modern seawater's $\delta^{18}O$ of ~0‰, with a mostly constant temperature of seawater over time. While this proposition was initially based on analyses of cherts (Perry and Tan, 1972), recent triple O isotope measurements in partially silicified lavas from the Nuvvuagittuq greenstone belt support the proposed low-$\delta^{18}O$ values of archean oceans (Bindeman and O'Neil, 2022). The increase of the $\delta^{18}O$ of seawater since the archean Eon was initially considered to result from juvenile mantle-derived water being progressively added to seawater while part of the hydrosphere was also continuously recycled towards the mantle (Perry and Tan, 1972). Alternatively the low-$\delta^{18}O$ values proposed for archean oceans was also ascribed to shallow oceans and emerged ridge systems that resulted in a reduced input of high-temperature hydrothermal fluids into archean oceans compared to modern analogues (Kasting et al., 2006; Jaffrés et al., 2007).

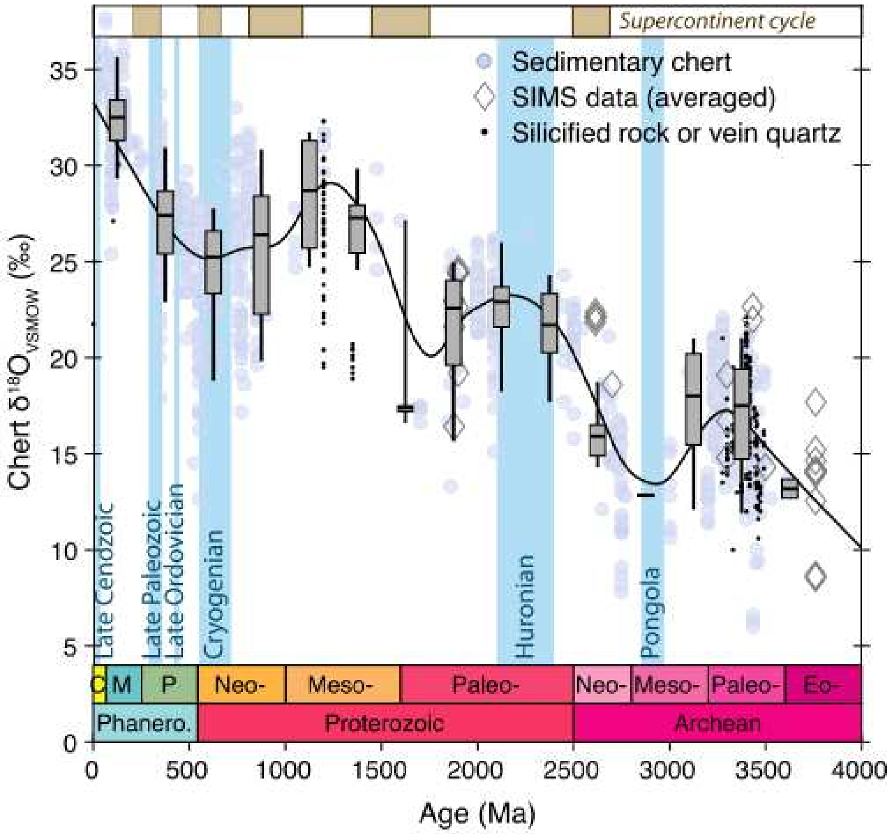

Figure 2-25. Secular evolution of O isotope composition of cherts since the Eoarchean Era (modified after Tatzel et al., 2022).

Secondly, an evolution of seawater temperature from ~70°C during the palaeoarchean Era to <10°C on the modern Earth was also proposed to explain the secular evolution of $\delta^{18}O$ values in cherts over time (Knauth and Lowe, 1978, 2003; Lowe et al., 2020; Robert and Chaussidon, 2006). All the studies that reached this conclusion considered that the O isotope composition of archean seawater was not different from the O isotope composition of modern oceans (Peters et al., 2020). This was mainly based on the fact that archean low-$\delta^{18}O$ oceans have not been reproduced by mass balance models of O isotope compositions of Earth's hydrosphere (e.g. Sengupta and Pack, 2018).

Lastly, a global diminution of diagenetic temperatures over time due to secular cooling of the Earth was also proposed to explain the variation of O isotope compositions of cherts (Kolodny and Epstein, 1976). Recent triple O isotope studies in archean cherts demonstrated that post-depositional interactions with diagenetic and hydrothermal fluids must have modified the isotopic composition of seawater-precipitated cherts, complicating the use of cherts to reconstruct the O isotope composition and the temperature of archean oceans (Sengupta et al., 2020; Yanchilina et al., 2020; Zakharov, et al., 2021; Ibarra et al., 2022; Zakharov et al., 2023). In modern cherts, Ibarra et al. (2022) observed a decrease in $\delta^{18}O$ and an increase in $\Delta'^{17}O$ with increasing burial depth (and therefore diagenetic temperature), showing that the post-depositional evolution of archean cherts must have caused important modifications of their O isotope composition. The relatively low $\delta^{18}O$ of archean cherts was also proposed by Tatzel et al. (2022) based on a numerical model to have resulted from a relatively hotter crustal geotherm compared to the modern one. Reconstructing the composition of palaeoarchean pore fluids including hydrothermal and diagenetic fluids that were responsible for the final isotopic composition of any chert (including archean ones) is probably the next step ahead in order to understand the composition and temperature of the archean seawater, as preserved in the O isotope composition of cherts.

2.4. Summary and bridge to next chapters

Three important pieces of information should be retained from this review part. Firstly, the composition of hydrothermally silicified rocks (lavas and clastic sediments) and seawater-precipitated cherts may constrain the composition and the temperature of archean hydrothermal fluids and seawater that contributed to their formation near the seafloor. Secondly, the O and Si isotopic composition of seafloor-derived silica-rich rocks can be tracked in TTGs to explain geological processes that recycled the seafloor during the Archean Eon. Thirdly, the 3.5-3.1 Barberton granitoid-greenstone terrain comprises silicified lavas, cherts and TTGs that allow us to explore the compositions of seawater and hydrothermal fluids as well as the processes that recycled the palaeoarchean seafloor.

Since metamorphic and weathering processes were demonstrated to have affected the studied Barberton terrain and could significantly modify the composition of Archean hydrothermal fluids, we decided to primarily evaluate the effects of metamorphism and weathering on the composition of investigated silicified lavas and cherts.

Part III.

Petrography, geochemistry and thermal evolution of silicified lavas and cherts from the palaeoarchean (3.5-3.2 Ga) Barberton greenstone belt: Disentangling the effects of near-seafloor silicification from subsequent modification

Manuscript in preparation. Co-authors of this study are Jean-Francois Moyen, Maud Boyet, Johanna Marin-Carbonne, Gary Stevens and Nicolas Olivier.

Abstract

Hydrothermally altered rocks (lavas and sediments) derived from the seafloor offer a unique opportunity to investigate geochemical interactions that operated between the hydrosphere and the lithosphere on the early Earth. However, post-depositional processes including metamorphism and late-stage interactions with other crustal fluids can partially or completely erase the original signature of hydrosphere-lithosphere interactions. Here we study silicified lavas and sediments from the Barberton greenstone belt that were hydrothermally altered near the palaeoarchean seafloor by seawater-derived hydrothermal fluids. We use petrographic, geochemical and thermometric data to distinguish the effects of near-seafloor hydrothermal silicification processes from those of subsequent fluid-rock interactions. We show that silicification occurred near the palaeoarchean seafloor at low temperature (< 150°C). A subsequent regional metamorphic event at higher temperature (> 280°C) has modified the mineralogy of the silicified rocks with re-crystallisation of some low-temperature phases such as clay minerals into higher temperature phases such as chlorite and muscovite. We further use La-Ce and Sm-Nd isotope systematics to demonstrate that interactions with post-archean meteoric fluids affected the composition of Ce due to its redox sensitivity but did not exert a significant influence on most immobile elements. By normalising the geochemistry of silicified lavas against fresh lava compositions, we show that the silicified rocks notably sequestrated K, Rb, Ba, U, Th and LREE, whereas Mg, Ca, Na and Fe were systematically removed by the silicifying fluids. Despite regional metamorphism and crustal fluid circulation, silicified lavas and clastic sediments of the Barberton greenstone belt still preserve some information about palaeoarchean near-seafloor hydrothermal fluids. Unlike what was recently proposed for other archean terranes, our data demonstrate that near-seafloor hydrothermalism did not communicate a seawater-like signatures (e.g. high Y/Ho ratios) to the silicified rocks of the Barberton greenstone belt. Provided that alterations due to metamorphic or other late-stage fluids are constrained, trace element geochemistry remains a powerful tool for distinguishing potential orthochemical cherts from silicified lavas and clastic sediments in palaeoarchean terranes.

Keywords: Hydrothermal fluid, Oxidised fluids, Palaeoarchean seafloor, Regional metamorphism, Silicification.

3.1. Introduction

Hydrothermal circulation of seawater-derived fluids modifies the mineralogical and geochemical composition of the upper oceanic crust and is an important component of elemental exchange between the hydrosphere and the lithosphere (Staudigel et al., 1981; Elderfield et al., 1999; Bach and Früh-Green, 2010; German and Seyfried, 2013; Coogan and Gillis, 2018b). Elemental exchange between the Phanerozoic ocean and the underlying crust has been established by measuring the mineralogical and geochemical compositions of ophiolite samples and from drill cores of modern altered oceanic crust (Alt and Teagle, 1999; Alt et al., 2010; Zhang and Smith-Duque, 2014). The geochemical composition of modern seafloor vent fluids is also measured from fluids that are sampled directly from the seafloor (Elderfield et al., 1999; Zakharov et al., 2021). The alteration of the topmost oceanic crust (up to 800 m below seafloor) is known to occur at temperatures that are lower than 200°C (Hart and Staudigel, 1982; Gillis and Robinson, 1990; Alt et al., 2010). Contrastingly, the lowermost oceanic crust (> 2000 m) undergoes higher-temperature alterations ranging from 300°C to 600°C) due to the percolation of fluids initially derived from seawater but heated at greater depth (Gillis and Robinson, 1990; Alt et al., 2010). Such knowledge of modern and Phanerozoic hydrothermal fluids and alteration processes makes it possible to study much older altered rocks that potentially represent oceanic crust for quantifying the chemical exchange that occurred between the hydrosphere and the lithosphere during the Archean Eon. Although greenstone belts dominated by ultramafic to mafic lavas are not universally established as fractions of the archean oceanic crust (Bickle et al., 1994), they have allowed investigating hydrosphere-lithosphere interactions on the archean Earth (Hofmann and Harris, 2008; Brengman and Fedo, 2018; Hofmann et al., 2022).

On the palaeoarchean Earth (3.6-3.2 Ga), the crust was dominantly covered with seawater (Bindeman et al., 2018) and displayed higher thermal fluxes than today (Tamblyn et al., 2023). Consequently, hydrosphere-lithosphere interactions were more intense than over the Phanerozoic Eon. Most remnants of the archean crust, as identified in greenstone belts worldwide, comprise silicified sediments (or secondary cherts) and lavas that were ascribed to interactions of the crust with seawater (Duchac and Hanor, 1987; Paris et al., 1985; Katijima et al., 2001; Brengman and Fedo, 2018; Hofmann et al., 2022). Associated with these rocks are also orthochemical cherts (or stricto sensu cherts) formed by direct precipitation from seawater (Knauth and Lowe, 1978; Marin-Carbonne et al., 2011; Ledevin et al., 2019; Lowe and Byerly, 2020). The water-rock interactions that drove the silicification of archean seafloor rocks (lavas or sediments) were also very important because they probably created the environment within which chemosynthetic life could flourish and facilitated its preservation though time (Javaux and Marshall, 2005; Hofmann and Harris, 2008; Alleon et al., 2021).

The mineralogical assemblages recorded by archean silicified rocks, and the estimates of temperatures of equilibration derived from these, have commonly been ascribed to original interactions with seawater-derived fluids (Rouchon and Orberger, 2008; Rouchon et al., 2009; Johnson and Wing, 2020). However, several authors believe that such a relationship cannot be so simple, and that subsequent regional metamorphism must have modified the primary, near seafloor hydrothermal signature (Xie et al., 1997; Hofmann et al., 2013; Grosch, 2018). Indeed, commonly used thermometric proxies for estimating the temperature of the hydrothermal silicification (e.g. chlorite chemistry, Raman spectroscopy of carbonaceous materials, fluid inclusion thermometry and oxygen isotope fractionation) can all be notably modified by regional metamorphism at temperatures exceeding 300 °C (Farber et al., 2016; Grosch, 2018; Deutschmann et al., 2022). Additionally, post-archean fluids related to weathering (e.g. Lowe and Byerly, 2007b) may have modified the geochemical composition of these rocks. Such effects have been highlighted by measuring the La-Ce isotope systematics in banded iron formation from the Moodies Group in the Barberton greenstone belt (Hayashi et al., 2004; Bonnand et al., 2020). In fact, cerium is a redox-sensitive element, and the La-Ce radiometric system can therefore be used as a proxy for tracing post-archean weathering effects.

We have investigated five different stratigraphic sections extending from silicified lavas at the base to silicified sediments or cherts at the top in the Onverwacht Group of the Barberton greenstone belt. Several researchers have demonstrated that the silicification of these rocks was due to interaction with seawater-derived hydrothermal fluids near the palaeoarchean seafloor (Paris et al., 1985; Lowe and Byerly, 1986; Duchac and Hanor, 1987; Hofmann and Harris, 2008; de Wit and Furnes, 2016). These rocks can therefore reveal the nature of hydrosphere-lithosphere interactions on the palaeoarchean Earth. The present study is aimed at: (1) petrographically and mineralogically characterizing the silicified sediments or cherts and silicified lavas; (2) constraining the mineralogical and geochemical influence of regional metamorphism and post-archean meteoric fluid circulations in these rocks; and (3) tracing the preserved geochemical signature of elemental exchange between the paleoarchean seawater-derived hydrothermal fluids and the lithosphere.

3.2. Geological setting

3.2.1. Regional geology

The 3.5-3.2 Ga Barberton greenstone belt (**Figure 3-1**) is located in the NW part of the Kaapvaal craton in Southern Africa. The Onverwacht Group in which the present study was conducted is the lowermost stratigraphic subdivision of the Barberton greenstone belt and largely consists of mafic to ultramafic volcanics that emplaced in a sub-oceanic setting (Armstrong et al., 1990; Lowe and Byerly, 1999; Byerly et al., 2019). It is overlain by large sedimentary successions belonging to the 3.3-3.2 Ga Fig Tree and Moodies groups (**Figure 3-1**) (Heubeck and Lowe, 1994; Heubeck, 2019; Drabon and Lowe, 2021). In the Onverwacht Group, some lava flows are silicified at their tops due to the circulation of seawater-derived hydrothermal fluids and overlain by sedimentary layers (Paris et al., 1985; Hofmann and Harris, 2008; Hofmann et al., 2013). The sedimentary layers are largely dominated by variably silicified clastic sediments, commonly identified as cherts, *lato-sensu*, although some detritus-free orthochemical cherts (or *stricto sensu* cherts) were also locally identified (Knauth and Lowe, 1978; Ledevin et al., 2019). Occasionally, non-silicified sediments are also preserved within the Onverwacht Group (Dziggel et al., 2002). The clastic sediments, silicified or not, are generally mafic in composition but felsic sediments occur also in some stratigraphic sections such as the Buck Reef Unit and the Theespruit rocks (Lanier and Lowe, 1982; Hofmann et al., 2013). In the rest of this paper, the term chert relates to silicified clastic sediments that are dominated by micro-quartz; it excludes clastic sediments that are not dominated by this micro-quartz (> 80 vol.%). Irrespective of the composition of original clastic sediments (i.e. felsic or mafic clasts), cherts are generally differentiated on the basis of their macroscopic appearance as grey, black and black-and-white chert (Lanier and Lowe, 1982; Hofmann et al., 2013; Ledevin et al., 2014).

A major geodynamic event deformed and metamorphosed the Onverwacht Group some 3.2 Ga ago. This age was determined by dating garnet, monazite and titanite from lower Onverwacht Group rocks in the Southern part of the belt which were subjected to high-pressure amphibolite facies conditions of ca 7.5 kbar and 550°C (Diener et al., 2005; Cutts et al., 2015). Despite folding, the portions of the Onverwacht Group that occurs above the Komati fault are generally agreed to represent a > 9 km-thick continuous and seafloor-deposited volcano-sedimentary succession in the Onverwacht anticline that comprises studied sections (Lowe and Byerly, 2007a; Hofmann and Harris, 2008). This succession includes four different geological formations, Komati, Hooggenoeg, Kromberg and Mendon formations (**Figure** 3-1) (see recent review by Byerly et al., 2019). Notably, the Sandspruit and Theespruit formations occurring below the Komati fault experienced burial to at least 25km during the 3.2 Ga amphibolite facies event and represent a much deeper crustal section that has been exhumed along the Komati fault at 3.2 Ga (Xie et al., 1997; Cloete, 1991; Tice et al., 2004; Kisters et al., 2003; Stevens and Moyen, 2007). Despite these structural complexities each one of these five formations is constituted by stratigraphic members that are typically made of one or several lava flows (generally with a silicified top) and overlying sediments (Hofmann and Harris, 2008; Byerly et al., 2019).

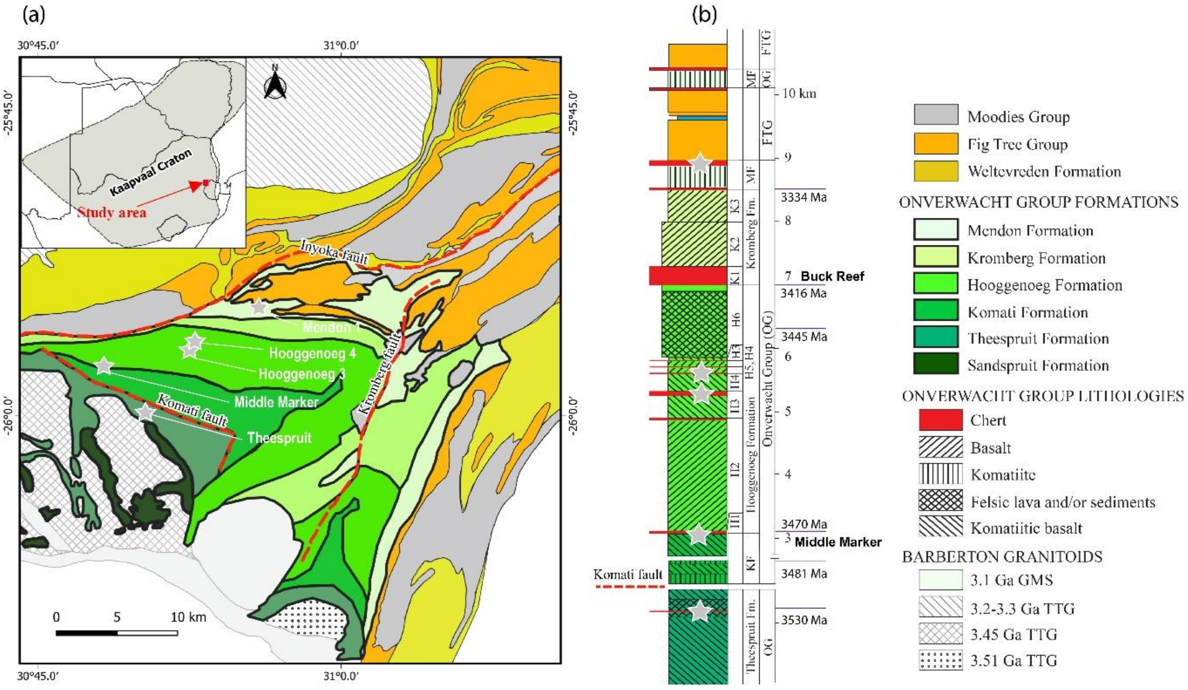

Figure 3-1. (a) Simplified geological map of the Barberton greenstone belt and (b) Stratigraphic succession of the central part of the Barberton greenstone belt modified after Anhaeusser (1981) and Hofmann and Harris (2008). Grey stars indicate the position of the studied sections on the map and on the stratigraphic succession.

3.2.2. Studied sections and samples

Studied samples originated from five different stratigraphic sections (**Figure 3-2**), which include both sedimentary layers and silicified lavas. The lithologies featured in **Figure 3-2** are based on petrographic descriptions at outcrop, hand-specimen and thin-section scales, and each section is named after the stratigraphic unit to which it belongs. Drone images of the studied sections are available in **Supplementary Figures A-1 to A-4**.

3.2.2.1. The Theespruit section

The Theespruit section was previously described by Hofmann and Harris (2008) and is part of the amphibolite facies portion of the Onverwacht Group. The felsic rocks of the Theespruit section were dated at ~3.52 Ga by Kröner et al. (2016). It is exposed in a river bed within the Tjakastad locality that was previously studied for lithological and mineralogical compositions by Diener et al. (2005) and Hofmann and Harris (2008). From the base upward, this section consists of pillowed and schistose amphibolitic lavas (> 30 m), a black chert layer (< 1 m) and schistose felsic sediments (~14m) (**Figure 3-2a**).

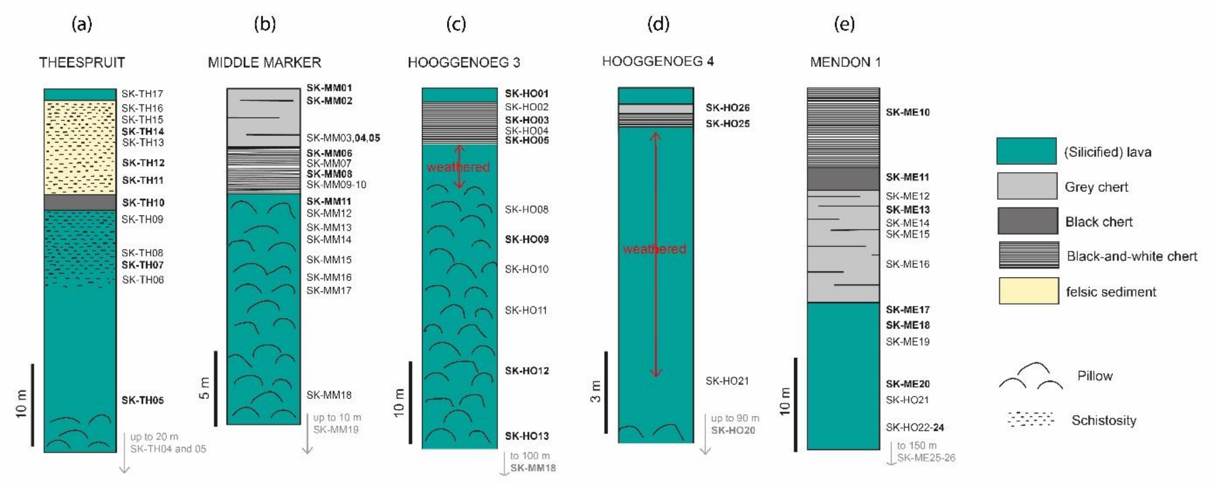

Figure 3-2. Detailed lithostratigraphic logs of the studied localities with an approximate location of collected samples: (a) Theespruit section, (b) Middle Marker section, (c) Hooggenoeg 3 section, (d) Hooggenoeg 4 section, e) Mendon 1 section. The location of each stratigraphic section on the geological map and stratigraphic succession of the Barberton greenstone belt are shown in Figure 1. In bold are samples that were selected for major and trace element, isotopic and thermometric analyses.

3.2.2.2. The Middle Marker section

The Middle Marker section comprises ~3.48 Ga old cherts and silicified lavas situated at the top of the Komati Formation (**Figures 3-1** and 3-**2b**). Our Middle Marker samples were collected from a ~ 7 m portion of Chert unit and from more than 30 m of the underlying silicified lavas (**Figure 3-2b**). The cherts were interpreted by Lanier and Lowe (1982) to represent silicified volcaniclastic components that were initially deposited in a relatively shallow sub-aqueous environment. These sediments currently occur as grey, black and black-and-white cherts that preserve primary sedimentary structures indicating a clastic origin.

3.2.2.3. The Hooggenoeg 3 and 4 sections

These two sections are located less than 800 m from one another although they respectively represent the top of Hooggenoeg 3 and 4 members (**Figure 3-1**). The emplacement age for these sections is bracketed between the 3.47 Ga age of detrital zircons from Hooggenoeg 4 chert and 3.41 Ga age felsic lavas from the Buck Reef Unit (**Figure 3-1**) (Armstrong et al., 1990; Laurent et al., 2020). The Hooggenoeg 3 section is made of >100 m-thick silicified and ocelli-bearing pillowed lava together with overlying ~6m-thick black-and-white cherts (**Figure 3-2c**) (Hofmann and Harris, 2008). Hooggenoeg 4 section includes a ~1m thick chert layer comprising grey and black-and-white chert layers as well as a lava sequence exceeding 100 m of thickness (**Figure 3-2d**). Notably, 5 to more than 8 m of the topmost lava underlying both Hooggenoeg 3 and Hooggenoeg 4 cherts were affected by a high degree of surface weathering such that they could not be sampled for the present study.

3.2.2.4. The Mendon 1 section

The Mendon 1 section (also called Msauli or Umsoli section in the literature; e.g. Heinrichs, 1984; Lowe and Byerly, 1986; Rouchon and Orberger, 2008) is named after the Mendon 1 Chert Unit situated at its top. The sedimentary portion of this section is slightly thicker than 20 m and comprises black-and-white, black and grey cherts that were previously interpreted to represent silicified volcano-clastic sediments (**Figure 3-2e**) (Stanistreet et al., 1981; Heinrichs, 1984; Rouchon and Orberger, 2008; Trower and Lowe, 2016). The deposition of these cherts was estimated to have occurred around 3.33 Ga based on U-Pb geochronology (Decker et al., 2015). These cherts are underlain by silicified lava units displaying various textures that include the hydrothermally induced zebraic texture as well as the magmatic spinifex texture (Hanor and Duschac, 1990; Hofmann and Harris, 2008). We sampled each chert units together with top 15 m occurring directly below the Mendon 1 chert layer for the present study (**Figure 3-2e**).

3.4. Materials and methods

After lithological description of the outcrops, representative samples were collected from each of the five different sections (**Figure 3-2**). The samples were cut into cm-thick rock slabs of which at least one slab per sample was dedicated to thin section and fine powder preparation. The prepared thin sections were used for petrographic investigation using a polarising microscope and a Scanning Electronic Microscope coupled with an Energy Dispersive

Spectrometer. A tungsten-carbide jaw crusher and an agate ball mill were used for rock powder preparation. Then, different analytical techniques were applied for the acquisition of reported mineralogical and geochemical data (i.e. Raman Spectroscopy, EPMA, XRF, ICPMS, MC-ICPMS, SIMS and TIMS).

3.4.1. Raman spectroscopy and the carbonaceous material thermometer

We acquired 113 Raman spectra of carbonaceous materials contained in six different chert samples (SK-MM02, SK-MM06, SK-HO02, SK-HO03, SK-HO25 and SK-ME11) representative of the Komati, Hooggenoeg 3, Hooggenoe 4 and Mendon 1 sections. These analyses were performed using InVia confocal Raman micro-spectrometer equipped with a 532 nm diode laser, a Peltier-cooled CCD detector of 1024 x 256 pixels, an automatized stage and a Leica DM 2500M optical microscope at Laboratoire Magmas et Volcans of Clermont Auvergne University. Before analytical sessions, the spectrometer was calibrated to a reference Si peak at 520.5 ± 0.5 cm^{-1}. Analyses were carried out on ca. 30 µm-thick polished thin sections and targeted carbonaceous materials that were covered by 4-6 µm of quartz in order to avoid detecting deteriorations due to polishing. Acquisition time was calibrated at 6x15s for each point. During acquisition, the laser beam passed through a 100X microscope objective under standard confocality (slit aperture set to 65 µm) with a final power of 1 to 4 mW at the analysed surface. Spatial resolutions of 1 to 3 µm and a spectral resolution better than 1 cm^{-1} was achieved. We used Wire 4.2 software to perform the following actions: (1) correct for phosphorescence effects by applying a linear baseline, (2) crop only the 1100 - 1850 cm^{-1} from the original spectra (acquired between 500 and 2400 cm-1), (3) deconvolute and fit the different curves corresponding to carbonaceous material peaks by a series of iterative calculations, and finally (4) measure the areas occupied by each peak.

The estimation of equilibrium temperature based on the Raman spectroscopy of carbonaceous materials relies on the release of heteroatoms and hydrogen as well as the progressive reorganisation of carbonaceous materials into crystalline graphite when subjected to continuously elevated temperatures (Beyssac et al., 2002). At low temperature (100 to 600°C), the Raman spectra of carbonaceous materials display the G peak of graphite at a shift of ~1580 cm^{-1} and four D peaks representing disorganised carbon at ~1350 cm^{-1} (D1), ~1610 cm^{-1} (D2), ~1450 cm^{-1} (D3) and ~1190 cm^{-1} (D4) respectively. Progressive reductions of D peaks and enhancement of the G peak during elevations of the temperature allowed Beyssac et al. (2002) to propose a thermometer that is applicable to samples that have experienced temperatures ranging between 300 and 600°C. This calibration is expressed as follows: T (°C) = -445*R2+641, where R2 is given by R2 = D1/(D1+D2+G), and spectral values (i.e. D1, D2 and G) are considered as integrated areas for the respective peaks (Beyssac et al., 2002).

3.4.2. Secondary ion mass spectrometry (SIMS)

The CAMECA 1280 HR SwissSIMS instrument was used for oxygen isotope analyses in quartz and carbonate phases at the University of Lausanne. Three quartz-carbonate couples from SK-ME18 (Mendon 1 section) and one couple from SK-MM11 sample (Komati section) were selected for 4 to 7 carbonate spots and 7 to 11 quartz spot analyses by SIMS. These analyses were conducted from 3 x 4 cm portions of thin sections that were pressed into indium mounts together with quartz and carbonate reference materials. The topography of the indium mounts did not exceed 5 microns of elevation difference, as determined with a Brucker GTA-K white light interferometer. At 10 kV, a 1.3 nA primary beam of Cs+ ions was focused to a 15-micron-sized spot diameter. The mass resolving power was set at 2400 using a 122 µm wide entrance slit, and 1 µm wide multi-collections exist slits to resolve mass interferences. Each O isotope analysis lasted ~3 minutes that included 30 s of pre-sputtering, followed by automatic signal optimization by centring the secondary beam, and 20 cycles of 5 sec of secondary ions collection. The data initially obtained as $^{18}O/^{16}O$ ratios were converted into the classical delta-notation relative to VSMOW reference [$\delta^{18}O = 1000*[(^{18}O/^{16}O_{sample}) - (^{18}O/^{16}O_{VSMOW})] / (^{18}O/^{16}O_{VSMOW})$]. Repeated analyses of UNIL-Q1 reference quartz allowed correcting quartz analyses for instrumental mass fractionation and provided an external error range (2 SD) of 0.35‰ for $\delta^{18}O$. Additionally, repeated analyses of the UNIL-C1 (2 SD = 0.46‰), UNIL-C4 (2 SD = 0.31‰) and KPIK (2 SD = 0.54‰) reference materials allowed correcting carbonate analyses for instrumental mass fractionation considering fractionation effects due to different major element compositions (i.e. calcite *versus* ankerite) (Rollion-Bard and Marin-Carbonne, 2011; Śliwiński et al., 2018). Details on these corrections can be found in **Supplementary Table A-1**.

3.4.3. Electron probe micro-analyses (EPMA)

Major and minor element compositions were measured for (1) the carbonate grains analysed by SIMS, and (2) for chlorites from five different samples (SK-MM02, SK-MM05, SK-ME24 and SK-ME13) using a CAMECA SX Five EPMA instrument at the University Clermont Auvergne. As required by the XMapTools software that was used to process these data (Lanari et al., 2014), we coupled x-ray maps of areas reaching 350 x 350 µm with qualitative analyses of specific zones within these areas. Qualitative analyses were performed with a current of 15 nA, an accelerating voltage of 15 kv and a counting time of 20 s. For acquisition of x-ray maps, a 100 nA current was applied with a dwell time of 0.1 s and a step size of 1 µm. The following internal standard were used for calibration in quantitative analyses: albite for Si, forsterite for Mg, fayalite for Fe, orthoclase for K and Al, anorthite for Ca, rhodonite for Mn and calcite for Ca.

3.4.4. Major and trace element analyses

Twenty-nine representative samples were analysed for major and trace elements at Stellenbosch University and Clermont Auvergne University, respectively. The volatile content or loss on ignition (LOI) was calculated after keeping small portions of rock powders in a muffle furnace at 1000°C for a duration of 30 minutes. For analyses of the non-volatile major elements, homogeneous discs were prepared by mixing 0.5 g of powder with 5 g of flux (32.8% $LiBO_2$ + 66.7% $Li_2B_4O_7$ + 0.5% LiI) and fusing the mixture at 1000 °C in an automatic Claisse M4 Gas Fusion instrument. A PAN analytical Axios Wavelength Dispersive x-ray fluorescence (XRF) spectrometer was used to quantify the major element concentrations at Stellenbosch University. Several reference materials (BE-N, JB-1, BHVO-A, JG-1, HUSG-1 and WITS-G) were analysed repetitively along with the samples and returned a 2 SD value that was lower than 0.7 wt.% for SiO_2 and Al_2O_3, and lower than 0.1 wt.% for all the other major oxides. The reference materials allowed estimating an accuracy of ±5 % range for the reported major element compositions (see **Supplementary Table A-2**).

Trace element concentrations were analysed from acid-dissolved powders using an ICP-MS 8900 at Laboratoire Magmas et Volcans, Clermont Auvergne University. Nearly 50 mg of powder and 200 mg of crystalline NH_4HF_2 were weighted into Savillex beakers and kept for 24h at 220 °C in a furnace. After receiving 1 ml of HNO_3 14N, the beakers were kept at 90 °C overnight and dried out on a hot plate. Three successive series of dissolution in 0.5 ml HNO_3 14N at 90 °C and drying on a hot plate allowed getting rid of residual F complexes. The samples were then completely dissolved in 30-40 ml of HNO_3 7N of which an aliquot corresponding to 2.5 % of the dissolved rock powder was taken for analysis. After complete evaporation, the aliquot was finally dissolved in solution made of HNO_3 0.4M - HF 0.05M and enriched to 2 ppm of In, Bi and Sb that served for monitoring the signal stability during the sequences of analysis and correcting the drift if necessary. We used a dilution factor of 5000. The counts per second measured in the solutions were converted to concentrations by bracketing our samples with repeated measurements of the USGS BHVO-2 certified standard. The signal of chemical blanks was insignificant but was still removed from unknowns to mitigate instrumental and chemistry-induced errors. Repeated analyses of G2, Bir-1a, UBN and IFG reference materials allows to estimate the repeatability and the accuracy of our measurements (see **Supplementary Table A-3**). The measured trace element concentrations of reference materials are in prefect agreement with published values (e.g. less than 5% for REEs, 2 SD).

3.4.5. Sm-Nd and La-Ce isotope analyses

Eleven samples were selected and processed along with the BHVO-2 standard and one chemical blank for analyses of ^{138}La-^{138}Ce and ^{147}Sm-^{143}Nd. These samples are representative of the different lithological types (i.e. silicified lavas, cherts, Theespruit sediments) and were selected considering their chondrite-normalised REE patterns (e.g. variable Ce anomaly). Depending on the REE contents, 50 to 300 mg of rock powders were weighted into Savillex beakers, dissolved using HF 29 N-HNO_3 14M in proportion 3:1 and placed during 48H on a hot plate. Once evaporated, samples were dissolved (and dried) several times in concentrated HNO_3. Final solutions were prepared by dissolving dry contents of the beakers in 5 to 18 ml of HCl 6N. Aliquots consisting of 94%, 5% and 1% of the prepared solutions were separated and were respectively used for (1) the separation of Ce and Ce isotopic measurement, (2) measurement of the Sm-Nd systematics using the isotope dilution technique (^{149}Sm-^{150}Nd mixed spike), and (3) determination of the La/Ce ratios by ICPMS, respectively.

Cerium fractions were isolated in 3 steps (see Israel et al., 2020). Firstly, the aliquots were loaded in HCl 2.5M into AG50W-X8 columns. Major elements were removed using HCl 2.5M and Ba using HNO_3 2M. Subsequently, LREEs were collected in HCl 6M and dried out. Then cerium was separated from the LREE fraction after its transformation into Ce^{4+} using a solution of HNO_3 10M + $NaBrO_3$. REEs under the 3+ form are not retained into the LNspec resin using this solution and the Ce fraction is collected latter in a 7 ml wash using HCl 6 N and H_2O_2. The obtained Ce fractions were separated again from potential residues of Ba using AG50W-X8 columns and HNO_3 2M and collected in HCl 6M. ICP-MS analyses of a small aliquot (1%) of the Ce fractions confirmed the success of the separation step before analyses of isotopic ratios. The separation of Sm and Nd aliquots started also with isolation of the LREE in the AG50W-X8 column. Separation of Nd and Sm is realized using diluted HCl (0.2 M and 0.5M, respectively) in a LN-Spec column.

Cerium isotopes were measured using a ThermoScientific^{TM} Triton plus TIMS at Clermont Auvergne University using the technique described in Bonnand et al. (2020) and Israel et al. (2020). Ce isotopes are routinely measured in oxide forms using double Re filaments. A typical analytical run comprises 27 blocks of 20 with signal integrations of 8 seconds. Corrections for (1) mass bias using ^{136}Ce/^{142}Ce = 0.01688; (2) oxide and (3) the effect of the ^{140}Ce tailing on the ^{138}Ce signals were done offline (Israel et al., 2020). Repeated analyses of Ce$_{LMV}$ synthetic reference material standard provided ^{138}Ce/^{142}Ce ratios of 0.2256992 ± 0.00000077 (34 ppm, n = 8) (**Supplementary Table A-4**). We also obtained a ^{138}Ce/^{142}Ce of 0.02256408 ± 0.00000023 (n = 1) for BHVO-2. All these values are consistent with previously published values (Bonnand et al., 2020; Israel et al., 2020).

Isotopic measurements for Nd and Sm were carried out using a Neptune Thermo Scientific Neptune Multicollector ICP-MS at Clermont Auvergne University. For Nd isotopic measurement, the JNdi-1 reference material (**Supplementary Table A-5**) was analysed after every 3 samples and values were normalized to the published value of 0.512099 for ^{143}Nd/^{144}Nd (Garçon et al., 2018). We operated corrections for instrumental fractionation (^{146}Nd/^{144}Nd = 0.7219) and spike composition offline. After corrections, the BHVO-2 standard provided ^{143}Nd/^{144}Nd and ^{147}Sm/^{144}Nd ratios of 0.513019 ± 0.000018 and 0.1500 respectively, that are consistent with published values (Li et al., 2012; Garçon et al., 2018). External precisions (2SD) are estimated at 0.5 epsilon unit for ^{143}Nd/^{144}Nd and 0.2% for ^{147}Sm/^{144}Nd ratios.

For high-precision La/Ce ratio measurement, we prepared gravimetrically 11 synthetic solutions with fixed La/Ce ratios ranging between 0.3 and 1.3. Solutions were prepared from La and Ce standards solution (ATSASOL®) for which the concentration was known with a precision of 0.2%. Three to five repetitive analyses of La and Ce counts in synthetic and natural solution using the Agilent ICP-MS 8900 instrument allowed determining precisely the La/Ce ratios of samples. The La/Ce ratios obtained by this technique are in good agreement with those calculated directly from trace element concentrations. The main advantage of this technique is that it allows considerably increasing the external precision (2SD) from > 2% when the La/Ce ratio is calculated from trace element concentrations to ~0.4% (see **Supplementary Table A-6**). The La/Ce ratio obtained for the BHVO standard is equal to 0.4048±0.0003 which is in perfect agreement with the value of 0.4053±0.0004 determined by isotopic dilution in (Schnabel et al., 2017). Measurement of La/Ce ratios using the two different methods (bulk trace element measurement and repeated analyses of La and Ce from the samples bracketed by synthetic solutions for which La/Ce ratios are known) are compared in **Supplementary Table A-6**.

3.5. Results

3.5.1. Petrography

As shown in **Figure 3-2**, the studied samples include silicified lavas, cherts (or pervasively silicified clastic sediments, i.e. containing more than 80 vol.% of silica) and schistose felsic sediments (silicified also but not pervasively). The latter represent the rocks observed at the top of the Theespruit section that are not silicified enough to classify as cherts. Representative macroscopic and microscopic aspects of these rocks are shown in **Figures 3-5**.

Figure 3-3. Representative outcrop aspects of silicified lavas and sediment lithofacies. Panels (a), (b) and (c) present different silicified lava while panels (d), (e) and (f) illustrate pervasively cherts and schistose felsic sediments. (a) shows pillows from the Theespruit Formation. (b) shows ocelli-bearing silicified lava from the Hooggenoeg 3 Formation. (c) shows zebraic-textured silicified lava from the Mendon 1 section with alternations of silicified lava portions and generally parallel chert veins, although some chert veins cross-cut the zebraic texture. (d) shows different bands of grey cherts with neatly different sediment grain sizes and eventual grading (see white triangle pointing to the top of a graded layer) crosscut by a black chert vein in the Mendon 1 section. (e) illustrates black-and-white chert showing cm- to dm-wide alternation of black and grey chert bands in the Middle Marker Unit. (f) is a photograph of black chert and schistose felsic sediments from the Theespruit section.

3.5.2.1. General descriptions of the main lithological types

A. Silicified lavas

Least-silicified lavas occur at the base of the sections and become progressively more silicified toward the interface with upper sedimentary layers. Overall, the silicified lavas are greenish to dark-greyish in colour. Well-preserved pillow lavas are identified in the Theespruit, Komati and Hooggenoeg 3 sections (**Figure 3-3a**) and occellar textures are observed in the

Hooggenoeg 3 section, e.g. sample SK-HO13 (**Figure 3-3b**). As observed in the Middle Marker and Mendon 1 sections, the lavas may locally acquire a hydrothermally-induced “zebraic” aspect (Paris et al., 1985; Duchac and Hanor, 1987) which is formed by centimetric bands of the silicified lava that are interspaced by parallel quartz- and carbonate-bearing veins (**Figure 3-3c**).

Under the microscope, least-silicified lavas display textures that, in part, reflect the volcanic origin of the rocks. Olivine and pyroxene phenocrysts, often pseudomorphed by epidote and chlorite, are set in a matrix containing different oxides (chromite and Fe-Ti oxides), feldspars, carbonates and quartz (**Figure 3-4a**). Partially silicified lavas show a heterogeneous texture depicting millimetre-scale quartz-rich and quartz-poor zones. Quartz-poor zones are rather dominated by phyllosilicates (muscovite and chlorite), oxides and epidote (**Figure 3-4b**). Finally, most intensely (or pervasively) silicified lavas have their magmatic minerals almost completely replaced by a fine-grained (<30 µm) quartz-rich assemblage (**Figure 3-4c**). Variable amounts of carbonates, phyllosilicates, Fe-Ti oxides and sulphides (pyrite, arsenopyrite, chalcopyrite and pentlandite) are scattered in this quartz-rich area. Automorphic chromite observed in many silicified lava samples represents the only magmatic mineral that survived the silicification process, although chromite is also partially replaced by Fe-Ti-oxide in the rim.

The lava samples of the Theespruit section show mineralogical assemblages that reflect their equilibration under amphibolite facies conditions (Diener et al., 2005; Cutts et al., 2014). At the base of the section, they occur as amphibolites and are majorly constituted by amphibole, carbonate, oxides and quartz. The uppermost part of the lava unit appears as a chlorite-bearing schist made of alternating, sub-millimetric quartz-rich and chlorite-rich layers containing also garnet and Fe-oxides.

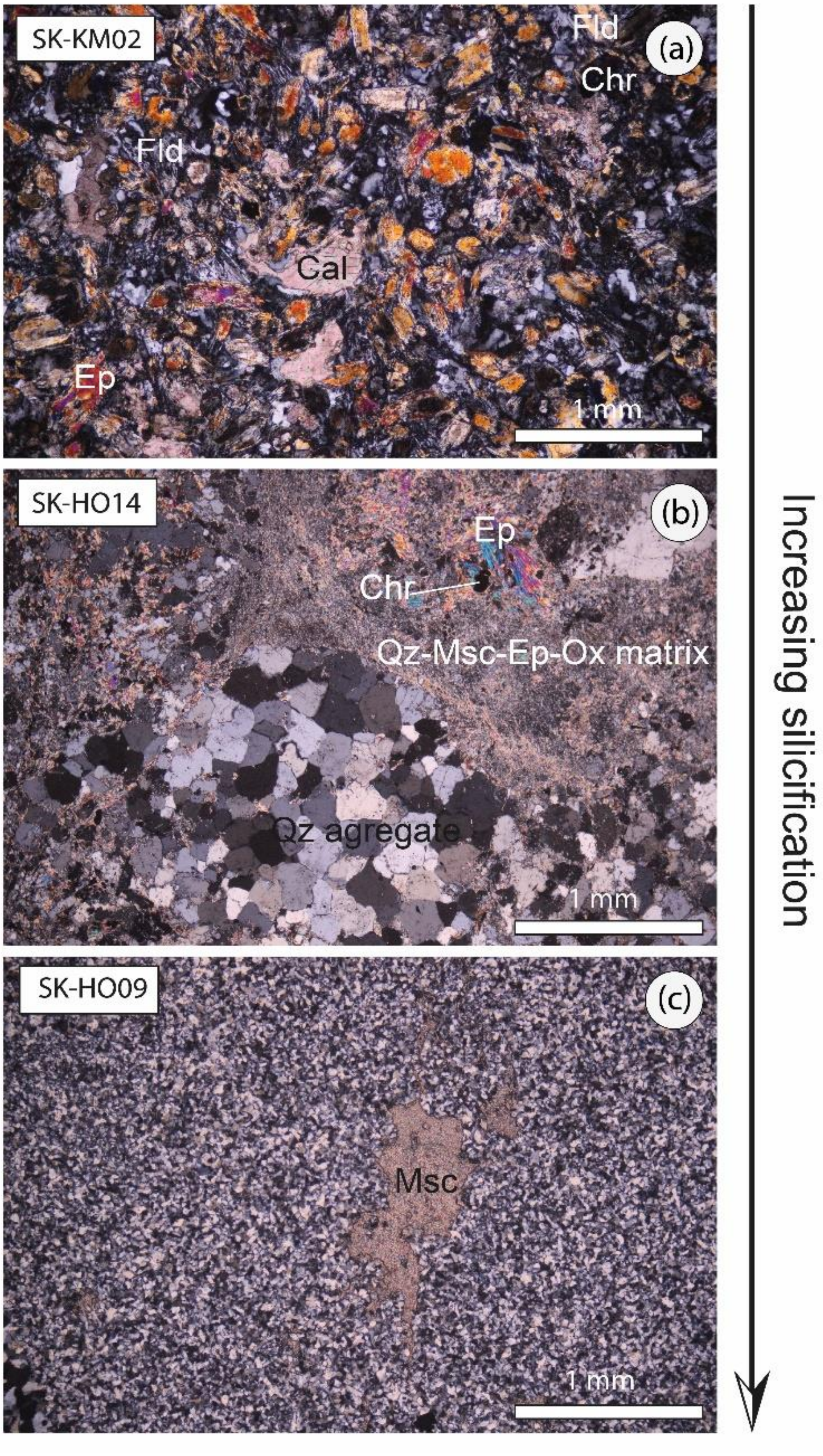

Figure 3-4. Representative microscopic aspects of the lava samples show the textural and mineralogical evolution due to intensifying silicification. (a) Least-silicified lava sample (SK-KM02) from the Middle Marker section, (b) Incompletely (or partly) silicified lava sample (SK-HO14) from the Hooggenoeg 3 section, and (c) Pervasively silicified lava sample (SK-HO09) from Hooggenoeg 9 section with a muscovite-rich zone. Fld: feldspath, Cal: calcite, Ep: epidote, Msc: muscovite, Ox: Fe-Ti oxide, Qz: quartz. All images were taken under polarised light.

B. Cherts

Black cherts are generally detritus free and are devoid of notable sedimentary features, with a pluri-decimetric to pluri-metric thickness (**Figure 3-3f**). They are dominated by micro-quartz (>90 vol.%) but contain also carbonates, sulphides, oxides, carbonaceous materials and minor apatite, except in the amphibolitic Theespruit section where the back cherts include an important amount of sericite surrounded by quartz (> 5 vol.%). In this unit, sericite follows the direction of schistosity and contains quartz inclusions suggesting that quartz and sericite were formed coevally.

Grey cherts generally feature sedimentary makers (**Figure 3-3d**). Under the microscope, the grey cherts may show a clastic texture with some pseudomorphs of detritic grains set in a quartz-rich matrix (**Figure 3-5a**) or a microquartz-dominated aspect (like most black cherts) (**Figure 3-5c**). Detrital grains of grey cherts range from slightly angular to rounded in shape. Apart from quartz clasts that are identified by discrete limits from the matrix, most of detrital grains are replaced by quartz-, phyllosilicate- (i.e. muscovite and chlorite) and oxide-bearing zones (**Figure 3-5b**). These silicified clasts are sometimes surrounded by an oxide-rich rim and are generally set in a quartz-dominated area containing also muscovite, carbonate, sulphides and oxides. In some cases, recrystallised grains display an assemblage of chlorite, oxide and minor carbonates in their rim. A particularly high amount of phyllosilicate phases (>25 vol.%) is observed in grey chert samples SK-MM04 and SK-ME13 (**Figure 3-2**) and suggests that they exceptionally did not reach a pervasive degree of silicification.

Black-and-white cherts consist of intercalations of black and white bands of chert at pluri-decimetre to sub-millimetre scales (**Figures 3-3e** and 3-**5b**). They generally depict sedimentary structures including grading and cross-bedding. In these black-and-white cherts, black layers are generally richer in carbonaceous material and Fe-oxides (**Figure 3-5c**) than white layers that are generally richer in muscovite; these features are therefore considered to control the colour of the individual layers in this unit. The common presence of detrital materials and minor greyish layers within the black bands of black-and-white chert distinguishes them from black cherts that are generally detritus-free. Additionally, unlike the black chert units that can reach a pluri-metric thickness, black bands of black-and-white chert units generally do not exceed a few decimetres in thickness.

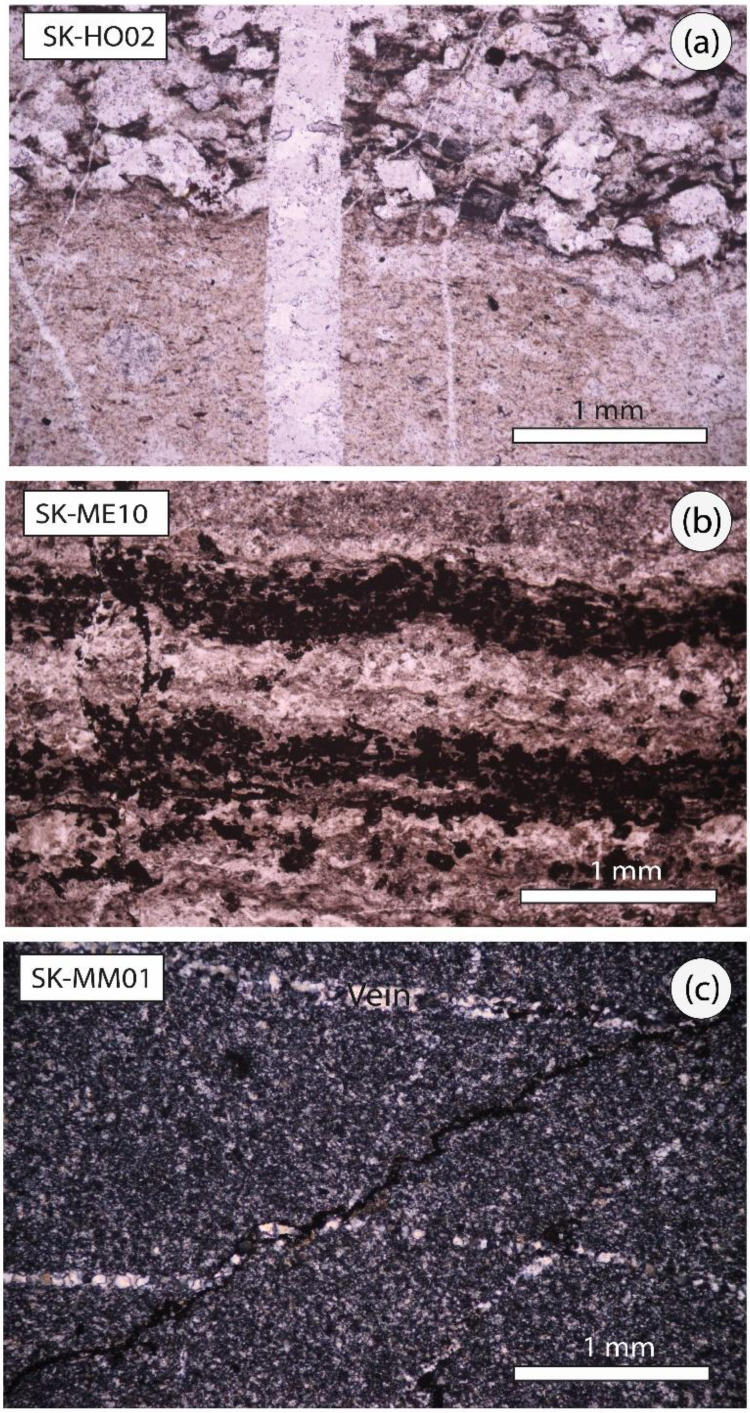

Figure 3-5. Representative microscopic aspects of studied cherts. (a) Alternation between coarse-grained and fine-grained silicified laminas in black-and-white chert sample SK-HO02; black bands are dominated by carbonaceous materials, oxides and coarser quartz grains whereas white bands are dominated by finer quartz grains, muscovite and chlorite. (b) Alternation of oxide-rich (black) and quartz-chlorite-muscovite rich (white) bands in black-and-white chert sample SK-MM11; quartz, chlorite and muscovite phases dominate white bands and black bands are dominated by oxides and carbonaceous materials. (c) Microtexture of grey chert SK-MM01 with a microcrystalline chert. Note the presence of quartz veins in all the different samples displayed. (a) and (b) were captured under natural light but (c) was taken under polarised light.

C. Schistose felsic sediments of the Theespruit section

Felsic sediments depicting a schistosity that is parallel to the bedding plane were observed at the top of the Theespruit section. They consist of quartz, sericite and oxide phases accompanied by accessory feldspar and garnet (**Figure 3-6**). They locally preserve cross-bedding structures at outcrop scale, despite their penetrative schistosity due to the amphibolitic metamorphism undergone by the Theespuit Formation. The schistosity is expressed by an alignment of sericite in the samples. The distinction between these schistose felsic sediments and the chert specimens previously described lies in the fact that the felsic sediments do not exceed 70 vol.% of silica phases, and therefore did not undergo pervasive silicification to become cherts.

Due to the high-grade metamorphism of this unit, it is impossible to distinguish the quartz due to regional metamorphic re-equilibration (Dziggel et al., 2002) from the quartz potentially due to near-seafloor silicification (Hofmann and Harris, 2008).

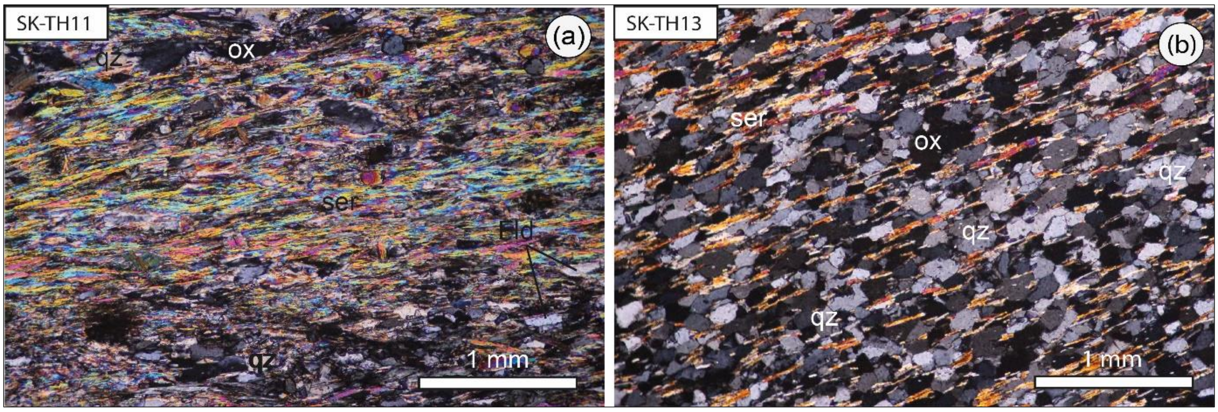

Figure 3-6. Microphotographs of the felsic schistose sediments from the Theespruit section taken under polarised light.

3.5.1.2. Textural evidence of different quartz, oxides and phyllosilicate generations

Above Komati fault where regional metamorphism did not reach high grades, textural observations at microscopic scale identify three different generations of secondary phases (i.e. quartz, phyllosilicates and oxides) in the studied samples as illustrated in **Figure 3-7**. The first generation consists of the fine-grained quartz-rich areas that have replaced the primary phases of the silicified lavas and sediments. In some samples, this area contains muscovite, chlorite and oxides that crystalized coevally with the dominant quartz, as demonstrated in **Figure 3-7a** by mutual inclusion in each other. In other samples, this secondary quartz-rich area rather contains carbonate (ankerite or calcite), oxide and sulphide preferentially (**Figure 3-7b**). The second generation of quartz consists of quartz veins that also contain accessory oxides and carbonates (**Figure 3-7c**). These quartz veins are pluri-decimetric to sub-millimetric in terms of thickness and are interpreted to have formed during a later stage of the silicification process. In some samples, we also observed muscovite-rich veinlets crosscutting the first generation of silica-rich areas that may be coeval with these quartz veins (**Figure 3-7d**). The third and last generation of secondary mineral growth is materialized by Fe-oxide veins crosscutting both the quartz-rich areas and veins (**Figure 3-7c**). These oxide-rich veins most likely formed after the main episode of silicification.

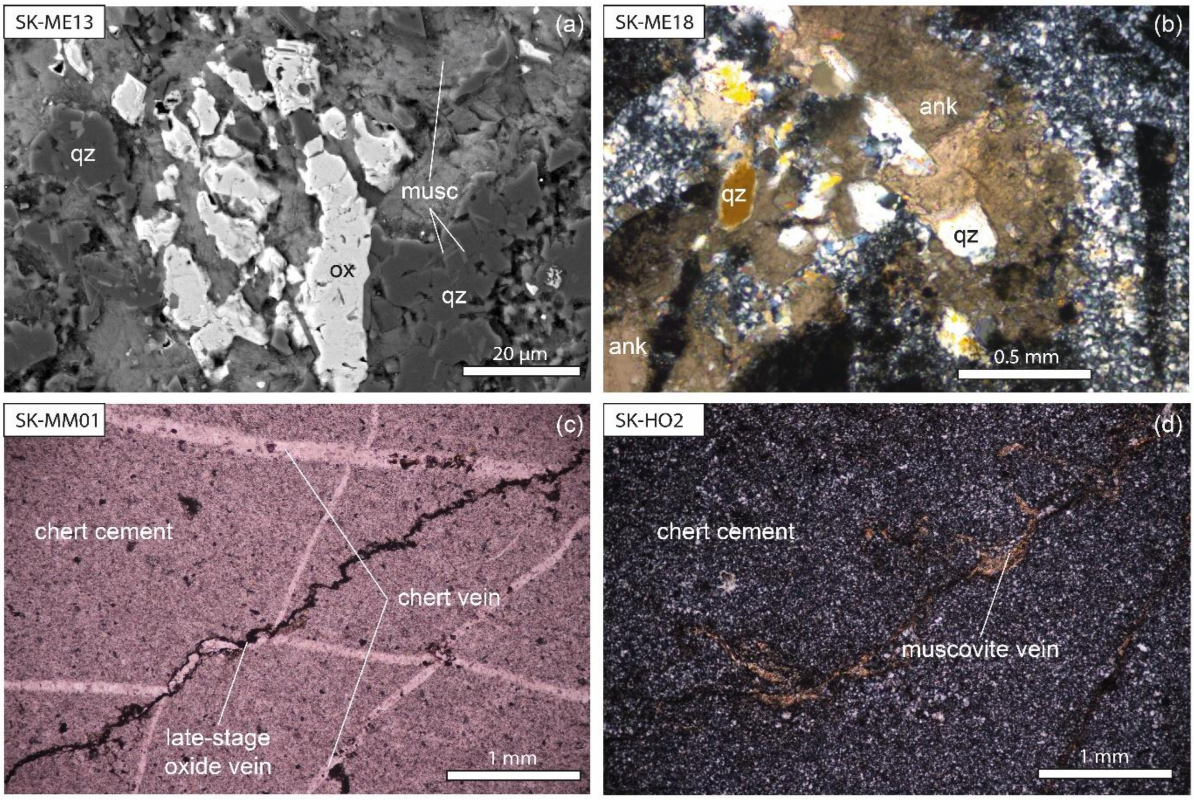

Figure 3-7. Selected images illustrating textural evidence of different episodes of secondary mineral precipitation in the silicified lavas and sediments. a) Association of Fe-oxide, muscovite and quartz (with inter-inclusions in each other) in SK-ME13 grey chert demonstrating that they formed coevally during an early stage of silicification. b) quartz-ankerite association in SK-ME18 silicified lava demonstrating coeval growth of quartz and carbonate. c) Early quartz-rich areas crosscut by quartz veins and a later oxide vein in SK-MM01 grey chert. d) Injection of muscovite vein in pre-existing silica-rich areas. Abbreviations: qz=quartz, ox=oxide, musc=muscovite, ank=ankerite.

3.5.2. Equilibrium temperatures

Here we present the results of three different thermometric techniques that were used to estimate equilibrium temperatures are recorded by the Onverwacht cherts located to the North of Komati Fault. The different techniques include (1) Raman spectroscopy of carbonaceous material, (2) chlorite chemistry and (3) SIMS-determined oxygen isotope fractionation between quartz and carbonate phases. Concerning the amphibolite-facies metamorphism that affected the Theespruit Formation, its peak temperature was estimated to >550°C based on the presence of staurotide-garnet-kyanite, and hornblende, epidote-garnet assemblages in metasedimentary and metamafic rocks, respectively (Diener et al., 2005; Cutts et al., 2014) and is not re-assessed here. Whereas Raman spectra of carbonaceous materials were acquired for cherts from four different sections (i.e. Middle Marker, Hooggenoeg 3, Hooggenoeg 4 and Mendon 1 sections), chlorite thermometry and oxygen isotope thermometry were only performed for the lower Middle Marker and the uppermost Mendon sections. For each section, these different analyses were conducted on distinct samples because the researched material (i.e. carbonaceous materials, chlorites and quartz-carbonate assemblages) do not coexist in the same samples.

3.5.2.1. Raman spectroscopy of carbonaceous material

Raman spectra of measured carbonaceous materials (**Figure 3-8**) provide peak temperatures of 361 ± 13 °C in the Middle Marker cherts (2SD, n=11), 333 ± 18 °C in the Hooggenoeg 3 chert (n=9), 343 ± 15 °C (n=10) in the Hooggenoeg 4 chert and 352 ± 13 in the Mendon 1 chert (n=15). Average temperatures per individual sample cover a narrow range of 333 to 366 °C and internal standard deviations are lower than 30°C. Carbonaceous materials of all the analysed samples are collectively consistent with equilibration at an average temperature of 347 °C, within a 2SD value of 50 °C representing the error range expected from this technique. This is consistent with results of previous studies that reported the Raman spectroscopy of carbonaceous material from the Onverwacht cherts (Tice et al., 2004; van Zuilen et al., 2007; Hofmann et al., 2013; Alleon et al., 2021).

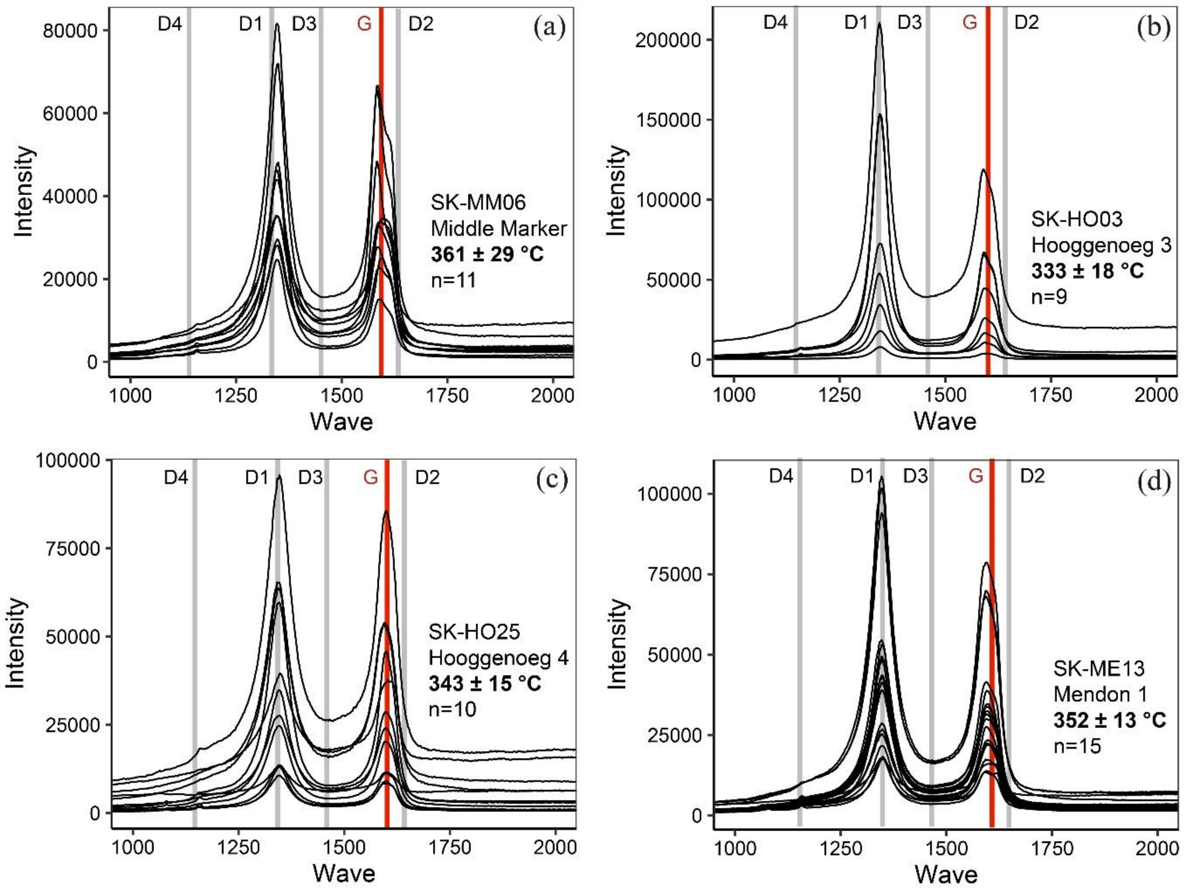

Figure 3-8. Raman spectra of carbonaceous materials from different sections: a) Mendon 1 section, b) Hooggenoeg 3 section, c) Hooggenoeg 4 section and d) Middle Marker section. The location of the different peaks of carbonaceous materials are shown by grey and black lines. A linear baseline was applied to original spectra that were also cropped to the displayed range of wavelength. Reported temperatures are average values and errors correspond to 2SD from measurements of 9 to 15 carbonaceous materials in individual samples.

3.5.2.2. Chlorite thermometry

Major element maps of chlorite-rich areas in selected silicified lava and chert samples from two different sections (i.e. the uppermost Middle Marker section and the lowermost Mendon 1 section) (**Figure 3-9**) allowed their equilibrium temperatures to be determined using the dynamic method of Vidal et al. (2016). Chlorite compositions were processed in X-map Tools software (Lanari et al., 2014). Resultant temperature maps and selected zones for equilibrium temperature determination are shown in **Figure 3-9**. The temperatures displayed by all chlorite rims are lower than those observed in cores due to higher SiO_2 and Al_2O_3 in the rims. The rim temperatures are therefore considered as unrepresentative of chlorite equilibration because processes like exhumation and weathering could have modified rim compositions after the peak equilibrium event. The cores of chlorite in the Middle Marker SK-MM05 sample are richer in SiO_2 (27-31 wt.%) and MgO (20-22 wt.%) but poorer in FeO (14-16 wt.%) than chlorite cores from the Mendon 1 SK-ME13 and SKME24 samples (23-25 wt.% SiO_2, 11-13 wt.% MgO and 27-29 wt.% FeO). Concerning FeO, it is richer in chlorite cores from Mendon 1 section (27-29 wt.%) than in those from Middle Marker section (14-16 wt.%). Despite this compositional difference, equilibrium temperatures calculated from Middle Marker and Mendon 1 chlorites are similar (**Figure 3-9**) and cover a narrow range extending between 275 and 291°C. Because analytical uncertainties of the chlorite thermometry can exceed 50°C of error (2SD) (Bourdelle, 2021), we consider that the chlorites equilibrated at an average temperature of 280 ± 50°C.

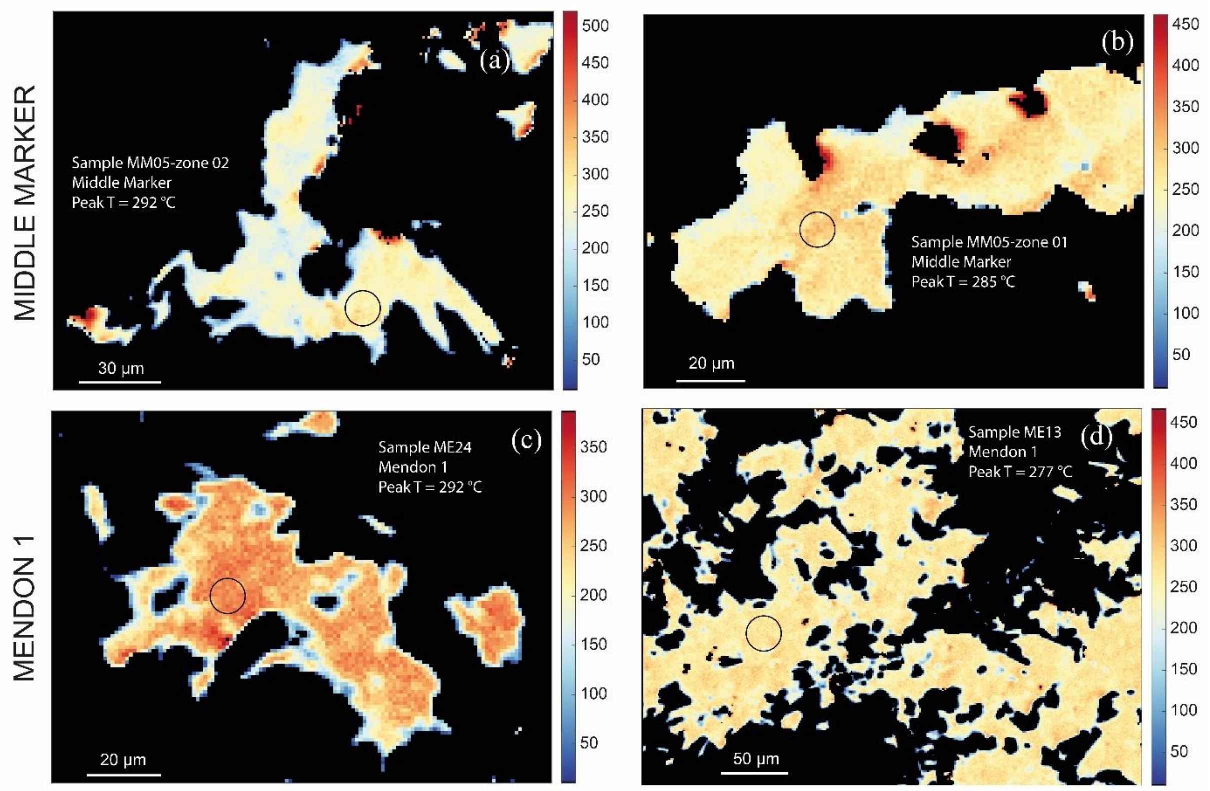

Figure 3-9. Thermal maps of chlorites obtained from the XmapTools software after the method described by Lanari et al. (2014) and Lanari and Piccoli (2020). (a) and (b) are from sample SK-MM05 from the Middle Marker section. (c) and (d) are from samples SK-ME13 and SK-ME24 from Mendon 1 section. Considered peak temperatures for each sample and the exact area from which they were estimated are also shown in the Figure. It is important mentioning that the method does not allow for a better precision than a 2 SD of 50 °C in estimated peak temperatures (Vidal et al., 2016).

3.5.2.3. Oxygen isotope thermometry

At equilibrium, the fractionation of oxygen isotopic ratios between quartz and carbonate phases precipitated from the same fluids ($\Delta^{18}O_{quartz\text{-}carbonate} = \delta^{18}O_{quartz} - \delta^{18}O_{carbonate}$) depends mainly on the temperature of the system (Clayton et al., 1972; Sharp and Kirschner, 1994). We measured oxygen isotope fractionation in quartz-carbonate assemblages of two silicified lava samples (Middle Marker SK-MM11 and Mendon 1 SK-ME18) by SIMS to determine their equilibrium temperature (**Figure 3-10**). In the three measured quartz-ankerite assemblages of Mendon 1 sample, the average $\delta^{18}O$ of ankerite obtained are respectively 9.8 ± 0.9 ‰, 10.5 ± 0.7 ‰ and 12.2 ± 1.5 ‰. The quartz phases associated with these ankerites have average $\delta^{18}O$ values of 15.4 ± 0.3 ‰, 14.8 ± 1.9 ‰ and 15.6 ± 0.3 ‰, respectively (**Figure 3-11**). The three different assemblages provide different $\Delta^{18}O_{\text{quartz-carbonate}}$ values of 5.6, 4.5 and 3.4 ‰, corresponding respectively to equilibrium temperatures of 122 °C, 181 °C and 236 °C (**Figure 3-10a-c**). These data are interpreted to show that the quartz and carbonate phases that we analysed in the Mendon 1 sample SK-ME18 equilibrated isotopically at different temperatures, and are therefore representative of at least two different thermal events: one at a temperature exceeding 280°C and another one at a temperature lower than 125 °C. The Middle Marker calcite displays a $\delta^{18}O$ value of 10.9 ± 0.5 ‰ (2SD, n=9) and associated quartz have a $\delta^{18}O$ value of 13.4 ± 0.7 ‰ (2SD, n=10) (**Figure 3-11**). Using these data, we obtain a $\Delta^{18}O_{\text{quartz-carbonate}}$ value of 2.4 ‰ and a temperature of 325 °C (**Figure 3-10d**).

To summarise the thermometric data, we obtained a consistent temperature of 347 (± 50) °C from Raman spectra of carbonaceous materials derived from four different stratigraphic levels in the Onverwacht Group (i.e. Middle Marker, Hooggenoeg 3, Hooggenoeg 4 and Mendon 1) (**Figure 3-8**). This temperature is similar within error to the temperature of 280 (± 50) °C obtained by chlorite chemistry in the Middle Marker and Mendon 1 sections (**Figure 3-9**). The fractionation of oxygen isotope between in the one quartz carbonate assemblage of the Middle Marker section that we analysed returns an equilibrium temperature of 325 °C that is consistent with the temperature determined from Raman spectra of carbonaceous material and chlorite chemistry (**Figure 3-10d**). On the other side, three different quartz-carbonate assemblages of the Mendon 1 silicified lavas provide notably different equilibrium temperatures (**Figure 3-10a-c**), suggesting that we analysed mineral populations that equilibrated at two different temperatures (i.e. at less than 122 °C and at more than 236 °C). This last temperature is consistent with the equilibrium temperature of ~240°C determined by Marin-Carbonne et al. (2011) based on O isotope fractionation between quartz and carbonates from a Mendon cherts sample.

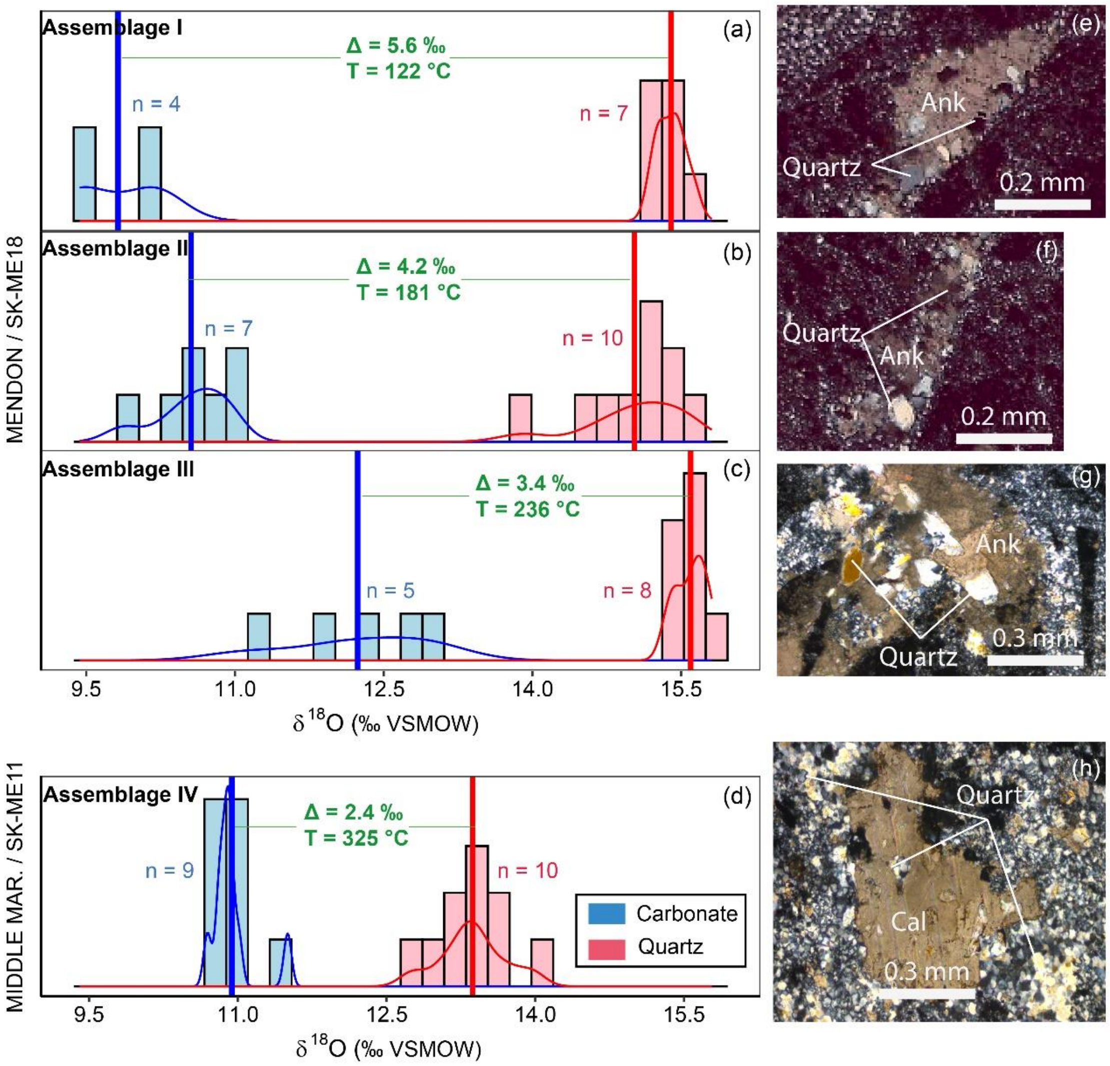

Figure 3-10. Distribution of $\delta^{18}O$ values and equilibrium temperatures obtained from analysed quartz (reddish) and carbonate (bluish) assemblages. (a), (b) and (c) present results of analyses in individual assemblages of the silicified lava sample SK-ME18 of Mendon section. (d) presents results obtained from the single assemblage of the silicified lava sample SK-MM11 that we analysed. Histograms and probability curves present the dispersion of the data from average values indicated by vertical lines. The reported equilibrium temperatures were calculated using the following equation: $\Delta = 0.87(\pm 0.06) \times 106/T^2$, with Δ = average $\delta^{18}O_{quartz}$ – average $\delta^{18}O_{carbonate}$. (e), (f), (g) and (h) show the petrography of the quartz-carbonate assemblages whose O isotope compositions are respectively displayed in (a), (b), (c) and (d).

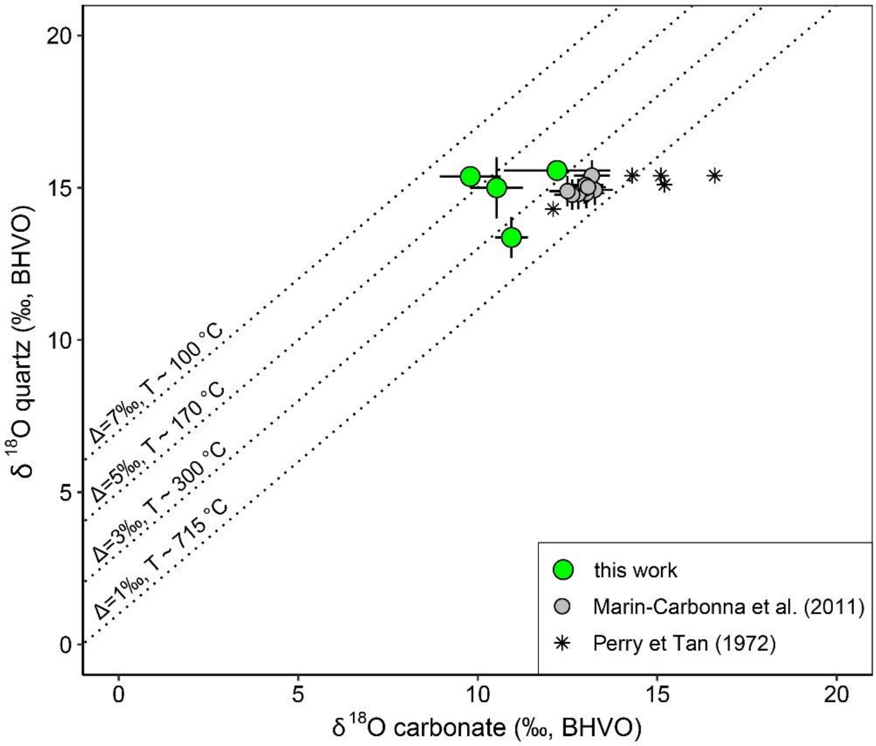

Figure 3-11. Comparison of O isotope fractionation (Δ) of quartz-carbonate assemblages of pervasively silicified lavas and sediments with those obtained by Perry and Tan (1972) and Marin-Carbonne et al. (2011) from Onverwacht cherts. The newly obtained O isotope fractionation extends the previous data towards lower equilibrium temperatures (as low as ~122 °C). The following equation was used to calculate the temperature lines shown on the graph: Δ (qz-cc) = 0.87(±0.06) × 106/T^2. Error bars are not reported for the data of Perry and Tan (1972) because they used bulk measurements that did not allow determining intra-mineral variations.

3.5.3. Bulk-rock geochemistry

3.5.3.1. Major and trace element compositions

Analyses of major and trace element concentrations in 29 selected sampled are provided in **Tables 3-1** and **3-2**, respectively. The location of these samples on the investigated sections are shown on **Figure 3-2**. Pervasively silicified lavas and most cherts display very high concentrations of SiO_2 (71-96 wt.%) that corroborate their quartz-dominated mineralogy. The SiO_2 concentration of the least silicified lavas from all localities (52-62 wt.%) and felsic sediments of the Theespruit section (69-79 wt.%) are relatively lower (e.g. **Figure 3-12a-b**). Lower concentrations of MgO, CaO, Fe_2O_3, MnO and LOI are observed in silicified lava and cherts compared to non-silicified lavas (**Figure 3-12a**) as expected from the observed replacement of primary magmatic phases by SiO_2. Samples SK-MM04 and SK-ME13 are characterised by lower SiO_2 concentrations but higher Al_2O_3 and K_2O concentrations compared to all the other chert samples (**Figure 3-12b**). These samples display higher volumes of phyllosilicate phases (>25 vol.%) than typical. Comparisons with previously published compositions demonstrate that our least-silicified lava samples are within the compositional field of Onverwacht lavas (**Figure 3-12**). Similarly, the Theespruit sediments are in the compositional field of felsic magmas cropping out in the Barberton greenstone belt. The Theespruit sediments and some cherts of the Middle Marker (SK-MM01 and SK-MM08) are characterised by lower concentrations of compatible elements like Cr and Ni and higher concentrations of REE (**Figure 3-12c**), Zr and Hf compared to other samples. In binary plots of REE *versus* TiO_2 (**Figure 3-12c**) and Th/Sc *versus* La/Yb (**Figure 3-12d**), the majority of our chert samples plot in the field of mafic lavas from the Onverwacht Group, whereas the schistose clastic sediments of the Theespruit section lay in the field of felsic lavas and granitoids (**Figure 3-12c-d**).

Table 3-1. Major element composition of analysed silicified lava and sediment samples

Sample	Section	Lithology	SiO_2	TiO	Fe_2O_3	Al_2O_3	MnO	MgO	CaO	Na_2O	K_2O	L.O.I.	Total
SK-TH05	Theespruit	lava	61.5	1.14	13.4	8.7	0.31	6.3	6.42	1.34	0.14	1.3	100.6
SK-TH07	Theespruit	lava	77.7	1.57	3.6	10.9	0.11	0.9	0.70	1.26	1.65	1.5	99.9
SK-TH11	Theespruit	sediment	60.7	0.33	2.1	25.1	0.02	1.8	0.25	2.90	2.23	3.7	99.1
SK-TH12	Theespruit	sediment	79.0	0.16	1.7	12.2	0.03	1.8	1.75	1.75	0.71	1.6	100.7
SK-TH14	Theespruit	sediment	71.7	0.21	2.2	15.8	0.06	0.9	2.31	5.38	1.16	1.4	101.2
SK-TH10	Theespruit	b chert	85.0	0.06	1.5	7.9	0.01	1.8	0.08	0.46	0.07	2.8	99.7
SK-MM01	Middle M.	bw chert	95.2	0.93	0.7	2.0	0.02	0.2	0.11	0.00	0.57	0.6	100.4
SK-MM06	Middle M.	bw chert	93.7	0.11	1.0	2.6	0.10	0.2	0.10	0.03	0.73	0.9	99.5
SK-MM08	Middle M.	bw chert	96.3	0.69	0.2	1.7	0.01	0.1	0.19	0.00	0.54	0.5	100.2
SK-MM04	Middle M.	bw chert	62.6	0.88	3.8	19.9	0.19	2.3	0.07	0.20	5.58	4.4	99.9
SK-MM10	Middle M.	lava	61.7	0.41	6.5	15.1	0.35	7.4	0.07	0.06	2.42	5.7	99.8
SK-MM11	Middle M.	lava	96.0	0.03	0.5	0.8	0.11	0.2	0.90	0.01	0.17	1.4	100.1
SK-KM02	Middle M.	lava	51.1	0.75	11.4	9.0	0.19	10.6	14.01	0.40	1.10	2.0	100.7
SK-HO01	Hoogg. 3	lava	76.3	0.22	8.7	6.5	0.15	4.8	0.04	0.01	0.04	3.3	100.1
SK-HO05	Hoogg. 3	bw chert	93.3	0.10	0.4	3.5	0.03	0.1	0.03	0.03	1.15	0.7	99.3
SK-HO09	Hoogg. 3	lava	97.5	0.04	0.3	1.6	0.04	bdl	0.02	0.04	0.37	0.3	100.2
SK-HO12	Hoogg. 3	lava	86.4	0.83	0.8	8.0	0.05	0.1	0.05	0.37	1.61	1.3	99.5
SK-HO13	Hoogg. 3	lava	85.1	1.13	1.3	8.4	0.02	0.6	0.06	0.49	1.33	1.7	100.1
SK-HO14	Hoogg. 3	lava	77.1	1.78	0.4	14.0	0.01	0.3	0.03	0.11	4.17	2.0	100.0
SK-HO20	Hoogg. 4	lava	52.6	0.41	10.9	11.3	0.23	11.6	6.85	2.70	0.49	3.4	100.5
SK-HO21	Hoogg. 4	lava	52.2	0.44	11.7	11.7	0.19	9.4	9.27	2.25	0.12	3.7	100.9
SK-HO25	Hoogg. 4	g chert	96.3	0.06	0.6	1.8	0.02	0.2	0.06	0.04	0.36	0.5	100.0
SK-HO26	Hoogg. 4	bw chert	89.2	0.30	1.0	6.3	0.02	0.2	0.05	0.08	1.83	1.0	99.9
SK-ME10	Mendon	bw chert	82.6	0.04	12.7	0.7	1.48	0.2	0.06	0.02	0.06	2.5	100.4
SK-ME11	Mendon	b chert	92.9	0.17	0.8	4.0	0.03	0.2	0.04	0.07	1.03	0.8	100.0
SK-ME13	Mendon	g chert	73.5	0.40	8.9	9.4	0.19	3.0	0.15	0.05	1.49	3.3	100.4
SK-ME17	Mendon	lava	89.4	0.09	2.1	3.5	0.17	1.1	1.10	0.02	0.83	2.2	100.5
SK-ME20	Mendon	lava	80.8	0.08	8.4	4.9	0.98	1.5	0.11	0.04	0.84	2.4	100.0
SK-ME24	Mendon	lava	91.1	0.10	1.9	4.3	0.02	0.6	0.04	0.01	1.02	1.0	100.1

Major element compositions were determined by XRF analyses at Stellenbosch University.
Abbreviations: b=black, g=grey, bw=black-and-white, bdl=below detection limit

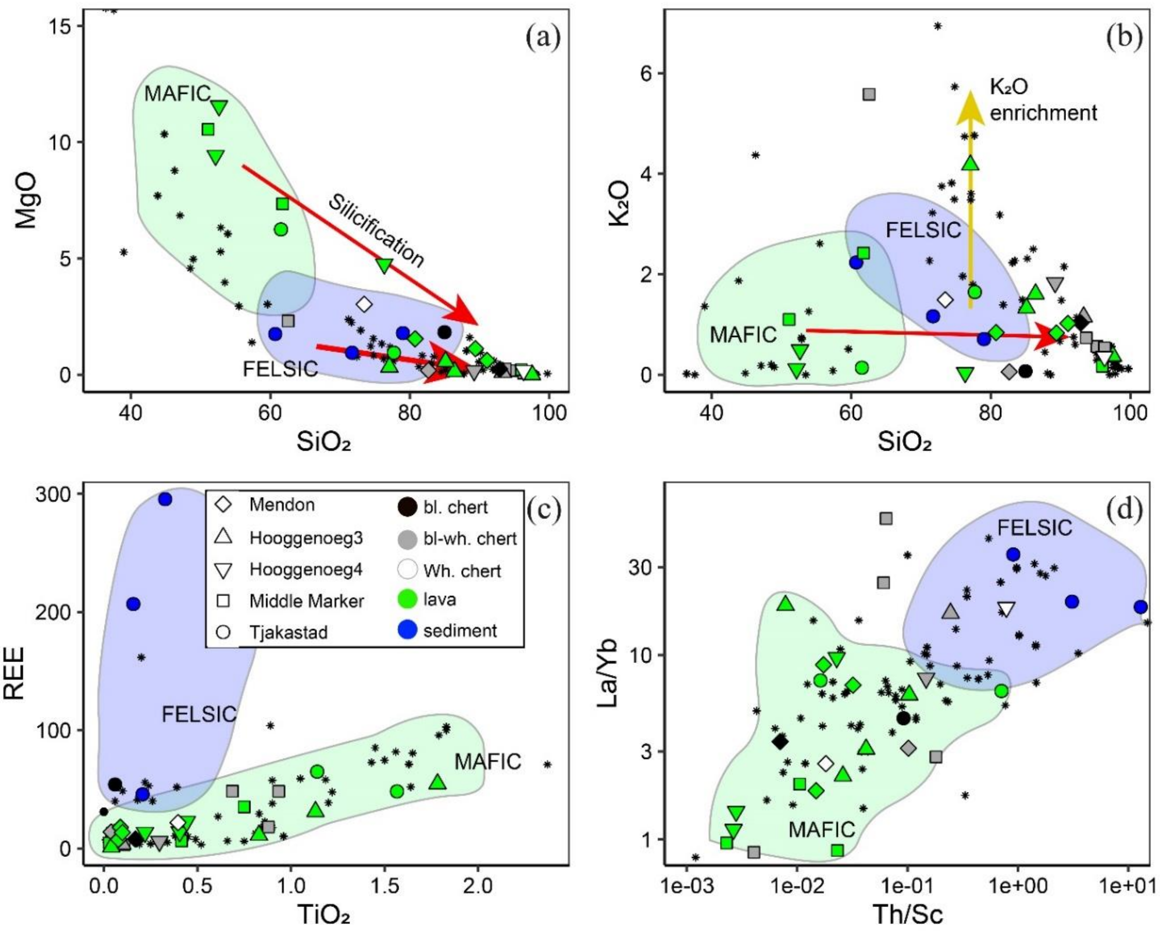

Figure 3-12. Selected major and trace element variations in the studied samples. (a) Decreasing MgO with increasing SiO_2 concentration; this feature was also observed for Fe_2O_3 and CaO. (b) Similar K_2O concentrations in variably silicified samples, with relatively high K_2O concentrations observed in samples that display 70-80 wt.% SiO_2. Arrows in (a) and (b) are based on the evolution of lava and chert compositions and may not apply for the Theespruit sediments that fully comprised in the field of felsic sediments. (c) TiO_2 versus total REE concentration displaying a positive correlation in silicified lava and chert samples from which the Theespruit sediments are removed. (d) La/Yb vs Th/Sc discriminating mafic from dominantly felsic compositions. The fields of mafic and felsic rocks from the Barberton greenstone belt are based on a compilation of published major and trace element compositions (Lahaye et al., 1995; Chavagnac, 2004; Furnes et al., 2012; Puchtel et al., 2013; Blichert-Toft et al., 2015; Agangi et al., 2018; Schneider et al., 2019). Black stars are representative samples of silicified lavas and cherts from the Onverwacht Group analysed previously (Hofmann and Harris, 2008; Rouchon and Orberger, 2008; Rouchon et al., 2009; Hofmann et al., 2013).

Table 3-2. Trace element composition of analysed silicified lavas, cherts and detrital sediments

Sample	Section	Lithology	Sc	Ti	V	Cr	Mn	Co	Ni	Cu	Ga	Ge	Rb	Sr	Zr	Nb	Ba	La	Ce	Pr
SK-TH05	Theespruit	lava	27.5	6645	210.5	367	2590	63.9	181	240.9	11.0	1.47	2.2	184	56	6.12	40	9.04	21.25	3.47
SK-TH07	Theespruit	lava	3.2	302	6.2	19	227	15.5	140	18.5	11.7	0.53	2.1	19	85	3.85	16	8.77	17.59	2.09
SK-TH11	Theespruit	sediment	4.0	1769	7.4	4.7	75	3.6	41	0.3	28.6	0.81	55.2	189	325	28.47	499	60.82	165.81	10.84
SK-TH12	Theespruit	sediment	2.0	869	2.8	5.1	169	1.8	2.9	2.2	15.1	0.60	25.4	115	182	17.18	276	53.14	94.77	9.36
SK-TH14	Theespruit	sediment	2.4	1211	18.4	16	309	6.0	21	31.3	19.5	0.55	27.0	589	105	2.05	305	10.88	19.92	2.21
SK-TH10	Theespruit	b chert	37.4	9719	275.8	521	853	40.4	98	113.5	14.2	0.71	52.2	127	78	8.85	160	6.75	19.72	2.73
SK-MM01	Middle Marker	bw chert	13.6	4951	75.6	772	78	44.6	241	177.8	3.8	0.29	18.2	8.9	60	9.86	68	7.96	19.43	2.73
SK-MM06	Middle Marker	bw chert	7.5	584	45.0	443	434	17.9	58	35.7	2.6	0.35	21.5	4.0	11	0.54	59	0.44	0.99	0.12
SK-MM08	Middle Marker	bw chert	10.6	4368	65.1	554	26	29.9	141	135.9	3.1	0.19	16.8	10	49	8.28	53	9.04	20.06	2.85
SK-MM04	Middle Marker	bw chert	79.6	5230	452.5	4661	1454	65.7	375	141.8	21.1	0.79	173.1	10	50	2.01	282	1.47	4.47	0.46
SK-MM10	Middle Marker	lava	61.9	2404	312.0	5094	2683	79.0	1006	39.4	14.9	1.02	68.1	7.6	24	0.79	114	0.66	1.85	0.17
SK-MM11	Middle Marker	lava	3.0	146	11.0	95	776	153.6	599	31.4	1.0	0.27	4.7	6.3	4.1	0.33	20	0.38	1.19	0.13
SK-KM02	Middle Marker	lava	30.4		223.7	648		45.6	160	61.3			9.3	452.7	52.4	2.63	88	3.36	9.30	1.43
SK-HO01	Hooggenoeg 3	lava	13.1	1276	124.7	2809	1035	56.9	1043	30.5	6.1	1.15	2.5	2.5	11	0.37	14	3.57	2.68	0.77
SK-HO05	Hooggenoeg 3	bw chert	2.6	613	94.4	1525	103	4.3	15	6.4	5.5	0.53	36.3	2.4	5.3	0.23	96	1.20	1.10	0.19
SK-HO09	Hooggenoeg 3	lava	2.4	231	31.8	572	114	2.9	6	2.1	1.8	0.22	12.4	5.0	2.2	0.05	61	0.39	0.31	0.07
SK-HO12	Hooggenoeg 3	lava	19.0	2078	176.7	532	238	14.2	83	25.2	8.4	1.07	74.0	3.0	17	0.74	155	1.48	3.16	0.44
SK-HO13	Hooggenoeg 3	lava	13.0	6934	178.8	114	141	16.4	87	36.7	11.6	0.47	42.9	23	105	5.34	62	3.86	10.37	1.51
SK-HO14	Hooggenoeg 3	lava	14.8	10834	263.8	175	26	6.8	35	10.7	19.4	0.38	95.5	8.6	159	8.17	628	7.51	17.53	2.38
SK-HO20	Hooggenoeg 4	lava	36.4	2459	222.1	919	1644	57.9	165	49.9	7.8	1.23	17.4	25	20	0.82	30	1.16	2.89	0.49
SK-HO21	Hooggenoeg 4	lava	39.1	2587	220.9	503	1404	52.9	123	76.5	10.3	1.37	2.7	118	22	0.92	27	2.42	3.77	0.87
SK-HO25	Hooggenoeg 4	g chert	1.4	362	6.2	19	339	5.1	25	12.4	2.3	0.46	11.9	3.1	39	2.72	32	2.34	5.62	0.71
SK-HO26	Hooggenoeg 4	bw chert	14.7	1726	150.4	583	189	6.4	34	14.7	7.1	0.55	58.9	5.5	32	2.23	136	0.96	2.21	0.28
SK-ME10	Mendon	bw chert	9.4	194	20.2	138	9277	20.2	135	4.8	1.8	1.93	2.0	14	5.7	0.45	39	2.35	4.33	0.51
SK-ME11	Mendon	b chert	10.6	1108	84.9	52	124	1.7	23	10.2	4.4	0.61	31.9	5.2	11	0.52	109	1.15	2.54	0.35
SK-ME13	Mendon	g chert	31.7	2419	213.6	257	1538	28.3	140	79.2	8.7	1.39	60.2	3.7	20	0.85	93	2.66	6.17	0.88
SK-ME17	Mendon	lava	12.4	479	72.3	1590	2133	24.0	100	6.9	3.5	0.66	26.2	5.9	3.8	0.14	76	3.91	6.24	0.75
SK-ME20	Mendon	lava	21.7	357	77.5	2671	5626	49.8	363	3.2	3.9	0.99	27.3	7.7	2.6	0.05	124	1.11	1.78	0.22
SK-ME24	Mendon	lava	12.7	561	76.4	1671	127	18.9	96	5.5	4.1	0.56	33.2	3.1	6.0	0.19	123	3.47	3.16	0.73

Sample	Section	Lithology	Pr	Nd	Sm	Eu	Gd	Tb	Dy	Y	Ho	Er	Tm	Yb	Lu	Hf	Ta	Pb	Th	U
SK-TH05	Theespruit	lava	3.47	16.08	3.59	1.34	3.41	0.51	2.78	12.69	0.52	1.39	0.20	1.24	0.18	1.47	0.36	1.51	0.45	0.12
SK-TH07	Theespruit	lava	2.09	8.09	2.13	0.26	2.46	0.43	2.69	14.20	0.54	1.46	0.22	1.37	0.18	1.78	0.23	6.22	2.23	0.90
SK-TH11	Theespruit	sediment	10.84	33.59	5.33	0.87	4.41	0.74	4.60	25.01	1.03	3.17	0.51	3.34	0.46	9.75	3.07	16.41	51.72	7.56
SK-TH12	Theespruit	sediment	9.36	29.04	4.62	0.63	3.97	0.64	3.86	24.78	0.81	2.44	0.39	2.73	0.42	5.45	1.60	11.73	6.25	2.68
SK-TH14	Theespruit	sediment	2.21	7.99	1.48	0.46	1.14	0.14	0.72	3.56	0.13	0.35	0.05	0.31	0.05	2.88	0.13	7.28	2.18	0.85
SK-TH10	Theespruit	b chert	2.73	11.82	2.72	0.90	2.45	0.39	2.56	14.76	0.55	1.57	0.23	1.48	0.21	2.07	0.56	3.68	3.44	1.06
SK-MM01	Middle Marker	bw chert	2.73	11.02	2.34	0.58	1.77	0.25	1.20	4.14	0.20	0.47	0.06	0.32	0.04	1.42	0.62	1.80	0.82	0.17
SK-MM06	Middle Marker	bw chert	0.12	0.54	0.14	0.05	0.18	0.03	0.22	1.34	0.05	0.15	0.02	0.16	0.02	0.26	0.04	1.58	1.36	0.43
SK-MM08	Middle Marker	bw chert	2.85	11.07	2.03	0.49	1.34	0.18	0.80	2.57	0.12	0.28	0.03	0.16	0.02	1.16	0.53	1.43	0.68	0.16
SK-MM04	Middle Marker	bw chert	0.46	2.03	0.65	0.26	1.32	0.29	2.51	16.43	0.62	1.85	0.27	1.73	0.24	1.48	0.13	4.82	0.32	0.17
SK-MM10	Middle Marker	lava	0.17	0.70	0.21	0.08	0.36	0.08	0.64	4.50	0.16	0.57	0.10	0.69	0.10	0.73	0.04	1.53	0.14	0.05
SK-MM11	Middle Marker	lava	0.13	0.56	0.17	0.04	0.33	0.07	0.54	3.75	0.13	0.39	0.07	0.43	0.06	0.09	0.01	1.84	0.07	0.03
SK-KM02	Middle Marker	lava	1.43	7.05	2.22	1.08	2.47	0.50	3.16	16.99	0.65	1.76	0.26	1.68	0.27	1.43	0.17	0.80	0.32	0.08
SK-HO01	Hooggenoeg 3	lava	0.77	2.89	0.72	0.22	0.81	0.13	0.74	3.26	0.14	0.38	0.06	0.37	0.06	0.32	0.03	0.38	0.30	0.10
SK-HO05	Hooggenoeg 3	bw chert	0.19	0.59	0.10	0.04	0.08	0.01	0.08	0.57	0.02	0.06	0.01	0.07	0.01	0.20	0.02	0.80	0.64	0.20
SK-HO09	Hooggenoeg 3	lava	0.07	0.23	0.05	0.02	0.04	0.01	0.04	0.20	0.01	0.02	0.00	0.02	0.00	0.06	-0.01	0.39	0.02	0.03
SK-HO12	Hooggenoeg 3	lava	0.44	2.05	0.54	0.22	0.69	0.12	0.87	5.74	0.20	0.62	0.10	0.67	0.10	0.52	0.04	0.62	0.49	0.16
SK-HO13	Hooggenoeg 3	lava	1.51	7.05	1.94	0.67	1.84	0.29	1.70	7.85	0.32	0.82	0.11	0.63	0.08	2.89	0.35	1.87	1.35	0.44
SK-HO14	Hooggenoeg 3	lava	2.38	10.17	2.51	0.81	3.19	0.54	3.67	22.07	0.82	2.44	0.37	2.43	0.36	4.30	0.54	1.10	0.63	0.23
SK-HO20	Hooggenoeg 4	lava	0.49	2.51	0.86	0.26	1.29	0.23	1.57	9.75	0.36	1.04	0.16	1.02	0.16	0.58	0.04	0.33	0.10	0.02
SK-HO21	Hooggenoeg 4	lava	0.87	4.30	1.38	0.54	2.12	0.38	2.62	15.05	0.58	1.66	0.26	1.70	0.26	0.66	0.04	0.43	0.11	0.03
SK-HO25	Hooggenoeg 4	g chert	0.71	2.65	0.58	0.16	0.54	0.09	0.47	2.05	0.08	0.18	0.02	0.13	0.02	0.96	0.19	1.02	1.10	0.29
SK-HO26	Hooggenoeg 4	bw chert	0.28	1.10	0.26	0.12	0.28	0.04	0.28	1.56	0.05	0.14	0.02	0.13	0.02	1.11	0.21	2.80	2.17	0.69
SK-ME10	Mendon	bw chert	0.51	2.06	0.55	0.31	0.86	0.15	1.00	6.71	0.23	0.68	0.11	0.75	0.12	0.13	0.08	1.29	0.96	0.31
SK-ME11	Mendon	b chert	0.35	1.49	0.33	0.14	0.42	0.08	0.53	3.16	0.12	0.33	0.05	0.34	0.05	0.29	0.06	0.40	0.07	0.10
SK-ME13	Mendon	g chert	0.88	4.17	1.13	0.44	1.60	0.27	1.78	10.27	0.38	1.09	0.16	1.03	0.16	0.59	0.07	0.68	0.58	0.18
SK-ME17	Mendon	lava	0.75	3.15	0.66	0.26	0.59	0.09	0.71	5.39	0.17	0.55	0.09	0.57	0.09	0.13	0.01	0.52	0.40	0.13
SK-ME20	Mendon	lava	0.22	1.02	0.40	0.21	0.63	0.10	0.70	6.08	0.17	0.53	0.09	0.60	0.10	0.09	0.02	0.44	0.32	0.11
SK-ME24	Mendon	lava	0.73	2.73	0.57	0.22	0.73	0.11	0.70	4.08	0.14	0.41	0.06	0.39	0.06	0.17	0.02	0.33	0.22	0.08

Trace element concentrations were analysed by ICPMS at Clermont Auvergne University. Sample SK-KM02 has been measured at Stellenbosch University following the routine technique described by Grosch et al. (2022).

Abbreviations: b=black, g=grey, bw=black-and-white.

In **Figure 3-13**, we show fresh lava normalised patterns of selected elements in the silicified lava samples (SiO_2 > 62 wt.%), with the aim of determining potential elemental exchanges between these rocks and the silicifying fluids. The normalising concentrations of fresh lava were taken from the literature and are specific for each section; they are given in **Supplementary Table A-7**. In **Figure 3-13**, HFSE and REE that are generally immobile in aqueous environments are used to define the maximal range of fresh-rock normalised values expected for non-mobilised elements. Elements that were sequestrated by the rocks should show normalised values that are relatively high, eventually exceeding the range of non-mobilised elements. On the other side, elements that were released by the rocks into the silicifying fluids should display normalised values that are considerably lower than the range of non-mobilised elements. Positive anomalies in alkalis (i.e. K, Rb and Ba) as well as in Pb and U are frequently observed, demonstrating the sequestration of these elements by the silicified lavas. On the other hand, Ca, Fe, Mg and Na display negative anomalies that support their mobilisation from the rocks to the silicifying fluids.

Chondrite-normalised (CN) rare earth element (REE) patterns are shown in **Figure 3-14**. Overall, the analysed samples display flat to positively sloped REE patterns ($(Ce/Yb)_{CN}$ = 0.6 – 31.5). The pervasively silicified lava samples have slightly higher La/Sm ratios $(La/Sm)_{CN}$ = 1.3 – 4.8) than less silicified counterparts ($(La/Sm)_{CN}$ = 0.9 - 3.1) (**Figure 3-14a-b**), showing that the silicified lavas gained subtle amounts of LREE that are unidentifiable from fresh rock normalized patterns displayed on **Figure 3-13**. The most fractionated patterns are displayed by the felsic Theespruit sediments (SK-TH11, SK-TH12 and SK-TH14) and Middle Marker cherts (SK-MM01 and SK-MM08) $(Ce/Yb)_{CN}$ > 9) (**Figure 3-14c-d**). Apart from these two chert samples that may have incorporated some felsic clast deposition, the majority of our chert samples display REE patterns (**Figure 13c**) that are similar to silicified lavas (**Figure 3-14b**). Positive and negative Eu anomalies (i.e., $Eu/Eu^* = 2 \times Eu_{CN} / (Sm_{CN} + Gd_{CN})$) are present in both the lava and chert samples (Eu/Eu* = 0.3 - 1.5). Two out of the three samples of schistose sediments from the Theespruit section display negative Eu anomalies down to 0.44. Concerning Ce, negative anomalies (i.e. $Ce/Ce^* = Ce_{CN} / ((Pr_{CN})^2 \times Nd_{CN})$) are common in our sample set for lavas and cherts (for example, Ce/Ce* = 0.40 and 0.54 in samples SK-HO01 and SK-HO05 respectively). Positive Ce anomalies were also measured in the Middle Marker lava SK-MM10 and the Theespruit schistose sediment sample SK-TH11 (Ce/Ce* = 1.44) and the chert SK-MM04 (Ce/Ce* = 1.30).

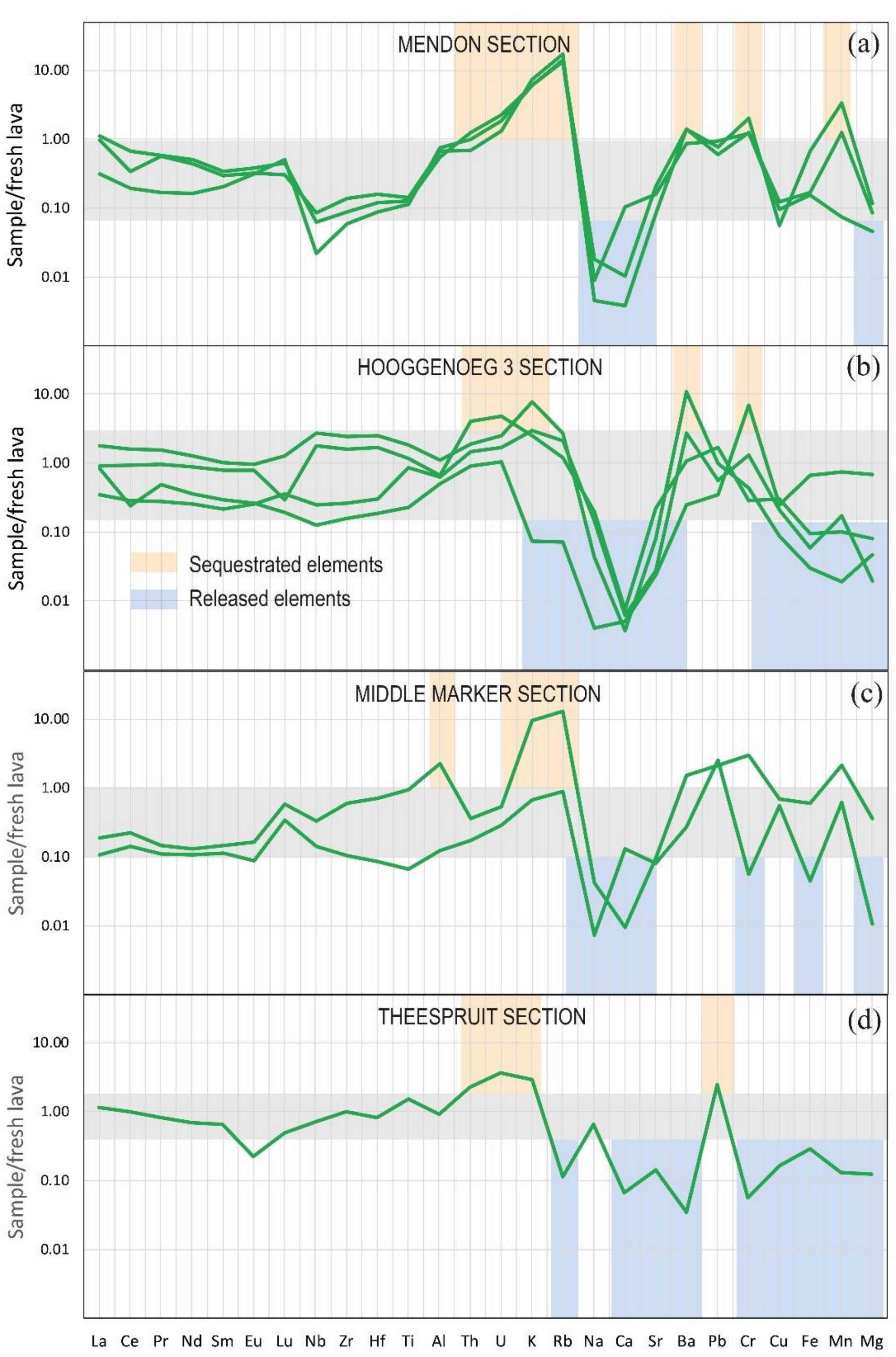

Figure 3-13. Fresh lava normalised profiles of major and trace element concentration in silicified lava samples displaying more than 70 wt.% of SiO_2 for (a) Mendon 1 section, (b) Hooggenoeg 3 section, (c) Middle Marker section and (d) Theespruit section. We note frequent positive anomalies in K, Rb, Ba, U and Pb illustrating that they were sequestrated by the silicified rocks and negative anomalies in Na, Ca, Fe and Mg showing that they were released into the hydrothermal fluids. Average fresh lava compositions used for normalisation were calculated based on the data published by Schneider et al. (2019) for the Theespruit and Komati (i.e. Middle Marker) samples, by Furnes et al. (2012) for the Hooggenoeg samples and by Lahaye et al. (1995) for the Mendon 1 samples.

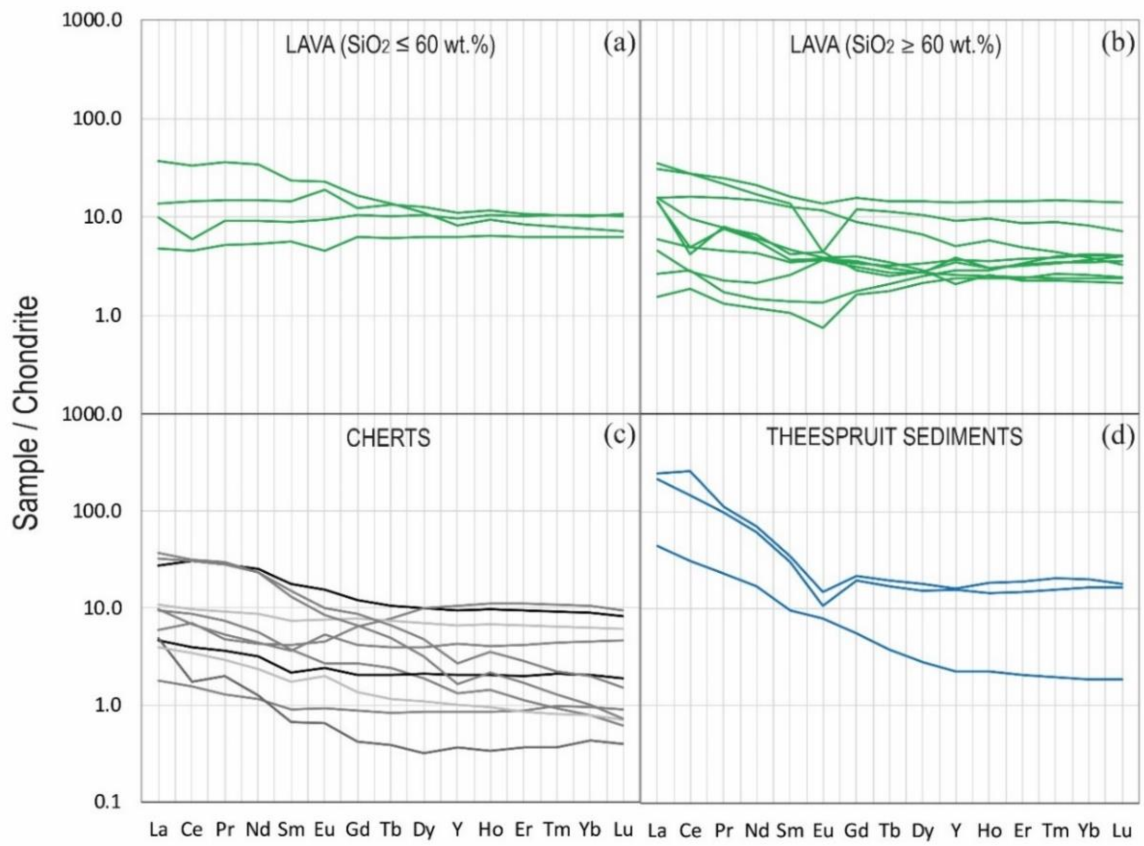

Figure 3-14. Chondrite normalised REE patterns of the different lithological types analysed (chondrites values are from Anders and Grevesse, 1989). The distinction between non silicified ($SiO_2 < 62$ wt.%) (a) and silicified lava ($SiO_2 > 62$ wt.%) (b) demonstrates that silicification did not drastically modify the REE patterns of the studied samples. (c) REE patterns of cherts showing that majority of these sediments are dominated by mafic clastics although some display a fractionated pattern due to contributions of felsic clasts. (d) LREE-enriched pattern of the felsic Theespruit clastic sediments displaying a negative anomaly in Eu in samples SK-TH11 and SK-TH12.

3.5.3.2. Sm-Nd and La-Ce isotopic compositions

Results of measurements of ^{138}La-^{138}Ce and ^{147}Sm-^{143}Nd systematics in eleven selected samples and the BHVO-2 reference basalt are presented in **Table 3-3** and **Figure 3-15**. Values for ^{138}La/^{142}Ce are calculated considering the equation ^{138}La/^{142}Ce = La/Ce×0.0082236 (considering masses and isotopic abundances reported in Schnabel et al., 2017). The ^{143}Nd/^{144}Nd and ^{147}Sm/^{144}Nd ratios of the analysed samples are widely variable. The Theespruit sediments have lower ^{143}Nd/^{144}Nd (0.510158 - 0.510772) and ^{147}Sm/^{144}Nd (0.094 to 0.112) than silicified lava samples (^{143}Nd/^{144}Nd = 0.511857 - 0.512147 and ^{147}Sm/^{144}Nd = 0.148 - 0.169). Cherts from the Middle Marker and Hooggenoeg 3 section display variable ^{147}Sm/^{144}Nd and ^{143}Nd/^{144}Nd ratios ranging between those of lava and Theespruit sediments (**Figure 3-15a**). In samples that are free of Ce anomalies, relatively narrow ranges of variation are observed for ^{138}Ce/^{142}Ce ratios (0.02256333 - 0.02257732) and ^{138}La/^{142}Ce ratios (0.0026 - 0.0045). Out of this range, high ^{138}La/^{142}Ce ratios of 0.0087 and 0.0107 were measured respectively in one lava

(SK-HO01) and one chert sample (SK-HO05) that are characterised by negative Ce anomalies (**Figure 3-15b**). The Theespruit sediments display the highest $^{138}Ce/^{142}Ce$ ratios (0.2257596 - 0.2257710) as expected from their felsic nature.

Table 3-3. Sm-Nd and La-Ce isotope data for selected silicified lavas and sediments

Sample	Section	Rock	Age(a)	$^{143}Nd/^{144}Nd$meas(b)	$^{147}Sm/^{144}Nd$(c)	εNdi(d)	$^{138}Ce/^{142}Ce$meas(b)	$^{138}La/^{142}Ce$(e)	εCei(d)
TH11*	Theespruit	Sediment	3500	0.510158 (11)	0.0957	-2.96	0.02257710 (18)	0.0030	5.25
TH12	Theespruit	Sediment	3500	0.510279 (09)	0.0944	0.03	0.02257732 (23)	0.0045	-0.25
TH14	Theespruit	Sediment	3500	0.510771 (09)	0.1115	1.93	0.02257596 (21)	0.0044	-0.26
TH10	Theespruit	b chert	3500	0.511637 (12)	0.1552	-0.95	0.02257208 (23)	0.004	-0.48
MM01	Middle M.	bw chert	3480	0.511134 (08)	0.1262	2.2	0.02256440 (24)	0.0033	-1.46
MM08	Middle M.	bw chert	3480	0.510847 (33)	0.1096	4.04	0.02256533 (20)	0.0036	-2.08
MM04*	Middle M.	bw chert	3480	0.512255 (11)	0.1781	0.73	0.02256721 (32)	0.0026	2.48
HO01*	Hoogg. 3	lava	3450	0.512475 (08)	0.1488	18.14	0.02256606 (29)	0.0107	-27.93
HO05*	Hoogg. 4	bw chert	3450	0.511813 (14)	0.1011	26.29	0.02256825 (41)	0.0087	-19.32
HO13	Hoogg. 5	lava	3450	0.512142 (09)	0.1688	2.56	0.02256333 (23)	0.003	-0.78
HO14	Hoogg. 6	lava	3450	0.511857 (10)	0.1483	6.1	0.02256586 (22)	0.0034	-1.14
BHVO-2				0.513047 (25)	0.1500		0.02256408 (23)	0.0032	

$^{147}Sm/^{144}Nd$ and $^{143}Nd/^{144}Nd$ isotope ratios were measured by MC-ICPMS, Ce isotopes by TIMS and La/Ce ratios by ICPMS.
*denotes samples that display a positive or negative Ce anomaly
Abbreviations: b=black, g=grey, bw=black-and-white
(a) Relative ages (Ma) are based on Armstrong et al. (1990) and Byerly et al. (2019).
(b) Reported uncertainties are internal precisions (2SE) in last decimal position. External precisions (2SD) calculated from repeated standard measurements are 0.50 epsilon unit for Nd and 0.34 for Ce.
(c) 2SD errors on $^{147}Sm/^{144}Nd$ are < 0.25%
(d) Initial εNdi and εCei were calculated using the following decay constants: 6.54×10^{-12} yr^{-1} for $\lambda^{147}Sm$, 2.37×10^{-12} yr^{-1} for ^{138}La β^- decay to ^{138}Ce and 4.44×10^{-12} yr^{-1} for ^{138}La β^+ decay to ^{138}Ba. CHUR compositions are taken from Bouvier et al. (2008) and Israel et al. (2020) for Sm-Nd and La-Ce systematics, respectively.
(e) 2SD errors on $^{138}La/^{142}Ce$ are < 0.4%.

In a $^{147}Sm/^{144}Nd$ vs $^{143}Nd/^{144}Nd$ isochron diagram, samples are aligned along a theoretical 3.4 Ga Sm-Nd isochron (starting from a chondritic composition), except two samples that are shifted on the left side (**Figure 3-15a**). These samples are SK-HO01 (lava) and SK-HO05 (chert) that are the two samples displaying negative cerium anomalies (**Figure 3-15c**). For the La-Ce systematics, most of the samples plot close to the theoretical 3.4 Ga isochron (**Figure 3-15b**). The four samples falling off the regression line are those characterised by negative (SK-HO01, SK-HO05) or positive Ce anomalies (SK-TH11 and SK-MM04) (**Figure 3-15c**). These samples have also extreme initial εNd and εCe values with values up to 27 and down to -27, respectively (**Table 3-3**). Such values confirm that measured parent/daughter ratios cannot be used to correct from the radioactive ingrowth because they have been modified since the rock emplacement. However we note that rocks from the same group have relatively close Ce and Nd isotopic compositions whether they display Ce anomalies or not. This suggest that the chemical modification that generated Ce anomalies occurred relatively recently. Thus, with the exception of samples that display Ce anomalies, the Sm-Nd and La-Ce isotope systematics of the analysed samples were not significantly disturbed since their deposition/eruption on the palaeoarchean seafloor.

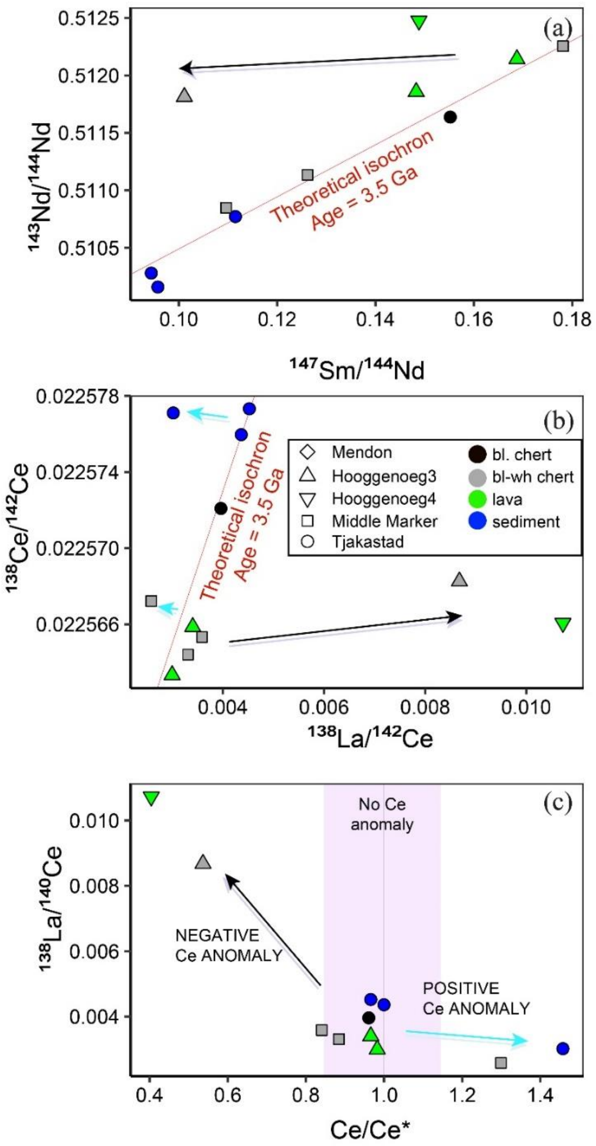

Figure 3-15. La-Ce and Sm-Nd isotope data for for selected silicified lavas and sediments. (a) Sm-Nd isochron diagram; (b) La-Ce isochron diagram; and (c) Ce/Ce* versus $^{138}La/^{142}Ce$. The red oblique lines represent a theoretical isochron of 3.5 Ga old material starting from a chondritic isotopic composition. The alignment of most samples along theoretical isochrons suggests that the parent/daughter ratios of the studied rocks have not been significantly modified by post emplacement processes. Two samples fall off the regression lines for both isotopic systematics, SK-H005 (chert) and SK-HOO1 (lava). These two samples have negative Ce anomalies as indicated by the black arrow in all panels. We note also that two samples deviate from the left-hand side of the $^{138}La/^{142}Ce$-$^{138}Ce/^{142}Ce$ regression. These samples are those characterized by positive anomalies, as indicated by the blue arrow in panel (c). Note that error bars are inferior to the symbols.

3.6. Discussion

We will firstly discuss the effects of post-silicification processes (i.e. weathering and regional metamorphism) on the mineralogy and geochemistry of the silicified lavas and sediments. Then, we will comment on the potential record of fluid-rock elemental exchange that operated during the silicification processes near the palaeoarchean seafloor. In this discussion, hydrothermal fluids are defined as seawater-derived fluids that have interacted with deep parts of the crust and thus can be enriched in silica. Metamorphic fluids are considered as fluids that are due to the metamorphic equilibration of minerals at relatively high temperature while meteoric are fluids involved in hydrological processes (e.g., precipitation, erosion, infiltration) in a continental setting.

3.6.1. Effects of modern meteoric fluids evidenced by La-Ce isotope systematics

Cerium exists under two valence states (+III and +IV). The behaviour of this element is a function of its redox state; in current ocean condition cerium is oxidized and therefore insoluble under its +IV forms. Today, oxidized weathering and hydrothermal fluids display negative Ce anomalies after having scavenged REEs from rocks, and this feature was reported to explain the negative Ce anomalies observed in modern oceans (Shimizu et al., 1994). The anoxic nature of archean environments is generally consistent with the lack of Ce anomalies in archean chemical sediments such as BIFs and thus in the coeval seawater (Bolhar et al., 2004; Hofmann, 2005). In the Barberton greenstone belt, negative Ce anomalies are observed in the Fig Tree and Moodies BIFs but the study of La-Ce radiometric system in these samples clearly shows that La/Ce fractionation and therefore cerium anomalies were formed recently during chemical weathering and fluid-rock interaction in an oxidised environment (Hayashi et al., 2004; Bonnand et al., 2020).

Nine out of the 29 samples that we analysed for trace element compositions display notably negative or positive Ce anomalies (**Figure 3-14**). Samples displaying Ce anomalies occur in all the studied sections and randomly belong to the different lithofacies groups identified in this study. In **Figure 3-15**, samples that are mostly free of Ce anomaly (with Ce/Ce* comprised between 0.85 and 1.15) align along theoretical 3.4 Ga Sm-Nd and La-Ce isochrons. These isochrons were calculated considering that the analysed rocks formed from a reservoir that had a chondritic composition. Their alignment along the theoretical isochron suggests that their parent-daughter (^{147}Sm/^{144}Nd and ^{138}La/^{142}Ce) ratios were not importantly modified after their emplacement on the seafloor. Contrastingly, the samples displaying negative Ce anomalies (^{138}La/^{142}Ce ratios) and those displaying positive Ce anomalies (^{138}La/^{142}Ce ratios) fall off the theoretical isochrons (**Figure 3-15**). Lower ^{147}Sm/^{144}Nd than predicted by the Sm-Nd theoretical isochrons for the measured ^{143}Nd/^{144}Nd are also observed in the two samples displaying the most pronounced negative Ce anomalies. Similar modifications have also been identified for the La-Ce and Sm-Nd isotopic systems in BIFs of the 3.22 Ga Moodies group and were explained by later addition of REE from a LREE-enriched but Ce-depleted oxidised fluid that generated the significant negative Ce anomalies (Bonnand et al., 2020). Here we note also for few samples a decrease of ^{138}La/^{142}Ce associated with positive Ce anomalies suggesting a preferential scavenging of La (and all the other LREE but Ce) by such oxidised fluids leaving an excess of Ce in the analysed rocks. The elevated amount of oxidised fluids that is needed for generating the observed Ce anomalies in the rocks cannot be achieved by a regional metamorphic event as previously proposed by Hayashi et al. (2004), and meteoric fluids in supra-continental context (Bonnand et al., 2020) are therefore considered here.

The number of analysed samples is definitely insufficient for determining unambiguously the timing of REE mobilisation by oxidised fluids within the studied samples as previously done by Bonnand et al. (2020) for the Moodies BIFs. However, the similarity of daughter isotope ratios (i.e. ^{138}Ce/^{140}Ce and ^{143}Nd/^{144}Nd) in lavas and sediments of the same stratigraphic units, independently of the presence or absence of Ce anomalies, is a strong indication that the Ce anomalies are relatively recent - likely younger than 1 Ga. Indeed, the large differences in parent (i.e. ^{147}Sm/^{144}Nd and ^{138}La/^{142}Ce) ratios within the samples displaying Ce anomalies have seemingly not existed for long enough to be recorded in daughter isotope ratios (i.e. radiogenic ingrowth). Consequently, the circulation of oxidised fluids that generated Ce anomalies must be relatively recent. This is consistent with the findings of Lowe and Byerly (2007b) who demonstrated that Phanerozoic meteoric fluids might have notably circulated in the Barberton greenstone belt and were responsible for the formation of iron pods in the Northern part of the Belt (e.g. De Wit et al., 1982). This episode of meteoric weathering may correspond to the formation of the late-stage oxides that were texturally observed to crosscut silica-rich areas and chert veins in some samples (**Figure 3-7c**). It may also have altered the composition of chlorite rims (**Figure 3-9**), thus affecting their record of equilibrium metamorphic temperature.

In order to verify whether late-stage oxidised meteoric fluids mobilised critically mobile elements like K, Rb, Ba, Pb and U (**Figure 3-13**) we searched for potential correlations between Ce anomalies and the anomalies of these elements in fresh-lava normalised elemental patterns. We find no correlation between Ce/Ce* ratios and the concentration or the anomalies of K, Rb, Ba, Pb and U in the silicified lavas (e.g. **Figure 3-16a-b**). There is also no correlation between Ce/Ce* ratios and the increase in SiO_2 concentration. Consequently, the weathering by post-archean oxidised fluids that generated variable Ce anomalies is not responsible for anomalous concentrations of alkalis, U and Pb in the silicified lava (**Figure 3-13**). On the other hand, the positive anomalies in these elements are well correlated with relatively high SiO_2 concentration (**Figure 3-16c-d**). Thus, the increase in K, Rb, Pb, Cs and Ba must be related to hydrothermal silicification near the mesoarchean seafloor (Hart and Staudigel, 1982; Hofmann and Harris, 2008; Rouchon and Orberger, 2008) and will be discussed in greater detail in **Section 3.5.3**.

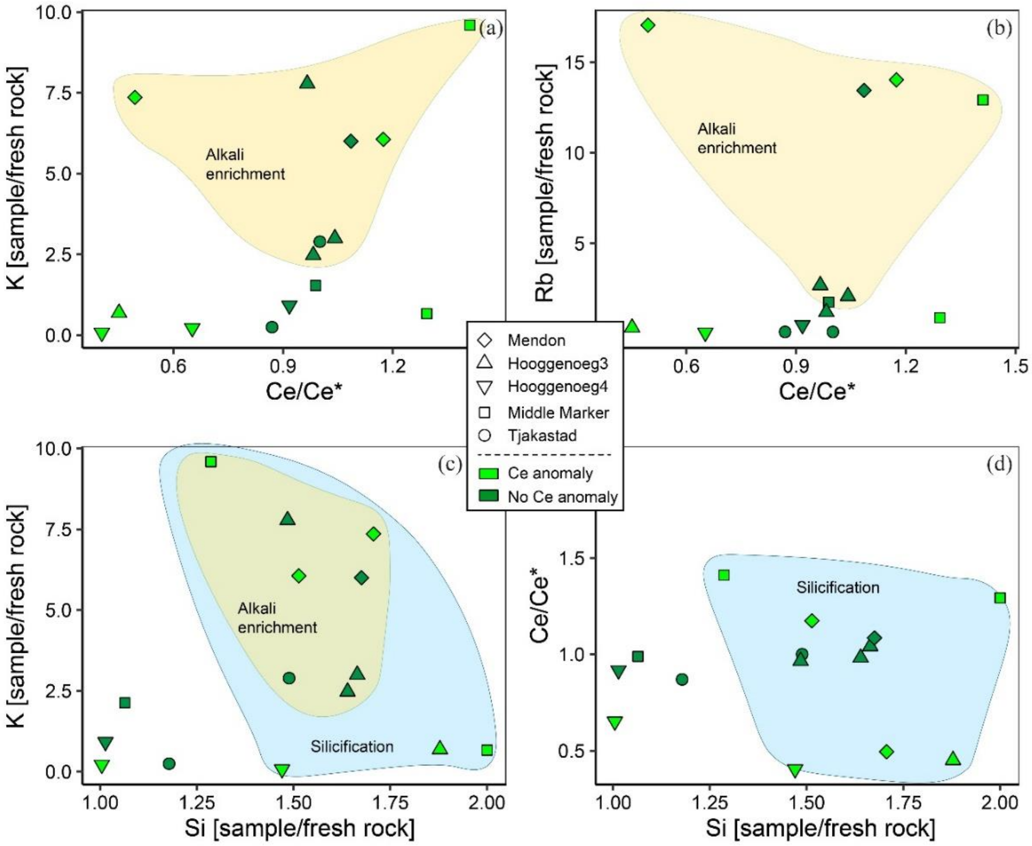

Figure 3-16. (a) and (b) Binary plots of Ce/Ce* ratios against K and Rb anomalies (i.e. sample/fresh rock concentration) showing no correlation between alkali and Ce anomalies. (c) Si anomaly plotted against K anomaly showing the correlation between Si and alkali anomalies. (d) Si anomaly versus Ce/Ce* demonstrating that Ce anomaly occurred independently from the silicification process. The yellowand blue areas respectively represent the zone of alkali enrichment and the zone of silica enrichment.

3.6.2. Regional metamorphism and significance of calculated temperatures

Above the Komati fault, the analysed silicified lavas and sediments are made of greenschist facies mineral assemblages (i.e. quartz-muscovite-chlorite-oxide-sulphide) that are constrained by Raman spectroscopy of carbonaceous materials and chlorite chemistry to have equilibrated between 280 and 360 °C (**Figures 3-8** and 3-**9**). This temperature range is consistent with the results of previous studies that utilised the same thermometric techniques on chert samples of the Onverwacht Group (Xie et al., 1997; Tice et al., 2004; Grosch et al., 2012; Grosch, 2018; Alleon et al., 2021; Zakharov et al., 2021). Oxygen isotope fractionation in quartz-carbonate assemblages return a large range of equilibrium temperatures (122 to 325 °C) (**Figures 3-10** and **11**). The notably large range of $\delta^{18}O$ values measured in ankerites and quartz phases of silicified lava sample SK-ME18 (**Figure 3-10a-c)** is interpreted to demonstrate that these minerals recorded a multistage evolution from an initial co-precipitation of quartz and ankerite at low temperature (< 122 °C) (Hofmann and Harris, 2008; Abraham et al., 2011;) to re-equilibration at higher temperature (> 236 °C) (Tice et al., 2004; Marin-Carbonne et al., 2011; Grosch, 2018; Zakharov et al., 2021). The high-temperature event must correspond to the apparition of greenschist-facies mineral assemblages formed at 280-360 °C. This event is largely accepted to represent a regional metamorphic event that might have been associated with the deformation of the belt around 3.2 Ga (Grosch, 2018). Other metamorphic events were also suggested to have affected the Barberton greenstone belt 3.1, 2.7 and 2.1 Ga ago (Weis and Wasserburg, 1987; Toulkeridis et al., 1998), and may have also contributed to the re-equilibration of the silicified lavas and sediments within the greenschist facies range of temperature. As there is no textural evidence of important fluid circulation between the silicification event (see silica-rich areas and chert veins; **Figure 3-7**) and the late-stage weathering process (see late-stage oxide veins; **Figure 3-7c**), we argue that regional metamorphism was isochemical and did not significantly affect the bulk-rock geochemistry of the studied rocks. In other word, no significant circulation of fluids is imputable to the regional metamorphism. However, it is almost certain that the current mineralogy of the studied samples is notably different from the one imparted by the near-seafloor silicification process as regional metamorphism must have notably re-equilibrated the mineralogy of the samples at 280-360 °C (Xie et al., 1997; Tice et al., 2004; Hofmann and Harris, 2008). For instance, as already suggested by Hofmann et al. (2013) and Saitoh et al. (2021), the observed muscovite and chlorite phases must have arisen from metamorphic recrystallization of clay minerals that were originally due to the near-seafloor silicification process.

The most interesting result of our thermometric analyses is that the quartz-carbonate assemblages of silicified lavas from the Onverwacht Group recorded different thermometric events in their variable oxygen isotope composition. This is a bridge between studies that identified a regional metamorphic event at > 300°C in cherts by thermometric analyses (Xie et al., 1997; Tice et al., 2004; Marin-Carbonne et al., 2011) and those arguing based on stable Si and O isotope measurements that silicification must have operated at less than 150 °C (Abraham et al., 2011; de Wit and Furnes, 2016). We consider the low-temperature event (~125 °C) constrained by one quartz-carbonate assemblage as characteristic of near-seafloor silicification before metamorphism. Similar results were also found by studies of fluid inclusion compositions that obtained a large range of homogenisation temperatures (60-300 °C) suggesting that even fluid inclusions observed in the Onverwacht cherts were also partly modified by the regional metamorphic event (de Vries and Touret, 2007; Marin-Carbonne et al., 2011; Farber et al., 2016; Deutschmann et al., 2022).

3.6.3. Are macroscopic types of cherts correlated with their origin?

The concentration of relatively immobile trace elements (REE and HFSE) in all the chert samples, regardless of their macroscopic classification (i.e. black, grey and black-and-white cherts) is comprised within the range of analysed silicified mafic lavas and felsic sediments that we analysed (**Figures 3-12** and 3-**14**). These immobile elements are more abundant in the analysed chert samples than in orthochemical sediments precipitated from seawater. Therefore, although previous studies have reported the presence orthochemical cherts in certain stratigraphic members of the Onverwacht Group (Knauth and Lowe, 1978; Ledevin et al., 2019; Lowe et al., 2020), all the analysed samples are considered to represent clastic sediments deposited on the palaeoarchean seafloor before being subsequently silicified by hydrothermal circulations (Lanier and Lowe, 1982; Heinrichs, 1984; Rouchon and Orberger, 2008; Hofmann et al., 2013; Lowe and Byerly, 2020). This is attested by sedimentary structures in the field, but also by the lack of common seawater signatures observed in typical orthochemical sediments (e.g. high Y/Ho ratio). We also note that the abundance of carbonaceous materials in black cherts and in black-and-white cherts is the major feature distinguishing them from grey cherts (Trower and Lowe, 2016). Although the reasons for this heterogeneous distribution of carbonaceous materials remains unknown, the apparent macroscopic differences between different types of chert are considered not to endorse a notable petrologic significance for the studied cherts which are all interpreted as pervasively silicified clastic sediments.

3.6.4. Geochemical modifications due to silicification and implications for silicifying hydrothermal fluids

The quartz-rich areas, quartz-rich veins and muscovite veins observed in the studied samples (**Figure 3-7**) are ascribed to different stages of silicification near the seafloor (Hofmann and Harris, 2008; Rouchon and Orberger, 2008; Ledevin et al., 2015). This silicification is common in archean seafloor-derived rocks where it has been ascribed to the hydrothermal circulation of seawater-derived hydrothermal fluids in the sub-oceanic crust (Shibuya et al., 2012; Brengman and Fedo, 2018; Hofmann et al., 2022). Harker diagrams and fresh lava-normalised patterns of multiple element concentrations in the silicified lavas demonstrate that silicification was roughly associated with an uptake of elements like K, Rb, Ba, Pb and U by the rocks, and release of Mg, Fe, Ca and Na into the fluids (**Figures 3-12** and 3-**13**). Additionally, chondrite-normalised REE patterns feature a slight enrichment of LREE (**Figure 3-14b**) in the silicified lavas comparatively to non-silicified lavas (**Figure 3-14b**). In other words, the silicified lavas have slightly higher La/Sm ratios than least-silicified lavas. We additionally observe randomly positive and negative Eu anomalies in the silicified rocks. Modern weathering has slightly modified the concentration of LREE and mostly the cerium concentration in some of the silicified samples (see **Section 3.5.1.)** but this process cannot explain the general enrichment of LREE or Eu anomalies. In fact, there is no correlation between Ce anomalies (i.e. Ce/Ce*) and Eu anomaly or LREE enrichments. Together with the increase in K, Rb, Ba, Pb and U, observed anomalies in Eu and enrichments in LREE are therefore linked to silicification near the palaeoarchean seafloor and not to the late-stage circulation of oxidised meteoric fluids. Furthermore, the fact that most samples align along a 3.4 Ga theoretical isochrone for both Sm-Nd and La-Ce isotopic systems (**Figure 3-15**) is an additional proof that LREE remained mostly immobile after silicification in samples that are free of Ce anomaly. This interpretation is consistent with the conclusions of Hanor and Duschac (1990), Hofmann and Harris (2008) and Rouchon and Orberger (2008) who used also trace element analyses to evaluate the mobility of elements in silicified lavas and sediments from the Onverwacht Group.

To constrain the potential temperature of the palaeoarchean silicifying fluids, we compare the mobilisation of elements by such fluids, as determined for the Onverwacht silicified lavas (**Figure 3-13**), with the well-established behaviour observed in altered portions of the modern oceanic crust that has interacted with hydrothermal fluids at well-known temperatures (Alt and Bach, 2006; Bach and Früh-Green, 2010; Coogan and Gillis, 2018b). In principle, the geochemical modifications undergone by a hydrothermally altered rock include (1) the release of some elements into hydrothermal fluids and (2) the uptake of other elements from the fluids. Today, the most phenomenal expression of hydrothermal discharge on the seafloor consists of high temperature (> 300°C) black or white "smokers" (German and Seyfried, 2013). Smokers are generally characterised by a positive anomaly in Eu due to the fact that Eu becomes considerably more soluble than all the other REEs at high temperature because it is present as Eu^{2+} (Bau, 1991; Hongo et al., 2007; Fowler and Zierenberg, 2015). The deep crustal zones where black smokers interact with the rocks to acquire their positive Eu anomaly are generally left with a negative Eu anomaly (Bach et al., 2003). On the other hand, smokers can transfer their positive Eu anomalies to chemical precipitates that they depose on the seafloor upon rapid cooling due to contact with colder seawater (Bau, 1991; German and Seyfried, 2013). They may also communicate the positive Eu anomaly to lavas and clastic sediments with which they interact on their way upwards the oceanic crust (Bach et al., 2003). In the archean context for example, a systematically positive Eu anomaly observed in silicified lavas from the Abitibi Greenstone Belt was ascribed to interaction with such high-temperature fluids and used as an evidence for the hydrothermal origin of silicification (Brengman and Fedo, 2018). In the studied Onverwacht samples, we did not observe an exclusively positive anomaly of Eu in the silicified lavas and clastic sediments. Instead, random positive Eu anomalies coexist with negative anomalies, suggesting that Eu was mobile within the silicified sections but was not preferentially sequestrated from the hydrothermal fluids (Gillis and Robinson, 1990; Bach et al., 2003). Consequently, the silicifying fluids were arguably not characterised by a positive anomaly in Eu and, thus, did not form by water-rock interaction at high temperature (e.g. >250°C; Mills and Elderfield, 1995).

For the silicified lavas and sediments of the Onverwacht Group, silicifying fluids might have been generated at relatively low temperature (Coogan and Gillis, 2018a), as they were arguably not characterised by a positive Eu anomaly. This can be explained by interactions with low-temperature (< 200 °C) hydrothermal fluids. In general, mineralogical and geochemical studies of altered lavas constitute the main source of information about the low-temperature alteration in the upper zone of the modern oceanic crust as these fluids cannot be sampled as easily as smokers are (Alt et al., 2010; Coogan and Gillis, 2018a). In these rocks, an uptake of alkalis, Pb and U is commonly observed as the solubility of these elements in the hydrothermal fluids decreases in the upper part of the crust (Hart and Staudigel, 1982; Hauff et al., 2003; Kelley et al., 2003). Lavas that are altered at low-temperature are also generally free of the systematically positive Eu anomaly that is commonly observed in high-temperature hydrothermal fluids (e.g. smokers), but present randomised negative and positive anomalies in Eu ascribed to the preferential mobilisation of this element upon plagioclase breakdown (Gillis and Robinson, 1990; Bach et al., 2003). Thus, we interpret the uptake of K, Rb, Ba, Pb and U, and the mobilisation of Eu anomalies in the studied samples as an additional proof that the observed silicification was due to a pervasive circulation of low-temperature (< 200 °C) hydrothermal fluids.

The low temperature of silicifying fluids, inferred from the comparison of trace element mobilisation in the studied samples with those observed in modern hydrothermal systems, is consistent with the lowest equilibrium temperature of ~125 °C provided by our oxygen isotope analyses (**Figure 3-10c**). This temperature is considered to provide the uppermost constrain on the silicification temperature that may actually be even lower (as low as < 100 °C; Kleine et al., 2018). An important difference from modern hydrothermal systems however is that the intense silicification, with SiO_2 concentration increasing up to almost the double of its initial value, has never been reported in the modern oceanic crust. The elevated frequency of silicification as a preferential form of low-temperature hydrothermal alteration observed in archean greenstone belts (e.g. Duchac and Hanor, 1987; Hofmann and Harris, 2008; Rouchon and Orberger, 2008; Brengman and Fedo, 2018; de Wit and Furnes, 2016; Hofmann et al., 2022) is most likely due to particular palaeoenvironmental conditions that are still to be determined. The ubiquitous silicification observed in near-seafloor archean rocks is generally correlated with inferences of high dissolved silica volume in archean oceans (Siever, 1992), but the origin of this silica remains enigmatic. Processes that were previously proposed to have caused silica enrichment in archean ocean include high-temperature water-rock interaction in the deep crust (Paris et al., 1985; Hofmann and Harris, 2008; André et al., 2022) and reverse weathering (Mackenzie and Kump, 1995; Trower and Fischer, 2019a) although further research is still needed to establish the effect of these processes on archean Si cycle.

3.6.5. Relative chronology of alteration and implications for the fluid record of archean near-seafloor-derived rocks

The different events demonstrated by our data to have modified the mineralogy or the geochemistry of the silicified lavas and cherts from the Onverwacht Group are summarised in **Figure 3-17**. After deposition or eruption on the palaeoarchean seafloor (Stage I), the studied rocks were silicified by seawater-derived hydrothermal fluids while residing near the seafloor (stage II). Subsequently, the rocks underwent regional metamorphism that was mostly isochemical as it did not generate notable elemental mobility (Stage III). Finally, the rocks interacted (or have been interacting) with oxidised fluids that are interpreted to reflect a post-archean episode of meteoric fluid circulations in the Belt (Stage IV).

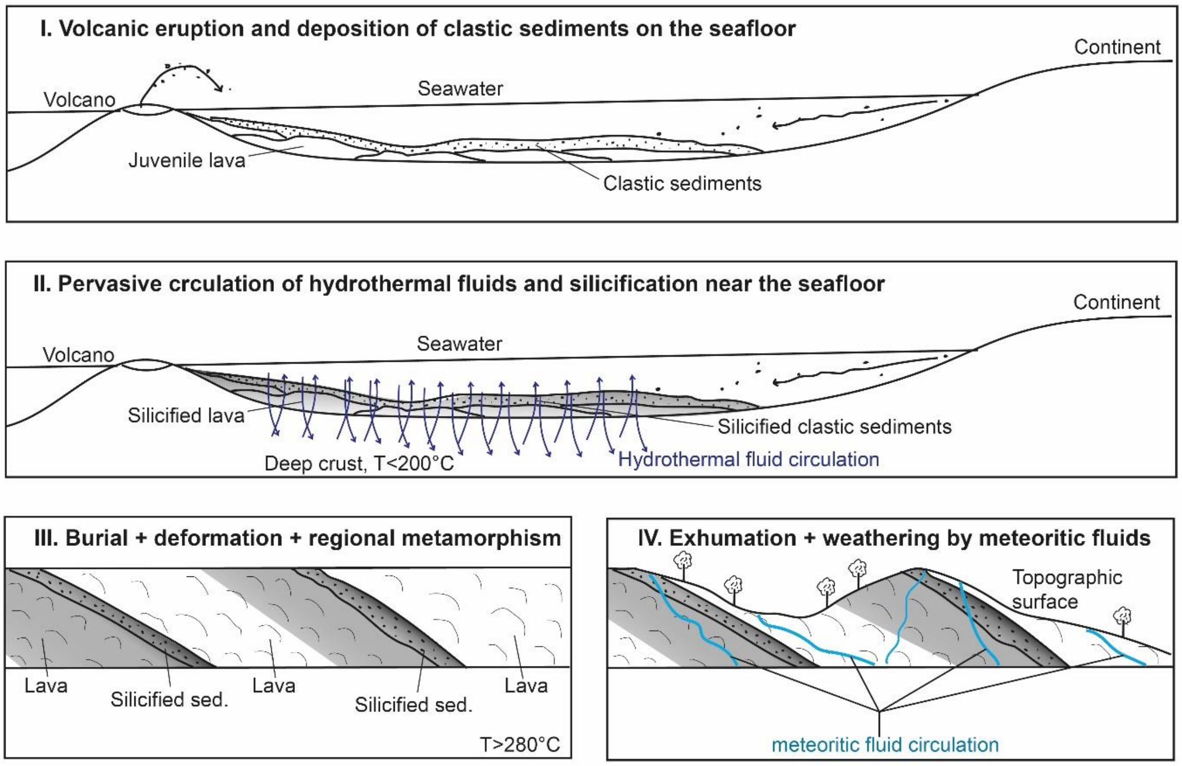

Figure 3-17. Summarised cartoon illustrating the history of the studied samples reconstructed based on the presented data with a focus on fluid-involving and temperature-involving processes. Stage I represents an episode of submarine volcanism followed by the deposition of continentally derived clastic sediments and/or remobilised pyroclastites. Stage II represents the episode of silicification near the seafloor at <150°C due to circulations of seawater-derived hydrothermal fluids that are heated at depth in the oceanic crusts. This episode must have operated in at least two different stages consisting of the silicification of the matrix and the formation of chert veins that crosscut the early silica-rich areas. Stage III represents the regional metamorphism at ~350°C that is recorded by the Raman spectra of carbonaceous material and chlorite composition, and that generated variable $\delta^{18}O$ values in quartz-carbonate assemblages. Finally, stage IV illustrates the circulation of meteoric fluids after exhumation of the studied samples near oxidised meteoric conditions that generated Ce anomalies in some samples. Grey areas represent silicified zones.

The distinction of different alteration events achieved in this study and summarised in **Figure 3-17** presents important implications for topical debates about the use of near-seafloor-derived rocks as proxies for archean seawater and hydrothermal fluids. We firstly confirm that episodes of elemental mobilisations are likely to have altered the geochemistry of most archean rocks, including the studied silicified lavas and cherts (Weis and Wasserburg, 1987b; Toulkeridis et al., 1998; Hayashi et al., 2004; Lowe and Byerly, 2007b; Bonnand et al., 2020).

We also show that diverse mineralogical and geochemical tools can allow differentiating the effect of these late-stage events (e.g. regional metamorphism and meteoric fluid circulation) from near-seafloor-derived geochemical signatures that represent the actual record of archean fluids. Therefore, it is possible to disentangle geochemical signatures that were generated near the archean seafloor from those due to later alterations by metamorphic and other crustal fluids. Another important implication of the study is that, in the Onverwacht Group, near-seafloor hydrothermal process did not ascribe seawater-like geochemical signatures (e.g., Y/Ho > 35, low REE concentration and positive La anomaly) to the studied silicified rocks. This disagrees with the idea that hydrothermal silicification could have ascribed seawater-like geochemical signatures to some volcanic and sedimentary materials of archean age, and thus promoted their erroneous qualification as orthochemical sediments (e.g. Fedo and Whitehouse, 2002; Bolhar et al., 2004; Brengman and Fedo, 2018). This idea has been used to question the orthochemical nature of some cherts or BIFs and even to refute their potential record of primitive life as proposed by other studies (Dauphas et al., 2004; Manning et al., 2006; Phillip Nutman et al., 2016), because microbial communities can hardly prosper in a lavas or be preserved in high current sediments. We demonstrate that silicified lavas and sediments (or *lato-sensu* cherts) kept the main features of their magmatic or clastic geochemistry such as their content in most HREE and HFSE. As hydrothermal fluids must have lost their seawater-derived geochemical signatures by interacting with the sub-oceanic crust (Hart and Staudigel, 1982; Mills and Elderfield, 1995; Alt et al., 2010; Coogan and Gillis, 2018a), we suggest that such fluids were incapable of ascribing seawater-like signatures to the studied rocks. The trace element composition of archean silicified rocks can therefore be hardly confused with that of orthochemical sediments. At least for the studied region, typical geochemical signatures of seawater should be maintained as diagnostic for orthochemical cherts or BIFs because these signatures are not expected to occur in silicified lavas and clastic sediments.

3.7. Conclusion

The analysis of various data types presented in this study allows disentangling three different events that collectively modified the mineralogical and/or geochemical composition of silicified lavas and sediments cropping out in the Onverwacht Group.

- The first process consists of **hydrothermal silicification** of near-seafloor lavas and clastic sediments by seawater-derived hydrothermal fluids. These fluids had interacted with the deep crust at a higher temperature, but not high enough to generate notable positive anomalies in Eu. The temperature of silicification is quantified here at < 125 °C by oxygen isotope fractionation in a single quartz-carbonate assemblage.

- The silicification process led to an increase of SiO_2 concentration materialised by the precipitation of silica. The silicification was also accompanied by a notable decrease in MgO, FeO and Na_2O concentrations and an increase in K_2O, Rb and Ba concentrations, as well as a slight and gradual increase in LREE concentrations, as informed by higher La/Sm ratios in the silicified lavas relative to unsilicifed ones. Despite slightly increasing the LREE content in the rocks, the hydrothermal silicification did not considerably modify the Sm-Nd and La-Ce isotope systematics.
- Following near-seafloor silicification, **regional metamorphism** recrystallised isochemically the mineralogical assemblages owed to near-seafloor silicification. Above the Komati fault, this process occurred at 280-360 °C as suggested by the chemistry of chlorite and the Raman spectra of carbonaceous material. It is also shown to have partially re-homogenised oxygen isotope distributions within quartz-carbonate assemblages.
- Finally, the **circulation of meteoric fluids** generated chemical modification that are recorded by the Sm-Nd and the La-Ce isotopic systematics in few samples. The La-Ce systematics is more prone to modification due to the redox sensitivity of Ce. This process is possibly responsible for the formation of late-stage oxides in the studied samples, and also of the geochemical modification of muscovite rim composition.

3.8. Supplementary Files

All the supplementary figures and tables cited in this part of the thesis are available in Appendices (see appendices A).

3.9. Bridge to Part VI

The most important finding of this **Part III** is that, despite metamorphism and meteoric weathering, the Barberton silicified lavas and cherts preserve geochemical signatures derived from the palaeoarchean seafloor. Particularly, the O isotope composition of quartz is observed to remain nearly constant while the O isotope composition of carbonates changes due to regional metamorphism (**Figure 3-10**). We can therefore focus on the isotopic composition of quartz in these rocks to constrain the properties of the fluids that generated the silica-rich rocks occurring in the Onverwacht Group. In the next part (**Part IV**), selected samples of pervasively silicified lavas and cherts analysed in this chapter, and new seawater-precipitated cherts from the Onverwacht Group, are studied to explore the O and Si isotopic composition of the silicifying hydrothermal fluids and its link with the reconstruction of seawater properties.

Part IV.

Oxygen and silicon isotopic compositions of archean silicified lava and cherts of the Onverwacht Group: implication for seafloor hydrothermalism and the nature of recycled components in the source of granitoids

This chapter is published in Chemical Geology Volume 670, 20 December 2024, 122407. Co-author of the manuscript are Professors David Zakharov, Johanna Marin-Carbonne, Maud Boyet, Jean-Francois Moyen, Tommaso Di-Rocco, Andreas Pack, Nicolas Olivier and Gary Stevens.

(Accessible at : https://doi.org/10.1016/j.chemgeo.2024.122407).

Abstract

Cherts are commonly used as proxies for archean environmental conditions such as oceanic temperature. However, because cherts encompass a wide variety of silica-rich rocks, including post-depositionally silicified of clastic sediments or chemical precipitates from seawater, reconstructions of the archean environment based on their O and Si isotopic compositions remain controversial. In this study, we present triple O isotope analyses associated with SIMS O and Si isotope measurements of palaeoarchean pervasively silicified lavas and clastic sediments, which have been less studied than the associated cherts within the Onverwacht Group (Barberton greenstone belt, South Africa). We also provide triple O isotopic compositions of seawater-precipitated cherts. The O and Si isotope composition of silicified clastic sediments and lavas is not considerably variable through the Onverwacht succession. These lithologies display relatively low δ^{18}O (11.3-14.9‰) and high Δ'^{17}O values (-0.05 to -0.07‰) attributed to precipitation of silica from hydrothermal fluids at less than 200 °C. Using these results, we reconstruct the approximate O isotope composition of the hydrothermal fluids. Water-rock interaction models suggest that this calculated fluid composition is consistent with the existence of low δ^{18}O oceans, but the exact δ^{18}O value of the palaeoarchean ocean remains elusive. Seawater-precipitated cherts show a mixture of hydrothermal- and seawater-like triple O isotope signatures, confirming that cherts are not straightforward proxies for constraining archean seawater composition or temperature. The average δ^{30}Si value of the pervasively silicified lavas and clastic sediments is positive (> +0.19‰) and compositionally similar to published values of the seawater-precipitated cherts. This suggests comparable δ^{30}Si values between archean hydrothermal fluids and seawater. A gradual increase of δ^{18}O values of silicified lavas and cherts from 10-13‰ to 15-20‰ observed along the Onverwacht succession is ascribed to local lithospheric cooling occurring between 3.47 Ga and 3.3 Ga, while Si isotope compositions remained mostly unchanged in the silica-rich rocks. As silicified lavas are likely part of materials that melted to generate palaeoarchean granitoids, the evolution of O isotopic compositions and the constancy of Si isotopic compositions may have characterised the silicified rocks that were recycled into different generations of granitoid sources. We propose that this may explain the variation of O isotopic compositions measured in different granitoid generations in the Barberton area.

Keywords: Chert, Silicified lava, Seafloor hydrothermalism, Palaeoarchean granitoids

4.1. Introduction

Interactions between seawater and submarine mafic rocks facilitated the generation of felsic and relatively buoyant continental crusts during the Archean Eon (Martin et al., 2014; André et al., 2019; Tamblyn et al., 2023). On the modern Earth, infiltration of seawater and water-rock reactions driven by heat deep in the oceanic crust plays an important role in altering the composition of the oceanic crust and generating hydrothermal fluids (Elderfield et al., 1999; Shanks, 2001; Alt and Bach, 2006; Alt et al., 2010; Yu et al., 2023; Zakharov et al., 2021a). Hydrothermal fluids are compositionally different from seawater, and modulate the balance of many dissolved elements on geologically long timescales (Shanks, 2001). For the Archean Eon, greenstone belts likely represent the best archives of seawater-rock interactions. Archean greenstone belts are often composed of silicified lavas in which magmatic minerals were replaced by quartz through hydrothermal alteration of the archean crust (e.g. Grosch and Slama, 2017; Hofmann et al., 2022). Some of these silicified lavas preserve their volcanic structures (e.g., pillows) and textures (e.g., spinifex and ocellar textures) while being completely replaced by a silica-rich matrix (Paris et al., 1985; Hanor and Duchac, 1990). This process is termed silicification and is likely an intrinsic feature of seawater-rock interaction below the silica-rich archean ocean.

In many greenstone belts, silicified lavas are intertwined with chert layers consisting of hydrothermally and/or diagenetically silicified clastic sediments and pure silica precipitated from seawater (Lanier and Lowe, 1982; Hofmann et al., 2013; Ledevin et al., 2019). These silica-rich lithologies not only reveal the chemistry of the archean seawater (Holmden and Muehlenbachs, 1993; Jaffrés et al., 2007; Tatzel et al., 2022) and hydrothermal fluids (van den Boorn et al., 2007; Hofmann and Harris, 2008; Brengman et al., 2016), but can constrain also the composition of the altered crust that was reworked in the magma sources of archean granitoids (Foley et al., 2003; Deng et al., 2019; André et al., 2019, 2022).

Recent measurements of O and Si isotope compositions in archean granitoids have firmly supported the contribution of seafloor-derived silica to their source (Vezinet et al., 2018; André et al., 2019; Deng et al., 2019; Wang et al., 2022; Lei et al., 2023). However, the potential compositional evolution of the recycled silicified lithologies is obstructing the interpretation of the O and Si isotopic variations of archean granitoids (e.g. Lei et al., 2023). Investigating of variations in O and Si isotopic compositions of silicified lavas and cherts from well-constrained stratigraphic and petrographic frameworks, within a single greenstone belt, is the next necessary step to understand the pathways of the recycled seafloor-derived silicified lithologies.

Another complicating factor is the progressive O and Si isotope evolutional trends recorded by global chert compilations, which have been differently interpreted as due to (1) secular cooling of oceans (Knauth and Lowe, 1978; Robert and Chaussidon, 2006; Lowe and Byerly, 2020), (2) to the evolution of seawater isotopic compositions (Jaffrés et al., 2007; Herwartz et al., 2021) or (3) to changes in diagenetic temperatures through time (Sengupta and Pack, 2018; Zakharov et al., 2021b). Importantly, several studies have highlighted the ambiguity in our understanding of the origin of archean cherts as they could form from various processes including hydrothermal and diagenetic silicification of precursor sedimentary or volcanic material as well as direct chemical precipitation form seawater (van den Boorn et al., 2007, 2010; Marin et al., 2010; Marin-Carbonne et al., 2011, 2012; Ledevin et al., 2014; Stefurak et al., 2015;). Moreover, in situ studies of O and Si isotopic variations in cherts have revealed the importance of diagenetic and late fluid circulation processes that can influence both O and Si isotope compositions of cherts (Marin et al., 2010; Marin-Carbonne et al., 2012; Cammack et al., 2018). Recent triple O isotope analyses (i.e. simultaneous measurements of $^{18}O/^{16}O$ and $^{17}O/^{16}O$ ratios) have also confirmed the importance of post-depositional processes such as diagenesis and regional metamorphism on O isotope compositions of cherts (Sengupta et al., 2020; Yanchilina et al., 2020; Ibarra et al., 2022; Zakharov et al., 2023). Due to the complexity of chert-forming processes, a quantitative determination of parental fluid O and Si isotope compositions is still challenging.

The first objective of this study was to constrain the isotopic composition of palaeoarchean hydrothermal fluids by characterizing Si ($^{28}Si/^{30}Si$) and O ($^{16}O/^{17}O/^{18}O$) isotopic compositions of samples, namely (1) silicified lavas, (2) silicified clastic sediments and (3) seawater-precipitated cherts, that represent different pathways of archean aqueous silica, leading to a diversity of chert-forming mechanisms. The second objective was to place new constrains on the O isotope composition and temperature of the palaeoarchean seawater using the diverse and well-characterised set of samples. Finally, the last objective was to provide a comprehensive suite of samples that could potentially represent the recycled material that contributed to the source of TTG magmas. This study was conducted on samples derived from the 3.5-3.3 Ga old Onverwacht Group of the Barberton greenstone belt, which includes portions of the palaeoarchean submarine mafic crust (Paris et al., 1985; Hofmann and Harris, 2008; de

Wit et al., 2011), and which is considered as analogous to the source of surrounding 3.5-3.1 Ga old granitoids (André et al., 2019, 2022; Deng et al., 2019; Lei et al., 2023).

4.2. Samples and methods

4.2.1. The Onverwacht Group

The Onverwacht Group is part of the 3.55-3.2 Ga Barberton greenstone belt located in the NE part of the Southern African Kaapvaal Craton (**Figure 4-1**). It is one of the best-preserved records of an archean seawater-altered crust, comprising alternating ultramafic to mafic lavas and silicified sediments that are commonly identified as “cherts” in the literature (Byerly et al., 1996; Hofmann and Harris, 2008; de Wit and Furnes, 2016). The Onverwacht Group includes six distinct geological formations that encompass in chronostratigraphic order the Sandspruit, Theespruit, Komati, Hooggenoeg, Kromberg and Mendon formations (Lowe and Byerly, 2007; Hofmann and Harris, 2008). Each of these formations is subdivided into different stratigraphic members and each member typically includes a mafic unit and a sedimentary or chert layer (**Figure 4-1b**). Each volcanic eruption was followed by a period (may be up to > 1 Ma) of volcanic quiescence during which cherts deposited and lava flow tops were silicified (Paris et al., 1985; Duchac and Hanor, 1987; Hofmann and Harris, 2008). The portion of the Onverwacht Group situated to the north of the Komati Fault (**Figure 4-1**) was affected by a regional greenschist-facies metamorphic event (300-400 °C) (Xie et al., 1997; Tice et al., 2004; Grosch, 2018; Alleon et al., 2021).

The chert units of the Onverwacht Group include pervasively silicified detrital sediments and pure silica precipitates that are all dominated by more than 90 vol.% by microquartz (Rouchon and Orberger, 2008; Hofmann et al., 2013; Ledevin et al., 2019). These pervasively silicified clastic sediments generally preserve sedimentary features including normal grading of clastic components at the outcrop scale (Lanier and Lowe, 1982; Paris et al., 1985; Duchac and Hanor, 1987; Rouchon and Orberger, 2008; Ledevin et al., 2014). They are by far the dominant member of the chert family, generally appearing in the field as black, grey or black-and-white banded chert layers (Lanier and Lowe, 1982; Lowe and Byerly, 1986; Hofmann et al., 2013; Lowe et al., 2020; **Figure 4-2a**). Pure chemical cherts are quite rare in the Onverwacht Group and may include the detritus-free banded chert layers of the Buck Reef Chert Unit located at the bottom of Kromberg Formation and similar rocks from the Mendon formation (Stefurak et al., 2015; Ledevin et al., 2019; Lowe and Byerly, 2020). The δ^{18}O value of cherts from the Onverwacht Group increases gradually from ~11 ‰ at the base, and the Buck

Reef Chert displays some of the highest $\delta^{18}O$ values of this stratigraphic succession (up to 22 ‰, see at 7 km) (**Figure 4-3a-b**) (Knauth and Lowe, 1978, 2003; Abraham et al., 2011; de Wit and Furnes, 2016; Lowe and Byerly, 2020). In contrast, the $\delta^{30}Si$ of these cherts does not show a systematic variation over the stratigraphic column (**Figure 4-3c**).

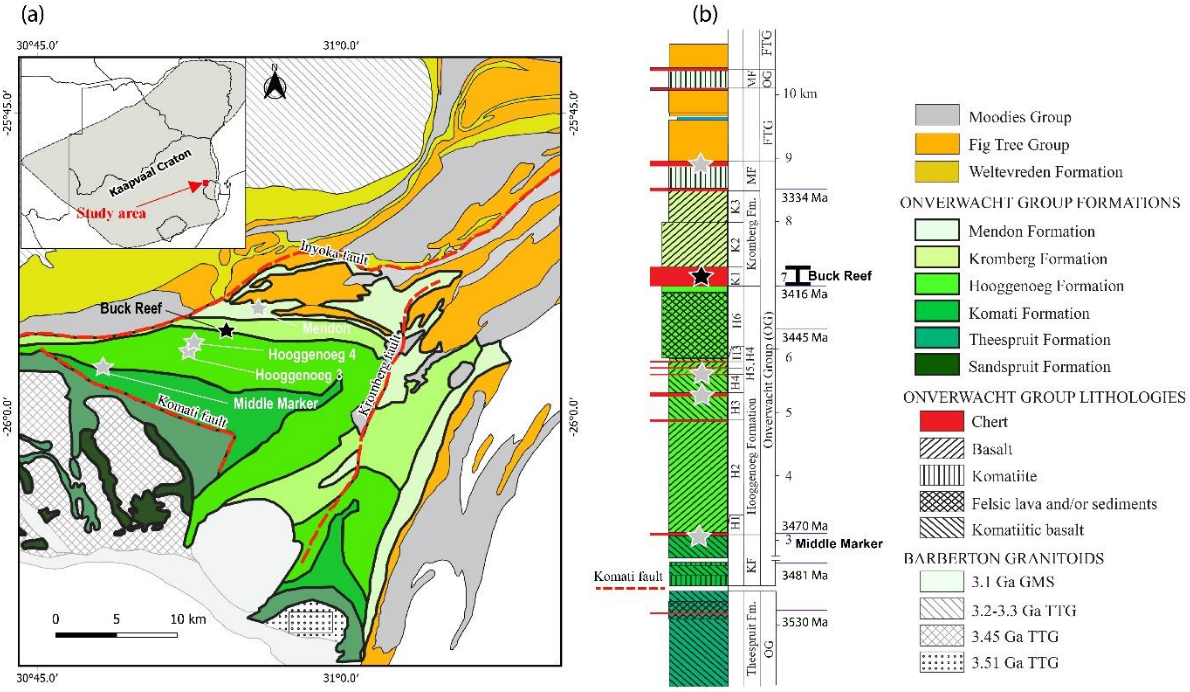

Figure 4-1. Geological map (a) and lithostratigraphy (b) of the Barberton greenstone belt. The geological map and lithostratigraphic section, together with existing geochronological constrains were modified from Hofmann (2005) and Byerly et al. (2019). Black stars are indicative of the Buck Reef Chert locality which represent seawater-precipitated cherts while the grey stars are representative of silicified clastic sediment and lavas from the Middle Marker, Hooggonoeg 3, Hooggenoe 4 and Mendon 1 stratigraphic members.

Lava units of the Onverwacht Group evolve downwards from pervasively silicified lava that recorded intense interactions with Si-rich hydrothermal fluids at the top, to non-silicified lava (Paris et al., 1985; Hofmann and Harris, 2008; Abraham et al., 2011). The silicified lavas feature original magmatic structures (e.g. pillows – see **Figure 4-2b** – and spinifex or ocellar textures) or structures that are typical of hydrothermal environments (e.g. brecciated textures) (Paris et al., 1985; Lowe and Byerly, 1986; Hofmann and Harris, 2008). Pervasively silicified lavas consist of >80 vol.% microscopic quartz (hereinafter microquartz) and minor assemblages of phyllosilicate phases (i.e. chlorite and muscovite), Fe-Ti oxides, carbonates and sulphides (Hofmann and Harris, 2008). Silicified lavas and cherts are all extremely fine-grained, such that separation of minor and accessory phases from quartz for selective isotopic analysis is not possible. Previously collected bulk-rock isotopic compositions of O and Si in partially and pervasively silicified lavas from the Onverwacht Group ($\delta^{18}O$ of 10.5-15.6‰ and $\delta^{30}Si$ of -0.64

to 0.74‰) are shown in **Figure 4-3** (Hofmann and Harris, 2008; Abraham et al., 2011; de Wit and Furnes, 2016).

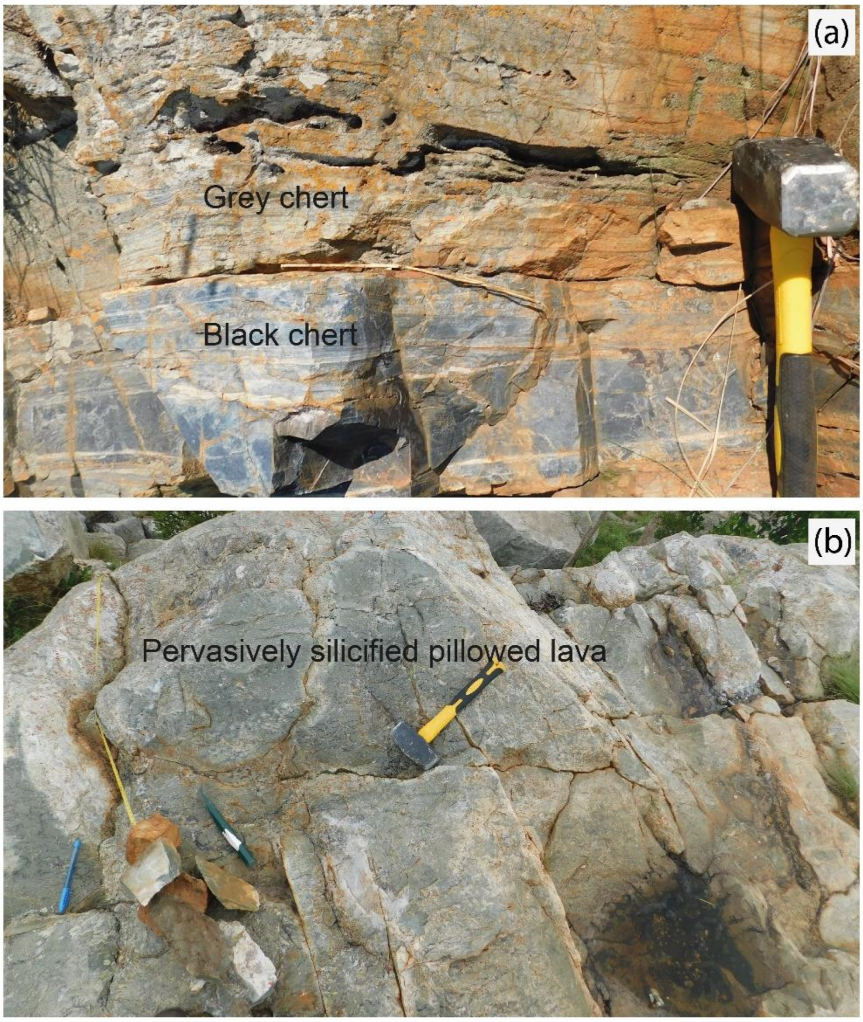

Figure 4-2. Illustration of field occurrence of pervasively silicified cherts (a) and pillowed lava (b). Note that the pervasively silicified lavas crop out as greenish lithologies with common preservation of their original volcanic structures (e.g. pillows), whereas cherts occur as grey and black layers locally preserving some sedimentary features.

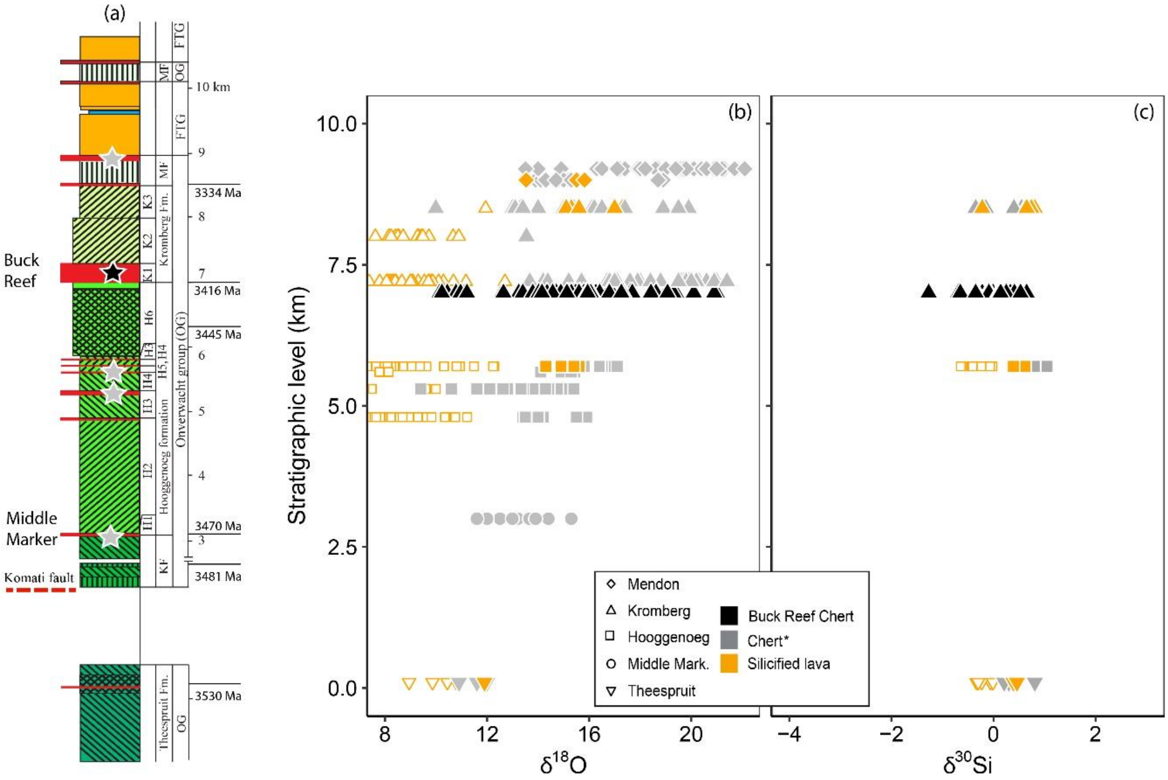

Figure 4-3. Stratigraphic succession of the Onverwacht Group (a) and a compilation of previously analysed oxygen (b) and silicon (c) isotopic compositions in cherts (including silicified clastic sediments and seawater-precipitated cherts) and silicified lava from the Onverwacht Group plotted against stratigraphic positions. In filled symbols are silicified lavas and cherts with an SiO_2 content exceeding 60 wt.%, while open symbols are lavas with a lower SiO_2 that is inferior to 60 wt.%. Only bulk-rock data are shown on this figure, and they were compiled from the following studies: Knauth and Lowe (1978, 2003), Hofmann and Harris (2008), Abraham et al. (2011), Geilert et al. (2014), de Wit and Furnes (2016), Lowe and Byerly (2020). The seawater-precipitated cherts of the Buck Reef Chert are plotted in black, while other cherts are in grey and silicified lava are in orange. The star (*) on cherts in the legend indicates that they may comprise pervasively silicified clastic sediments and seawater-precipitated cherts that were not clearly distinguished in the literature.

4.2.2. Sample description

In this study, we analysed three different groups of samples: (1) silicified lava, (2) silicified clastic sediments and (3) seawater-precipitated cherts. The first sample group comprises six pervasively silicified lava samples collected respectively from the Middle Marker (number of samples or n=1; SK-MM11), Hooggeonoeg 3 (n=2; SK-HO09 and SK-HO12) and Mendon 1 (n=3; SK-ME17, SK-ME18 and SK-ME20) members of the Onverwacht Group (**Figure 4-1**). These samples derived from variable depths below chert layers (1 to 40 m), but they all contain more than 90 vol.% of microquartz testifying their pervasive silicification. The second group of samples includes seven cherts representing pervasively silicified clastic sediments derived from the Middle Marker (n=4; MM07-11, MM07-10, MM24 and

MMJLog53), Hooggenoeg 3 (n=1; SK-HO05) and Hooggenoeg 4 (n=2; SK-HO25 and SK-HO26) stratigraphic members. Finally, the third sample group is constituted by nine seawater-precipitated chert samples that originated from the Buck Reef Chert (Buck4A plus eight ICDP samples obtained from the BARB4 ICDP drill core) located at the base of the Kromberg Formation (Ledevin et al., 2019; Lowe et al., 2020).

Petrographic descriptions allow identifying four different types of quartz in both the silicified lavas and silicified clastic sediment samples that we analysed by SIMS (**Figure 4-4**). The first and most dominant type is a microquartz made of micron-sized (<30 µm) crystals that make up more than 90% of the rock (**Figure 4-4a**) with minor phases of phyllosilicates (chlorite and muscovite), carbonates, oxides, sulphides and phosphates. The second type of quartz corresponds to veins (**Figure 4-4b-c**) made of coarser quartz crystals (<70 µm), with additional minor assemblages of Fe oxide and carbonate phases. The third quartz type corresponds to megaquartz (**Figure 4-4c**). The coarse-grained quartz crystals (>150 µm) occur as void-filling aggregates. Finally, the fourth type of quartz is represented by inclusions within carbonate phases (i.e. calcite in SK-MM11 and ankerite in SK-ME18). These quartz inclusions are made of polycrystalline assemblages to monocrystalline euhedral quartz (**Figure 4-4d**).

4.2.3. O and Si isotope analyses

In addition to published datasets on O and Si isotope variations in cherts and silicified lavas from the Onverwacht Group (**Figure 4-3**) Knauth and Lowe, 1978, 2003; Hofmann and Harris, 2008; Abraham et al., 2011; Marin-Carbonne et al., 2011; Geilert et al., 2014; Stefurak et al., 2015; de Wit and Furnes, 2016; Hayles et al., 2019; Zakharov et al., 2021), here we analysed the triple O isotope composition of all the samples described in the previous section excepted one silicified lava (SK-ME18). We also conducted SIMS analyses in five selected samples including one silicified clastic sediment (SK-HO25) and four pervasively silicified lavas (SK-MM11, SK-HO09, SK-ME17 and SK-ME18) that are representative of three different geological formations of the Barberton greenstone belt, namely the Komati, Hooggenoeg and Mendon formations.

4.2.3.1. Notations

The delta notation of stable isotope ratios in a sample quantifies their relative difference from ratios of the same isotopes in a reference material (i.e. V-SMOW for O and NBS-28 for Si isotopes) and is expressed in **Equations 4-1** to **3-4**:

$$\delta^{X}O = 1000 \times [(^{X}O/^{16}O_{sample}) - (^{X}O/^{16}O_{VSMOW})] / (^{X)}O/^{16}O_{VSMOW}) \quad \textbf{(Equation 4-1)}$$

with X representing either 18 or 17;

$$\delta^{30}Si = 1000 \times [(^{30}Si/^{28}Si_{sample}) - (^{30}Si/^{28}O_{NBS\text{-}28})] / (^{30}Si/^{28}Si_{NBS\text{-}28}) \quad \textbf{(Equation 4-2)}$$

The definition of $\Delta'^{17}O$ is given by:

$$\Delta'^{17}O = \delta'^{17}O - 0.528 \times \delta'^{18}O \quad \textbf{(Equation 4-3)}$$

where $\delta'^{17}O$ and $\delta'^{18}O$ are linearized delta expressions:

$$\delta'^{18(17)}O = 1000 \times \ln(\delta^{18(17)}O /1000 + 1). \quad \textbf{(Equation 4-4)}$$

4.3.3.1. Secondary ion mass spectrometry (SIMS)

Analyses of O and Si isotopic compositions of quartz by secondary ion mass spectrometry were carried out within the SwissSIMS laboratory at the University of Lausanne (UNIL), using the CAMECA 1280 HR secondary ion mass spectrometer. Selected zones (3 x 4 cm) of thin sections were imaged under a polarising microscope, isolated by a high precision diamond wire-saw and pressed into indium mounts together with the UNIL-Q1 reference quartz (Seitz et al., 2017). The surface of indium mounts did not exceed 5 microns of elevation difference, as determined with a Brucker GTA-K white light interferometer. After carbon coating and imaging by scanning electron microscopy at the Laboratoire Magmas et Volcans, University Clermont Auvergne, the carbon coat was removed by polishing, and the surface of each mount was cleaned with pure ethanol and distilled water, then dried in an oven and coated with a ~ 20 nm-thick gold layer. The samples were measured during two O isotope analyses sessions and two Si isotope session.

A 10 kV primary beam of Cs^{+} ions was tuned at 1.3 nA for O isotopes and ~ 2nA for Si isotopes and focused to a diameter of 15 μm. A current of -10 kV was applied using an electron gun to compensate the charge following the routine SIMS procedure. The mass resolving power was set at 2400 using an entrance slit of 122 microns and multicollection exit slit of 1. Each O isotope analysis lasted ~ 3 minutes that included 30 s of pre-sputtering, followed by automatic signal optimization by centring the secondary beam, and 20 cycles of 5 s of secondary ion collection. For Si isotope measurements, analysis time was 3.5 minutes and included 1 minute of pre-sputtering of the targeted surface, automatic centring of the secondary ions and 25 cycles of 5 s of measurements. $^{16}O^{-}$, $^{18}O^{-}$, $^{28}Si^{-}$ and $^{30}Si^{-}$ were detected in multicollection mode using Faraday cups; L'2 trolley for $^{16}O^{-}$ and $^{28}Si^{-}$ (using a 10^{10} Ω resistor for $^{16}O^{-}$ and 10^{11} Ω resistor for $^{28}Si^{-}$) and H1 trolley for $^{18}O^{-}$ and $^{30}Si^{-}$ (both using a 10^{11} Ω resistor).

Repeated analyses of UNIL-Q1 reference quartz allowed correcting for instrumental mass fractionation and provided an external error (2 S.D.) of 0.2 – 0.6‰ for $\delta^{18}O$ and 0.5 – 0.7‰ for $\delta^{30}Si$ values depending on the analytical sessions.

4.3.3.2. Triple O isotopic analyses

Triple O isotopic analyses of 1-2 mg of silica chips isolated from each sample were done at the Geoscience Centre of Göttingen University, following the method previously described by Pack et al. (2016). The analysis of O isotopes was conducted by laser fluorination-assisted mass spectrometry. The O_2 gas was liberated from silica by a reaction with BrF_5 and purified from potential contaminants via a series of cryogenic traps. The purified O_2 was then absorbed onto 5 Å molecular sieves, and subsequently passed through a gas chromatograph via a He gas flow at 10 mL/min. After the evacuation of He carrier gas, the resultant O_2 was measured in dual inlet mode using a MAT253 instrument. The San Carlos olivine standard ($\Delta'^{17}O$ = -0.052‰) was used for calibrations of $\delta^{17}O$ on V-SMOW scale. The analytical reproducibility (i.e. the 2 S.D. value obtained from repeated analyses of San Carlos olivine) was better than ± 0.6‰ for $\delta^{18}O$ and ± 0.02‰ for $\Delta'^{17}O$. We also used the laser fluorination technique to analyse the $\delta^{18}O$ values of duplicates of the samples at the University of Lausanne. During these analyses, repeated measurements of the $\delta^{18}O$ value of LS1 quartz standard ($\delta^{18}O$=18.1‰) provided an external reproducibility (2 S.D.) of 0.2 ‰.

4.4. Modelling komatiite-seawater interaction and triple O isotope composition of resulting fluids

To model the triple O isotope and chemical composition of aqueous fluids produced by equilibrium reaction between a komatiite and seawater, we used a modelling software that computes heterogeneous aqueous-mineral equilibria. The CHIM-XPT program (Reed et al., 2010) was used to compute dissolved aqueous species and equilibrium minerals as a function of changing bulk composition, representing a series of titration steps of komatiite into 1L of solution. The equilibrium speciation of aqueous species and mineral saturation indices (i.e., logQ/K's) are computed by the CHIM-XPT software for a series of incremental titration steps with intermittent calculation of equilibrium speciation by minimization of the Gibbs Free Energy of the system. The thermodynamic and related data for calculation of aqueous and mineral species are given in the description of the modelling software, particularly in the SOLTHERM database used by the CHIM-XPT software (Reed et al., 2010). CHIM-XPT uses

Newton-Raphson method to solve a system of simultaneous mass-balance and mass-action equations and compute equilibrium activities of the aqueous and mineral species. In this study, we simulated an archean seawater-komatiite reaction at 200°C and 150 bars.

The initial compositions of reacting seawater and komatiite were set in the beginning of the calculation and the water/rock ratio is defined as a function of titrated komatiite. The initial seawater composition was taken as a close analogue to the modern seawater (Berner and Berner, 1996), with the only modification that H_4SiO_4 concentration was fixed by an equilibrium with amorphous silica at 25°C and the sulfate concentration is set extremely low. Such seawater (see **Supplementary Table B-1)** represents a simplified composition of reduced archean seawater that was probably saturated in silica, as attested by the abundance of cherts in archean greenstone belts. The model is not aimed to fully reproduce the details of chemical speciation of the archean seawater as it remains poorly constrained. However, this simple aqueous-mineral equilibrium reaction modelling is used to constrain the mass balance of the O isotope exchange trajectory between fluids and silicate rocks, where O is a major element, and silicate minerals and H_2O are major phases. The major elemental composition of seawater used in the calculations was set to (in mmol/kg): Cl = 594, Na = 457, Ca = 10.2, Mg = 53.6, K = 10.0, H_4SiO_4 = 15.7. The molality of Fe^{2+} (total dissolved species) and HCO_3- ions were set to 0.2 and 389 µmol/kg, respectively. The composition of titrated komatiitic rock was taken as follows: Na_2O = 0.1 wt. %, K_2O = 0.01 wt. %, MgO = 28.1 wt.%, FeO = 12.8 wt.%, Al_2O_3 = 4.4, SiO_2 = 47.3 wt.%.

To track the O isotope budget of the reaction, we assigned an isotope composition of mantle-derived lava to the fresh unaltered komatiite: $\delta^{18}O = 5.7‰$ and a $\Delta'^{17}O = -0.06‰$ (Pack et al., 2016). Two end-member seawater compositions were used in the calculation. In the first case, seawater was taken with $\delta^{18}O$ and $\Delta'^{17}O$ values of 0‰. In the second case, we used a seawater with $\delta^{18}O$ of -10‰ and a $\Delta'^{17}O$ of +0.01‰ to reflect a potential low-$\delta^{18}O$ seawater proposed for the archean Earth (Jaffrés et al., 2007; Sengupta and Pack, 2018; Zakharov et al., 2021; Bindeman and O'Neil, 2022). The triple O isotope composition of modelled equilibrium fluids was calculated using the mass-balance of O moles in the system distributed between equilibrium minerals and H_2O, taking into account mineral-water equilibrium fractionation factors derived from Yapp (1990), Zheng (1993) and Wostbrock and Sharp (2021). The $^{17}O/^{16}O$ fractionation factor is derived from the relationship $^{17/16}\alpha = {}^{18/16}\alpha^{\theta}$. The theta value ($\theta$) of 0.527 is adapted to calculate the ^{17}O fractionation factor based on this relationship for quartz-water equilibrium fractionation at 200 °C (Wostbrock and Sharp, 2021).

4.3. Results

4.3.1. Measured O and Si isotopic compositions

The triple O isotopic compositions measured in Göttingen and the $\delta^{18}O$ values measured in duplicate samples at UNIL by laser-fluorination are available in **Table 4-1.** In addition, the O and Si isotopic compositions acquired by SIMS are summarized in **Table 4-2** (the detailed dataset is provided in **Supplementary Tables B-2 and B-3**). The $\delta^{18}O$ values measured by SIMS and laser fluorination (both at Göttingen and Lausanne) are similar within the range of analytical error of the respective methods. SIMS analyses enabled the independent measurement of $\delta^{18}O$ and $\delta^{30}Si$ of four types of quartz identified in our samples, i.e. microquartz, quartz vein, megaquartz and quartz inclusions in carbonates (**Figure 4-4**). These four different quartz types display similar $\delta^{18}O$ and $\delta^{30}Si$ values in samples collected from the same geological formations (i.e. Komati, Hooggenoeg and Mendon formations) (**Figure 4-5**). Because the only silicified clastic sediments analysed by SIMS (SK-HO25) is indistinguishable (within error) from the silicified lava of the Hooggenoeg Formation (SK-HO09) in terms of Si and O isotope compositions, their compositions are combined in **Figure 4-5**.

Table 4-1. Measured triple O isotopic compositions

Sample	**Unit**	**Lithofacies**	**meters below sediment**	**$\delta^{18}O$ (‰)_UNIL**	**$\delta^{18}O$ (‰)**	**$\delta^{17}O$ (‰)**	**$\delta'^{18}O$ (‰)**	**$\delta'^{17}O$ (‰)**	**$\Delta'^{17}O$ (‰)**
SK-ME17	Mendon 1	Silicified lava	9 m	14.9	14.8	7.7	14.7	7.7	-0.06
SK-ME20	Mendon 1	Silicified lava	14 m	15.1	14.2	7.4	14.1	7.4	-0.06
SK-H009	Hooggenoeg 3	Silicified pillow	15 m	14.0	12.7	6.6	12.6	6.6	-0.07
SK-HO12	Hooggenoeg 3	Silicified pillow	35 m	13.8	12.8	6.7	12.8	6.7	-0.06
SK-MM11	Middle Marker	Silicified pillow	1 m	13.1	12.3	6.4	12.2	6.4	-0.05
SK-HO25	Hooggenoeg 4	silicified sediment		14.2	13.8	7.2	13.7	7.1	-0.06
SK-H026	Hooggenoeg 4	silicified sediment		13.8	13.2	6.9	13.2	6.9	-0.06
SK-H005	Hooggenoeg 3	silicified sediment		12.4	11.7	6.1	11.7	6.1	-0.06
MM07-11	Middle Marker	silicified sediment		12.1	11.3	5.9	11.2	5.9	-0.05
MM07-10	Middle Marker	silicified sediment		12.7	11.9	6.2	11.9	6.2	-0.07
MM24	Middle Marker	silicified sediment		12.8	12.5	6.5	12.4	6.5	-0.07
MMJLog53	Middle Marker	silicified sediment			13.0	6.7	12.9	6.7	-0.07
Buck4A	Buck Reef	seawater-prec. chert			16.4	8.5	16.3	8.5	-0.07
BBDP12724	Buck Reef	seawater-prec. chert			19.9	10.3	19.7	10.3	-0.09
BBDP11265	Buck Reef	seawater-prec. chert			20.3	10.6	20.1	10.5	-0.10
BBDP8545	Buck Reef	seawater-prec. chert			19.9	10.4	19.7	10.3	-0.09
BBDP13784	Buck Reef	seawater-prec. chert			19.5	10.1	19.3	10.1	-0.11
BBDP8545	Buck Reef	seawater-prec. chert			19.9	10.4	19.7	10.3	-0.10
BBDP8545	Buck Reef	seawater-prec. chert			19.3	10.0	19.1	10.0	-0.10
BBDP13784	Buck Reef	seawater-prec. chert			19.3	10.0	19.1	10.0	-0.10
BBDP13784	Buck Reef	seawater-prec. chert			17.7	9.2	17.6	9.2	-0.10

Table 4-2. Summary of SIMS-determined oxygen and silicon isotopic compositions

				OXYGEN ISOTOPE DATA			SILICON ISOTOPE DATA		
Sample	Formation	Lithofacies	quartz type	#spots	$\delta^{18}O$ (‰)	2 S.D.	#spots	$\delta^{30}Si$ (‰)	2 S.D.
SK-ME17	Mendon	Sililicified lava	matrix	*16*	15.54	0.37	*13*	0.65	0.72
			Granoblast	*15*	15.51	0.47	*16*	0.07	0.74
			vein	*9*	15.71	0.20	*9*	0.13	0.91
SK-ME18	Mendon	Silicified lava	matrix	*26*	15.13	0.59	*24*	0.75	1.63
			Granoblast	*19*	15.41	0.45	*20*	0.75	0.89
			vein	*15*	15.26	0.49	*15*	1.38	1.02
			Incl. Ank.	*7*	14.90	1.25	*4*	-0.57	0.89
SK-HO25	Hooggenoeg	Black chert	matrix	*18*	14.10	0.77	*17*	0.81	1.03
			Granoblast	*6*	14.34	0.27	*4*	1.12	0.92
			vein	*16*	14.24	0.47	*16*	0.49	1.14
SK-HO09	Hooggenoeg	Silicified lava	matrix	*13*	14.52	0.38	*11*	1.24	0.65
SK-MM11	Komati	Silicified lava	matrix	*25*	13.49	0.39	*23*	0.25	1.81
			Granoblast	*6*	13.55	0.52	*6*	0.09	0.95
			Incl. Carb.	*5*	13.09	0.44	*4*	-0.01	1.45

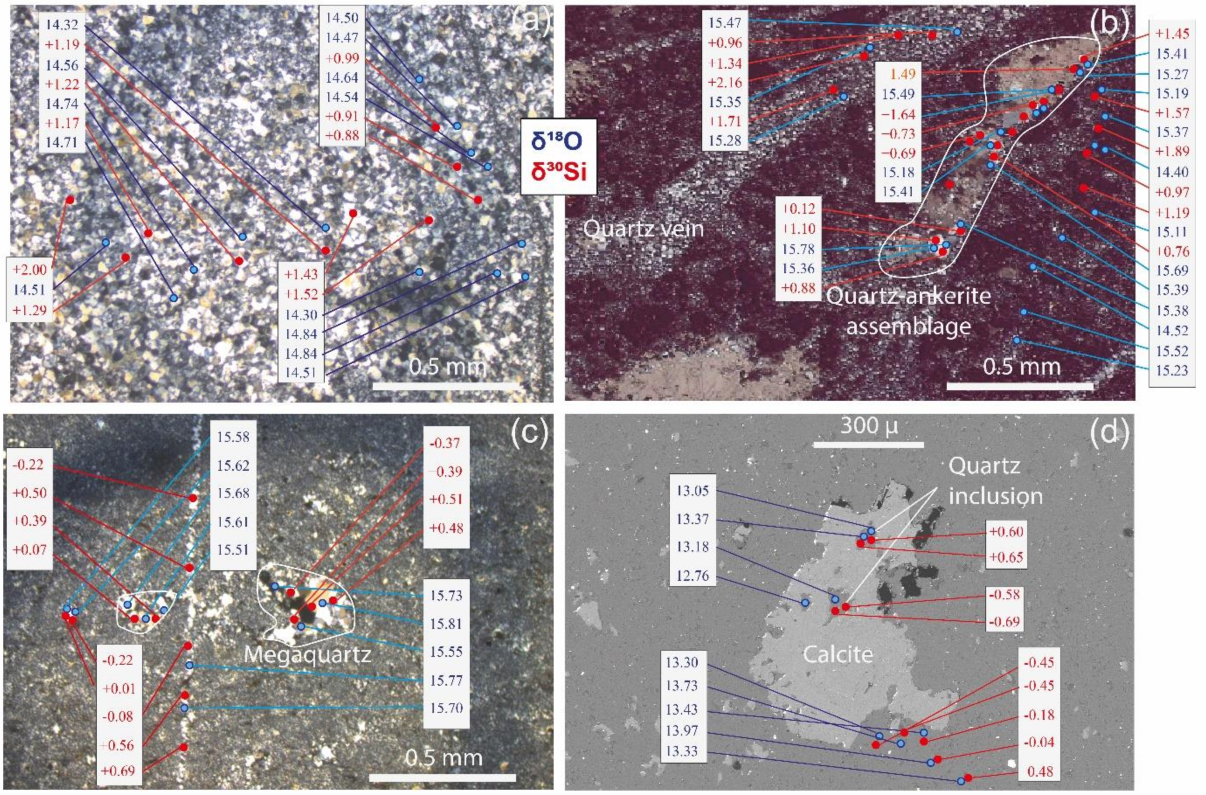

Figure 4-4. Selected petrographic features of the analysed quartz types with the SIMS $\delta^{18}O$ (in blue) and $\delta^{30}Si$ values (in red) of analysed spots. (a): microquartz of the silicified pillowed lava SK-HO09. (b): microquartz, veins and inclusions in carbonate in sample SK-ME18. (c): an aggregate of granoblastic quartz occurring in the fine-grained matrix and in a relatively thin quartz vein of sample SK-HO25. (d): a back-scattered electron image of sample SK-MM11 showing analysed quartz inclusions in calcite.

4.3.1.1. Isotopic composition of silicified lavas and silicified clastic sediments

The bulk $\delta^{18}O$ measured in pervasively silicified lavas ranges between 12.3 and 14.9‰, while pervasively silicified sediment have $\delta^{18}O$ values ranging between 11.3 and 14.2‰. These values are lower than the $\delta^{18}O$ values of seawater-precipitated cherts that extend between 16.4

to 20.3‰ (**Figures 4-5** and **4-6**). Average $\delta^{18}O$ values analysed by SIMS in the silicified lava and clastic sediment samples also range between 13.5 and 15.5‰. Individual samples depict narrow $\delta^{18}O$ variations (< 2‰) comprising the different quartz types that were analysed (i.e. i.e. microquartz, quartz veins, megaquartz and quartz inclusions in carbonates). Although quartz inclusions in carbonate phases typically extend to slightly lower $\delta^{18}O$ values in SK-MM11 (13.1 ± 0.4‰) and SK-ME18 (14.9 ± 1.3‰) silicified lava samples (**Table 4-2** and **Figure 4-4**), quartz inclusion in carbonate remains indistinguishable from the other types of quartz within the analytic error (2 S.D.= 0.6‰). Both SIMS and laser fluorination display a similar pattern of increasing $\delta^{18}O$ values (**Figure 4-5**) that is overall consistent with stratigraphic increase of $\delta^{18}O$ values in cherts upwards through the Onverwacht succession (**Figure 4-3**). The $\Delta'^{17}O$ of pervasively silicified lava and silicified clastic sediment samples range between -0.07 to and -0.05‰, covering a narrower range with higher values than seawater-precipitated cherts from the Buck Reef Unit (-0.12 to -0.07‰) (**Figure 4-6**).

The $\delta^{30}Si$ values of the analysed spots vary between -2.1 and +2.3 ‰ with no textural control on this variable within our error limits (2 S.D. = 0.5 – 0.7‰) (**Figure 4-5**). Average values of $\delta^{30}Si$ per sample are generally positive, ranging between +0.19 and +1.24, consistently with bulk-rock analyses of Si isotopes in the silicified lavas and silicified clastic sediments from the Onverwacht Group (Abraham et al., 2011; Geilert et al., 2014). Unlike $\delta^{18}O$, there is no general stratigraphic trend of $\delta^{30}Si$ variation along the Onverwacht Group in our dataset. This is consistent with the absence of a positive correlation between $\delta^{18}O$ and $\delta^{30}Si$ values in pervasively silicified lavas and clastic sediments throughout the Onverwacht stratigraphy contrary to previous observation (Abraham et al., 2011). However this positive correlation between $\delta^{18}O$ and $\delta^{30}Si$ was observed in a combination of non-silicified lava, silicified lava and chert samples with variable SiO_2 content (39.7 to 100 wt.%) (see **Supplementary Figure B-1**) in the Onverwactht Group.

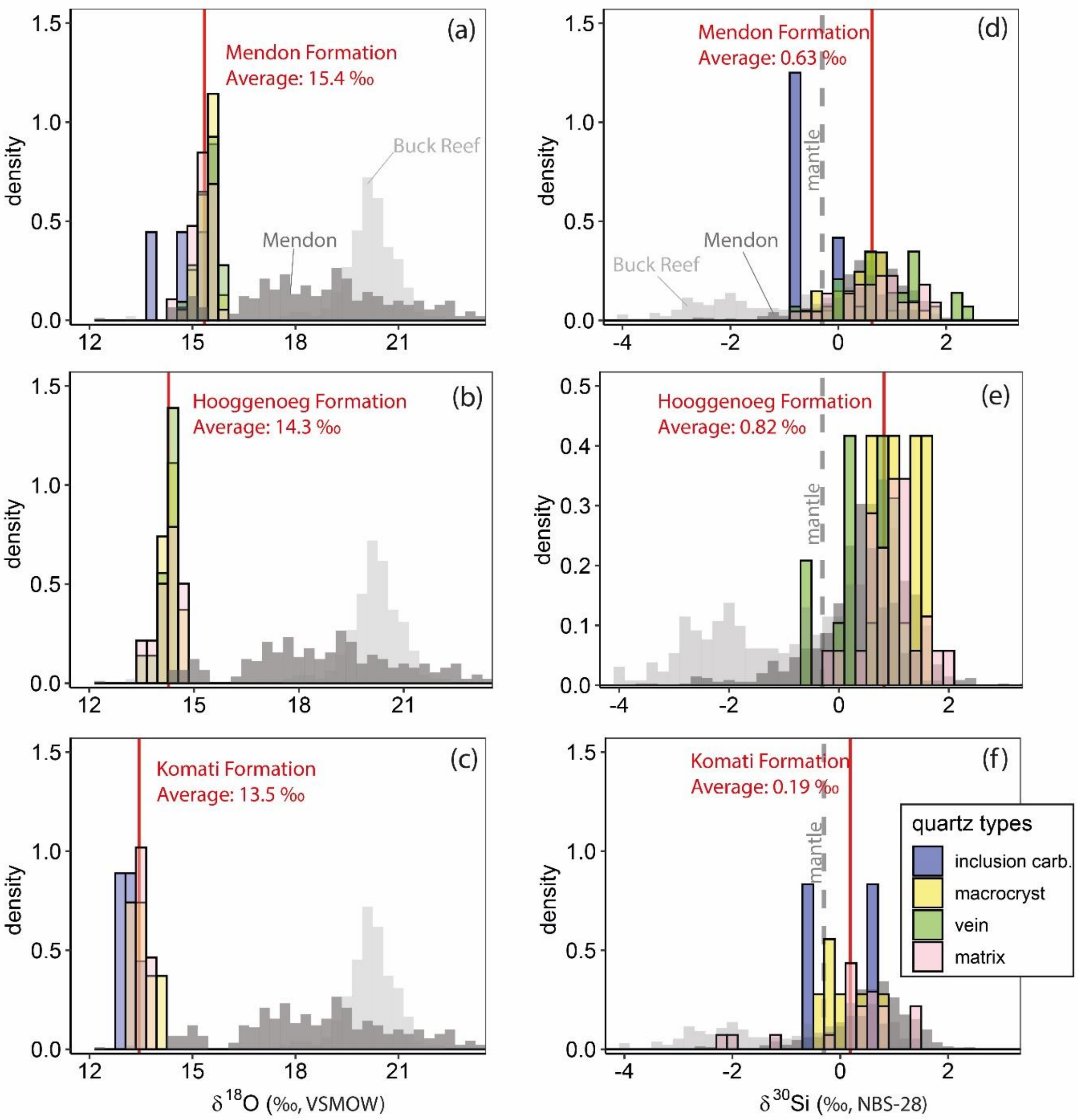

Figure 4-5. (a) to (f) Histograms presenting the SIMS-determined variations of O and Si isotopic compositions classified by microquartz matrix, quartz vein, megaquartz and carbonate-included quartz analyses within the Komati, Hooggenoeg and Mendon samples. The compositions of silicified lava and clastic sediments analysed in this study are compared with isotopic variations in seawater-precipitated Buck Reef and Mendon cherts published by Marin-Carbonne et al. (2011) and Stefurak et al. (2015).

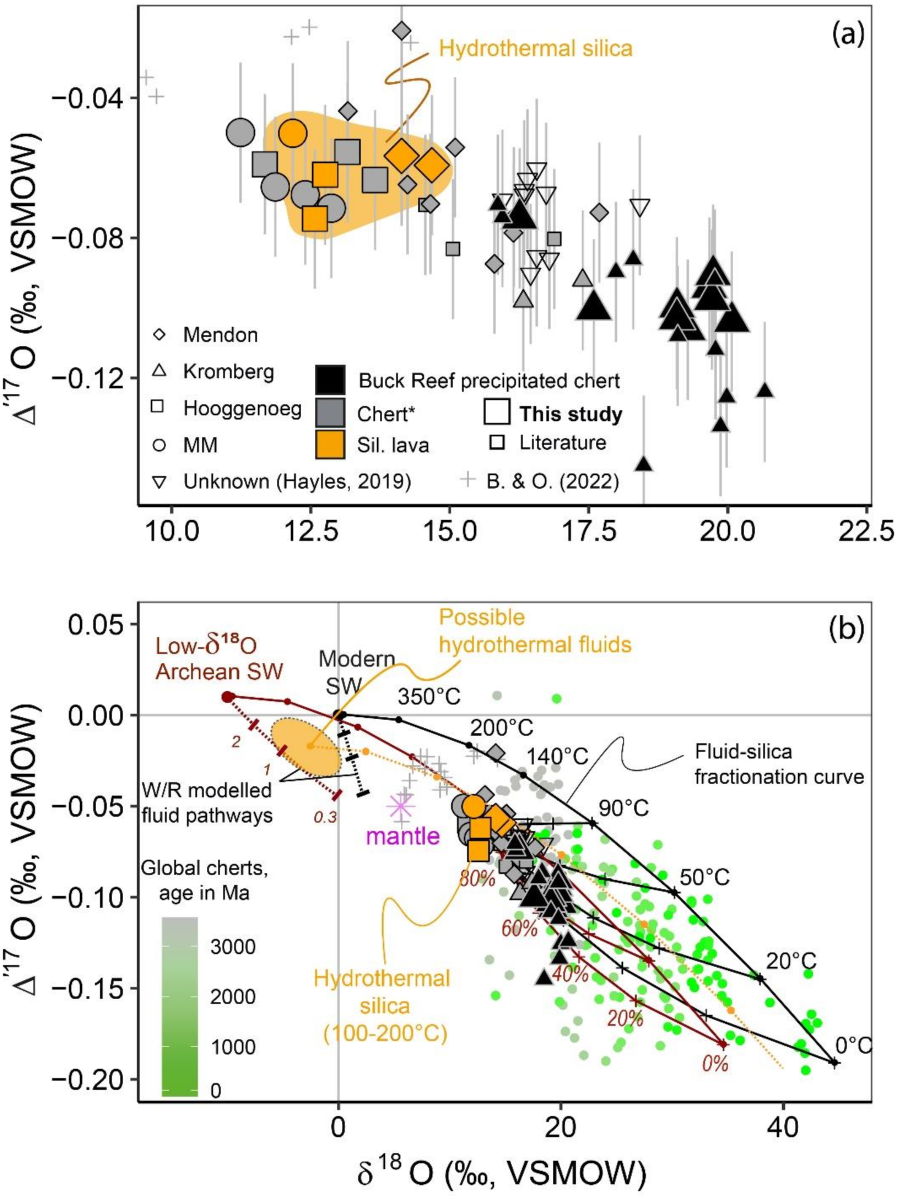

Figure 4-6. Triple O isotopic compositions of the Onverwacht cherts and silicified lavas analysed in this study compared with previous analyses of the Onverwacht cherts (Hayles et al., 2019; Liljestrand et al., 2020; Lowe et al., 2020; Sengupta et al., 2020; Zakharov et al., 2021) and with the global record of cherts (Zakharov et al., 2021). For comparison, silicified lavas from the Nuvvuagittuq greenstone belt (Bindeman and O'Neil, 2022) are shown as grey crosses. The fractionation curve between silica and fluids are drawn after the equations of Sharp et al. (2016). The star (*) on cherts indicates that they comprise pervasively silicified clastic sediments that we analysed and cherts of unknown nature from the literature that may be both silicified clastic sediments and seawater-precipitated cherts. The proposed field of hydrothermal silica and fluids are shown in orange. The 'W/R modelled fluid pathways' are based on numerical models of water-rock interactions and calculations of triple O isotopic composition of the fluids at equilibrium. Results of mixing calculations between pure seawater-precipitated and hydrothermal silica are also shown considering two different compositions for the archean seawater: one with a low $\delta^{18}O$ value of -10‰ and another one with a modern-day like oceanic composition ($\delta^{18}O$ = 0‰).

4.3.1.2. Isotopic composition of seawater-precipitated cherts

The bulk $\delta^{18}O$ values of seawater-precipitated chert samples from the Buck Reef Chert measured by laser fluorination are high and relatively variable (16.4-20.3‰) (**Table 4-1** and **Figure 4-6**). These values are consistent with previously published $\delta^{18}O$ values compositions of the Buck Reef seawater-precipitated cherts measured both in-situ by SIMS and on bulk-rock samples (Stefurak et al., 2015; Lowe et al., 2020). The $\Delta'^{17}O$ values of the seawater-precipitated samples is relatively low and covers also a wide range (-0.12 to - 0.07‰) (**Figure 4-6**).

4.3.2. Modelling results

In our model of seawater-komatiite interactions at 200 °C, secondary minerals include amphiboles (e.g. tremolite and actinolite), chlorites (e.g. daphnite, clinochlore) and serpentines (e.g. chrysotile) that precipitated in equilibrium with a residual fluid, which represents the silicifying hydrothermal fluid (**Figure 4-7a**). The triple O isotope composition of seawater considered in the model influences considerably the isotopic composition of modelled hydrothermal fluid. When a seawater characterised by a $\delta^{18}O$ of -10‰ and a $\Delta'^{17}O$ of 0.01‰ is considered in the model, the $\delta^{18}O$ of computed hydrothermal fluid remains negative, ranging between -10 and -0.1‰ across different water/rock ratios (10^5 to 0.3) (**Figure 4-7b**). If the triple O isotopic composition of modern seawater is considered ($\delta^{18}O$=0‰ and $\Delta'^{17}O$=0‰), the computed $\delta^{18}O$ of hydrothermal fluid increases from 0 to 2‰ over the considered range of water/rock ratio (**Figure 4-6b**). Notably, the $\Delta'^{17}O$ of the modelled hydrothermal is generally negative, ranging from+0.01 to -0.04, and shows insignificant variation between the two different seawater compositions considered in the model (**Figure 4-6c**).

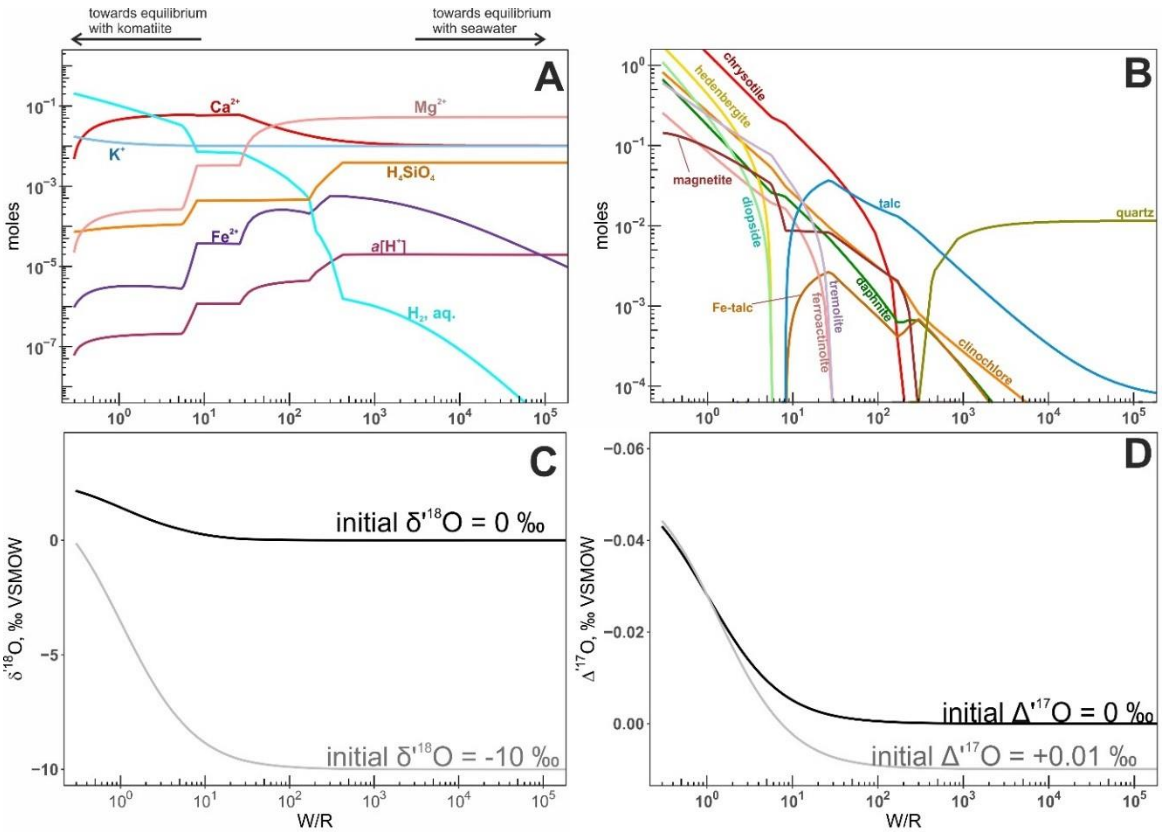

Figure 4-7. Graphic representation of the output of the aqueous-mineral equilibrium modelling and calculated O isotope composition of the fluids. The komatiite-seawater reaction is computed in CHIM-XPT and is post-processed for O isotope calculation. The horizontal axes in all panels denote the compositional change of the system due to titration progress of komatiite into the 1020 g of seawater solution. The mass ratio of titrated komatiite to solution is shown as water/rock ratio (W/R). A) Total moles of major dissolved specie in the fluids showing significant variations controlled by aqueous-mineral equilibria, excluding Na^+, Cl-, Al^{3+}, HCO^{3-} and SO_4^2. In addition, a measure of pH is shown in terms of aqueous activity of H^+ species (a[H+]). Molality of aqueous H_2 is also shown to emphasize the reducing nature of the reaction. A list of individual aqueous species and their molalities is given in Supplementary File A. B) Moles of equilibrium minerals produced by the komatiite-seawater reaction. C) The computed $\delta'^{18}O$ value of the equilibrium H_2O is shown for to initial compositions – i.e. modern-day like seawater (initial $\delta^{18}O$ = 0 ‰) and a potential low-$\delta^{18}O$ archean seawater (initial $\delta^{18}O$ = -10 ‰). D) The computed $\Delta'^{17}O$ values of the equilibrium H_2O. The theta value of 0.527 is used to calculate the triple O isotope fractionation factors 17/16α=18/16αθ.

4.4. Discussion

The silicified lavas, silicified clastic sediments and seawater-precipitated cherts investigated in this study are among the best records of palaeoarchean seawater-derived hydrothermal fluids that circulated during their formation near the seafloor between 3.47 and 3.3 Ga ago (**Figure 4-1**) (Van Den Boorn et al., 2007; Abraham et al., 2011; Marin-Carbonne et al., 2011, 2013; de Wit and Furnes, 2016). Notably, a distinct difference in O isotope composition identified between hydrothermally silicified lavas or clastic sediments and the seawater-precipitated cherts, is not evidenced in Si isotope composition (**Figures 4-5** and **4-7**). These features represent important and new aspects in understanding the composition and temperature of the palaeoarchean hydrothermal fluids and seawater from which silica precipitated. Nevertheless, it is important also to consider the potential influence of late-stage processes such as regional metamorphism that affected the entire Barberton greenstone belt around 3.2 Ga ago (Xie et al., 1997; Tice et al., 2004; Grosch, 2018). This metamorphism could potentially modify the isotopic composition of the studied rocks (Knauth and Lowe, 2003). To address these considerations, we first explore the potential effects of regional metamorphism on the measured isotopic compositions. Subsequently, we discuss their implications for the O and Si isotopic composition of paleoarchean near-seafloor fluid compositions, and then we evaluate how the composition of seawater-precipitated cherts may have changed following alteration by hydrothermal fluids. Finally, we provide novel constrains linking temporal variations in the O isotope composition of silicified lavas and cherts and O isotope variations occurring in the Barberton TTGs. It is important to note that we differentiate here "regional metamorphism" from "seafloor hydrothermalism". Seafloor hydrothermal processes are near-contemporaneous with sedimentation and eruption of the studied rocks, while regional metamorphism significantly postdates these events.

4.4.1. Effects of regional metamorphism

The temperature of regional metamorphism in the Onverwacht Group was constrained to 300-450 °C by analyses of chlorite chemistry (Xie et al., 1997) and Raman spectrometry of carbonaceous materials (Tice et al., 2004). A voluminous flow of metamorphic fluids may have an effect on the measured O isotope compositions cherts because O is abundant in most fluids. Previously, $\delta^{18}O$ values that are lower than ~16‰ in cherts from basal formations of the Onverwacht Group (i.e. Komati and Hooggenoeg Formations) (**Figure 4-3**) were ascribed to the circulation of regional metamorphic fluids at 300-400 °C around 3.45 Ga, and therefore discarded from Paleoenvironmental reconstructions (Knauth and Lowe, 2003). However, thermometric analyses identify the 300-400 °C regional metamorphic event even in the stratigraphically upper Buck Reef Chert and Mendon cherts that were argued to preserve seawater-derived elevated $\delta^{18}O$ values (**Figures 4-2, 4-5 and 4-6**) (Tice et al., 2004; Alleon et al., 2021; Zakharov et al., 2021). Independent thermometers (e.g. chlorite compositions and Raman spectrometry of carbonaceous matter) have demonstrated that a 300-400 °C metamorphic event affected all the silicified lithologies of the Barberton greenstone belt regardless of their stratigraphic position (Xie et al., 1997; Tice et al., 2004; Grosch, 2018). This eliminates regional metamorphism as the primary cause of the observed isotopic differences between the lower (i.e. Middle Marker and Hooggenoeg) and upper (i.e. Buck Reef and Mendon) chert layers of the Onverwacht Group (**Figure 4-1b**). For regional metamorphism to significantly alter the O isotope composition of cherts, it would require operating at high fluid/rock ratio (that is metamorphic fluid, not the original seawater-derived hydrothermal fluids) to recrystallise the silica with fluid isotope composition far from equilibrium, or it would need to re-homogenise the silica phases with other minerals (e.g., Hyslop et al., 2008). Re-crystallisation at relatively low fluid/rock ratio during regional metamorphism is unlikely to have importantly affected the isotopic composition of analysed silica (Perry and Tan, 1972; Marin-Carbonne et al., 2014). Consequently, based on consistent regional metamorphism temperature spanning from the Komati to the Mendon formation, this event is unlikely to explain the difference in δ^{18}O values displayed by cherts and silicified lavas across the Onverwacht Group (**Figures 4-3** and **4-5**). Thus, the O isotope composition of silica phases from silicified lavas, silicified clastic sediments and seawater-precipitated cherts, whatever its value (i.e. higher or lower than 16‰) can provide critical insights into the temperature and the composition of the palaeoarchean hydrothermal fluids and seawater from which they precipitated.

4.4.2. Insights for the isotopic composition of palaeoarchean hydrothermal fluids

Numerous field observation and detailed petrographic studies suggested that the studied silicified lavas and clastic sediments are due to interaction of original rocks with hydrothermal fluids (e.g. Paris et al., 1985; Hofmann and Harris, 2008). Although the O and Si isotope composition of these hydrothermal fluids remain poorly constrained, their determination may ameliorate constrains on seawater composition and temperature (e.g. Knauth and Lowe, 2003; Lowe et al., 2020; Tatzel et al., 2024). Therefore, we use here the O and Si isotopic composition of the pervasively silicified lavas and cherts that we have analysed to constrain the isotopic composition of the palaeoarchean silicifying hydrothermal fluids. The pervasive silicification of the analysed silicified clastic sediments and lavas (e.g. **Figure 4-2**) informs that they are dominantly constituted by hydrothermal silica, and are therefore ideal for constraining hydrothermal fluids.

The average δ^{30}Si values of the silicified clastic sediments and lavas are generally positive (>+0.19 ‰). These values suggest that kinetic fractionations did not intervene during hydrothermal silicification as kinetic fractionation would produce negative δ^{30}Si in hydrothermal silica (Kleine et al., 2018). Although a model of dynamic fractionation of Si isotopes between fluids and precipitating silica has been used for thermometric purposes (e.g. Dupuis et al., 2015; Tatzel et al., 2024), Abraham et al. (2011) observed a gradual increase in δ^{30}Si values upwards silicified lavas flows that they ascribed to a Rayleigh-type fractionation in the fluids due to silica precipitation. This complicates the use of a dynamic model to recalculate the possible Si isotopic composition of silicifying fluids. We note however that the δ^{30}Si values of the silicified clastic sediments and lavas are as positive as most seawater-precipitated cherts of palaeoarchean age (van den Boorn et al., 2007, 2010; Marin-Carbonne et al., 2011; Geilert et al., 2014). Thus hydrothermally precipitated silica did not necessarily feature negative δ^{30}Si values as previously considered. Here, we therefore propose similar Si isotope composition for the different fluids involved in the precipitation of silica near the palaeoarchean seafloor, namely the palaeoarchean seawater and hydrothermal fluids.

Mostly negative δ^{30}Si values were measured in the seawater-precipitated cherts and interpreted to reflect a post-depositional input of hydrothermal fluids (van den Boorn et al., 2007; Geilert et al., 2014). However, the positive δ^{30}Si values that we have measured in hydrothermally silicified lavas and clastic sediments rather support the alternative model that negative δ^{30}Si values of some cherts may be due to Rayleigh dynamic fractionation (Marin-Carbonne et al., 2011) or kinetic fractionation (Kleine et al., 2018). Sugitani (1992) proposed that the aqueous Si content of archean seawater was primarily derived from hydrothermal fluid discharges, a view supported also by the similarity in δ^{30}Si between seawater-precipitated cherts and hydrothermally-silicified clastic sediments and lavas.

The O isotope composition of silica fractions is consistent with hydrothermal silicification of the analysed clastic sediments and lava samples that we analysed. These samples have an O isotope composition (δ^{18}O = 11.3-14.8‰ and Δ'^{17}O = -0.05 to - 0.07‰) which differs from that of the seawater-precipitated Buck Reef Cherts (δ^{18}O = 16.4 to 20.3‰ and Δ'^{17}O = -0.07 to -0.1 ‰) (**Figure 4-6**). Contrary to previous suggestions (e.g. Lowe et al., 2020), even the triple O isotope composition of Buck Reef cherts is not compatible with simple precipitation from seawater (see **Section 4.4.3**.). Considering the previously proposed temperature range of hydrothermal silicification (i.e. 100-200 °C) (Lowe and Byerly, 1986; Cloete, 1991; Hofmann and Harris, 2008; Abraham et al., 2011; de Wit and Furnes, 2016), we calculate the isotopic composition of hydrothermal fluids and obtain negative δ^{18}O (-8 to 0‰) and Δ'^{17}O values (-0.04 to 0‰) (**Figure 4-6**). Although silicification of lavas and clastic sediments resulted from both descending flux of seawater-derived fluids and an ascending flux derived from the deep crust, our rough estimation cannot definitively discriminate the O isotope composition of each one of these fluids. We observe that the negative $\delta^{18}O$ values calculated for archean hydrothermal fluids is different from positive $\delta^{18}O$ values measured in modern hydrothermal fluids (Elderfield et al., 1999; Shanks, 2001; Zakharov et al., 2021a), although both fluids depict negative $\Delta'^{17}O$.

Our model of seawater-komatiite reaction (**Figure 4-7**) can provide a first-order estimation of the most likely composition of seawater that existed during the palaeoarchean Era. In the model, hydrothermal fluids obtained using a virtual archean seawater with an extremely low $\delta^{18}O$ of -10 ‰ and a $\Delta'^{17}O$ of 0.01 ‰ (Jaffrés et al., 2007) roughly reproduces the negative $\delta^{18}O$ of hydrothermal fluids reconstructed from silica compositions (**Figure 4-6**). This supports lower $\delta^{18}O$ value in archean oceans compared to modern analogues (Jaffrés et al., 2007; Bindeman and O'Neil, 2022), although it cannot allow estimating the exact $\delta^{18}O$ value of the palaeoarchean seawater. According to the model, modern seawater-derived hydrothermal fluids are too high in $\delta^{18}O$ to explain the O isotope composition of measured silicified lavas and clastic sediments. Although Sengupta et al. (2020) proposed high $\delta'^{18}O$ of 1‰ for the archean seawater, recent numerical modelling studies are consistent with our results as they also suggested a low $\delta'^{18}O$ of -2 to -10‰ in the palaeoarchean seawater (Herwartz et al., 2021; Tatzel et al., 2022).

4.4.3. Post-depositional modification of seawater-precipitated cherts

While we provide new measurements of seawater-precipitated cherts, it has been recognized that near-seafloor diagenesis of cherts is an important factor controlling the O isotope composition of cherts (Kolodny and Epstein, 1976; Marin-Carbonne et al., 2011; Yanchilina et al., 2020; Ibarra et al., 2022; Zakharov et al., 2023). With the novel triple O isotope data, we observe that seawater-precipitated cherts such as the Buck Reef Cherts exhibit an evolution from the hydrothermal silica endmember towards higher $\delta^{18}O$ and lower $\Delta'^{17}O$ values (**Figure 4-6a**). The hydrothermal component is constrained by measurements of silicified rocks produced by precipitation of silica from hydrothermal fluids (**Figure 4-6a)** (Hofmann and Harris, 2008).

A simple mixing model of measured hydrothermal silica (i.e. silicified rocks) with estimated seawater-precipitated silica (**Figure 4-6b**) in the triple O space reproduce the variation of O isotope composition in seawater-precipitated cherts. However, both a modern-day-like seawater displaying $\delta^{18}O$ close to 0‰ (Knauth and Lowe, 1978, 2003; Lowe et al., 2020) and assumed archean seawater with an extremely low $\delta^{18}O$ of -10‰ (Jaffrés et al., 2007; Tatzel et al., 2022) allow the mixing model to cover the full range of seawater-precipitated chert compositions. Additionally, seawater temperatures of 0 to 60 °C are all capable of reproducing the O isotope composition of seawater-precipitated cherts from the Onverwacht Group. Thus, due to post-depositional interaction of seawater-precipitated cherts with hydrothermal fluids, it is difficult to reconstruct archean seawater compositions or temperatures in a straightforward manner using chert's isotopic composition. Indeed, post-depositional fluid circulations at diagenetic stage create complex mixing schemes even in the triple O isotope compositions of the Cenozoic seawater-precipitated cherts recovered from the modern seafloor (see compilation in **Figure 4-6**) (Kolodny and Epstein, 1976; Yanchilina et al., 2020; Ibarra et al., 2022).

4.4.4. Origin of stratigraphic variations in O isotope compositions

The $\delta^{18}O$ values of silicified lavas and cherts increase up the stratigraphic section of the Onverwacht group (**Figure 4-3 and 4-5a**), unlike $\delta^{30}Si$ values that do not change considerably through the stratigraphic section. The lowermost member measured here is Middle Marker and shows $\delta^{18}O$ values of 10-13‰, and the uppermost member, Mendon 1, has a $\delta^{18}O$ of ~15‰, that extends up to 20‰ if we consider previously published data (**Figure 4-5a**). While Si-isotopes do not display this evolution, the stratigraphic variation of O isotope represents an important signal recorded in the Onverwacht Group (**Figure 4-3**) but its origin remains unconstrained (Knauth and Lowe, 1978, 2003; de Wit and Furnes, 2016).

To understand the primary causes behind the stratigraphic variations of $\delta^{18}O$ values in cherts and silicified lavas, we consider the theoretical dependence of their O isotope composition on several factors: (1) the composition of the archean seawater, (2) the composition of the reacting crustal formations, (3) the ratio of interacting water/rock abundances, and (4) the thermal condition of the system during silica precipitation or seafloor silicification. The three first variables are unlikely to have played a major role in the case of the Onverwacht formations for the following reasons. First, it is difficult to explain a $\delta^{18}O$ variation of >4 ‰ in seawater during the 180 Ma in which the seafloor formation cropping out to the North of Komati fault emplaced (**Figure 4-1**). Although the details of archean O isotope balance are not well-constrained, the change of >4 ‰ over a course of 180 Ma is unlikely. This is due to mass-balance considerations of the O isotope budget. The residence timescale for O in seawater is large (i.e. several tens of Ma) due to its abundance reflecting relative sizes of its sources and sinks (Muehlenbachs, 1998). Specifically, buffering by the balance of seawater circulation in the greenstone formations and weathering is unlikely to change the composition of seawater in a dramatic fashion (Meuhlenbachs and Clayton, 1976). Secondly, the variability of $\delta^{18}O$ in the pre-silicified rocks is expected to be minimal because the Komati, Hooggenoeg and Mendon lavas are all mantle-derived komatiites and basalts with $\delta^{18}O$ likely around 5.5±1 ‰ (Valley et al., 1998) (**Figures 4-2** and **4-5a-c**). Finally, although the fluid/rock ratio of former hydrothermal reactions is quite hard to estimate (Alt and Bach, 2006; Coogan and Gillis, 2018), all the studied samples were pervasively silicified to a similar extent (> 90 vol.% quartz) supporting constant fluid/rock ratios during hydrothermal fluid circulations (Paris et al., 1985; Duchac and Hanor, 1987; Abraham et al., 2011). Based on this argumentation, the changes in thermal conditions of the hydrothermal systems (e.g. Tatzel et al., 2022) might be a critical component explaining the increase of $\delta^{18}O$ values between 3.48 and 3.3 Ga.

We propose that the stratigraphic variations of O isotope compositions in the Onverwacht silicified lavas and cherts was due to local lithospheric cooling associated with the evolution of the Barberton greenstone belt. The secular and global cooling of the Earth has been demonstrated to largely explain $\delta^{18}O$ changes observed in global chert compilations (Tatzel et al., 2022). Similarly, a local lithospheric cooling related to the evolution of the Barberton greenstone belt would account for the upward increase of $\delta^{18}O$. As the silicification of seafloor lava and the formation of overlying chert layers occurred likely on a long timescale (likely exceeding 1 Ma or at least several thousands of years), volcanic eruptions are not considered to be the main driver of heat during the hydrothermal circulations. Regional geothermal gradient is a possible candidate as the source of heat for hydrothermal circulation of seawater-derived hydrothermal fluids that caused silicification. The evolution of the Barberton greenstone belt from a hot, thin and juvenile greenstone succession to a relatively colder, thicker and stable continent (Lowe and Byerly, 2007a; Moyen et al., 2021; Drabon et al., 2019, 2024) might have been accompanied by a progressive cooling at lithospheric scale that explains the long-term and vertical increase of $\delta^{18}O$ values in cherts and lavas of the Onverwacht Group.

4.4.5. Implications for the origin of archean granitoids

Although there is no physical relationship between the analysed silica-rich rocks and granitoids of the Barberton area, the evolution of O and Si isotopic compositions in these silica-rich rocks offer insights into the composition of analogous lithologies reworked in the source of the Barberton TTGs (André et al., 2022). Elevated $\delta^{18}O$ (4.4-6.9‰, measured in zircon) and

δ^{30}Si values (-0.14 to 0.25‰: measured whole rock and zircon composition) were recently published for the Barberton granitoids (**Figure 4-8**). These data were interpreted to support the reworking of seafloor-derived silicified lavas and cherts in the source of the Barberton granitoids (Wang et al., 2022; André et al., 2019; Deng et al., 2019; Lei et al., 2023). Notably, similar Si but different O isotope compositions have been observed between the pre-3.3 Ga (δ^{18}O= 4.4-6.0‰ and δ^{30}Si= -0.05 to 0.20‰) and post-3.3 Ga granitoids (δ^{18}O= 4.9-6.9‰ and δ^{30}Si= -0.14 to 0.17‰) (**Figure 4-8**). To explain this decoupled evolution of O and Si isotopes in the granitoids, we propose that it reflects the near-constant δ^{30}Si values and chrono-stratigraphically increasing δ^{18}O values (from 10-12‰ to 16-19‰) of silicified clastic sediments and lavas derived from the seafloor (**Figures 4-3**, **4-5** and **4-7**). In this perspective, the older seafloor-derived silica that was reworked into 3.45 Ga TTGs was likely lower in δ^{18}O than the younger seafloor-derived silica reworked in post-3.3 Ga TTGs, but they all must have displayed a similar range of δ^{30}Si values. If true, then an increasing fraction of younger seafloor-derived components was incorporated in the source region of younger granitoids. This demonstrates a close link between mafic rocks emplaced at the surface of the Earth and their recycling into the source zone of palaeoarchean granitoids. Determining the exact age of the silicified rocks that were reworked in the source zone of the Barberton TTGs remains challenging, but previous Nd and Hf isotopic measurements in the TTGs suggested that their source was still juvenile upon melting (Moyen et al., 2019). Thus, the Onverwacht rocks might be very close in composition to seafloor-derived lithologies reworked in the source of the Barberton granitoids. Unlike other terrains where TTG melts have been proposed to originate from the same Hadean crust over more than 1 Ga based on the study of ^{146}Sm-^{142}Nd short-lived isotope systematics (e.g. O'Neil and Carlson, 2017), we suggest that different generations of seafloor-derived components were systematically recycled into the source region of the Barberton granitoids over time. Thus, various mechanisms for forming granitic rocks may have co-existed on the early Earth.

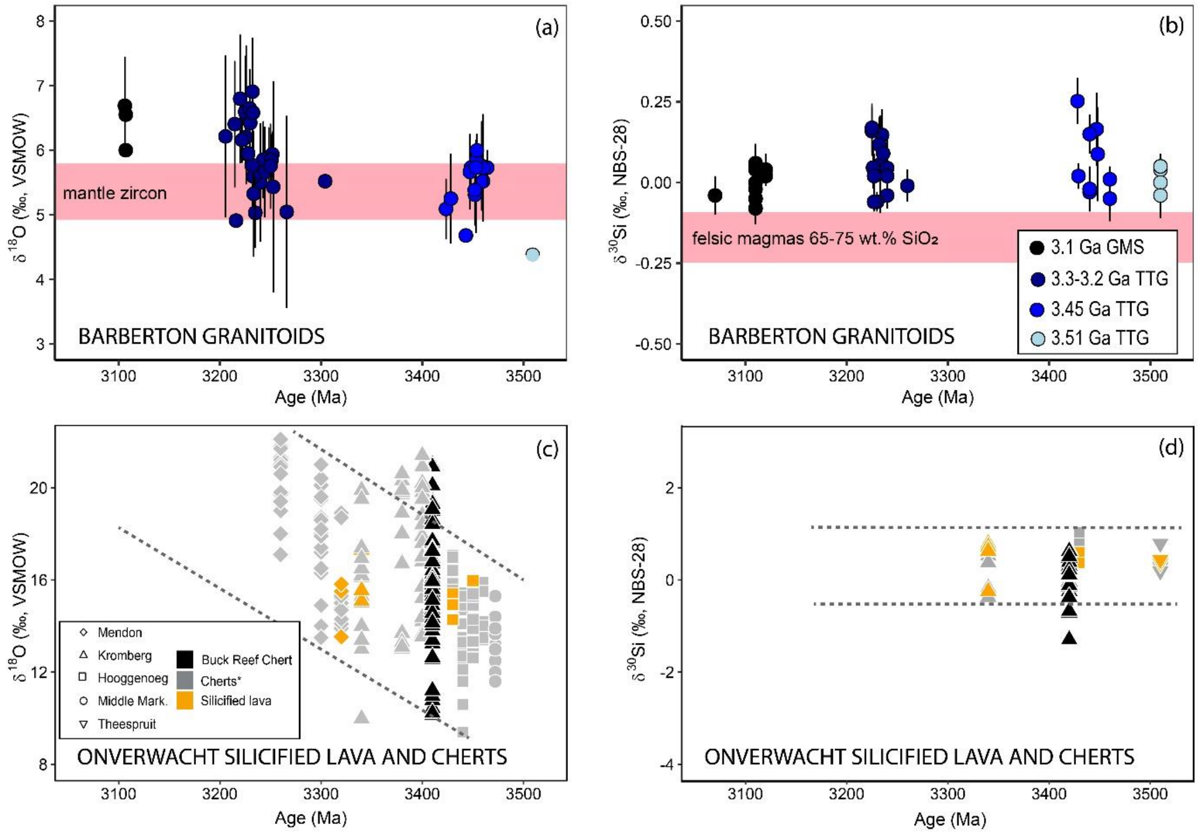

Figure 4-8. Variations of $\delta^{18}O$ in zircons (a) and $\delta^{30}Si$ in TTG magmas (b) in the Barberton granitoids compared with the evolution of $\delta^{18}O$ (c) and $\delta^{30}Si$ (d) in the Onverwacht silicified lava and cherts. Compositions featured in plates (a) and (b) were compiled from previously published datasets (Valley et al., 2005; André et al., 2019; Deng et al., 2019; Wang et al., 2022; Lei et al., 2023). Oxygen isotopic compositions were exclusively measured from magmatic zircons whereas silicon isotopic ratios include measurements from the bulk-rock but also from zircons. The equation of Guitreau et al. (2022) was used to convert the $\delta^{30}Si$ values of zircons into the bulk-rock values shown on the Figure. Note that $\delta^{30}Si$ signatures are higher than mantle values in all the Barberton TTGs, whereas $\delta^{18}O$ signatures only reach notably elevated only in those that are younger than 3.23 Ga. The symbols of (c) and (d) are the same as in Figures 3 and 6. The star (*) on cherts in the legend indicates that they may comprise pervasively silicified clastic sediments and seawater-precipitated cherts that were not clearly distinguished in the literature.

4.5. Conclusion

- The compositions of silicified clastic sediments and lava, and seawater-precipitated cherts of the Onverwhacht Group, Barberton greenstone belt, constrain the hydrothermal silica endmember in the triple O isotope space. The silicified rocks have lower $\delta^{18}O$ (silicified lava = 12.3-14.9‰ and silicified clastic sediments = 11.3-14.2‰) and higher $\Delta'^{17}O$ values (-0.07 to -0.05‰) than seawater-precipitated cherts (16.4 to 20.3‰ of $\delta^{18}O$ and -0.12 to -0.07‰ of $\Delta'^{17}O$). These values are best explained by a low-temperature (100-200 °C) hydrothermal alteration that obscures the record of seawater temperature and composition in pure seawater-precipitated cherts.

- Considering the possible silicification temperature range of 100-200 °C, the triple O isotope composition of the archean silicifying fluid is likely negative in both δ^{18}O and Δ'^{17}O. Numerical modelling of komatiite-seawater reaction and mass-balance calculation of O isotope composition in equilibrium fluids suggests that the silicifying hydrothermal fluids must have originated from a palaeoarchean seawater with a negative δ^{18}O value. However, the exact O isotope composition and temperature of this palaeoarchean seawater is challenging to reconstruct.
- A slight but evident increase of δ^{18}O values upwards the Onverwacht stratigraphy (from ~10-13‰ to 15-20 ‰) is observed both in the hydrothermally silicified lavas and clastic sediments. As changes in seawater δ^{18}O and temperature are unlikely to evolve dramatically over the formation of the Onverwacht Group, this variation is likely due to lithospheric cooling of the Barberton greenstone belt.
- The exclusively positive values of average δ^{30}Si (+0.19 to +1.24 ‰) measured in the hydrothermally silicified lava are like positive δ^{30}Si values that were previously ascribed to archean seawater-precipitated cherts, suggesting that seawater-derived and hydrothermal silica were relatively close in Si isotopic composition. This discards Si isotope composition as an efficient tool for discriminating seawater-precipitated from hydrothermally formed cherts.
- The evolution of δ^{18}O values in silicified rocks from the Onverwacht Group over time is correlated with the evolution observed in the Barberton granitoids, suggesting that different generations of granitoid sources reworked distinct generations of seawater-derived rocks. Accordingly, at least in some parts of the palaeoarchean Earth, the recycling of seafloor-derived rocks into the deep source of granitoids might have been active. This insight enhances our understanding of the geological processes that contributed to the formation of ancient granitic complexes.

4.6. Supplementary material

All the supplementary figures and tables related to this part of the thesis are available in Appendices (see Appendices B).

4.7. Bridge to Part V

In this part, we have observed a correlation between the evolutions of O isotope compositions in silica-rich rocks derived from the palaeoarchean seafloor and in the Barberton TTGs over time. Building on this correlation, **Part V** uses the database of O and Si isotope compositions in both the silica-rich rocks and TTGs to discuss about the composition and the proportion of silica-rich rocks in the source zone of the Barberton TTGs. New constrains on the reworked silica-rich rocks allow discussing the geodynamic significance of these rocks as components of the TTG source zone.

Part V.

Recycling of silica-rich rocks from the seafloor to the TTG source zone: Reappraisal of O and Si isotopic compositions combined with thermodynamic modelling

5.1. Context and purpose

Oxygen and silicon isotopic compositions of palaeoarchean TTGs or their zircons support the reworking of seafloor-derived silicified lavas and cherts in the source zone of these granitoids (see **Sub-section 4.4.5**., Trail et al., 2018; Deng et al., 2019; André et al., 2019, 2022; Lei et al., 2023). This qualitative identification of paleoarchean recycling processes was a significant progress in our understanding of crustal geodynamics on the early Earth. It firmly precluded geodynamic models that cannot explain the presence of seafloor-derived rocks in the source zone of TTG magmas. For example, melting a deep basaltic crust completely isolated from the hydrosphere (e.g. Smithies et al., 2021) cannot account for the production of most paleoarchean TTG magmas with elevated $\delta^{18}O$ and $\delta^{30}Si$ values. However, despite this important progress, fundamental problems on the significance of O and Si isotopic compositions of paleoarchean TTGs and their zircons persist.

Firstly, the O and Si isotopic composition of primary TTG melts remain hard to constrain, hampering an unambiguous characterization of the source magma. Bulk-rock TTG samples and zircons are the main samples studied to determine the isotopic composition of TTG melts, but each of them has its limitations. Bulk-rock isotopic compositions measured in rock samples could depart from the original isotopic composition of the primitive melt due to fractional crystallization (**Figure 5-1**) (e.g. Lackey et al., 2008), metamorphism and weathering processes (Faure and Harris, 1991). Therefore, bulk-rock O isotope data are generally not believed to represent the signature of the primary TTG melt, which motivates the use of zircon as a proxy for the isotopic composition of granitic magmas. However O and Si isotopes are all known to fractionate between zircon and felsic melt (Valley et al., 1994; Lackey et al., 2008; Qin et al., 2016; Trail et al., 2020; Guitreau et al., 2022), and this fractionation is often overlooked in the study of granitoid source zones based on O isotope compositions. For example, several studies have interpreted zircons with a $\delta^{18}O$ of 5.0-5.9‰ as due to the presence of fresh basalts derived from the mantle alone in the TTGs source (e.g. Trail et al., 2018; Wang et al., 2022; Lei, et al., 2023). In particular, Lei et al. (2023) proposed that Si and O isotopic compositions are decoupled in ~3.45 Ga old TTGs from the Barberton granitoid-greenstone terrain because they measured higher $\delta^{30}Si$ in TTG's zircon compared to mantle values but a mantle-like $\delta^{18}O$ in TTG-hosted zircon. The decoupling of O and Si isotopic compositions proposed by Lei et al. (2023) is problematic because silica-rich rocks derived from the seafloor, that were suggested to explain the Si isotopic composition of the Barberton TTG melts, should have generated mantle-different signatures both for O and Si isotope compositions in the Barberton TTGs

(Deng et al., 2019). Exploring the relationship that exists between the isotopic composition of zircon and bulk-rock specimens may reveal the significance of decoupled O and Si isotopic compositions that was proposed by Lei et al. (2023) based on zircon analyses.

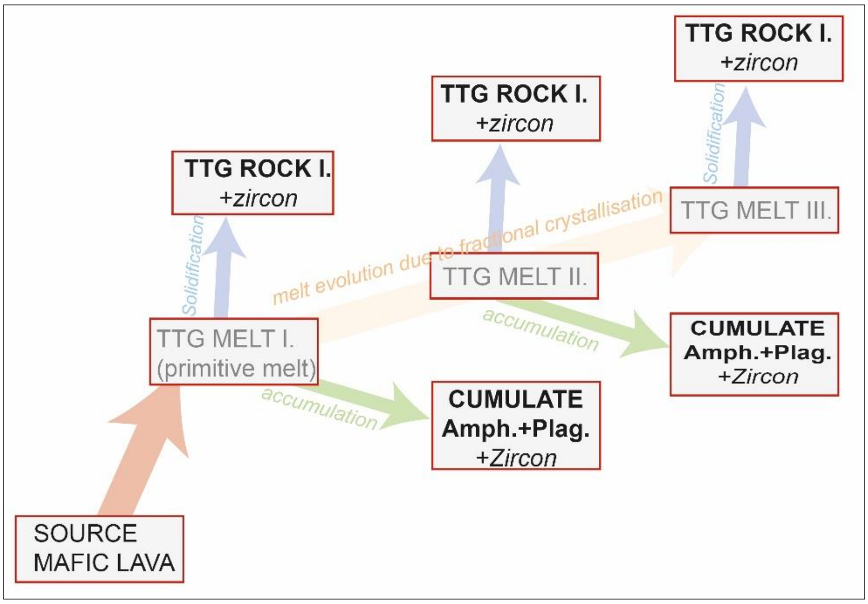

Figure 5-1. Conceptual illustration of TTG melt evolution from a primary melt derived directly from the source zone due to fractional crystallisation and crystal accumulation. In bold are the variety of materials expected in natural TTG plutons. Because O and Si isotopes can fractionate between the melt and the cumulate, these processes should be considered when using the O and Si isotopic compositions measured in bulk-rock or zircon samples to characterise the source zone of TTG melts.

The second unsolved problem is that, although O and Si isotopic analyses support the reworking of seafloor-derived silica-rich rocks in the source zone of paleoarchean TTGs, determining the composition, proportion and burial depth that characterized these silica-rich rocks remains a challenge. In fact, we cannot yet discriminate burial which is considered as due to passive accumulation of young lavas and clastic sediments on the seafloor (Hernández-Uribe, 2024), from active transportation of materials from the seafloor to the deep Earth, for example due to subduction-like processes (Roman and Arndt, 2020; Arndt, 2023). This is still hampering an unambiguous use of O and Si isotopic compositions of TTG melts to constrain geodynamic processes that operated on the early Earth (Vezinet et al., 2018; Lei, et al., 2023). Considering supracrustal rocks preserved in archean greenstone belts as proxies for similar rocks reworked in source zone of TTG magmas is the only way to fill this gap. This would help constraining the composition, proportion and possible burial depth of reworked silica-rich rocks (Deng et al., 2019), and discriminating burial from transport as the recycling mode responsible for the occurrence of seafloor-derived rocks in the source zone of TTGs. Indeed, seafloor-derived rocks buried passively towards the deep crust (> 20 km) could melt in any geodynamic context (Hartnady et al., 2022; Tamblyn et al., 2023), but more preferentially in intra-crustal and infra-crustal settings (Smithies et al., 2009) or due to delamination from the base of the crust (Bédard, 2018). In contrast, seafloor-derived rocks that remained in the shallow crust (e.g. < 5km deep) could only be reworked in the TTG source zone if subduction-like processes transported them (Deng et al., 2019; Wang et al., 2022). Briefly, estimating the possible burial depth of reworked silica-rich rocks in the submarine crust could help discriminating the influence of passive burial from that of active transportation/subduction in the reworking of the seafloor-derived rocks.

In this part of the thesis, supra-crustal formations of the Onverwacht Group are considered as compositionally and stratigraphically equivalent to similar rocks that were reworked in the source zone of the Barberton TTGs. The main pitfall with this consideration is that the reworked rocks, which are by definition not accessible for analysis anymore, may have been different, either in composition or in stratigraphic thickness from the rocks that are currently accessible in the Onverwacht Group (Clemens et al., 2006). However, the hypothesis that Onverwacht silica-rich rocks are analogous to the reworked silica-rich rocks is supported by the nearly juvenile Hf and Nd isotopic compositions of the Barberton TTGs (both εNd and εHf mainly comprised between -2 and +2, with T_{DM} ~150 Ma older than emplacement), suggesting that the source of the Barberton TTGs was most likely coeval with the Onverwacht Formations (Moyen et al., 2019). Furthermore, the correlation of the evolution of O isotope compositions in the Barberton TTGs and in silica-rich rocks from the Onverwacht Group (Barberton greenstone belt) (see **Part IV**) supports the reworking of different generations of silicified lavas in the source zone of the Barberton granitoids. Consequently, the Onverwacht rocks represent the only accessible source of information on the composition of silica-rich lithologies reworked in the source zone of the Barberton Granitoids and can therefore be used to improve our understanding of the composition, proportions, and burial depth of the reworked supracrustal rocks.

This chapter discusses the isotopic composition, proportion and burial position in the crust of seafloor-derived silica-rich rocks that were reworked in the source zone of the Barberton TTGs. It aims to determine the thermodynamic conditions in which these rocks melted and the possible geodynamic processes that could explain their transportation at depth. Following this introductory section, the second section presents (1) a compilation of O and Si isotopic composition in bulk-rock sample and zircons from the Barberton TTGs and (2) results of a simplified thermodynamic model simulating the melting of a silicified lava and a non-silicified lava. Then, the third section presents the different interpretations and discussions arising from these observations, including (1) the determination of the original O and Si isotopic composition of the TTG melt, (2) the composition and proportion of silica-rich seafloor-derived rocks reworked in the source zone of these granitoids, and (3) the possible burial depth and geodynamic process responsible for the reworking of the silica-rick rocks. Finally, the fourth section presents a more general overview of the advantages and disadvantages of using stable isotope signatures to constrain palaeoarchean geodynamic models.

5.2. Observations: isotopic database and numerical modelling results

Two types of observations are discussed in this part of the thesis, namely (1) the O and Si isotopic compositions of bulk-rock samples and zircons from the Barberton TTGs and (2) the results of a numerical thermodynamic model that explores melting of silicified and non-silicified lavas at different conditions of pressure, temperature, and water content.

5.2.1. Oxygen and silicon isotopic composition measured in the Barberton TTGs

5.2.1.1. A brief note on the database

A list of the different TTGs for which O or Si isotope compositions are discussed in this thesis is presented in **Table 5-1**. For each pluton, the number of bulk-rock and zircon analyses that we produced or collected from the literature is given

Table 5-1. Summary of the dataset of O and Si isotope compositions in the Barberton TTGs

		Oxygen isotope composition						Silicon isotope composition	
		Bulk-rock samples			Zircon grains			Bulk-rock samples	Zircon grains
TTG body	Age (Ga)	This study (a)	Literature (b)	Tot.	This study (a)	Literature (c)	Tot.	Literature (d)	Literature (e)
Stolzburg (dyke)	3.21					5	5		
Kaap Valley	3.22	1	16	17	52	16	68	3	5
Honingklip	3.22					3	3		10
Nelshoogte	3.23	2		2	54	12	66	3	5
Weergevonden (dyke)	3.23					16	16		
Uitvogenden	3.23					30	30		5
Rooihoogte Pass	3.24					29	29		
Batavia	3.25					47	47		4
Badplaas	3.25					52	52	1	11
Eerstehoek	3.43					7	7		5
Theespruit	3.45	1		1	16	39	55	3	5
Stolzburg	3.45	2		2	19	45	64	4	5
Weergevonden	3.46					3	3		
Total		**6**	**16**	**22**	**141**	**304**	**445**	**14**	**55**

Data sources: (a) this study, (b) Faure and Harris (1991), (c) Lei et al. (2023), Valley et al. (2005) and Wang et al. (2022), (d) Guitreau et al. (2022) and Lei et al. (2023) , (e) André et al. (2019) and Deng et al. (2019).

This study is mainly based on O and Si isotopic compositions of bulk-rock samples and zircons from 3.45-3.2 Ga old TTG bodies cropping out in the Barberton granitoid-greenstone terrain (**Table 5-1** and **Figure 5-2**), including previously published and newly acquired data. Oxygen isotope compositions of bulk-rock samples from the Kaap Valley pluton (n=16) were taken from Faure and Harris (1991) which is the only study to have reported the bulk-rock O isotope composition of the Barberton TTGs that we found in the literature (to the best of our knowledge). The bulk-rock Si isotope compositions (n=18) of the Stolzburg, Theespruit, Kaap Valley, Nelshoogte and Baadplaas plutons were compiled from the studies of André et al. (2019) and Deng et al. (2019). The O isotope composition of zircons from the Barberton TTGs was compiled from Lei et al. (2023), Valley et al. (2005) and Wang et al. (2022), while Si isotope composition of zircons from the Barberton TTGs (n=55) was taken from Lei et al. (2023) and Guitreau et al. (2022). Of all these studies, only two studies Wang et al. (2022) and Lei et al. (2023) reported bulk-rock major and trace element compositions of their samples.

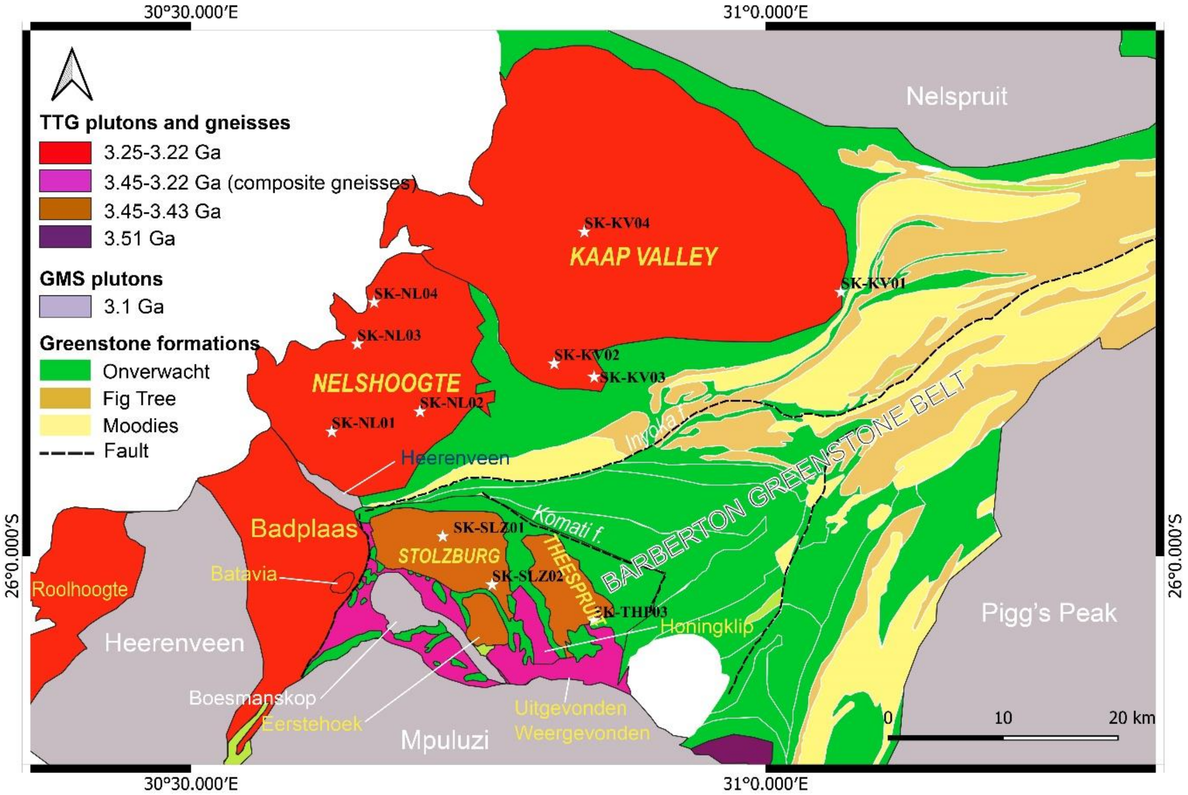

Figure 5-2. Simplified geological map of the Barberton Granitoid-Greenstone Terrain. The location of outcrops from which the eleven samples analysed in this study were collected is represented with white stars. The names of plutons for isotopic compositions are discussed in this study are written in yellow, and among these, the names plutons for which we produced new data are in capital letter.

In addition to the data that were compiled from previous studies, we analysed also 11 new samples (**Table 5-1**) from 5 different plutons (**Figure 5-2**). These include 4 samples from the

Kaap Valley pluton (3.22 Ga), 4 samples from the Nelshoogte pluton (3.23 Ga), 1 sample from the Theespruit pluton (3.45 Ga) and 2 samples from the Stolzburg pluton (3.45 Ga). The location of these samples is shown in **Figure 5-2**. Among these samples, only 6 samples were analysed for O isotope composition of bulk-rock powders and only 8 samples were analysed for O isotope composition of zircon separates. We did not analyse the bulk-rock O isotope composition of all the samples because we initially wanted to investigate the isotopic composition of zircon. Although we wanted to analyse the O isotope composition of zircon for all the 11 samples, zircon was absent from 3 of these samples. Our newly produced dataset presents simultaneous analyses of O isotope compositions in bulk-rock powders and zircons for three samples (SK-THP03, SK-NL04 and SK-SLZ02), which is a first opportunity to compare these two different data types for the Barberton TTGs.

The O isotope compositions of the zircons were quantified by SIMS at the University of Lausanne, according to the analytical procedure described in **Parts III** and **IV** of the thesis. The reproducibility of these analyses was 0.4‰ (2SD) as determined by repeated measurements of the 91500 zircon standard ($\delta^{18}O = 9.86 \pm 0.11$). Cathodo-luminescence images of the analysed zircons were also acquired at Laboratoire Magmas et Volcans using a JEOL 5910 LV scanning electron microscope (SEM). The O isotope composition of bulk-rock samples was measured by gas-source mass spectrometry at the University of Lausanne with an external uncertainty of ±0.1‰, following the method described in **Part IV** of the thesis. Finally, the bulk-rock major element compositions of the 11 TTG samples were determined by XRF analyses at the Stellenbosch University, following the method described in **Part III** of this thesis.

The data discussed in this study are summarised in Tables **5-1** to **5-4**. The complementary data acquired in this study (i.e. major element, bulk-rock O isotope and zircon O isotope compositions of eleven TTG samples) are presented first (**Table 5-2**). Then **Table 5-3** reports the average O and Si isotope compositions of bulk-rock samples per TTG pluton, and **Table 5-4** presents average O and Si isotope compositions of zircon populations per plutons

5.2.1.2. Oxygen isotope composition in the Barberton TTGs and their zircons

A. Bulk-rock O isotope composition

Bulk-rock $\delta^{18}O$ values of the TTG samples analysed in this study vary between +6.9 and +8.1‰, consistent with the bulk-rock $\delta^{18}O$ range of +6.0 to +8.5‰ published by Faure and Harris (1991) for the Kaap Valley pluton (**Figure 5-3a**). Collectively, these data allow calculating average $\delta^{18}O$ per TTG body of +7.0 to +7.6‰, with 2SD up to 1.3‰ (**Table 5-3**).

In the six samples analysed jointly for bulk-rock O isotope and major element compositions, the bulk-rock $\delta^{18}O$ values are not notably correlated with SiO_2 concentration (**Figure 5-3b**). We observe the same O isotope compositions for trondhjemites with an SiO_2 concentration comprised between 67.1 and 73.5 wt.% and tonalites displaying a lower SiO_2 concentration of 58.2 to 63.6 wt.% (**Figure 5-3a,b**).

Table 5-2. Major element, bulk-rock $\delta^{18}O$ and average zircon $\delta^{18}O$ in analysed TTG samples from the Barberton Granitoid greenstone belt

Sample	TTG body	Type	$\delta^{18}O$	$\delta^{18}O_{Zrc}$		$\Delta^{18}O_{WR-Zrc}$	SiO_2	TiO_2	Al_2O_3	MgO	CaO	K_2O	Na_2O	Fe_2O_3	L.O.I.	Total
				Average	2SD											
SK-KV01	Kaap Valley	Ton.		5.7	0.5		63.6	0.5	15.3	3	4.8	1.3	4.3	5.2	1.9	99.9
SK-KV02	Kaap Valley	Trond.	7.9				67.1	0.4	15.6	1.8	3.8	1.2	4.9	3.8	1.2	99.8
SK-KV03	Kaap Valley	Trond.		5.6	0.5		67.3	0.5	15.1	2	3.6	1.1	4.9	4.2	1.6	100.2
SK-KV04	Kaap Valley	Trond.		5.4	0.3		70.2	0.3	15.6	1.3	3.3	1.4	5.2	2.9	0.6	100.7
SK-NL01	Nelshoogte	Trond.	8.1				72.8	0.3	15.1	0.6	2.9	1.1	4.9	2.3	0.7	100.6
SK-NL02	Nelshoogte	Trond.		5.2	0.1		73.5	0.2	14.4	0.5	2.3	1.8	4.7	2.1	0.7	100.3
SK-NL03	Nelshoogte	Trond.		5.7	1.1		70	0.4	15.2	1.3	3.3	1	4.8	3.2	1.1	100.3
SK-NL04	Nelshoogte	Ton.	7.2	5.6	0.9	1.6	58.2	0.9	13.9	6.6	5.6	1.1	3.5	8.6	2	100.3
SK-THP03	Theespruit	Trond.	7.4	5.9	1	1.5	72.2	0.3	15	1	2.5	1.4	5.4	2.3	0.6	100.6
SK-SLZ01	Stolzburg	Trond.	6.9				72.4	0.2	15.3	0.4	2.1	1.9	5.6	1.7	0.5	100
SK-SLZ02	Stolzburg	Ton.	7.2	4.8	0.6	2.4	60.1	1	18.4	2.2	5.2	1.6	5.7	4.8	1.4	100.4

Table 5-3. Average $\delta^{18}O$ and $\delta^{30}Si$ measured in bulk-rock samples from Barberton TTG bodies

TTG body	Age (Ga)	$\delta^{18}O$			$\delta^{30}Si$		
		n	Av.	2SD	*n*	Av.	2SD
Kaap Valley	3.22	*17*	7.5	1.3	*3*	-0.03	0.09
Nelshoogte	3.23	*2*	7.6	1.3	*3*	0.02	0.13
Badplaas	3.25				*1*	-0.01	
Theespruit	3.45	*1*	7.4		*3*	0.03	0.2
Stolzburg	3.45	*2*	7	0.4	*4*	0.03	0.14

Data source: O isotope compositions are from this study and Faure and Harris (1991), whereas Si isotope compositions are from Deng et al. (2019) and André et al. (2019).

Table 5-4. Average $\delta^{18}O$ and $\delta^{30}Si$ measured in zircons from Barberton TTG bodies

TTG body	Age (Ga)	$\delta^{18}O$			$\delta^{30}Si$		
		n	Av.	2SD	*n*	Av.	2SD
Stolzburg (dyke)	3.21	*5*	6.4	1			
Kaap Valley	3.22	*68*	5.7	0.7	*5*	-0.23	0.07
Honingklip	3.22	*3*	6.8	1	*10*	-0.27	0.13
Nelshoogte	3.23	*66*	5.6	1	*5*	-0.39	0.18
Weergevonden (dyke)	3.23	*16*	6.9	0.8			
Uitvogenden	3.23	*30*	6.6	0.5	*5*	-0.27	0.08
Rooihoogte Pass	3.24	*29*	5.7	0.7			
Batavia	3.25	*47*	5.7	1	*4*	-0.39	0.11
Badplaas	3.25	*52*	5.5	1	*11*	-0.3	0.16
Eerstehoek	3.43	*7*	5.3	0.7	*5*	-0.15	0.07
Theespruit	3.45	*55*	5.8	0.8	*5*	-0.31	0.16
Stolzburg	3.45	*64*	5.4	1.5	*5*	-0.24	0.1
Weergevonden	3.46	*3*	5.7	0.8			

Data source: O isotope compositions are from this study and Valley et al. (2005), Wang et al. (2022) and Lei et al. (2023). Si isotope compositions are from Guitreau et al. (2022) and Lei et al. (2023).

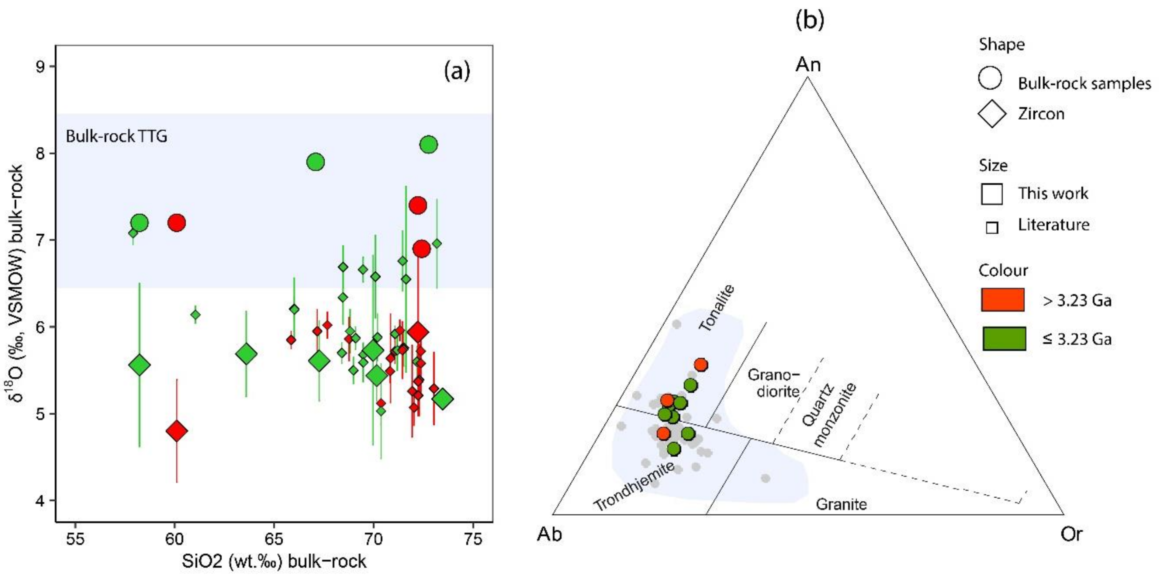

Figure 5-3. Major element and O isotope composition of newly analysed TTG samples. Panel (a) is a binary plot of bulk-rock SiO_2 content versus δ^{18}O values in both bulk-rock samples and zircon. Plate (b) is an An-Ab-Or diagram showing the difference between trondhjemitic and tonalitic samples. Samples derived from TTG bodies that are older than 3.23 Ga (red) are differentiated from younger samples (green). The light-blue area is a field representing the data published by Wang et al. (2022) and Lei et al. (2023). The field of the Barberton TTGs is based on the data of Faure and Harris (1991) in plate (a), and on the compilation of Moyen et al. (2019) in plate (b). Error bars are covered by the symbols when absent and generally represent 2SD values.

B. Zircon O isotope composition

The newly acquired δ^{18}O values of individual zircon spots featuring typical magmatic textures (e.g. **Figure 5-4**), such as oscillatory and sector zoning in cathodo-luminescence images, range between 4.4 and 6.8‰ (**Figure 5-5a**). These values are consistent with the δ^{18}O values of 3.5 to 7.8‰ obtained by previous studies in individual zircons from the Barberton TTGs (**Figure 5-5a**) (Lei et al., 2023; Valley et al., 2005; Wang et al., 2022). In seven out of the eight samples for which we analysed the O isotope composition of zircons, average δ^{18}O values of magmatic zircons per sample range between 5.2 and 5.9‰, with 2SD values of 0.5 to 1.1‰ (e.g. **Figure 5-5**). These values are consistent with the average values of 5.3 ± 0.6‰ obtained in zircons of mantle-derived ultramafic lavas (i.e. kimberlites, Page et al., 2007), that are commonly interpreted as characteristic of zircons from granitic magmas due to melting of mantle-derived mafic lavas (e.g. Drabon et al., 2024; Lei et al., 2023; Trail et al., 2018; Wang et al., 2022). One sample (SK-SLZ01) displays an average δ^{18}O of 4.8‰ that is lower than all the other samples that we analysed, and lower than the mantle range. The δ^{18}O values measured in zircons of SK-SLZ01 sample are also relatively lower than the δ^{18}O value of previously analysed zircons from the Stolzburg pluton (see **Figure 5-5k**), probably reflecting intra-pluton variations in the O isotope composition of TTG melts.

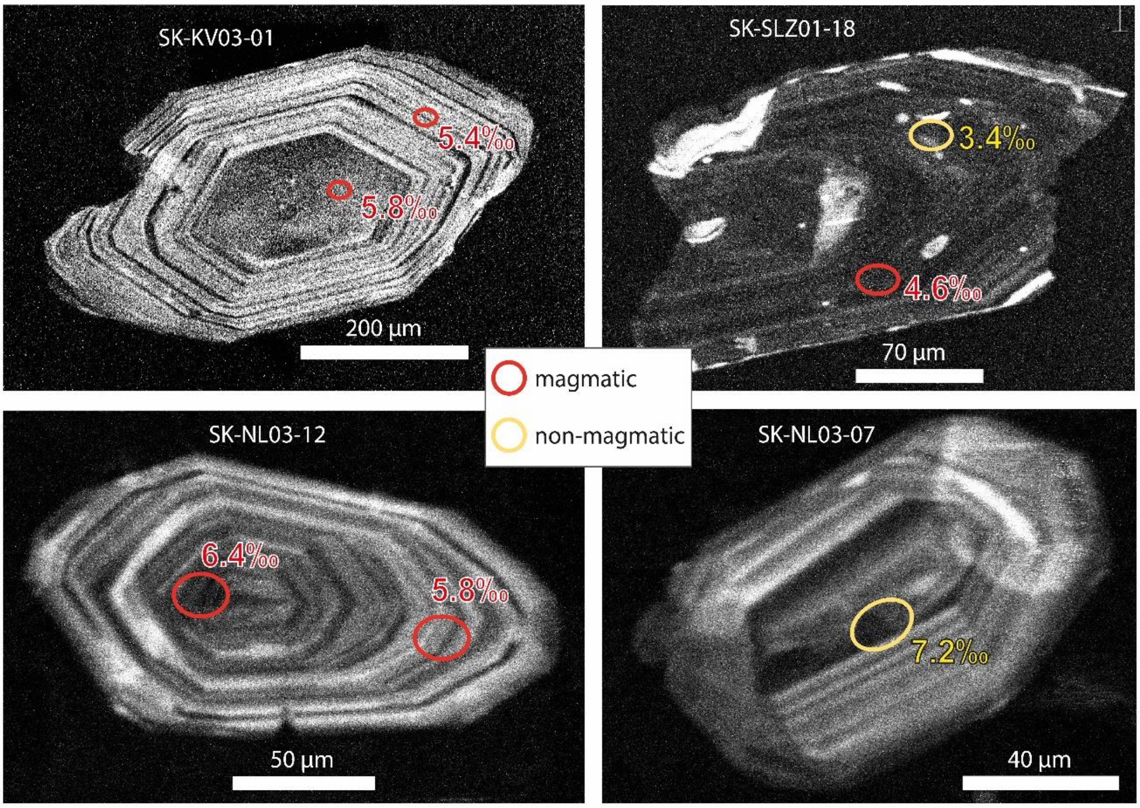

Figure 5-4. Cathodo-luminescence images of representative zircons analysed for O isotope composition and featuring an oscillatory zoning. The spots of SIMS analyses are shown with their respective $\delta^{18}O$ values. Note the textural evidence of local metamictization in grains SK-SLZ01-18 and SK-NL03-07 where non-magmatic values are observed.

Collectively, the newly acquired and the previously published data allow calculating average zircon $\delta^{18}O$ values per pluton of +5.3 to +6.9‰ with a 2SD value comprised between 0.4 and 1.5‰ (**Table 5-4** and **Figure 5-6**). Average zircons of TTG bodies (pluton or dyke) that are younger than 3.23 Ga show similar to higher $\delta^{18}O$ values compared to average zircons from older TTGs (**Figure 5-5**), as initially observed by Wang et al. (2022). In TTGs that are older than 3.24 Ga, average zircon ranges between 5.3 and 5.7‰ in $\delta^{18}O$, which is comprised in accepted range of mantle-derived zircons (5.6±0.3‰). Contrastingly, the average zircon of TTGs that are younger than 3.23 Ga display $\delta^{18}O$ values up to 6.9‰ (e.g. Weergenvonden TTG; Figure 5-6), that exceed the range of commonly accepted values for mantle-derived zircons. The Stolzburg and Weergenvonden bodies include samples (or magma injections) that are both older and younger than 3.24 Ga and in which zircons display notably different $\delta^{18}O$ values (**Figure 5-5c** and **j**).

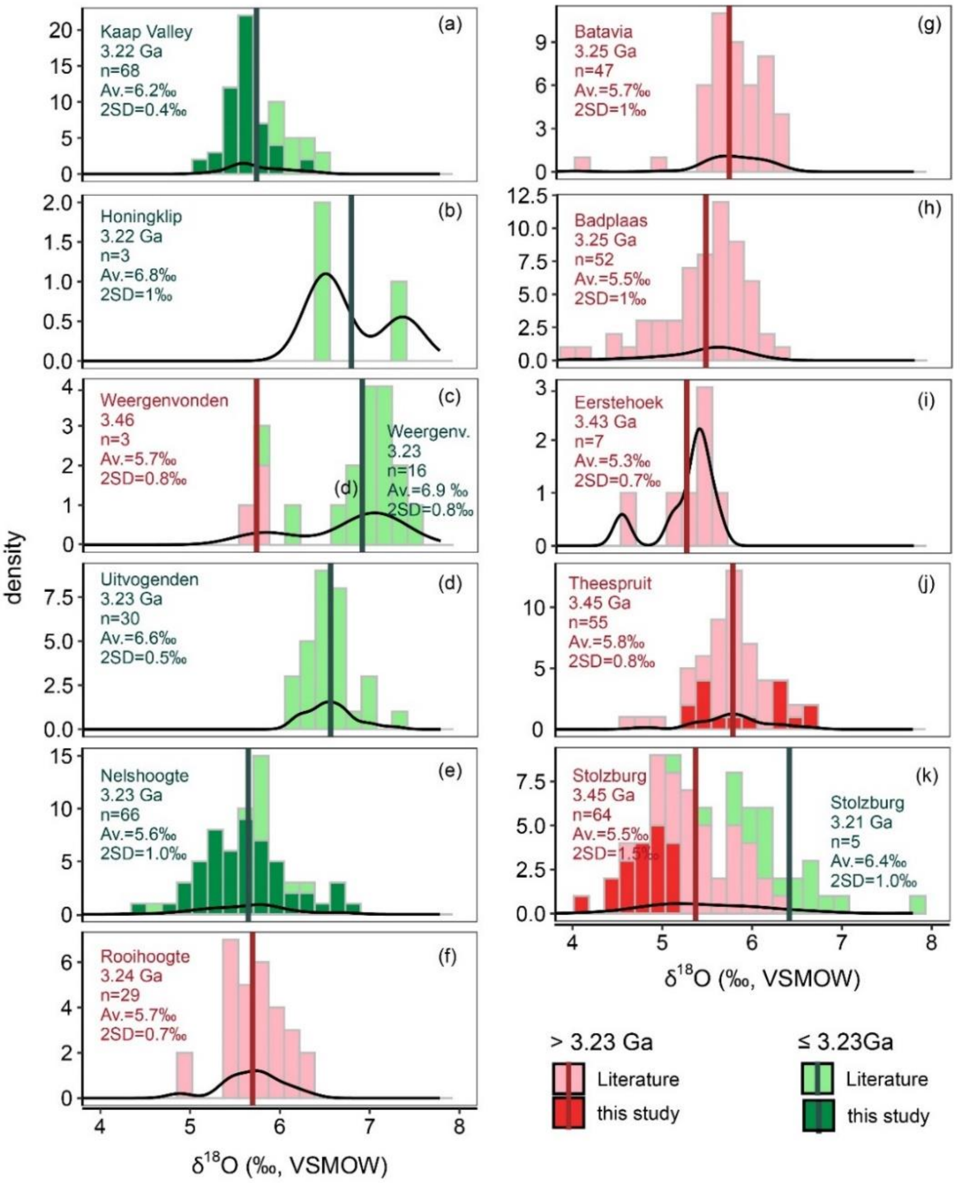

Figure 5-5. Distribution of δ^{18}O in magmatic zircons from different TTG bodies cropping out in the Barberton Granitoid-Greenstone Terrain. Data from the different TTG bodies are arranged in chronological order from the youngest in panel (a) to the oldest in panel (k). The figure distinguishes zircons derived from samples that are older than 3.23 Ga (pink) from those that are younger than this date (green) because this date corresponds to a major change in the O isotope composition of the Barberton TTG melts (Wang et al., 2022). Vertical lines depict the average composition of each zircon population.

Metamorphic zones were generally avoided during O isotope analyses of zircons based on cathode-luminescence textures, yet some spots are completely removed from magmatic composition despite their magmatic textures. In samples SK-NL03, SK-NL04 and SK-THP03, these non-magmatic zones display higher δ^{18}O (7.1-9.9‰) compared to magmatic zones (**Figures 5-4**). Contrastingly, in sample SK-SLZ01, zones are considerably lower in δ^{18}O (up to 3.3‰) than magmatic zones. The non-magmatic zones (based on O isotope composition) could be due to metamictisation of these parts of zircons that may have enhanced the mobility of oxygen without generating metamorphic textures. The non-magmatic O isotope compositions will therefore be excluded from the following discussion and were excluded from the calculation of the average compositions shown in **Table 5-4**.

C. Difference of $\delta^{18}O$ between bulk-rock samples and zircon

Figure 5-3a illustrates the difference in $\delta^{18}O$ between TTG samples and their zircons and shows that zircons generally have lower $\delta^{18}O$ values than those measured in whole-rock samples. The value of $\Delta^{18}O_{melt\text{-}Zrc}$ ranges between 1.5 and 2.4‰ for three samples for which we analysed $\delta^{18}O$ values both in bulk-rock samples and zircons. This range of $\Delta^{18}O_{melt\text{-}Zrc}$ is consistent with values found in previous studies that analysed coevally the O isotope composition of zircon and bulk-rock samples in felsic magmatic rocks (Valley et al., 1994; Lackey et al., 2008; Zakharov et al., 2022).

5.2.1.3. Silicon isotope composition in the Barberton TTGs and their zircons

All Si isotope compositions discussed in this study derived from the literature (see **Sub-section 5.2.1.1.**).

A. Bulk-rock Si isotope composition

The $\delta^{30}Si$ of individual TTG samples are comprised between -0.06 and +0.15‰, which is higher than the range of ~ -0.20 to -0.17 expected in modern granitoids at SiO_2 concentration of 66-70 wt% (André et al., 2019). The average $\delta^{30}Si$ of individual plutons calculated based on existing bulk-rock analyses is comprised in a narrow range of -0.03 to +0.03‰, with 2SD values of 0.09 to 0.20‰ (**Table 5-3**).

B. Zircon Si isotope composition

The $\delta^{30}Si$ of individual magmatic zircons from the Barberton TTGs ranges between -0.50 and -0.10 ‰. In every TTG body, the average $\delta^{30}Si$ of zircon is comprised between -0.39 and -0.15 ‰, with a 2SD extending from ± 0.07 to ± 0.18‰ (**Table 5-4** and **Figure 5-6**). The average $\delta^{30}Si_{zrc}$ of the Barberton TTGs is generally at the higher end of the field defined by A-type, I-type and S-type granitoids.

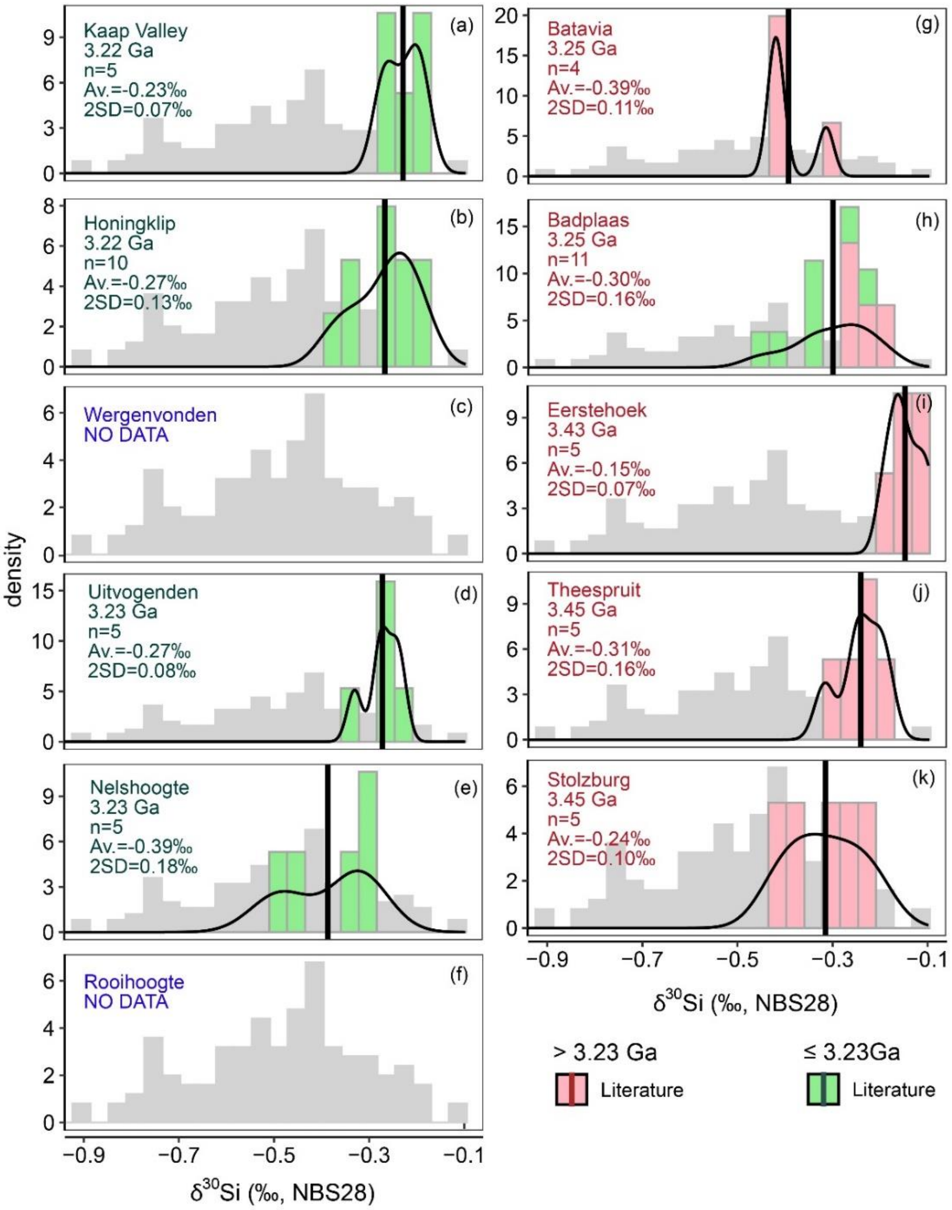

Figure 5-6. Distribution of δ^{30}Si in magmatic zircons from different TTG bodies cropping out in the Barberton Granitoid-Greenstone Terrain. Data of the different TTG bodies are arranged from the youngest in Panel (a) to the oldest in Panel (k). A distinction between zircons from samples that are older than 3.23 Ga and those that are younger than 3.23 Ga is performed because this is the date when an O isotope change was observed in the Barberton TTGs. In the background, the distribution of δ^{30}Si values in zircons of A-type, I-type and S-type granites analysed by Guitreau et al. (2022) is shown in light grey.

5.2.2. Numerical modelling

In support to the compiled isotopic database, we performed also a numerical model with the goal of understanding the thermodynamic conditions in which the isotopic signature of silica-rich rocks derived from the seafloor was transmitted to TTG magmas. Previous experimental and numerical studies successfully reproduced the major and trace element composition of TTGs by simulating basalt melting in different conditions of pressure, temperature and H_2O content (Rapp et al., 1991; Stevens and Moyen, 2007; Laurie and Stevens, 2012; Nagel et al., 2012; Palin et al., 2016; Johnson et al., 2017). However, most of these studies were performed before we knew that the source zone of TTGs contained a seafloor-derived silica-rich component. The major and trace element composition of melts produced by silica-rich rocks derived from the seafloor has not been explored neither experimentally nor numerically, and the influence of these rocks on the major element geochemistry of natural TTGs therefore remains unexplored. To fill this gap, we have performed a simple numerical model that simulates the proportion and composition of the primary liquid and the nature of residual phases appearing upon melting of both silicified lavas and non-silicified lavas. The modelling method is briefly described in the next section before the presentation of its results.

5.2.2.1. Description of the thermodynamic model

Partial melting of an average silicified lava and an average non-silicified lava from the Onverwacht Group was simulated numerically using the Perple_X software (Connolly et al., 2011) that incorporates the complete thermodynamic database and solution models of Holland and Powell (2011) and Holland et al. (2018). The different parameters considered in the model, including (1) the oxides constituting the system (NCKFMASHTO: Na_2O–CaO–K_2O–FeO–MgO–Al_2O_3–SiO_2–H2O–TiO_2–O_2), (2) thermodynamic models for the solid solutions and (3) the composition of possible sources, here we used an average silicified lava and an average non-silicified lava, both presented in **Table 5-5**. The water-fractionated or dry equilibrium model considers that pure aqueous fluids were removed systematically from the system unless they were dissolved into pre-existing melt upon their apparition. The average compositions of silicified lavas used in the model was calculated using the composition of representative silicified lavas that were analysed in this thesis (see **Section III**, **Table 3-1**) and published in previous works of Hofmann and Harris (2008). Similarly, the average composition of non-silicified lavas was calculated from the compilation of Furnes et al. (2013). An O_2 concentration of 0.18 wt.% was added also to both systems to achieve a Fe^{2+}/Fe^{3+} ratio of ~0.4 in the system (Middlemost, 1989). Two endmember models were performed for each of these two different sources. The first model simulated water-saturated equilibrium, while the second model simulated water-fractionated (or dry) equilibrium, and both models were run between 530 and 1030 °C and along a hot archean geotherm of 900 °C/GPa (pressure range 0.6 to 1.1 GPa) (Johnson et al., 2017).

Table 5-5. Parameters considered in the thermodynamic model

Oxides	Models	Source material	Composition (wt.%)									
			SiO_2	Al_2O_3	FeO	MgO	CaO	K_2O	Na_2O	TiO_2	H_2O	O_2
Na_2O–CaO–K_2O–FeO–MgO–Al_2O_3–SiO_2–H_2O–TiO_2–O_2 (NCKFMASHTO)	Melt(HGPH), St(W), Ctd(W), Ep(HP11), Fsp(C1), Gt(HGP), Opx(HGP), Cpx(HGP), Crd(HGP), Bi(HGP), Mica(W), cAmph(G), IlHm(A), Sp(HGP)	Average silicified lava	80.28	4.98	6.23	2.72	0.36	1.64	0.15	0.56	3.08	0.18
		Average fresh lava	51.27	12.37	10.78	9.54	7.85	0.59	2.14	0.88	4.59	0.18

5.2.2.2. Proportion of equilibrium minerals and liquid

We describe firstly equilibrium minerals and liquid proportions that were obtained by our model in water-saturated conditions and closed system (**Figure 5-7a and b**). In these conditions, partial melting of silicified lavas occurs in the presence of biotite, amphibole, quartz and H_2O, and is associated with the growth of garnet, and orthopyroxene (i.e. in amphibolite facies). Upon disappearance of biotite and amphibole from the system, melting continues in the presence of quartz, garnet and orthopyroxene (in eclogite facies) until the silicified lavas are completely melted shortly before the system reaches 900 °C (**Figure 5-7a**). Concerning non-silicified lavas, they also produce, in water-saturated conditions, large proportions of melts at relatively low temperature (> 30 vol.% at 730 °C) and in the presence of biotite, plagioclase, quartz and garnet (**Figure 5-7b**). Once quartz and plagioclase are consumed off the non-silicified lava system, partial melting starts to operate only in the presence of amphibole and peritectic garnet and pyroxene. An important observation from our model is that, in a closed system, complete melting of silicified lavas in water-saturated conditions could occur before reaching 900 °C, while non-silicified lavas are only partially melted. Implicitly, the contribution of silicified lavas could be over-represented in the melt and missing or under-represented in the residue.

Concerning water-fractionated (or dry) conditions, the average silicified lava melts in the presence of a large quantity of quartz (> 65 vol.%) that remains stable up to considerably high temperatures, co-existing with biotite and amphibole at low temperature (< 870 °C) and with peritectic garnet and orthopyroxene at higher temperatures (**Figure 5-7c**). Therefore, the melting degree is considerably low, around 25 vol.% of melt only at ~1020 °C. Concerning the average non-silicified lava, it melts in the presence of amphibole, quartz, feldspar, and peritectic pyroxenes at low temperature (< 880 °C), with peritectic garnet appearing after the disappearance of quartz and amphibole at higher temperature. In water-fractionated conditions, the proportion of melt produced by silicified lavas is relatively lower than that produced by non-silicified lavas at temperatures exceeding 850 °C, contrastingly to what is observed in water-saturated conditions.

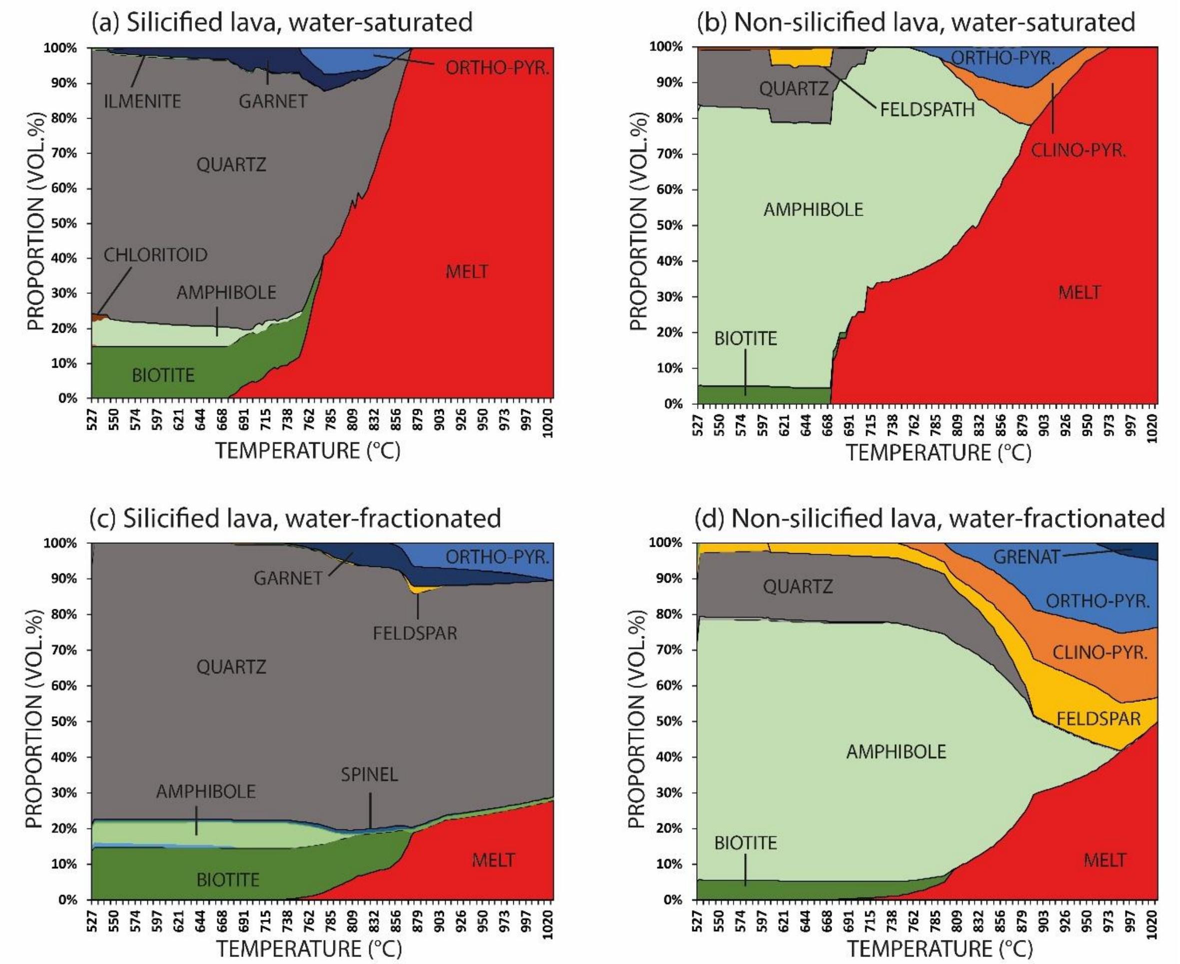

Figure 5-7. Proportions of phases equilibrated in numerical thermodynamic models. Plates (a) and (b) feature the proportions of different phases upon thermodynamic equilibrium of an average silicified lava and non-silicified lava respectively in a water-saturated system. Plates (c) and (d) illustrate the same results in a water-fractionated (or dry) system. Note that models are not calibrated for very silicic compositions; thus the results in the q+L field are questionable

5.2.2.3. Major element composition of the modelled melt

Unsurprisingly, the compositions of liquids produced by melting of an average silicified lava are considerably different from those of liquids extracted from non-silicified lavas (**Figure 5-8**). The composition of melts produced by silicified lavas in the model are generally richer in K_2O (i.e. closer to orthose endmember) than natural TTGs both in water-saturated lavas (**Figure 5-8a**) and in water-fractionated conditions (**Figure 5-8c**). When the proportion of melt is still lower than ~5 vol.%, the melt produced by a silicified lavas in water-saturated conditions display TTG like compositions but such low degrees of melting are not viable for explaining the trace element composition and the volume of natural TTG bodies. Concerning the non-silicified lavas, they generate TTG like melt in both a water-saturated once they reach a melting degree of 20-40 vol.% both in water-saturated and water-fractionated conditions. However, the non-silicified lavas produce trondhjemitic to tonalitic liquids that are close the proposed field of primitive TTG melt only in water-saturated conditions (**Figure 5-8b**). The melts produced by the non-silicified lavas in water-fractionated conditions are rather granodioritic in the conditions of pressure and temperature considered in the model.

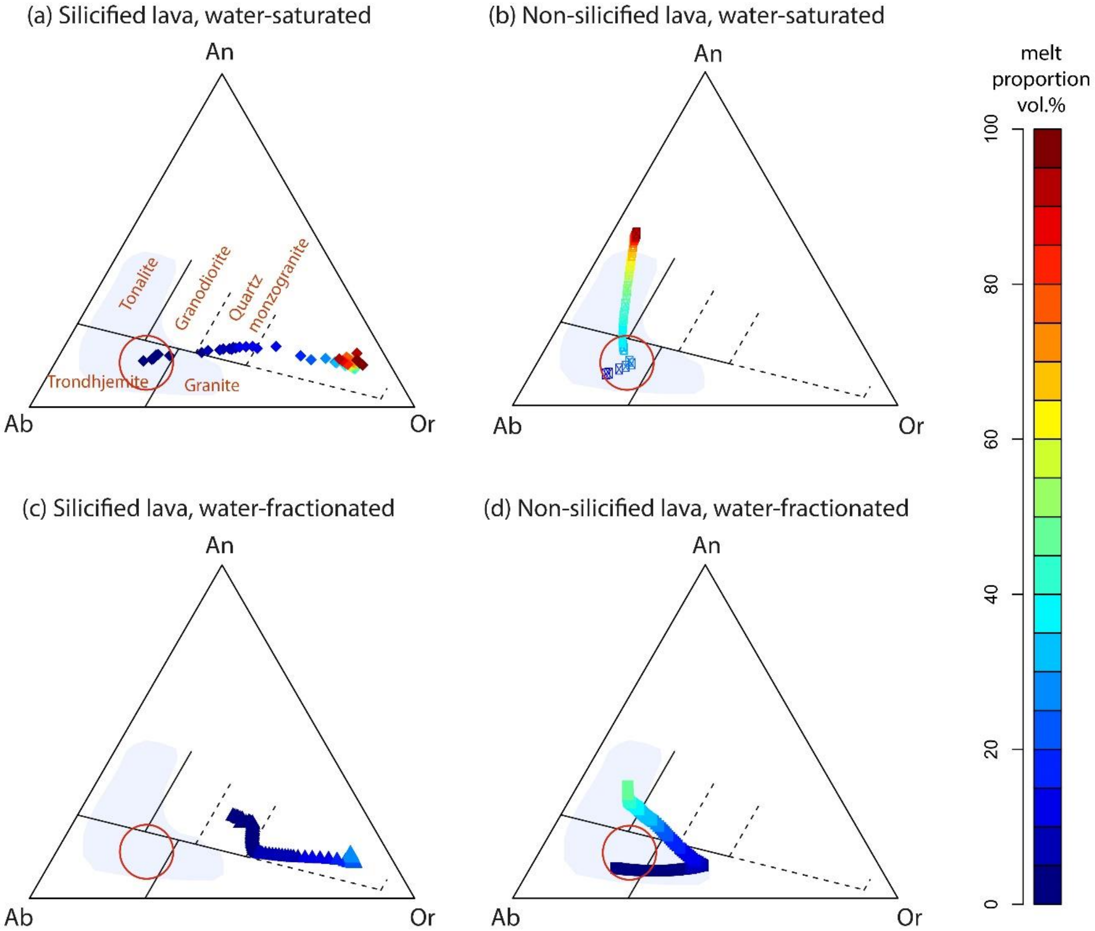

Figure 5-8. Anorthite-albite-orthoclase (An-Ab-Or) diagrams illustrating the composition of liquids generated by melting of an average silicified lava and an average non-silicified lava in water-saturated (a and b) and water-fractionated (c and d) systems. The red circle represents a possible field of primitive TTG melt based on reconstructions of Laurent et al. (2020) and Rollinson (2021). The blue zone was drawn based on the compilation of Barberton TTG compositions by Moyen et al. (2019). Note that non-silicified lavas could generate TTG melts in water-saturated conditions and silicified lavas alone are not likely to have generated TTG melts.

5.3. Interpretations and discussion

This section is subdivided in three different sub-section. The first sub-section discusses the O and Si isotopic composition of TTG magmas based on their average bulk-rock and zircon compositions. Then, the second sub-section discusses the proportion and isotopic composition of silica-rich rocks that were reworked in the source zone of distinct generations of TTGs based on both isotopic measurements and modelling. Finally, the third subsection uses the possible location of silica-rich rocks in the Onverwacht Group stratigraphic succession to estimate their burial depth in the palaeoarchean crust upon involvement in TTG melting and provide new geodynamic implications.

5.3.1. Determining the O and Si isotope composition of primitive TTG magmas

The $\delta^{18}O$ and $\delta^{30}Si$ of primitive TTG melts are important for characterising the source zone of TTGs but iare only accessible from indirect proxies such as bulk-rock and zircon analyses. In this part, we compare the isotopic composition of the TTG melts obtained by the two different approaches (i.e. bulk-rock and zircon analyses).

5.3.1.1. Isotopic composition of the melt obtained from bulk-rock analyses

Calculating the average $\delta^{18}O$ and $\delta^{30}Si$ values of a pluton from bulk-rock measurements of representative samples is the simplest way to estimate the isotopic composition of the primitive TTG melt. However, the fact that fractional crystallisation (**Figure 5-1**), metamorphism and weathering can modify the isotopic composition of TTGs has been considered as drawback for considering average bulk-rock compositions as representative of the original melt.

In individual TTG bodies from the Barberton granitoid-greenstone terrain, large variations are observed for $\delta^{18}O$ (2SD = 0.4-1.3‰) and $\delta^{30}Si$ (2SD = 0.09-0.20‰). The variations of $\delta^{18}O$ values particularly extend beyond analytical errors (2SD = 0.4‰ $\delta^{18}O$ values) (**Table 5-3**) and are therefore not due to analytical limitations. They may rather reflect multiple parameters including (1) fractional crystallisation (Lackey et al., 2008; Guitreau et al., 2022) or secondary alteration of the granitoids (e.g. Faure and Harris, 1991), (2) lack of representativeness of analysed samples due to their small number, and 3) original isotopic heterogeneities in the primary melt. Oxygen and silicon are both major constituents of TTGs, and, as the Barberton TTGs did not record an intense episode of fluid circulation, metamorphism or weathering processes cannot explain the large variation of O and Si isotope compositions in individual TTG bodies. Although gold-rich fluids circulated in northern part of the Barberton Granitoid-Greenstone Terrain around 3 Ga ago or later (e.g. Agangi et al., 2019), no petrographic evidence demonstrates that these fluids affected the studied TTG plutons. In addition, low fluid/rock ratios at metamorphic or weathering stage could not dramatically modify the O and Si isotopic composition of the Barberton TTGs.

In contrast with large inter-sample dispersion, inter-pluton differences in the average bulk-rock $\delta^{18}O$ and $\delta^{30}Si$ per TTG body cover narrow ranges of variation (7.0 – 7.6‰ and -0.03 to +0.03‰, respectively). In addition, individual bulk-rock samples analysed in this study (**Table 5-2**) are comprised in a narrow range of $\delta^{18}O$ values (6.9 – 8.1‰) independently of their SiO_2 concentration (**Figures 5-3b**). Thus, processes related to fractional crystallisation cannot have considerably modified the average O and Si isotope composition of the Barberton TTG plutons. Calculated average $\delta^{18}O$ and $\delta^{30}Si$ per TTG body must be close to original values. A calculation of O isotope evolution in the TTG liquid and solid fractions upon cooling confirms this interpretation (**Figures 5-9**). The calculation is based on phase proportions predicted by thermodynamic modelling on a cooling path, and melt-mineral isotopic fractionation factors calculated from the database of Faure and Harris (1991) (**Table 5-6**). This calculation shows that fractional crystallization could not significantly change the composition of the Barberton TTG melt as its $\delta^{18}O$ variation is predicted to have not exceeded 0.5‰ (especially for Kaap Valley pluton). Unknown fractionation of Si isotopes between the TTG melt and its major minerals precludes modelling the evolution of $\delta^{30}Si$ during fractional crystallisation, but fractional crystallisation could not change importantly the $\delta^{30}Si$ of the melt (Deng et al., 2019).

Table 5-6. Calculation parameters derived from Perple-X model of fractionation of a tonalitic melt and results of O isotope evolution during fractional crystallisation of a TTG magma.

T[°C]	1050	980	910	840	770	700
Proportions (mol%)(a)						
System	100.0	100.0	100.0	100.0	100.0	100.0
Plagioclase		4.4	11.3	18.8	22.8	28.4
Opx			0.7	3.1		
hornblend				1.1	10.1	12.6
quartz						4.7
Liquid	100.0	95.6	87.7	76.5	66.9	54.3
Solid	0.0	4.4	12.3	23.5	33.1	45.7
$\delta^{18}O$ (‰, VSMOW)						
System	7.5	7.5	7.5	7.5	7.5	7.5
Plagioclase(b)		7.2	7.2	7.2	7.2	7.2
Ortho-pyroxene(b)			5.7	5.7	5.7	5.7
hornblend(b)				5.4	5.4	5.4
quartz(b)						9.7
$\Delta^{18}O_{WR-mineral}$(b)						
Plagioclase		0.3	0.3	0.3	0.3	0.3
Opx			1.8	1.8	1.8	1.8
hornblend				2.1	2.1	2.1
quartz						-2.2
Liquid (calculated)(c)	**7.5**	**7.5**	**7.6**	**7.7**	**7.9**	**8.0**
Solid (calculated)(c)		**7.2**	**6.9**	**6.8**	**6.6**	**6.9**

(a) The proportions of phases were obtained from a thermodynamic model along a cooling pathway at a fixed pressure of 0.5 GPa, using the igneous dataset of Holland et al. (2018) and MAGEMin software. The major element composition of sample SK-KV02 (see **Table 5-2**) was considered in this model. (b) O isotope compositions of minerals and $\Delta^{18}O_{WR-ZRC}$ values are based on the database published by Faure and Harris (1991) for the Kaap-Valley pluton. (c) The O isotope composition of residual liquid was based on mass balance calculations.

The fact that average bulk-rock $\delta^{18}O$ and $\delta^{30}Si$ values per TTG body are comprised in narrow ranges (despite large 2SD values) suggests that these values are close to (i.e. less than 0.5‰ different from) the composition of original TTG melts. Yet, since the large 2SD values of bulk-rock compositions in individual plutons may be due to processes that are independent of primitive melt composition, it is important to compare them with results obtained from zircon analyses.

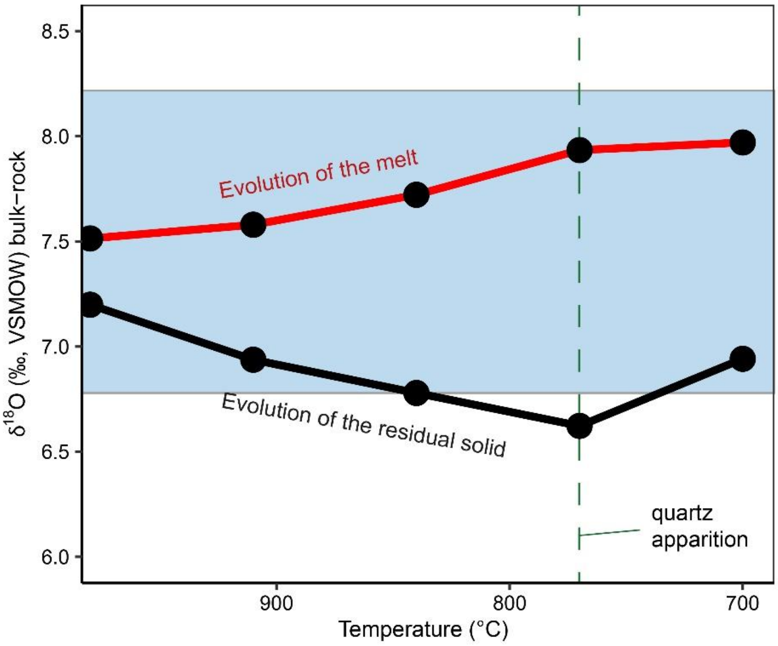

Figure 5-9. Modelled evolution of $\delta^{18}O$ in the residual liquid and solid phases in a cooling TTG magma compared to the range of bulk-rock TTG composition. The blue field shows the range of $\delta^{18}O$ in measured bulk-rock samples from the Barberton TTGs (this study and Faure and Harris, 1991).

5.3.1.2. Isotopic composition of the TTG melt obtained from zircon composition

Zircon is a good proxy to determine the O and Si isotopic composition of TTG melts because zircon forms early in the TTG magma, and therefore captures the isotopic composition of the un-differentiated melt (Page et al., 2007; Fu et al., 2008; Guitreau et al., 2022). In addition, zircon is very resistant to post-magmatic processes (Hawkesworth and Kemp, 2006) and the characteristic textures of magmatic zircons (e.g. **Figure 5-4**) allow to distinguish them from metamorphic zircon that may have lost their magmatic O and Si isotopic composition.

In the Barberton TTGs, we observe intra-pluton and inter-pluton variations in the $\delta^{18}O$ (2SD = 0.5-0.8‰) and $\delta^{30}Si$ (2SD = 0.07-0.11‰) of zircon that may be due to (1) analytical uncertainty (typically 2SD>0.4‰), (2) heterogeneity in the primary TTG melts and (3) differences in the temperature of zircon precipitation. The large analytical errors arising from in situ analyses of O and Si isotope compositions of zircon hinder a precise calculation of the isotopic composition of TTGs using these data. Additionally, zircons separated from different samples within the same TTG body are different in their $\delta^{18}O$ values, supporting the existence of isotopic heterogeneities in original TTG melts that, in turn, may reflect heterogeneities existing in the source region.

We note that, in any TTG body from the Barberton granitoid-greenstone terrain, the average $\delta^{18}O$ and $\delta^{30}Si$ of zircon is different from that of bulk-rock samples (**Table 5-3**). This notable difference can only be explained by the fractionation of Si and O isotopes between TTG melts and crystallised zircons (Valley et al., 1994; Lackey et al., 2008; Harris et al., 2015; Qin et al., 2016; Trail et al., 2020; Guitreau et al., 2022). As $\Delta^{18}O_{melt\text{-}zrc}$ and $\Delta^{30}Si_{melt\text{-}zrc}$ are generally positive, it is possible to question the common consideration that a $\delta^{18}O$ value of ~5.3 ±0.3‰ measured in zircons of a TTG indicates that these felsic magmas originated from melting of mantle-derived magmas (e.g. Page et al., 2007; Vezinet et al., 2018; Smithies et al., 2021; Wang et al., 2022; Lei et al., 2023; Drabon et al., 2024). This consideration is based on comparisons of the $\delta^{18}O$ value of zircons from granitoids, with that of kimberlitic zircons (Mattey et al., 1994; Page et al., 2007) and mantle-derived magmas (Eiler, 2019; Eiler et al., 2000). Indeed, kimberlite-hosted zircons display $\delta^{18}O$ values that are within error equivalent to bulk-rock $\delta^{18}O$ values of the hosting ultramafic and mantle-derived magmas (Mattey et al., 1994; Page et al., 2007). It has been also shown that the fractionation of $\delta^{18}O$ between zircon and a magma from which it crystallises in equilibrium ($\Delta^{18}O_{melt\text{-}zrc}$) depends on the temperature and the concentration of SiO_2 in the magma (Valley et al., 1994; Lackey et al., 2008). Thus, the $\delta^{18}O$ value of zircon can be similar to (or less than 0.3‰ lower than) that of ultramafic rocks in equilibrium (Mattey et al., 1994; Page et al., 2007), but up to ~1.5‰ lower than that of felsic magmas as observed in **Figure 5-3a** (Lackey et al., 2008; Zakharov et al., 2022). It is therefore unrealistic to consider mantle-like $\delta^{18}O$ values (5.3 ±0.3‰) in zircons from the Barberton TTGs as indicating origination from melting of a non-altered mantle-derived basalt.

To estimate the O and Si isotopic composition of average TTG melts from which zircon crystallised, we need to correct average zircon compositions for melt-zircon isotopic fractionation. For this purpose, we consider the calibration of magma-zircon O isotope fractionation proposed by Lackey et al. (2008) and the calibration of granitic magma-zircon Si isotope fractionation proposed by Guitreau et al. (2022) that are expressed in **Equations 5-1** and **5-2**:

$$\Delta^{18}O_{(melt-ZRC)} = 0.0612 \times SiO_2 - 2.5 \quad \textbf{(Equation 5-1)}$$

and,

$$\Delta^{30}Si_{(melt-ZRC)} = 0.0054 \times \frac{10^6}{T^2} \times SiO_2 \quad \textbf{(Equation 5-2)}$$

We also consider for every TTG body an average SiO_2 concentration of 69 wt.% and a temperature of 800 °C. These considered parameters are satisfactorily close to average values obtained respectively by bulk-rock major element (e.g. Anhaeusser and Robb, 1980; Kleinhanns et al., 2003; Clemens et al., 2006; Anhaeusser, 2010) and Ti-in-zircon analyses in archean TTGs (e.g. Fu et al., 2008; Guitreau et al., 2022). Although the actual SiO_2 concentrations and temperatures of the primary TTG melts may deviate slightly (± 2 wt.% and ± 50 °C) from the considered values, this slight deviation cannot generate dramatic changes in the respective $\Delta^{18}O_{\text{melt-ZRC}}$ and $\Delta^{30}Si_{\text{melt-ZRC}}$ values that we obtain from empirical calibrations.

From these calibrations, we obtain $\Delta^{18}O_{\text{melt-ZRC}}$ and $\Delta^{30}Si_{\text{melt-ZRC}}$ values of 1.6‰ and 0.33‰. The empirically calculated $\Delta^{18}O_{\text{melt-ZRC}}$ value is within error compatible to $\Delta^{18}O_{\text{WR-ZRC}}$ calculated from the new data acquired in this study (**Table 5-2** and **Figure 5-3a**). In addition, the $\delta^{18}O$ (7.1 to 8.4‰) and $\delta^{30}Si$ values (-0.06 to +0.33‰) that we calculated for average TTG melts of the different bodies based on average zircon composition (**Table 5-7** and **Figure 5-10**) are within error comparable to those provided by average bulk-rock compositions as illustrated in **Figure 5-11**. Thus, both average bulk-rock and zircon-reconstructed $\delta^{18}O$ and $\delta^{30}Si$ values of the TTG melt may be close to actual values of original melts. However, large 2SD variations of $\delta^{18}O$ and $\delta^{30}Si$ values are observed both for average TTG melts calculated from average bulk-rock analyses (**Table 5-3**) and for those reconstructed using zircon composition presented in **Table 5-7**. These large variations do not allow to obtain an unambiguous 1:1 correlation between these equivalent variables in **Figure 5-11**. These variations could be partly due to intra-pluton melt heterogeneity as evidenced by the large range of O isotope composition in zircons from the different plutons, and particularly of the Stolzburg pluton (**Figure 5-5k**).

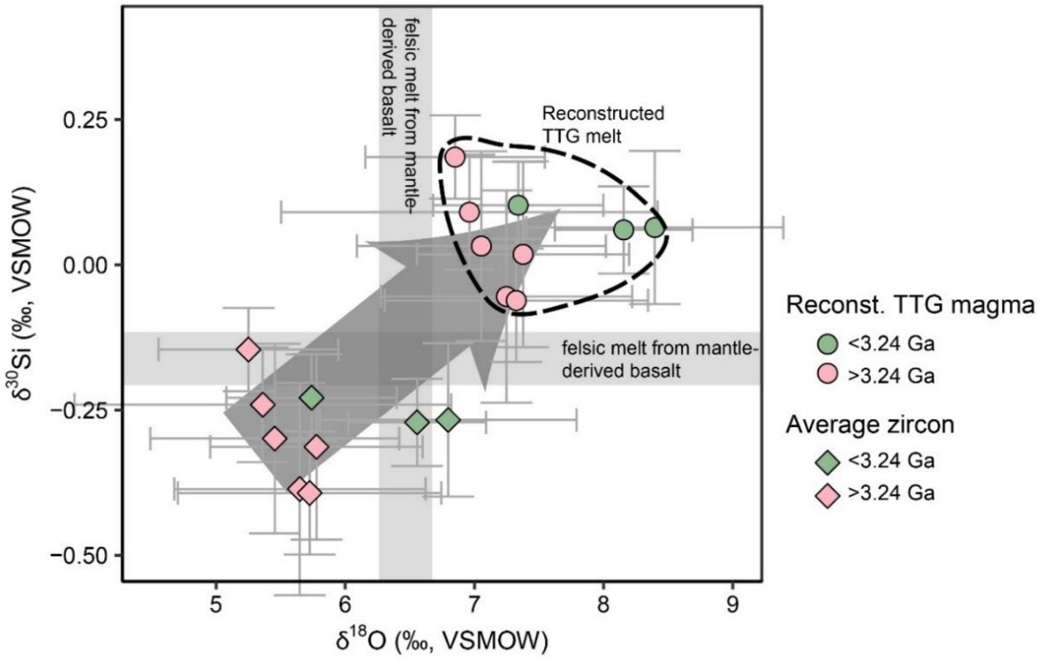

Figure 5-10. Plot of δ^{18}O values versus δ^{30}Si values illustrating the difference between the isotopic composition of average zircons and the calculated isotopic composition of melts from which they precipitated. Featured data are average values calculated for the different TTGs as given in **Table 5-7**. The grey arrow illustrates the trend of Si and O isotope fractionation between the TTG magma and the precipitated zircons. The arrays of felsic melt produced by mantle-derived magmas are taken from André et al. (2019) for δ^{30}Si and Bindeman et al. (2005) for δ^{18}O .

Table 5-7. δ^{18}O and δ^{30}Si of average melts from the Barberton TTG bodies calculated from average zircon composition

TTG body	Age (Ga)	calculated $\Delta^{18}O_{melt-ZRC}$	$\delta^{18}O_{melt}$		calculated $\Delta^{30}Si_{melt-ZRC}$	$\delta^{30}Si_{melt}$	
			Av.	2SD		Av.	2SD
Badplaas	3.25	1.6	7.1	1	0.33	0.03	0.16
Nelshoogte	3.23	1.6	7.2	1	0.33	-0.05	0.18
Kaap Valley	3.22	1.6	7.3	0.7	0.33	0.1	0.07
Theespruit	3.45	1.6	7.4	0.8	0.33	0.02	0.16
Stolzburg	3.45	1.6	7	1.5	0.33	0.09	0.1
Stolzburg	3.21	1.6	8	1	0.33	0.33	
Weergevonden	3.46	1.6	7.3	0.8	0.33	0.33	
Weergevonden	3.23	1.6	8.5	0.8	0.33	0.33	
Batavia	3.25	1.6	7.3	1	0.33	-0.06	0.11
Rooihoogte Pass	3.24	1.6	7.3	0.7	0.33	0.33	
Uitvogenden	3.23	1.6	8.2	0.5	0.33	0.06	0.08
Eerstehoek	3.43	1.6	6.9	0.7	0.33	0.19	0.07
Honingklip	3.22	1.6	8.4	1	0.33	0.06	0.13

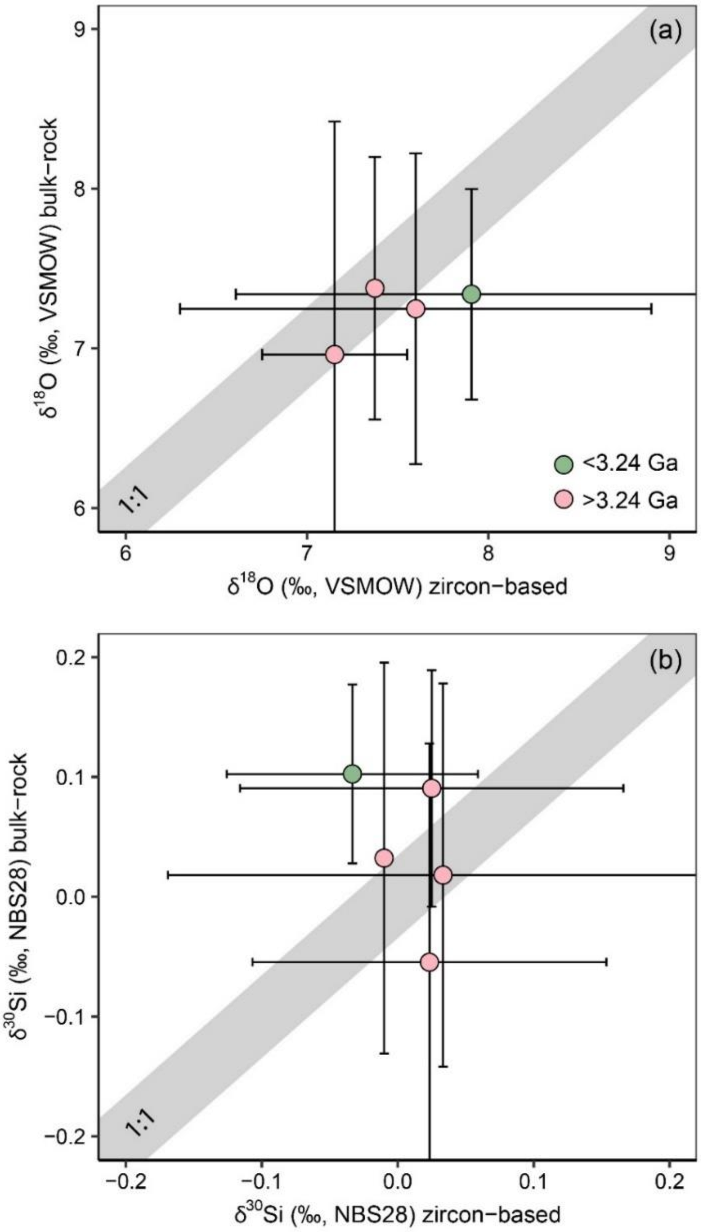

Figure 5-11. Comparison between O and Si isotopic compositions of the TTG magmas estimated based on zircon and bulk-rock data. Only the plutons for which O or Si isotope compositions are simultaneously available for zircon and bulk-rock samples are shown in this graph. The grey line was drawn to illustrate the expected positive correlation in case the compared parameters are equivalent. On plate (a) we note a 1:1 correlation between the $\delta^{18}O$ isotope compositions of TTG magmas calculated based on their zircon composition and issued by bulk-rock measurements. On plate (b) we note that the $\delta^{30}Si$ values proposed for the TTG magma based on bulk-rock measurements and reconstructed based zircon compositions are equivalent within error but do not achieve a perfect 1:1 correlation. Error bars are 2SD values encompassing analytical errors and intra-pluton dispersion.

We further note that the average $\delta^{18}O$ and $\delta^{30}Si$ of all the Barberton TTG magmas are collectively higher than the respective values of ~6.5‰ (Bindeman et al., 2005) and ~0.19‰ (André et al., 2019) expected for felsic magmas issued by melting of non-altered mantle-derived magmas. Therefore, contrasting with the recent proposition of Lei et al. (2023), we do not identify any decoupling between Si and O isotopes in the Barberton TTGs. The decoupled Si and O isotopic signatures were proposed by considering the $\delta^{18}O$ of ~5.0-5.8‰ in zircons as representative of TTG originating from melting of a non-altered mantle-derived magma (Lei et al., 2023). However, after reconstructing the approximate composition of the TTG magmas, we find not only that O and Si isotope compositions are not decoupled in the Barberton TTGs, but also that they collectively support the presence of a component characterised by heavier O and Si isotopic compositions in the source region of the TTGs (compared to mantle-derived lavas) (**Figure 5-10**). Silica-rich rocks (silicified lavas and cherts) derived from the seafloor have been proposed to represent this silica-rich endmember (Deng et al., 2019; André et al., 2019, 2022; Lei et al., 2023), and their proportion and isotopic composition in the source zone of the Barberton greenstone belt is discussed in the next sub-section.

5.3.2. Proportion and isotopic composition of reworked silica-rich lavas

An important feature of the Barberton TTGs is that their zircons extend to higher $\delta^{18}O$ values in younger TTGs (< 3.23 Ga in age) compared to older ones (**Figure 5-5**). In contrast, the $\delta^{30}Si$ values of the zircons and bulk-rock samples are almost constant over time (e.g. **Figure 5-6**) (Wang et al., 2022; Lei et al., 2023). This difference in the evolution of O and Si isotope compositions has been ascribed in **Part IV** of this thesis to isotopic variations in seafloor-derived silica-rich rocks over time based on variations of O isotopic compositions observed in silicified lavas from the Onverwacht Group over time (i.e. upwards the stratigraphic column) (**Figure 5-12a**). In the Onverwacht Group, the $\delta^{18}O$ value of silicified lavas and cherts containing more than 60 wt.% of SiO_2 increases from ~11‰ to > 14‰, while their $\delta^{30}Si$ value remains constant around 0 to 1‰ (**Figure 12b**). Building on this observation, the goal of this section is to evaluate the proportion and composition of silica-rich rocks reworked in the source zone of specific TTGs generations in the Barberton granitoid-greenstone terrain by combining results of numerical modelling data with interpretations of isotopic data.

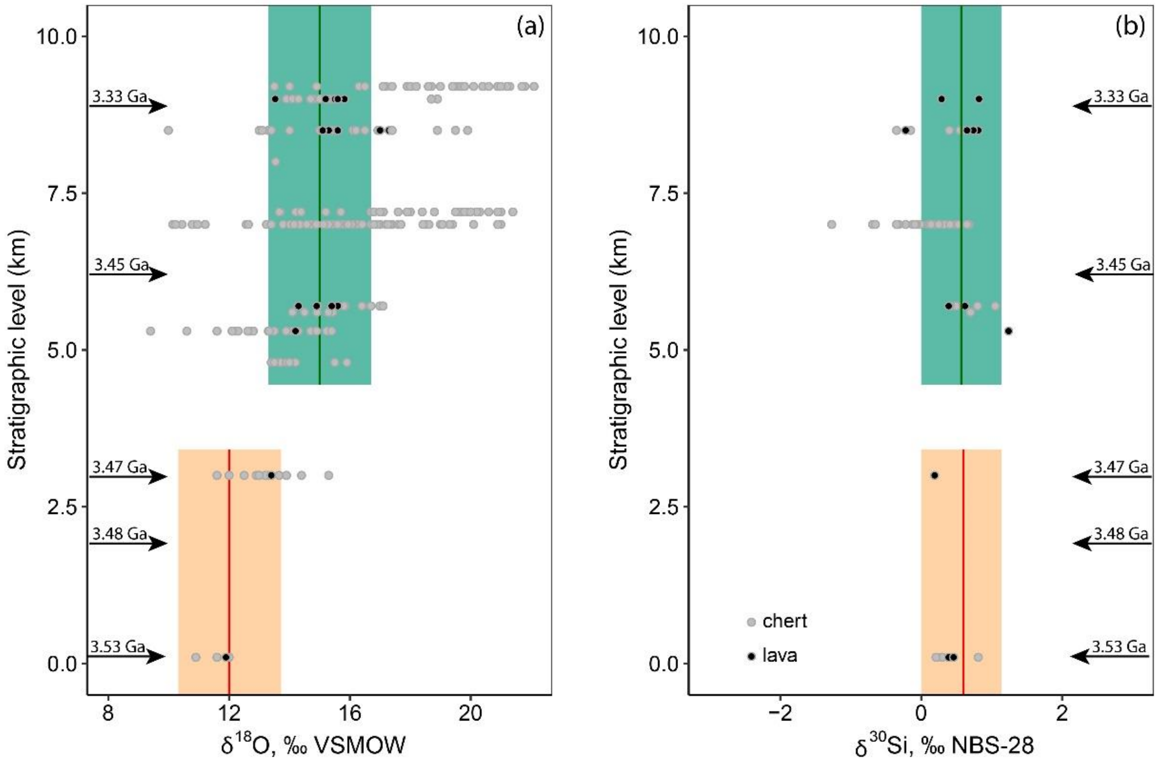

Figure 5-12. Si and O isotopic composition of silicified lavas (black) and cherts (grey) from the Onvewacht Group. Red and green lines depict compositions of average seafloor derived silica (i.e. silicified lava + chert) used in models presented further in this manuscript (Section 4.2). Note the change of O isotope composition and the mostly invariable Si isotope composition over time. Black arrows show different stratigraphic levels with known age (taken from the review of Byerly et al., 2019). Orange and green ranges are potential compositions of average seafloor derived silica-rich rocks considering the volumetric dominance of silicified lavas over cherts. Data sources: Knauth and Lowe (1978, 2003), Hofmann and Harris (2008), Abraham et al. (2011), Geilert et al. (2014), de Wit and Furnes (2016), Lowe et al. (2020) and **Part IV** of this study. Only samples with an SiO_2 concentration exceeding 65 wt.% are shown in this figure.

Our numerical thermodynamic model shows that silicified lavas alone cannot generate felsic melts with a TTG-like composition as the generated melts are more potassic than natural TTGs (**Figure 5-8a,c**). This is not surprising because the silicification of lavas and clastic sediments near the palaeoarchean seafloor was accompanied by an uptake of alkalis elements including K and a release of Mg, Fe, Ca and Na (e.g. **Part III**. of this thesis, Hofmann and Harris, 2008; Rouchon and Orberger, 2008). The silicified lavas are therefore unable to generate TTG-like melts because TTGs are Na-rich and sodic plagioclase-dominated magmatic rocks. The incorporation of silicified lavas and cherts into TTGs as evidenced by Si and O isotopic compositions must therefore be due to mixing with melts generated by a typical archean basalt that has been accepted to represent the major component of TTG source zones (Smithies et al., 2009; Johnson et al., 2017; Moyen and Laurent, 2018). Indeed, partial melts of an average non-silicified lava from the Barberton greenstone belt (**Table 5-5**) globally reproduce the composition of the Barberton TTGs in our numerical model (**Figure 5-8b,d**). The primary tonalitic to trondhjemitic TTG melt that has been proposed in the literature is only achieved in a water-saturated environment, corroborating the notion that TTG melts were generated by water-fluxed melting (Laurie and Stevens, 2012). This is also confirmed by the high-degree of melting observed for silicified lavas compared to non-silicified lavas in water-saturated conditions, which can allow transmitting efficiently the isotopic composition of the silica-rich rocks to seafloor-derived rocks. Based on these results of our numerical model in two extreme conditions (i.e. water saturated and dry conditions), we assume for the rest of the discussion that TTG melts were produced in a water-present context due to ~30 wt.% melting of an average non-silicified Barberton basalt and a ~70 wt.% melting of non-silicified lavas (i.e. at temperatures that did not exceed 900 °C).

To determine the potential proportion of silica-rich rocks reworked in the source zone of the Barberton TTGs, we perform a simple mixing (in the $\delta^{18}O$ vs. $\delta^{30}Si$ space and in major element compositions) between the melt derived from non-altered juvenile lavas and the one issued by the average silicified lava (**Figure 5-13**). The different parameters considered in the mixing model are provided in **Table 5-8**. Within uncertainty, the calculated mixing curves considering two different silica endmembers with different O isotope compositions (i.e. silicified lava 1 with $\delta^{18}O$=12‰ and silicified lava 2 with $\delta^{18}O$=15‰, see **Table 5-8**) traverse TTG melts reconstructed both from zircon and bulk-rock compositions (**Figure 5-13**). According to our calculation, 10 to 25 vol.% proportion of the Barberton TTG melts originated from silica-rich rocks derived from the seafloor. This melt proportion is definitely higher than the proportion silicified lavas in the Barberton granitoid-greenstone terrain, and we ascribe this to the overrepresentation of silicified lava-derived melt to a higher degree of partial melting in water-saturated conditions (**Figure 5-7**). A major element mixing of modelled liquids shown in **Figure 5-13c** demonstrates that the proportion of 10-25 vol.% melt derived from silicified lavas is consistent with the possible primitive major element composition of the Barberton TTG magma. While this proportion range represents average estimations per TTG body, the input of silicified lava-derived melts could be heterogeneous throughout the melting event, and this would partly explain the isotopic variations observed in bulk-rock and zircon analyses. We note also that higher proportions of silicified lava-derived melts (up to 70 vol.%) could explain the formation of potassic granitoids coevally with TTGs in the Barberton area, although such rocks have been identified as pebbles in the ~3.2 Ga old Moodies conglomerates (Sanchez-Garrido, 2011; Agangi et al., 2018).

Considering the different melting degree, we suggest that 5 to 12 vol.% of silica-rich rocks derived from the seafloor and 95 to 88 vol.% of non-silicified lavas in the source zone of the Barberton TTGs. The proposed proportion of melt issued by silicified lavas and cherts is notably higher than that of less than the 5 vol.% of cherts estimated by Deng et al. (2019). This is explained by the composition of the chert endmember considered by Deng et al. (2019) (i.e. 25‰ of $\delta^{18}O$ and +2‰ of $\delta^{30}Si$) that is significantly different from the values that were actually measured in the silicified rocks from the Onverwacht Group (**Figure 5-12**).

Table 5-8. Parameters considered in the mixing calculations to determine the proportion of silica-rich rocks reworked in the source

Material	$\delta^{18}O$	$\delta^{30}Si$	$\Delta^{18}O_{source-melt}$	$\Delta^{30}Si_{source-melt}$
Silicified lava 1	15(a)	0.8(a)	+1(d)	+0.05(f)
Silicified lava 2	12(a)	0.8(a)	+1(d)	+0.05(f)
Non-silicified lava	5.6(b)	-0.29(c)	-0.8(e)	-0.11(g)

Sources of used values:

(a) Values obtained from the compilation of Si and O isotopic composition in silicified lavas and cherts of the Barberton granitoid-greenstone terrain (Figure 5-12)
(b) Eiler et al. (2000) and Eiler (2019);
(c) (Yu et al., 2018);
(d) values estimated based on fractionations of O isotopes between quartz and TTG melts in equilibrium (see Faure and Harris, 1991), taking into account the proportions inferred from thermodynamic modelling;
(e) estimated by Bindeman et al. (2005);
(f) values estimated based on recent measurements of Si isotopes in migmatites by Murphy et al. (2024), considering the proportions of phases inferred from thermodynamic modelling;
(g) Estimated from André et al. (2019).

Due to the impossibility of quantifying three different parameters (i.e. the O and Si isotope composition and the proportion of reworked silicified lavas) based on the isotopic composition of TTG melts alone, our mixing calculation considered the isotopic composition of silica-rich rocks from the Onverwacht Group (**Figure 5-12**). This means that the proportions that we have obtained are only correct if the reworked silicified lavas were compositionally similar to equivalent rocks preserved in the Onverwacht Group. We acknowledge also that the mixing calculation does not constrain independently the O and Si isotopic compositions of the silica-rich rocks reworked in the Barberton granitoid-greenstone terrain. Yet, this calculation can explain the apparition of higher $\delta^{18}O$ TTGs magmas after 3.23 Ga ago, despite the large uncertainties on estimated TTG magma composition. Indeed, the obtained mixing pathways (**Figure 5-13a,b**) confirm that an increase in the maximum of $\delta^{18}O$ values of silicified lavas (e.g. from 10-13‰ to 11-15‰) (**Figure 5-12**) could explain the change in the range of O isotope composition in TTG melts that appeared around 3.23 Ga ago, as already suggested in **Part IV**. This observation is also consistent with our working hypothesis considering that silicified lavas from the Onverwacht Group are good proxies for the reworked analogues. Thus, the burial depth to which the silica-rich lavas was located in the crust due to passive accumulation of younger rocks on the seafloor can be estimated by comparing the calculated values with natural values measured in the Onverwacht Group, which allows evaluating potential geodynamic scenarios in the next section.

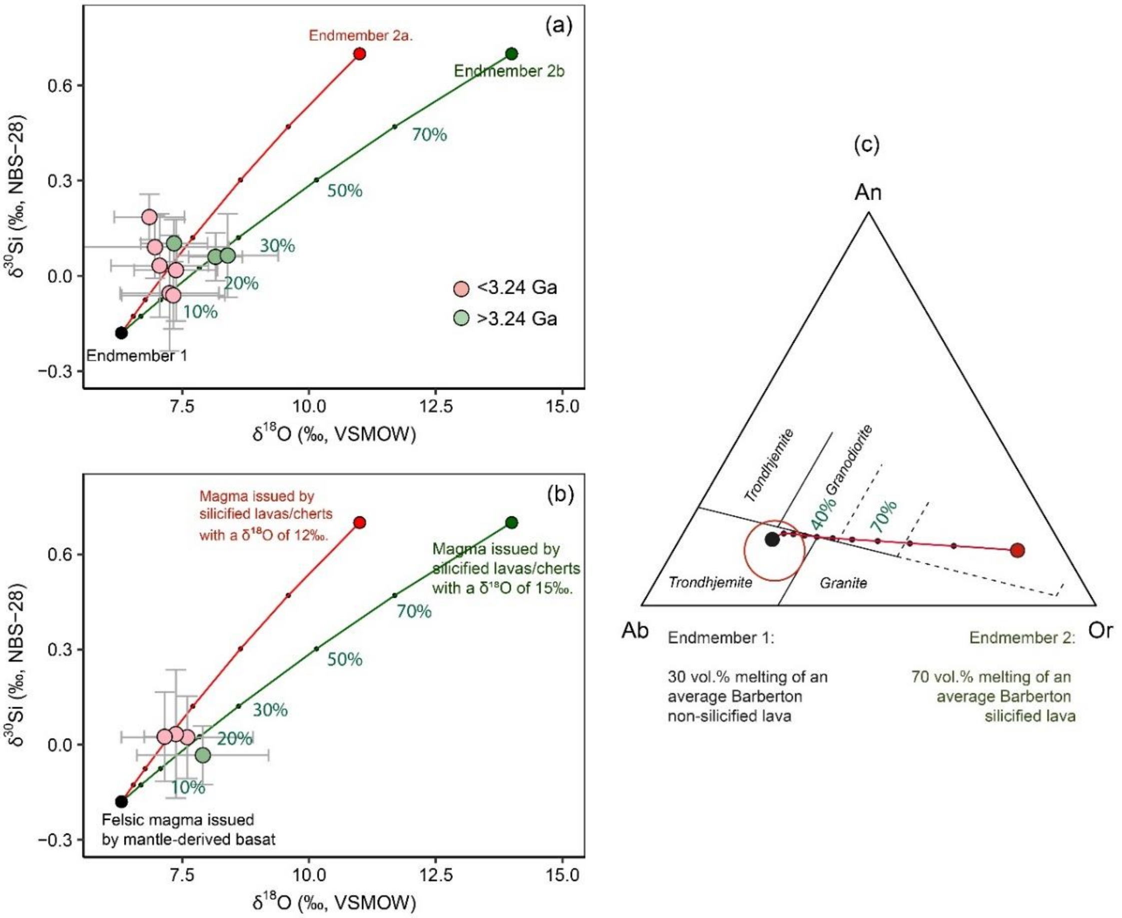

Figure 5-13. Model of mixing between felsic melt generated by fresh (non-silicified lavas) and melt generated by silicified lavas. Plate (a) shows the position of primitive TTG magmas that were reconstructed from zircon composition. Plate (b) shows the position of average pluton compositions for the four TTGs with bulk-rock analyses of Si and O isotopes (Stolzburg, Theespruit, Nelshoogte and Kaap Valley). Plate (c) shows a mixing curve between the melt originating from silicified lavas and the melt originating from non-silicified lavas in the Anorthite-Albite-Orthoclase ternary diagram.

5.3.3. Stratigraphic position of reworked silicified lavas and geodynamic implication

A simple evidence of seafloor-derived silicified lavas and cherts in the source zone of the Barberton TTGs cannot allow discriminating the different possible geodynamic scenarios

(Vezinet et al., 2018; Lei et al., 2023). In fact, melting at the base of a stratigraphically over-thickened crust (Bédard, 2006; Smithies et al., 2009; Johnson et al., 2017), melting in a vertically-sank portion of stagnant crust (Van Kranendonk, 2011; Van Kranendonk et al., 2014Sizova et al., 2015), and melting of a subducted crust (Clemens et al., 2006; Moyen and van Hunen, 2012; Van Hunen and Moyen, 2012) are all consistent with the incorporation of melts produced by silicified lavas and cherts in the Barberton TTGs. Here, we couple the results of our magma mixing calculation (**Figures 5-12**) with known isotopic composition of silicified lavas and cherts from the Onverwacht Group (**Figures 5-13**) to estimate the stratigraphic position, and therefore the burial depth of recycled seafloor-derived rocks. Then, the estimated burial depth in the Onverwacht Group of so determined lithologies is incorporated to the discussion about processes that transported seafloor-derived rocks to depth. It is noteworthy to keep in mind that the discussion provided in the present sub-section is valid only if the Onverwacht Group is equivalent to the archean crust that produced the different generations of TTGs cropping out in the Barberton area.

The silica-rich rocks displaying a δ^{18}O of ~11-13‰ that explain the O and Si isotopic composition of the oldest TTGs (>3.23 Ga) (**Figure 5-13**) corresponds to silicified lavas and cherts from the base of the Onverwacht Group that were emplaced before 3.46 Ga ago, as parts of the Theespruit and Komati formations (**Figure 5-13**). On the other hand, only silicified lavas and cherts that are younger than 3.46 Ga in the Onverwacht Group (i.e. belonging to the Hooggenoeg, Kromberg and Mendon formations) have a δ^{18}O that is high enough (~15‰) to explain the relatively high δ^{18}O values of some post-3.23 Ga TTG magmas. This suggests that, in addition to the old silicified lavas reworked in the source zone of pre-3.23 Ga TTGs, younger silica-rich rocks provided an additional contribution to the source zone of the post-3.23 Ga TTGs, resulting in a wider range of δ^{18}O values.

A critical look at the continuous chrono-stratigraphic evolution of O and Si isotope compositions in the Onverwacht Group (**Figure 5-12**) suggests that, shortly before the the different episodes of TTG melting (i.e. 3.45-3.46 and 3.28-3.22 Ga), silicified lavas and cherts that contributed to the TTG source zone were located at relatively shallow levels (<10 km) in the stratigraphic section. This discards melting within or at the base of an over-thickened crust as responsible for the generation of TTG melts in the Barberton (Bédard, 2006; Johnson et al., 2017; Smithies et al., 2009, 2019). In fact, at P-T conditions expected at less than 10 km of thickness, the volcano-sedimentary successions could not have undergone partial melting yet. Some researchers have suggested that density-driven processes such as crustal overturn and sagduction/delamination were prominent on the early Earth and could explain the reworking of seafloor-derived rocks in the source zone of TTGs (Van Kranendonk, 2011; Van Kranendonk et al., 2009, 2014; Sizova et al., 2015). However, thermodynamic models suggested that delamination processes affected only the lower crust, which means that the topmost 5 km cannot be recycled by these processes (Sizova et al., 2015). In addition, overturn is unlikely to have occasioned the formation of the Barberton TTGs because their Si and O isotopic compositions do not evidence an initial formation of TTG melts at the base of the crust before the recycling of silica-rich rocks derived from the seafloor. Thus, the inferred stratigraphic position of reworked silicified lavas and cherts is inconsistent with both melting of a mafic crust in intra-crustal or infra-crustal settings and melting events due to density-driven processes.

After excluding the two competing scenarios, we tentatively suggest that subduction-like processes (Clemens et al., 2006; Moyen and Stevens, 2006; Martin et al., 2014) are best indicated to explain the transportation of silicified lavas and cherts towards the source region of the Barberton TTGs (**Figure 5-14**). Stratigraphically-shallow volcano-sedimentary formations could have been transported towards the deep sources of TTGs by horizontal movements followed by plunging ones like in modern arc zones (Bindeman et al., 2005; Clemens et al., 2006; Van Hunen and Moyen, 2012). The observation that the youngest 3.24 to 3.22 Ga old TTG melts covered a large range of $\delta^{18}O$ values is consistent with a reworking of silicified lavas and cherts covering a wider array of $\delta^{18}O$ (from <12 to >15‰) in their sources (**Figure 5-14**). It is possible that silicified lavas and cherts that are younger than 3.46 Ga with a $\delta^{18}O$ of more than ~15‰ started being reworked in the TTG source region around 3.24 Ga ago but this does not necessarily mean that plate tectonics started at this date (e.g. Wang et al., 2022). Considering the episodic nature of TTG magmatism in the Barberton granitoid-greenstone terrain (see different generations of plutons in **Figure 5-2**), we speculate that palaeoarchean subduction-like processes that recycled silicified lavas and cherts were episodic, in contrast to the long-lived Phanerozoic subductions. Slab-breaking as proposed by Nebel et al. (2018) is a good way to explain the interruption of incipient subductions that led to periodic TTG melting. More importantly, the Si and O isotopic composition is not consistent with a change from stagnant lid to plate tectonic scenario Barberton Granitoid-Greenstone Terrain around 3.2 Ga ago as proposed by Wang et al., (2022).

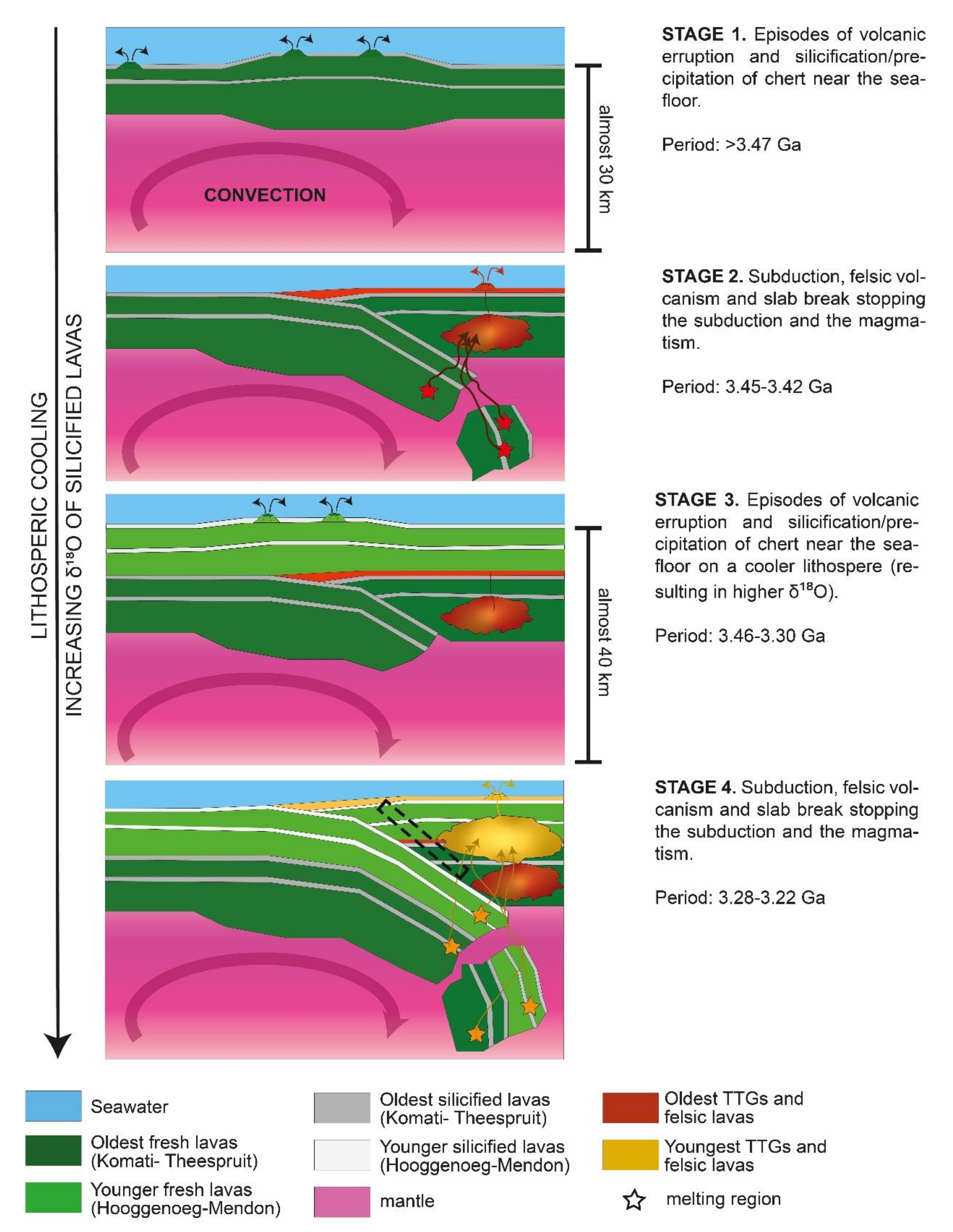

Figure 5-14. Cartoons explaining the evolution of $\delta^{18}O$ in the Barberton TTG melts by incorporation of different generations of silicified lavas (and cherts) in their source zone. Although no cartoon is at absolute scale, a relative scale is given. Note also that the thickness of silicified leva levels are overestimated on this Figure for illustration purposes. The dashed box in the last cartoon represents the geological formations that are still accessible in the Onverwacht Group.

5.4. Outlook on stable isotope compositions in TTGs as a tool for constraining archean geodynamic processes

Since the study of Wilde et al. (2001), who argued that the O isotope composition of the 4.36 Ga old Jack-Hills zircons traces the reworking of supra-crustal rocks derived from the seafloor in Hadean granitoid source zones, multiple stable isotope systems (e.g. O, Si, B, Li and Ca) have been analysed in archean granitoids (e.g. Cavosie et al., 2005; Reimink et al., 2016; Vezinet et al., 2018; André et al., 2019; Smit et al., 2019; Deng et al., 2019; Wang et al., 2020; Antonelli et al., 2021; Smithies et al., 2021; Wang et al., 2022; Lei et al., 2023). The main purpose of these analyses has been to constrain the nature of geodynamic processes that led to the formation of primitive continents on Earth. This approach of studying archean geodynamic processes stemmed from the struggle of field observations, elemental geochemistry and radiogenic isotope analyses to discriminate archean granitoids that were generated in subduction zones from granitoids formed in other contexts including intra-crustal and infra-crustal settings or due to delamination processes (Martin, 1993; Moyen and Stevens, 2006; Smithies et al., 2009; Bédard, 2018; Sotiriou et al., 2022). Here, I comment on the results of recent stable isotope studies and elaborate an opinion on factors that have hindered an unambiguous determination of archean geodynamic processes using stable isotope analyses in archean TTGs, including (1) uncertainty on the stable isotope composition of primitive TTG melts, (2) uncertainty on the nature of reworked material, and (3) difficulty to discriminate passive burial by accumulation of younger lavas from modern-like subduction.

5.4.1. Uncertainty on the stable isotope composition of primitive TTG melt

The difficulty to establish a link between measured isotopic composition of bulk-rock samples and minerals (e.g. zircon) and the actual isotopic composition of the primitive TTG melt is commonly overlooked but not necessarily insignificant. Bulk-rock compositions can represent modified melts due to petrogenetic processes such as fractional crystallisation, magma mixing or separation (e.g. Doucet et al., 2020; Laurent et al., 2020), or due to late-stage processes such as metamorphism and weathering (e.g. Faure and Harris, 1991). Isotopic analyses in isolated minerals are also not fully reliable as they depend on the composition of a possibly evolved melt that crystallised the considered mineral (e.g. Reimink et al., 2016), and on empirical calibrations allowing to reconstruct the isotopic composition of the primitive melt based on mineral compositions (e.g. Guitreau et al., 2022). For example, backed by previous studies of O isotope behaviours in magmatic systems, we have pointed that overlooking zircon-melt O isotope fractionation (up to -1.5‰) was at the source of an erroneous consideration of zircons with a $\delta^{18}O$ value of 5.6 ± 0.3‰ as reflecting fresh mantle-derived lavas at the source of TTGs (e.g. ; Wang et al., 2022). While an efficient use of stable isotope data requires to know the potential effects of syn- and post-magmatic processes on the measured values, these effects are generally overlooked for isotopic systems that were not very well constrained empirically (e.g. B and Li). Thus, proposed isotopic compositions of TTG melts for these systems (e.g. B and Li) could be revised in future studies if magmatic fractionations are identified.

5.4.2. Uncertainty on the nature of reworked material

Incapacity to determine unambiguously the reworked seafloor-derived materials based on isotopic compositions measured in primitive TTG melts can generate important errors in proposed models of archean geodynamic settings. For instance, Antonelli et al. (2021) ascribed low $\delta^{44}Ca$ values that they measured in 4.0-28 Ga old TTGs to subduction of shales and carbonates derived from the seafloor; but this interpretation is inconsistent with the scarcity of carbonate platforms in the geological record before the Mesoarchean Era, and the low- $\delta^{44}Ca$ (up to -1‰) of archean carbonates assumed in the study of Antonelli et al. (2021) has not yet been reported for any natural carbonate sample. Another example can be found in the study of Smit et al. (2019) who proposed that archean TTGs melts did not incorporate materials derived from the seafloor because they featured mantle-like signatures in B isotopic compositions, unlike the modern seawater, serpentinites and arc lavas. This consideration of modern altered rocks as analogous to archean counterparts is at odds with the fact that the hydrosphere-crust system probably operated differently during the Archean Eon than on the modern Earth (Bindeman et al., 2018; Albarede et al., 2020). An important insight is also provided by the study of Wang et al. (2020), who coupled B isotope with Li isotope analyses in TTGs and showed that the archean “altered oceanic crust”, that was reworked in some TTGs, could be free of B isotope anomalies, unlike modern serpentinites and seawater. Additionally, a progressive rise of $\delta^{18}O$ between 3.5 and 3.1 Ga ago in zircons from the Coorg Block TTGs in Southern Indian was interpreted to reflect an increase in the $\delta^{18}O$ and in the proportion of shales that were reworked in their source zone over time, with implications for the consolidation of archean continents (Roberts and Santosh, 2018). Contrastingly, in this study, we show that a similar evolution in the O isotope composition of TTG melts over time could arise also from isotopic evolutions of hydrothermally altered rocks derived from the seafloor, without any implication for the composition and proportion of ancient continents.

The few examples of stable isotope studies presented above show that geodynamic models that were based on stable isotope compositions of archean TTGs strongly depend on the proxies that were considered to explain measured isotopic compositions. Multi-isotopic characterisations of recycling signatures identified in archean TTGs, when possible coupled with analyses of natural samples of considered proxies (e.g. the silica-rich rocks analysed in this thesis), could improve our understanding of proposed geodynamic processes, as performed in this study for O and Si isotopes.

5.4.3. Can we really discriminate passive burial from transport in geochemical signatures of recycling?

Finally, distinguishing subduction from burial processes using stable isotope data alone is probably impossible (Vezinet et al., 2018; Lei et al., 2023). This distinction could however be enabled by coupling the stable isotope data with geological evidence, that must therefore have been preserved. As explored in this study, the imperative of a constrained geological context may require to postulate that geological formations located in the vicinities of analysed TTGs were equivalent in composition and in chrono-stratigraphic succession to the reworked counterparts (**Figure 5-12**). However, only a few archean terrains preserve complete supracrustal sequences and different generations of TTGs that could help constraining the nature and stratigraphic position of recycled materials for geodynamic interpretations. The stable isotope composition of isolated granitoids or detrital minerals can qualitatively identify the recycling of silicified lavas but cannot distinguish unambiguously archean subductions and burial processes, unless chronologically related to a unique event at the surface of the Earth such as the Great Oxygenation Event (~2.5 Ga) (e.g. Moreira et al., 2023). In fact, Moreira et al.(2023) demonstrated that oxidised rocks from the seafloor were rapidly subducted towards the source zone of TTGs soon after the Great Oxygenation Event, supporting that plate tectonics was already operational then. In most cases, however, a firm demonstration that supracrustal rocks accessible at the surface of the Earth are chrono-stratigraphically analogous to similar rocks reworked in the source zone of specific TTGs remains complicated. A definitive understanding of processes that transported seafloor-derived rocks towards the source zone of TTG melts may simply be out of reach for most stable isotopic systems.

5.5. Summary of this part

This part of the thesis was based on a compilation of O and Si isotopic compositions of 3.45-3.22 Ga TTG bodies cropping out in the Barberton granitoid-greenstone terrain, and on a thermodynamic model that simulates the melting of an average silicified and non-silicified lava from the Onverwacht Group. The results of this study can be summarised as follows:

- The isotopic O and Si isotopic composition of TTG melts calculated based on average zircons compositions is consistent with average bulk-rock $\delta^{18}O$ and $\delta^{30}Si$ for each TTG body. Numerical modelling reveals also that fractional crystallisation did not considerably change the O isotope composition of bulk-rock TTG samples from the original composition of TTG melts. The large dispersions observed in Si and O isotopic compositions of TTG zircons are partly ascribed to heterogeneity at the scale of the pluton due to an heterogeneous source zone.
- The isotopic compositions of O and Si were coupled in the primary TTG melt, unlike previously proposed by Lei et al. (2023), and are collectively consistent with the reworking of seafloor-derived silicified lavas in the source zone of the Barberton TTGs. The proportion of melt derived from silicified lavas is estimated to 10-25 vol.%, corresponding to the presence of 5-12 vol.% of silicified lavas in the source zone of the Barberton granitoids.
- Estimated O and Si isotopic compositions of reworked silica-rich rocks are associated with measured isotopic compositions of natural rocks from the Onverwacht Group to estimate the burial depth of the reworked rocks in the palaoarchean submarine crust. These results suggest that the reworked seafloor-derived rocks were not buried passively to depths exceeding 10 km before their reworking. Therefore, a subduction(-like) process represents the only way to explain the reworking of seafloor-derived silica-rich rocks in the source zone of the Barberton TTGs.

5.6. Supplementary Files

The Supplementary Table cited in this part of the thesis is available in Appendices (Appendix C).

Part VI.

Conclusions and perspectives

6.1. Major results and their implications

This doctoral research was aimed (1) to constrain the properties (composition and temperature) of palaeoarchean hydrothermal fluids and seawater based on the composition of silicified lavas and cherts (including silicified clastic sediments and seawater-precipitated cherts) from the Barberton greenstone belt, and (2) to improve our understanding of processes that recycled silica-rich rocks from the seafloor to the source zone of the Barberton TTGs. The thesis is subdivided in three interconnected studies, and the main results of each of these studies are summarised below with their implications.

Firstly, in **Part III** of the thesis, different mineralogical and geochemical tools collectively distinguish the mineralogical and geochemical effects of regional metamorphism and late-stage circulations of oxidised fluids from effects of hydrothermal silicification near the palaeoarchean seafloor. Chlorite chemistry, Raman spectroscopy of carbonaceous materials and O isotope fractionation in quartz-carbonate assemblages provide an equilibrium temperature of more than 280 °C in the analysed silicified lavas and cherts, which is interpreted as the temperature of regional metamorphism. In absence of textural evidence of important fluid circulation at metamorphic stage, we consider that this regional metamorphism did not significantly affect the bulk-rock composition of the studied silica-rich rocks. In addition, the mobilisation of REE during late-stage events is constrained by La-Ce and Sm-Nd isotope systematics and we demonstrate that positive or negative Ce anomalies observed in a few samples are due to circulations of post-archean oxidised fluids. In silicified lavas that were not affected by this late-stage alteration, an increase in K, Ba, Cs, LREE, Pb and U concentration, and a decrease of Mg, Fe and Na concentration are associated with hydrothermal silicification near the seafloor. The uptake of alkalis is interpreted to show that silicification occurred at low temperature (< 150 °C), which is confirmed by the lowest equilibrium temperature of ~125 °C calculated from O isotope fractionation in a particularly preserved quartz-carbonate assemblage. In addition, positive and negative Eu anomalies observed in the silicified lavas and cherts suggest that the silicifying hydrothermal fluid were generally free of positive Eu anomaly, reflecting fluid-rock interaction at less than 250 °C. Finally, REE and HFSE concentrations in the analysed silicified lavas and secondary cherts are considerably higher than expected in seawater-precipitated sediments and generally remain affiliated to the trace element composition of fresh protoliths and free of seawater-like features such as elevated Y/Ho ratios. Therefore, we support that hydrothermal silicification could not generate seawater-like trace element properties in silicified lavas, and consider that trace REE+Y patterns can successfully identify seawater-precipitated cherts of unique paleo-environmental significance.

Secondly, in **Part IV**, analyses of triple O and Si isotopic compositions of pervasively silicified lavas, silicified clastic sediments (or secondary cherts) and seawater-precipitated cherts from the Onverwacht Group provide new constrains on (1) the O isotope composition of silicifying hydrothermal fluids, (2) the post-depositional evolution of seawater-precipitated cherts and (3) the thermal evolution of the Onverwacht Group. Relative to seawater-precipitated cherts, lower $\delta^{18}O$ values and higher $\Delta'^{17}O$ values are observed in pervasively silicified lavas and clastic sediments, and these values reveal a negative $\delta^{18}O$ for the silicifying hydrothermal fluids. A simplified model of water-rock interaction supports that these hydrothermal fluids must have originated from a palaeoarchean seawater that was lower in $\delta^{18}O$ value than modern oceans. The triple O isotope compositions of seawater-precipitated cherts shows that they were considerably modified by the circulation of hydrothermal fluids and may have lost their capacity to reconstruct the composition and temperature of the palaeoarchean seawater. Additionally, in the analysed silicified lavas and sediment, we obtained positive $\delta^{30}Si$ values that are similar to those previously reported for seawater-precipitated cherts in the Onverwacht Group. Therefore, unlike commonly believed, a positive $\delta^{30}Si$ value is not a guarantee for a pure orthochemical origin for a chert and a negative $\delta^{30}Si$ should not be regarded as diagnostic for silica precipitation from hydrothermal fluids. Instead, we suggest that the palaeoarchean seawater and hydrothermal fluids may have featured significantly similar $\delta^{30}Si$ values, inferring that hydrothermal fluids possibly represented the major source of aqueous Si in palaeoarchean oceans. Moreover, we observe a gradual increase in the $\delta^{18}O$ values of silicified lavas and cherts upwards the Onverwacht Group and ascribe this evolution to progressive changes in the regional geothermal gradient, probably due to crustal thickening. By constraining the isotopic composition of hydrothermal silica, this study exposes the importance of previously excluded silicified lavas and clastic sediments in solving long-lived problems on the Palaeo-environmental significance of the commonly analysed seawater-precipitated cherts.

Finally, in **Part V**, the properties of silicified lavas and cherts recycled towards the source zone of different generations of TTG melts and geodynamic processes responsible for their recycling are discussed based on O and Si isotopic compositions coupled with thermodynamic modelling results. The silicified lavas reworked in the source zone of the Barberton TTGs are proposed to have been equivalent in composition and stratigraphic position to silicified lavas and cherts preserved in the Onverwacht Group, and the isotopic change observed in the

Barberton TTGs over time is ascribed to a progressive recycling of younger units towards the source zone of TTG melts. After inferences on the possible stratigraphic position of the lavas and cherts reworked in the source zone of the Barberton TTGs, subduction-like processes are proposed to explain the recycling of near-seafloor lithologies towards the source zone of the TTGs. The vertical accumulation of mafic lavas in the Onverwacht Group and the periodicity of TTG formation further suggest that such the proposed subductions were sporadic, unlike modern subductions that are almost continuous in time. We further speculate that slab breakoff was common during the Palaeoarchean Era due to a hotter crustal geotherm compared to the modern one, which precluded continued subductions.

Maybe the most important scientific contribution of this study is the demonstration that variations in the isotopic composition of palaeoarchean seafloor rocks over time must be considered in the use of stable isotope compositions of TTGs to characterise palaeoarchean geodynamic processes. Isotopic variations in granitic magmas that were previously interpreted to imply important geodynamic changes could simply reflect a change in the nature of the recycled material over time within the same geodynamic framework. This invites to re-think the way we interpret geochemical signatures of recycled seafloor lithologies observed in TTGs in terms of their geodynamic implication. Understanding the evolution of isotopic compositions in seafloor rocks recycled towards the deep Earth over time appears to be a key condition for the acquisition of realistic geodynamic models for the archean world. The future of stable isotope geochemistry as a tool for studying archean geodynamic processes probably resides in intimate interactions between low-temperature and high-temperature geochemical and petrological studies that were traditionally considered as different sub-disciplines of Earth sciences. In this thesis, the conjunction of low-temperature and high-temperature geochemistry of O and Si isotopes allows providing new insights into the geodynamic evolution of the Barberton Granitoid-Greenstone Terrain and its possible implications for archean dynamics.

6.2. Perspectives

To constrain the budget of different major elements in archean oceans, the elemental exchanges between the silicifying hydrothermal fluids and near-seafloor rocks constrained in this study could be integrated in a broader study comprising also elemental mobilisations due to the formation of archean paleo-sols and to high-temperature hydrothermal systems. Such a general study is needed to understand variations that may have operated in seawater composition since the Archean Eon but it is too ambitious study for being achieved within the next few months, or even years. For perspectives that may be addressed in a continued investigation of our samples on a relatively shorter run, I have spotted three simple but very important questions.

Firstly, the origin of the Si and alkalis that were dissolved in the silicifying hydrothermal fluids and subsequently sequestrated by the analysed silicified lavas and cherts remains unconstrained. This thesis has supported that these elements originated from deeper within the crust from reactions between the seawater-derived fluids and the mafic to ultramafic crust, but this hypothesis remains unverified. Part of these elements (especially K which is rare in mafic rocks) could also have originated from eroded continents. Deep crustal rocks representing the potential region where the silicifying lavas scavenged their Si and alkali content could be studied to quantify the temperature of the hydrothermal fluids in the deep crust and understand their possible compositional evolution during ascent towards the upper zones where silica precipitated. As suggested by Hoffman et al. (1986), serpentinised lavas occurring at the base of some geological formations such as the Komati and the Weltevreden formations are good candidates for deep crustal rocks altered by the descending flux of hydrothermal fluids. This suggestion is consistent with the results of water-rock interaction run in **Part IV** of this thesis that reproduces the formation of serpentine due to fluid-rock interaction at ~200 °C. We collected, in addition to the samples investigated in this study, serpentinite specimens from the Weltevreden formation that we did not have enough time to analyse in detail through the last three years. A detailed mineralogical and geochemical study, including in-situ analysis of O isotope compositions of carbonates and serpentine, could help to evaluate the possibility that the serpentinites provided the amount of Si dissolved in the hydrothermal silicifying fluids.

Secondly, the O isotope composition of zircons that may have crystallised from TTG melts produced by melting of fresh basalts is still to be determined, since zircon grains displaying a mantle-like $\delta^{18}O$ of 5.6±0.3‰ could have formed from magmas that had incorporated seafloor-derived silica-rich rocks. This argument urges to determine the actual O isotope composition of zircons precipitated from a TTG melt generated by melting of a pure mantle-derived basaltic lava. In my opinion, studies of Moreira et al. (2020) and Smithies et al. (2021) provided valuable clues in solving this question as they observed that zircons of the earliest TTG in most cratons featured 4.5-5‰ in $\delta^{18}O$. Although these values are generally interpreted to represent the contribution of a high-temperature altered deep crustal component, the $\delta^{18}O$ values of 4.5-5‰ (Moreira et al., 2020; Smithies et al., 2021) could reflect that of zircon precipitating from felsic melts originated from pure, non-altered lavas. In fact, this range of $\delta^{18}O$ values matches perfectly a $\delta^{18}O$ of ~4.8‰ that can be calculated empirically for zircons from a felsic magma that formed by melting of a non-altered felsic melt, even if we acknowledge that fractional crystallisation could lead to variations of ~0.5‰ in the residual melt, and therefore in its zircons. In this study, we obtained an average $\delta^{18}O$ value of 4.8 in sample SK-SLZ01, which could represent a portion of the Stolzburg pluton that was fortuitously isolated from the contribution of melts derived from silicified lavas or cherts. To test this hypothesis, we may measure the Si isotopic compositions of our zircons by MC-ICPMS to check if, as expected, only SK-SLZ01 zircons will not display high $\delta^{30}Si$ value documenting mixing between melts issued by silicified lavas and melts originated from fresh basalts.

Thirdly, the seafloor-derived component of TTG source zones has been suggested to feature more radiogenic Hf isotope ratios compared to non-silicified lavas, explaining part of the range of Hf isotope composition in TTGs (Vezinet et al., 2019). However, so far, only a few studies have explored the Hf isotope composition of silica-rich rocks derived from the palaeoarchean seafloor (e.g. Garçon et al., 2017; Viehmann et al., 2020). We could complete the radiogenic Nd and Ce isotope dataset reported in this thesis with Hf isotope analyses to understand the potential modification of ^{176}Lu-^{176}Hf during the silicification of palaeoarchean near-seafloor rocks. This would also provide new clues for the development of a seawater array in the εNd versus εHf environment (Vervoort et al., 2011). While thinking of this perspective, I had a first look at the Lu/Hf elemental ratio of the studied samples (data give in **Table 3-1**). **Figure 6-1** demonstrates that this ratio could be modified by the silicification process as also noticed by (André et al., 2019), but unlike (André et al., 2019) who observed that the Lu/Hf ratio decreases with silicification, our data feature a component of increasing Lu/Hf ratio with increasing SiO_2. Analyses of Lu and Hf isotopic compositions in the studied samples would (1) improve our capacity to trace the recycling of seafloor-derived silicified rocks, and (2) complete the understanding the origin of fractionated Hf isotope composition in archean oceans that was mainly ascribed to selective erosion of continents (e.g. Viehmann et al., 2018).

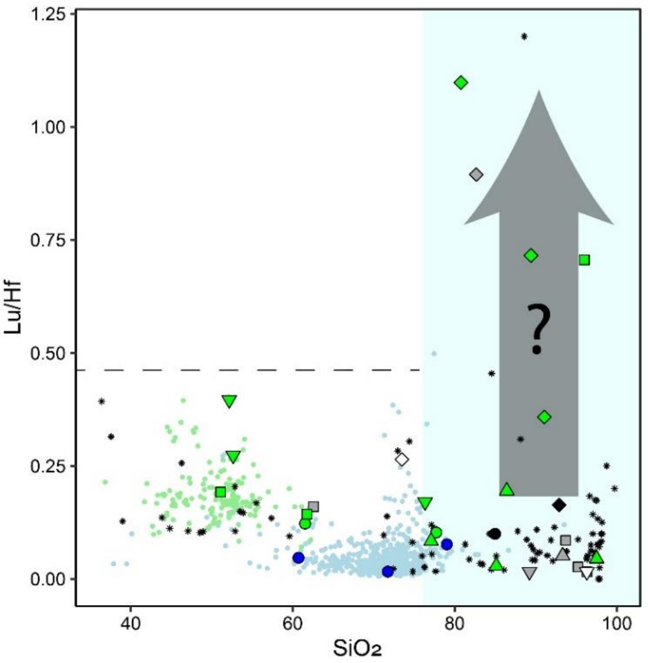

Figure 6-1. Evidence of possible modification of Lu/Hf ratio in the silicified lavas. Symbols are like in Figure 3-12 and a compilation of mafic (small green dots) lavas and granitoids (small blue dots) is also shown. The increase in Lu/Hf ratio (grey arrow) associated with silicification opens to new questions on the origin of the seawater Lu-Hf isotope composition previously constrained for the Archean seawater.

Résumé étendu de la thèse en Français

Cette partie est une synthèse générale de la thèse en langue Française. Elle est adressée aux potentiels lecteurs francophones tel qu'exigé par l'Ecole Doctorale des Sciences Fondamentales de l'UCA pour les thèses rédigées en Anglais au sein de cette institution.

Introduction générale

Parce que la Terre reste la seule planète où l'on connaisse des formes de vie complexes, plusieurs études ont cherché à comprendre les conditions environnementales ayant conduit à l'émergence de la vie sur Terre. La primitive vie ayant évolué dans des conditions sous-marines, les roches d'âge paléoarchéen (3.6-3.2 Ga) ayant résidé au niveau du plancher océanique peuvent avoir enregistré dans leur composition chimique et minéralogique les propriétés des fluides supergènes tels que l'eau de mer et les fluides hydrothermaux avec lesquelles les cellules primitives ont interagi (Perry, 1967; Knauth and Lowe, 1978; Lowe and Byerly, 2020). Des études minéralogiques et géochimiques menées sur ces roches du plancher océanique Paléarchéennes sont capables de reconstruire la composition et la température de l'eau de mer et des fluides hydrothermaux qui ont vu des formes primitives de vie apparaitre sur Terre. Ces roches se retrouvent au sein des ceintures de roches vertes telles que la ceinture de Barberton étudiée dans cette thèse.

Des niveaux de laves silicifiées et cherts, incluant d'une part des sédiments clastiques silicifiés et d'autre part des sédiments précipités chimiquement de l'eau de mer, ont permis de reconstituer les propriétés de l'eau de mer et des fluides hydrothermaux archéens (Robert and Chaussidon, 2006; Jaffrés et al., 2007; Hofmann and Harris, 2008;Abraham et al., 2011). Ces roches sont aussi essentielles dans l'étude de l'origine de la vie parce qu'elles contiennent souvent des traces de matière organique considérées comme les traces de la vie primitive (Javaux and Marshall, 2005). Alors que la circulation des fluides hydrothermaux a favorisé la silicification des laves et sédiments clastiques déposés dans la partie supérieure de la croute sous-marine archéenne, les cherts précipités de l'eau de mer sont généralement associés à la précipitation de la silice saturée dans l'eau de mer archéenne. Ainsi, la plupart des travaux géochimiques antérieurs visant à reconstruire la composition et la température de l'eau de mer se sont focalisés sur l'analyse des cherts. Toutefois, les compositions et températures reconstituées à partir de ces études de cherts sont controversés car les cherts ont subi une histoire post-dépôt complexe qui a vraisemblablement affecté leur enregistrement géochimique. Ainsi, l'étude de l'histoire post-dépôt des cherts permettra de mieux contraindre les interactions fluide-roche archéennes pour une meilleure caractérisation des environnements dans lesquels la vie est apparue. Dans cette thèse, nous explorons la géochimie des laves et sédiments clastiques silicifiés grâce à la circulation des fluides hydrothermaux, qui ont été jusqu'à présent moins étudiés que les cherts précipités de l'eau de mer, afin d'améliorer notre compréhension de l'enregistrement des propriétés des fluides hydrothermaux et de l'eau de mer dans l'ensemble des roches riches en silice du plancher océanique archéen.

Cependant, des processus tardifs tels que le métamorphisme régional et l'altération supergène peuvent modifier l'enregistrement minéralogique et géochimique des propriétés des fluides au sein des roches d'âge Paléoarchéennes (Lowe and Byerly, 2007; Marin-Carbonne et al., 2011). Ceci constitue l'un des problèmes majeurs auxquels il faut faire face dans l'étude de la composition minéralogique et géochimique des roches Archéennes. Des travaux récents ont montré que ces processus tardifs peuvent altérer la plupart des signatures minéralogiques et géochimiques que nous utilisons couramment pour déterminer la température de l'eau de mer et celle des fluides hydrothermaux durant l'Archéen (Bonnand et al., 2020; Liljestrand et al., 2020). Ainsi, il est important de comprendre les effets potentiels des processus tardifs (métamorphisme et altération météoritique) sur la minéralogie et la géochimique des roches riches en silice venues du plancher océanique archéen avant d'utiliser ces compositions pour contraindre les propriétés des fluides.

Des études géochimiques ont également montré que des roches silicifiées venues du plancher océanique étaient présentes dans la zone source des granitoïdes ou méta-granitoïdes de la série tonalite-trondhjemite-granodiorite (TTG) dominant les vestiges des continents primitifs (André et al., 2019; Deng et al., 2019). Ceci permet d'étudier les circonstances qui ont conduit à l'apparition de ces premiers continents. La présence des continents a joué un rôle essentiel dans l'évolution de la vie primitive en apportant les nutriments nécessaires au métabolisme des premières cellules (Martin et al., 2006; Flament et al., 2008). De ce fait, comprendre les processus qui ont généré ces granitoïdes est donc essentiel dans l'étude de l'origine de la vie sur Terre. Cependant, le cadre géodynamique dans lequel les TTGs se sont formés est controversé depuis plus d'un demi-siècle. On distingue des modèles proposant la fusion d'une plaque lithosphérique enfouie en zone de subduction et divers autres modèles suggérant des fusions intra-plaques, infra-plaques ou encore dues à des processus de délamination sur une terre archéenne dépourvue de tectonique de plaques (Cawood et al., 2018; Nebel et al., 2018). Alors que ces processus auraient pu coexister sur Terre durant la période Paléo-archéenne, il reste difficile de distinguer les TTGs formés dans un contexte similaire à la subduction moderne des TTGs formés dans d'autres contextes géodynamiques (Lei et al., 2023). Cette distinction est importante parce qu'elle permettrait de comprendre la manière dont la dynamique terrestre a évolué dans le temps et à appréhender son influence sur l'environnement et le développement du vivant. Les traces de recyclage des laves silicifiées et cherts venues du plancher océanique, qui ont été identifiées dans la composition des TTGs, constituent un outil important pouvant permettre de dissocier les différents contextes géodynamiques potentiellement responsables de la formation des TTGs. Pour y parvenir, il suffirait de discriminer la subduction, d'une part, d'un enfouissement passif dû à l'accumulation des laves et sédiments plus jeunes au niveau du plancher océanique, d'autre part.

Afin de contraindre les propriétés des fluides hydrothermaux responsables de la silicification au niveau du plancher océanique et de l'eau de mer à l'Archéen, cette thèse a étudié différents aspects minéralogiques et géochimiques des laves silicifiés et cherts affleurant au sein des roches archéennes de la région de Barberton. Cette thèse a aussi analysé la composition des TTGs pour comprendre les processus qui recyclaient des roches venues du plancher océaniques vers leur zone source. Les uatre objectifs majeurs suivants ont été poursuivis dans cette étude :

- Différencier les transformations minéralogiques et géochimiques issues des interactions fluides-plancher océaniques paléoarchéennes des effets des processus tardifs tels que l métamorphisme et l'altération météorique ;
- Utiliser les échantillons les mieux préservés de laves silicifiés et cherts pour déterminer les propriétés géochimiques et la température des fluides hydrothermaux responsables de la silicification au niveau du plancher océanique archéen ;
- Evaluer le potentiel des cherts pour reconstruire précisément la composition et la température de l'eau de mer pour des reconstitutions paléo-environnementales ; et enfin,
- Coupler la composition des laves silicifiées, cherts et TTGs pour contraindre le cadre géodynamique qui opérait dans la région de Barberton durant la période Paléoarchéenne.

Après une revue de la littérature essentielle à la compréhension des discussions conduites dans la thèse (**Partie II**), le reste de cette thèse comprend trois parties. La **Partie III** de la thèse constitue une première étude actuellement en relecture à *Geochimica et Cosmochimica Acta*. Ce manuscript présente des nouvelles analyses pétrographiques, géochimiques et thermométriques visant à différencier les signatures des processus tardifs, notamment du métamorphisme et de l'altération supergène, des effets des processus précoces opérés au niveau du plancher océanique tels que l'altération (silicification) hydrothermale. Ensuite, la **Partie IV** de la thèse comporte une deuxième étude qui est en cours de révision pour publication à *Chemical Geology* et qui contraint la composition des fluides hydrothermaux ayant interagi avec le plancher océanique préservé dans la ceinture de roches vertes de la région de Barberton. La **Partie V** présente des résultats d'un travail en cours visant à déterminer le contexte géodynamique de formation des TTG de la région de Barberton grâce à une réinterprétation des compositions isotopiques de l'O et du Si au sein de ces roches, couplée avec des résultats de modélisation thermodynamique de la fusion partielle des laves fraiches et silicifiées. Enfin, les conclusions majeures et perspectives de la thèse sont présentées dans la **Partie IV**. Les points suivants synthétisent chacune des principales parties de la thèse.

Présentation du premier article (Partie III)

« Pétrographie, géochimie et thermométrie des laves silicifiées et cherts de la ceinture des roches vertes de Barberton : Distinguer l'altération près du plancher océanique des modification tardives »

Contexte, matériels et méthodes utilisées dans la Partie III

L'étude du système hydrosphère-croûte actuel a révélé que la circulation des fluides hydrothermaux dérivés de l'eau de mer au sein de la croute océanique contribue à la composition l'eau de mer moderne. L'interaction entre la croûte océanique et les fluides hydrothermaux génère une croûte océanique altérée dont la minéralogie et la géochimie sont associées à la nature des fluides avec lesquelles elle a interagi à différentes températures et pressions. Ainsi, l'étude des roches archéennes altérées par la circulation des fluides hydrothermaux au sein de la croûte océanique peut reconstruite les propriétés des fluides similaires durant l'Archéen. Les laves et sédiments clastiques silicifiés que l'on retrouvés dans la plupart des terrains archéennes, par exemple, sont utilisables pour cette fin parce qu'ils présentent des évidences texturales et pétrographiques d'une origine hydrothermale (brèches et veines par exemple). Cependant, la plupart des laves et sédiments silicifiés d'âge Archéen ont été affectés par des processus tardifs incluant le métamorphisme et l'interaction avec des fluides météoritiques lors de leur mise à l'affleurement. Ces processus peuvent avoir effacé, au moins en partie, les signatures hydrothermales des roches silicifiées. Ainsi, il convient de contraindre l'impact des processus tardifs (métamorphisme et altération météoritique) sur la minéralogie et la géochimie des roches silicifiées archéennes avant de les utiliser pour étudier la nature des fluides archéennes.

Dans ce manuscript, j'ai étudié différents aspects de la pétrographie et de la géochimie des laves et cherts (essentiellement représentés par des sédiments clastiques) afin de (1) distinguer les effets de l'altération hydrothermale sur le plancher océanique Archéen des effets des processus tardifs, et (2) de contraindre certaines propriétés physico-chimiques (e.g. la température) des fluides hydrothermales qui ont causé la silicification près du plancher océanique archéen.

Stratigraphiquement, la ceinture des roches vertes de Barberton est constituée de trois Groupes géologiques: d'une part le Groupe d'Onverwacht (3.5-3.3 Ga), et d'autre part les Groupes de Fig Tree et Moodies (3.3-3.2 Ga) (**Figure 3-1**) (Byerly et al., 2019). Cette étude a porté essentiellement sur le Groupe d'Onverwacht qui représente une croute juvénile sous-marine Paléoarchéenne constituée essentiellement des laves ultrabasiques à basiques, avec des intercalations sédimentaires mineures et de rares niveaux de laves felsiques. Le Groupe d'Onverwacht est subdivisé en six Formations géologiques principales qui sont à leur tour subdivisés en différents membres, et chaque membre se compose d'une ou plusieurs coulées de laves surplombées par une couche sédimentaire. Les sédiments d'Onverwacht ainsi que les sommets de la plupart de coulées de laves sont généralement silicifiées, si bien que la plupart des sédiments apparaissent actuellement comme des cherts secondaires (ou non précipités directement de l'eau de mer) (Hofmann and Harris, 2008; Abraham et al., 2011). Ce sont ces laves et sédiments silicifiées (ou cherts secondaires) d'Onverwacht qui ont été étudiés dans cette **Partie III** de la thèse.

Au cours d'une campagne de terrain dans la ceinture des roches vertes de Barberton, nous avons collecté des échantillons de laves silicifiées et sédiments silicifiés ou cherts de différents âges sur cinq sections stratigraphiques différentes. La première section est issue de la Formation de la Theespruit datée à 3.53 Ga, et comprend des laves silicifiées à la base, suivies des sédiments felsiques silicifiés au sommet. La deuxième section est issue de la Formation de la Komati au niveau du Middle Marker situé à son sommet et datée à 3.47 Ga. Les troisième et quatrième sections appartiennent à la Formation d'Hooggenoeg, et enfin, la cinquième section appartient à la Formation de Mendon. Ces sections ont en commun le fait d'avoir des laves silicifiées à la base et des cherts (sédiments silicifiés) au sommet. Tandis que les quatre dernières sections se trouvent dans une zone où elles ont subi un métamorphisme de faciès schiste vert, la section de la Theespruit a enregistré un métamorphisme de faciès amphibolite. Tel qu'illustré sur la **Figure 3-2** plusieurs échantillons ont été collectés sur le terrain pour cette étude.

Après une préparation de lames minces, poudres et plots en indium pour certains échantillons sélectionnés, trois types d'analyses ont été effectuées :

- Analyses pétrographiques : les observations pétrographiques ont été effectuées avec un microscope polarisant, puis complétées par des séances de microscopie électronique à balayage.
- Analyses thermométriques : ces analyses incluent (1) la cartographie des chlorites, (2) la spectroscopie Raman des matériaux carbonatés, (3) et l'analyse par sonde ionique (SIMS) de la composition isotopique de l'oxygène dans des couples quartz-carbonate, qui ont permis de calculer des températures d'équilibre.
- Analyses géochimiques (roche totale) : celles-ci incluent des mesures de concentration des éléments majeurs par spectrométrie à rayons X, des analyses d'éléments en trace par spectrométrie de masse, la mesure des isotopes du Sm et du Nd au Neptune, et enfin, la mesure des isotopes du Ce au TIMS.

Résultats de la partie III

Les résultats de cette étude sont subdivisés en trois groupes, notamment des résultats pétrographiques, thermométriques et géochimiques.

Sur le plan pétrographique les laves silicifiés se distinguent des cherts et sédiments felsiques partiellement silicifiés par leurs apparences macroscopiques et microscopiques (**Figures 3-3** à **3-7**). Les laves présentent différents degrés de silicification. Les laves les moins silicifiés montrent encore des textures rappelant leur origine magmatique, avec des pseudomorphes de phénocristaux (d'olivine ou pyroxène probablement) remplacés par des assemblages à chlorite et épidote, dans une matrice contenant des oxydes tels que la chromite et les oxydes de fer et de titane. Les laves partiellement silicifiés ont des textures hétérogènes avec des zones riches en quartz et des zones pauvres en quartz. Les zones pauvres en quartz sont dominées par des phyllosilicates tels que des micas et chlorites, et aussi par des oxydes. Enfin, les laves complétement silicifiées sont dominées par une matrice riche en quartz et à l'échelle microscopique leur texture est identique à celle des cherts, bien qu'elles préservent plus fréquemment des chromites et qu'elles montrent des structures magmatiques sur le terrain. Les cherts sont distingués en cherts gris, cherts noirs et cherts noir-et-blanc sur la base de leur apparence macroscopique sur le terrain. Il faut noter que la matrice de micro-quartz domine tous les types de cherts. Alors que les cherts gris présentent fréquemment des résidus de phases détritiques à l'échelle millimétrique à microscopique témoignant de leur origine clastique, les cherts noirs sont généralement dépourvus de ces évidences de résidus détritiques. De plus, les cherts noirs doivent leur couleur à des matériaux carbonatés, des oxydes et des sulfures plus abondants, tandis que les cherts gris contiennent plutôt plus de phyllosilicates. Les cherts noir-et-blanc, enfin, sont faits d'une alternance de lits blanchâtres et des lits noirs à des échelles métriques à pluri-centimétriques. Bien que les cherts étudiés soient essentiellement des sédiments détritiques silicifiés, nous les avons différenciés des sédiments felsiques de la section de la Theespruit qui ne sont pas assez riches en quartz pour appartenir à la catégorie des cherts. Ces sédiments contiennent plutôt une quantité importante de muscovite et du grenat suite à leur métamorphisme en faciès amphibolite.

Nous avons calculé des températures d'équilibres issues des spectres Raman des matériaux carbonés, de la cartographie d'éléments majeurs dans les chlorites, et du fractionnement des isotopes d'oxygène dans des assemblages quartz-carbonate. Les deux dernières techniques ont été appliquées seulement sur des échantillons de la section du Middle Marker et du Mendon, tandis que la première technique a été opérée pour toutes les autres sections, excepté la section de la Theespruit. La cartographie Raman a donné une température de 347 (± 50) °C pour l'ensemble de la partie supérieure du Groupe d'Onverwacht couvrant une épaisseur stratigraphique continue de ~9 km (**Figure 3-8**). La cartographie des chlorites a aussi donné une température moyenne de 280 (± 50) °C dans les sections du Middle Marker et de Mendon (**Figure 3-9**). Enfin, et de manière plus importante, le fractionnement des isotopes d'oxygène au sein des couples quartz-carbonate a donné un large intervalle de températures d'équilibre, variant entre 125 et 325 °C (**Figures 3-10** et **3-11**). Cette variation suggère que les couples quartz-carbonate équilibrés initialement à relativement basse température auraient subi un événement tardif qui a redistribué leurs isotopes d'oxygène, expliquant une tendance vers des températures d'équilibre de plus en plus élevées.

La silicification est corrélée avec un enrichissement en SiO_2 des compositions des roches totales, s'accompagnant d'une augmentation de la concentration des alcalins tels que K, Rb et Ba (**Figures 3-12** et **3-13**). La silicification s'accompagne aussi d'une nette diminution de la concentration en Ca, Fe, Mg et Na. Les rapports de concentrations d'éléments immobiles tels que Yb, Sc, Th, Ta, Nb, Zr préservent des valeurs caractéristiques des protolithes, et n'auraient donc pas été affectés par la silicification. Les spectres des terres rares suggèrent qu'un léger enrichissement en LREE aurait accompagné le processus de silicification (**Figure 3-14**). De plus, des anomalies positives et négatives en Eu et Ce témoignent de la mobilisation de ces deux éléments. Afin de comprendre l'origine des anomalies en Ce, nous avons analysé le système de longue vie ^{138}La-^{138}Ce d'échantillons présentant ou ne présentant pas d'anomalies en Ce. Malgré les légères augmentations des REE observées, les échantillons ne présentant pas d'anomalie en Ce s'alignent le long des isochrones ^{138}La-^{138}Ce et ^{147}Sm-^{143}Nd théoriques suggérant que les roches analysées auraient une source proche d'un manteau non différencié il y a ~3.4 Ga (**Figure 3-15**). Par contre, les échantillons présentant des anomalies négatives en Ce sont éloignés des isochrones théoriques vers des valeurs ^{138}La/^{142}Ce plus élevés et des valeurs ^{147}Sm/^{144}Nd plus basses.

Discussion et implications majeures de la Partie III

La discussion de cette partie de la thèse s'est amorcée par une évaluation des effets des processus tardifs tels que l'effet de la circulation des fluides météoritiques et du métamorphisme régional. Ensuite, des points plus centrés sur le plancher océanique paléoarchéen tels que la signification des types de cherts observés macroscopiquement, la nature des fluides hydrothermaux responsables de la silicification et l'implication de l'étude sur la discrimination des roches du plancher océanique Archéen sont discutés.

Considérant que le cérium existe sous différentes valences (+III et +IV), et que la mobilisation des terres rares par des fluides oxydés peut fractionner le cérium des autres terres rares (Bonnand et al., 2020), la première partie de la discussion propose que les anomalies de Ce soient dues à la circulation tardive des fluides oxydés. Contrairement aux autres LREE le cerium est immobile en milieu oxydé. La mobilisation différentielles des LREE permet de générer des anomalies positives (pertes de LREE sauf Ce) ou négatives (gain de LREE sauf Ce). Puisqu'aucune corrélation n'apparait entre les anomalies en Ce et la concentration en SiO_2, ou l'enrichissement en alcalins (**Figure 3-16**), nous avons conclu que la silicification ne peut pas être responsable des anomalies en Ce, ce qui concorde avec l'aspect anoxique des océans archéens. De plus, parce que des rapports fluide/roche élevés sont nécessaires pour mobiliser suffisamment de terres rares et générer les anomalies en Ce observées, nous avons proposé que le métamorphisme régional ne peut pas expliquer ce phénomène. Seule la circulation des fluides météoriques, supportée par la présence de veines d'oxydes tardives au sein des roches analysées, semble expliquer les anomalies en Ce observées. En tenant compte du fait que les rapports en isotopes radiogéniques ne sont pas notablement différents entre les échantillons présentant une anomalie en Ce et ceux en dépourvus, nous proposons que les circulations des fluides météoriques ayant généré les anomalies en Ce observées étaient plus jeunes que 1 Ga, et sont peut-être très récentes.

Nous proposons que les températures élevées de 280-360 °C obtenues par cartographie des chlorites et spectroscopie Raman des matériaux carbonatées enregistrent un événement de métamorphisme tardif (Tice et al., 2004; Marin-Carbonne et al., 2011). Vu que cet événement a affecté de manière indifférenciée des roches d'âge variable (3.5-3.3 Ga), nous le rattachons à l'événement tectonique majeur qui a structuré la ceinture de Barberton il y a environ 3.2 Ga. De manière plus importante, une basse température de ~125 °C est obtenue par la mesure des isotopes d'oxygène dans un couple quartz-carbonate suggérant que certaines roches n'ont pas enregistrées les conditions du métamorphisme régional. Cette température est interprétée comme plus proche de la température de silicification en accord avec des températures calculées antérieurement grâce aux inclusions fluides (Farber et al., 2016). L'effet du métamorphisme sur différents thermomètres utilisées pour calculer la température de la silicification démontre qu'il faut prendre des précautions avant d'attacher une température calculée au sein des roches archéennes à l'hydrothermalisme au niveau du plancher océanique.

Connaissant les effets des processus métamorphiques et météoritiques, les données géochimiques ont été utilisées pour discuter l'origine des cherts analysés et caractériser les fluides hydrothermaux responsables de la silicification. Les concentrations élevées des éléments immobiles (HFSE et HREE) montent que tous les cherts analysés représentent des sédiments clastiques silicifiés. Les différences texturales sont simplement expliquées par un apport hétérogène de matériaux carbonatés dont l'origine demeure inconnue et des oxydes. De plus, alors que de constantes anomalies positives en Eu ont été suggérées comme caractéristiques des laves silicifiées archéennes, similairement aux fumeurs noirs modernes, les échantillons analysés présentent plutôt de faibles anomalies aussi bien positives que négatives en Eu. Ces anomalies sont interprétées comme des évidences de la mobilisation de l'Eu suite à l'altération des plagioclases par des fluides hydrothermaux de basse température (Coogan and Gillis, 2018a). La séquestration des métaux alcalins rappelant ce qui s'observe essentiellement au sein des parties supérieures de la croute océanique moderne ayant interagi avec des fluides d'une température inférieure à 150 °C (Hart and Staudigel, 1982) confirme aussi la basse température de la silicification (et donc des fluides hydrothermaux).

Enfin, nous avons abordé des implications importantes pour notre façon d'aborder la géochimie des roches riches en silice dérivées du plancher océanique pour des études paléo-environnementales. Alors que l'altération hydrothermale des basaltes et sédiments a été proposée pour expliquer des signatures géochimiques de l'eau de mer (e.g. Y/Ho > 30) dans des laves silicifiées de la région d'Abitibi (Brengman and Fedo, 2018), notre étude suggère que même après une longue interaction avec des fluides hydrothermaux les basaltes et sédiments clastiques silicifiés demeuraient nettement distincts géochimiquement des sédiments purement précipités de l'eau de mer Archéenne. Ainsi, identifier les signatures de l'eau de mer dans la composition en éléments en trace des cherts demeure fiable pour identifier les cherts précipités de l'eau de à utiliser pour des reconstitutions paléo-environnementales parce que ces signatures ne peuvent pas s'acquérir autrement, du moins pour le cas de Barberton.

Brève synthèse de la partie III

En résumé, cette partie de la thèse a utilisé des données pétrographiques, thermométriques et géochimiques afin de différencier les signatures des processus survenus au niveau du plancher océanique Paléoarcheen de celles issues des processus tardifs tels que le métamorphisme et la circulation des fluides météoritiques. Le métamorphisme régional a recristallisé les roches analysées à plus de 280 °C et les anomalies en Ce sont dues à la circulation des fluides météoritiques. La silicification s'est opérée à des températures plus basses que 150 °C, ce qui explique l'absence d'anomalies positives en Eu dans les fluides hydrothermaux et l'enrichissement en métaux alcalins au sein des roches silicifiées. La préservation des signatures géochimiques issues de la silicification au niveau du plancher océanique a motivé l'analyse des isotopes d'oxygène et silicium pour contraindre encore mieux les fluides responsables de la silicification.

Présentation du deuxième article (Partie IV).

« Compositions isotopiques en oxygène et silicium des laves silicifiés et cherts paleoarchéens d'Onverwacht : Implication sur l'hydrothermalisme au plancher océanique et la nature des composantes recyclées dans la zone source des granitoïdes. »

Contexte, échantillons et méthodes

Nous avons observé dans la **Partie III** que les isotopes d'oxygène dans le quartz restaient largement insensibles au métamorphisme (**Figure 3-10**). Cette deuxième partie de notre étude a donc cherché à explorer la signification des compositions isotopiques de O et Si que nous mesurons dans les cherts et laves silicifiées du Groupe d'Onverwacht. La composition isotopique de O et Si au sein de ces roches constitue un traceur paléo-environnemental important permettant de reconstituer la composition isotopique et la température des fluides (Robert and Chaussidon, 2006; Hofmann and Harris, 2008; André et al., 2022). Certains auteurs ont utilisé la composition isotopique de O des cherts pour reconstruire des températures de l'eau de mer archéenne élevées, au-delà de 70 °C (Lowe et al., 2020). En revanche, d'autres études interprètent les températures calculées à partir de la composition isotopique des cherts de Barberton comme des épisodes de circulation de fluides post-dépôt (Kolodny and Epstein, 1976; Zakharov et al., 2021). De plus, les compositions isotopiques du Si ont démontré le recyclage des roches riches en silice dérivées du plancher océanique vers la zone source des TTGs. Une évolution progressive de la composition isotopique de l'O des granitoïdes de Barberton a été observée alors que la composition isotopique du Si demeure largement constante dans ces plutons (André et al., 2019; Deng et al., 2019; Wang et al., 2022). La signification de ce découplage entre isotopes de l'oxygène et du silicium dans les TTGs (Lei et al., 2023) reste débattue. Dans cette étude, nous avons donc analysé la composition isotopique de plusieurs types de roches silicifiées issues de la ceinture de roches vertes de Barberton, afin de (1) contraindre les compositions possibles des fluides hydrothermaux et de l'eau de mer paléoarchéenne, et (2) de comprendre l'origine de l'évolution isotopique observée au sein des TTGs de Barberton.

Les différents types d'échantillons analysés dans cette étude incluent :

- Des laves complétement silicifiées issues de trois formations géologiques différentes du Groupe d'Onverwacht, notamment la Formation de la Komati (section du Middle Marker), la Formation d'Hoggenoeg, et la Formation de Mendon ;
- Des cherts secondaires (ou sédiments clastiques silicifiées) issues de ces trois différentes sections;
- Et enfin, des cherts précipités d'eau de mer issues de l'Unité de Buck Reef, particulièrement connue pour en contenir (Lowe et al., 2020). Ces derniers échantillons proviennent du forage BARB4 ICDP et sont les seuls échantillons de cette thèse que nous n'avons pas prélevés nous-même sur le terrain.

Tous ces échantillons analysés dans cette étude présentent une concentration en SiO_2 supérieure à 90 wt.% qui permet de les considérer comme analogues à de la silice purs. Ils permettent de reconstituer les compositions des fluides hydrothermaux et de l'eau de mer (Sharp et al., 2016). Pour tous ces différents types d'échantillons, nous avons effectué des analyses des trois isotopes de l'oxygène ($^{18}O/^{17}O/^{16}O$) à l'université de Göttingen par fluorination laser couplée à la spectrométrie de masse à source gazeuse (erreur 2SD sur $\delta^{18}O$

et $\Delta^{17}O$ obtenue par analyse répétitive de standard : ± 0.6‰ and ± 0.02‰ respectivement). Les rapports $^{18}O/^{16}O$ ont été également analysés à l'Université de Lausanne pour la plupart des échantillons puisque cette technique permet une meilleure précision (2SD de ± 0.2‰). Cinq échantillons dont quatre laves silicifiées ont aussi été sélectionnés pour l'analyse de la composition isotopique de l'oxygène et du silicium in-situ par SIMS sur des points de ~15 µm de diamètre, avec d'assez bonnes précisions (2SD $\delta^{18}O$ de ± 0.2-0.6‰ et 2SD $\delta^{30}Si$ de ± 0.5-0.7‰). Au sein de ces échantillons, différents types de quartz reconnus pétrographiquement, notamment des micro-quartz, megaquartz, veines de quartz, et inclusions de quartz au sein de carbonates ont été respectivement analysés. En plus des différentes analyses géochimiques, nous avons aussi réalisé un modèle d'interaction eau-roche permettant de déterminer la composition isotopique de l'O au sein des fluides hydrothermaux en fonction de la composition d'eau de mer considérée.

Résultats

Les résultats obtenus de cette étude sont doubles. Ils incluent d'une part la mesure de composition isotopique d'O et du Si dans les laves silicifiées et cherts, et d'autre part les résultats numériques d'interaction eau-roche.

En ce qui concerne les compositions isotopiques d'oxygène et de silicium au sein des roches mesurées, nos résultats peuvent être synthétisés en quatre points essentiels. (1) Les laves et sédiments clastiques silicifiés diffèrent nettement des cherts précipités de l'eau de mer en termes de composition isotopique de l'oxygène. En effet, le $\delta^{18}O$ de ces laves et sédiments silicifiés varie entre 11,3 et 14,9‰, ce qui est relativement bas comparé aux cherts pures précipités de l'eau de mer dont le $\delta^{18}O$ varie entre 16,4 et 20,3‰ (**Table 4-1, Figure 4-6**). De plus, le $\Delta'^{17}O$ varie entre -0,07 et -0,05‰ dans les laves et sédiments clastiques silicifiés, ce qui est plus élevé que les de valeurs -0,12 à -0,07‰ obtenues dans les cherts précipités de l'eau de mer. (2) Le $\delta^{18}O$ des laves et sédiments clastiques silicifiés augmente progressivement de 11-13‰ à la base de la succession d'Onverwacht à 14-16‰ vers le sommet de cette succession (**Figure 4-5**). (3) Les $\delta^{30}Si$ mesurés dans les laves et sédiments silicifiés sont généralement positifs (0,19 to 1,24‰), et donc presque identiques aux valeurs antérieurement mesurées pour des cherts précipités à partir de l'eau de mer. (4) Dans un même échantillon, les différents types de quartz analysés lors de cette étude ne montrent pas de différence notable en termes de composition isotopique, suggérant qu'ils seraient co-génétiques dans chaque échantillon (**Table 4-2**, **Figure 4-5**).

Notre modèle numérique d'interaction eau-roche permet de déterminer les différents minéraux qui auraient résulté de l'altération des basaltes de la croûte sous-marine durant la formation des fluides hydrothermaux responsables de la silicification du plancher océanique (**Figure 4-7**). Ces minéraux incluent des amphiboles (tremolite et actinolite), chlorites (daphnite, clinochlore) et serpentines (chrysotile). De plus, le modèle montre que la composition isotopique de l'oxygène des fluides hydrothermaux générés (i.e. responsables de la silicification) est essentiellement dépendante de la composition isotopique de l'eau de mer considérée. Des fluides avec un $\delta^{18}O$ négatif se forment si l'eau de mer possède également un $\delta^{18}O$ négatif, alors que, pour l'eau de mer actuelle qui a un $\delta^{18}O$ proche de ~0‰, on observe un $\delta^{18}O$ plutôt positif dans les fluides hydrothermaux modélisés (similairement aux valeurs mesurées précédemment sur des fluides collectés au niveau du plancher océanique).

Discussion

La discussion des résultats obtenus dans cette étude s'articule autour de cinq points : (1) l'effet du métamorphisme régional, (2) la composition isotopique des fluides hydrothermaux Paléoarchéens, (3) l'effet de ces fluides sur la préservation des signatures issues de l'eau de mer dans les cherts précipités de l'eau de mer, (4) l'origine des variations stratigraphiques des compositions isotopiques de l'oxygène, et enfin (5) la signification des variations isotopiques observées dans les TTGs de Barberton.

Knauth and Lowe (2003) ont proposé que les cherts de la base du groupe d'Onverwacht ont subi un métamorphisme important qui auraient considérablement modifié la composition isotopique de leur oxygène, contrairement aux cherts du haut de la séquence stratigraphique. Cependant, nous notons que tous les cherts de la ceinture de Barberton ont enregistré le même événement métamorphique autours de 3.2 Ga mais restent quand même isotopiquement différents. De plus, nous rappelons que des rapports fluides/roche très élevés sont nécessaires pour que le métamorphisme transforme considérablement la composition isotopique d'un chert, ce qui n'est pas envisageable sur base des textures des cherts de Barberton. Ainsi, tel que déjà introduit dans la **Partie III** de cette thèse, nous suggérons que les signatures isotopiques observées pour la silice des roches silicifiées de Barberton soient principalement liées aux processus d'interaction fluide-roche au niveau du plancher océanique archéen, et puissent donc servir à étudier la composition des fluides hydrothermaux et de l'eau de mer.

Nous considérons que les laves et sédiments clastiques d'Onverwacht sont essentiellement constitués de quartz dû à l'altération hydrothermale sur le plancher océanique, et utilisons donc leur composition isotopique pour discuter la nature des fluides hydrothermaux. Les δ^{30}Si positifs mesurés dans les laves et sédiments silicifiés suggèrent que le fractionnement cinétique était insignifiant lors du remplacement des minéraux primaires par le quartz hydrothermal. Ces valeurs étant non-différentiables de la composition isotopique des cherts précipités de l'eau de mer, elles suggèrent que les fluides hydrothermaux étaient presque similaires à l'eau de mer en composition isotopique du Si. Concernant les isotopes d'oxygène, les laves et sédiments silicifiés (SiO_2 > 90 wt.%) sont compris dans un champ restreint dans le diagramme présentant les valeurs de $\delta`^{18}$O en fonction de Δ'^{17}O (**Figure 4-6**). Ce champ permet de calculer des fluides hydrothermaux avec un δ^{18}O négatif, et donc différent de celui des fluides hydrothermaux modernes. Notre modèle numérique d'interaction eau-roche a démontré que ceci ne peut être expliqué que si l'eau de mer avait des valeurs négatives de δ^{18}O durant l'Archéen (Jaffrés et al., 2007; Bindeman and O'Neil, 2022).

Dans le diagramme δ'^{18}O – Δ'^{17}O (**Figure 4-6**), les cherts précipités chimiquement à partir de l'eau de mer évoluent depuis le champ des laves et sédiments clastiques silicifiés vers des valeurs de δ'^{18}O plus élevées et de Δ'^{17}O plus basses. Ceci est interprété ici comme un mélange entre des quartz issus de l'eau de mer et des quartz issus de la circulation post-dépôt des fluides riches en Si. Etant donné que des circulations intenses de fluides hydrothermales opéraient dans la croûte, comme montré par l'intense silicification des laves et sédiments clastiques, il est possible que les cherts précipités par l'eau de mer aient considérablement interagi avec les fluides responsables de la silicification au niveau du plancher océanique. Notre modèle simplifié de mélange montre cependant que l'eau de mer moderne avec un δ^{18}O proche de ~0‰ et une eau de mer archéenne avec un δ^{18}O beaucoup plus bas pourraient toutes bien expliquer la composition des cherts précipités de l'eau de mer de Barberton, si on prend en compte le mélange avec de la silice hydrothermale. Aussi, les températures de précipitation variant entre 0 et 60 °C sont toutes acceptables. Les compositions isotopiques de l'oxygène dans les cherts sont donc de mauvais marqueurs des propriétés de l'océan, car ils ont été intensément altérés au niveau du plancher océanique (Liljestrand et al., 2020).

Pour comprendre l'origine des variations temporelles du δ^{18}O (**Figures 4-3** et **4-5**) des laves silicifiées et cherts observés le long de la succession stratigraphique d'Onverwacht, nous avons réfléchi sur d'éventuels changements de plusieurs paramètres clés au cours de l'évolution de la ceinture: (1) changement du δ^{18}O de l'eau de mer ou de la croûte, (2) des rapports fluide/roche durant la silicification, et (3) des conditions thermiques du système hydrothermal. La composition isotopique de l'oxygène de la croute basaltique archéenne a toujours été autour de ~5,6‰ et ne peut donc pas être à l'origine du changement observé (Wang et al., 2023). Aussi, le $\delta^{18}O$ de l'eau de mer ne peut pas changer considérablement en l'espace de 300 Ma tel qu'il serait suggéré par le changement observé dans les roches riches en silice d'Onverwacht. De plus, vu que tous les échantillons étudies contiennent plus de 90 wt.% de SiO_2, nous considérons que les rapports fluide/roche qui les ont générés étaient similaires et n'expliquent pas les variations en $\delta^{18}O$. Ainsi, en nous basant sur le modèle numérique de Tatzel et al. (2022), nous suggérons que le changement thermique (refroidissement progressif) du système hydrothermal pourrait expliquer la variation de la composition isotopique de l'oxygène. Ce changement serait dû à l'épaississement de la croute qui a progressivement éloigné le plancher océanique des flux de chaleur mantelliques.

Enfin, une compilation des compositions isotopiques de l'O et du Si dans les granitoïdes de Barberton permet de corréler l'augmentation du $\delta^{18}O$ dans les roches riches en silice d'Onverwacht avec une augmentation similaire observée au sein des granitoïdes de Barberton dans le temps (**Figure 4-8**). La constance de la composition isotopique du Si dans les granitoïdes se corrèle également avec la constance du $\delta^{30}Si$ dans différentes générations de roches silicifiées d'Onverwacht. Ces observations démontrent que différentes générations de roches silicifiés doivent avoir été recyclées vers la zone source des granitoïdes de différents âges affleurant à Barberton. Ce modèle est différent de celui établi pour des parties du craton Nord-Américain où une même source basique a été recyclée successivement pour former des granitoïdes pendant plus d'1 Ga. De ce fait, différents contextes de formations de granitoïdes auraient coexisté sur la terre paléoarchéenne.

Bref résumé de la Partie IV

Dans cette étude, la mesure des compositions isotopique d'oxygène et du silicium dans des laves silicifiées et cherts de Barberton a permis d'identifier le composant de silice hydrothermal au sein des roches du plancher océanique paléoarchéen. Ceci a permis de montrer que les fluides hydrothermaux paléoarchéens auraient un $\delta^{18}O$ négatif associé à des valeurs encore plus basses dans l'océan archéen que nous ne pouvons pas définir de manière non-ambiguë. La circulation des fluides hydrothermaux est proposée pour expliquer l'altération des cherts précipités d'eau de mer. Ce processus a altéré l'enregistrement des propriétés de l'eau de mer paléoarchéenne. Des variations du $\delta^{18}O$ observées au sein des cherts et laves silicifiées d'Onverwacht dans le temps sont associées à un refroidissement crustal dû à l'épaississement de la croute. Enfin, une corrélation entre l'évolution isotopique des roches riches en silice du plancher océanique archéen et celle observée dans les granitoïdes est considérée comme une preuve que les des différentes générations de granitoïdes observés à Barberton provenaient des sources contenant différentes générations de roches recyclées du plancher océanique.

Nouvelles contraintes sur les roches silicifiées recyclées et implications géodynamiques : Evaluation des compositions en O et Si des TTGs et modélisation thermodynamique (Partie V)

Contexte et objectifs

Les compositions isotopiques du silicium et de l'oxygène ont permis aux travaux antérieurs de tracer le recyclage des roches silicifiées venues du plancher océanique vers la zone source des TTGs de Barberton (André et al., 2019; Deng et al., 2019; Trail et al., 2018). Ceci a montré qu'il y avait bien une composante supergène dans la zone source de ces magmas, ce qui a permis d'éliminer les modèles qui suggéraient que ces TTGs seraient issus de la cristallisation fractionnée des liquides mantéliques. Cependant, deux questions importantes restent non-résolues à ce jour. Premièrement, nous ignorons à quel point les compositions isotopiques que nous mesurons dans des zircons séparés ou bien dans des échantillons de roche totale sont proches des compositions des liquides primitifs qui ont généré les plutons de TTGs. En effet, les TTGs tels que nous les connaissons actuellement auraient résulté des processus de cristallisation fractionnée et d'accumulation des phases minérales qui seraient capables de modifier la composition isotopique des magmas. De plus, durant leur évolution géologique, les roches de la série TTGs doivent avoir interagi avec des fluides hydrothermaux, métamorphiques ou météoriques capables d'affecter leur composition isotopique (Faure and Harris, 1991). On considère que les zircons des TTGs, résistants aux interactions avec les fluides, ont de plus cristallisé précocement et reflètent donc la composition du magma primitif (Hawkesworth and Kemp, 2006). Cependant, les compositions isotopiques des zircons et des liquides silicatés à l'équilibre montrent un fractionnement isotopique (Valley et al., 1994; Lackey et al., 2008; Trail et al., 2020; Guitreau et al., 2022), et les compositions des zircons devraientt donc être corrigées du fractionnement pour pouvoir révéler la composition isotopique des magmas primitifs des TTGs. Certains travaux ont négligé les effets du fractionnement zircon-magma en proposant que les zircons qui montrent un $\delta^{18}O$ de 5.3±0.3‰ étaient issus des TTGs générés par des roches basaltiques non-altérés venues du manteau. Puisque cette considération a conduit à proposer que les isotopes d'O et Si étaient découplés dans les TTGs (Lei et al., 2023), il convient de s'intéresser au fractionnement zircon-magma des isotopes d'oxygène afin de comprendre la signification du découplage entre les isotopes d'oxygène et silicium.

De plus, les propriétés des laves et sédiments silicifiés recyclés dans la zone source des TTGs de Barberton, c'est-à-dire leur composition isotopique, leur proportion dans la zone source et leur profondeur d'enfouissement dans la croûte sous-marine sont inconnues. La profondeur d'enfouissement liée à l'activité volcanique au niveau du plancher océanique est importante parce qu'elle permettrait de discriminer les TTGs dont la zone source contenaient des roches transportées par subduction de ceux dont les roches silicifiées de la source y ont été passivement enfouies (Laurent et al., 2024). En effet, si les roches recyclées n'ont jamais été passivement enfouies à forte profondeurs, alors leur présence dans la zone source des TTGs peut seulement s'expliquer par des processus similaires aux subductions modernes. Déterminer la profondeur d'enfouissement (passive) des roches recyclées constitue donc un moyen de contribuer à l'étude des processus géodynamiques qui opéraient sur la terre primitive.

Dans cette partie de la thèse, nous avons utilisé les compositions isotopiques de l'oxygène et du silicium des roches totales et zircons des TTGs de Barberton ainsi que des résultats de modèles thermodynamiques afin de discuter (1) la composition isotopique des magmas de TTG primitifs, (2) la proportion des roches silicifiées dans leur zone source et (3) les processus géologiques responsables du recyclage de ces roches. Pour y parvenir, nous avons considéré les roches d'Onverwacht comme étant de bons analogues des roches recyclées dans la zone source des TTGs de Barberton.

Observations

Dans un premier lieu, nous avons joint de nouvelles analyses des compositions isotopiques d'oxygène sur des échantillons de roche totale et zircons de TTGs de Barberton à une compilation des compositions isotopiques de Si et O dans ces TTGs et leurs zircons. Trois observations majeures découlent de ces données. Premièrement, un changement de la composition isotopique de l'oxygène dans les zircons des TTGs s'observe à partir de 3.23 Ga avec l'apparition de valeurs de $\delta^{18}O$ de plus en plus élevées dans les TTG jeunes, dépassant nettement le champ de zircons mantelliques, alors que les zircons des TTGs plus vieilles sont généralement compris dans ce champ de zircons mantelliques (**Figure 5-5** et **5-6**). Deuxièmement, il y a une différence notable entre les valeurs du $\delta^{18}O$ et du $\delta^{30}Si$ des zircons et celles des roches totales rappelant le fractionnement des isotopes d'oxygène entre roche totale et zircon (**Figure 5-1**). Enfin, nous observons de larges gammes de variations aussi bien du $\delta^{18}O$ que du $\delta^{30}Si$ dans les populations de roches totales et zircons des différents plutons.

En second lieu, nous avons effectué un modèle thermodynamique de fusion de laves silicifiées et de laves non-silicifiés en conditions saturées en eau et en conditions sèches, le long d'un géotherme chaud de 900 °C/GPa (~25.7 °C/km). Ce modèle permet de d'appréhender d'une part la nature et la proportion des phases minérales coexistant avec le liquide en différentes conditions de pression et de température, et d'autre part la composition en éléments majeurs des liquides formés (**Figures 5-7** and **5-8**). En conditions saturées en eau, nous avons trouvé que les laves silicifiées peuvent fondre complétement avant que le système n'atteigne 900 °C, alors que les laves non-silicifiés ne sont que partiellement fondues. Ceci conduirait à une surreprésentation de la composante laves silicifiées dans la fraction liquide et sa sous-représentation dans le solide résiduel. En conditions sèches (sans eau libre), les laves silicifiées sont beaucoup moins fertiles parce que le quartz reste stable en grande proportion jusqu'à haute température. Dans ces conditions, les laves silicifiées sont moins représentées dans le liquide formé que les laves non-silicifiés. En ce qui concerne la composition des liquides formés, nous avons trouvé que les laves silicifiés génèrent des liquides plutôt potassiques et ne peuvent donc pas expliquer seules la formation des TTGs. Les laves non-silicifiés génèrent des liquides proches des compositions généralement acceptées pour les magmas TTG primitifs à des taux de fusion acceptables seulement dans les conditions saturées en eau.

Interprétations et discussions

Trois points principaux sont abordés sur base des observations de cette étude : (1) le lien entre les mesures et la composition isotopique probable des liquides primitifs, (2) la proportion et composition isotopique des roches riches en silice recyclés, et (3) la profondeur d'enfouissement de ces roches avec ses implications géodynamiques.

La composition isotopique des liquides primitifs a été premièrement débattue dans cette étude sur la base des compositions moyennes isotopiques de l'oxygène et du silicium des roches totales de chaque pluton. Nous suggérons que ces moyennes sont généralement comprises dans une gamme restreinte ($\delta^{18}O$ = 7,0-7,6‰ and $\delta^{30}Si$ = -0,03 to +0,03‰, respectivement) et qu'elles sont proches de la composition isotopique des magmas de TTG primitifs. Nous démontrons grâce à un modèle numérique (**Figure 5-9**) que la cristallisation fractionnée ne peut pas modifier considérablement la composition isotopique de l'oxygène dans les liquides résiduels. Aussi, considérant qu'il n'y a pas d'évidence d'une forte interaction entre les TTG et les fluides métamorphique et météoriques, nous suggérons que ces fluides ne peuvent pas avoir affecté la composition isotopique des roches totales moyennes des TTGs de Barberton. Une large dispersion observée autour des roches totales moyennes pour chaque pluton suggère que la composition isotopique de l’oxygène et du silicium au sein des plutons serait hétérogène. Les compositions isotopiques des zircons confirment cette hypothèse car elles donnent des valeurs différentes pour des échantillons venant d’un même pluton. Le fait que ces zircons aient des valeurs différentes de composition isotopique de l’O et du Si comparativement aux roches totales suggère que leur composition ne représente pas la composition isotopique des magmas primitifs contrairement à ce qui a été inféré récemment (Wang et al., 2022). Par contre, après avoir appliqué des corrections empiriques du fractionnement des isotopes de l’oxygene et du silicium (Lackey et al., 2008; Guitreau et al., 2022), nous obtenons des compositions isotopiques des liquides TTGs similaires à celles obtenues pour les roches totales moyennes par pluton (**Figures 5-10** et **5-11**). Ces compositions montrent aussi une large gamme de dispersion et nous proposons donc que les compositions isotopiques des liquides de TTGs seraient hétérogènes à l’échelle des plutons, bien que des erreurs analytiques et processus magmatiques ou tardifs peuvent aussi avoir contribué partiellement aux larges variations observées. Les liquides de TTGs calculés ne montrent aucun découplage entre les compositions isotopiques de l’oxygène et du silicium contrairement à ce qui a été proposé récemment (Lei et al., 2023), et leur compositions isotopiques sont tous en accord avec le recyclage de roches silicifiées venues du plancher océanique Archéen.

Vu qu’il est impossible de déterminer conjointement les compositions isotopiques et la proportion des roches silicifiées recyclées dans la zone source des TTGs, nous avons considéré la composition des roches silicifiées affleurant à Barberton pour simplifier nos estimations. En prenant compte des résultats de notre modèle thermodynamique, nous avons effectué un calcul de mélange des liquides issus de la fusion d’une lave non-silicifiée et ceux issus de la fusion d’une lave silicifiée pour déterminer la proportion des roches silicifiées dans la source des TTGs de Barberton (**Figure 5-13**). Le modèle montre que le mélange des deux types de liquides explique la composition isotopique des TTGs. Il montre aussi que 10 à 25 vol.% des TTGs correspondent aux liquides issues de la fusion des roches silicifiées dérivées du plancher océanique. En tenant compte de la différence de taux de fusion entre lave silicifiée et lave fraiche, ceci correspondrait, dans les conditions saturées en eau proposées, à 5 à 12 vol.% de roche silicifiés dans la zone source. La modélisation suggère aussi e qu’une augmentation du

$\delta^{18}O$ des roches recyclées de ~12 à ~15‰ expliquerait la variation isotopique des TTGs de Barberton autour de 3.23 Ga.

Replacée dans la succession stratigraphique d'Onverwacht (**Figure 5-12**), la composition isotopique des laves recyclés ainsi estimée montre que ces laves ne pouvaient pas être enfouies à de très grandes profondeur au moment de leur fusion. Elles seraient restées peu profondes (< 10 km), ce qui est incompatible avec leur fusion dans la zone de stabilité de grenat si la croute était stagnante. Ceci suggère que la fusion de ces roches dans la zone source des TTGs de Barberton devait être due à un transport physique, de très près similaires à la subduction moderne. Ainsi, la fusion d'une portion de croûte ayant subi la subduction est envisagée pour expliquer la formation des TTGs de Barberton. Par contre, vu que les TTGs se formaient de manière épisodique, une subduction sporadique est proposée et expliquée par des ruptures de croute encore trop chaude et flexible pour entretenir des processus de subduction plus soutenus dans le temps, comme on en observe aujourd'hui (Nebel et al., 2018).

Perspective sur l'utilisation des isotopes stables pour contraindre les processus géodynamiques Archéens

Pour finir avec une discussion générale sur l'utilisation des isotopes stables en vue de comprendre la géodynamique Archéenne, nous avons effectué une relecture des travaux récents sur ce sujet (Cavosie et al., 2005; Reimink et al., 2016; Vezinet et al., 2018; André et al., 2019; Deng et al., 2019; Smit et al., 2019; Antonelli et al., 2021; Smithies et al., 2021; Wang et al., 2020; Wang et al., 2022; Lei et al., 2023) afin de comprendre les défis qui restent à relever. Trois principales faiblesses ont été identifiées dans ces récents travaux antérieurs. Premièrement, il est difficile de savoir si les minéraux mesurés pour les compositions isotopiques ont réellement préservé la composition du magma primitif. En effet, pour certains isotopes les fractionnements isotopiques au sein des systèmes magmatiques demeurent peu contraints. Deuxièmement, la nature des matériaux recyclés est souvent difficile à déterminer, ce qui peut conduire à des interprétations peu vérifiables. Par exemple, une étude a interprété l'augmentation du $\delta^{18}O$ au sein des TTGs indiens (Coorg Block) comme due à une augmentation de quantité de sédiments argileux recyclés, traduisant l'émergence graduelle des continents, alors que dans ce travail nous montrons qu'une pareille évolution peut s'observer sans l'influence des continents. Enfin troisièmement, il est difficile de distinguer les effets de l'enfouissement (passive et due à l'accumulation de laves) de ceux du transport (dû à des contraintes actives, exemple : la subduction) dans les signatures isotopiques des granitoïdes, si ces signatures ne sont pas couplées avec d'autres données géologiques (e.g. des formations géologiques représentant les roches recyclés). Vu que ces données géologiques sont généralement rares pour la terre archéenne, les processus géologiques qui opéraient au niveau du plancher océanique sont difficiles à contraindre de manière certaine. Des études multi-isotopiques au sein des TTGs, préférentiellement couplées à l'analyses des restes des lithologies recyclées, sont proposées comme une piste intéressante à poursuivre, tel qu'explorée dans cette thèse.

Brève synthèse de la Partie V

Cette étude utilise la composition isotopique de Si et O dans les roches totales et zircons des TTGs de Barberton, couplées à des modèles thermodynamiques de fusion partielle, pour discuter sur la composition isotopique des liquides primitifs de TTGs, la proportion et la composition des roches silicifiées venues du plancher océanique vers leur zone source, ainsi que la profondeur d'enfouissement et les processus géologiques responsables du recyclage de ces roches. Nous proposons que : (1) les compositions isotopiques de l'oxygène et du silicium étaient couplés dans les liquides primitifs des TTG, (2) qu'elles reflètent le recyclage des roches du plancher océanique (5 à 12 vol.% de roches silicifiées) vers la zone source de TTGs, et (3) que la plupart des roches recyclées n'étaient pas enfouies passivement à forte profondeur, ce qui suggère que la subduction soit le processus responsable de leur recyclage.

Conclusions de la thèse (Partie VI)

Cette recherche doctorale visait premièrement à contraindre les propriétés (composition et température) des fluides hydrothermaux et de l'eau de mer du Paléo-archéen sur la base de la composition des laves et des cherts (y compris les sédiments clastiques silicifiés et les cherts précipités par l'eau de mer) de la ceinture de roches vertes de Barberton. Deuxièmement, elle visait à améliorer notre compréhension des processus qui ont conduit au recyclage des roches riches en silice du plancher océanique vers la zone source des TTGs de Barberton. La thèse est divisée en trois études interconnectées, et les principaux résultats de chacune de ces études sont résumés ci-dessous avec leurs implications.

Premièrement, dans la partie III de la thèse, différents outils minéralogiques et géochimiques identifient collectivement les effets minéralogiques et géochimiques du métamorphisme régional et des circulations tardives de fluides oxydés. Ces effets sont distingués de ceux de la silicification hydrothermale près du plancher océanique Paléoarchéen. La chimie des chlorites, la spectroscopie Raman des matériaux carbonés et le fractionnement isotopique de l'oxygène dans les assemblages quartz-carbonate démontrent que le métamorphisme régional a recristallisé les laves et les cherts à plus de 280 °C. En l'absence de preuves texturales d'une circulation importante de fluides au stade métamorphique, nous considérons que le métamorphisme n'a pas considérablement affecté la composition chimique de la roche totale pour les échantillons de roches riches en silice étudiées. En outre, les anomalies positives ou négatives en Ce observées dans quelques échantillons sont attribuées à des circulations de fluides oxydés post-archéens. Dans les laves silicifiées qui n'ont pas été affectées par cette altération tardive, une augmentation de la concentration en K, Ba, Cs, LREE, Pb et U, et une diminution de la concentration en Mg, Fe et Na sont associées à la silicification hydrothermale près du plancher océanique. L'absorption d'alcalins est interprétée comme montrant que la silicification s'est produite à basse température (< 150 °C), ce qui est confirmé par la température d'équilibre la plus basse de ~125 °C calculée à partir du fractionnement isotopique de l'oxygène dans un assemblage de quartz-carbonate particulièrement préservé. En outre, les anomalies en Eu positives et négatives observées dans les laves et les cherts silicifiés suggèrent que les fluides hydrothermaux responsables de la silicification étaient généralement exempts d'anomalie positives en Eu, ce qui montre que ces fluides se sont formés par interaction entre l'eau de mer et la croûte à une température globalement inférieure à 250 °C. Enfin, les concentrations en REE et en HFSE dans les laves silicifiées et les cherts secondaires analysés sont considérablement plus élevées que celles attendues dans les sédiments précipités de l'eau de mer et restent généralement affiliées à la composition en éléments traces des protolithes frais et exempts de caractéristiques semblables à celles de l'eau de mer, telles que des rapports Y/Ho élevés. Par conséquent, cette thèse soutient que la silicification hydrothermale n'a pas pu générer des propriétés d'éléments traces semblables à celles de l'eau de mer dans les laves silicifiées, et que les compositions d'éléments traces restent robustes pour identifier les cherts précipités par l'eau de mer qui sont d'une importance paléo-environnementale unique.

Deuxièmement, dans la partie IV, les analyses des compositions isotopiques triple de l’oxygène et des compositions isotopiques du Si des laves silicifiées, des sédiments clastiques silicifiés (ou cherts secondaires) et des cherts précipités de l'eau de mer fournissent de nouvelles contraintes sur (1) la composition isotopique de l’oxygène des fluides hydrothermaux responsables de la silicification, (2) l'évolution post-dépôt des cherts précipités à l'eau de mer et (3) l'évolution thermique dans la croute durant le dépôt du groupe d'Onverwacht. Par rapport aux cherts précipités dans l'eau de mer, des valeurs $\delta'^{18}O$ plus faibles et des valeurs $\Delta'^{17}O$ plus élevées sont observées dans les laves et les sédiments clastiques silicifiés, et ces valeurs permettent de reconstruire un $\delta^{18}O$ négatif pour les fluides hydrothermaux responsables de la silicification. Un modèle simplifié d'interactions eau-roche confirme que ces fluides hydrothermaux doivent provenir d'une eau de mer Paléo-archéenne avec une valeur de $\delta^{18}O$ inférieure à celle des océans modernes. La composition isotopique triple de l'oxygène des cherts précipités de l'eau de mer suggère qu'ils ont été considérablement modifiés par la circulation des fluides hydrothermaux et qu'ils ont peut-être perdu leur capacité à reconstituer la composition et la température de l'eau de mer du Paléo-archéen. En outre, les laves et sédiments silicifiés analysés, présentent des valeurs positives de $\delta^{30}Si$ qui sont similaires à celles rapportées précédemment pour les cherts précipités par l'eau de mer dans le groupe d'Onverwacht. Par conséquent, contrairement à ce que l'on croit généralement, une valeur $\delta^{30}Si$ positive ne garantit pas une origine orthochimique pure pour un chert et une valeur $\delta^{30}Si$ négative ne doit pas être considérée comme un diagnostic de précipitation de silice à partir de fluides hydrothermaux. Au contraire, nous suggérons que l'eau de mer paléoarchéenne et les fluides hydrothermaux ont pu être proches en termes de valeurs de $\delta^{30}Si$, déduisant que les fluides hydrothermaux représentaient peut-être la principale source du Si dissout dans les océans paléoarchéen. En outre, nous observons une augmentation progressive des valeurs $\delta^{18}O$ des laves silicifiées et des cherts vers le haut du groupe d'Onverwacht, et attribuons cette évolution à des changements progressifs du gradient géothermique régional, probablement dus à l'épaississement de la croute. Cette étude révèle l'importance des laves silicifiées et des sédiments clastiques qui étaient précédemment exclus des travaux visant à comprendre la signification paléo-environnementale des cherts paléoarchéens.

Enfin, dans la partie V, les propriétés des laves et des cherts silicifiés recyclés vers la zone source de différentes générations de TTG et les processus géodynamiques responsables de leur recyclage sont discutés sur la base d'une réévaluation des compositions isotopiques de l'oxygène et du silicium, associée à des résultats de modélisation thermodynamique. Les laves silicifiées fondues dans la zone source des TTG de Barberton peuvent avoir été équivalentes en composition et en position stratigraphique aux laves silicifiées et aux cherts préservés dans le groupe d'Onverwacht, et le changement isotopique observé dans les TTG de Barberton au cours du temps est attribué à un recyclage progressif d'unités plus jeunes du plancher océanique vers la zone source de fontes TTG. Après la détermination de la position stratigraphique possible des laves et des cherts remaniés dans la zone source des TTG de Barberton, des processus de type subduction sont proposés pour expliquer le recyclage des lithologies proches du plancher océanique vers la zone source des TTG de Barberton. L'accumulation verticale de laves mafiques dans le groupe d'Onverwacht et la périodicité de la formation des TTG suggèrent en outre que ces subductions étaient sporadiques, contrairement aux subductions modernes qui sont presque continues dans le temps. Le transport de roches supracrustales altérées par l'hydrosphère en profondeur semble avoir joué un rôle important dans le développement des premiers continents sur Terre.

La contribution scientifique la plus importante de cette étude est peut-être la démonstration que les variations de la composition isotopique des roches du plancher océanique du Paléoarchéen au cours du temps doivent être prises en compte dans l'utilisation des isotopes stables pour caractériser les processus géodynamiques. Des variations isotopiques observées dans les magmas granitiques qui étaient auparavant interprétées comme dues à des changements géodynamiques importants durant l'Archéen pourraient simplement refléter un changement de la composition des matériaux recyclés. Cette proposition invite à repenser la façon dont nous interprétons les signatures géochimiques des lithologies recyclées des fonds marins pour proposer des modèles géodynamiques ; elle plaide pour l'importance de comprendre les variations des compositions isotopiques des roches des fonds marins recyclées vers la source des granitoïdes. L'avenir de l'utilisation de la géochimie des isotopes stables pour étudier les processus géodynamiques archéens réside probablement dans une interdisciplinarité couplant les études géochimiques et pétrologiques à basse et haute température qui étaient traditionnellement considérées comme des sous-disciplines assez différentes en sciences de la Terre.

Bibliographic references

Abbott, D. H. (1996). Plumes and hotspots as sources of greenstone belts. *Lithos*, *37*(2–3), 113–127. https://doi.org/10.1016/0024-4937(95)00032-1

Abraham, K., Hofmann, A., Foley, S. F., Cardinal, D., Harris, C., Barth, M. G., & Andre, L. (2011). Coupled silicon-oxygen isotope fractionation traces Archaean silicification. *Earth and Planetary Science Letters*, *301*(1–2), 222–230. https://doi.org/10.1016/j.epsl.2010.11.002

Abraham, K., Opfergelt, S., Fripiat, F., Cavagna, A. J., de Jong, J. T. M., Foley, S. F., André, L., & Cardinal, D. (2008). δ30Si and δM29Si Determinations on USGS BHVO-1 and BHVO-2 Reference Materials with a New Configuration on a Nu Plasma Multi-Collector ICP-MS. *Geostandards and Geoanalytical Research*, *32*(2), 193–202. https://doi.org/10.1111/j.1751-908X.2008.00879.x

Ackerman, L., Žák, J., Kachlík, V., Pašava, J., Žák, K., Pack, A., Veselovský, F., & Strnad, L. (2023). The significance of cherts as markers of Ocean Plate Stratigraphy and paleoenvironmental conditions: New insights from the Neoproterozoic–Cambrian Blovice accretionary wedge, Bohemian Massif. *Geoscience Frontiers*, *14*(1). https://doi.org/10.1016/j.gsf.2022.101478

Agangi, A., Hofmann, A., Eickmann, B., & Marin-Carbonne, J. (2019). Mesoarchaean Gold Mineralisation in the Barberton Greenstone Belt: A Review. In A. Kroner & A. Hofmann (Eds.), *The Archean Geology of the Kaapvaal Craton, Southern Africa, Regional Geology Reviews* (pp. 171–184). Springer Nature. https://doi.org/10.1007/978-3-319-78652-0_7

Agangi, A., Hofmann, A., & Elburg, M. A. (2018). A review of Palaeoarchaean felsic volcanism in the eastern Kaapvaal craton : Linking plutonic and volcanic records. *Geoscience Frontiers*, *9*(3), 667–688. https://doi.org/10.1016/j.gsf.2017.08.003

Albarede, F., Thibon, F., Blichert-Toft, J., & Tsikos, H. (2020). Chemical archeoceanography. *Chemical Geology*, *548*(April), 119625. https://doi.org/10.1016/j.chemgeo.2020.119625

Alleon, J., Bernard, S., Olivier, N., Thomazo, C., & Marin-carbonne, J. (2021). Inherited geochemical diversity of 3 . 4 Ga organic. *Communications Earth & Environment*, *2021*, 4–10. https://doi.org/10.1038/s43247-020-00066-7

Alleon, J., Bernard, S., Olivier, N., Thomazo, C., & Marin-Carbonne, J. (2021). Inherited geochemical diversity of 3.4 Ga organic films from the Buck Reef Chert, South Africa. *Communications Earth and Environment*, *2*(1), 4–10. https://doi.org/10.1038/s43247-020-00066-7

Alleon, J., & Summons, R. E. (2019). Organic geochemical approaches to understanding early life. *Free Radical Biology and Medicine*, *140*(March), 103–112. https://doi.org/10.1016/j.freeradbiomed.2019.03.005

Alt, J. C., & Bach, W. (2006). Oxygen isotope composition of a section of lower oceanic crust, ODP Hole 735B. *Geochemistry, Geophysics, Geosystems*, *7*(12). https://doi.org/10.1029/2006GC001385

Alt, J. C., Laverne, C., Coggon, R. M., Teagle, D. A. H., Banerjee, N. R., Morgan, S., Smith-Duque, C. E., Harris, M., & Galli, L. (2010). Subsurface structure of a submarine hydrothermal system in ocean crust formed at the East Pacific Rise, ODP/IODP Site 1256. *Geochemistry, Geophysics, Geosystems*, *11*(10), 1–28. https://doi.org/10.1029/2010GC003144

Alt, J. C., & Teagle, D. A. H. (1999). The uptake of carbon during alteration of ocean crust. *Geochimica et Cosmochimica Acta*, *63*(10), 1527–1535. https://doi.org/10.1016/S0016-7037(99)00123-4

Anders, E., & Grevesse, N. (1989). Abundances of the elements: Meteoritic and solar. *Geochimica et Cosmochimica Acta*, *53*(1), 197–214. https://doi.org/10.1016/0016-7037(89)90286-X

André, L., Abraham, K., Hofmann, A., Monin, L., Kleinhanns, I. C., & Foley, S. (2019). Early continental crust generated by reworking of basalts variably silicified by seawater. *Nature Geoscience*. https://doi.org/10.1038/s41561-019-0408-5

André, L., Cardinal, D., Alleman, L. Y., & Moorbath, S. (2006). Silicon isotopes in ~3.8 Ga West Greenland rocks as clues to the Eoarchaean supracrustal Si cycle. *Earth and Planetary Science Letters*, *245*(1–2), 162–173. https://doi.org/10.1016/j.epsl.2006.02.046

André, L., Monin, L., & Hofmann, A. (2022). The origin of early continental crust: New clues from coupling Ge/Si ratios with silicon isotopes. *Earth and Planetary Science Letters*, *582*. https://doi.org/10.1016/j.epsl.2022.117415

Anhaeusser, C. R. (1981). Geotectonic evolution of the archaean successions in the barberton mountain land, south africa. *Developments in Precambrian Geology*, *4*(C), 137–160. https://doi.org/10.1016/S0166-2635(08)70011-2

Anhaeusser, C. R. (2010). Magmatic and structural characteristics of the ca. 3440 ma theespruit pluton, barberton mountain land, South Africa. *American Journal of Science*, *310*(9), 1136–1167. https://doi.org/10.2475/09.2010.14

Anhaeusser, C. R. (2014). Archaean greenstone belts and associated granitic rocks - A review. *Journal of African Earth Sciences*, *100*, 684–732. https://doi.org/10.1016/j.jafrearsci.2014.07.019

Anhaeusser, C. R. (2019). The geology and tectonic evolution of the northwest part of the Barberton Greenstone Belt , South Africa : A review. *South African Journal of Geology*, *122*, 1–34.

Anhaeusser, C. R., & Robb, L. J. (1980). Regional and detailed field and geochemical studies of Archean trondhjemitic gneisses, migmatites and greenstone xenoliths in the southern part of the Barberton Mountain Land, South Africa. *Precambrian Research*, *11*(3–4), 373–397. https://doi.org/10.1016/0301-9268(80)90073-X

Antonelli, M. A., Kendrick, J., Yakymchuk, C., Guitreau, M., Mittal, T., & Moynier, F. (2021). Calcium isotope evidence for early Archaean carbonates and subduction of oceanic crust. *Nature Communications*, *12*(1). https://doi.org/10.1038/s41467-021-22748-2

Aquila, Q. (2024). *Explorer la géochimie des océans archéens avec les Formations de fer rubanées (BIF) : apport des compositions isotopiques Hf-N*. Université Clermont Auvergne.

Armstrong, R. A., Compston, W., de Wit, M. J., & Williams, I. S. (1990). The stratigraphy of the 3.5-3.2 Ga Barberton Greenstone Belt revisited: a single zircon ion microprobe study. *Earth and Planetary Science Letters*, *101*(1), 90–106. https://doi.org/10.1016/0012-821X(90)90127-J

Arndt, N. (1998). Were komatiites wet? *Geology*, *26*(8), 739–742. https://doi.org/10.1130/0091-7613(1998)026<0739:WKW>2.3.CO;2

Arndt, N. (2023). How did the continental crust form: No basalt, no water, no granite. *Precambrian Research*, *397*(September), 107196. https://doi.org/10.1016/j.precamres.2023.107196

Bach, W., Bernhard, P. E., Hart, S. R., & Blusztajn, J. S. (2003). Geochemistry of hydrothermally altered oceanic crust: DSDP/ODP Hole 504B-Implications for seawater-crust exchange budgets and Sr-and Pb-isotopic evolution of the mantle. *Geochemistry, Geophysics, Geosystems*, *4*(3), 40–55. https://doi.org/10.1029/2002GC000419

Bach, W., & Früh-Green, G. L. (2010). Alteration of the oceanic lithosphere and implications for seafloor processes. *Elements*, *6*(3), 173–178.

https://doi.org/10.2113/gselements.6.3.173

Bao, H., Cao, X., & Hayles, J. A. (2016). Triple Oxygen Isotopes: Fundamental Relationships and Applications. *Annual Review of Earth and Planetary Sciences*, *44*, 463–492. https://doi.org/10.1146/annurev-earth-060115-012340

Bau, M. (1991). Rare-earth element mobility during hydrothermal and metamorphic fluid-rock interaction and the significance of the oxidation state of europium. In *Chemical Geology* (Vol. 93).

Bédard, J. H. (2006). A catalytic delamination-driven model for coupled genesis of Archaean crust and sub-continental lithospheric mantle. *Geochimica et Cosmochimica Acta*, *70*(5), 1188–1214. https://doi.org/10.1016/j.gca.2005.11.008

Bédard, J. H. (2018). Stagnant lids and mantle overturns: Implications for Archaean tectonics, magmagenesis, crustal growth, mantle evolution, and the start of plate tectonics. *Geoscience Frontiers*, *9*(1), 19–49. https://doi.org/10.1016/j.gsf.2017.01.005

Bédard, J. H. (2024). A gradual Proterozoic transition from an Unstable Stagnant Lid to the modern Plate Tectonic system. *Journal of the Geological Society*, *181*. https://doi.org/10.1144/jgs2024-023

Beyssac, O., Goffé, B., Chopin, C., & Rouzaud, J. N. (2002). Raman spectra of carbonaceous material in metasediments: a new geothermometer - Beyssac - 2002 - Journal of Metamorphic Geology - Wiley Online Library. *Journal of Metamorphic Geology*, *20*(9), 859–871. https://onlinelibrary.wiley.com/doi/abs/10.1046/j.1525-1314.2002.00408.x

Bickle, M. J., Nisbet, E. G., & Martin, A. (1994). Archean Greenstone Belts Are Not Oceanic Crust Author (s): M . J . Bickle , E . G . Nisbet and A . Martin Published by : The University of Chicago Press Stable URL : https://www.jstor.org/stable/30068540 Archean Greenstone Belts Are Not Oceanic Crust ’. *The University of Chicago Press*, *102*(2), 121–137.

Bindeman, I. N. (2021). Triple Oxygen Isotopes in Evolving Continental Crust, Granites, and Clastic Sediments. *Reviews in Mineralogy and Geochemistry*, *86*(1), 241–290. https://doi.org/10.2138/rmg.2021.86.08

Bindeman, I. N., Eiler, J. M., Yogodzinski, G. M., Tatsumi, Y., Stern, C. R., Grove, T. L., Portnyagin, M., Hoernle, K., & Danyushevsky, L. V. (2005). Oxygen isotope evidence for slab melting in modern and ancient subduction zones. *Earth and Planetary Science Letters*, *235*(3–4), 480–496. https://doi.org/10.1016/j.epsl.2005.04.014

Bindeman, I. N., & O’Neil, J. (2022). Earth’s earliest hydrosphere recorded by the oldest hydrothermally-altered oceanic crust: Triple oxygen and hydrogen isotopes in the 4.3-3.8 Ga Nuvvuagittuq belt, Canada. *Earth and Planetary Science Letters*, *586*, 117539. https://doi.org/10.1016/j.epsl.2022.117539

Bindeman, I. N., Zakharov, D. O., Palandri, J., Greber, N. D., Dauphas, N., Retallack, G. J., Hofmann, A., Lackey, J. S., & Bekker, A. (2018). Rapid emergence of subaerial landmasses and onset of a modern hydrologic cycle 2.5 billion years ago. *Nature*, *557*(7706), 545–548. https://doi.org/10.1038/s41586-018-0131-1

Blichert-Toft, J., Arndt, N. T., Wilson, A., & Coetzee, G. (2015). Hf and Nd isotope systematics of early Archean komatiites from surface sampling and ICDP drilling in the Barberton Greenstone Belt, South Africa. *American Mineralogist*, *100*(11–12), 2396–2411. https://doi.org/10.2138/am-2015-5325

Bolhar, R., Kamber, B. S., Moorbath, S., Fedo, C. M., & Whitehouse, M. J. (2004). Characterisation of early Archaean chemical sediments by trace element signatures. *Earth and Planetary Science Letters*, *222*(1), 43–60. https://doi.org/10.1016/j.epsl.2004.02.016

Bonnand, P., Israel, C., Boyet, M., Doucelance, R., & Auclair, D. (2019). Radiogenic and stable Ce isotope measurements by thermal ionisation mass spectrometry. *Journal of*

Analytical Atomic Spectrometry, *34*(3), 504–516. https://doi.org/10.1039/c8ja00362a

Bonnand, P., Lalonde, S. V, Boyet, M., Heubeck, C., Homann, M., Nonnotte, P., Foster, I., Konhauser, K. O., & Köhler, I. (2020). Post-depositional REE mobility in a Paleoarchean banded iron formation revealed by La-Ce geochronology : A cautionary tale for signals of ancient oxygenation. *Earth and Planetary Science Letters*, *547*, 116452. https://doi.org/10.1016/j.epsl.2020.116452

Bourdelle, F. (2021). *Low-Temperature Chlorite Geothermometry and Related Recent Analytical Advances: A Review*.

Bouvier, A., Vervoort, J. D., & Patchett, P. J. (2008). The Lu-Hf and Sm-Nd isotopic composition of CHUR: Constraints from unequilibrated chondrites and implications for the bulk composition of terrestrial planets. *Earth and Planetary Science Letters*, *273*(1–2), 48–57. https://doi.org/10.1016/j.epsl.2008.06.010

Brengman, L. A., & Fedo, C. M. (2018). Development of a mixed seawater-hydrothermal fluid geochemical signature during alteration of volcanic rocks in the Archean (2 . 7 Ga) Abitibi Greenstone Belt , Canada. *Geochimica et Cosmochimica Acta*, *227*, 227–245. https://doi.org/10.1016/j.gca.2018.02.019

Brengman, L. A., Fedo, C. M., & Whitehouse, M. J. (2016). Micro-scale silicon isotope heterogeneity observed in hydrothermal quartz precipitates from the >3.7 Ga Isua Greenstone Belt, SW Greenland. *Terra Nova*, *28*(1), 70–75. https://doi.org/10.1111/ter.12192

Brown, M., Johnson, T., & Gardiner, N. J. (2020). Plate Tectonics and the Archean Earth. *Annual Review of Earth and Planetary Sciences*, *48*, 291–320. https://doi.org/10.1146/annurev-earth-081619-052705

Byerly, B. L., Lowe, D. R., Drabon, N., Coble, M. A., Burns, D. H., & Byerly, G. R. (2018). Hadean zircon from a 3.3 Ga sandstone, Barberton greenstone belt, South Africa. *Geology*, *46*(11), 967–970. https://doi.org/10.1130/G45276.1

Byerly, G. R., Kröner, A., Lowe, D. R., Todt, W., & Walsh, M. M. (1996). Prolonged magmatism and time constraints for sediment deposition in the early Archean Barberton greenstone belt: Evidence from the Upper Onverwacht and Fig Tree groups. *Precambrian Research*, *78*(1-3 SPEC. ISS.), 125–138. https://doi.org/10.1016/0301-9268(95)00073-9

Byerly, G. R., Lowe, D. R., & Heubeck, C. (2019). Geologic Evolution of the Barberton Greenstone Belt—A Unique Record of Crustal Development, Surface Processes, and Early Life 3.55–3.20 Ga. In *Earth's Oldest Rocks*. Elsevier B.V. https://doi.org/10.1016/b978-0-444-63901-1.00024-1

Cammack, J. N., Spicuzza, M. J., Cavosie, A. J., Van Kranendonk, M. J., Hickman, A. H., Kozdon, R., Orland, I. J., Kitajima, K., & Valley, J. W. (2018). SIMS microanalysis of the Strelley Pool Formation cherts and the implications for the secular-temporal oxygen-isotope trend of cherts. *Precambrian Research*, *304*, 125–139. https://doi.org/10.1016/j.precamres.2017.11.005

Catling, D. C., & Zahnle, K. J. (2020). The Archean atmosphere. *Science Advances*, *6*(February), 1–16.

Cavosie, A. J., Valley, J. W., & Wilde, S. A. (2005). Magmatic δ18O in 4400-3900 Ma detrital zircons: A record of the alteration and recycling of crust in the Early Archean. *Earth and Planetary Science Letters*, *235*(3–4), 663–681. https://doi.org/10.1016/j.epsl.2005.04.028

Cawood, P. A., Hawkesworth, C. J., Pisarevsky, S. A., Dhuime, B., Capitanio, F. A., & Nebel, O. (2018). Geological archive of the onset of plate tectonics. *Philosophical Transactions of the Royal Society A: Mathematical, Physical and Engineering Sciences*, *376*(2132). https://doi.org/10.1098/rsta.2017.0405

Charnay, B., Wolf, E. T., Marty, B., & Forget, F. (2020). Is the Faint Young Sun Problem for Earth Solved? *Space Science Reviews*, *216*(5), 1–22. https://doi.org/10.1007/s11214-020-00711-9

Chavagnac, V. (2004). A geochemical and Nd isotopic study of Barberton komatiites (South Africa): Implication for the Archean mantle. *Lithos*, *75*(3–4), 253–281. https://doi.org/10.1016/j.lithos.2004.03.001

Chelle-Michou, C., McCarthy, A., Moyen, J. F., Cawood, P. A., & Capitanio, F. A. (2022). Make subductions diverse again. *Earth-Science Reviews*, *226*(January), 103966. https://doi.org/10.1016/j.earscirev.2022.103966

Clayton, R. N., O'Neil, J. R., & Mayeda, T. K. (1972). Oxygen isotope exchange between quartz and water. *Journal of Geophysical Research*, *77*(17), 3057–3067. https://doi.org/10.1029/jb077i017p03057

Clemens, J. D., Belcher, R. W., & Kisters, A. F. M. (2010). *The Heerenveen Batholith , Barberton Mountain Land , South Africa : Mesoarchaean , Potassic , Felsic Magmas Formed by Melting of an Ancient Subduction Complex*. *51*(5), 1099–1120. https://doi.org/10.1093/petrology/egq014

Clemens, J. D., Yearron, L. M., & Stevens, G. (2006). Barberton (South Africa) TTG magmas : Geochemical and experimental constraints on source-rock petrology , pressure of formation and tectonic setting. *Precambrian Research*, *151*, 53–78. https://doi.org/10.1016/j.precamres.2006.08.001

Cloete, M. (1991). An overview of metamorphism of the Barberton Greenstone belt. In *ICDP Project 280-Two Cratons and an OrogençExcursion Guidebook and Review Articles for a Field Workshop through Selected Archean Terranes of Swaziland, South Africa and Zimbabwe.* (pp. 84–98).

Compston, W., & Pidgeon, R. T. (1986). Jack Hills, evidence of more very old detrital zircons in Western Australia. *Nature*, *321*(6072), 766–769. https://doi.org/10.1038/321766a0

Condie, K. C. (2014). How to Make a Continent: Thirty-five Years of TTG Research. In *Evolution of Archean Crust and Early Life* (Issue January). https://doi.org/10.1007/978-94-007-7615-9

Condie, K. C. (2019). Earth's Oldest Rocks and Minerals. In M. J. Van Kranendonk, V. C. Bennett, & J. E. Hoffmann (Eds.), *Earth's Oldest Rocks* (pp. 5–24). Elsevier.

Condie, K. C., & Stern, R. J. (2023). Ophiolites: Identification and tectonic significance in space and time. *Geoscience Frontiers*, *14*(6), 101680. https://doi.org/10.1016/j.gsf.2023.101680

Connolly, B. D., Puchtel, I. S., Walker, R. J., Arevalo, R., Piccoli, P. M., Byerly, G., Robin-popieul, C., & Arndt, N. (2011). Highly siderophile element systematics of the 3 . 3 Ga Weltevreden komatiites , South Africa : Implications for early Earth history. *Earth and Planetary Science Letters*, *311*(3–4), 253–263. https://doi.org/10.1016/j.epsl.2011.09.039

Coogan, L. A., & Gillis, K. M. (2018a). Low-Temperature Alteration of the Seafloor: Impacts on Ocean Chemistry. *Annual Review of Earth and Planetary Sciences*, *46*, 21–45. https://doi.org/10.1146/annurev-earth-082517-010027

Coogan, L. A., & Gillis, K. M. (2018b). Temperature dependence of chemical exchange during seafloor weathering: Insights from the Troodos ophiolite. *Geochimica et Cosmochimica Acta*, *243*, 24–41. https://doi.org/10.1016/j.gca.2018.09.025

Cotten, J., Le Dez, A., Bau, M., Caroff, M., Maury, R. C., Dulski, P., Fourcade, S., Bohn, M., & Brousse, R. (1995). Origin of anomalous rare-earth element and yttrium enrichments in subaerially exposed basalts: Evidence from French Polynesia. *Chemical Geology*, *119*(1–4), 115–138. https://doi.org/10.1016/0009-2541(94)00102-E

Crawford, M. L., & Hollister, L. S. (1986). Metamorphic fluids: the evidence from fluid inclusions. *Fluid-Rock Interactions during Metamorphism*, *1971*, 1–35.

https://doi.org/10.1007/978-1-4612-4896-5_1

Cutts, K. A., Stevens, G., Hoffmann, J. E., Buick, I. S., Frei, D., & Münker, C. (2014). Paleo- to mesoarchean polymetamorphism in the barberton granite-greenstone belt, south africa: Constraints from U-Pb monazite and Lu-Hf garnet geochronology on the tectonic processes that shaped the belt. *Bulletin of the Geological Society of America*, *126*(3–4), 251–270. https://doi.org/10.1130/B30807.1

Cutts, K. A., Stevens, G., & Kisters, A. (2015). Reply to “paleo- to mesoarchean polymetamorphism in the barberton granite-greenstone belt, South Africa: Constraints from U-Pb monazite and Lu-Hf garnet geochronology on the tectonic processes that shaped the belt: Discussion” by M. Brown. *Bulletin of the Geological Society of America*, *127*(11–12), 1558–1563. https://doi.org/10.1130/B31304.1

Dauphas, N., Van Zuilen, M., Wadhwa, M., Davis, A. M., Marty, B., & Janney, P. E. (2004). Clues from Fe isotope variations on the origin of early Archean BIFs from Greenland. *Science*, *306*(5704), 2077–2080. https://doi.org/10.1126/science.1104639

de Vries, S. T., & Touret, J. L. R. (2007). Early Archaean hydrothermal fluids; a study of inclusions from the ~ 3.4 Ga Buck Ridge Chert, Barberton Greenstone Belt, South Africa. *Chemical Geology*, *237*(3–4), 289–302. https://doi.org/10.1016/j.chemgeo.2006.06.027

de Wit, M. J. E. (1982). Gliding and overthrust nappe tectonics in the Barberton Greenstone Belt. *Journal of Structural Geology*, *4*(2), 117–136.

de Wit, M. J., & Furnes, H. (2016). 3.5-Ga hydrothermal fields and diamictites in the Barberton Greenstone Belt-Paleoarchean crust in cold environments. *Science Advances*, *2*(2), 1–12. https://doi.org/10.1126/sciadv.1500368

de Wit, M. J., Furnes, H., & Robins, B. (2011). Geology and tectonostratigraphy of the Onverwacht Suite , Barberton Greenstone Belt , South Africa. *Precambrian Research*, *186*(October 2015), 1–27. https://doi.org/10.1016/j.precamres.2010.12.007

De Wit, M. J., Hart, R., Martin, A., & Abbott, P. (1982). Archean abiogenic and probable biogenic structures associated with mineralized hydrothermal vent systems and regional metasomatism, with implications for greenstone belt studies. *Economic Geology*, *77*(8), 1783–1802. https://doi.org/10.2113/gsecongeo.77.8.1783

Decker, N. B., Byerly, G. R., Thompson Stiegler, M., Lowe, D. R., & Stefurak, E. (2015). High resolution tephra and U/Pb chronology of the 3.33-3.26Ga Mendon Formation, Barberton Greenstone Belt, South Africa. *Precambrian Research*, *261*, 54–74. https://doi.org/10.1016/j.precamres.2015.02.003

Deng, Z., Chaussidon, M., Guitreau, M., Puchtel, I. S., & Dauphas, N. (2019). An oceanic subduction origin for Archean granitoids revealed by silicon isotopes. *Nature Geoscience*, *12*(September), 774–779. https://doi.org/10.1038/s41561-019-0407-6

Deutschmann, C., Hopp, J., Trieloff, M., & Ott, U. (2022). Entrapment history of aqueous fluids in Archean cherts from the Barberton Greenstone Belt, South Africa. *Precambrian Research*, *368*(September 2021), 106502. https://doi.org/10.1016/j.precamres.2021.106502

Diener, J. F. A., Stevens, G., Kisters, A. F. M., & Poujol, M. (2005). Metamorphism and exhumation of the basal parts of the Barberton greenstone belt, South Africa: Constraining the rates of Mesoarchaean tectonism. *Precambrian Research*, *143*(1–4), 87–112. https://doi.org/10.1016/j.precamres.2005.10.001

Dilek, Y., & Furnes, H. (2014). Ophiolites and their origins. *Elements*, *10*(2), 93–100. https://doi.org/10.2113/gselements.10.2.93

Ding, T., Wan, D., Bai, R., Zhang, Z., Shen, Y., & Meng, R. (2005). Silicon isotope abundance ratios and atomic weights of NBS-28 and other reference materials. *Geochimica et Cosmochimica Acta*, *69*(23), 5487–5494.

https://doi.org/10.1016/j.gca.2005.06.015

Doucet, L. S., Laurent, O., Ionov, D. A., Mattielli, N., Debaille, V., & Debouge, W. (2020). Archean lithospheric differentiation: Insights from Fe and Zn isotopes. *Geology*, *48*(10), 1028–1032. https://doi.org/10.1130/G47647.1

Drabon, N., Galić, A., Mason, P. R. D., & Lowe, D. R. (2019). Provenance and tectonic implications of the 3.28–3.23 Ga Fig Tree Group, central Barberton greenstone belt, South Africa. *Precambrian Research*, *325*(July 2018), 1–19. https://doi.org/10.1016/j.precamres.2019.02.010

Drabon, N., Kirkpatrick, H. M., Byerly, G. R., & Wooden, J. L. (2024). Trace elements in zircon record changing magmatic processes and the multi-stage build-up of Archean proto-continental crust. *Geochimica et Cosmochimica Acta*, *373*(March), 136–150. https://doi.org/10.1016/j.gca.2024.03.014

Drabon, N., & Lowe, D. R. (2021). Progressive accretion recorded in sedimentary rocks of the 3.28−3.23 Ga Fig Tree Group, Barberton Greenstone Belt. *GSA Bulletin*, *September*, 1–19. https://doi.org/10.1130/b35973.1

Duchac, K. C., & Hanor, J. S. (1987). Origin and timing of the metasomatic silification of an early Archean komatiite sequuence, Barberton Mountain Land, South Africa. *Precambrian Research*, *37*, 125–146.

Dupuis, R., Benoit, M., Nardin, E., & Méheut, M. (2015). Fractionation of silicon isotopes in liquids: The importance of configurational disorder. *Chemical Geology*, *396*(239), 254. https://doi.org/10.1126/science.ns-3.50.59

Dziggel, A., Stevens, G., Poujol, M., Anhaeusser, C. R., & Armstrong, R. A. (2002). Metamorphism of the granite – greenstone terrane south of the Barberton greenstone belt , South Africa : an insight into the tectono-thermal evolution of the ‘ lower ’ portions of the Onverwacht Group. *Precambrian Research*, *114*, 221–247.

Eiler, J. M. (2019). Oxygen isotope variations of basaltic lavas and upper mantle rocks. *Stable Isotope Geochemistry*, *43*, 319–364. https://doi.org/10.1515/9781501508745-008

Eiler, J. M., Crawford, A., Elliott, T., Farley, K. A., Valley, J. W., & Stolper, E. M. (2000). Oxygen isotope geochemistry of oceanic-arc lavas. *Journal of Petrology*, *41*(2), 229–256. https://doi.org/10.1093/petrology/41.2.229

Elderfield, H., Wheat, C. G., Mottl, M. J., Monnin, C., & Spiro, B. (1999). Fluid and geochemical transport through oceanic crust: A transect across the eastern flank of the Juan de Fuca Ridge. *Earth and Planetary Science Letters*, *172*(1–2), 151–165. https://doi.org/10.1016/S0012-821X(99)00191-0

Farber, K., Dziggel, A., Meyer, F. M., & Harris, C. (2016). Petrology , geochemistry and fluid inclusion analysis of altered komatiites of the Mendon Formation in the BARB4 drill core , Barberton greenstone belt , South Africa. *South African Journal of Geology*, *119*(4), 639–654. https://doi.org/10.2113/gssajg.119.4.639

Faure, K., & Harris, C. (1991). Oxygen and carbon isotope geochemistry of the 3 . 2 Ga Kaap Valley tonalite , Barberton greenstone belt , South Africa. *Precambrian Research*, *52*(1956), 301–319.

Fedo, C. E., & Whitehouse, M. J. (2002). Metasomatic origin of quartz-pyroxene rock, Akilia, Greenland, and implications earth’s earliest life. *Science*, *296*(5572), 1448–1452. https://doi.org/10.1126/science.1070336

Flament, N., Coltice, N., & Rey, P. F. (2008). A case for late-Archaean continental emergence from thermal evolution models and hypsometry. *Earth and Planetary Science Letters*, *275*(3–4), 326–336. https://doi.org/10.1016/j.epsl.2008.08.029

Foley, S. F., Buhre, S., & Jacob, D. E. (2003). Evolution of the Archaean crust by delamination and shallow subduction. *Nature*, *421*(6920), 249–252. https://doi.org/10.1038/nature01319

Fowler, A. P. G., & Zierenberg, R. A. (2015). Rare Earth Element Concentrations in Geothermal Fluids and Epidote from the Reykjanes Geothermal System , Iceland. *Proceedings of the World Geothermal Congress 2015*, *April*, 19–25.

Fralick, P., & Riding, R. (2015). Steep Rock Lake: Sedimentology and geochemistry of an Archean carbonate platform. *Earth-Science Reviews*, *151*, 132–175. https://doi.org/10.1016/j.earscirev.2015.10.006

Fu, B., Page, F. Z., Cavosie, A. J., Fournelle, J., Kita, N. T., Lackey, J. S., Wilde, S. A., & Valley, J. W. (2008). Ti-in-zircon thermometry: Applications and limitations. *Contributions to Mineralogy and Petrology*, *156*(2), 197–215. https://doi.org/10.1007/s00410-008-0281-5

Furnes, H., Banerjee, N., Muehlenbachs, K., Staudigel, H., & de Wit, M. J. (2004). Early Life Recorded in Archean Pillow Lavas. *Science*, *304*(April), 578–582.

Furnes, H., de Wit, M., & Robins, B. (2013). A review of new interpretations of the tectonostratigraphy, geochemistry and evolution of the Onverwacht Suite, Barberton Greenstone Belt, South Africa. *Gondwana Research*, *23*(2), 403–428. https://doi.org/10.1016/j.gr.2012.05.007

Furnes, H., Robins, B., & De Wit, M. J. (2012). Geochemistry and petrology of lavas in the upper onverwacht suite, Barberton Mountain Land, South Africa. *South African Journal of Geology*, *115*(2), 171–210. https://doi.org/10.2113/gssajg.115.2.171

Galili, N., Shemesh, A., Yam, R., Brailovsky, I., Sela-adler, M., Schuster, E. M., Collom, C., Bekker, A., Planavsky, N., Macdonald, F. A., Préat, A., Rudmin, M., Trela, W., & Sturesson, U. (2019). From Marine Iron Oxides. *Science*, *473*(August), 469–473.

Garçon, M. (2021). Episodic growth of felsic continents in the past 3.7 Ga. *Science Advances*, *7*(39). https://doi.org/10.1126/sciadv.abj1807

Garçon, M., Boyet, M., Carlson, R. W., Horan, M. F., Auclair, D., & Mock, T. D. (2018). Factors influencing the precision and accuracy of Nd isotope measurements by thermal ionization mass spectrometry. *Chemical Geology*, *476*(December 2017), 493–514. https://doi.org/10.1016/j.chemgeo.2017.12.003

Garçon, M., Carlson, R. W., Shirey, S. B., Arndt, N. T., Horan, M. F., & Mock, T. D. (2017). Erosion of Archean continents: The Sm-Nd and Lu-Hf isotopic record of Barberton sedimentary rocks. *Geochimica et Cosmochimica Acta*, *206*, 216–235. https://doi.org/10.1016/j.gca.2017.03.006

Geilert, S., Vroon, P. Z., & van Bergen, M. J. (2014). Silicon isotopes and trace elements in chert record early Archean basin evolution. *Chemical Geology*, *386*, 133–142. https://doi.org/10.1016/j.chemgeo.2014.07.027

German, C. R., & Seyfried, W. E. (2013). Hydrothermal Processes. In *Treatise on Geochemistry: Second Edition* (2nd ed., Vol. 8). Elsevier Ltd. https://doi.org/10.1016/B978-0-08-095975-7.00607-0

Gillis, K. M., & Robinson, P. T. (1990). Patterns and Process of Alteration in the Lavas and Dykes of the Troodos Ophiolite, Cyprus. *Journal of Geophysical Research*, *95*(523–548).

Grant, A. (1986). The isocon diagram - A simple solution to Gresens' Equation for metamorphic alteration. *Economic Geology*, *81*, 1976–1982.

Grant, J. A. (2005). Isocon analysis : A brief review of the method and applications. *Physics and Chemistry of the Earth*, *30*, 997–1004. https://doi.org/10.1016/j.pce.2004.11.003

Grosch, E. G. (2018). Metamorphic processes preserved in early Archean supracrustal rocks of the Barberton Greenstone Belt, South Africa. *Geological Society Special Publication*, *478*. https://doi.org/10.6084/m9.figshare.c.4139102

Grosch, E. G., Ndlela, S., Murphy, D., McLoughlin, N., Trubac, J., & Slama, J. (2022). Geochemistry of mafic-ultramafic rocks of the 3.33 Ga Kromberg type-section, Barberton greenstone belt, South Africa: Implications for early Earth geodynamic processes. *Chemical Geology*, *605*(February), 120947. https://doi.org/10.1016/j.chemgeo.2022.120947

Grosch, E. G., & Slama, J. (2017). Evidence for 3.3-billion-year-old oceanic crust in the Barberton greenstone belt, South Africa. *Geology*, *45*(8), 695–698. https://doi.org/10.1130/G39035.1

Grosch, E. G., Vidal, O., Abu-alam, T., & Mcloughlin, N. (2012). P - T Constraints on the Metamorphic Evolution of the Paleoarchean Kromberg T Barberton Greenstone Belt , South Africa. *Journal of Petrology*, *53*(3). https://doi.org/10.1093/petrology/egr070

Grosch, E. G., Viola, G., & Ndlela, S. (2020). Geological record of Paleoarchean oceanic flake tectonics preserved in the c. 3.3 Ga Kromberg volcanic type-section, Barberton greenstone belt, South Africa. *Precambrian Research*, *346*. https://doi.org/10.1016/j.precamres.2020.105815

Guitreau, M., Gannoun, A., Deng, Z., Chaussidon, M., Moynier, F., Barbarin, B., & Marin-Carbonne, J. (2022). Stable isotope geochemistry of silicon in granitoid zircon. *Geochimica et Cosmochimica Acta*, *316*, 273–294. https://doi.org/10.1016/j.gca.2021.09.029

Hanor, J. S., & Duschac, K. C. (1990). Isovolumetric Silicification of Early Archean Komatiites : Geochemical Mass Balances and Constraints on Origin. *The Journal of Geology*, *98*(6), 863–877.

Harris, C., le Roux, P., Cochrane, R., Martin, L., Duncan, A. R., Marsh, J. S., le Roex, A. P., & Class, C. (2015). The oxygen isotope composition of Karoo and Etendeka picrites: High δ18O mantle or crustal contamination? *Contributions to Mineralogy and Petrology*, *170*(1). https://doi.org/10.1007/s00410-015-1164-1

Hart, S. R., & Staudigel, H. (1982). The control of alkalies and uranium in seawater by ocean crust alteration. *Earth and Planetary Science Letters*, *58*(2), 202–212. https://doi.org/10.1016/0012-821X(82)90194-7

Hartnady, M. I. H., Johnson, T. E., Schorn, S., Hugh Smithies, R., Kirkland, C. L., & Richardson, S. H. (2022). Fluid processes in the early Earth and the growth of continents. *Earth and Planetary Science Letters*, *594*. https://doi.org/10.1016/j.epsl.2022.117695

Hauff, F., Hoernle, K., & Schmidt, A. (2003). Sr-Nd-Pb composition of Mesozoic Pacific oceanic crust (Site 1149 and 801, ODP Leg 185): Implications for alteration of ocean crust and the input into the Izu-Bonin-Mariana subduction system. *Geochemistry, Geophysics, Geosystems*, *4*(8). https://doi.org/10.1029/2002GC000421

Hawkesworth, C. J., & Kemp, A. I. S. (2006). Using hafnium and oxygen isotopes in zircons to unravel the record of crustal evolution. *Chemical Geology*, *226*(3–4), 144–162. https://doi.org/10.1016/j.chemgeo.2005.09.018

Hayashi, T., Tanimizu, M., & Tanaka, T. (2004). Origin of negative Ce anomalies in Barberton sedimentary rocks, deduced from La-Ce and Sm-Nd isotope systematics. *Precambrian Research*, *135*(4 SPEC. ISS.), 345–357. https://doi.org/10.1016/j.precamres.2004.09.004

Hayles, J. A., Yeung, L. Y., Homann, M., Banerjee, A., Jiang, H., Shen, B., & Lee, C.-T. (2019). Three Billion Year Secular Evolution of the Triple Oxygen Isotope Composition of Marine Chert. *Submitted to Earth and Planetary Science Letters*, 1–30.

Heinrichs, T. (1984). The Umsoli chert, turbidite testament for a major phreatoplinian event at the onverwacht/fig tree transition (Swaziland supergroup, Archaean, South Africa). *Precambrian Research*, *24*(3–4), 237–283. https://doi.org/10.1016/0301-9268(84)90061-5

Hernández-Uribe, D. (2024). Generation of Archaean oxidizing and wet magmas from mafic crustal overthickening. *Nature Geoscience*, 8–10. https://doi.org/10.1038/s41561-024-

01489-z

Herwartz, D., Pack, A., & Nagel, T. J. (2021). A CO2 greenhouse efficiently warmed the early Earth and decreased seawater 18O/16O before the onset of plate tectonics. *Proceedings of the National Academy of Sciences of the United States of America*, *118*(23). https://doi.org/10.1073/pnas.2023617118

Herzberg, C., Condie, K., & Korenaga, J. (2010). Thermal history of the Earth and its petrological expression. *Earth and Planetary Science Letters*, *292*(1–2), 79–88. https://doi.org/10.1016/j.epsl.2010.01.022

Herzberg, C. T., & Ohtani, E. (1988). Origin of komatiite at high pressures. *Earth and Planetary Science Letters*, *88*(3–4), 321–329. https://doi.org/10.1016/0012-821X(88)90088-X

Heubeck, C. (2019). *The Moodies Group—a High-Resolution Archive of Archaean Surface Processes and Basin-Forming Mechanisms*. https://doi.org/10.1007/978-3-319-78652-0_6

Heubeck, C., & Lowe, D. R. (1994). Depositional and tectonic setting of the Archean Moodies Group, Berberton Greenstone Belt, South Africa. *Precambrian Research*, *66*, 257–290.

Hickman-lewis, K., Cavalazzi, B., Foucher, F., & Westall, F. (2018). Most ancient evidence for life in the Barberton greenstone belt : Microbial mats and biofabrics of the ~ 3 . 47 Ga Middle Marker horizon. *Precambrian Research*, *312*(April), 45–67. https://doi.org/10.1016/j.precamres.2018.04.007

Hoefs. (2009). Stable isotope geochemistry. In *Stable Isotope Geochemistry*. https://doi.org/10.1017/cbo9780511809323.008

Hoffman, S. E., Wilson, M., & Stakes, D. S. (1986). Inferred oxygen isotope profile of Archean oceanic crust, Onverwacht Group, South Africa. *Nature*, *321*, 55–58.

Hofmann, A. (2005). The geochemistry of sedimentary rocks from the Fig Tree Group , Barberton greenstone belt : Implications for tectonic , hydrothermal and surface processes during mid-Archaean times. *Precambrian Research*, *143*, 23–49. https://doi.org/10.1016/j.precamres.2005.09.005

Hofmann, A., Bolhar, R., Orberger, B., & Foucher, F. (2013). Cherts of the Barberton Greenstone Belt, South Africa: Petrology and Trace-Element Geochemistry of 3.5 To 3.3 Ga Old Silicified Volcaniclastic Sediments. *South African Journal of Geology*, *116*(2), 297–322. https://doi.org/10.2113/gssajg.116.2.297

Hofmann, A., & Harris, C. (2008). Silica alteration zones in the Barberton greenstone belt : A window into subseafloor processes 3.5-3.3 Ga ago. *Chemical Geology*, *257*, 224–242. https://doi.org/10.1016/j.chemgeo.2008.09.015

Hofmann, A., Jodder, J., Xie, H., Bolhar, R., Whitehouse, M., & Elburg, M. (2022). The Archaean geological history of the Singhbhum Craton, India – a proposal for a consistent framework of craton evolution. *Earth-Science Reviews*, *228*(January), 103994. https://doi.org/10.1016/j.earscirev.2022.103994

Hofmann, A., & Wilson, A. H. (2007). Chapter 5.5 Silicified Basalts, Bedded Cherts and Other Sea Floor Alteration Phenomena of the 3.4 Ga Nondweni Greenstone Belt, South Africa. *Developments in Precambrian Geology*, *15*(07), 571–605. https://doi.org/10.1016/S0166-2635(07)15055-6

Holland, T. J. B., Green, E. C. R., & Powell, R. (2018). Melting of peridotites through to granites: A simple thermodynamic model in the system KNCFMASHTOCr. *Journal of Petrology*, *59*(5), 881–900. https://doi.org/10.1093/petrology/egy048

Holland, T. J. B., & Powell, R. (2011). An improved and extended internally consistent thermodynamic dataset for phases of petrological interest, involving a new equation of state for solids. *Journal of Metamorphic Geology*, *29*(3), 333–383.

https://doi.org/10.1111/j.1525-1314.2010.00923.x

Holmden, C., & Muehlenbachs, K. (1993). The 18O/16O Ratio of 2-Billion-Year-Old Seawater Inferred from Ancient Oceanic Crust. *Science*, *259*, 1733–1736.

Hongo, Y., Obata, H., Gamo, T., Nakaseama, M., Ishibashi, J., Konno, U., Saegusa, S., Ohkubo, S., & Tsunogai, U. (2007). Rare earth elements in the hydrothermal system at Okinawa Trough back-arc basin. *Geochemical Journal*, *41*(1), 1–15. https://doi.org/10.2343/geochemj.41.1

Hyslop, E. V., Valley, J. W., Johnson, C. M., & Beard, B. L. (2008). The effects of metamorphism on O and Fe isotope compositions in the Biwabik Iron Formation, northern Minnesota. *Contributions to Mineralogy and Petrology*, *155*(3), 313–328. https://doi.org/10.1007/s00410-007-0244-2

Ibarra, D. E., Yanchilina, A. G., Lloyd, M. K., Methner, K. A., Chamberlain, C. P., Yam, R., Shemesh, A., & Stolper, D. A. (2022). Triple oxygen isotope systematics of diagenetic recrystallization of diatom opal-A to opal-CT to microquartz in deep sea sediments. *Geochimica et Cosmochimica Acta*, *320*, 304–323. https://doi.org/10.1016/j.gca.2021.11.027

Israel, C., Boyet, M., Doucelance, R., Bonnand, P., Frossard, P., Auclair, D., Bouvier, A., & Geoinstitut, B. (2020). Formation of the Ce-Nd mantle array : crustal extraction vs . recycling by subduction. *Earth and Planetary Science Letters*, *530*, 1–11.

J De Ronde, C. E., Der Channer, D. M., Faure, K., Bray, C. J., & C Spooner, E. W. (1997). Fluid chemistry of Archean seafloor hydrothermal vents: Implications for the composition of circa 3.2 Ga seawater. In *Geochimica et Cosmochimica Acta* (Vol. 61, Issue 19).

Jaffrés, J. B. D., Shields, G. A., & Wallmann, K. (2007). The oxygen isotope evolution of seawater: A critical review of a long-standing controversy and an improved geological water cycle model for the past 3.4 billion years. *Earth-Science Reviews*, *83*(1–2), 83–122. https://doi.org/10.1016/j.earscirev.2007.04.002

Jagoutz, O., Schmidt, M. W., Enggist, A., Burg, J. P., Hamid, D., & Hussain, S. (2013). TTG-type plutonic rocks formed in a modern arc batholith by hydrous fractionation in the lower arc crust. *Contributions to Mineralogy and Petrology*, *166*(4), 1099–1118. https://doi.org/10.1007/s00410-013-0911-4

Javaux, E. J., & Marshall, C. P. (2005). Tracking the record of early life. In *Pre-Cambrian to Palaeozoic Palaeopalynology and Palaeobotany.* (Vol. 2005, pp. 27–31).

Johnson, B. W., & Wing, B. A. (2020). Limited Archaean continental emergence reflected in an early Archaean 18O-enriched ocean. *Nature Geoscience*, *13*(3), 243–248. https://doi.org/10.1038/s41561-020-0538-9

Johnson, T. E., Brown, M., Gardiner, N. J., Kirkland, C. L., & Smithies, R. H. (2017). Earth's first stable continents did not form by subduction. *Nature*, *543*(7644), 239–242. https://doi.org/10.1038/nature21383

Kamber, B. S. (2010). *Archean mafic – ultramafic volcanic landmasses and their effect on ocean – atmosphere chemistry*. *274*, 19–28. https://doi.org/10.1016/j.chemgeo.2010.03.009

Kareem, K., & Byerly, G. R. (2003). Petrology and geochemistry of 3.3 Ga komatiites-Weltevreden formation, Barberton Greenstone Belt. *Lunar and Planetary Science*, 1–2.

Kasting, J. F., Howard, M. T., Wallmann, K., Veizer, J., Shields, G., & Jaffrés, J. (2006). Paleoclimates, ocean depth, and the oxygen isotopic composition of seawater. *Earth and Planetary Science Letters*, *252*(1–2), 82–93. https://doi.org/10.1016/j.epsl.2006.09.029

Katijima, K., Mauyama, S., Utsunomiya, S., & Liou, J. G. (2001). Sea-floor hydrothermal alteration at an Archaean mid-ocean ridge. *Journal of Metamorphic Geology*, *19*, 583–599.

Kelley, K. A., Plank, T., Ludden, J., & Staudigel, H. (2003). Composition of altered oceanic crust at ODP Sites 801 and 1149. *Geochemistry, Geophysics, Geosystems*, *4*(6). https://doi.org/10.1029/2002GC000435

Kisters, A. F. M., & Anhaeusser, C. R. (1995). The structural significance of the Steynsdorp pluton and anticline within the tectono- magmatic framework of the Barberton Mountain Land. *South African Journal of Geology*, *98*, 43–51.

Kisters, A. F. M., Belcher, R. W., Poujol, M., & Dziggel, A. (2010). Continental growth and convergence-related arc plutonism in the Mesoarchaean : Evidence from the Barberton granitoid-greenstone terrain , South Africa. *Precambrian Research*, *178*(1–4), 15–26. https://doi.org/10.1016/j.precamres.2010.01.002

Kisters, A. F. M., Stevens, G., Dziggel, A., & Armstrong, R. A. (2003). Extensional detachment faulting and core-complex formation in the southern Barberton granite – greenstone terrain , South Africa : evidence for a 3 . 2 Ga orogenic collapse. *Precambrian Research*, *127*, 355–378. https://doi.org/10.1016/j.precamres.2003.08.002

Kleine, B. I., Stefánsson, A., Halldórsson, S. A., Whitehouse, M. J., & Jónasson, K. (2018). Silicon and oxygen isotopes unravel quartz formation processes in the Icelandic crust. *Geochemical Perspectives Letters*, *7*, 5–11. https://doi.org/10.7185/geochemlet.1811

Kleinhanns, I. C., Kramers, J. D., & Kamber, B. S. (2003). Importance of water for Archaean granitoid petrology : a comparative study of TTG and potassic granitoids from Barberton Mountain Land, South Africa. *Contribution to Mineralogy and Petrology*, *145*, 377–389. https://doi.org/10.1007/s00410-003-0459-9

Knauth, L. P., & Lowe, D. R. (1978). Oxygen isotope geochemistry of cherts from the Onverwacht (3.4 billion years) Group, Transvaal, South Africa, with implications for secular variations in the isotopic composition of cherts. In *Earth and Planetary Science Letters* (Vol. 41).

Knauth, L. P., & Lowe, D. R. (2003). High Archean climatic temperature inferred from oxygen isotope geochemistry of cherts in the 3 . 5 Ga Swaziland Supergroup , South Africa. *Geological Society of America Bulletin*, *5*, 566–580.

Kolodny, Y., & Epstein, S. (1976). Stable isotope geochemistry of deep sea cherts. *Geochimica et Cosmochimica Acta*, *40*(10), 1195–1209. https://doi.org/10.1016/0016-7037(76)90155-1

Kröner, A., Anhaeusser, C. R., Hoffmann, J. E., Wong, J., Geng, H., Hegner, E., Xie, H., Yang, J., & Liu, D. (2016). Chronology of the oldest supracrustal sequences in the Palaeoarchaean Barberton Greenstone Belt, South Africa and Swaziland. *Precambrian Research*, *279*, 123–143. https://doi.org/10.1016/j.precamres.2016.04.007

Kusky, T. M., & Polat, A. (1999). Growth of granite – greenstone terranes at convergent margins , and stabilization of Archean cratons. *Tectonophysics*, *305*, 43–73.

Lackey, J. S., Valley, J. W., Chen, J. H., & Stockli, D. F. (2008). Dynamic magma systems, crustal recycling, and alteration in the Central Sierra Nevada batholith: The oxygen isotope record. *Journal of Petrology*, *49*(7), 1397–1426. https://doi.org/10.1093/petrology/egn030

Lahaye, Y., Arndt, N., Byerly, G., Chauvel, C., Fourcade, S., & Gruau, G. (1995). The influence of alteration on the trace-element and Nd isotopic compositions of komatiites. *Chemical Geology*, *126*, 43–64.

Lanari, P., & Piccoli, F. (2020). New horizons in quantitative compositional mapping - Analytical conditions and data reduction using XMapTools. *IOP Conference Series: Materials Science and Engineering*, *891*(1). https://doi.org/10.1088/1757-899X/891/1/012016

Lanari, P., Vidal, O., Andrade, V. De, Dubacq, B., Grosch, E. G., Schwartz, S., Lanari, P., Vidal, O., Andrade, V. De, Dubacq, B., Lewin, E., & Xmaptools, A. (2014).

XMapTools : A MATLAB © -based program for electron microprobe X-ray image processing and geothermobarometry. *Computers and Geosciences*.

Lanier, W. P., & Lowe, D. R. (1982). Sedimentology of the middleker (3.4 Ga), Onverwacht group, Transvaal, South Africa. *Precambrian Research*, *18*, 237–260.

Laurent, O., Björnsen, J., Wotzlaw, J.-F., Bretscher, S., Pimenta Silva, M., Moyen, J.-F., Ulmer, P., & Bachmann, O. (2020). Earth's earliest granitoids are crystal-rich magma reservoirs tapped by silicic eruptions. *Nature Geoscience*, *13*(2), 163–169. https://doi.org/10.1038/s41561-019-0520-6

Laurent, O., Guitreau, M., Bruand, E., & Moyen, J. (2024). At the Dawn of Continents: Archean Tonalite-Trondhjemite- Granodiorite Suites. *Elements*, *20*, 174–179. https://doi.org/10.2138/gselements.20.3.174

Laurent, O., Martin, H., Moyen, J. F., & Doucelance, R. (2014). The diversity and evolution of late-Archean granitoids: Evidence for the onset of "modern-style" plate tectonics between 3.0 and 2.5 Ga. *Lithos*, *205*, 208–235. https://doi.org/10.1016/j.lithos.2014.06.012

Laurie, A., & Stevens, G. (2012). Water-present eclogite melting to produce Earth's early felsic crust. *Chemical Geology*, *314–317*, 83–95. https://doi.org/10.1016/j.chemgeo.2012.05.001

Lawrence, M. G., Greig, A., Collerson, K. D., & Kamber, B. S. (2006). Rare earth element and yttrium variability in South East Queensland waterways. *Aquatic Geochemistry*, *12*(1), 39–72. https://doi.org/10.1007/s10498-005-4471-8

Ledevin, M., Arndt, N., Chauvel, C., Jaillard, E., & Simionovici, A. (2019). The sedimentary origin of black and white banded cherts of the Buck Reef, Barberton, South Africa. *Geosciences (Switzerland)*, *9*(10), 17–24. https://doi.org/10.3390/geosciences9100424

Ledevin, M., Arndt, N., Davaille, A., Ledevin, R., & Simionovici, A. (2015). The rheological behaviour of fracture-filling cherts: Example of Barite Valley dikes, Barberton Greenstone Belt, South Africa. *Solid Earth*, *6*(1), 253–269. https://doi.org/10.5194/se-6-253-2015

Ledevin, M., Arndt, N., Simionovici, A., Jaillard, E., & Ulrich, M. (2014). Silica precipitation triggered by clastic sedimentation in the Archean : New petrographic evidence from cherts of the Kromberg type section , South Africa. *Precambrian Research*, *255*, 316–334. https://doi.org/10.1016/j.precamres.2014.10.009

Lei, K., Wang, H., Wang, X., Zhang, Q., & Li, X. (2023). Decoupled Zircon Si–O Isotopes Tracing the Supracrustal Silicification and Komatiitic-Derived Fluids in the Source of TTGs. *Geophysical Research Letters*, *50*(16), 1–9. https://doi.org/10.1029/2023GL104002

Lei, K., Zhang, Q., Liu, Y., Lu, K., Wu, L. G., He, S., & Li, X. H. (2023). Heavy silicon and oxygen isotope signatures of TTGs formed in distinct tectonic settings. *Precambrian Research*, *397*(October), 107202. https://doi.org/10.1016/j.precamres.2023.107202

Li, C. F., Li, X. H., Li, Q. L., Guo, J. H., Li, X. H., & Yang, Y. H. (2012). Rapid and precise determination of Sr and Nd isotopic ratios in geological samples from the same filament loading by thermal ionization mass spectrometry employing a single-step separation scheme. *Analytica Chimica Acta*, *727*, 54–60. https://doi.org/10.1016/j.aca.2012.03.040

Liljestrand, F. L., Knoll, A. H., Tosca, N. J., Cohen, P. A., Macdonald, F. A., Peng, Y., & Johnston, D. T. (2020). The triple oxygen isotope composition of Precambrian chert. *Earth and Planetary Science Letters*, *537*, 116167. https://doi.org/10.1016/j.epsl.2020.116167

Lowe, D. R., & Byerly, G. R. (1986). Archean flow-top alteration zones formed initially in a low-temperature sulphate-rich environment. *Nature*, *324*, 245–248.

Lowe, D. R., & Byerly, G. R. (1999). *Geologic evolution of the Barberton Grenstone Belt,* *South Africa* (The Geological Society of America (ed.)).

Lowe, D. R., & Byerly, G. R. (2007a). An overview of the geology of the Barberton greenstone belt and vicinity: implications for early crustal development. In M. J. Van Kranendonk, R. H. Smithies, & V. C. Bennett (Eds.), *Developments in Precambrian Geology* (Vol. 15, Issue 07, pp. 481–526). Elsevier B.V. https://doi.org/10.1016/S0166-2635(07)15053-2

Lowe, D. R., & Byerly, G. R. (2007b). Ironstone bodies of the Barberton greenstone belt, South Africa: Products of a Cenozoic hydrological system, not Archean hydrothermal vents! *Bulletin of the Geological Society of America*, *119*(1–2), 65–87. https://doi.org/10.1130/B25997.1

Lowe, D. R., & Byerly, G. R. (2020). The non-glacial and non-cratonic origin of an early Archean felsic volcaniclastic unit, Barberton Greenstone Belt, South Africa. *Precambrian Research*, *341*(September 2019), 105647. https://doi.org/10.1016/j.precamres.2020.105647

Lowe, D. R., Ibarra, D. E., Drabon, N., & Chamberlain, C. P. (2020). Constraints on surface temperature 3.4 billion years ago based on Triple Oxygen isotopes from the Barberton greenstone belt, South Africa, and the problem of sample selection. *American Journal of Science*, *320*(9). https://doi.org/10.2475/11.2020.02

Lugmair, G. W., & Marti, K. (1978). Lunar initial 143Nd-144Nd; Differential evolution of the lunar crust and mantle. *Earth and Planetary Science Letters*, *39*, 349–357.

Luz, B., & Barkan, E. (2010). Variations of 17O/16O and 18O/16O in meteoric waters. *Geochimica et Cosmochimica Acta*, *74*, 6276–6286. https://doi.org/10.1016/j.gca.2010.08.016

Mackenzie, F. T., & Kump, L. R. (1995). Reverse Weathering, Clay Mineral Formation, and Oceanic Element Cycles. *Science*, *270*(5236), 586–586. https://doi.org/10.1126/science.270.5236.586

Maliva, R. G., Knoll, A. H., & Simonson, B. M. (2005). Secular change in the Precambrian silica cycle: Insights from chert petrology. *Bulletin of the Geological Society of America*, *117*(7–8), 835–845. https://doi.org/10.1130/B25555.1

Manning, C. E., Mojzsis, S. J., & Harrison, T. M. (2006). Geology, age and origin of supracrustal rocks at Akilia, West Greenland. *American Journal of Science*, *306*(5), 303–366. https://doi.org/10.2475/05.2006.02

Marin-Carbonne, J., Chaussidon, M., Boiron, M.-C., & Robert, F. (2011). A combined in situ oxygen, silicon isotopic and fluid inclusion study of a chert sample from Onverwacht Group (3.35Ga, South Africa): New constraints on fluid circulation. *Chemical Geology*, *286*(3–4), 59–71. https://doi.org/10.1016/j.chemgeo.2011.02.025

Marin-Carbonne, J., Chaussidon, M., & Robert, F. (2012). Micrometer-scale chemical and isotopic criteria (O and Si) on the origin and history of Precambrian cherts: Implications for paleo-temperature reconstructions. *Geochimica et Cosmochimica Acta*, *92*, 129–147. https://doi.org/10.1016/j.gca.2012.05.040

Marin-Carbonne, J., Faure, F., Chaussidon, M., Jacob, D., & Robert, F. (2013). A petrographic and isotopic criterion of the state of preservation of Precambrian cherts based on the characterization of the quartz veins. *Precambrian Research*, *231*, 290–300. https://doi.org/10.1016/j.precamres.2013.03.019

Marin, J., Chaussidon, M., & Robert, F. (2010). Microscale oxygen isotope variations in 1.9 Ga Gunflint cherts: Assessments of diagenesis effects and implications for oceanic paleotemperature reconstructions. *Geochimica et Cosmochimica Acta*, *74*(1), 116–130. https://doi.org/10.1016/j.gca.2009.09.016

Martin, H. (1987). Petrogenesis of archaean trondhjemites, tonalites, and granodiorites from Eastern Finland: Major and trace element geochemistry. *Journal of Petrology*, *28*(5), 921–953. https://doi.org/10.1093/petrology/28.5.921

Martin, H. (1993). The mechanisms of petrogenesis of the Archaean continental crust-Comparison with modern processes. *Lithos*, *30*(3–4), 373–388. https://doi.org/10.1016/0024-4937(93)90046-F

Martin, H., Albarède, F., Claeys, P., Gargaud, M., Marty, B., Morbidelli, A., & Pinti, D. L. (2006). Building of a habitable planet. In *Earth, Moon and Planets* (Vol. 98, Issues 1–4, pp. 97–151). https://doi.org/10.1007/s11038-006-9088-4

Martin, H., & Moyen, J. F. (2002). Secular changes in tonalite-trondhjemite-granodiorite composition as markers of the progressive cooling of Earth. *Geology*, *30*(4), 319–322. https://doi.org/10.1130/0091-7613(2002)030<0319:SCITTG>2.0.CO;2

Martin, H., Moyen, J. F., Guitreau, M., Blichert-Toft, J., & Le Pennec, J. L. (2014). Why Archaean TTG cannot be generated by MORB melting in subduction zones. *Lithos*, *198–199*(1), 1–13. https://doi.org/10.1016/j.lithos.2014.02.017

Martin, H., Smithies, R. H., Rapp, R., Moyen, J. F., & Champion, D. (2005). An overview of adakite, tonalite-trondhjemiten-granodiorite (TTG), and sanukitoid: Relationships and some implications for crustal evolution. *Lithos*, *79*(1-2 SPEC. ISS.), 1–24. https://doi.org/10.1016/j.lithos.2004.04.048

Marty, B., Avice, G., Bekaert, D. V., & Broadley, M. W. (2018). Salinity of the Archaean oceans from analysis of fluid inclusions in quartz. *Comptes Rendus - Geoscience*, *350*(4), 154–163. https://doi.org/10.1016/j.crte.2017.12.002

Mattey, D., Lowry, D., & Macpherson, C. (1994). Oxygen isotope composition of mantle peridotite. *Earth and Planetary Science Letters*, *128*(3–4), 231–241. https://doi.org/10.1016/0012-821X(94)90147-3

McLennan, S. M., Taylor, S. R., & Kröner, A. (1983). Geochemical evolution of Archean shales from South Africa. I. The Swaziland and Pongola Supergroups. *Precambrian Research*, *22*(1–2), 93–124. https://doi.org/10.1016/0301-9268(83)90060-8

Meija, J., Coplen, T. B., Berglund, M., Brand, W. A., De Bièvre, P., Gröning, M., Holden, N. E., Irrgeher, J., Loss, R. D., Walczyk, T., & Prohaska, T. (2016). Isotopic compositions of the elements 2013 (IUPAC Technical Report). *Pure and Applied Chemistry*, *88*(3), 293–306. https://doi.org/10.1515/pac-2015-0503

Meuhlenbachs, K., & Clayton, R. N. (1976). Oxygen Isotope Composition of the Oceanic Crust and Its Bearing on Seawater. *J Geophys Res*, *81*(23), 4365–4369. https://doi.org/10.1029/jb081i023p04365

Middlemost, E. A. K. (1989). Iron oxidation ratios, norms and the classification of volcanic rocks. *Chemical Geology*, *77*(1), 19–26. https://doi.org/10.1016/0009-2541(89)90011-9

Mills, R. A., & Elderfield, H. (1995). Rare earth element geochemistry of hydrothermal deposits from the active TAG Mound, 26°N Mid-Atlantic Ridge. *Geochimica et Cosmochimica Acta*, *59*(17), 3511–3524. https://doi.org/10.1016/0016-7037(95)00224-N

Moreira, H., Storey, C., Bruand, E., Darling, J., Fowler, M., Cotte, M., Villalobos-Portillo, E. E., Parat, F., Seixas, L., Philippot, P., & Dhuime, B. (2023). Sub-arc mantle fugacity shifted by sediment recycling across the Great Oxidation Event. *Nature Geoscience*, *16*(10), 922–927. https://doi.org/10.1038/s41561-023-01258-4

Moreira, H., Storey, C., Fowler, M., Seixas, L., & Dunlop, J. (2020). Petrogenetic processes at the tipping point of plate tectonics: Hf-O isotope ternary modelling of Earth's last TTG to sanukitoid transition. *Earth and Planetary Science Letters*, *551*. https://doi.org/10.1016/j.epsl.2020.116558

Moyen, J.-F., Stevens, G., Kisters, A. F. M., Belcher, R. W., & Lemirre, B. (2019). TTG Plutons of the Barberton Granitoid-Greenstone Terrain, South Africa. In *Earth's Oldest Rocks*. https://doi.org/10.1016/b978-0-444-63901-1.00025-3

Moyen, J. F. (2009). Lithos High Sr / Y and La / Yb ratios : The meaning of the " adakitic signature .” *Lithos*, *112*, 556–574. http://dx.doi.org/10.1016/j.lithos.2009.04.001

Moyen, J. F., & Laurent, O. (2018). Archaean tectonic systems: A view from igneous rocks. *Lithos*, *302–303*, 99–125. https://doi.org/10.1016/j.lithos.2017.11.038

Moyen, J. F., & Stevens, G. (2006). Experimental constraints on TTG petrogenesis: Implications for archean geodynamics. *Geophysical Monograph Series*, *164*, 149–175. https://doi.org/10.1029/164GM11

Moyen, J. F., Stevens, G., & Kisters, A. (2006). Record of mid-Archaean subduction from metamorphism in the Barberton terrain, South Africa. *Nature*, *442*(7102), 559–562. https://doi.org/10.1038/nature04972

Moyen, J. F., & van Hunen, J. (2012). Short-term episodicity of Archaean plate tectonics. *Geology*, *40*(5), 451–454. https://doi.org/10.1130/G322894.1

Moyen, J. F., Zeh, A., Cuney, M., Dziggel, A., & Carrouée, S. (2021). The multiple ways of recycling Archaean crust: A case study from the ca. 3.1 Ga granitoids from the Barberton Greenstone Belt, South Africa. *Precambrian Research*, *353*(November 2020), 105998. https://doi.org/10.1016/j.precamres.2020.105998

Moyen, J., Stevens, G., Kisters, A. F. M., Belcher, R. W., & Lemirre, B. (2019). TTG Plutons of the Barberton Granitoid- Greenstone Terrain , South Africa. In *Earth’s Oldest Rocks* (pp. 615–648).

Muehlenbachs, K. (1998). The oxygen isotopic composition of the oceans, sediments and the seafloor. *Chemical Geology*, *145*(3–4), 263–273. https://doi.org/10.1016/S0009-2541(97)00147-2

Mühlberg, M., Stevens, G., Moyen, J., Kisters, A. F. M., & Lana, C. (2021). Thermal evolution of the Stolzburg Block , Barberton granitoid-greenstone terrain , South Africa : Implications for Paleoarchean tectonic processes. *Precambrian Research*, *359*(February 2020), 106082. https://doi.org/10.1016/j.precamres.2020.106082

Murphy, M. E., Macdonald, J. E., Fischer, S., Gardiner, N. J., White, R. W., & Savage, P. S. (2024). Silicon isotopes in an Archaean migmatite confirm seawater silicification of TTG sources. *Geochimica et Cosmochimica Acta*, *368*(January), 34–49. https://doi.org/10.1016/j.gca.2024.01.018

Nabelek, P. I. (1987). General equations for modeling fluid/rock interaction using trace element and isotopes. *Geochemica et Cosmochimica Acta*, *51*, 1765–1769.

Nagel, T. J., Hoffmann, J. E., & Münker, C. (2012). Generation of Eoarchean tonalite-trondhjemite-granodiorite series from ahickened mafic arc crust. *Geology*, *40*(4), 375–378. https://doi.org/10.1130/G32729.1

Nakamura, K., & Kato, Y. (2004). Carbonatization of oceanic crust by the seafloor hydrothermal activity and its significance as a CO2 sink in the Early Archean. *Geochimica et Cosmochimica Acta*, *68*(22), 4595–4618. https://doi.org/10.1016/j.gca.2004.05.023

Nebel, O., Capitanio, F. A., Moyen, J. F., Weinberg, R. F., Clos, F., Nebel-Jacobsen, Y. J., & Cawood, P. A. (2018). When crust comes of age: On the chemical evolution of Archaean, felsic continental crust by crustal drip tectonics. *Philosophical Transactions of the Royal Society A: Mathematical, Physical and Engineering Sciences*, *376*(2132). https://doi.org/10.1098/rsta.2018.0103

Newton, R. C. (1989). Metamorphic fluids in the deep crust. *Annual Review of Earth and Planetary Sciences*, *17*, 385–412.

O’Neil, J., & Carlson, R. W. (2017). Building Archean cratons from Hadean mafic crust. *Scientific Reports*, *355*(6330), 1199–1202. https://doi.org/10.1126/science.aah3823 1202

O’Neil, J., Carlson, R. W., Francis, D., & Stevenson, R. K. (2008). Neodymium-142 evidence for hadean mafic crust. *Science*, *321*(5897), 1828–1831. https://doi.org/10.1126/science.1161925

O'Neil, J., Carlson, R. W., Paquette, J., Francis, D., Neil, J. O., Carlson, R. W., Paquette, J., Francis, D., Neil, J. O., Carlson, R. W., Paquette, J., & Francis, D. (2012). Formation age and metamorphic history of the Nuvvuagittuq Greenstone Belt. *Precambrian Research*, *220–221*, 23–44.

O'Nions. (1979). Geochemical and cosmochemical applications of Nd isotope analysis. *Annual Review of Earth and Planetary Sciences*, *7*, 11–38.

Page, F. Z., Fu, B., Kita, N. T., Fournelle, J., Spicuzza, M. J., Schulze, D. J., Viljoen, F., Basei, M. A. S., & Valley, J. W. (2007). Zircons from kimberlite: New insights from oxygen isotopes, trace elements, and Ti in zircon thermometry. *Geochimica et Cosmochimica Acta*, *71*(15), 3887–3903. https://doi.org/10.1016/j.gca.2007.04.031

Palin, R. M., White, R. W., & Green, E. C. R. (2016). Partial melting of metabasic rocks and the generation of tonalitic–trondhjemitic–granodioritic (TTG) crust in the Archaean: Constraints from phase equilibrium modelling. *Precambrian Research*, *287*, 73–90. https://doi.org/10.1016/j.precamres.2016.11.001

Paris, I., Stanistreet, I. G., & Hughes, M. J. (1985). Cherts of the Barberton greenstone belt ainterpreted as products of submarine exhalative activity. *Journal of Geology*, *93*, 111–129.

Perry, E. C., & Lefticariu, L. (2007). Formation and Geochemistry of Precambrian Cherts. *Treatise on Geochemistry*, 1–21.

Perry, E. C., & Tan, F. C. (1972). Significance of Oxygen and Carbon Isotope Variations in Early Precambrian Cherts and Carbonate Rocks of Southern Africa. *Geological Society of America Bulletin*, *83*(March), 647–664.

Perry Jr, E. C. (1967). The oxygen isotope chemistry of ancient cherts. *Earth and Planetary Science Letters*, *3*(July), 62–66.

Peter, S., & Shields, G. (1997). Introduction and Basic Principles of Isotope Geochemistrt. In *Radiogenic Isotope Geochemistry of Sedimentary and volcanic rocks* (pp. 1–10).

Peters, S. T. M., Szilas, K., Sengupta, S., Kirkland, C. L., Garbe-Schönberg, D., & Pack, A. (2020). >2.7 Ga metamorphic peridotites from southeast Greenland record the oxygen isotope composition of Archean seawater. *Earth and Planetary Science Letters*, *544*, 116331. https://doi.org/10.1016/j.epsl.2020.116331

Phillip Nutman, A., Bennett, V. C., L Friend, C. R., Van Kranendonk, M. J., Chivas, A., Phillip, A., L, C. R., & Kranendonk, V. (2016). *Rapid emergence of life shown by discovery of 3,700-million-year-old Rapid emergence of life shown by discovery of 3,700-million-year-old microbial structures microbial structures Recommended Citation Recommended Citation*. https://ro.uow.edu.au/smhpapershttps://ro.uow.edu.au/smhpapers/4157

Poitrasson, F. (2017). Silicon isotope geochemistry. *Non-Traditional Stable Isotopes*, *82*, 289–344. https://doi.org/10.2138/rmg.2017.82.8

Puchtel, I. S., Blichert-Toft, J., Touboul, M., Walker, R. J., Byerly, G. R., Nisbet, E. G., & Anhaeusser, C. R. (2013). Insights into early Earth from Barberton komatiites: Evidence from lithophile isotope and trace element systematics. *Geochimica et Cosmochimica Acta*, *108*, 63–90. https://doi.org/10.1016/j.gca.2013.01.016

Puchtel, I. S., Hofmann, A. W., Mezger, K., Jochum, K. P., Shchipansky, A. A., & Samsonov, A. V. (1998). Oceanic plateau model for continental crustal growth in the Archaean: A case study from the Kostomuksha greenstone belt, NW Baltic Shield. *Earth and Planetary Science Letters*, *155*(1–2), 57–74. https://doi.org/10.1016/s0012-821x(97)00202-1

Qin, T., Wu, F., Wu, Z., & Huang, F. (2016). First-principles calculations of equilibrium fractionation of O and Si isotopes in quartz, albite, anorthite, and zircon. *Contributions to Mineralogy and Petrology*, *171*(11), 1–14. https://doi.org/10.1007/s00410-016-1303-3

Rapp, R. P., Watson, E. B., & Miller, C. F. (1991). Partial melting of amphibolite/eclogite and the origin of Archean trondhjemites and tonalites. *Precambrian Research*, *51*(1–4), 1–25. https://doi.org/10.1016/0301-9268(91)90092-O

Reed, M. H., Spycher, N. F., & Palandri, J. (2010). Users Guide for CHIM-XPT: A Program for Computing Reaction Processes in Aqueous-Mineral-Gas Systems and MINTAB Guide. *Journal of Chemical Information and Modeling*, *53*(9), 1689–1699.

Reimann, S., Heubeck, C. E., Fugmann, P., Rensburg, D. J. J. Van, & Zametzer, A. (2021). Syndepositional hydrothermalism selectively preserves records of one of the earliest benthic ecosystems , Moodies Group (3 . 22 Ga), Barberton Greenstone Belt , South Africa. *South African Journal of Geology*, *124*, 253–278.

Reimink, J. R., Davies, J. H. F. L., Chacko, T., Stern, R. A., Heaman, L. M., Sarkar, C., Schaltegger, U., Creaser, R. A., & Pearson, D. G. (2016). No evidence for Hadean continental crust within Earth's oldest evolved rock unit. *Nature Geoscience*, *9*(10), 777–780. https://doi.org/10.1038/ngeo2786

Robb, L. J., Barton, J. M., Kable, E. J. D., & Wallace, R. C. (1986). Geology, geochemistry and isotopic characteristics of the Archean Kaap Valley pluton, Barberton Mountain Land, South Africa. *Precambrian Research*, *31*(1986), 1–366.

Robert, F., & Chaussidon, M. (2006). A paleotemperature curve for the Precambrian oceans based on silicon isotopes in cherts. *Nature*, *443*, 969–972.

Roberts, N. M. W., & Santosh, M. (2018). Capturing the Mesoarchean Emergence of Continental Crust in the Coorg Block, Southern India. *Geophysical Research Letters*, *45*(15), 7444–7453. https://doi.org/10.1029/2018GL078114

Robin-Popieul, C. C. M., Arndt, N. T., Chauvel, C., Byerly, G. R., Sobolev, A. V., & Wilson, A. (2012). A new model for barberton komatiites: Deep critical melting with high melt retention. *Journal of Petrology*, *53*(11), 2191–2229. https://doi.org/10.1093/petrology/egs042

Rollinson, H. (2021). Do all Archaean TTG rock compositions represent former melts? In *Precambrian Research* (Vol. 367). Elsevier B.V. https://doi.org/10.1016/j.precamres.2021.106448

Rollion-Bard, C., & Marin-Carbonne, J. (2011). Determination of SIMS matrix effects on oxygen isotopic compositions in carbonates. *Journal of Analytical Atomic Spectrometry*, *26*(6), 1285–1289. https://doi.org/10.1039/c0ja00213e

Roman, A., & Arndt, N. (2020). Differentiated Archean oceanic crust: its thermal structure, mechanical stability and a test of the sagduction hypothesis. *Geochimica et Cosmochimica Acta*, *278*, 65–77.

Rosman, K. J. R., & Taylor, P. D. P. (1998). Isotopic compositions of the elements 1997 (Technical Report). *Pure and Applied Chemistry*, *70*(1), 217–235. https://doi.org/10.1351/pac199870010217

Rouchon, V., & Orberger, B. (2008). Origin and mechanisms of K-Si-metasomatism of ca. 3.4-3.3 Ga volcaniclastic deposits and implications for Archean seawater evolution: Examples from cherts of Kittys Gap (Pilbara craton, Australia) and Msauli (Barberton Greenstone Belt, South Africa). *Precambrian Research*, *165*(3–4), 169–189. https://doi.org/10.1016/j.precamres.2008.06.003

Rouchon, V., Orberger, B., Hofmann, A., & Pinti, D. L. (2009). *Diagenetic Fe-carbonates in Paleoarchean felsic sedimentary rocks (Hooggenoeg Formation , Barberton greenstone belt , South Africa): Implications for CO 2 sequestration and the chemical budget of seawater*. *172*, 255–278. https://doi.org/10.1016/j.precamres.2009.04.010

Saitoh, M., Olivier, N., Garçon, M., Boyet, M., Thomazo, C., Alleon, J., Moyen, J. F., Motto-Ros, V., & Marin-Carbonne, J. (2021). Metamorphic origin of anastomosing and wavy laminas overprinting putative microbial deposits from the 3.22 Ga Moodies Group

(Barberton Greenstone Belt). *Precambrian Research*, *362*. https://doi.org/10.1016/j.precamres.2021.106306

Sanchez-garrido, C. J. M. G. (2011). *The petrogenesis of the older (> 3.0 Ga) potassic granitoids of eastern Mpumalanga (South Africa) and Swaziland : An investigation of crustal formation processes in the early Earth* (Issue December).

Schmitz, M., & Heubeck, C. (2021). Constraints on deformation mechanisms of the Barberton Greenstone Belt from regional stratigraphic and structural data of the synorogenic Moodies Group. *Precambrian Research*, *362*(February), 106177. https://doi.org/10.1016/j.precamres.2021.106177

Schnabel, C., Münker, C., & Strub, E. (2017). La-Ce isotope measurements by multicollector-ICPMS. *Journal of Analytical Atomic Spectrometry*, *32*(12), 2360–2370. https://doi.org/10.1039/c7ja00256d

Schneider, K. P., Hoffmann, J. E., Münker, C., Patyniak, M., Sprung, P., Roerdink, D., Wissenschaften, G., & Berlin, F. U. (2019). Petrogenetic evolution of metabasalts and metakomatiites of the lower Onverwacht Group , Barberton Greenstone Belt (South Africa). *Chemical Geology*, *511*(August 2018), 152–177. https://doi.org/10.1016/j.chemgeo.2019.02.020

Sengupta, S., & Pack, A. (2018). Triple oxygen isotope mass balance for the Earth’s oceans with application to Archean cherts. *Chemical Geology*, *495*(July), 18–26. https://doi.org/10.1016/j.chemgeo.2018.07.012

Sengupta, S., Peters, S. T. M., Reitner, J., Duda, J. P., & Pack, A. (2020). Triple oxygen isotopes of cherts through time. *Chemical Geology*, *554*(July), 119789. https://doi.org/10.1016/j.chemgeo.2020.119789

Shanks, W. C. (2001). Stable isotopes in seafloor hydrothermal systems: Vent fluids, hydrothermal deposits, hydrothermal alteration, and microbial processes. *Stable Isotope Geochemistry*, *43*, 469–525. https://doi.org/10.1515/9781501508745-011

Sharp, Z. (2017). *Principles of Stable Isotope Geochemistry*.

Sharp, Z. D., Gibbons, J. A., Maltsev, O., Atudorei, V., Pack, A., Sengupta, S., Shock, E. L., & Knauth, L. P. (2016). A calibration of the triple oxygen isotope fractionation in the SiO2-H2O system and applications to natural samples. *Geochimica et Cosmochimica Acta*, *186*, 105–119. https://doi.org/10.1016/j.gca.2016.04.047

Sharp, Z. D., & Kirschner, D. L. (1994). Quartz-calcite oxygen isotope thermometry: A calibration based on natural isotopic variations. *Geochimica et Cosmochimica Acta*, *58*(20), 4491–4501. https://doi.org/10.1016/0016-7037(94)90350-6

Shibuya, T., Kitajima, K., Komiya, T., Terabayashi, M., & Maruyama, S. (2007). Middle Archean ocean ridge hydrothermal metamorphism and alteration recorded in the Cleaverville area, Pilbara Craton, Western Australia. *Journal of Metamorphic Geology*, *25*(7), 751–767. https://doi.org/10.1111/j.1525-1314.2007.00725.x

Shibuya, T., Tahata, M., Kitajima, K., Ueno, Y., Komiya, T., Yamamoto, S., Igisu, M., Terabayashi, M., Sawaki, Y., Takai, K., Yoshida, N., & Maruyama, S. (2012). Depth variation of carbon and oxygen isotopes of calcites in Archean altered upperoceanic crust: Implications for the CO 2 flux from ocean to oceanic crust in the Archean. *Earth and Planetary Science Letters*, *321–322*, 64–73. https://doi.org/10.1016/j.epsl.2011.12.034

Shimizu, H., Amano, M., & Masuda, A. (1991). La-Ce and Sm-Nd systematics of siliceous sedimentary rocks: a clue to marine environment in their deposition. *Geology*, *19*(4), 369–371. https://doi.org/10.1130/0091-7613(1991)019<0369:LCASNS>2.3.CO;2

Shimizu, H., Tachikawa, K., Masuda, A., & Nozaki, Y. (1994). Cerium and neodymium isotope ratios and REE patterns in seawater from the North Pacific Ocean. *Geochimica et Cosmochimica Acta*, *58*(1), 323–333. https://doi.org/10.1016/0016-7037(94)90467-7

Siever, R. (1992). The silica cycle in the Precambrian. *Geochimica et Cosmochimica Acta*, *56*, 3265–3272. https://doi.org/10.1109/LSP.2004.830109

Sizova, E., Gerya, T., Stüwe, K., & Brown, M. (2015). Generation of felsic crust in the Archean: A geodynamic modeling perspective. *Precambrian Research*, *271*, 198–224. https://doi.org/10.1016/j.precamres.2015.10.005

Śliwiński, M. G., Kitajima, K., Spicuzza, M. J., Orland, I. J., Ishida, A., Fournelle, J. H., & Valley, J. W. (2018). SIMS Bias on Isotope Ratios in Ca-Mg-Fe Carbonates (Part III): δ18O and δ13C Matrix Effects Along the Magnesite–Siderite Solid-Solution Series. *Geostandards and Geoanalytical Research*, *42*(1), 49–76. https://doi.org/10.1111/ggr.12194

Smit, M. A., Scherstén, A., Næraa, T., Emo, R. B., Scherer, E. E., Sprung, P., Bleeker, W., Mezger, K., Maltese, A., Cai, Y., Rasbury, E. T., & Whitehouse, M. J. (2019). Formation of Archean continental crust constrained by boron isotopes. *Geochemical Perspectives Letters*, *12*(2019), 23–26. https://doi.org/10.7185/geochemlet.1930

Smithies, R. H., Champion, D. C., & Van Kranendonk, M. J. (2009). Formation of Paleoarchean continental crust through infracrustal melting of enriched basalt. *Earth and Planetary Science Letters*, *281*(3–4), 298–306. https://doi.org/10.1016/j.epsl.2009.03.003

Smithies, R. H., Lu, Y., Johnson, T. E., Kirkland, C. L., Cassidy, K. F., Champion, D. C., Mole, D. R., Zibra, I., Gessner, K., Sapkota, J., De Paoli, M. C., & Poujol, M. (2019). No evidence for high-pressure melting of Earth's crust in the Archean. *Nature Communications*, *10*(1). https://doi.org/10.1038/s41467-019-13547-x

Smithies, R. H., Lu, Y., Kirkland, C. L., Johnson, T. E., Mole, D. R., Champion, D. C., Martin, L., Jeon, H., Wingate, M. T. D., & Johnson, S. P. (2021). Oxygen isotopes trace the origins of Earth ' s earliest continental crust. *Nature*, *592*(July 2020). https://doi.org/10.1038/s41586-021-03337-1

Sotiriou, P., Polat, A., Windley, B. F., & Kusky, T. (2022). Temporal variations in the incompatible trace element systematics of Archean volcanic rocks: Implications for tectonic processes in the early Earth. *Precambrian Research*, *368*(June 2021), 106487. https://doi.org/10.1016/j.precamres.2021.106487

Sotiriou, P., Polat, A., Windley, B., & Kusky, T. (2023). Temporal variations in the incompatible trace element systematics of Archean TTGs: Implications for crustal growth and tectonic processes in the early Earth. *Earth-Science Reviews*, *236*(November 2022), 104274. https://doi.org/10.1016/j.earscirev.2022.104274

Stanistreet, I. G., de Wit, M. J., & Fripp, R. E. P. (1981). Do graded units of accretionary spheroids in the Barberton Greenstone Belt indicate Archean deep water environment? *Nature*, *293*(280–283).

Staudigel, H., Hart, S. R., & Richardson, S. H. (1981). Alteration of the oceanic crust: Processes and timing. *Earth and Planetary Science Letters*, *52*(2), 311–327. https://doi.org/10.1016/0012-821X(81)90186-2

Steefel, C., Org, E., Steefel, C. I., & Maher, K. (2009). *Title Fluid-rock interaction: A reactive transport approach Publication Date Fluid-Rock Interaction: A Reactive Transport Approach*.

Stefurak, E. J. T., Fischer, W. W., & Lowe, D. R. (2015). Texture-specific Si isotope variations in Barberton Greenstone Belt cherts record low temperature fractionations in early Archean seawater. *Geochimica et Cosmochimica Acta*, *150*, 26–52. https://doi.org/10.1016/j.gca.2014.11.014

Stefurak, E. J. T., Lowe, D. R., Zentner, D., & Fischer, W. W. (2014). Primary silica granules-A new mode of Paleoarchean sedimentation. *Geology*, *42*(4), 283–286. https://doi.org/10.1130/G35187.1

Stevens, G., & Moyen, J. (2007). Metamorphism in the Barberton granite greenstone terrain: a record of Paleoarchean accretion. In M. J. van Kranendonk, R. H. Smithies, & V. C. Bennett (Eds.), *Precambrian Ophiolites and Related Rocks*. https://doi.org/10.1016/S0166-2635(07)15057-X

Stoll, E., Drabon, N., & Lowe, D. R. (2021). Provenance and paleogeography of Archean Fig Tree siliciclastic rocks in the East-Central Barberton Greenstone Belt , South Africa. *Precambrian Research*, *354*(June 2020), 106041. https://doi.org/10.1016/j.precamres.2020.106041

Sugahara, H., Sugitani, K., Mimura, K., Yamashita, F., & Yamamoto, K. (2010). A systematic rare-earth elements and yttrium study of Archean cherts at the Mount Goldsworthy greenstone belt in the Pilbara Craton: Implications for the origin of microfossil-bearing black cherts. *Precambrian Research*, *177*(1–2), 73–87. https://doi.org/10.1016/j.precamres.2009.10.005

Sugitani, K. (1992). Geochemical characteristics of Archean cherts and other sedimentary rocks in the Pilbara Block, Western Australia: evidence for Archean seawater enriched in hydrothermally-derived iron and silica. *Precambrian Research*, *57*(1–2), 21–47. https://doi.org/10.1016/0301-9268(92)90093-4

Sugitani, K., Horiuchi, Y., Adachi, M., & Sugisaki, R. (1996). Anomalously low Al2O3/TiO2 values for Archean cherts from the Pilbara Block, Western Australia - Possible evidence for extensive chemical weathering on the early earth. *Precambrian Research*, *80*(1–2), 49–76. https://doi.org/10.1016/s0301-9268(96)00005-8

Sun, H., Chaussidon, M., Robert, F., Tian, S., Deng, Z., & Moynier, F. (2023). Triple silicon isotope insights into the formation of Precambrian cherts. *Earth and Planetary Science Letters*, *607*. https://doi.org/10.1016/j.epsl.2023.118069

Tamblyn, R., Hermann, J., Hasterok, D., Sossi, P., Pettke, T., & Chatterjee, S. (2023). Hydrated komatiites as a source of water for TTG formation in the Archean. *Earth and Planetary Science Letters*, *603*, 117982. https://doi.org/10.1016/j.epsl.2022.117982

Tanaka, M., Shimizu, H., Nozak, Y., Ikeuch, Y., & Masuda, A. (1990). 138Ce / 142Ce and 143Nd / 144Nd ratios in seawater samples. *Geochemical Journal*, *24*(5), 309–314. https://doi.org/10.2343/geochemj.24.309

Tappe, S., Kjarsgaard, B. A., Kurszlaukis, S., Nowell, G. M., & Phillips, D. (2014). Petrology and Nd–Hf Isotope Geochemistry of the Neoproterozoic Amon Kimberlite Sills, Baffin Island (Canada): Evidence for Deep Mantle Magmatic Activity Linked to Supercontinent Cycles. *Journal of Petrology*, *55*(10), 2003–2042. https://doi.org/10.1093/petrology/egu048

Tatzel, M., Frings, P. J., Oelze, M., Herwartz, D., Lünsdorf, N. K., & Wiedenbeck, M. (2022). Chert oxygen isotope ratios are driven by Earth’s thermal evolution. *Proceedings of the National Academy of Sciences*, *120*, 2017. https://doi.org/10.1073/pnas

Tatzel, M., Oelze, M., Frick, D. A., Di Rocco, T., Liesegang, M., Stuff, M., & Wiedenbeck, M. (2024). Silicon and oxygen isotope fractionation in a silicified carbonate rock. *Chemical Geology*, *658*(August 2023), 122120. https://doi.org/10.1016/j.chemgeo.2024.122120

Tice, M., & Lowe, D. R. (2006). The origin of carbonaceous matter in pre-3 . 0 Ga greenstone terrains : A review and new evidence from the 3 . 42 Ga ... Related papers A review and new evidence from the 3 . 42 Ga Buck Reef Chert. *Earth Science Reviews*, *76*, 259–300. https://doi.org/10.1016/j.earscirev.2006.03.003

Tice, M. M., Bostick, B. C., & Lowe, D. R. (2004). Thermal history of the 3.5–3.2 Ga Onverwacht and Fig Tree Groups, Barberton greenstone belt, South Africa, inferred by Raman microspectroscopy of carbonaceous material. *Geology*, *32*(1), 37. https://doi.org/10.1130/G19915.1

Toulkeridis, T., Goldstein, S. L., Clauer, N., Kro, A., Todt, W., & Schidlowski, M. (1998).

Sm – Nd , Rb – Sr and Pb – Pb dating of silicic carbonates from the early Archaean Barberton Greenstone Belt , South Africa Evidence for post-depositional isotopic resetting at low temperature. *Precambrian Research*, *92*(92), 129–144.

Trail, D., Boehnke, P., Savage, P. S., Liu, M. C., Miller, M. L., & Bindeman, I. (2018). Origin and significance of Si and O isotope heterogeneities in Phanerozoic, Archean, and Hadean zircon. *Proceedings of the National Academy of Sciences of the United States of America*, *115*(41), 10287–10292. https://doi.org/10.1073/pnas.1808335115

Trail, D., Savage, P., Moynier, F., Trail, D., Savage, P., & Moynier, F. (2020). *Experimentally determined Si isotope fractionation between zircon and quartz To cite this version : HAL Id : insu-02916949 Experimentally determined Si isotope fractionation between zircon and quartz.*

Trower, E. J., & Fischer, W. W. (2019a). Precambrian Si isotope mass balance, weathering, and the significance of the authigenic clay silica sink. *Sedimentary Geology*, *384*, 1–11. https://doi.org/10.1016/j.sedgeo.2019.02.008

Trower, E. J., & Fischer, W. W. (2019b). Precambrian Si isotope mass balance , weathering , and the signi fi cance of the authigenic clay silica sink. *Sedimentary Geology*, *384*, 1–11. https://doi.org/10.1016/j.sedgeo.2019.02.008

Trower, E. J., & Lowe, D. R. (2016). Sedimentology of the ~3.3 Ga upper Mendon Formation, Barberton Greenstone Belt, South Africa. *Precambrian Research*, *281*, 473–494. https://doi.org/10.1016/j.precamres.2016.06.003

Valley, J. W., Chiarenzelli, J. R., & McLelland, J. M. (1994). Oxygen isotope geochemistry of zircon. *Earth and Planetary Science Letters*, *126*(4), 187–206. https://doi.org/10.1016/0012-821X(94)90106-6

Valley, J. W., Kinny, P. D., Schulze, D. J., & Spicuzza, M. J. (1998). Zircon megacrysts from kimberlite: Oxygen isotope variability among mantle melts. *Contributions to Mineralogy and Petrology*, *133*(1–2), 1–11. https://doi.org/10.1007/s004100050432

Valley, J. W., Lackey, J. S., Cavosie, A. J., Clechenko, C. C., Spicuzza, M. J., Basei, M. A. S., Bindeman, I. N., Ferreira, V. P., Sial, A. N., King, E. M., Peck, W. H., Sinha, A. K., & Wei, C. S. (2005). 4.4 billion years of crustal maturation: Oxygen isotope ratios of magmatic zircon. *Contributions to Mineralogy and Petrology*, *150*(6), 561–580. https://doi.org/10.1007/s00410-005-0025-8

van den Boorn, S. H. J. M., van Bergen, M. J., Nijman, W., & Vroon, P. Z. (2007). Dual role of seawater and hydrothermal fluids in Early Archean chert formation: Evidence from silicon isotopes. *Geology*, *35*(10), 939–942. https://doi.org/10.1130/G24096A.1

van den Boorn, S. H. J. M., van Bergen, M. J., Vroon, P. Z., de Vries, S. T., & Nijman, W. (2010). Silicon isotope and trace element constraints on the origin of ∼3.5 Ga cherts: Implications for Early Archaean marine environments. *Geochimica et Cosmochimica Acta*, *74*(3), 1077–1103. https://doi.org/10.1016/j.gca.2009.09.009

Van Hunen, J., & Moyen, J. F. (2012). Archean subduction: Fact or fiction? *Annual Review of Earth and Planetary Sciences*, *40*, 195–219. https://doi.org/10.1146/annurev-earth-042711-105255

van Hunen, J., & van den Berg, A. P. (2008). Plate tectonics on the early Earth: Limitations imposed by strength and buoyancy of subducted lithosphere. *Lithos*, *103*(1–2), 217–235. https://doi.org/10.1016/j.lithos.2007.09.016

Van Kranendonk, M. J. (2011). Cool greenstone drips and the role of partial convective overturn in Barberton greenstone belt evolution. *Journal of African Earth Sciences*, *60*(5), 346–352. https://doi.org/10.1016/j.jafrearsci.2011.03.012

Van Kranendonk, M. J., Kröner, A., Hegner, E., & Connelly, J. (2009). Age, lithology and structural evolution of the c. 3.53 Ga Theespruit Formation in the Tjakastad area, southwestern Barberton Greenstone Belt, South Africa, with implications for Archaean tectonics. *Chemical Geology*, *261*(1–2), 115–139. https://doi.org/10.1016/j.chemgeo.2008.11.006

Van Kranendonk, M. J., Kröner, A., Hoffman, J. E., Nagel, T., & Anhaeusser, C. R. (2014). Just another drip: Re-analysis of a proposed mesoarchean suture from the Barberton mountain land, South Africa. *Precambrian Research*, *254*, 19–35. https://doi.org/10.1016/j.precamres.2014.07.022

van Zuilen, M. A., Chaussidon, M., Rollion-Bard, C., & Marty, B. (2007). Carbonaceous cherts of the Barberton Greenstone Belt, South Africa: Isotopic, chemical and structural characteristics of individual microstructures. *Geochimica et Cosmochimica Acta*, *71*(3), 655–669. https://doi.org/10.1016/j.gca.2006.09.029

Vervoort, J. D., Plank, T., & Prytulak, J. (2011). The Hf-Nd isotopic composition of marine sediments. *Geochimica et Cosmochimica Acta*, *75*(20), 5903–5926. https://doi.org/10.1016/j.gca.2011.07.046

Vezinet, A., Pearson, D. G., Thomassot, E., Stern, R. A., Sarkar, C., Luo, Y., & Fisher, C. M. (2018). Hydrothermally-altered mafic crust as source for early Earth TTG: Pb/Hf/O isotope and trace element evidence in zircon from TTG of the Eoarchean Saglek Block, N. Labrador. *Earth and Planetary Science Letters*, *503*, 95–107. https://doi.org/10.1016/j.epsl.2018.09.015

Vezinet, A., Thomassot, E., Pearson, D. G., Stern, R. A., Luo, Y., & Sarkar, C. (2019). Extreme δ18O signatures in zircon from the Saglek Block (North Atlantic Craton) document reworking of mature supracrustal rocks as early as 3.5 Ga. *Geology*, *47*(7), 605–608. https://doi.org/10.1130/G46086.1

Vidal, O., Lanari, P., Munoz, M., Bourdelle, F., & Andrade, V. D. E. (2016). Deciphering temperature , pressure and oxygen-activity conditions of chlorite formation. *Clay Minerals*, *51*(July 2015), 615–633. https://doi.org/10.1180/claymin.2016.051.4.06

Viehmann, S., Bau, M., Hoffmann, J. E., & Münker, C. (2018). Decoupled Hf and Nd isotopes in suspended particles and in the dissolved load of Late Archean seawater. *Chemical Geology*, *483*(December 2017), 111–118. https://doi.org/10.1016/j.chemgeo.2018.01.017

Viehmann, S., Reitner, J., Tepe, N., Hohl, S. V., Van Kranendonk, M., Hofmann, T., Koeberl, C., & Meister, P. (2020). Carbonates and cherts as archives of seawater chemistry and habitability on a carbonate platform 3.35 Ga ago: Insights from Sm/Nd dating and trace element analysis from the Strelley Pool Formation, Western Australia. *Precambrian Research*, *344*(August 2019), 105742. https://doi.org/10.1016/j.precamres.2020.105742

Wang, D., Romer, R. L., Guo, J. hui, & Glodny, J. (2020). Li and B isotopic fingerprint of Archean subduction. *Geochimica et Cosmochimica Acta*, *268*, 446–466. https://doi.org/10.1016/j.gca.2019.10.021

Wang, H., Wilson, A., Yang, J., Li, Q., Tang, G., Feng, L., & Jia, L. (2023). No 18O-depleted mantle source for Archean komatiite. *Science Bulletin*, *68*(1), 53–55. https://doi.org/10.1016/j.scib.2022.12.017

Wang, X., Tang, M., Moyen, J., Wang, D., Kröner, A., Xia, X., Xie, H., Anhaeusser, C., Hofmann, A., Li, J., & Li, L. (2022). The onset of deep recycling of supracrustal materials at the Paleo-Mesoarchean boundary. *National Science Review*, *9*, 1–9.

Weis, D., & Wasserburg, G. . (1987a). Rb□Sr and Sm□Nd systematics of cherts and other siliceous deposits. *Geochimica et Cosmochimica Acta*, *51*(4), 959–972. https://doi.org/10.1016/0016-7037(87)90108-6

Weis, D., & Wasserburg, G. J. (1987b). RbSr and SmNd isotope geochemistry and chronology of cherts from the Onverwacht Group (3.5 AE), South Africa* * Division Contribution No. 4326 (527). *Geochimica et Cosmochimica Acta*, *51*(4), 973–984. https://doi.org/10.1016/0016-7037(87)90109-8

Westall, F., De Wit, M. J., Dann, J., Gaast, S. Van Der, De Ronde, C. E. J., & Gerneke, D. (2001). *Early Archean fossil bacteria and biofilms in hydrothermally-influenced sediments from the Barberton greenstone belt , South Africa*. *106*, 93–116.

Wilde, S. A., Valley, J. W., Peck, W. H., & Graham, C. M. (2001). Evidence from detrital zircons for the existence of continental crust and oceans on the Earth 4.4 Gyr ago. *Nature*, *409*(6817), 175–178. https://doi.org/10.1038/35051550

Willbold, M., & Stracke, A. (2010). Formation of enriched mantle components by recycling of upper and lower continental crust. *Chemical Geology*, *276*(3–4), 188–197. https://doi.org/10.1016/j.chemgeo.2010.06.005

Windley, B. F., Kusky, T., & Polat, A. (2021). Onset of plate tectonics by the Eoarchean. *Precambrian Research*, *352*(July 2020), 105980. https://doi.org/10.1016/j.precamres.2020.105980

Wit, M. J. De, Roering, C., Hart, R. J., Armstrong, R. A., Ronde, C. E. J. De, Green, R. W. E., Tredoux, M., Peberdy, E., & Hart, R. A. (1992). Formation of an Archaean continent. *Nature*, *357*, 553–562.

Wostbrock, J. A. G., & Sharp, Z. D. (2021). Triple oxygen isotopes in silica-water and carbonate-water systems. *Triple Oxygen Isotope Geochemistry*, *86*, 367–400. https://doi.org/10.2138/rmg.2021.86.11

Xie, X., Byerly, G. R., & Ferrell, R. E. (1997). IIb trioctahedral chlorite from the Barberton greenstone belt: Crystal structure and rock composition constraints with implications to geothermometry. *Contributions to Mineralogy and Petrology*, *126*(3), 275–291. https://doi.org/10.1007/s004100050250

Yanchilina, A. G., Yam, R., Kolodny, Y., & Shemesh, A. (2020). From diatom opal-A δ18O to chert δ18O in deep sea sediments. *Geochimica et Cosmochimica Acta*, *268*, 368–382. https://doi.org/10.1016/j.gca.2019.10.018

Yapp, C. J. (1990). Oxygen isotopes in iron (III) oxides. 1. Mineral-water fractionation factors. *Chemical Geology*, *85*(3–4), 329–335. https://doi.org/10.1016/0009-2541(90)90010-5

Yu, H. M., Li, Y. H., Gao, Y. J., Huang, J., & Huang, F. (2018). Silicon isotopic compositions of altered oceanic crust: Implications for Si isotope heterogeneity in the mantle. *Chemical Geology*, *479*(April 2017), 1–9. https://doi.org/10.1016/j.chemgeo.2017.12.013

Yu, H. M., Yang, L., Zhang, G. L., & Huang, F. (2023). Silicon isotopic compositions of altered Oceanic crust samples from IODP U1365 and U1368: Effect of low-temperature seawater alteration. *Chemical Geology*, *624*(November 2022), 121424. https://doi.org/10.1016/j.chemgeo.2023.121424

Zakharov, D. O., Marin-Carbonne, J., Alleon, J., & Bindeman, I. N. (2021). Triple Oxygen Isotope Trend Recorded by Precambrian Cherts : A Perspective from Combined Bulk and in situ Secondary Ion Probe Measurements. *Reviews in Mineralogy and Geochemistry*, *86*, 323–365.

Zakharov, D. O., Marin-Carbonne, J., Pack, A., Di Rocco, T., Robyr, M., & Vennemann, T. (2023). In-situ and Triple Oxygen Isotope Characterization of Seafloor Drilled Cherts: Marine Diagenesis and Its Bearing on Seawater Reconstructions. *Geochemistry, Geophysics, Geosystems*. https://doi.org/10.1029/2022gc010741

Zakharov, D. O., Tanaka, R., Butterfield, D. A., & Nakamura, E. (2021). A New Insight Into Seawater-Basalt Exchange Reactions Based on Combined δ18O—Δ′17O—87Sr/86Sr Values of Hydrothermal Fluids From the Axial Seamount Volcano, Pacific Ocean. *Frontiers in Earth Science*, *9*(September), 1–17. https://doi.org/10.3389/feart.2021.691699

Zakharov, D. O., Zozulya, D. R., & Rubatto, D. (2022). Low-δ18O Neoarchean precipitation recorded in a 2.67 Ga magmatic-hydrothermal system of the Keivy granitic complex, Russia. *Earth and Planetary Science Letters*, *578*, 117322. https://doi.org/10.1016/j.epsl.2021.117322

Zhang, G.-L., & Smith-Duque, C. (2014). Seafloor basalt alteration and chemical change in ultra thinly sedimented South Pacific. *Geochemistry, Geophysics, Geosystems*, *15*, 4692–4711. https://doi.org/10.1002/2013GC005141.Received

Zheng, Y.-F. (1993). Calculation of oxygen isotope fractionation in hydroxyl-bearing silicates. *Earth and Planetary Science Letters*, *121*, 247–263.

Appendices

A. Supplementary materials related to Part III.

B. Supplementary materials related to Part IV.

C. Supplementary material related to Part V.

A. Supplementary material related to Part III.

Supplementary Figure A-1. Drone images of the Theespruit section with approximate sample location

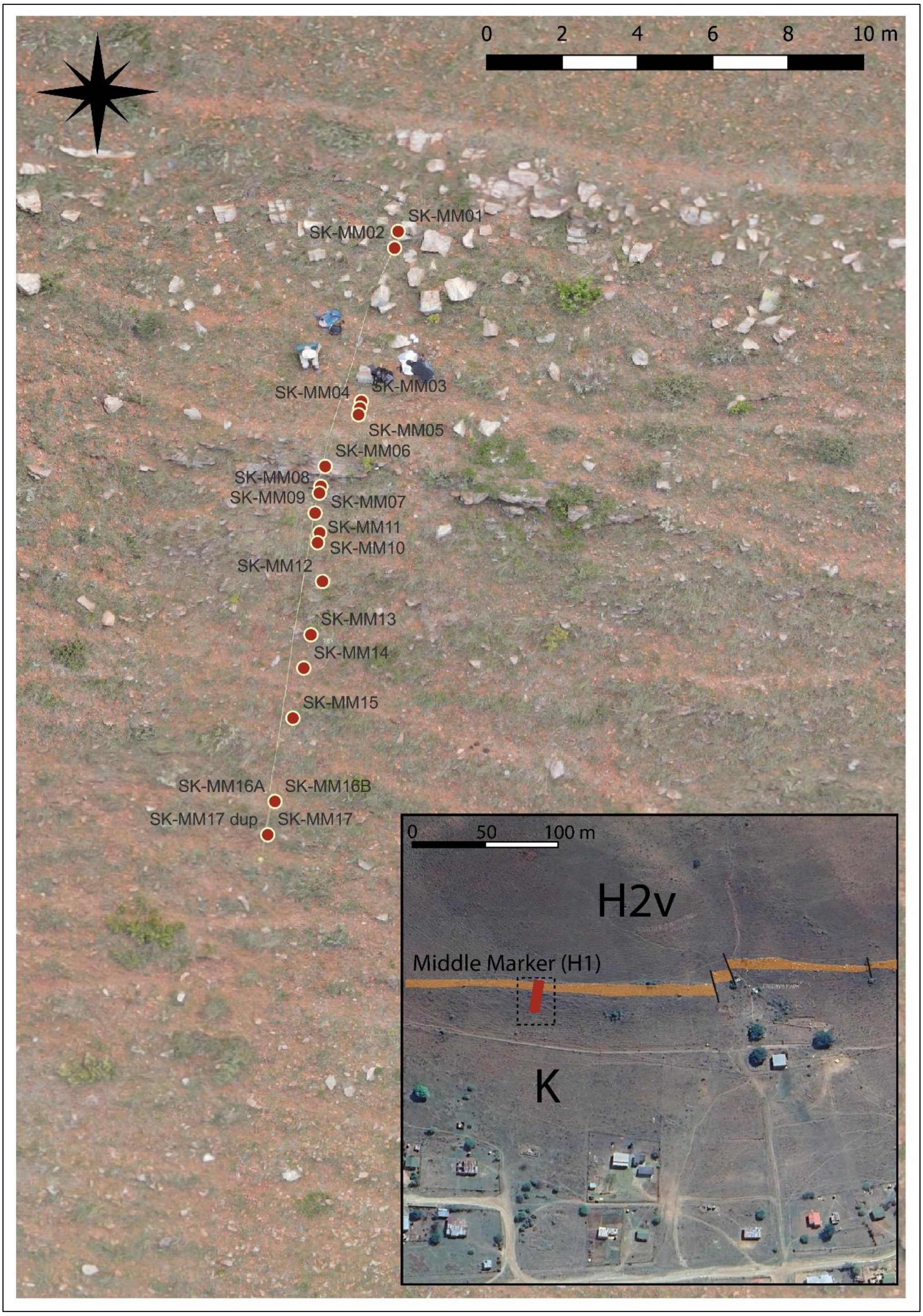

Supplementary Figure A-2. Drone images of the Middle Marker section with approximate sample location

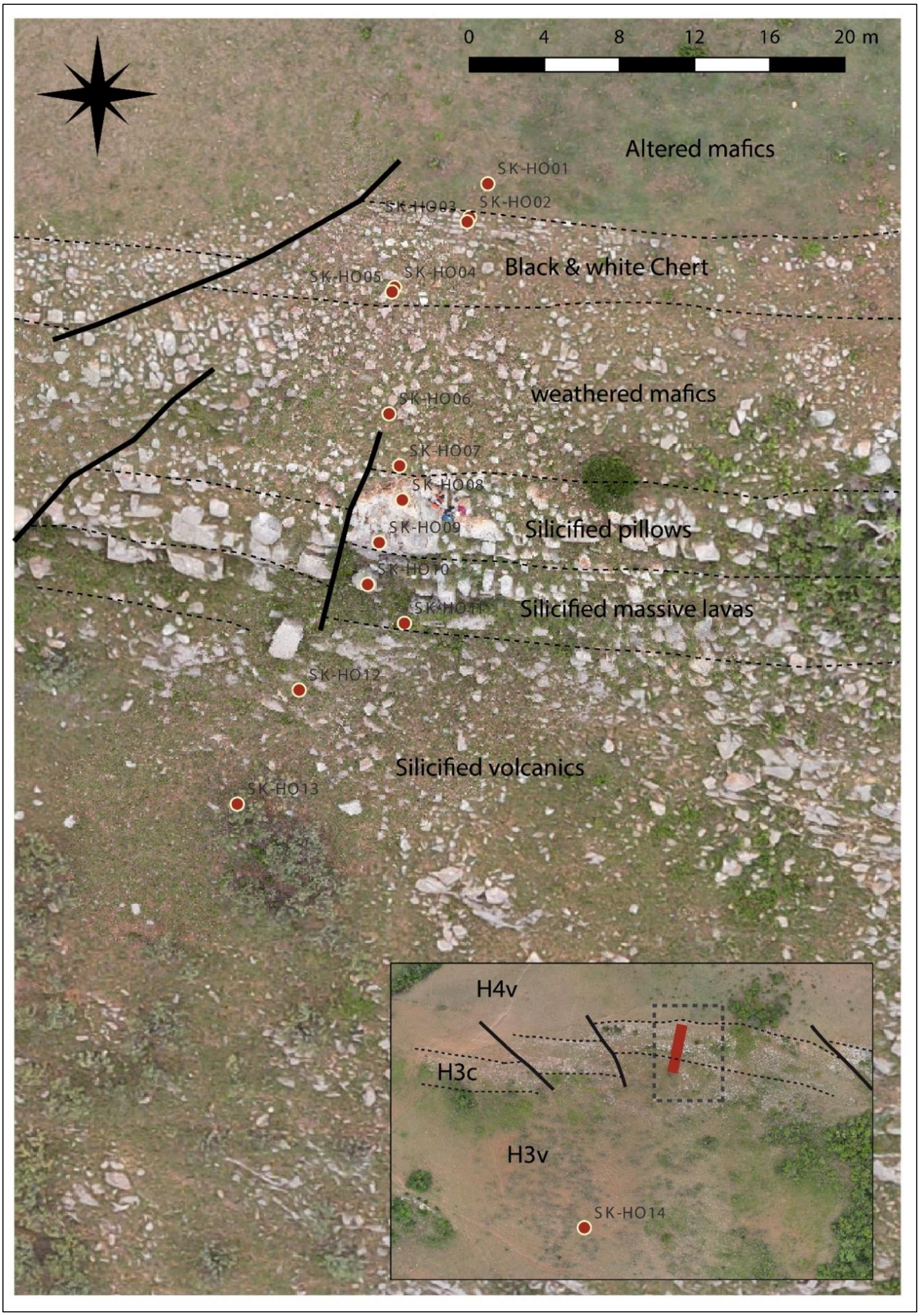

Supplementary Figure A-3. Drone images of the Hooggenoeg 3 section with approximate sample location.

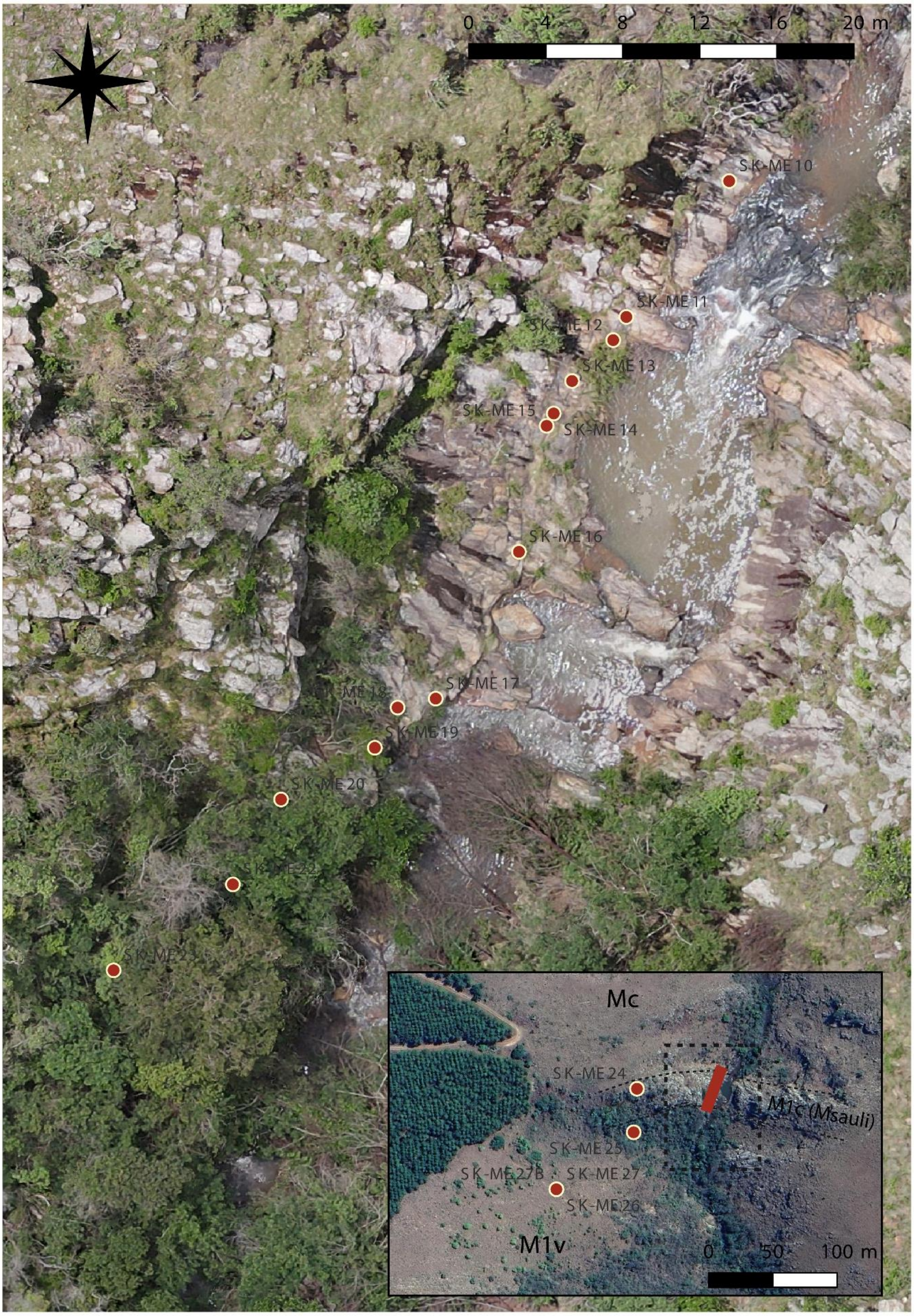

Supplementary Figure A-4. Drone images of the Mendon 1 section with approximate sample location

Supplementary Table A-1. SIMS-determined O isotope compositions of reference materials and samples

ID	δ^{18}O mesured			Δ^{18}O dol-ank mes.	Δ^{18}O dol-ank cal.	Cal. IMF	δ^{18}O real	Fe#	SiO2		FeO		MnO		MgO		CaO	
	n	Average	2 S.D.						Av.	2 S.D.	Av.	2 S.D.	Av.	2 S.D.	Av.	2 S.D.	Av.	2 S.D.
UNIL-C4	10	15.8	0.31	9.0		0.7	**16.5**	0.79	0.00	0.01	24.81	0.82	2.02	0.12	3.62	0.47	27.33	0.31
KPIK	8	-2.0	0.54	0.0		9.7	**7.6**	0.00	0.00	0.01	0.03	0.03	0.01	0.02	21.19	0.14	31.18	0.31
Zi01 (UNIL-C1)	7	15.2	0.46	6.6		3.1	**18.3**	0.11	0.00	0.01	0.08	0.04	0.05	0.04	0.39	0.03	55.10	0.55
d18O-SKME18a-Ank@1		9.3	0.16		8.1	1.6	**10.9**	0.32	0.00	0.00	11.00	1.58	2.00	0.77	12.86	1.37	28.69	3.44
d18O-SKME18a-Ank@2		9.0	0.11		8.1	1.6	**10.6**	0.33	0.03	0.16	9.84	1.57	3.79	1.23	11.30	1.51	27.70	3.58
d18O-SKME18a-Ank@3		9.3	0.16		8.1	1.6	**10.9**	0.31	0.00	0.00	9.00	1.18	4.22	1.13	11.00	1.75	26.95	4.22
d18O-SKME18a-Ank@4		8.4	0.18		8.2	1.4	**9.8**	0.36	0.02	0.14	8.92	1.85	3.63	0.95	8.90	1.94	23.18	4.70
d18O-SKME18a-Ank@5		8.7	0.16		8.1	1.6	**10.3**	0.31	0.00	0.00	10.49	1.53	1.93	1.28	13.00	1.31	28.67	2.66
d18O-SKME18a-Ank@6		9.0	0.15		8.2	1.5	**10.5**	0.34	0.00	0.00	9.41	1.72	4.22	0.94	10.47	1.61	27.59	3.61
d18O-SKME18a-Ank@7		9.2	0.12		8.2	1.5	**10.7**	0.34			10.38	2.09	3.87	0.89	11.07	1.20	28.29	3.35
d18O_P551_030423_ME18b_AnkA@1		8.7	0.10		8.2	1.5	**10.2**	0.35	2.77	7.51	7.48	2.12	3.26	1.07	7.81	2.73	20.57	5.90
d18O_P551_030423_ME18b_AnkA@2		7.9	0.09		8.1	1.6	**9.4**	0.32	0.42	0.79	8.76	1.62	3.93	1.07	10.38	2.30	26.38	4.89
d18O_P551_030423_ME18b_AnkA@3		7.9	0.12		8.2	1.5	**9.4**	0.34	1.05	1.72	7.56	1.48	3.44	1.45	8.10	2.27	21.00	5.09
d18O_P551_030423_ME18b_AnkA@4		8.6	0.12		8.1	1.6	**10.1**	0.32	0.18	0.39	9.28	1.41	3.64	1.48	10.85	1.53	27.33	4.28
d18O_P551_030423_ME18b_AnkB@1		13.8	0.18		7.9	1.8	**15.6**	0.28	0.10	0.31	9.29	1.71	1.04	0.54	13.65	1.45	29.02	3.26
d18O_P551_030423_ME18b_AnkB@2		11.3	0.14		8.2	1.5	**12.8**	0.34	0.31	0.68	9.67	2.17	2.51	1.06	10.45	2.12	26.10	4.79
d18O_P551_030423_ME18b_AnkB@3		10.7	0.15		8.1	1.6	**12.2**	0.33	0.22	0.42	9.48	2.13	1.57	0.66	10.87	2.34	26.78	6.03
d18O_P551_030423_ME18b_AnkB@4		10.3	0.15		8.0	1.6	**12.0**	0.31	0.28	0.54	9.30	2.26	3.54	2.28	11.66	2.42	28.16	4.35
d18O_P551_030423_ME18b_AnkB@5		11.4	0.10		8.1	1.5	**12.9**	0.33	0.39	0.55	9.11	2.00	2.82	1.89	10.29	1.81	24.68	4.66
d18O_P551_030423_ME18b_AnkB@6		9.4	0.14		8.0	1.7	**11.1**	0.30	0.19	0.40	9.00	1.86	4.73	1.19	11.54	1.73	26.54	3.20
d18O_P551_030423_MM11B_Calc@3		7.9	0.10				**11.0**		1.06	0.93	0.61	0.50	1.71	0.61	0.00	0.00	51.82	3.37
d18O_P551_030423_MM11B_Calc@4		7.8	0.15				**10.9**		4.77	1.00	0.61	0.49	1.32	0.57	0.04	0.19	50.88	3.21
d18O_P551_030423_MM11B_Calc@5		7.8	0.16				**10.9**		2.90	1.67	0.66	0.65	0.89	0.60	0.22	0.42	52.66	3.66
d18O_P551_030423_MM11B_Calc@6		7.7	0.18				**10.8**		6.26	1.58	0.58	0.50	1.18	0.50	0.01	0.11	49.53	4.98
d18O_P551_030423_MM11B_Calc@7		8.4	0.13				**11.5**		1.83	1.40	0.71	0.51	1.59	0.59	0.02	0.16	51.44	3.88
d18O_P551_030423_MM11B_Calc@8		7.8	0.15				**10.9**		3.43	1.38	0.64	0.48	1.57	0.56	0.00	0.00	48.87	4.54
d18O_P551_030423_MM11B_Calc@9		7.7	0.10				**10.8**		6.86	4.23	0.53	0.50	1.12	0.60	0.00	0.00	50.20	4.65
d18O_P551_030423_MM11B_Calc@10		7.6	0.22				**10.7**		1.59	1.24	0.47	0.50	1.31	0.51	0.00	0.00	53.14	3.14
d18O_P551_030423_MM11b_qz6@1		7.8	0.10				**10.9**		1.30	1.03	0.50	0.50	1.53	0.62	0.00	0.00	52.12	3.51
UNIL-Q1	38	4.3	0.35			5.6	9.9											
d18O-SKME18a-qz6@1		9.6					15.2											
d18O-SKME18a-qz6@2		9.9					15.5											
d18O-SKME18a-qz6@3		8.3					13.9											
d18O-SKME18a-qz6@4		9.9					15.5											
d18O-SKME18a-qz6@5		9.0					14.6											
d18O-SKME18a-qz3@2		9.2					14.8											
d18O-SKME18a-qz3@3		9.5					15.1											
d18O-SKME18a-qz3@4		9.9					15.5											
d18O-SKME18a-qz3@5		9.3					14.9											
d18O-SKME18a-qz3@6		9.5					15.1											
d18O_P551_030423_ME18b_Qz3B@1		9.8					15.4											
d18O_P551_030423_ME18b_Qz3B@02		9.7					15.3											
d18O_P551_030423_ME18b_Qz3B@03		10.0					15.6											
d18O_P551_030423_ME18b_Qz3B@04		9.9					15.5											
d18O_P551_030423_ME18b_Qz3B@05		9.7					15.3											
d18O_P551_030423_ME18b_Qz3B@06		9.6					15.2											

ID		**δ^{18}O mesured**		**Δ^{18}O dol-ank mes.**	**Δ^{18}O dol-ank cal.**	**Cal. IMF**	**δ^{18}O real**	**Fe#**	**SiO2**		**FeO**		**MnO**		**MgO**		**CaO**	
	n	**Average**	**2 S.D.**						**Av.**	**2 S.D.**	**Av.**	**2 S.D.**	**Av.**	**2 S.D.**	**Av.**	**2 S.D.**	**Av.**	**2 S.D.**
d18O_P551_030423_ME18b_Qz3B@07		9.8					15.4											
d18O_P551_030423_ME18b_Qz3B@08		10.1					15.7											
d18O_P551_030423_ME18b_Qz3B@09		9.8					15.4											
d18O_P551_030423_ME18b_Qz3B@10		10.2					15.8											
d18O_P551_030423_ME18b_Qz3B@11		9.8					15.4											
d18O_P551_030423_ME18b_Qz3B@12		10.1					15.7											
d18O_P551_030423_ME18b_Qz3B@13		9.9					15.5											
d18O_P551_030423_ME18b_Qz3B@14		10.0					15.6											
d18O_P551_030423_ME18b_Qz3B@15		10.0					15.6											
d18O_P551_030423_MM11b_qz6@2		7.6					13.2											
d18O_P551_030423_MM11b_qz6@3		7.5					13.0											
d18O_P551_030423_MM11b_qz6@4		7.8					13.4											
d18O_P551_030423_MM11b_qz6@5		7.2					12.8											
d18O_P551_030423_MM11b_qz3@1		7.7					13.3											
d18O_P551_030423_MM11b_qz3@2		7.9					13.4											
d18O_P551_030423_MM11b_qz3@3		8.2					13.7											
d18O_P551_030423_MM11b_qz3@4		8.4					14.0											
d18O_P551_030423_MM11b_qz3@5		7.8					13.3											
d18O_P551_030423_MM11b_qz3@6		8.0					13.5											

Supplementary Table A-2. Major element data of analysed reference materials obtained by XFR analyses

Sample name			**Meas. date/time**	**Al2O3**	**CaO**	**Cr2O3**	**Fe2O3**	**K2O**	**MgO**	**MnO**	**Na2O**	**P2O5**	**SiO2**	**TiO2**	**L.O.I.**	**Sum Of Conc.**
BE-N																
Basalt Reference values				**9.98**	**13.99**		**12.70**	**1.42**	**13.06**	**0.20**	**3.22**	**1.04**	**38.22**	**2.61**		**96.45**
BE-N	**STD**	MajorBasic32+Zn	08/11/2021 12:45	10.15	14.09	0.05	12.93	1.39	13.14	0.20	3.22	1.08	38.55	2.66		97.46
BE-N	**STD**	MajorBasic32+Zn	06/12/2021 10:00	10.14	14.20	0.05	12.91	1.39	13.10	0.20	3.19	1.09	38.43	2.63		97.33
BE-N	**STD**	MajorBasic32+Zn	10/12/2021 09:39	10.20	14.20	0.05	12.88	1.40	13.08	0.19	3.18	1.09	38.35	2.66		97.28
BE-N	**std**	MajorBasic32+Zn	04/02/2022 14:56	10.15	14.16	0.05	12.91	1.41	13.04	0.19	3.21	1.09	38.51	2.66		97.38
BE-N	**std**	MajorBasic32+Zn	24/02/2022 11:01	10.19	14.23	0.05	12.90	1.42	13.20	0.19	3.15	1.08	38.45	2.64		97.50
BE-N	**std**	MajorBasic32+Zn	04/03/2022 10:52	10.21	14.17	0.05	12.89	1.41	13.15	0.20	3.17	1.08	38.45	2.64		97.42
BE-N	**std**	MajorBasic32+Zn	10/03/2022 14:58	10.20	14.21	0.05	12.87	1.41	13.07	0.20	3.17	1.08	38.50	2.65		97.41
BE-N	**std**	MajorBasic32+Zn	17/03/2022 09:14	10.17	14.19	0.05	12.93	1.41	13.09	0.20	3.12	1.08	38.52	2.63		97.39
BE-N	**std**	MajorBasic32+Zn	24/03/2022 10:33	10.20	14.28	0.04	12.86	1.42	13.15	0.20	3.18	1.10	38.59	2.66		97.68
BE-N	**STD**	MajorBasic32+Zn	13/04/2022 10:48	10.17	14.11	0.05	12.83	1.41	13.12	0.20	3.16	1.08	38.36	2.64		97.13
BE-N	**STD**	MajorBasic32+Zn	26/04/2022 09:23	10.17	14.06	0.05	12.89	1.41	13.17	0.20	3.16	1.08	38.55	2.65		97.39
Average				10.18	14.17	0.05	12.89	1.41	13.12	0.20	3.17	1.08	38.48	2.65		97.40
2SD				0.05	0.13	0.01	0.06	0.02	0.10	0.01	0.06	0.01	0.16	0.02		
Relative standard deviation (%)				1.96	1.31		1.50	1.04	0.45	1.46	1.38	4.08	0.68	1.35		0.99

JB-1				**14.53**	**9.33**	**0.07**	**8.99**	**1.42**	**7.81**	**0.15**	**2.75**	**0.26**	**52.46**	**1.30**		**99.07**
Basalt (depleted) Reference values																
JB-1	**STD**	MajorBasic32+Zn	08/11/2021 12:54	14.94	9.33	0.06	8.92	1.44	7.91	0.16	2.94	0.27	52.14	1.30		99.41
JB-1	**STD**	MajorBasic32+Zn	06/12/2021 10:09	14.97	9.41	0.06	8.89	1.43	7.93	0.16	2.93	0.27	52.06	1.31		99.42

Sample name			**Meas. date/time**	**Al2O3**	**CaO**	**Cr2O3**	**Fe2O3**	**K2O**	**MgO**	**MnO**	**Na2O**	**P2O5**	**SiO2**	**TiO2**	**L.O.I.**	**Sum Of Conc.**
JB-1	**STD**	MajorBasic32+Zn	10/12/2021 09:48	14.60	9.44	0.07	8.86	1.43	7.87	0.16	2.88	0.28	53.04	1.30		99.93
JB-1	**std**	MajorBasic32+Zn	04/02/2022 15:05	14.90	9.41	0.07	8.90	1.44	7.88	0.16	2.94	0.28	52.82	1.30		100.10
JB-1	**std**	MajorBasic32+Zn	24/02/2022 11:11	15.07	9.42	0.06	8.89	1.46	7.88	0.16	2.93	0.28	53.02	1.32		100.49
JB-1	**std**	MajorBasic32+Zn	04/03/2022 11:01	14.99	9.42	0.06	8.93	1.44	7.90	0.17	2.95	0.28	53.09	1.31		100.54
JB-1	**std**	MajorBasic32+Zn	10/03/2022 15:08	15.04	9.41	0.06	8.89	1.44	7.88	0.15	2.88	0.28	52.27	1.31		99.61
JB-1	**std**	MajorBasic32+Zn	17/03/2022 09:23	14.09	9.40	0.07	8.90	1.45	7.84	0.16	2.87	0.28	52.88	1.31		99.25
JB-1	**std**	MajorBasic32+Zn	24/03/2022 10:41	15.01	9.45	0.06	8.87	1.44	7.88	0.16	2.97	0.28	52.13	1.32		99.57
JB-1	**std**	MajorBasic32+Zn	13/04/2022 15:07	14.99	9.30	0.06	8.89	1.44	7.88	0.16	2.97	0.28	52.04	1.31		99.32
JB-1	**std**	MajorBasic32+Zn	26/04/2022 09:32	14.13	9.32	0.07	8.89	1.45	7.91	0.16	2.93	0.29	52.13	1.31		98.59
Average				14.79	9.39	0.06	8.89	1.44	7.89	0.16	2.93	0.28	52.51	1.31		99.66
2SD				0.72	0.10	0.01	0.04	0.02	0.05	0.01	0.07	0.01	0.90	0.01		
Relative standard deviation (%)				1.81	0.66	6.42	1.07	1.54	1.03	7.10	6.45	6.24	0.10	0.78		0.60
BHVO-1																
Basalt Reference values				**13.69**	**11.43**	**0.04**	**12.32**	**0.53**	**7.21**	**0.17**	**2.31**	**0.28**	**49.79**	**2.74**	**0.52**	**101.03**
BHVO-1	**STD**	MajorBasic32+Zn	17/09/2021 09:49	14.02	11.46	0.04	12.35	0.51	7.23	0.17	2.33	0.30	50.00	2.73		101.14
BHVO-1	**STD**	MajorBasic32+Zn	28/10/2021 16:02	14.00	11.42	0.03	12.28	0.52	7.23	0.16	2.34	0.29	50.16	2.74		101.17
BHVO-1	**STD**	MajorBasic32+Zn	08/11/2021 13:13	14.02	11.47	0.04	12.38	0.52	7.28	0.17	2.33	0.29	50.16	2.73		101.39
BHVO-1	**STD**	MajorBasic32+Zn	06/12/2021 10:27	14.01	11.54	0.03	12.34	0.52	7.24	0.16	2.34	0.30	50.18	2.73		101.39
BHVO-1	**std**	MajorBasic32+Zn	04/02/2022 15:23	13.93	11.53	0.04	12.34	0.52	7.24	0.17	2.31	0.29	49.94	2.73		101.04
BHVO-1	**std**	MajorBasic32+Zn	24/02/2022 11:29	14.03	11.56	0.04	12.33	0.53	7.21	0.17	2.31	0.29	50.23	2.75		101.45
BHVO-1	**std**	MajorBasic32+Zn	04/03/2022 11:20	13.97	11.59	0.04	12.36	0.53	7.29	0.17	2.34	0.29	50.12	2.74		101.44
BHVO-1	**std**	MajorBasic32+Zn	10/03/2022 15:26	14.01	11.56	0.04	12.34	0.53	7.25	0.17	2.32	0.30	50.15	2.75		101.42
BHVO-1	**std**	MajorBasic32+Zn	17/03/2022 09:41	14.00	11.60	0.04	12.39	0.53	7.23	0.17	2.30	0.29	50.49	2.74		101.78
BHVO-1	**std**	MajorBasic32+Zn	24/03/2022 11:00	13.98	11.52	0.04	12.33	0.52	7.27	0.17	2.32	0.29	50.40	2.73		101.57
BHVO-1	**std**	MajorBasic32+Zn	13/04/2022 15:25	14.01	11.44	0.04	12.32	0.52	7.26	0.17	2.30	0.29	49.96	2.73		101.04
BHVO-1	**std**	MajorBasic32+Zn	26/04/2022 09:50	14.00	11.50	0.03	12.36	0.53	7.26	0.17	2.29	0.29	50.34	2.73		101.50
Average				14.00	11.52	0.04	12.34	0.52	7.25	0.17	2.32	0.29	50.18	2.74		101.36
2SD				0.05	0.12	0.01	0.06	0.01	0.05	0.01	0.03	0.01	0.34	0.02		
Relative standard deviation (%)				2.25	0.75		0.19	0.43	0.50	0.34	0.27	5.48	0.78	0.22		0.33
JG-1																
Granodiorite Reference values				**14.20**	**2.18**	**0.01**	**2.14**	**3.97**	**0.74**	**0.06**	**3.39**	**0.10**	**72.30**	**0.26**		**99.35**
JG-1	**STD**	MajorBasic32+Zn	28/10/2021 16:12	14.68	2.16	bdl	2.09	3.99	0.66	0.07	3.52	0.10	72.46	0.26		99.99
JG-1	**STD**	MajorBasic32+Zn	08/11/2021 13:31	14.46	2.16	bdl	2.10	4.01	0.67	0.06	3.54	0.10	72.68	0.26		100.04
JG-1	**STD**	MajorBasic32+Zn	06/12/2021 10:45	14.45	2.18	bdl	2.10	4.01	0.66	0.06	3.51	0.10	72.58	0.26		99.91
JG-1	**STD**	MajorBasic32+Zn	10/12/2021 10:24	14.80	2.19	0.01	2.08	3.99	0.67	0.06	3.46	0.10	72.60	0.26		100.22
JG-1	**std**	MajorBasic32+Zn	04/02/2022 15:32	14.75	2.18	bdl	2.08	3.98	0.66	0.07	3.53	0.09	72.25	0.26		99.85
JG-1	**std**	MajorBasic32+Zn	24/02/2022 11:38	14.76	2.18	bdl	2.11	4.03	0.67	0.06	3.49	0.10	72.84	0.26		100.50
JG-1	**std**	MajorBasic32+Zn	04/03/2022 11:29	14.77	2.18	0.01	2.10	4.00	0.67	0.06	3.53	0.10	72.34	0.26		100.02
JG-1	**std**	MajorBasic32+Zn	10/03/2022 15:35	14.63	2.19	bdl	2.10	3.99	0.66	0.06	3.54	0.10	72.30	0.26		99.83
JG-1	**std**	MajorBasic32+Zn	17/03/2022 09:50	14.46	2.18	bdl	2.11	4.01	0.67	0.06	3.48	0.10	72.64	0.26		99.97
JG-1	**std**	MajorBasic32+Zn	24/03/2022 11:09	14.59	2.18	0.00	2.11	4.00	0.67	0.06	3.48	0.10	72.80	0.26		100.25

Sample name			Meas. date/time	Al2O3	CaO	Cr2O3	Fe2O3	K2O	MgO	MnO	Na2O	P2O5	SiO2	TiO2	L.O.I.	Sum Of Conc.
JG-1	**std**	MajorBasic32+Zn	13/04/2022 15:35	14.65	2.16	0.01	2.09	4.01	0.68	0.06	3.52	0.10	72.28	0.26		99.82
JG-1	**std**	MajorBasic32+Zn	26/04/2022 09:59	14.25	2.16	0.01	2.10	3.99	0.66	0.07	3.50	0.10	72.70	0.26		99.80
Average				14.60	2.18	0.01	2.10	4.00	0.67	0.06	3.51	0.10	72.54	0.26		100.02
2SD				0.34	0.02	0.01	0.02	0.03	0.01	0.01	0.05	0.01	0.42	0.00		
Relative standard deviation (%)				2.85	0.23	14.89	1.99	0.78	9.91	0.79	3.49	2.23	0.33	0.00		0.67

Quality control for 2010-2011																
Average HUSG			**13/01/1900 17:55**	**13.75**	**1.52**	**0.00**	**3.78**	**4.66**	**1.04**	**0.06**	**2.57**	**0.21**	**69.77**	**0.54**	**0.73**	**98.65**
STDEV			**00/01/1900 04:51**	**0.20**	**0.04**	**0.00**	**0.14**	**0.06**	**0.04**	**0.01**	**0.18**	**0.01**	**0.54**	**0.02**	**0.05**	**0.71**
MIN			**13/01/1900 00:57**	**13.04**	**1.48**	**0.00**	**3.64**	**4.55**	**0.94**	**0.05**	**2.30**	**0.20**	**68.42**	**0.52**	**0.53**	**97.23**
MAX			**14/01/1900 07:06**	**14.30**	**1.63**	**0.01**	**4.56**	**4.80**	**1.22**	**0.08**	**3.30**	**0.23**	**70.96**	**0.60**	**0.80**	**100.40**
HUSG-1	**STD**	MajorBasic32+Zn	08/11/2021 13:03	14.18	1.55	bdl	3.74	4.64	1.01	0.05	2.77	0.21	70.41	0.54	0.80	99.90
HUSG-1	**STD**	MajorBasic32+Zn	06/12/2021 10:18	14.17	1.56	bdl	3.71	4.64	1.02	0.06	2.79	0.21	70.58	0.54	0.80	100.08
HUSG-1	**STD**	MajorBasic32+Zn	10/12/2021 09:57	14.21	1.57	bdl	3.70	4.64	1.01	0.05	2.77	0.21	70.60	0.54	0.80	100.10
HUSG-1	**std**	MajorBasic32+Zn	04/02/2022 15:14	14.20	1.57	bdl	3.70	4.62	1.03	0.06	2.79	0.21	70.37	0.54	0.80	99.89
HUSG-1	**std**	MajorBasic32+Zn	24/02/2022 11:20	14.15	1.55	bdl	3.71	4.64	1.03	0.05	2.72	0.21	70.57	0.55	0.80	99.98
HUSG-1	**std**	MajorBasic32+Zn	04/03/2022 11:11	14.25	1.57	bdl	3.71	4.67	1.01	0.06	2.75	0.21	70.68	0.55	0.80	100.26
HUSG-1	**std**	MajorBasic32+Zn	10/03/2022 15:17	14.22	1.57	bdl	3.68	4.64	1.03	0.06	2.74	0.21	70.27	0.55	0.80	99.77
HUSG-1	**std**	MajorBasic32+Zn	17/03/2022 09:32	14.15	1.57	bdl	3.75	4.65	1.02	0.05	2.71	0.22	70.68	0.54	0.80	100.14
HUSG-1	**M-1**	MajorBasic32+Zn	24/03/2022 10:51	14.27	1.56	bdl	3.71	4.64	1.00	0.05	2.76	0.22	70.60	0.54	0.80	100.15
HUSG-1	**STD**	MajorBasic32+Zn	13/04/2022 15:16	14.20	1.56	bdl	3.70	4.63	1.03	0.06	2.74	0.22	70.67	0.54	0.80	100.15
HUSG-1	**STD**	MajorBasic32+Zn	26/04/2022 09:41	14.20	1.56	bdl	3.73	4.64	1.03	0.06	2.76	0.22	70.81	0.54	0.80	100.35
Average				14.20	1.56	#DIV/0!	3.71	4.64	1.02	0.06	2.75	0.21	70.57	0.54	0.80	100.07
2SD				0.08	0.02	#DIV/0!	0.04	0.02	0.02	0.01	0.05	0.01	0.32	0.01	0.00	
Relative standard deviation (%)				3.30	2.72	#DIV/0!	1.69	0.31	2.31	13.93	7.22	0.54	1.15	0.06	9.58	1.44

WITS-G																
Granite Reference values				**11.53**	**1.51**		**3.58**	**4.46**	**0.10**	**0.05**	**2.97**	**0.04**	**74.53**	**0.29**	**0.08**	**99.14**
WITS-G				**11.73**	**1.44**		**3.43**	**4.29**	**0.21**	**0.03**	**2.39**	**0.05**	**74.26**	**0.29**	**0.07**	**98.19**
WITS-G (AUG)				**12.01**	**1.46**		**3.51**	**4.26**	**0.05**	**0.02**	**2.39**	**0.06**	**74.56**	**0.30**	**0.07**	**98.69**
WITS-G (OCT)				**11.52**	**1.47**		**3.47**	**4.33**	**0.00**	**0.05**	**2.37**	**0.03**	**73.57**	**0.28**	**0.07**	**97.14**
WITS-G (DEC)				**11.45**	**1.47**		**3.50**	**4.39**	**0.06**	**0.05**	**2.45**	**0.04**	**75.45**	**0.28**	**0.07**	**99.22**
Average reference value				**11.65**	**1.47**	_	**3.50**	**4.34**	**0.08**	**0.04**	**2.51**	**0.04**	**74.47**	**0.29**	**0.07**	**98.48**
WITS-G	**STD**	MajorBasic32+Zn	30/08/2021 14:54	12.30	1.50	bdl	3.41	4.46	0.04	0.05	2.83	0.04	74.19	0.27	0.07	**99.16**
WITS-G	**STD**	MajorBasic32+Zn	14/09/2021 13:22	12.27	1.49	bdl	3.42	4.47	0.03	0.05	2.85	0.05	74.18	0.26	0.07	**99.14**
WITS-G	**STD**	MajorBasic32+Zn	17/09/2021 09:58	12.25	1.50	bdl	3.40	4.46	0.02	0.05	2.80	0.04	74.81	0.27	0.07	**99.67**
WITS-G	**STD**	MajorBasic32+Zn	28/10/2021 16:30	12.25	1.49	bdl	3.38	4.48	0.02	0.05	2.86	0.05	74.99	0.27	0.07	**99.91**
WITS-G	**STD**	MajorBasic32+Zn	08/11/2021 13:22	12.27	1.47	bdl	3.39	4.46	0.02	0.04	2.85	0.04	74.92	0.26	0.07	**99.79**
WITS-G	**STD**	MajorBasic32+Zn	06/12/2021 10:36	12.24	1.50	bdl	3.38	4.47	0.03	0.05	2.85	0.05	74.21	0.27	0.07	**99.12**
WITS-G	**STD**	MajorBasic32+Zn	10/12/2021 10:15	12.31	1.51	bdl	3.40	4.46	0.02	0.04	2.85	0.05	74.21	0.27	0.07	**99.19**
WITS-G	**std**	MajorBasic32+Zn	24/02/2022 11:47	12.25	1.51	bdl	3.39	4.46	0.03	0.05	2.79	0.05	74.95	0.27	0.07	**99.82**
WITS-G	**std**	MajorBasic32+Zn	04/03/2022 11:38	12.32	1.52	bdl	3.39	4.46	0.03	0.05	2.86	0.05	74.23	0.27	0.07	**99.25**

Sample name			Meas. date/time	Al2O3	CaO	Cr2O3	Fe2O3	K2O	MgO	MnO	Na2O	P2O5	SiO2	TiO2	L.O.I.	Sum Of Conc.
WITS-G	**std**	MajorBasic32+Zn	10/03/2022 15:44	12.28	1.50	bdl	3.38	4.45	0.03	0.05	2.85	0.05	74.95	0.27	0.07	**99.88**
WITS-G	**std**	MajorBasic32+Zn	17/03/2022 10:00	12.25	1.52	bdl	3.38	4.46	0.02	0.05	2.84	0.05	74.10	0.27	0.07	**99.01**
WITS-G	**std**	MajorBasic32+Zn	24/03/2022 11:18	12.30	1.50	bdl	3.37	4.46	0.03	0.05	2.85	0.05	74.26	0.27	0.07	**99.21**
WITS-G	**std**	MajorBasic32+Zn	13/04/2022 15:44	12.26	1.48	bdl	3.35	4.44	0.03	0.05	2.79	0.05	74.95	0.27	0.07	**99.74**
WITS-G	**std**	MajorBasic32+Zn	26/04/2022 10:08	12.32	1.48	-0.01	3.38	4.46	0.04	0.05	2.83	0.05	74.13	0.27	0.07	**99.07**
Average				12.27	1.50	#DIV/0!	3.39	4.46	0.03	0.05	2.84	0.05	74.53	0.27	0.07	99.45
2SD				0.06	0.03	#DIV/0!	0.03	0.02	0.01	0.01	0.05	0.01	0.77	0.01	0.00	
Relative standard deviation (%)				5.42	0.71		5.37	0.02	73.08	3.08	4.51	19.23	0.01	7.43	12.50	0.32

Supplementary Table A-3. Trace element data of reference materials obtained by ICP-MS analyses

	Sc	Ti	V	Cr	Co	Ni	Cu	Ge	Rb	Sr	Y	Zr	Nb	Ba	La	Ce	Pr	Nd	Sm	Eu	Tb	Gd	Dy	Ho	Er	Tm	Yb	Lu	Hf	Ta	Pb	Th	U
Bir_1a	43.7	5851.6	325.3	402.5	52.0	168.6	122.7	1.4	0.19	109.0	15.8	14.7	0.54	6.33	0.60	1.87	0.37	2.37	1.06	0.50	0.35	1.90	2.56	0.57	1.66	0.25	1.65	0.25	0.59	0.038	3.5	0.028	0.009
Bir_1a	42.8	5540.5	316.1	381.1	51.2	167.4	119.6	1.4	0.18	105.4	15.3	14.2	0.52	6.24	0.59	1.84	0.37	2.29	1.08	0.51	0.35	1.86	2.51	0.57	1.63	0.25	1.62	0.24	0.57	0.037	3.4	0.032	0.008
Bir_1a	45.4	5856.7	321.3	397.9	53.8	177.0	121.9	1.4	0.19	110.0	16.1	14.9	0.54	6.45	0.61	1.93	0.38	2.43	1.11	0.54	0.37	1.94	2.63	0.59	1.73	0.26	1.66	0.25	0.59	0.041	3.7	0.030	0.011
Bir_1a	42.7	5607.1	318.8	376.8	51.5	171.8	119.4	1.4	0.19	109.3	15.7	14.7	0.54	6.43	0.59	1.90	0.37	2.35	1.08	0.51	0.36	1.90	2.56	0.59	1.68	0.26	1.62	0.25	0.57	0.028	2.8	0.028	0.010
Bir_1a	41.8	5380.6	305.3	359.0	49.3	160.2	114.6	1.2	0.17	98.6	14.1	13.3	0.50	5.87	0.55	1.70	0.34	2.16	0.99	0.47	0.32	1.71	2.34	0.53	1.50	0.22	1.48	0.22	0.53	0.024	2.5	0.025	0.010
Bir_1a	43.8	5948.4	340.2	396.3	54.7	170.6	127.6	1.4	0.19	104.6	15.0	14.1	0.52	6.29	0.58	1.81	0.36	2.30	1.07	0.50	0.35	1.84	2.48	0.56	1.61	0.25	1.57	0.24	0.57	0.028	2.7	0.027	0.000
Bir_1a	42.8	5658.7	325.5	392.1	52.5	171.9	123.6	1.5	0.19	111.6	16.2	15.2	0.55	6.65	0.62	1.98	0.38	2.41	1.11	0.53	0.36	1.93	2.62	0.60	1.71	0.27	1.70	0.25	0.60	0.040	3.5	0.033	0.011
Bir_1a	42.4	5808.2	331.4	396.8	52.9	173.6	120.7	1.5	0.19	108.6	15.9	15.0	0.54	6.60	0.61	1.94	0.38	2.41	1.11	0.53	0.36	1.96	2.63	0.59	1.70	0.26	1.70	0.25	0.59	0.038	3.5	0.032	0.009
BIR-1a	42.0	5492.4	317.5	398.8	52.5	169.1	119.1	1.4	0.20	110.5	15.9	15.0	0.53	6.56	0.60	1.96	0.37	2.40	1.09	0.52	0.36	1.92	2.61	0.59	1.70	0.26	1.70	0.25	0.60	0.031	2.9	0.029	0.010
BIR-1a	41.6	5740.3	326.3	409.2	52.7	170.4	119.3	1.4	0.19	109.1	15.8	14.8	0.53	6.46	0.59	1.91	0.37	2.34	1.10	0.52	0.36	1.90	2.61	0.58	1.71	0.26	1.66	0.25	0.59	0.031	2.9	0.030	0.011
BIR-1a	44.5	5983.1	341.2	429.9	54.5	179.6	123.9	1.5	0.20	111.6	16.1	15.2	0.55	6.68	0.63	1.93	0.39	2.48	1.13	0.54	0.37	1.99	2.64	0.59	1.73	0.27	1.73	0.26	0.62	0.032	3.0	0.030	0.011
Average	**43.0**	**5715.2**	**324.4**	**394.6**	**52.5**	**170.9**	**121.1**	**1.4**	**0.19**	**108.0**	**15.6**	**14.7**	**0.53**	**6.41**	**0.60**	**1.89**	**0.37**	**2.36**	**1.09**	**0.51**	**0.36**	**1.90**	**2.56**	**0.58**	**1.67**	**0.25**	**1.64**	**0.25**	**0.59**	**0.033**	**3.1**	**0.029**	**0.009**
2 S.D.	2.3	372.2	20.1	34.8	3.0	9.7	6.5	0.1	0.02	7.3	1.2	1.1	0.03	0.44	0.04	0.15	0.02	0.16	0.07	0.04	0.03	0.14	0.18	0.04	0.13	0.03	0.14	0.02	0.05	0.010	0.8	0.004	0.006
2 S.D. %	5.2	6.5	6.2	8.8	5.7	5.7	5.3	9.8	8.62	6.8	7.4	7.5	5.66	6.86	6.86	7.93	6.38	6.90	6.41	7.36	7.73	7.45	6.85	7.01	7.75	10.01	8.32	7.96	7.97	30.949	24.4	15.262	65.660
Reference (Georem)	43.2	5746.0	320.6	392.9	52.2	168.9	120.7	1.5	0.21	108.6	15.6	14.8	0.55	6.75	0.63	1.92	0.37	2.40	1.11	0.52	0.36	1.81	2.54	0.57	1.68	0.26	1.63	0.25	0.58	0.041	3.0	0.033	0.011
Difference %	**-0.4**	**-0.5**	**1.2**	**0.4**	**0.6**	**1.2**	**0.4**	**-3.9**	**-10.38**	**-0.5**	**0.2**	**-1.0**	**-3.71**	**-4.98**	**-4.70**	**-1.67**	**-0.28**	**-1.77**	**-2.24**	**-1.04**	**-1.83**	**4.74**	**0.90**	**1.02**	**-0.57**	**-0.59**	**0.85**	**-0.71**	**0.62**	**-19.352**	**3.1**	**-10.465**	**-13.323**

	Sc	Ti	V	Cr	Co	Ni	Cu	Ge	Rb	Sr	Y	Zr	Nb	Ba	La	Ce	Pr	Nd	Sm	Eu	Tb	Gd	Dy	Ho	Er	Tm	Yb	Lu	Hf	Ta	Pb	Th	U
G2	3.7	2832.0	34.2	6.1	4.4	2.1	9.8	0.8	164.86	471.9	9.9	335.8	12.00	1862.78	85.60	160.80	16.40	52.10	6.97	1.43	0.51	4.01	2.08	0.35	0.95	0.12	0.71	0.10	7.99	0.777	34.2	23.900	1.820
G2	3.4	2841.7	33.4	5.5	4.2	2.1	9.1	0.8	160.94	455.9	9.4	323.3	11.50	1812.11	83.60	155.44	15.80	50.00	6.71	1.39	0.50	3.90	1.98	0.34	0.91	0.12	0.67	0.09	7.67	0.738	33.1	23.000	1.740
G2	3.7	2998.1	35.1	6.4	4.7	2.2	10.0	1.0	175.83	498.9	10.3	355.1	12.60	1977.21	90.50	167.24	17.10	54.30	7.21	1.49	0.53	4.19	2.19	0.37	0.99	0.12	0.74	0.10	8.24	0.798	35.9	24.100	1.820
G2	3.5	2789.2	33.3	6.8	4.3	2.0	8.5	0.8	163.59	465.1	9.6	351.0	11.90	1846.21	86.10	160.87	16.44	52.67	7.00	1.44	0.52	4.07	2.13	0.35	0.96	0.12	0.72	0.10	8.63	0.787	29.9	25.735	1.841
G2	3.4	2835.6	33.5	7.0	4.3	1.9	8.8	0.8	159.51	446.4	9.0	337.8	11.44	1799.71	83.81	153.78	15.75	50.07	6.62	1.35	0.49	3.88	2.02	0.34	0.92	0.11	0.68	0.10	8.05	0.739	27.9	24.151	1.724
G2	3.3	2975.9	34.9	7.1	4.5	2.0	9.1	0.9	162.64	454.1	9.1	343.4	11.67	1834.31	85.75	156.27	15.93	50.58	6.71	1.39	0.48	3.92	2.04	0.34	0.92	0.11	0.70	0.10	8.28	0.749	28.6	24.547	0.000
G2	3.5	2806.1	34.2	7.1	4.5	1.9	9.8	0.9	164.80	468.0	9.9	336.3	12.17	1868.60	85.12	159.48	16.28	51.79	7.01	1.43	0.51	4.09	2.16	0.36	0.96	0.12	0.71	0.10	8.01	0.787	30.6	24.059	1.959
G2	3.9	3172.6	37.8	7.6	4.9	2.3	11.1	1.0	184.02	522.5	10.8	373.5	13.48	2077.46	94.89	175.83	17.98	57.12	7.74	1.58	0.57	4.53	2.36	0.40	1.05	0.14	0.79	0.11	8.89	0.874	34.1	26.365	2.166
G2	3.9	3172.6	37.8	7.6	4.9	2.3	11.1	1.0	184.02	522.5	10.8	373.5	13.48	2077.46	94.89	175.83	17.98	57.12	7.74	1.58	0.57	4.53	2.36	0.40	1.05	0.14	0.79	0.11	8.89	0.874	34.1	26.365	2.166
Average	**3.6**	**2936.0**	**34.9**	**6.8**	**4.5**	**2.1**	**9.7**	**0.9**	**168.91**	**478.4**	**9.9**	**347.8**	**12.25**	**1906.21**	**87.81**	**162.84**	**16.63**	**52.86**	**7.08**	**1.45**	**0.52**	**4.13**	**2.15**	**0.36**	**0.97**	**0.12**	**0.72**	**0.10**	**8.29**	**0.791**	**32.0**	**24.691**	**1.693**
2 S.D.	0.5	304.6	3.5	1.4	0.5	0.3	1.8	0.2	19.46	58.1	1.3	34.5	1.57	219.05	8.96	16.68	1.74	5.53	0.84	0.16	0.06	0.50	0.27	0.05	0.10	0.02	0.08	0.01	0.85	0.103	5.7	2.371	1.312
2 S.D. %	12.7	10.4	10.1	20.7	11.9	16.2	19.0	19.5	11.52	12.2	13.4	9.9	12.81	11.49	10.21	10.24	10.46	10.47	11.80	11.31	12.33	12.20	12.77	12.83	10.56	14.99	11.68	11.64	10.25	13.034	17.7	9.601	77.494
Reference (Georem)	3.7	2876.2	35.1	7.9	4.5	3.5	11.0	1.1	168.50	474.9	9.9	319.0	12.00	1860.00	88.40	161.20	16.90	53.80	7.19	1.41	0.50	4.23	2.28	0.37	0.93	0.12	0.72	0.10	7.78	0.834	30.0	24.500	1.960
Difference %	**-2.0**	**2.1**	**-0.5**	**-13.8**	**0.9**	**-39.7**	**-11.9**	**-16.7**	**0.24**	**0.7**	**-0.1**	**9.0**	**2.07**	**2.48**	**-0.67**	**1.02**	**-1.59**	**-1.75**	**-1.51**	**3.08**	**4.90**	**-2.48**	**-5.84**	**-2.76**	**4.29**	**-1.43**	**0.05**	**-0.57**	**6.61**	**-5.110**	**6.8**	**0.781**	**-13.630**

	Sc	Ti	V	Cr	Co	Ni	Cu	Ge	Rb	Sr	Y	Zr	Nb	Ba	La	Ce	Pr	Nd	Sm	Eu	Tb	Gd	Dy	Ho	Er	Tm	Yb	Lu	Hf	Ta	Pb	Th	U
Ben	22.7	16158.4	233.8	364.8	59.8	261.0	70.5	1.5	47.50	1397.9	29.2	273.9	111.92	1028.17	81.10	153.23	17.40	65.90	12.10	3.71	1.33	9.86	6.38	1.08	2.66	0.32	1.84	0.24	5.90	5.700	4.6	10.600	2.430
Ben	22.1	15529.9	229.7	356.5	59.9	261.6	69.0	1.6	47.30	1371.9	28.6	268.9	111.40	1023.48	80.60	151.36	17.20	64.50	11.90	3.63	1.32	9.62	6.29	1.08	2.58	0.32	1.77	0.24	5.68	5.610	4.5	10.600	2.410
Ben	22.0	15428.8	228.6	353.8	60.0	259.9	68.3	1.6	46.90	1358.5	28.4	266.5	110.55	1017.77	79.80	148.51	17.00	64.10	11.80	3.64	1.29	9.57	6.17	1.07	2.54	0.32	1.74	0.24	5.56	5.500	4.5	10.100	2.320
Ben	23.5	16245.3	243.2	368.4	63.7	277.6	74.0	1.8	48.95	1452.2	30.1	283.6	117.46	1043.43	82.88	156.52	17.57	67.62	12.33	3.82	1.37	10.14	6.58	1.13	2.67	0.32	1.89	0.25	5.90	5.794	4.7	10.842	2.443
Average	**22.6**	**15840.6**	**233.8**	**360.8**	**60.8**	**265.0**	**70.4**	**1.6**	**47.66**	**1395.1**	**29.1**	**273.2**	**112.83**	**1028.21**	**81.10**	**152.40**	**17.29**	**65.53**	**12.03**	**3.70**	**1.33**	**9.80**	**6.35**	**1.09**	**2.61**	**0.32**	**1.81**	**0.24**	**5.76**	**5.651**	**4.6**	**10.535**	**2.401**
2 S.D.																																	
2 S.D. %																																	
Reference (Georem)	22.0	15642.8	235.0	360.0	60.0	267.0	72.0	1.2	47.00	1370.0	30.0	260.0	105.00	1025.00	82.00	152.00	17.50	67.00	12.20	3.60	1.30	9.70	6.40	1.10	2.50	0.34	1.80	0.24	5.60	5.700	4.0	10.400	2.400
Difference %	**2.6**	**1.3**	**-0.5**	**0.2**	**1.4**	**-0.7**	**-2.2**	**34.4**	**1.41**	**1.8**	**-3.1**	**5.1**	**7.46**	**0.31**	**-1.10**	**0.27**	**-1.19**	**-2.19**	**-1.38**	**2.77**	**2.05**	**1.01**	**-0.71**	**-1.01**	**4.55**	**-6.63**	**0.57**	**1.37**	**2.85**	**-0.858**	**14.3**	**1.303**	**0.030**

	Sc	**Ti**	**V**	**Cr**	**Co**	**Ni**	**Cu**	**Ge**	**Rb**	**Sr**	**Y**	**Zr**	**Nb**	**Ba**	**La**	**Ce**	**Pr**	**Nd**	**Sm**	**Eu**	**Tb**	**Gd**	**Dy**	**Ho**	**Er**	**Tm**	**Yb**	**Lu**	**Hf**	**Ta**	**Pb**	**Th**	**U**

	Sc	**Ti**	**V**	**Cr**	**Co**	**Ni**	**Cu**	**Ge**	**Rb**	**Sr**	**Y**	**Zr**	**Nb**	**Ba**	**La**	**Ce**	**Pr**	**Nd**	**Sm**	**Eu**	**Tb**	**Gd**	**Dy**	**Ho**	**Er**	**Tm**	**Yb**	**Lu**	**Hf**	**Ta**	**Pb**	**Th**	**U**
UB_N (ppm)	11.9	570.1	60.8	2163.0	96.9	1824.0	24.0	1.1	3.30	7.2	2.6	3.8	0.04	21.05	0.30	0.77	0.11	0.61	0.20	0.09	0.06	0.32	0.43	0.10	0.28	0.05	0.30	0.05	0.14	-0.002	11.9	0.054	0.049
UB_N (ppm)	11.5	531.8	57.8	2150.1	91.6	1803.9	23.3	1.0	3.06	6.6	2.3	3.4	0.04	19.51	0.27	0.68	0.10	0.55	0.19	0.07	0.05	0.30	0.38	0.09	0.26	0.04	0.28	0.04	0.12	-0.001	10.3	0.051	0.040
UB_N (ppm)	12.7	588.3	64.9	2455.2	103.5	2059.6	26.2	1.2	3.45	7.5	2.6	3.9	0.05	21.99	0.31	0.79	0.12	0.62	0.22	0.09	0.06	0.34	0.44	0.10	0.30	0.05	0.31	0.05	0.14	-0.002	12.0	0.058	0.000
Average	**12.0**	**563.4**	**61.2**	**2256.1**	**97.4**	**1895.8**	**24.5**	**1.1**	**3.27**	**7.1**	**2.5**	**3.7**	**0.04**	**20.85**	**0.30**	**0.75**	**0.11**	**0.59**	**0.21**	**0.08**	**0.06**	**0.32**	**0.42**	**0.10**	**0.28**	**0.04**	**0.30**	**0.05**	**0.13**	**-0.002**	**11.4**	**0.054**	**0.030**
2 S.D.	0.5	21.1	2.5	132.8	4.1	109.2	1.2	0.1	0.14	0.3	0.1	0.2	0.00	0.89	0.02	0.04	0.01	0.03	0.01	0.01	0.00	0.02	0.03	0.01	0.02	0.00	0.01	0.00	0.01	0.000	0.7	0.002	0.020
2 S.D. %	3.8	3.7	4.1	5.9	4.2	5.8	4.7	6.8	4.19	4.5	4.7	4.6	6.51	4.27	5.12	5.71	5.79	5.20	4.98	7.50	5.92	4.67	6.39	5.73	5.60	6.83	3.85	2.24	7.48	-26.863	6.3	4.548	66.667
Reference (Chauvel)	11.4	659.0	73.6	2148.0	96.5	1830.0	25.2		3.27	7.1	2.4	3.6	0.60	27.40	0.32	0.79	0.12	0.60	0.22	0.08	0.06	0.32	0.42	0.09	0.29		0.29	0.05	0.13	0.013	12.2	0.060	0.059
Difference %	**5.6**	**-14.5**	**-16.9**	**5.0**	**0.9**	**3.6**	**-2.8**	**#DIV/0!**	**-0.03**	**0.5**	**5.4**	**2.6**	**-92.88**	**-23.90**	**-5.58**	**-5.36**	**-3.15**	**-1.84**	**-3.97**	**-0.21**	**-1.54**	**0.94**	**-1.70**	**1.15**	**-3.21**	**#DIV/0!**	**1.48**	**0.03**	**0.14**	**-111.926**	**-6.6**	**-10.044**	**-49.610**

JB_3	30.4	8285.2	375.3	57.9	33.6	35.7	181.1	1.1	14.09	400.9	25.1	90.7	2.01	229.18	8.25	20.81	3.18	15.23	4.09	1.28	0.72	4.58	4.41	0.94	2.60	0.39	2.49	0.36	2.65	0.125	5.8	1.304	0.472
JB_3	34.7	8695.6	391.5	60.3	37.1	38.5	201.1	1.3	14.75	416.6	26.1	93.8	2.07	235.79	8.52	21.50	3.29	15.94	4.24	1.36	0.75	4.75	4.67	0.97	2.66	0.40	2.54	0.38	2.73	0.127	5.9	1.346	0.477
Average	**32.6**	**8490.4**	**383.4**	**59.1**	**35.4**	**37.1**	**191.1**	**1.2**	**14.42**	**408.8**	**25.6**	**92.2**	**2.04**	**232.49**	**8.38**	**21.16**	**3.24**	**15.59**	**4.17**	**1.32**	**0.73**	**4.67**	**4.54**	**0.95**	**2.63**	**0.39**	**2.52**	**0.37**	**2.69**	**0.126**	**5.9**	**1.325**	**0.474**
2 S.D.																																	
2 S.D. %																																	
Reference (Georem)	33.3	8690.0	383.0	60.4	36.3	38.8	198.0	1.1	15.10	403.0	27.0	98.3	2.30	245.00	8.89	21.50	3.11	15.60	4.27	1.31	0.75	4.47	4.55	0.79	2.61	0.41	2.62	0.39	2.68	0.150	5.6	1.270	0.480
Difference %	**-2.2**	**-2.3**	**0.1**	**-2.2**	**-2.6**	**-4.4**	**-3.5**	**4.6**	**-4.50**	**1.4**	**-5.1**	**-6.2**	**-11.36**	**-5.11**	**-5.70**	**-1.59**	**4.09**	**-0.08**	**-2.39**	**0.80**	**-2.05**	**4.39**	**-0.17**	**20.80**	**0.73**	**-3.74**	**-3.85**	**-4.26**	**0.42**	**-15.828**	**5.6**	**4.317**	**-1.176**

	Sc	**Ti**	**V**	**Cr**	**Co**	**Ni**	**Cu**	**Ge**	**Rb**	**Sr**	**Y**	**Zr**	**Nb**	**Ba**	**La**	**Ce**	**Pr**	**Nd**	**Sm**	**Eu**	**Tb**	**Gd**	**Dy**	**Ho**	**Er**	**Tm**	**Yb**	**Lu**	**Hf**	**Ta**	**Pb**	**Th**	**U**
JB_1a	27.4	7878.8	198.4	406.4	39.0	137.4	53.0	1.3	36.29	439.3	22.3	134.5	27.06	479.55	35.90	64.26	6.98	25.58	4.92	1.47	0.70	4.63	3.99	0.82	2.21	0.32	2.00	0.30	3.46	1.659	7.1	8.980	1.564
Reference (Georem)	27.8	7732.0	200.3	408.0	38.5	139.5	54.5	1.0	38.15	443.4	22.9	140.1	27.57	495.10	37.74	65.93	7.10	26.15	5.10	1.48	0.70	4.70	4.07	0.81	2.23	0.32	2.10	0.31	3.47	1.738	6.4	8.970	1.615
Ecart	**-1.5**	**1.9**	**-1.0**	**-0.4**	**1.3**	**-1.5**	**-2.8**	**32.2**	**-4.87**	**-0.9**	**-2.6**	**-4.0**	**-1.85**	**-3.14**	**-4.87**	**-2.53**	**-1.62**	**-2.16**	**-3.54**	**-0.94**	**-0.10**	**-1.54**	**-1.95**	**2.36**	**-1.15**	**-0.36**	**-4.96**	**-5.02**	**-0.25**	**-4.560**	**9.9**	**0.110**	**-3.146**

	Sc	Ti	V	Cr	Co	Ni	Cu	Ge	Rb	Sr	Y	Zr	Nb	Ba	La	Ce	Pr	Nd	Sm	Eu	Tb	Gd	Dy	Ho	Er	Tm	Yb	Lu	Hf	Ta	Pb	Th	U
IFG	0.2	22.5	1.6	4.4	3.3	23.8	10.0	14.6	0.29	3.5	9.7	0.8	0.07	2.13	2.31	3.54	0.39	1.63	0.38	0.35	0.11	0.68	0.80	0.20	0.63	0.09	0.59	0.09	0.02	0.003	5.1	0.044	0.015
IFG	0.2	23.2	1.7	4.3	3.3	24.0	10.2	14.9	0.29	3.5	9.5	0.8	0.07	2.05	2.29	3.44	0.38	1.62	0.38	0.35	0.11	0.67	0.78	0.20	0.60	0.09	0.56	0.08	0.02	0.002	4.9	0.041	0.013
IFG	0.2	22.4	1.9	4.5	3.5	23.8	10.3	14.7	0.30	3.4	9.4	0.8	0.07	2.06	2.29	3.41	0.38	1.59	0.39	0.36	0.11	0.68	0.78	0.20	0.60	0.09	0.56	0.09	0.02	0.003	5.1	0.043	0.015
Average	**0.2**	**22.7**	**1.7**	**4.4**	**3.3**	**23.9**	**10.2**	**14.7**	**0.29**	**3.5**	**9.5**	**0.8**	**0.07**	**2.08**	**2.30**	**3.46**	**0.38**	**1.61**	**0.38**	**0.35**	**0.11**	**0.67**	**0.79**	**0.20**	**0.61**	**0.09**	**0.57**	**0.09**	**0.02**	**0.003**	**5.0**	**0.042**	**0.014**
2 S.D.	0.0	0.4	0.2	0.1	0.1	0.1	0.2	0.2	0.00	0.1	0.2	0.0	0.00	0.06	0.02	0.09	0.00	0.02	0.00	0.00	0.00	0.01	0.02	0.00	0.02	0.00	0.02	0.00	0.00	0.000	0.1	0.002	0.001
2 S.D. %	4.3	1.8	10.2	1.5	4.1	0.5	1.6	1.2	0.51	2.0	1.8	2.1	2.02	3.07	0.82	2.66	1.05	1.43	0.93	1.03	1.37	0.87	2.37	0.53	4.10	3.55	3.98	2.93	1.63	14.985	2.5	5.001	7.202
Reference (Georem)	0.3	0.0	0.0	17.4	0.0	23.9	0.0	0.0	0.29	3.6	9.1	0.6	0.10	2.02	2.71	3.90	0.43	1.73	0.40	0.36	0.11	0.67	0.79	0.21	0.62	0.09	0.58	0.09	0.02	0.172	2.5	0.043	0.021
Difference %	**-25.7**			**-74.6**		**-0.2**			**1.04**	**-4.0**	**4.3**	**41.1**	**-25.41**	**2.77**	**-15.03**	**-11.29**	**-10.68**	**-6.87**	**-4.47**	**-2.83**	**-3.64**	**0.85**	**-0.54**	**-3.23**	**-2.17**	**-1.53**	**-2.02**	**-2.35**	**13.89**	**-98.376**	**100.1**	**-2.432**	**-32.405**

Supplementary Table A-4. Ce isotope ratios of the Ce-LMV standard determined by TIMS

Analysis ID	sample name	Signals $^{138}Ce^{16}O$	 $^{142}Ce^{16}O$	Corrected ratios $^{138}Ce/^{142}Ce$	 2s.e.
1	Ce-LMV 1000ng	0.24	10.64	0.02257053	0.00000021
2	Ce-LMV 1000ng	0.16	7.28	0.02256975	0.00000028
3	Ce-LMV 1000ng	0.21	9.53	0.02257032	0.00000021
4	Ce-LMV 1000ng	0.17	7.80	0.02256944	0.00000025
5	Ce-LMV 1000ng	0.20	9.01	0.02256952	0.00000024
6	Ce-LMV 1000ng	0.13	5.99	0.02256970	0.00000027
7	Ce-LMV 1000ng	0.13	5.79	0.02256998	0.00000028
8	Ce-LMV 1000ng	0.15	6.78	0.02257009	0.00000029
	Average			0.02256992	
	2SD			0.00000072	
	2SD (ppm)			32	
	Reference value (Israel et al. 2023)			**0.02257036**	

Supplementary Table A-5. Nd isotope ratios of JNdi reference materials determined by MC-ICPMS and correction factors.

analysis ID	**measured 143Nd/144Nd**	**2SE**	**Correction 143/144Nd**
1	0.511965	0.000007	1.000260968
2	0.511972	0.000008	1.000248078
3	0.511961	0.000007	1.000270152
4	0.511933	0.000006	1.000324679
5	0.511918	0.000008	1.000353839
6	0.511904	0.000007	1.00038111
Average Standard JNdi	**0.511942**		
2 SD	0.000056		
2SD (ppm)	109		
Literrature value (Garçon et al., 2018)	**0.512099**		

Supplementary Table A-6. Comparison of La/Ce ratios obtained by two different methods and calculations of $^{138}La/^{142}Ce$ ratios.

N[(a)]	Name	La/Ce[(b)]	La/Ce[(c)]	2SD[(d)]	2SD%	$^{138}La/^{142}Ce$[(e)]
3	BHVO		0.4048	0.0003	0.07	0.0033
4	TH11	0.3668	0.3779	0.0008	0.19	0.0031
4	TH12	0.5607	0.5662	0.0019	0.30	0.0047
3	TH14	0.5462	0.5461	0.0007	0.11	0.0045
3	TH10	0.3423	0.4959	0.0008	0.14	0.0041
4	MM01	0.4097	0.4144	0.0007	0.16	0.0034
3	MM08	0.4506	0.4491	0.0022	0.46	0.0037
4	MM04	0.3289	0.3233	0.0015	0.43	0.0027
4	HO01	1.3321	1.3423	0.0049	0.33	0.0110
4	HO05	1.0909	1.0861	0.0061	0.52	0.0089
3	HO13	0.3722	0.3750	0.0012	0.29	0.0031
3	HO14	0.4284	0.4260	0.0011	0.24	0.0035
Average					0.27	

(a) Number of duplicates analysed by bracketing the samples with prepared synthetic solutions

(b) La/Ce ratio calculated from trace element data

(c) La/Ce ratio calculated from bracketing rock samples with prepared syntentic silutions

(d) 2SD errors on La/Ce ratios measured by bracketing rock samples with synthetic solutions. These errors were calculated from values proded by the three to 4 diplicates of each sample.

(e) $^{138}La/^{142}Ce$=0.0082236 x La/Ce, with the ratio of 0.0082236 calculated from the data of natural rock standards published by Schnebel et al. (2017)

Supplementary Table A-7. Average composition of fresh lavas used for normalising the composition of silicified lavas

Average lava	La	Ce	Pr	Nd	Sm	Eu	Lu	Nb	Zr	Hf	TiO2	Al2O3	Th	U	K2O	Rb	Na2O	CaO	Sr	Ba	Pb	Cr	Cu	Fe2O3	MnO	MgO
THEESPRUIT	7.63	17.66	2.54	11.72	3.25	1.17	0.37	5.44	85.0	2.18	1.03	12.0	0.985	0.245	0.57	18.7	2.0	10.5	136	454	2.56	329	114.0	12.6	0.23	7.6
KOMATI	3.49	8.37	1.16	5.27	1.46	0.49	0.18	2.36	39.7	1.03	0.45	6.6	0.401	0.097	0.25	5.3	1.3	7.0	79	74	0.72	1707	56.5	11.0	0.16	20.6
HOOGGENOEG	4.24	11.17	1.56	8.03	2.47	0.86	0.29	2.97	66.0	1.72	0.96	12.9	0.336	0.093	0.54	35.5	2.5	7.9	107	58	1.11	403	122.2	13.2	0.18	7.0
MENDON	3.55	9.23	1.28	6.25	1.94	0.68	0.20	2.21	43.8	1.06	0.70	6.4	0.321	0.058	0.14	1.9	2.2	10.4	38	89	0.56	1323	56.5	12.5	0.22	13.3

These values were calculated from published fresh lava compositions in the different formations.

B. Supplementary material related to Part IV.

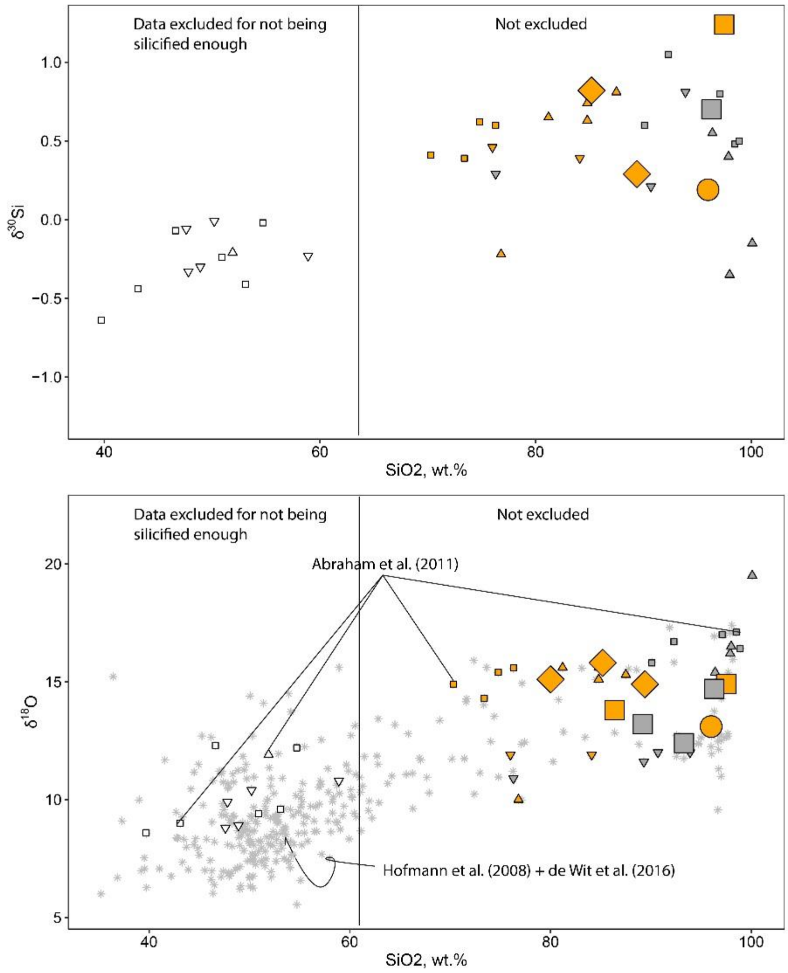

Supplementary Figure B-1. SiO_2 concentration versus $\delta^{18}O$ values in the analysed samples.

Supplementary Table B-1. Compositions of seawater and lava used in the numerical model of water-roch interaction.

Initial komatiite composition		Initial reduced high-Si seawater	
Oxides	wt. %	Component species	Moles
SiO2	47.3	H2O	5.55E+01
Al2O3	4.4	Cl-	5.94E-01
MgO	28.1	SO4--	2.81E-11
FeO	12.8	HCO3-	3.89E-04
CaO	7.4	HS-	3.32E-11
Na2O	0.1	H4SiO4	1.57E-02
K2O	0.01	Al+++	3.47E-12
		Ca++	1.02E-02
δ17O komatiite	2.95	Mg++	5.36E-02
δ18O komatiite	5.7	Fe++	2.30E-07
		K+	9.97E-03
		Na+	4.57E-01

Supplementary Table B-2. Details of SIMS measurements of O isotope compositions in quartz

		18O/16O	16O/Coeff	18O/Coeff						
Spot#		H'2/L'2	L'2	H'2	yield	% yield	δ^{18}O mes.	2Se int	IMF	**δ^{18}O corr.**
d18O_P549_310323_Paine@1	2.22	2.0132E-03	2.3601E+09	4.7516E+06	1.06E+09	100.0	4.01	0.11	-5.79	
d18O_P549_310323_Paine@2	2.22	2.0132E-03	2.3783E+09	4.7879E+06	1.07E+09	100.7	4.00	0.12	-5.80	
d18O_P549_310323_Paine@3	2.22	2.0137E-03	2.3760E+09	4.7845E+06	1.07E+09	100.7	4.23	0.13	-5.57	
d18O_P549_310323_Paine@4	2.22	2.0134E-03	2.3687E+09	4.7694E+06	1.07E+09	100.5	4.10	0.10	-5.70	
d18O_P549_310323_Paine@5	2.21	2.0133E-03	2.3569E+09	4.7449E+06	1.06E+09	100.1	4.04	0.09	-5.76	
d18O_P549_310323_Paine@6	2.23	2.0136E-03	2.3830E+09	4.7986E+06	1.07E+09	100.5	4.18	0.10	-5.62	
d18O_P549_310323_Paine@7	2.23	2.0139E-03	2.3818E+09	4.7966E+06	1.07E+09	100.6	4.34	0.13	-5.46	
d18O_P549_310323_Paine@08	2.23	2.0136E-03	2.3758E+09	4.7838E+06	1.07E+09	100.3	4.18	0.13	-5.62	
d18O_P549_310323_HO25a_qz4@1	2.23	2.0222E-03	2.3551E+09	4.7627E+06	1.06E+09	99.4	8.46	0.13		**14.18**
d18O_P549_310323_HO25a_qz4@2	2.23	2.0209E-03	2.3165E+09	4.6816E+06	1.04E+09	97.8	7.82	0.13		**13.55**
d18O_P549_310323_HO25a_qz4@3	2.23	2.0223E-03	2.3140E+09	4.6797E+06	1.04E+09	97.8	8.51	0.09		**14.24**
d18O_P549_310323_HO25a_qz4@4	2.22	2.0215E-03	2.3683E+09	4.7873E+06	1.06E+09	100.2	8.14	0.14		**13.87**
d18O_P549_310323_HO25a_qz4@5	2.22	2.0223E-03	2.3513E+09	4.7553E+06	1.06E+09	99.6	8.52	0.12		**14.25**
d18O_P549_310323_HO25a_qz4@6	2.22	2.0225E-03	2.3381E+09	4.7287E+06	1.05E+09	98.9	8.64	0.13		**14.37**
d18O_P549_310323_Paine@09	2.22	2.0130E-03	2.3703E+09	4.7713E+06	1.07E+09	100.2	3.86	0.11	-5.94	
d18O_P549_310323_HO25a_qz4@7	2.22	2.0221E-03	2.3455E+09	4.7429E+06	1.05E+09	99.2	8.45	0.13		**14.18**
d18O_P549_310323_HO25a_qz4@8	2.22	2.0226E-03	2.3727E+09	4.7990E+06	1.07E+09	100.4	8.66	0.11		**14.39**
d18O_P549_310323_HO25_qz1@1	2.26	2.0222E-03	2.4093E+09	4.8722E+06	1.06E+09	100.2	8.48	0.11		**14.21**
d18O_P549_310323_HO25_qz1@2	2.26	2.0220E-03	2.3922E+09	4.8369E+06	1.06E+09	99.6	8.36	0.11		**14.09**
d18O_P549_310323_HO25_qz1@3	2.25	2.0209E-03	2.4221E+09	4.8948E+06	1.08E+09	101.2	7.83	0.15		**13.56**
d18O_P549_310323_HO25_qz1@4	2.24	2.0213E-03	2.4538E+09	4.9597E+06	1.09E+09	103.0	8.04	0.12		**13.77**
d18O_P549_310323_Paine@10	2.24	2.0133E-03	2.3865E+09	4.8047E+06	1.07E+09	100.4	4.02	0.13	-5.78	
d18O_P549_310323_HO25_qz1@5	2.24	2.0221E-03	2.3843E+09	4.8215E+06	1.07E+09	100.3	8.42	0.10		**14.15**
d18O_P549_310323_HO25_qz1@6	2.24	2.0205E-03	2.4330E+09	4.9162E+06	1.09E+09	102.4	7.65	0.14		**13.38**
d18O_P549_310323_HO25_qz1@7	2.23	2.0214E-03	2.4363E+09	4.9249E+06	1.09E+09	102.6	8.07	0.14		**13.80**
d18O_P549_310323_HO25_qz1@8	2.23	2.0205E-03	2.4226E+09	4.8948E+06	1.09E+09	102.3	7.65	0.09		**13.38**
d18O_P549_310323_SK-HO25b_qz4@1	2.22	2.0225E-03	2.3753E+09	4.8042E+06	1.07E+09	100.5	8.64	0.10		**14.37**
d18O_P549_310323_SK-HO25b_qz4@2	2.22	2.0226E-03	2.3631E+09	4.7795E+06	1.06E+09	100.1	8.67	0.11		**14.40**
d18O_P549_310323_Paine@11	2.22	2.0130E-03	2.3828E+09	4.7965E+06	1.07E+09	100.9	3.88	0.09	-5.92	
d18O_P549_310323_SK-HO25b_qz4@3	2.22	2.0224E-03	2.3752E+09	4.8035E+06	1.07E+09	100.5	8.55	0.13		**14.28**
d18O_P549_310323_SK-HO25b_qz4@4	2.23	2.0225E-03	2.3770E+09	4.8077E+06	1.07E+09	100.5	8.65	0.13		**14.38**
d18O_P549_310323_SK-HO25b_qz4@5	2.22	2.0224E-03	2.3645E+09	4.7822E+06	1.06E+09	100.1	8.58	0.13		**14.31**
d18O_P549_310323_SK-HO25b_qz4@6	2.22	2.0229E-03	2.3718E+09	4.7977E+06	1.07E+09	100.6	8.81	0.13		**14.54**
d18O_P549_310323_SK-HO25b_qz4@7	2.22	2.0224E-03	2.3688E+09	4.7906E+06	1.07E+09	100.4	8.59	0.10		**14.32**
d18O_P549_310323_SK-HO25b_qz4@8	2.22	2.0222E-03	2.3695E+09	4.7915E+06	1.07E+09	100.3	8.50	0.09		**14.23**
d18O_P549_310323_Paine@12	2.23	2.0132E-03	2.3858E+09	4.8030E+06	1.07E+09	100.9	4.00	0.14	-5.80	
d18O_P549_310323_SKHO25b_qz3@1	2.23	2.0222E-03	2.3711E+09	4.7950E+06	1.06E+09	100.2	8.49	0.11		**14.22**
d18O_P549_310323_SKHO25b_qz3@2	2.23	2.0226E-03	2.3758E+09	4.8053E+06	1.07E+09	100.4	8.67	0.10		**14.40**
d18O_P549_310323_SKHO25b_qz3@3	2.22	2.0224E-03	2.3501E+09	4.7528E+06	1.06E+09	99.4	8.56	0.16		**14.29**
d18O_P549_310323_SKHO25b_qz3@4	2.22	2.0230E-03	2.3567E+09	4.7675E+06	1.06E+09	99.7	8.85	0.09		**14.58**
d18O_P549_310323_SKHO25b_qz3@5	2.23	2.0224E-03	2.3825E+09	4.8182E+06	1.07E+09	100.7	8.59	0.11		**14.31**
d18O_P549_310323_SKHO25b_qz3@6	2.23	2.0223E-03	2.3795E+09	4.8121E+06	1.07E+09	100.6	8.51	0.13		**14.24**
d18O_P549_310323_Paine@13	2.23	2.0131E-03	2.3899E+09	4.8110E+06	1.07E+09	101.0	3.95	0.11	-5.85	
d18O_P549_310323_SKHO25b_qz1@1	2.23	2.0223E-03	2.3793E+09	4.8118E+06	1.07E+09	100.5	8.54	0.12		**14.27**
d18O_P549_310323_SKHO25b_qz1@2	2.23	2.0225E-03	2.3772E+09	4.8077E+06	1.07E+09	100.4	8.64	0.15		**14.37**
d18O_P549_310323_SKHO25b_qz1@3	2.18	2.0230E-03	2.4061E+09	4.8675E+06	1.10E+09	103.7	8.86	0.11		**14.59**
d18O_P549_310323_SKHO25b_qz1@4	2.23	2.0231E-03	2.3787E+09	4.8122E+06	1.06E+09	100.2	8.94	0.12		**14.67**
d18O_P549_310323_SKHO25b_qz1@5	2.25	2.0228E-03	2.3833E+09	4.8206E+06	1.06E+09	99.9	8.77	0.12		**14.50**
d18O_P549_310323_SKHO25b_qz1@6	2.25	2.0221E-03	2.4430E+09	4.9402E+06	1.09E+09	102.2	8.43	0.11		**14.16**
d18O_P549_310323_Paine@14	2.25	2.0135E-03	2.4138E+09	4.8601E+06	1.07E+09	101.0	4.16	0.10	-5.64	
d18O_P549_310323_SKHO25b_qz1@7	2.25	2.0226E-03	2.3885E+09	4.8310E+06	1.06E+09	100.0	8.66	0.10		**14.39**
d18O_P549_310323_SKHO25b_qz1@8	2.25	2.0223E-03	2.3986E+09	4.8508E+06	1.07E+09	100.5	8.52	0.12		**14.25**
d18O_P549_310323_SKHO25b_qz1@9	2.24	2.0217E-03	2.3994E+09	4.8507E+06	1.07E+09	100.6	8.22	0.12		**13.95**
d18O_P549_310323_SKHO25b_qz1@10	2.24	2.0222E-03	2.3989E+09	4.8514E+06	1.07E+09	100.8	8.50	0.15		**14.23**
d18O_P549_310323_SKHO09_qz2@1	2.24	2.0228E-03	2.4342E+09	4.9237E+06	1.09E+09	102.2	8.78	0.09		**14.51**
d18O_P549_310323_SKHO09_qz2@02	2.24	2.0232E-03	2.4113E+09	4.8786E+06	1.08E+09	101.2	8.98	0.13		**14.71**
d18O_P549_310323_Paine@15	2.24	2.0138E-03	2.4065E+09	4.8462E+06	1.07E+09	101.1	4.29	0.14	-5.51	
d18O_P549_310323_SKHO09_qz2@03	2.24	2.0233E-03	2.4395E+09	4.9357E+06	1.09E+09	102.6	9.01	0.13		**14.74**
d18O_P549_310323_SKHO09_qz2@04	2.25	2.0229E-03	2.4418E+09	4.9395E+06	1.08E+09	101.9	8.83	0.13		**14.56**
d18O_P549_310323_SKHO09_qz2@05	2.25	2.0224E-03	2.4440E+09	4.9431E+06	1.08E+09	102.0	8.59	0.12		**14.32**
d18O_P549_310323_SKHO09_qz2@06	2.25	2.0222E-03	2.4359E+09	4.9257E+06	1.08E+09	101.8	8.47	0.11		**14.20**
d18O_P549_310323_SKHO09_qz2@07	2.25	2.0235E-03	2.4263E+09	4.9093E+06	1.08E+09	101.4	9.11	0.17		**14.84**
d18O_P549_310323_SKHO09_qz2@08	2.25	2.0228E-03	2.4065E+09	4.8680E+06	1.07E+09	100.8	8.78	0.10		**14.51**
d18O_P549_310323_Paine@16	2.23	2.0134E-03	2.3980E+09	4.8280E+06	1.07E+09	101.0	4.09	0.11	-5.71	
d18O_P549_310323_SKHO09_qz2@09	2.24	2.0223E-03	2.4180E+09	4.8899E+06	1.08E+09	101.6	8.50	0.13		**14.23**
d18O_P549_310323_SKHO09_qz2@10	2.23	2.0229E-03	2.4285E+09	4.9125E+06	1.09E+09	102.2	8.81	0.15		**14.54**
d18O_P549_310323_SKHO09_qz2@11	2.24	2.0231E-03	2.4046E+09	4.8647E+06	1.08E+09	101.1	8.91	0.09		**14.64**
d18O_P549_310323_SKHO09_qz2@12	2.24	2.0227E-03	2.4222E+09	4.8974E+06	1.08E+09	101.8	8.74	0.10		**14.47**
d18O_P549_310323_SKHO09_qz2@13	2.24	2.0228E-03	2.4068E+09	4.8686E+06	1.07E+09	101.1	8.77	0.09		**14.50**
d18O_P549_310323_Paine@17	2.24	2.0129E-03	2.3967E+09	4.8246E+06	1.07E+09	100.8	3.85	0.15	-5.95	
d18O_P548_310323_Paine@1	2.25	2.0140E-03	2.5101E+09	5.0553E+06	1.12E+09	100.0	4.37	0.12	-5.43	
d18O_P548_310323_Paine@2	2.25	2.0139E-03	2.5006E+09	5.0360E+06	1.11E+09	99.5	4.35	0.14	-5.45	
d18O_P548_310323_Paine@3	2.25	2.0140E-03	2.4988E+09	5.0326E+06	1.11E+09	99.4	4.38	0.14	-5.42	
d18O_P548_310323_Paine@4	2.25	2.0140E-03	2.4900E+09	5.0149E+06	1.11E+09	99.1	4.41	0.10	-5.39	
d18O_P548_310323_Paine@5	2.25	2.0140E-03	2.4898E+09	5.0145E+06	1.11E+09	99.2	4.40	0.16	-5.40	
d18O_P548_310323_Paine@6	2.25	2.0140E-03	2.4899E+09	5.0143E+06	1.11E+09	99.3	4.38	0.09	-5.42	
d18O_P548_310323_Paine@7	2.28	2.0140E-03	2.5511E+09	5.1380E+06	1.12E+09	100.3	4.38	0.12	-5.42	
d18O_P548_310323_MM11a_qz1@1	2.28	2.0216E-03	2.5309E+09	5.1163E+06	1.11E+09	99.7	8.18	0.09		**13.56**
d18O_P548_310323_MM11a_qz1@02	2.28	2.0209E-03	2.4910E+09	5.0343E+06	1.09E+09	98.1	7.84	0.09		**13.22**
d18O_P548_310323_MM11a_qz1@03	2.27	2.0217E-03	2.5206E+09	5.0957E+06	1.11E+09	99.5	8.22	0.14		**13.60**
d18O_P548_310323_MM11a_qz1@04	2.27	2.0219E-03	2.5356E+09	5.1264E+06	1.12E+09	100.2	8.31	0.10		**13.68**

Spot#		18O/16O H'2/L'2	16O/Coeff L'2	18O/Coeff H'2	yield	% yield	δ^{18}O mes.	2Se int	IMF	**δ^{18}O corr.**
d18O_P548_310323_MM11a_qz1@05	2.27	2.0217E-03	2.5349E+09	5.1245E+06	1.12E+09	100.1	8.21	0.14		**13.59**
d18O_P548_310323_MM11a_qz1@06	2.26	2.0210E-03	2.5277E+09	5.1085E+06	1.12E+09	100.2	7.89	0.09		**13.27**
d18O_P548_310323_Paine@8	2.26	2.0141E-03	2.5131E+09	5.0618E+06	1.11E+09	99.6	4.44	0.14	-5.36	
d18O_P548_310323_MM11a_qz1@07	2.26	2.0211E-03	2.5221E+09	5.0975E+06	1.12E+09	100.0	7.95	0.11		**13.32**
d18O_P548_310323_MM11a_qz1@08	2.26	2.0210E-03	2.5255E+09	5.1039E+06	1.12E+09	100.2	7.89	0.11		**13.26**
d18O_P548_310323_MM11a_qz1@09	2.26	2.0212E-03	2.5318E+09	5.1171E+06	1.12E+09	100.3	7.96	0.10		**13.33**
d18O_P548_310323_MM11a_qz1@10	2.26	2.0218E-03	2.5279E+09	5.1107E+06	1.12E+09	100.2	8.26	0.09		**13.64**
d18O_P548_310323_MM11a_qz1@11	2.26	2.0209E-03	2.5261E+09	5.1051E+06	1.12E+09	100.2	7.85	0.13		**13.23**
d18O_P548_310323_MM11a_qz1@12	2.26	2.0217E-03	2.5147E+09	5.0839E+06	1.11E+09	99.8	8.23	0.11		**13.60**
d18O_P548_310323_Paine@9	2.25	2.0141E-03	2.5152E+09	5.0656E+06	1.12E+09	100.0	4.45	0.09	-5.35	
d18O_P548_310323_MM11a_qz1@13	2.25	2.0212E-03	2.5256E+09	5.1047E+06	1.12E+09	100.5	7.99	0.12		**13.37**
d18O_P548_310323_MM11a_qz1@14	2.26	2.0213E-03	2.5266E+09	5.1067E+06	1.12E+09	100.4	8.01	0.15		**13.39**
d18O_P548_310323_ME17b_qz3@1	2.26	2.0256E-03	2.5206E+09	5.1058E+06	1.12E+09	100.1	10.17	0.15		**15.55**
d18O_P548_310323_ME17b_qz3@2	2.26	2.0260E-03	2.5079E+09	5.0810E+06	1.11E+09	99.5	10.35	0.16		**15.73**
d18O_P548_310323_ME17b_qz3@3	2.26	2.0261E-03	2.4809E+09	5.0265E+06	1.10E+09	98.3	10.44	0.10		**15.81**
d18O_P548_310323_ME17b_qz3@4	2.26	2.0257E-03	2.5157E+09	5.0958E+06	1.11E+09	99.9	10.21	0.09		**15.58**
d18O_P548_310323_Paine@10	2.26	2.0138E-03	2.5148E+09	5.0647E+06	1.11E+09	99.8	4.31	0.13	-5.49	
d18O_P548_310323_ME17b_qz3@5	2.26	2.0257E-03	2.5208E+09	5.1067E+06	1.12E+09	100.1	10.24	0.12		**15.62**
d18O_P548_310323_ME17b_qz3@6	2.26	2.0259E-03	2.5173E+09	5.0996E+06	1.11E+09	99.7	10.30	0.14		**15.68**
d18O_P548_310323_ME17b_qz3@7	2.26	2.0257E-03	2.5182E+09	5.1010E+06	1.11E+09	99.8	10.24	0.10		**15.61**
d18O_P548_310323_ME17b_qz3@8	2.26	2.0256E-03	2.5184E+09	5.1014E+06	1.11E+09	99.8	10.17	0.12		**15.55**
d18O_P548_310323_MM17b_qz4@1	2.26	2.0261E-03	2.5160E+09	5.0976E+06	1.11E+09	99.7	10.40	0.10		**15.77**
d18O_P548_310323_MM17b_qz4@2	2.27	2.0259E-03	2.5162E+09	5.0977E+06	1.11E+09	99.5	10.33	0.09		**15.70**
d18O_P548_310323_Paine@11	2.27	2.0141E-03	2.5244E+09	5.0844E+06	1.11E+09	99.8	4.42	0.11	-5.38	
d18O_P548_310323_MM17b_qz4@4	2.21	2.0259E-03	2.5138E+09	5.0925E+06	1.14E+09	101.8	10.31	0.11		**15.69**
d18O_P548_310323_MM17b_qz4@5	2.27	2.0262E-03	2.5430E+09	5.1528E+06	1.12E+09	100.5	10.50	0.12		**15.87**
d18O_P548_310323_MM17b_qz4@6	2.27	2.0256E-03	2.5334E+09	5.1319E+06	1.11E+09	99.8	10.18	0.10		**15.55**
d18O_P548_310323_MM17b_qz4@7	2.27	2.0258E-03	2.5366E+09	5.1388E+06	1.12E+09	100.1	10.29	0.14		**15.67**
d18O_P548_310323_MM17b_qz4@8	2.27	2.0257E-03	2.5218E+09	5.1083E+06	1.11E+09	99.6	10.23	0.12		**15.60**
d18O_P548_310323_Paine@12	2.27	2.0147E-03	2.5313E+09	5.0996E+06	1.11E+09	99.8	4.72	0.10	-5.08	
d18O_P548_310323_MM17b_qz4@9	2.27	2.0260E-03	2.5233E+09	5.1121E+06	1.11E+09	99.8	10.36	0.10		**15.74**
d18O_P548_310323_MM17b_qz4@10	2.28	2.0261E-03	2.5267E+09	5.1192E+06	1.11E+09	99.4	10.42	0.11		**15.80**
d18O_P548_310323_ME17b_qz1@1	2.28	2.0258E-03	2.5153E+09	5.0955E+06	1.10E+09	98.8	10.26	0.15		**15.64**
d18O_P548_310323_ME17b_qz1@2	2.28	2.0259E-03	2.5183E+09	5.1019E+06	1.11E+09	99.2	10.32	0.12		**15.69**
d18O_P548_310323_ME17b_qz1@3	2.27	2.0257E-03	2.5038E+09	5.0716E+06	1.10E+09	98.8	10.20	0.12		**15.57**
d18O_P548_310323_ME17b_qz1@4	2.27	2.0258E-03	2.5051E+09	5.0749E+06	1.10E+09	98.9	10.27	0.13		**15.65**
d18O_P548_310323_Paine@13	2.27	2.0143E-03	2.5333E+09	5.1030E+06	1.12E+09	100.0	4.55	0.11	-5.25	
d18O_P548_310323_ME17b_qz1@5	2.27	2.0259E-03	2.5065E+09	5.0779E+06	1.10E+09	98.9	10.33	0.11		**15.71**
d18O_P548_310323_ME17b_qz1@6	2.27	2.0253E-03	2.5299E+09	5.1239E+06	1.12E+09	100.0	10.03	0.09		**15.41**
d18O_P548_310323_ME17b_qz1@7	2.26	2.0254E-03	2.5056E+09	5.0751E+06	1.11E+09	99.2	10.08	0.11		**15.45**
d18O_P548_310323_ME17b_qz1@8	2.27	2.0257E-03	2.5061E+09	5.0768E+06	1.10E+09	99.0	10.20	0.10		**15.58**
d18O_P548_310323_ME17b_qz1@9	2.27	2.0257E-03	2.5175E+09	5.1000E+06	1.11E+09	99.5	10.25	0.11		**15.62**
d18O_P548_310323_ME17b_qz1@10	2.27	2.0256E-03	2.5739E+09	5.2137E+06	1.13E+09	101.7	10.16	0.10		**15.54**
d18O_P548_310323_Paine@14	2.31	2.0140E-03	2.5700E+09	5.1761E+06	1.11E+09	99.8	4.38	0.11	-5.42	
d18O_P548_310323_Paine@15	2.30	2.0145E-03	2.5619E+09	5.1608E+06	1.11E+09	99.7	4.63	0.13	-5.17	

		H'2/L'2	L'2	H'2	yield	% yield	d18O	2Se int	IMF	**d18O c**
d18O-290323-P0481-Paine@1	1.37	2.0136E-03	1.4937E+09	3.0077E+06	1.09E+09	100.0	4.18	0.21	-5.62	
d18O-290323-P0481-Paine@2	1.38	2.0138E-03	1.4894E+09	2.9995E+06	1.08E+09	99.4	4.31	0.21	-5.49	
d18O-290323-P0481-Paine@3	1.38	2.0137E-03	1.4845E+09	2.9895E+06	1.08E+09	99.1	4.26	0.19	-5.54	
d18O-290323-P0481-Paine@4	1.37	2.0133E-03	1.4751E+09	2.9697E+06	1.07E+09	98.7	4.04	0.17	-5.76	
d18O-290323-P0481-Paine@5	1.37	2.0144E-03	1.4772E+09	2.9757E+06	1.08E+09	99.0	4.59	0.16	-5.21	
d18O-290323-P0481-Paine@6	1.37	2.0138E-03	1.4803E+09	2.9802E+06	1.08E+09	99.2	4.29	0.19	-5.51	
d18O-290323-P0481-Paine@3c	1.36	2.0143E-03	1.5035E+09	3.0277E+06	1.11E+09	101.8	4.56	0.19	-5.24	
d18O-290323-P0481-Paine@4c	1.36	2.0145E-03	1.4975E+09	3.0166E+06	1.10E+09	101.4	4.62	0.23	-5.18	
d18O-290323-P0481-Paine@5b	1.36	2.0144E-03	1.4996E+09	3.0210E+06	1.10E+09	101.5	4.58	0.17	-5.22	
d18O-290323-P0481-Paine@6b	1.36	2.0140E-03	1.4923E+09	3.0053E+06	1.10E+09	101.1	4.38	0.16	-5.42	
d18O-290323-P0481-Paine@8	1.35	2.0138E-03	1.4870E+09	2.9945E+06	1.10E+09	101.2	4.31	0.22	-5.49	
d18O-290323-P0481-Paine@9	1.34	2.0139E-03	1.4801E+09	2.9806E+06	1.10E+09	101.1	4.32	0.22	-5.48	
d18O-290323-P0550-Paine@1	1.34	2.0138E-03	1.4848E+09	2.9901E+06	1.11E+09	101.7	4.28	0.25	-5.52	
d18O-290323-P0550-Paine@2	1.34	2.0136E-03	1.4768E+09	2.9748E+06	1.10E+09	101.4	4.19	0.20	-5.61	
d18O-290323-P0550-Paine@3	1.34	2.0143E-03	1.4741E+09	2.9684E+06	1.10E+09	101.3	4.54	0.23	-5.26	
d18O-290323-P0550-Paine@4	1.34	2.0142E-03	1.4661E+09	2.9527E+06	1.10E+09	100.9	4.47	0.18	-5.33	
d18O-290323-P0550-Paine@5	1.34	2.0137E-03	1.4657E+09	2.9515E+06	1.10E+09	100.9	4.22	0.15	-5.58	
d18O-290323-P0550-Paine@6	1.34	2.0142E-03	1.4633E+09	2.9476E+06	1.10E+09	100.7	4.47	0.19	-5.33	
d18O-SKME18a-Ank@1	1.33	2.0239E-03	2.0315E+09	4.1114E+06	1.52E+09	139.9	9.32	0.16		**10.01**
d18O-SKME18a-Ank@2	1.33	2.0233E-03	2.0447E+09	4.1369E+06	1.54E+09	141.1	9.05	0.11		**9.74**
d18O-SKME18a-Ank@3	1.33	2.0238E-03	1.9505E+09	3.9476E+06	1.47E+09	134.8	9.28	0.16		**9.97**
d18O-SKME18a-Ank@4	1.33	2.0221E-03	2.0045E+09	4.0531E+06	1.51E+09	138.6	8.42	0.18		**9.11**
d18O-SKME18a-Ank@5	1.33	2.0226E-03	2.0425E+09	4.1312E+06	1.54E+09	141.3	8.66	0.16		**9.35**
d18O-SKME18a-Ank@6	1.33	2.0232E-03	2.0110E+09	4.0684E+06	1.51E+09	139.2	8.96	0.15		**9.66**
d18O-SKME18a-Ank@7	1.33	2.0236E-03	2.0005E+09	4.0482E+06	1.51E+09	138.4	9.20	0.12		**9.89**
d18O-290323-P0550-Paine@7	1.33	2.0135E-03	1.4586E+09	2.9367E+06	1.10E+09	101.0	4.13	0.13	-5.67	
d18O-SKME18a-qz6@1	1.33	2.0246E-03	1.4193E+09	2.8738E+06	1.07E+09	98.1	9.69	0.12		**15.18**
d18O-SKME18a-qz6@2	1.33	2.0252E-03	1.4349E+09	2.9069E+06	1.08E+09	99.3	9.99	0.14		**15.48**
d18O-SKME18a-qz6@3	1.33	2.0220E-03	1.4024E+09	2.8357E+06	1.06E+09	97.2	8.39	0.20		**13.88**
d18O-SKME18a-qz6@4	1.33	2.0253E-03	1.4180E+09	2.8720E+06	1.07E+09	98.1	10.03	0.14		**15.52**
d18O-SKME18a-qz6@5	1.33	2.0234E-03	1.3811E+09	2.7945E+06	1.04E+09	95.7	9.07	0.13		**14.56**
d18O-290323-P0550-Paine@8	1.33	2.0136E-03	1.4556E+09	2.9312E+06	1.10E+09	100.9	4.18	0.15	-5.62	
d18O-SKME18a-qz3@1	1.32	2.0188E-03	1.3915E+09	2.8093E+06	1.05E+09	96.6	6.77	0.17		**12.26**
d18O-SKME18a-qz3@2	1.32	2.0238E-03	1.4058E+09	2.8439E+06	1.06E+09	97.7	9.29	0.18		**14.78**
d18O-SKME18a-qz3@3	1.32	2.0245E-03	1.3860E+09	2.8062E+06	1.05E+09	96.4	9.62	0.13		**15.12**
d18O-SKME18a-qz3@4	1.32	2.0252E-03	1.4159E+09	2.8675E+06	1.07E+09	98.5	9.97	0.19		**15.46**
d18O-SKME18a-qz3@5	1.32	2.0241E-03	1.3951E+09	2.8239E+06	1.06E+09	97.1	9.42	0.18		**14.91**

Spot#		18O/16O H'2/L'2	16O/Coeff L'2	18O/Coeff H'2	yield	% yield	δ^{18}O mes.	2Se int	IMF	**δ^{18}O corr.**
d18O-SKME18a-qz3@6	1.32	2.0245E-03	1.4233E+09	2.8814E+06	1.08E+09	99.2	9.61	0.17		**15.11**
d18O-290323-P0550-Paine@9	1.32	2.0140E-03	1.4480E+09	2.9164E+06	1.10E+09	100.9	4.37	0.18	-5.43	
d18O-SKME18a-qz1@3	1.31	2.0252E-03	1.4312E+09	2.8984E+06	1.09E+09	100.1	9.96	0.17		**15.45**
d18O-SKME18a-qz1@2	1.31	2.0242E-03	1.4317E+09	2.8960E+06	1.09E+09	100.1	9.46	0.18		**14.95**
d18O-SKME18a-qz1@1	1.32	2.0245E-03	1.4439E+09	2.9222E+06	1.10E+09	100.7	9.63	0.21		**15.12**
d18O-SKME18a-qz1@4	1.31	2.0237E-03	1.4215E+09	2.8767E+06	1.08E+09	99.4	9.22	0.21		**14.71**
d18O-SKME18a-qz1@5	1.32	2.0244E-03	1.4214E+09	2.8784E+06	1.08E+09	99.2	9.58	0.17		**15.07**
d18O-SKME18a-qz1@6	1.32	2.0247E-03	1.4278E+09	2.8909E+06	1.09E+09	99.7	9.71	0.18		**15.20**
d18O-290323-P0550-Paine@10	1.32	2.0136E-03	1.4504E+09	2.9206E+06	1.10E+09	101.2	4.17	0.16	-5.63	
d18O-SKME17a-Qz3@1	1.32	2.0253E-03	1.4181E+09	2.8720E+06	1.08E+09	98.8	10.03	0.17		**15.53**
d18O-SKME17a-Qz3@2	1.32	2.0247E-03	1.4189E+09	2.8729E+06	1.08E+09	99.0	9.72	0.18		**15.21**
d18O-SKME17a-Qz3@3	1.31	2.0255E-03	1.4175E+09	2.8713E+06	1.08E+09	99.1	10.11	0.15		**15.61**
d18O-SKME17a-Qz3@4	1.32	2.0249E-03	1.4185E+09	2.8721E+06	1.08E+09	99.1	9.80	0.16		**15.29**
d18O-SKME17a-Qz3@5	1.32	2.0250E-03	1.4145E+09	2.8644E+06	1.07E+09	98.7	9.88	0.20		**15.37**
d18O-SKME17a-Qz3@6	1.32	2.0240E-03	1.4270E+09	2.8882E+06	1.08E+09	99.6	9.38	0.13		**14.87**
d18O-SKME17a-Qz3@7	1.32	2.0255E-03	1.4201E+09	2.8754E+06	1.08E+09	99.2	10.13	0.17		**15.62**
d18O-290323-P0550-Paine@11	1.31	2.0137E-03	1.4466E+09	2.9140E+06	1.10E+09	101.3	4.26	0.25	-5.54	
d18O-SKME17a-Qz1@1	1.31	2.0250E-03	1.4212E+09	2.8779E+06	1.08E+09	99.6	9.86	0.22		**15.36**
d18O-SKME17a-Qz1@2	1.31	2.0257E-03	1.4241E+09	2.8849E+06	1.09E+09	99.8	10.24	0.15		**15.73**
d18O-SKME17a-Qz1@3	1.31	2.0247E-03	1.4420E+09	2.9197E+06	1.10E+09	101.1	9.72	0.21		**15.21**
d18O-SKME17a-Qz1@4	1.32	2.0250E-03	1.4290E+09	2.8936E+06	1.08E+09	99.5	9.86	0.16		**15.35**
d18O-SKME17a-Qz1@5	1.32	2.0260E-03	1.4215E+09	2.8801E+06	1.08E+09	98.9	10.37	0.16		**15.86**
d18O-SKME17a-Qz1@6	1.32	2.0247E-03	1.4244E+09	2.8844E+06	1.08E+09	99.1	9.73	0.13		**15.23**
d18O-290323-P0550-Paine@12	1.32	2.0141E-03	1.4503E+09	2.9210E+06	1.10E+09	100.9	4.42	0.20	-5.38	
		H'2/L'2	L'2	H'2	yield	% yield	d18O	2Se int	IMF	**d18O c**
d18O_Paine_Calib@1	1.54	2.0147E-03	1.6969E+09	3.4187E+06	1.10E+09	100.7	4.74	0.11	-5.06	
d18O_Paine_Calib@2	1.55	2.0142E-03	1.6988E+09	3.4216E+06	1.10E+09	100.6	4.48	0.14	-5.32	
d18O_Paine_Calib@3	1.55	2.0142E-03	1.6983E+09	3.4207E+06	1.10E+09	100.6	4.47	0.16	-5.33	
d18O_Paine_Calib@4	1.54	2.0140E-03	1.6952E+09	3.4142E+06	1.10E+09	100.6	4.38	0.18	-5.42	
d18O_Paine_Calib@5	1.54	2.0141E-03	1.6951E+09	3.4140E+06	1.10E+09	100.8	4.43	0.11	-5.37	
d18O_Paine_Calib@6	1.54	2.0135E-03	1.7090E+09	3.4413E+06	1.11E+09	101.6	4.16	0.16	-5.64	
d18O_Paine_P551@1	1.54	2.0143E-03	1.6868E+09	3.3978E+06	1.10E+09	100.4	4.54	0.14	-5.26	
d18O_Paine_P551@02	1.54	2.0140E-03	1.6861E+09	3.3969E+06	1.09E+09	100.2	4.40	0.20	-5.40	
d18O_Paine_P551@03	1.54	2.0144E-03	1.6803E+09	3.3837E+06	1.09E+09	100.0	4.59	0.14	-5.21	
d18O_Paine_P551@04	1.54	2.0137E-03	1.6793E+09	3.3827E+06	1.09E+09	100.1	4.24	0.15	-5.56	
d18O_Paine_P551@05	1.53	2.0142E-03	1.6796E+09	3.3830E+06	1.09E+09	100.2	4.47	0.11	-5.33	
d18O_Paine_P551@06	1.54	2.0143E-03	1.6821E+09	3.3891E+06	1.09E+09	100.2	4.52	0.15	-5.28	
d18O_P551_030423_MM11B_Calc@1	1.54	2.0567E-03	2.1269E+09	4.3745E+06	1.38E+09	126.7	25.70	0.12		**28.83**
d18O_P551_030423_MM11B_Calc@2	1.54	2.0557E-03	2.1317E+09	4.3819E+06	1.38E+09	126.8	25.18	0.12		**28.31**
d18O_P551_030423_MM11B_Calc@3	1.53	2.0210E-03	2.2159E+09	4.4782E+06	1.44E+09	132.2	7.90	0.10		**11.03**
d18O_P551_030423_MM11B_Calc@4	1.53	2.0208E-03	2.0367E+09	4.1158E+06	1.33E+09	121.7	7.80	0.15		**10.93**
d18O_P551_030423_MM11B_Calc@5	1.53	2.0208E-03	2.0903E+09	4.2242E+06	1.36E+09	124.7	7.80	0.16		**10.93**
d18O_P551_030423_MM11B_Calc@6	1.54	2.0207E-03	2.1036E+09	4.2504E+06	1.37E+09	125.4	7.73	0.18		**10.85**
d18O_Paine_P551@07	1.54	2.0147E-03	1.6765E+09	3.3763E+06	1.09E+09	100.0	4.76	0.16	-5.04	
d18O_P551_030423_MM11B_Calc@7	1.53	2.0220E-03	2.1537E+09	4.3548E+06	1.40E+09	128.5	8.39	0.13		**11.52**
d18O_P551_030423_MM11B_Calc@8	1.53	2.0209E-03	2.2091E+09	4.4644E+06	1.44E+09	131.9	7.82	0.15		**10.94**
d18O_P551_030423_MM11B_Calc@9	1.53	2.0206E-03	2.1019E+09	4.2472E+06	1.37E+09	125.6	7.70	0.10		**10.83**
d18O_P551_030423_MM11B_Calc@10	1.55	2.0204E-03	2.1644E+09	4.3729E+06	1.40E+09	128.2	7.59	0.22		**10.71**
d18O_P551_030423_MM11b_qz6@1	1.55	2.0208E-03	2.1976E+09	4.4408E+06	1.42E+09	130.1	7.76	0.10		**10.89**
d18O_P551_030423_MM11b_qz6@2	1.55	2.0210E-03	1.6658E+09	3.3668E+06	1.07E+09	98.4	7.86	0.18		**13.18**
d18O_Paine_P551@08	1.55	2.0148E-03	1.6956E+09	3.4163E+06	1.09E+09	100.2	4.78	0.16	-5.02	
d18O_P551_030423_MM11b_qz6@3	1.55	2.0207E-03	1.6501E+09	3.3341E+06	1.07E+09	97.6	7.72	0.14		**13.05**
d18O_P551_030423_MM11b_qz6@4	1.55	2.0213E-03	1.6328E+09	3.2997E+06	1.06E+09	96.7	8.05	0.17		**13.37**
d18O_P551_030423_MM11b_qz6@5	1.55	2.0201E-03	1.6209E+09	3.2745E+06	1.05E+09	96.0	7.44	0.11		**12.76**
d18O_P551_030423_MM11b_qz3@1	1.55	2.0212E-03	1.7025E+09	3.4410E+06	1.10E+09	100.9	7.97	0.11		**13.30**
d18O_P551_030423_MM11b_qz3@2	1.55	2.0214E-03	1.7146E+09	3.4660E+06	1.11E+09	101.6	8.10	0.11		**13.43**
d18O_P551_030423_MM11b_qz3@3	1.55	2.0221E-03	1.7123E+09	3.4622E+06	1.11E+09	101.4	8.40	0.16		**13.73**
d18O_Paine_P551@09	1.55	2.0137E-03	1.6956E+09	3.4144E+06	1.10E+09	100.3	4.26	0.18	-5.54	
d18O_P551_030423_MM11b_qz3@4	1.55	2.0225E-03	1.7020E+09	3.4423E+06	1.10E+09	100.6	8.64	0.11		**13.97**
d18O_P551_030423_MM11b_qz3@5	1.55	2.0212E-03	1.7025E+09	3.4413E+06	1.10E+09	100.6	8.00	0.12		**13.33**
d18O_P551_030423_MM11b_qz3@6	1.55	2.0217E-03	1.6964E+09	3.4296E+06	1.10E+09	100.3	8.22	0.16		**13.55**
d18O_P551_030423_MM11b_qz2@1	1.55	2.0221E-03	1.6894E+09	3.4159E+06	1.09E+09	100.1	8.44	0.13		**13.77**
d18O_P551_030423_MM11b_qz2@2	1.55	2.0222E-03	1.6951E+09	3.4279E+06	1.09E+09	100.2	8.49	0.13		**13.82**
d18O_P551_030423_MM11b_qz2@3	1.55	2.0215E-03	1.6917E+09	3.4195E+06	1.09E+09	100.1	8.12	0.18		**13.45**
d18O_Paine_P551@10	1.55	2.0144E-03	1.6948E+09	3.4139E+06	1.10E+09	100.4	4.59	0.17	-5.21	
d18O_P551_030423_MM11b_qz2@4	1.55	2.0213E-03	1.6981E+09	3.4323E+06	1.10E+09	100.5	8.05	0.15		**13.37**
d18O_P551_030423_MM11b_qz2@5	1.55	2.0217E-03	1.6874E+09	3.4114E+06	1.09E+09	99.8	8.24	0.11		**13.56**
d18O_P551_030423_MM11b_qz1@1	1.55	2.0218E-03	1.6974E+09	3.4318E+06	1.10E+09	100.5	8.27	0.18		**13.59**
d18O_P551_030423_MM11b_qz1@2	1.54	2.0211E-03	1.6933E+09	3.4231E+06	1.10E+09	100.4	7.93	0.21		**13.26**
d18O_P551_030423_MM11b_qz1@3	1.54	2.0212E-03	1.6660E+09	3.3674E+06	1.08E+09	98.8	7.97	0.14		**13.30**
d18O_P551_030423_MM11b_qz1@4	1.54	2.0222E-03	1.6937E+09	3.4251E+06	1.10E+09	100.5	8.45	0.16		**13.78**
d18O_Paine_P551@11	1.54	2.0133E-03	1.6927E+09	3.4079E+06	1.10E+09	100.5	4.04	0.17	-5.76	
d18O_P551_030423_MM11b_qz1@5	1.54	2.0221E-03	1.6902E+09	3.4178E+06	1.09E+09	100.2	8.42	0.13		**13.75**
d18O_P551_030423_ME18c_qz4@1	1.54	2.0251E-03	1.7023E+09	3.4475E+06	1.10E+09	101.0	9.90	0.12		**15.23**
d18O_P551_030423_ME18c_qz4@2	1.54	2.0240E-03	1.7128E+09	3.4665E+06	1.11E+09	101.7	9.35	0.17		**14.68**
d18O_P551_030423_ME18c_qz4@3	1.54	2.0250E-03	1.6875E+09	3.4173E+06	1.10E+09	100.3	9.87	0.11		**15.20**
d18O_P551_030423_ME18c_qz4@4	1.53	2.0254E-03	1.6884E+09	3.4196E+06	1.10E+09	101.1	10.07	0.14		**15.40**
d18O_P551_030423_ME18c_qz4@5	1.53	2.0255E-03	1.6829E+09	3.4085E+06	1.10E+09	100.7	10.13	0.16		**15.45**
d18O_Paine_P551@12	1.53	2.0139E-03	1.6876E+09	3.3976E+06	1.10E+09	100.8	4.34	0.14	-5.46	
d18O_P551_030423_ME18c_qz4@6	1.54	2.0250E-03	1.6977E+09	3.4379E+06	1.10E+09	101.1	9.88	0.12		**15.21**
d18O_P551_030423_ME18c_qz4@7	1.53	2.0260E-03	1.6858E+09	3.4153E+06	1.10E+09	100.7	10.37	0.16		**15.69**
d18O_P551_030423_ME18c_qz4@8	1.53	2.0247E-03	1.6692E+09	3.3796E+06	1.09E+09	99.9	9.73	0.21		**15.06**
d18O_P551_030423_ME18c_qz4@9	1.53	2.0247E-03	1.6866E+09	3.4150E+06	1.10E+09	100.8	9.75	0.11		**15.07**

Spot#		18O/16O H'2/L'2	16O/Coeff L'2	18O/Coeff H'2	yield	% yield	δ^{18}O mes.	2Se int	IMF	δ^{18}O corr.
d18O_P551_030423_ME18c_qz4@10	1.53	2.0252E-03	1.6689E+09	3.3813E+06	1.09E+09	99.7	9.97	0.22		**15.29**
d18O_P551_030423_ME18c_qz1@1	1.53	2.0250E-03	1.6924E+09	3.4272E+06	1.10E+09	101.0	9.87	0.20		**15.20**
d18O_Paine_P551@13	1.53	2.0138E-03	1.6829E+09	3.3889E+06	1.10E+09	100.7	4.27	0.15	-5.53	
d18O_P551_030423_ME18c_qz1@2	1.53	2.0250E-03	1.6842E+09	3.4108E+06	1.10E+09	100.9	9.89	0.15		**15.22**
d18O_P551_030423_ME18c_qz1@3	1.53	2.0252E-03	1.6889E+09	3.4204E+06	1.11E+09	101.3	9.97	0.21		**15.29**
d18O_P551_030423_ME18c_qz1@4	1.53	2.0258E-03	1.6765E+09	3.3981E+06	1.10E+09	100.7	10.29	0.17		**15.61**
d18O_P551_030423_ME18c_qz1@5	1.53	2.0254E-03	1.6797E+09	3.4021E+06	1.10E+09	100.7	10.07	0.17		**15.39**
d18O_P551_030423_ME18c_qz1@6	1.53	2.0251E-03	1.6814E+09	3.4053E+06	1.10E+09	100.9	9.95	0.13		**15.27**
d18O_P551_030423_ME18c_qz1@7	1.53	2.0246E-03	1.6831E+09	3.4078E+06	1.10E+09	100.9	9.66	0.18		**14.99**
d18O_Paine_P551@14	1.52	2.0143E-03	1.6782E+09	3.3805E+06	1.10E+09	100.9	4.52	0.14	-5.28	
d18O_P551_030423_ME18c_qz1@8	1.52	2.0247E-03	1.6952E+09	3.4320E+06	1.11E+09	101.9	9.70	0.13		**15.03**
d18O_P551_030423_ME18c_qz1@9	1.52	2.0234E-03	1.6320E+09	3.3023E+06	1.07E+09	98.1	9.09	0.17		**14.41**
d18O_P551_030423_ME18b_AnkA@1	1.53	2.0227E-03	2.3333E+09	4.7196E+06	1.53E+09	139.9	8.72	0.10		**9.37**
d18O_P551_030423_ME18b_AnkA@2	1.53	2.0210E-03	2.3667E+09	4.7831E+06	1.55E+09	141.6	7.86	0.09		**8.52**
d18O_P551_030423_ME18b_AnkA@3	1.53	2.0211E-03	2.3026E+09	4.6539E+06	1.51E+09	138.1	7.91	0.12		**8.56**
d18O_P551_030423_ME18b_AnkA@4	1.52	2.0224E-03	2.3585E+09	4.7698E+06	1.55E+09	141.9	8.56	0.12		**9.21**
d18O_Paine_P551@15	1.52	2.0145E-03	1.6806E+09	3.3856E+06	1.10E+09	101.1	4.62	0.14	-5.18	
d18O_P551_030423_ME18b_AnkB@1	1.53	2.0329E-03	2.2888E+09	4.6529E+06	1.50E+09	137.2	13.82	0.18		**14.47**
d18O_P551_030423_ME18b_AnkB@2	1.53	2.0279E-03	2.3158E+09	4.6962E+06	1.52E+09	138.9	11.33	0.14		**11.98**
d18O_P551_030423_ME18b_AnkB@3	1.52	2.0266E-03	2.3667E+09	4.7963E+06	1.55E+09	142.3	10.67	0.15		**11.32**
d18O_P551_030423_ME18b_AnkB@4	1.53	2.0259E-03	2.3445E+09	4.7496E+06	1.54E+09	140.8	10.32	0.15		**10.97**
d18O_P551_030423_ME18b_AnkB@5	1.53	2.0280E-03	2.3916E+09	4.8499E+06	1.57E+09	143.5	11.37	0.10		**12.02**
d18O_P551_030423_ME18b_AnkB@6	1.52	2.0241E-03	2.3458E+09	4.7482E+06	1.54E+09	141.0	9.45	0.14		**10.10**
d18O_Paine_P551@16	1.52	2.0142E-03	1.6737E+09	3.3710E+06	1.10E+09	100.7	4.47	0.13	-5.33	
d18O_P551_030423_ME18b_Qz3B@1	1.52	2.0254E-03	1.6541E+09	3.3501E+06	1.09E+09	99.7	10.08	0.13		**15.41**
d18O_P551_030423_ME18b_Qz3B@02	1.52	2.0251E-03	1.6806E+09	3.4035E+06	1.10E+09	101.2	9.95	0.14		**15.27**
d18O_P551_030423_ME18b_Qz3B@03	1.52	2.0258E-03	1.7001E+09	3.4427E+06	1.12E+09	102.2	10.26	0.14		**15.59**
d18O_P551_030423_ME18b_Qz3B@04	1.52	2.0255E-03	1.6692E+09	3.3809E+06	1.10E+09	100.3	10.14	0.15		**15.47**
d18O_P551_030423_ME18b_Qz3B@05	1.52	2.0251E-03	1.6627E+09	3.3664E+06	1.09E+09	100.1	9.93	0.17		**15.25**
d18O_P551_030423_ME18b_Qz3B@06	1.52	2.0250E-03	1.6575E+09	3.3563E+06	1.09E+09	99.9	9.86	0.17		**15.18**
d18O_Paine_P551@17	1.52	2.0144E-03	1.6741E+09	3.3725E+06	1.10E+09	100.9	4.60	0.15	-5.20	
d18O_P551_030423_ME18b_Qz3B@07	1.52	2.0254E-03	1.6658E+09	3.3739E+06	1.10E+09	100.3	10.08	0.24		**15.41**
d18O_P551_030423_ME18b_Qz3B@08	1.52	2.0260E-03	1.6510E+09	3.3452E+06	1.09E+09	99.4	10.36	0.17		**15.69**
d18O_P551_030423_ME18b_Qz3B@09	1.52	2.0254E-03	1.6754E+09	3.3933E+06	1.10E+09	101.0	10.05	0.15		**15.38**
d18O_P551_030423_ME18b_Qz3B@10	1.52	2.0262E-03	1.6736E+09	3.3913E+06	1.10E+09	100.7	10.45	0.12		**15.78**
d18O_P551_030423_ME18b_Qz3B@11	1.52	2.0253E-03	1.6673E+09	3.3768E+06	1.10E+09	100.3	10.03	0.15		**15.36**
d18O_P551_030423_ME18b_Qz3B@12	1.52	2.0259E-03	1.6403E+09	3.3230E+06	1.08E+09	98.8	10.35	0.16		**15.67**
d18O_Paine_P551@18	1.52	2.0145E-03	1.6763E+09	3.3767E+06	1.10E+09	101.2	4.65	0.14	-5.15	
d18O_P551_030423_ME18b_Qz3B@13	1.52	2.0255E-03	1.6567E+09	3.3560E+06	1.09E+09	99.9	10.13	0.16		**15.46**
d18O_P551_030423_ME18b_Qz3B@14	1.52	2.0258E-03	1.6582E+09	3.3594E+06	1.09E+09	99.8	10.29	0.18		**15.62**
d18O_P551_030423_ME18b_Qz3B@15	1.52	2.0258E-03	1.6452E+09	3.3330E+06	1.08E+09	99.1	10.26	0.18		**15.59**
d18O_P551_030423_ME18b_Qz4@1	1.52	2.0256E-03	1.6673E+09	3.3772E+06	1.10E+09	100.6	10.17	0.14		**15.50**
d18O_P551_030423_ME18b_Qz4@2	1.51	2.0255E-03	1.6647E+09	3.3706E+06	1.10E+09	100.7	10.14	0.13		**15.47**
d18O_P551_030423_ME18b_Qz4@3	1.52	2.0252E-03	1.6649E+09	3.3718E+06	1.10E+09	100.6	9.95	0.12		**15.28**
d18O_Paine_P551@19	1.52	2.0144E-03	1.6759E+09	3.3746E+06	1.10E+09	101.2	4.59	0.17	-5.21	
d18O_P551_030423_ME18b_Qz4@4	1.52	2.0253E-03	1.6725E+09	3.3865E+06	1.10E+09	100.7	10.03	0.12		**15.35**
d18O_P551_030423_ME18b_Qz4@5	1.52	2.0247E-03	1.6535E+09	3.3474E+06	1.09E+09	99.7	9.70	0.16		**15.03**
d18O_P551_030423_ME18b_Qz1@1	1.52	2.0250E-03	1.6704E+09	3.3826E+06	1.10E+09	100.9	9.86	0.16		**15.19**
d18O_P551_030423_ME18b_Qz1@02	1.52	2.0253E-03	1.6680E+09	3.3771E+06	1.10E+09	100.8	10.04	0.18		**15.37**
d18O_P551_030423_ME18b_Qz1@03	1.51	2.0234E-03	1.6638E+09	3.3664E+06	1.10E+09	100.6	9.07	0.20		**14.40**
d18O_P551_030423_ME18b_Qz1@04	1.51	2.0248E-03	1.6744E+09	3.3903E+06	1.11E+09	101.2	9.76	0.14		**15.08**
d18O_Paine_P551@20	1.52	2.0142E-03	1.6753E+09	3.3743E+06	1.11E+09	101.2	4.50	0.18	-5.30	
d18O_P551_030423_ME18b_Qz1@05	1.52	2.0248E-03	1.6636E+09	3.3684E+06	1.10E+09	100.5	9.78	0.17		**15.11**
d18O_P551_030423_ME18b_Qz1@06	1.51	2.0254E-03	1.6693E+09	3.3799E+06	1.10E+09	101.0	10.07	0.17		**15.39**
d18O_P551_030423_ME18b_Qz1@07	1.51	2.0245E-03	1.6704E+09	3.3820E+06	1.10E+09	101.2	9.63	0.16		**14.96**
d18O_P551_030423_ME18b_Qz1@08	1.51	2.0244E-03	1.6053E+09	3.2489E+06	1.06E+09	97.4	9.60	0.19		**14.92**
d18O_P551_030423_ME18b_Qz1@09	1.51	2.0254E-03	1.6829E+09	3.4068E+06	1.11E+09	101.9	10.05	0.22		**15.38**
d18O_P551_030423_ME18b_Qz1@10	1.51	2.0256E-03	1.6844E+09	3.4135E+06	1.11E+09	101.9	10.19	0.13		**15.52**
d18O_P551_030423_ME18b_Qz1@11	1.51	2.0251E-03	1.6712E+09	3.3846E+06	1.10E+09	101.1	9.91	0.13		**15.23**
d18O_Paine_P551@21	1.51	2.0140E-03	1.6677E+09	3.3588E+06	1.10E+09	100.9	4.39	0.14	-5.41	

Supplementary Table B-1. Details of SIMS measurements of Si isotope compositions in quartz

Spot#		30Si/28Si H'2/L'2	28Si/Coeff L'2	yield	δ^{30}Si measured	2se	IMF	δ^{30}Si corrected
d30Si_P548_050423_paine@1	2.00	3.2701E-02	9.4409E+07	4.7281E+07	-42.34	0.14	-42.24	
d30Si_P548_050423_paine@2	2.00	3.2678E-02	9.4808E+07	4.7371E+07	-43.01	0.13	-42.91	
d30Si_P548_050423_paine@3	2.00	3.2652E-02	9.4871E+07	4.7411E+07	-43.77	0.16	-43.67	
d30Si_P548_050423_paine@4	2.00	3.2682E-02	9.4370E+07	4.7266E+07	-42.88	0.18	-42.78	
d30Si_P548_050423_paine@5	2.00	3.2703E-02	9.1383E+07	4.5793E+07	-42.28	0.15	-42.18	
d30Si_P548_050423_paine@6	1.99	3.2714E-02	9.1396E+07	4.5874E+07	-41.96	0.15	-41.86	
d30Si_P548_050423_paine@7	1.99	3.2708E-02	8.9734E+07	4.5034E+07	-42.12	0.18	-42.02	
d30Si_P548_050423_paine@8	1.99	3.2726E-02	8.9417E+07	4.5011E+07	-41.61	0.13	-41.51	
d30Si_P548_050423_paine@9	1.98	3.2709E-02	8.9294E+07	4.4987E+07	-42.11	0.23	-42.01	
d30Si_P548_050423_ME17b_qz3@1	1.98	3.2734E-02	8.7484E+07	4.4118E+07	-41.37	0.18		**0.48**
d30Si_P548_050423_ME17b_qz3@2	1.98	3.2731E-02	8.9794E+07	4.5274E+07	-41.47	0.16		**0.39**
d30Si_P548_050423_ME17b_qz3@3	1.98	3.2735E-02	9.0799E+07	4.5962E+07	-41.35	0.20		**0.51**
d30Si_P548_050423_ME17b_qz3@4	1.98	3.2705E-02	8.8477E+07	4.4716E+07	-42.23	0.18		**-0.37**
d30Si_P548_050423_ME17b_qz3@5	1.98	3.2731E-02	8.8239E+07	4.4650E+07	-41.46	0.18		**0.39**
d30Si_P548_050423_ME17b_qz3@6	1.98	3.2720E-02	8.9364E+07	4.5169E+07	-41.79	0.17		**0.07**
d30Si_P548_050423_ME17b_qz3@7	1.98	3.2721E-02	9.0131E+07	4.5570E+07	-41.75	0.18		**0.11**
d30Si_P548_050423_ME17b_qz3@8	1.98	3.2715E-02	8.9431E+07	4.5264E+07	-41.91	0.14		**-0.06**

Spot#		30Si/28Si H'2/L'2	28Si/Coeff L'2	yield	δ^{30}Si measured	2se	IMF	**δ^{30}Si corrected**
d30Si_P548_050423_ME17b_qz4@1	1.97	3.2732E-02	8.8967E+07	4.5230E+07	-41.43	0.21		**0.43**
d30Si_P548_050423_ME17b_qz4@2	1.96	3.2710E-02	9.0734E+07	4.6259E+07	-42.07	0.12		**-0.22**
d30Si_P548_050423_ME17b_qz4@3	1.96	3.2735E-02	8.9683E+07	4.5654E+07	-41.35	0.14		**0.50**
d30Si_P548_050423_ME17b_qz4@4	1.97	3.2718E-02	8.9612E+07	4.5556E+07	-41.84	0.18		**0.01**
d30Si_P548_050423_paine@9b	1.97	3.2706E-02	8.8533E+07	4.4908E+07	-42.18	0.11	-42.08	
d30Si_P548_050423_paine@10	1.97	3.2709E-02	8.9056E+07	4.5254E+07	-42.11	0.13	-42.01	
d30Si_P548_050423_ME17b_qz4@5	1.97	3.2714E-02	8.9488E+07	4.5488E+07	-41.94	0.17		**-0.08**
d30Si_P548_050423_ME17b_qz4@6	1.97	3.2737E-02	8.9065E+07	4.5321E+07	-41.29	0.19		**0.56**
d30Si_P548_050423_ME17b_qz4@7	1.96	3.2741E-02	8.9786E+07	4.5765E+07	-41.16	0.16		**0.69**
d30Si_P548_050423_ME17b_qz4@8	1.96	3.2693E-02	8.9035E+07	4.5500E+07	-42.56	0.20		**-0.71**
d30Si_P548_050423_ME17b_qz4@9	1.96	3.2716E-02	8.9463E+07	4.5700E+07	-41.91	0.14		**-0.05**
d30Si_P548_050423_ME17b_qz1@1	1.96	3.2743E-02	8.6642E+07	4.4264E+07	-41.11	0.17		**0.74**
d30Si_P548_050423_ME17b_qz1@2	1.96	3.2746E-02	8.6184E+07	4.3873E+07	-41.01	0.18		**0.85**
d30Si_P548_050423_ME17b_qz1@3	1.96	3.2750E-02	8.6426E+07	4.4071E+07	-40.90	0.16		**0.95**
d30Si_P548_050423_ME17b_qz1@4	1.96	3.2751E-02	8.6672E+07	4.4282E+07	-40.88	0.14		**0.97**
d30Si_P548_050423_paine@11	1.96	3.2711E-02	9.0600E+07	4.6244E+07	-42.03	0.13	-41.93	
d30Si_P548_050423_ME17b_qz1@5	1.95	3.2713E-02	8.6313E+07	4.4192E+07	-41.98	0.15		**-0.13**
d30Si_P548_050423_ME17b_qz1@6	1.95	3.2752E-02	8.6241E+07	4.4292E+07	-40.83	0.15		**1.03**
d30Si_P548_050423_ME17b_qz1@7	1.94	3.2737E-02	8.5016E+07	4.3733E+07	-41.28	0.14		**0.57**
d30Si_P548_050423_ME17b_qz1@8	1.94	3.2729E-02	8.6307E+07	4.4515E+07	-41.53	0.17		**0.33**
d30Si_P548_050423_MM11a_qz1@1	1.94	3.2726E-02	8.8888E+07	4.5876E+07	-41.59	0.21		**0.26**
d30Si_P548_050423_MM11a_qz1@2	1.94	3.2722E-02	8.9155E+07	4.6018E+07	-41.73	0.13		**0.12**
d30Si_P548_050423_MM11a_qz1@3	1.94	3.2727E-02	8.9964E+07	4.6484E+07	-41.57	0.14		**0.29**
d30Si_P548_050423_paine@12	1.93	3.2733E-02	8.8035E+07	4.5577E+07	-41.40	0.13	-41.30	
d30Si_P548_050423_MM11a_qz1@4	1.93	3.2728E-02	8.9496E+07	4.6281E+07	-41.54	0.13		**0.31**
d30Si_P548_050423_MM11a_qz1@5	1.93	3.2722E-02	8.8192E+07	4.5620E+07	-41.72	0.19		**0.13**
d30Si_P548_050423_MM11a_qz1@6	1.93	3.2748E-02	8.9066E+07	4.6149E+07	-40.96	0.20		**0.89**
d30Si_P548_050423_MM11a_qz1@7	1.93	3.2734E-02	9.0690E+07	4.7045E+07	-41.38	0.18		**0.48**
d30Si_P548_050423_MM11a_qz1@8	1.93	3.2728E-02	8.8106E+07	4.5736E+07	-41.53	0.14		**0.32**
d30Si_P548_050423_MM11a_qz1@9	1.94	3.2741E-02	8.9421E+07	4.6181E+07	-41.15	0.11		**0.70**
d30Si_P548_050423_MM11a_qz1@10	1.93	3.2712E-02	8.8995E+07	4.6108E+07	-42.00	0.11		**-0.15**
d30Si_P548_050423_paine@13	1.92	3.2720E-02	8.7274E+07	4.5393E+07	-41.78	0.14	-41.68	
d30Si_P548_050423_paine@14	1.92	3.2716E-02	8.7855E+07	4.5695E+07	-41.90	0.15	-41.80	
d30Si_P550_050423_paine@1	1.90	3.2706E-02	8.9180E+07	4.6869E+07	-42.19	0.20	-42.09	
d30Si_P550_050423_paine@2	1.90	3.2706E-02	8.8812E+07	4.6752E+07	-42.18	0.13	-42.08	
d30Si_P550_050423_paine@3	1.90	3.2717E-02	8.7476E+07	4.6047E+07	-41.88	0.18	-41.78	
d30Si_P550_050423_paine@4	1.90	3.2722E-02	8.6993E+07	4.5779E+07	-41.73	0.15	-41.63	
d30Si_P550_050423_paine@5	1.90	3.2720E-02	8.7697E+07	4.6234E+07	-41.77	0.18	-41.67	
d30Si_P550_050423_paine@6	1.89	3.2720E-02	8.8071E+07	4.6535E+07	-41.78	0.18	-41.68	
d30Si_P550_050423_paine@6b	1.89	3.2718E-02	8.7941E+07	4.6545E+07	-41.83	0.12	-41.73	
d30Si_P550_050423_ME18a_qz6@1	1.89	3.2719E-02	8.6868E+07	4.6057E+07	-41.81	0.16		**0.09**
d30Si_P550_050423_ME18a_qz6@2	1.88	3.2691E-02	8.5907E+07	4.5617E+07	-42.63	0.19		**-0.73**
d30Si_P550_050423_ME18a_qz6@3	1.89	3.2685E-02	8.5537E+07	4.5368E+07	-42.79	0.19		**-0.89**
d30Si_P550_050423_ME18a_qz6@4	1.88	3.2690E-02	8.7064E+07	4.6274E+07	-42.65	0.15		**-0.75**
d30Si_P550_050423_ME18a_qz3@1	1.88	3.2738E-02	8.3997E+07	4.4694E+07	-41.24	0.16		**0.66**
d30Si_P550_050423_ME18a_qz3@2	1.87	3.2741E-02	8.2851E+07	4.4204E+07	-41.15	0.15		**0.75**
d30Si_P550_050423_ME18a_qz3@3	1.87	3.2707E-02	8.2800E+07	4.4284E+07	-42.16	0.18		**-0.26**
d30Si_P550_050423_ME18a_qz3@4	1.87	3.2741E-02	8.1250E+07	4.3441E+07	-41.17	0.20		**0.74**
d30Si_P550_050423_ME18a_qz3@5	1.88	3.2733E-02	8.3145E+07	4.4287E+07	-41.41	0.16		**0.49**
d30Si_P550_050423_ME18a_qz1a@1a	1.87	3.2742E-02	8.6524E+07	4.6237E+07	-41.14	0.18		**0.76**
d30Si_P550_050423_paine@7	1.87	3.2698E-02	8.8533E+07	4.7313E+07	-42.41	0.16	-42.31	
d30Si_P550_050423_ME18a_qz1a@2	1.87	3.2738E-02	8.6381E+07	4.6097E+07	-41.24	0.17		**0.66**
d30Si_P550_050423_ME18a_qz1a@3	1.87	3.2724E-02	8.4342E+07	4.4982E+07	-41.65	0.17		**0.25**
d30Si_P550_050423_ME18a_qz1a@4	1.87	3.2729E-02	8.7702E+07	4.6898E+07	-41.52	0.16		**0.38**
d30Si_P550_050423_paine@8	1.87	3.2704E-02	8.9941E+07	4.8053E+07	-42.26	0.14	-42.16	
d30Si_P550_050423_ME18a_qz1a@5	1.87	3.2711E-02	9.0129E+07	4.8222E+07	-42.03	0.17		**-0.13**
d30Si_P550_050423_ME18a_qz1a@6	1.87	3.2728E-02	8.8247E+07	4.7215E+07	-41.55	0.11		**0.35**
d30Si_P550_050423_ME18a_qz1b@1	1.87	3.2686E-02	8.9231E+07	4.7815E+07	-42.78	0.18		**-0.88**
d30Si_P550_050423_ME18a_qz1b@2	1.87	3.2720E-02	8.6785E+07	4.6526E+07	-41.77	0.15		**0.13**
d30Si_P550_050423_ME18a_qz1b@3	1.86	3.2711E-02	8.6857E+07	4.6598E+07	-42.05	0.14		**-0.15**
d30Si_P550_050423_ME18a_qz1b@4	1.86	3.2699E-02	8.8376E+07	4.7399E+07	-42.39	0.21		**-0.49**
d30Si_P550_050423_paine@9	1.56	3.2723E-02	7.2468E+07	4.6330E+07	-41.69	0.15	-41.59	
d30Si_P550_050423_ME18a_qz1b@5	1.58	3.2698E-02	7.6864E+07	4.8581E+07	-42.43	0.15		**-0.61**
d30Si_P550_050423_ME17a_qz3@1	1.60	3.2704E-02	7.2952E+07	4.5731E+07	-42.24	0.19		**-0.41**
d30Si_P550_050423_ME17a_qz3@2	1.61	3.2706E-02	7.3472E+07	4.5667E+07	-42.18	0.19		**-0.36**
d30Si_P550_050423_ME17a_qz3@3	1.62	3.2737E-02	7.3023E+07	4.5095E+07	-41.27	0.20		**0.56**
d30Si_P550_050423_ME17a_qz3@4	1.62	3.2723E-02	7.4751E+07	4.6060E+07	-41.68	0.18		**0.15**
d30Si_P550_050423_ME17a_qz3@5	1.63	3.2719E-02	7.3884E+07	4.5337E+07	-41.80	0.20		**0.02**
d30Si_P550_050423_paine@10	1.63	3.2724E-02	7.5761E+07	4.6462E+07	-41.67	0.19	-41.57	
d30Si_P550_050423_ME17a_qz3@8	1.64	3.2701E-02	7.5454E+07	4.6049E+07	-42.33	0.18		**-0.51**
d30Si_P550_050423_ME17a_qz1@1	1.64	3.2757E-02	7.4437E+07	4.5411E+07	-40.68	0.18		**1.14**
d30Si_P550_050423_ME17a_qz1@2	1.64	3.2742E-02	7.5247E+07	4.5804E+07	-41.14	0.21		**0.69**
d30Si_P550_050423_ME17a_qz1@3	1.65	3.2740E-02	7.5096E+07	4.5584E+07	-41.20	0.18		**0.63**
d30Si_P550_050423_ME17a_qz1@4	1.65	3.2730E-02	7.5625E+07	4.5919E+07	-41.48	0.12		**0.35**
d30Si_P550_050423_ME17a_qz1@5	1.64	3.2728E-02	7.5290E+07	4.5804E+07	-41.53	0.20		**0.30**
d30Si_P550_050423_paine@11	1.64	3.2698E-02	7.6818E+07	4.6792E+07	-42.42	0.19	-42.32	

		30Si/28Si H'2/L'2	28Si/Coeff L'2	yield	d30Si	2se	IMF	**d30Si NBS28**
d30Si_Paine_P551@11	2.21	3.2687E-02	1.0529E+08	4.7732E+07	-42.75	0.14	-42.65	
d30Si_Paine_P551@12	2.20	3.2673E-02	1.0536E+08	4.7810E+07	-43.16	0.11	-43.06	
d30Si_Paine_P551@13	2.21	3.2677E-02	1.0527E+08	4.7704E+07	-43.03	0.14	-42.93	
d30Si_P551_030423_MM11b_qz6@1	2.20	3.2660E-02	1.0328E+08	4.6930E+07	-43.54	0.14		**-0.58**
d30Si_P551_030423_MM11b_qz6@2	2.20	3.2656E-02	1.0259E+08	4.6698E+07	-43.66	0.11		**-0.69**

Spot#		30Si/28Si H'2/L'2	28Si/Coeff L'2	yield	δ^{30}Si measured	2se	IMF	**δ^{30}Si corrected**
d30Si_P551_030423_MM11b_qz6@3	2.20	3.2700E-02	1.0015E+08	4.5593E+07	-42.37	0.15		**0.60**
d30Si_P551_030423_MM11b_qz6@4	2.19	3.2702E-02	1.0047E+08	4.5788E+07	-42.32	0.16		**0.65**
d30Si_P551_030423_MM11b_qz3@1	2.19	3.2676E-02	1.0440E+08	4.7695E+07	-43.07	0.15		**-0.11**
d30Si_P551_030423_MM11b_qz3@2	2.18	3.2673E-02	1.0389E+08	4.7581E+07	-43.14	0.20		**-0.18**
d30Si_Paine_P551@07	2.18	3.2666E-02	1.0305E+08	4.7273E+07	-43.34	0.13	-43.24	
d30Si_P551_030423_MM11b_qz3@3	2.18	3.2664E-02	1.0409E+08	4.7713E+07	-43.42	0.15		**-0.45**
d30Si_P551_030423_MM11b_qz3@4	2.18	3.2678E-02	1.0325E+08	4.7430E+07	-43.00	0.14		**-0.04**
d30Si_P551_030423_MM11b_qz3@5	2.18	3.2696E-02	1.0268E+08	4.7206E+07	-42.48	0.11		**0.48**
d30Si_P551_030423_MM11b_qz3@6	2.17	3.2708E-02	1.0356E+08	4.7705E+07	-42.13	0.16		**0.83**
d30Si_P551_030423_MM11b_qz2@1	2.17	3.2702E-02	1.0307E+08	4.7460E+07	-42.32	0.19		**0.65**
d30Si_P551_030423_MM11b_qz2@2	2.17	3.2697E-02	1.0179E+08	4.6900E+07	-42.44	0.14		**0.53**
d30Si_P551_030423_MM11b_qz2@3	2.17	3.2613E-02	1.0248E+08	4.7322E+07	-44.91	0.17		**-1.94**
d30Si_Paine_P551@08	2.16	3.2691E-02	1.0214E+08	4.7325E+07	-42.62	0.16	-42.52	**0.35**
d30Si_P551_030423_MM11b_qz2@4	2.15	3.2698E-02	1.0259E+08	4.7620E+07	-42.41	0.12		**0.55**
d30Si_P551_030423_MM11b_qz2@5	2.16	3.2637E-02	1.0199E+08	4.7302E+07	-44.22	0.16		**-1.25**
d30Si_P551_030423_MM11b_qz1@1	2.16	3.2725E-02	9.9564E+07	4.6184E+07	-41.62	0.14		**1.34**
d30Si_P551_030423_MM11b_qz1@2	2.15	3.2727E-02	1.0228E+08	4.7529E+07	-41.57	0.12		**1.40**
d30Si_P551_030423_MM11b_qz1@3	2.14	3.2687E-02	1.0236E+08	4.7723E+07	-42.73	0.13		**0.23**
d30Si_P551_030423_MM11b_qz1@4	2.14	3.2689E-02	1.0195E+08	4.7587E+07	-42.70	0.10		**0.26**
d30Si_P551_030423_MM11b_qz1@5	2.14	3.2725E-02	1.0170E+08	4.7446E+07	-41.62	0.20		**1.34**
d30Si_Paine_P551@09	2.14	3.2664E-02	1.0182E+08	4.7499E+07	-43.42	0.11	-43.32	
d30Si_P551_030423_MM11b_qz1@6	2.14	3.2607E-02	1.0056E+08	4.6925E+07	-45.07	0.11		**-2.11**
d30Si_P551_030423_MM11b_qz1@7	2.14	3.2699E-02	1.0184E+08	4.7690E+07	-42.38	0.13		**0.58**
d30Si_P551_030423_MM11b_qz1@8	2.13	3.2708E-02	1.0073E+08	4.7264E+07	-42.14	0.12		**0.83**
d30Si_P551_030423_ME18c_qz4@1	2.13	3.2713E-02	1.0166E+08	4.7736E+07	-41.99	0.13		**0.97**
d30Si_P551_030423_ME18c_qz4@2	2.13	3.2725E-02	1.0080E+08	4.7275E+07	-41.63	0.16		**1.33**
d30Si_Paine_P551@14	2.13	3.2678E-02	1.0172E+08	4.7757E+07	-43.01	0.21	-42.91	
d30Si_P551_030423_ME18c_qz4@3	2.13	3.2702E-02	1.0004E+08	4.7048E+07	-42.30	0.14		**0.66**
d30Si_P551_030423_ME18c_qz4@4	2.12	3.2702E-02	9.9633E+07	4.7002E+07	-42.30	0.14		**0.66**
d30Si_P551_030423_ME18c_qz4@5	2.12	3.2726E-02	9.8289E+07	4.6417E+07	-41.59	0.14		**1.38**
d30Si_P551_030423_ME18c_qz4@6	2.12	3.2724E-02	9.9935E+07	4.7162E+07	-41.66	0.13		**1.30**
d30Si_P551_030423_ME18c_qz4@7	2.12	3.2754E-02	9.8663E+07	4.6573E+07	-40.79	0.14		**2.18**
d30Si_P551_030423_ME18c_qz4@8	2.11	3.2725E-02	9.8811E+07	4.6760E+07	-41.64	0.10		**1.32**
d30Si_P551_030423_ME18c_qz4@9	2.11	3.2720E-02	9.8605E+07	4.6777E+07	-41.77	0.16		**1.19**
d30Si_Paine_P551@15	2.11	3.2686E-02	1.0066E+08	4.7761E+07	-42.78	0.12	-42.68	
d30Si_P551_030423_ME18c_qz4@10	2.11	3.2758E-02	9.8318E+07	4.6615E+07	-40.66	0.16		**2.31**
d30Si_P551_030423_ME18c_qz1@1	2.11	3.2733E-02	9.7635E+07	4.6324E+07	-41.40	0.17		**1.57**
d30Si_P551_030423_ME18c_qz1@2	2.10	3.2729E-02	9.6011E+07	4.5621E+07	-41.51	0.16		**1.45**
d30Si_P551_030423_ME18c_qz1@3	2.10	3.2717E-02	1.0227E+08	4.8662E+07	-41.86	0.11		**1.10**
d30Si_P551_030423_ME18c_qz1@4	2.10	3.2734E-02	9.9282E+07	4.7228E+07	-41.37	0.17		**1.59**
d30Si_P551_030423_ME18c_qz1@5	2.10	3.2704E-02	1.0063E+08	4.7906E+07	-42.26	0.14		**0.70**
d30Si_P551_030423_ME18c_qz1@6	2.10	3.2743E-02	9.7428E+07	4.6346E+07	-41.11	0.12		**1.85**
d30Si_Paine_P551@16	2.10	3.2690E-02	1.0059E+08	4.7906E+07	-42.67	0.12	-42.57	
d30Si_P551_030423_ME18c_qz1@7	2.09	3.2737E-02	9.7835E+07	4.6779E+07	-41.28	0.15		**1.68**
d30Si_P551_030423_ME18c_qz1@8	2.09	3.2727E-02	9.9980E+07	4.7886E+07	-41.58	0.12		**1.38**
d30Si_P551_030423_ME18c_qz1@9	2.09	3.2707E-02	1.0118E+08	4.8375E+07	-42.14	0.16		**0.82**
d30Si_P551_030423_ME18b_Qz3B@1	2.09	3.2729E-02	9.7624E+07	4.6719E+07	-41.52	0.11		**1.45**
d30Si_P551_030423_ME18b_Qz3B@02	2.09	3.2730E-02	9.8475E+07	4.7187E+07	-41.47	0.17		**1.49**
d30Si_P551_030423_ME18b_Qz3B@03	2.08	3.2735E-02	9.9204E+07	4.7675E+07	-41.32	0.14		**1.64**
d30Si_P551_030423_ME18b_Qz3B@04	2.08	3.2706E-02	9.7148E+07	4.6681E+07	-42.20	0.14		**0.76**
d30Si_Paine_P551@17	2.08	3.2661E-02	1.0018E+08	4.8166E+07	-43.50	0.15	-43.40	
d30Si_P551_030423_ME18b_Qz3B@05	2.08	3.2698E-02	9.7717E+07	4.6986E+07	-42.43	0.12		**0.53**
d30Si_P551_030423_ME18b_Qz3B@06	2.08	3.2701E-02	9.8813E+07	4.7490E+07	-42.34	0.16		**0.63**
d30Si_P551_030423_ME18b_Qz3B@07	2.08	3.2690E-02	9.7279E+07	4.6812E+07	-42.66	0.15		**0.30**
d30Si_P551_030423_ME18b_Qz3B@08	2.07	3.2703E-02	9.7410E+07	4.6972E+07	-42.27	0.12		**0.70**
d30Si_P551_030423_ME18b_Qz3B@09	2.07	3.2705E-02	9.9001E+07	4.7727E+07	-42.21	0.17		**0.76**
d30Si_P551_030423_ME18b_Qz3B@10	2.07	3.2684E-02	9.7840E+07	4.7189E+07	-42.84	0.18		**0.12**
d30Si_P551_030423_ME18b_Qz3B@11	2.07	3.2710E-02	9.9764E+07	4.8125E+07	-42.08	0.13		**0.88**
d30Si_P551_030423_ME18b_Qz3B@12	2.07	3.2717E-02	1.0194E+08	4.9193E+07	-41.87	0.16		**1.10**
d30Si_Paine_P551@18	2.07	3.2682E-02	9.9710E+07	4.8167E+07	-42.90	0.19	-42.80	
d30Si_P551_030423_ME18b_Qz3B@13	2.07	3.2708E-02	9.6338E+07	4.6569E+07	-42.12	0.16		**0.84**
d30Si_P551_030423_ME18b_Qz3B@14	2.07	3.2708E-02	9.5331E+07	4.6105E+07	-42.14	0.14		**0.82**
d30Si_P551_030423_ME18b_Qz3B@15	2.07	3.2703E-02	9.7232E+07	4.7075E+07	-42.27	0.14		**0.69**
d30Si_P551_030423_ME18b_Qz4@1	2.06	3.2724E-02	9.7286E+07	4.7165E+07	-41.66	0.11		**1.31**
d30Si_P551_030423_ME18b_Qz4@2	2.06	3.2712E-02	9.7542E+07	4.7304E+07	-42.01	0.13		**0.96**
d30Si_P551_030423_ME18b_Qz4@3	2.06	3.2738E-02	9.6479E+07	4.6911E+07	-41.26	0.13		**1.71**
d30Si_P551_030423_ME18b_Qz4@4	2.05	3.2725E-02	9.7132E+07	4.7315E+07	-41.63	0.12		**1.34**
d30Si_P551_030423_ME18b_Qz4@5	2.05	3.2753E-02	9.6891E+07	4.7185E+07	-40.80	0.16		**2.16**
d30Si_P551_030423_ME18b_Qz1@1	2.05	3.2733E-02	9.5874E+07	4.6740E+07	-41.39	0.14		**1.57**
d30Si_P551_030423_ME18b_Qz1@02	2.05	3.2744E-02	9.6450E+07	4.7128E+07	-41.08	0.14		**1.89**
d30Si_P551_030423_ME18b_Qz1@04	2.05	3.2713E-02	9.5412E+07	4.6648E+07	-41.99	0.12		**0.97**
d30Si_P551_030423_ME18b_Qz1@05	2.04	3.2720E-02	9.8300E+07	4.8161E+07	-41.78	0.12		**1.19**
d30Si_Paine_P551@21	2.03	3.2670E-02	9.8139E+07	4.8319E+07	-43.25	0.18	-43.15	
d30Si_Paine_P549@1	1.98	3.2698E-02	9.2497E+07	4.6722E+07	-42.41	0.16	-42.31	
d30Si_Paine_P549@2	1.98	3.2666E-02	9.2124E+07	4.6587E+07	-43.37	0.18	-43.27	
d30Si_Paine_P549@3	1.97	3.2661E-02	9.2997E+07	4.7131E+07	-43.51	0.15	-43.41	
d30Si_Paine_P549@04	1.97	3.2681E-02	9.2363E+07	4.6869E+07	-42.91	0.15	-42.81	
d30Si_Paine_P549@05	1.97	3.2668E-02	9.2348E+07	4.6813E+07	-43.30	0.17	-43.20	
d30Si_Paine_P549@06	1.97	3.2695E-02	9.2495E+07	4.6983E+07	-42.50	0.13	-42.40	
d30Si_P549_030423_HO25a_Qz4@1	1.96	3.2661E-02	9.5071E+07	4.8410E+07	-43.50	0.13		**-0.67**
d30Si_P549_030423_HO25a_Qz4@2	1.96	3.2721E-02	8.9288E+07	4.5533E+07	-41.74	0.17		**1.09**
d30Si_P549_030423_HO25a_Qz4@3	1.96	3.2710E-02	8.7636E+07	4.4630E+07	-42.08	0.20		**0.75**
d30Si_P549_030423_HO25a_Qz4@4	1.96	3.2723E-02	9.0924E+07	4.6293E+07	-41.69	0.12		**1.14**
d30Si_P549_030423_HO25a_Qz4@5	1.96	3.2688E-02	9.2626E+07	4.7331E+07	-42.70	0.13		**0.13**

Spot#		30Si/28Si H'2/L'2	28Si/Coeff L'2	yield	δ^{30}Si measured	2se	IMF	**δ^{30}Si corrected**
d30Si_P549_030423_HO25a_Qz4@6	1.95	3.2691E-02	9.0259E+07	4.6221E+07	-42.62	0.16		**0.21**
d30Si_Paine_P549@07	1.95	3.2675E-02	9.1582E+07	4.6989E+07	-43.10	0.16	-43.00	
d30Si_P549_030423_HO25a_Qz4@7	1.95	3.2683E-02	8.9205E+07	4.5656E+07	-42.86	0.16		**-0.03**
d30Si_P549_030423_HO25a_Qz4@8	1.95	3.2665E-02	9.7121E+07	4.9865E+07	-43.40	0.15		**-0.57**
d30Si_P549_030423_HO25a_Qz1@1	1.95	3.2697E-02	8.8895E+07	4.5677E+07	-42.45	0.13		**0.39**
d30Si_P549_030423_HO25a_Qz1@2	1.94	3.2706E-02	8.9675E+07	4.6139E+07	-42.19	0.18		**0.64**
d30Si_P549_030423_HO25a_Qz1@3	1.94	3.2721E-02	9.2120E+07	4.7427E+07	-41.74	0.14		**1.10**
d30Si_P549_030423_HO25a_Qz1@4	1.94	3.2710E-02	8.8843E+07	4.5790E+07	-42.08	0.19		**0.75**
d30Si_Paine_P549@08	1.93	3.2666E-02	9.1891E+07	4.7489E+07	-43.34	0.13	-43.24	
d30Si_P549_030423_HO25a_Qz1@5	1.94	3.2711E-02	8.6950E+07	4.4918E+07	-42.05	0.24		**0.79**
d30Si_P549_030423_HO25a_Qz1@6	1.93	3.2716E-02	9.6301E+07	4.9792E+07	-41.89	0.17		**0.94**
d30Si_P549_030423_HO25a_Qz1@7	1.93	3.2701E-02	9.1251E+07	4.7199E+07	-42.33	0.14		**0.51**
d30Si_P549_030423_HO25a_Qz1@8	1.93	3.2681E-02	9.0716E+07	4.7078E+07	-42.93	0.18		**-0.10**
d30Si_P549_030423_HO25a_Qz1@9	1.93	3.2714E-02	8.7644E+07	4.5419E+07	-41.96	0.17		**0.88**
d30Si_P549_030423_HO25a_Qz1@10	1.93	3.2704E-02	9.3290E+07	4.8380E+07	-42.23	0.13		**0.60**
d30Si_P549_030423_HO9_Qz2@1	1.93	3.2752E-02	9.0675E+07	4.7055E+07	-40.83	0.12		**2.00**
d30Si_Paine_P549@09	1.93	3.2677E-02	9.1983E+07	4.7654E+07	-43.03	0.13	-42.93	
d30Si_P549_030423_HO9_Qz2@02	1.92	3.2728E-02	9.1522E+07	4.7548E+07	-41.54	0.15		**1.29**
d30Si_P549_030423_HO9_Qz2@03	1.92	3.2724E-02	8.9952E+07	4.6748E+07	-41.66	0.11		**1.17**
d30Si_P549_030423_HO9_Qz2@04	1.92	3.2725E-02	9.0921E+07	4.7361E+07	-41.62	0.16		**1.22**
d30Si_P549_030423_HO9_Qz2@05	1.92	3.2724E-02	8.9609E+07	4.6708E+07	-41.65	0.19		**1.19**
d30Si_P549_030423_HO9_Qz2@06	1.92	3.2733E-02	9.0075E+07	4.7007E+07	-41.40	0.18		**1.43**
d30Si_P549_030423_HO9_Qz2@07	1.91	3.2736E-02	8.9656E+07	4.6932E+07	-41.31	0.16		**1.52**
d30Si_P549_030423_HO9_Qz2@08	1.91	3.2714E-02	9.0602E+07	4.7456E+07	-41.95	0.15		**0.88**
d30Si_Paine_P549@10	1.91	3.2703E-02	9.1762E+07	4.8081E+07	-42.29	0.14	-42.19	
d30Si_P549_030423_HO9_Qz2@09	1.91	3.2715E-02	9.0156E+07	4.7223E+07	-41.92	0.16		**0.91**
d30Si_P549_030423_HO9_Qz2@10	1.91	3.2718E-02	9.1092E+07	4.7691E+07	-41.84	0.11		**0.99**
d30Si_P549_030423_HO9_Qz2@11	1.91	3.2718E-02	9.6705E+07	5.0672E+07	-41.83	0.15		**1.00**
d30Si_P549_030423_HO25b_Qz3@1	1.91	3.2719E-02	8.6128E+07	4.5151E+07	-41.81	0.14		**1.02**
d30Si_P549_030423_HO25b_Qz3@2	1.91	3.2702E-02	8.9040E+07	4.6720E+07	-42.30	0.12		**0.53**
d30Si_P549_030423_HO25b_Qz3@3	1.90	3.2729E-02	9.0075E+07	4.7298E+07	-41.52	0.13		**1.31**
d30Si_P549_030423_HO25b_Qz3@4	1.90	3.2739E-02	8.8356E+07	4.6533E+07	-41.22	0.18		**1.61**
d30Si_Paine_P549@11	1.90	3.2673E-02	9.1531E+07	4.8164E+07	-43.15	0.14	-43.05	
d30Si_P549_030423_HO25b_Qz4@1	1.90	3.2712E-02	8.9204E+07	4.6918E+07	-42.01	0.18		**0.83**
d30Si_P549_030423_HO25b_Qz4@2	1.90	3.2714E-02	8.9316E+07	4.7017E+07	-41.96	0.11		**0.88**
d30Si_P549_030423_HO25b_Qz4@3	1.90	3.2692E-02	8.8948E+07	4.6897E+07	-42.61	0.17		**0.22**
d30Si_P549_030423_HO25b_Qz4@4	1.89	3.2706E-02	9.0511E+07	4.7879E+07	-42.19	0.13		**0.65**
d30Si_P549_030423_HO25b_Qz4@5	1.90	3.2716E-02	8.9462E+07	4.7087E+07	-41.90	0.18		**0.93**
d30Si_P549_030423_HO25b_Qz4@6	1.90	3.2719E-02	8.9909E+07	4.7291E+07	-41.79	0.12		**1.04**
d30Si_Paine_P549@12	1.90	3.2693E-02	8.9451E+07	4.7021E+07	-42.55	0.17	-42.45	
d30Si_P549_030423_HO25b_Qz4@7	1.88	3.2693E-02	8.9295E+07	4.7427E+07	-42.55	0.14		**0.28**
d30Si_P549_030423_HO25b_Qz4@8	1.88	3.2714E-02	8.8757E+07	4.7149E+07	-41.95	0.16		**0.88**
d30Si_P549_030423_HO25b_Qz1@1	1.88	3.2748E-02	8.7257E+07	4.6319E+07	-40.94	0.19		**1.89**
d30Si_P549_030423_HO25b_Qz1@2	1.88	3.2721E-02	8.9225E+07	4.7389E+07	-41.76	0.15		**1.08**
d30Si_P549_030423_HO25b_Qz1@3	1.88	3.2724E-02	8.7371E+07	4.6467E+07	-41.67	0.17		**1.16**
d30Si_Paine_P549@13	1.88	3.2688E-02	8.9965E+07	4.7941E+07	-42.73	0.15	-42.63	
d30Si_P549_030423_HO25b_Qz1@4	1.88	3.2723E-02	8.7971E+07	4.6803E+07	-41.68	0.13		**1.15**
d30Si_P549_030423_HO25b_Qz1@5	1.88	3.2736E-02	8.5568E+07	4.5612E+07	-41.30	0.18		**1.53**
d30Si_P549_030423_HO25b_Qz1@6	1.88	3.2678E-02	8.9640E+07	4.7802E+07	-43.00	0.15		**-0.17**
d30Si_P549_030423_HO25b_Qz1@7	1.87	3.2704E-02	8.8091E+07	4.7075E+07	-42.23	0.18		**0.60**
d30Si_P549_030423_HO25b_Qz1@8	1.87	3.2707E-02	8.8640E+07	4.7346E+07	-42.17	0.14		**0.66**
d30Si_Paine_P549@14	1.87	3.2682E-02	8.9728E+07	4.7984E+07	-42.88	0.17	-42.78	

C. Supplementary material related to Part V.

Supplementary Table C-1. SIMS-determined O isotope composition of zircon grains.

Sample #	Ipr (nA)	18O/16O H'2/L'2	16O/Coeff L'2	yield	d18Oraw	2se	2SD	IMF	**d18OVSMOW**
d18O_030524_91500@1	1.966E+00	2.030E-03	2.092E+09	1.064E+09	12.56	0.14		2.70	
d18O_030524_91500@2	1.964E+00	2.029E-03	2.094E+09	1.066E+09	11.77	0.10		1.91	
d18O_030524_91500@3	1.961E+00	2.029E-03	2.080E+09	1.061E+09	11.84	0.12		1.98	
d18O_030524_91500@4	1.960E+00	2.030E-03	2.101E+09	1.072E+09	12.21	0.10		2.35	
d18O_030524_91500@5	1.956E+00	2.029E-03	2.083E+09	1.065E+09	11.72	0.13		1.86	
d18O_030524_91500@6	1.952E+00	2.028E-03	2.079E+09	1.065E+09	11.54	0.10		1.68	
d18O_030524_91500@7	1.951E+00	2.029E-03	2.092E+09	1.072E+09	12.02	0.11		2.16	
d18O_030524_91500@8	1.949E+00	2.028E-03	2.088E+09	1.071E+09	11.34	0.10		1.48	
d18O_030524_91500@9	1.951E+00	2.028E-03	2.084E+09	1.068E+09	11.46	0.12	0.26	1.60	
d18O_030524_91500@10	1.948E+00	2.028E-03	2.083E+09	1.070E+09	11.53	0.12		1.67	
d18O_030524_91500@11	1.944E+00	2.028E-03	2.079E+09	1.069E+09	11.41	0.12		1.55	
d18O_030524_91500@12	1.943E+00	2.028E-03	2.073E+09	1.067E+09	11.16	0.10		1.30	
d18O_030524_91500@13	1.937E+00	2.029E-03	2.071E+09	1.069E+09	12.02	0.13			
d18O_030524_91500@14	1.937E+00	2.028E-03	2.066E+09	1.067E+09	11.53	0.12		1.67	
d18O_030524_91500@15	1.936E+00	2.028E-03	2.073E+09	1.071E+09	11.48	0.12	0.36	1.62	

Sample #	Ipr (nA)	18O/16O	16O/Coeff						
		H'2/L'2	L'2	yield	d18Oraw	2se	2SD	IMF	**d18OVSMOW**
d18O_030524_THP03-01@1	1.934E+00	2.020E-03	1.999E+09	1.034E+09	7.56	0.18			**5.86**
d18O_030524_THP03-01@2	1.930E+00	2.023E-03	1.971E+09	1.021E+09	8.77	0.27			**7.08**
d18O_030524_THP03-02@1	1.930E+00	2.021E-03	1.996E+09	1.034E+09	8.10	0.21			**6.40**
d18O_030524_THP03-02@2	1.931E+00	2.028E-03	1.914E+09	9.913E+08	11.61	0.15			**9.91**
d18O_030524_THP03-03@1	1.930E+00	2.021E-03	2.006E+09	1.040E+09	8.04	0.23			**6.34**
d18O_030524_THP03-03@2	1.931E+00	2.020E-03	2.002E+09	1.037E+09	7.39	0.13			**5.69**
d18O_030524_THP03-04@1	1.927E+00	2.021E-03	1.995E+09	1.035E+09	7.94	0.21			**6.24**
d18O_030524_THP03-04@2	1.924E+00	2.024E-03	1.951E+09	1.014E+09	9.20	0.23			**7.50**
d18O_030524_THP03-05@1	1.924E+00	2.021E-03	2.005E+09	1.042E+09	7.66	0.19			**5.96**
d18O_030524_THP03-06@1	1.925E+00	2.019E-03	2.016E+09	1.047E+09	7.07	0.12			**5.38**
d18O_030524_THP03-06@2	1.927E+00	2.020E-03	2.006E+09	1.041E+09	7.22	0.17			**5.53**
d18O_030524_THP03-07@1	1.923E+00	2.024E-03	1.949E+09	1.013E+09	9.30	0.18			**7.60**
d18O_030524_THP03-08@1	1.920E+00	2.019E-03	2.005E+09	1.044E+09	7.11	0.13			**5.41**
d18O_030524_THP03-08@2	1.918E+00	2.022E-03	1.963E+09	1.024E+09	8.32	0.16			**6.63**
d18O_030524_THP03-09@1	1.917E+00	2.019E-03	2.016E+09	1.051E+09	7.06	0.10			**5.37**
d18O_030524_THP03-09@2	1.917E+00	2.021E-03	1.995E+09	1.041E+09	8.05	0.24			**6.36**
d18O_030524_91500@17	1.918E+00	2.029E-03	2.041E+09	1.064E+09	11.86	0.12		2.00	
d18O_030524_THP03-10@1	1.917E+00	2.021E-03	1.987E+09	1.037E+09	8.00	0.20			**6.30**
d18O_030524_THP03-10@2	1.919E+00	2.020E-03	1.990E+09	1.037E+09	7.21	0.13			**5.52**
d18O_030524_THP03-11@1	1.917E+00	2.022E-03	1.994E+09	1.040E+09	8.38	0.18			**6.68**
d18O_030524_THP03-11@2	1.919E+00	2.024E-03	1.957E+09	1.020E+09	9.16	0.14			**7.47**
d18O_030524_THP03-13@1	1.918E+00	2.019E-03	2.006E+09	1.045E+09	7.05	0.13			**5.35**
d18O_030524_NL03-01@1	1.917E+00	2.019E-03	2.013E+09	1.050E+09	7.07	0.12			**5.37**
d18O_030524_NL03-01@2	1.917E+00	2.024E-03	2.002E+09	1.044E+09	9.24	0.18			**7.55**
d18O_030524_NL03-02@1	1.916E+00	2.020E-03	1.986E+09	1.037E+09	7.44	0.17			**5.74**
d18O_030524_91500@18	1.917E+00	2.029E-03	2.046E+09	1.067E+09	11.84	0.12		1.98	
d18O_030524_NL03-03@1	1.918E+00	2.021E-03	1.987E+09	1.036E+09	7.78	0.13			**6.09**
d18O_030524_NL03-03@2	1.920E+00	2.020E-03	1.976E+09	1.029E+09	7.62	0.18			**5.92**
d18O_030524_NL03-04@1	1.918E+00	2.021E-03	1.993E+09	1.039E+09	7.74	0.17			**6.05**
d18O_030524_NL03-05@1	1.917E+00	2.017E-03	1.940E+09	1.012E+09	6.10	0.17			**4.40**
d18O_030524_NL03-05@2	1.914E+00	2.020E-03	1.993E+09	1.041E+09	7.56	0.16			**5.87**
d18O_030524_NL03-06@1	1.912E+00	2.020E-03	1.993E+09	1.042E+09	7.26	0.15			**5.56**
d18O_030524_NL03-06@2	1.911E+00	2.019E-03	2.004E+09	1.049E+09	7.09	0.11			**5.39**
d18O_030524_NL03-07@1	1.910E+00	2.023E-03	1.946E+09	1.019E+09	8.89	0.57			**7.20**
d18O_030524_91500@19	1.909E+00	2.028E-03	2.027E+09	1.062E+09	11.49	0.10		1.63	
d18O_030524_NL03-10@1	1.906E+00	2.020E-03	1.993E+09	1.045E+09	7.34	0.13			**5.64**
d18O_030524_NL03-10@2	1.904E+00	2.021E-03	1.972E+09	1.035E+09	7.71	0.14			**6.01**
d18O_030524_NL03-11@1	1.902E+00	2.020E-03	1.971E+09	1.036E+09	7.28	0.13			**5.58**
d18O_030524_NL03-12@1	1.903E+00	2.021E-03	1.964E+09	1.032E+09	8.10	0.18			**6.40**
d18O_030524_NL03-12@2	1.904E+00	2.020E-03	1.971E+09	1.035E+09	7.49	0.14			**5.80**
d18O_030524_NL03-15@1	1.903E+00	2.019E-03	1.983E+09	1.042E+09	7.06	0.13			**5.36**
d18O_030524_NL03-15@2	1.903E+00	2.019E-03	1.976E+09	1.039E+09	6.99	0.10			**5.29**
d18O_030524_NL03-17@1	1.902E+00	2.020E-03	1.986E+09	1.045E+09	7.16	0.11			**5.47**
d18O_030524_91500@20	1.901E+00	2.029E-03	2.003E+09	1.054E+09	11.73	0.10		1.87	
d18O_030524_NL03-17@2	1.900E+00	2.019E-03	1.886E+09	9.923E+08	6.75	0.17			**5.05**
d18O_030524_NL03-19@1	1.899E+00	2.022E-03	1.959E+09	1.031E+09	8.33	0.14			**6.63**
d18O_030524_NL03-20@1	1.897E+00	2.022E-03	1.953E+09	1.030E+09	8.38	0.24			**6.68**
d18O_030524_NL03-23@1	1.895E+00	2.022E-03	1.925E+09	1.016E+09	8.49	0.18			**6.79**
d18O_030524_NL03-24@1	1.897E+00	2.019E-03	1.960E+09	1.033E+09	6.93	0.13			**5.23**
d18O_030524_NL03-25@1	1.896E+00	2.020E-03	1.950E+09	1.028E+09	7.38	0.11			**5.68**
d18O_030524_NL03-26@1	1.895E+00	2.020E-03	1.950E+09	1.029E+09	7.55	0.10			**5.85**
d18O_030524_NL03-27@1	1.892E+00	2.019E-03	1.961E+09	1.036E+09	6.96	0.13			**5.27**
d18O_030524_91500@21	1.891E+00	2.029E-03	2.004E+09	1.060E+09	11.66	0.11		1.80	
d18O_030524_91500@24	1.876E+00	2.028E-03	2.010E+09	1.071E+09	11.37	0.16	0.70	1.51	
d18O_030524_NL04-01@1	1.875E+00	2.018E-03	1.935E+09	1.032E+09	6.53	0.11			**4.84**
d18O_030524_NL04-01@2	1.875E+00	2.022E-03	1.894E+09	1.010E+09	8.41	0.17			**6.72**
d18O_030524_NL04-02@1	1.874E+00	2.021E-03	1.944E+09	1.037E+09	7.66	0.11			**5.97**
d18O_030524_NL04-02@2	1.873E+00	2.020E-03	1.927E+09	1.029E+09	7.60	0.14			**5.90**
d18O_030524_NL04-03@1	1.870E+00	2.018E-03	1.937E+09	1.035E+09	6.58	0.10			**4.88**

Sample #	Ipr (nA)	18O/16O H'2/L'2	16O/Coeff L'2	yield	d18Oraw	2se	2SD	IMF	**d18OVSMOW**
d18O_030524_NL04-03@2	1.868E+00	2.019E-03	1.924E+09	1.030E+09	6.78	0.16			**5.08**
d18O_030524_NL04-04@1	1.868E+00	2.019E-03	1.941E+09	1.039E+09	6.83	0.13			**5.13**
d18O_030524_NL04-04@2	1.867E+00	2.018E-03	1.938E+09	1.038E+09	6.63	0.12			**4.94**
d18O_030524_NL04-05@1	1.865E+00	2.020E-03	1.943E+09	1.042E+09	7.54	0.12			**5.84**
d18O_030524_NL04-05@2	1.864E+00	2.020E-03	1.938E+09	1.040E+09	7.56	0.16			**5.87**
d18O_030524_91500@25	1.862E+00	2.028E-03	1.991E+09	1.069E+09	11.39	0.15		1.53	
d18O_030524_NL04-07@1	1.862E+00	2.021E-03	1.920E+09	1.031E+09	8.04	0.22			**6.35**
d18O_030524_NL04-07@2	1.861E+00	2.025E-03	1.937E+09	1.041E+09	9.68	0.30			**7.99**
d18O_030524_NL04-08@1	1.860E+00	2.019E-03	1.921E+09	1.033E+09	7.04	0.12			**5.34**
d18O_030524_NL04-08@2	1.856E+00	2.020E-03	1.936E+09	1.043E+09	7.41	0.16			**5.71**
d18O_030524_NL04-09@1	1.853E+00	2.020E-03	1.933E+09	1.043E+09	7.31	0.12			**5.61**
d18O_030524_NL04-10@1	1.852E+00	2.019E-03	1.923E+09	1.038E+09	7.02	0.14			**5.32**
d18O_030524_NL04-11@1	1.852E+00	2.019E-03	1.920E+09	1.037E+09	6.93	0.12			**5.24**
d18O_030524_NL04-11@2	1.852E+00	2.020E-03	1.917E+09	1.035E+09	7.14	0.15			**5.44**
d18O_030524_NL04-12@1	1.853E+00	2.020E-03	1.926E+09	1.040E+09	7.37	0.13			**5.68**
d18O_030524_NL04-13@1	1.852E+00	2.019E-03	1.954E+09	1.055E+09	7.09	0.10			**5.40**
d18O_030524_91500@26	1.849E+00	2.028E-03	1.978E+09	1.070E+09	11.38	0.11		1.52	
d18O_030524_NL04-13@2	1.848E+00	2.019E-03	1.944E+09	1.052E+09	6.80	0.12			**5.11**
d18O_030524_NL04-19@1	1.849E+00	2.020E-03	1.940E+09	1.049E+09	7.34	0.11			**5.64**
d18O_030524_NL04-19@2	1.847E+00	2.020E-03	1.933E+09	1.047E+09	7.36	0.13			**5.66**
d18O_030524_NL04-21@1	1.847E+00	2.020E-03	1.913E+09	1.036E+09	7.24	0.15			**5.54**
d18O_030524_NL04-21@2	1.845E+00	2.021E-03	1.912E+09	1.037E+09	7.92	0.13			**6.22**
d18O_030524_NL04-22@1	1.843E+00	2.020E-03	1.921E+09	1.043E+09	7.22	0.10			**5.53**
d18O_030524_NL04-22@2	1.840E+00	2.021E-03	1.905E+09	1.035E+09	7.79	0.15			**6.09**
d18O_030524_NL04-24@1	1.840E+00	2.019E-03	1.846E+09	1.003E+09	6.71	0.26			**5.01**
d18O_030524_NL02-02@1	1.839E+00	2.019E-03	1.931E+09	1.050E+09	6.90	0.11			**5.20**
d18O_030524_NL02-02@2	1.840E+00	2.019E-03	1.919E+09	1.043E+09	6.83	0.14			**5.13**
d18O_030524_91500@27	1.838E+00	2.028E-03	1.975E+09	1.075E+09	11.34	0.16		1.48	
d18O_030524_KV04-01@1	1.836E+00	2.020E-03	1.919E+09	1.046E+09	7.32	0.10			**5.63**
d18O_030524_KV04-01@2	1.835E+00	2.020E-03	1.902E+09	1.037E+09	7.19	0.10			**5.49**
d18O_030524_KV04-02@1	1.835E+00	2.020E-03	1.914E+09	1.043E+09	7.21	0.13			**5.51**
d18O_030524_KV04-02@2	1.836E+00	2.019E-03	1.917E+09	1.044E+09	6.95	0.12			**5.26**
d18O_030524_KV04-03@1	1.833E+00	2.019E-03	1.892E+09	1.032E+09	6.97	0.12			**5.27**
d18O_030524_KV04-03@2	1.831E+00	2.020E-03	1.902E+09	1.039E+09	7.19	0.11			**5.49**
d18O_030524_KV01-03@1	1.828E+00	2.020E-03	1.927E+09	1.054E+09	7.20	0.10			**5.50**
d18O_030524_KV01-04@1	1.829E+00	2.020E-03	1.928E+09	1.054E+09	7.31	0.14			**5.61**
d18O_030524_KV01-04@2	1.829E+00	2.021E-03	1.928E+09	1.054E+09	8.03	0.15			**6.33**
d18O_030524_KV01-05@1	1.829E+00	2.020E-03	1.931E+09	1.056E+09	7.33	0.11			**5.63**
d18O_030524_91500@28	1.827E+00	2.028E-03	1.967E+09	1.077E+09	11.27	0.11		1.41	
d18O_030524_KV01-05@2	1.823E+00	2.020E-03	1.919E+09	1.053E+09	7.60	0.10			**5.91**
d18O_030524_KV01-06@1	1.821E+00	2.020E-03	1.905E+09	1.046E+09	7.30	0.13			**5.60**
d18O_030524_KV01-06@2	1.822E+00	2.021E-03	1.942E+09	1.066E+09	7.69	0.45			**6.00**
d18O_030524_KV01-07@1	1.822E+00	2.020E-03	1.917E+09	1.052E+09	7.25	0.13			**5.55**
d18O_030524_KV01-07@2	1.821E+00	2.020E-03	1.916E+09	1.052E+09	7.21	0.11			**5.52**
d18O_030524_KV01-08@1	1.820E+00	2.020E-03	1.901E+09	1.044E+09	7.28	0.13			**5.58**
d18O_030524_KV01-10@1	1.819E+00	2.020E-03	1.918E+09	1.054E+09	7.48	0.15			**5.78**
d18O_030524_KV01-10@2	1.817E+00	2.020E-03	1.910E+09	1.051E+09	7.31	0.12			**5.62**
d18O_030524_KV01-11@1	1.817E+00	2.020E-03	1.910E+09	1.052E+09	7.25	0.12			**5.55**
d18O_030524_KV01-12@1	1.818E+00	2.020E-03	1.900E+09	1.045E+09	7.26	0.12			**5.56**
d18O_030524_91500@29	1.819E+00	2.028E-03	1.940E+09	1.066E+09	11.48	0.12		1.62	
d18O_030524_KV01-12@2	1.818E+00	2.020E-03	1.893E+09	1.041E+09	7.62	0.12			**5.92**
d18O_030524_91500@30	1.809E+00	2.030E-03	1.914E+09	1.058E+09	12.44	0.13			
d18O_030524_91500@31	1.810E+00	2.029E-03	1.912E+09	1.057E+09	11.76	0.10		1.90	
d18O_030524_91500@32	1.809E+00	2.029E-03	1.908E+09	1.054E+09	11.67	0.14	0.23	1.81	
d18O_030524_KV01-14@2	1.806E+00	2.019E-03	1.781E+09	9.859E+08	6.78	0.23			**5.06**
d18O_030524_KV01-16@1	1.804E+00	2.020E-03	1.885E+09	1.045E+09	7.27	0.10			**5.55**
d18O_030524_KV01-16@2	1.802E+00	2.020E-03	1.873E+09	1.039E+09	7.50	0.12			**5.79**
d18O_030524_KV01-24@1	1.802E+00	2.020E-03	1.874E+09	1.040E+09	7.57	0.11			**5.85**
d18O_030524_KV01-24@2	1.803E+00	2.020E-03	1.858E+09	1.031E+09	7.35	0.12			**5.63**

Sample #	Ipr (nA)	18O/16O H'2/L'2	16O/Coeff L'2	yield	d18Oraw	2se	2SD	IMF	**d18OVSMOW**
d18O_030524_KV03-01@1	1.801E+00	2.020E-03	1.894E+09	1.052E+09	7.46	0.11			**5.74**
d18O_030524_KV03-01@2	1.800E+00	2.019E-03	1.895E+09	1.053E+09	7.07	0.13			**5.36**
d18O_030524_91500@33	1.797E+00	2.028E-03	1.915E+09	1.065E+09	11.51	0.14		1.65	
d18O_030524_KV03-02@1	1.796E+00	2.020E-03	1.880E+09	1.047E+09	7.26	0.11			**5.54**
d18O_030524_KV03-02@2	1.798E+00	2.020E-03	1.880E+09	1.046E+09	7.28	0.11			**5.57**
d18O_030524_KV03-03@1	1.799E+00	2.020E-03	1.894E+09	1.053E+09	7.33	0.15			**5.62**
d18O_030524_KV03-03@2	1.798E+00	2.020E-03	1.903E+09	1.059E+09	7.33	0.12			**5.62**
d18O_030524_KV03-05@1	1.795E+00	2.020E-03	1.890E+09	1.053E+09	7.33	0.12			**5.62**
d18O_030524_KV03-05@2	1.793E+00	2.020E-03	1.896E+09	1.057E+09	7.38	0.12			**5.66**
d18O_030524_KV03-06@1	1.792E+00	2.020E-03	1.895E+09	1.057E+09	7.23	0.13			**5.51**
d18O_030524_KV03-06@2	1.794E+00	2.020E-03	1.900E+09	1.059E+09	7.37	0.10			**5.65**
d18O_030524_KV03-07@1	1.792E+00	2.020E-03	1.885E+09	1.052E+09	7.31	0.12			**5.59**
d18O_030524_KV03-08@1	1.789E+00	2.020E-03	1.887E+09	1.055E+09	7.33	0.12			**5.61**
d18O_030524_91500@34	1.788E+00	2.028E-03	1.900E+09	1.063E+09	11.57	0.10		1.71	
d18O_030524_KV03-09@1	1.788E+00	2.021E-03	1.861E+09	1.041E+09	8.06	0.22			**6.34**
d18O_030524_KV03-10@1	1.788E+00	2.019E-03	1.876E+09	1.049E+09	7.11	0.14			**5.39**
d18O_030524_KV03-11@1	1.786E+00	2.020E-03	1.865E+09	1.044E+09	7.32	0.10			**5.60**
d18O_030524_KV03-14@1	1.784E+00	2.020E-03	1.879E+09	1.053E+09	7.45	0.14			**5.73**
d18O_030524_KV03-14@2	1.782E+00	2.020E-03	1.862E+09	1.045E+09	7.13	0.14			**5.42**
d18O_030524_KV03-15@1	1.783E+00	2.019E-03	1.842E+09	1.033E+09	6.87	0.17			**5.15**
d18O_030524_KV03-16@1	1.782E+00	2.020E-03	1.874E+09	1.052E+09	7.38	0.13			**5.66**
d18O_030524_KV03-17@1	1.781E+00	2.020E-03	1.862E+09	1.046E+09	7.21	0.10			**5.50**
d18O_030524_KV03-17@2	1.777E+00	2.020E-03	1.862E+09	1.047E+09	7.20	0.12			**5.48**
d18O_030524_KV03-18@1	1.775E+00	2.019E-03	1.864E+09	1.050E+09	7.02	0.12			**5.30**
d18O_030524_91500@35	1.777E+00	2.028E-03	1.892E+09	1.065E+09	11.61	0.10		1.75	
d18O_030524_KV03-18@2	1.777E+00	2.021E-03	1.858E+09	1.045E+09	7.70	0.18			**5.98**
d18O_030524_KV03-21@1	1.777E+00	2.020E-03	1.863E+09	1.048E+09	7.46	0.10			**5.74**
d18O_030524_KV03-21@2	1.775E+00	2.020E-03	1.857E+09	1.046E+09	7.15	0.14			**5.44**
d18O_030524_SLZ01-01@1	1.773E+00	2.019E-03	1.848E+09	1.042E+09	6.81	0.20			**5.09**
d18O_030524_SLZ01-01@2	1.772E+00	2.019E-03	1.861E+09	1.050E+09	6.70	0.12			**4.98**
d18O_030524_SLZ01-02@1	1.772E+00	2.019E-03	1.866E+09	1.053E+09	6.85	0.12			**5.13**
d18O_030524_SLZ01-02@2	1.771E+00	2.017E-03	1.843E+09	1.041E+09	6.09	0.12			**4.37**
d18O_030524_SLZ01-03@1	1.770E+00	2.018E-03	1.850E+09	1.045E+09	6.50	0.14			**4.78**
d18O_030524_SLZ01-03@2	1.769E+00	2.018E-03	1.852E+09	1.047E+09	6.57	0.14			**4.85**
d18O_030524_SLZ01-05@1	1.766E+00	2.017E-03	1.870E+09	1.059E+09	6.10	0.13			**4.38**
d18O_030524_91500@36	1.767E+00	2.028E-03	1.872E+09	1.059E+09	11.45	0.13		1.59	
d18O_030524_SLZ01-05@2	1.768E+00	2.019E-03	1.858E+09	1.051E+09	6.67	0.16			**4.95**
d18O_030524_SLZ01-06@1	1.767E+00	2.018E-03	1.853E+09	1.049E+09	6.56	0.12			**4.84**
d18O_030524_SLZ01-06@2	1.765E+00	2.018E-03	1.853E+09	1.050E+09	6.23	0.10			**4.51**
d18O_030524_SLZ01-08@1	1.763E+00	2.018E-03	1.853E+09	1.051E+09	6.49	0.10			**4.77**
d18O_030524_SLZ01-08@2	1.762E+00	2.018E-03	1.855E+09	1.053E+09	6.52	0.13			**4.80**
d18O_030524_SLZ01-10@1	1.762E+00	2.011E-03	1.840E+09	1.044E+09	2.83	0.19			**1.12**
d18O_030524_SLZ01-14@1	1.761E+00	2.018E-03	1.839E+09	1.044E+09	6.38	0.15			**4.66**
d18O_030524_SLZ01-15@1	1.760E+00	2.018E-03	1.850E+09	1.051E+09	6.52	0.15			**4.80**
d18O_030524_SLZ01-15@2	1.757E+00	2.019E-03	1.839E+09	1.046E+09	6.86	0.11			**5.14**
d18O_030524_SLZ01-16@1	1.756E+00	2.019E-03	1.838E+09	1.047E+09	6.66	0.12			
d18O_030524_91500@37	1.756E+00	2.028E-03	1.861E+09	1.060E+09	11.46	0.14		1.60	
d18O_030524_SLZ01-16@2	1.757E+00	2.019E-03	1.833E+09	1.044E+09	6.85	0.14			**5.13**
d18O_030524_SLZ01-18@1	1.759E+00	2.018E-03	1.828E+09	1.039E+09	6.33	0.12			**4.61**
d18O_030524_SLZ01-18@2	1.757E+00	2.015E-03	1.844E+09	1.049E+09	5.07	0.14			**3.36**
d18O_030524_SLZ01-21@1	1.754E+00	2.017E-03	1.836E+09	1.047E+09	5.77	0.17			**4.05**
d18O_030524_SLZ01-21@2	1.752E+00	2.015E-03	1.825E+09	1.042E+09	5.02	0.16			**3.31**